

# Investigating the Physical, Chemical and Electronic Properties of Chromium Oxide Layers and Gold Clusters on Surfaces: Implications for Photocatalysis

By

Abdulrahman S Alotabi

Thesis
Submitted to Flinders University
for the degree of

**Doctor of Philosophy** 

College of Science and Engineering
November 2023

In the name of Allah, the Most Gracious, the Most Merciful

"... and say, My Lord, increase me in knowledge."

Al-Quran, Ta-Ha, 20:114

# **Table of Contents**

Table of Contents	i
Abstract	v
Declaration	vii
Acknowledgements	viii
List of Publications and Conference Presentations	X
List of Figures	xiii
List of Tables	xviii
Abbreviations	xix
Chapter 1: Introduction	1
1.1 Background	2
1.2 Basic Principles of One-step Overall Water Splitting on a Photocatalyst	3
1.3 Photocatalyst	6
1.3.1 Light-Harvesting of Photocatalysts	6
1.3.2 Band Gap Engineering – Doping	6
1.3.3 Photogenerated Charge Separation	7
1.3.3.1 Enhancement of Photogenerated Charge Separation	7
1.3.3.1.1 Particle Size and Morphology	7
1.3.3.1.2 Crystalline Phases and Junctions	8
1.3.3.1.3 Facet Control	8
1.4 Photocatalysts for water splitting	9
1.4.1 Titanium Dioxide	9
1.4.2 Strontium Titanate	10
1.5 Co-catalysts for photocatalytic water splitting	12
1.5.1 Gold Clusters as Co-catalysts	13
1.5.1.1 Characterization of Gold Clusters	14
1.5.1.1.1 Electron microscopy	14
1.5.1.1.2 Photoelectron spectroscopy	
1.5.1.1.2.1 X-ray Photoelectron Spectroscopy	17
1.5.1.1.2.2 Ultraviolet Photoelectron Spectroscopy	21
1.5.1.1.2.3 Metastable Impact Electron Spectroscopy	
1.5.1.1.3 X-ray Absorption Spectroscopy	
1.5.2 Challenges in Co-catalysts	
1.5.2.1 Back Reactions	
1.5.2.2 Stability of Co-catalyst	
1.6 Metal Oxide Layers for Photocatalytic Water Splitting	
1.6.1 Nickel Oxide Layer to Suppress Back Reactions	27

1.6	6.2 Chromium Oxide Layer to Suppress Back Reactions	27
1.6	6.3 Other Metal Oxide Layers	29
1.7	Applications of Metal Oxide Layers for Other Photocatalysis Reactions	34
1.8	Thesis Outline	36
1.9	References	37
Chapte	er 2: Experimental Techniques	52
2.1	X-ray Photoelectron Spectroscopy	53
2.2	Ultraviolet Photoelectron Spectroscopy	57
2.3	Near-Edge X-ray Absorption Fine Structure	58
2.4	X-ray Diffraction	58
2.5	Neutral Impact Collision Ion Scattering Spectroscopy	59
2.6	Scanning Electron Microscopy	61
2.7	Atomic Force Microscopy	61
2.8	Laser Scanning Confocal Microscope	62
2.9	Scanning Transmission Electron Microscopy	62
2.10	References	63
Chapte	0	) <sub>2</sub> upon
Annea		
3.1	Abstract	
3.2	Introduction	
3.3	Experimental	
	3.1 Material and sample preparation	
	3.2 Methods	
3.4	Results and Discussion	
	4.1 Room temperature studies	
3.4	4.2 Annealing studies	75
3.4	4.3 Surface morphology studies	80
3.5	Conclusions	
3.6	References	83
Chapte	,	
	CiO <sub>3</sub> Particles upon High-Temperature Annealing	
4.1	Abstract	
4.2	Introduction	
4.3	Experimental	
4.3	1 1	
	3.2 Methods	
4.4	Results and Discussion	
4.4		
4.4	4.2 Cr-oxide layer on P25, BLTO and Al:SrTiO <sub>3</sub> particles – after annealing	95

4.4	4.3	Change of surface electronic properties upon annealing	101
4.4.4		Change of bulk electronic properties upon annealing	
4.4.5		Photocatalytic water splitting	
		nclusions	109
4.6	Ref	erences	110
Chapto TiO2 F		Cr <sub>2</sub> O <sub>3</sub> Layer Inhibits Agglomeration of Phosphine-Protected Au <sub>9</sub> Cl <sub>1</sub> 115	usters on
5.1	Abs	stract	116
5.2	Intr	oduction	117
5.3	Exp	perimental	118
5.3	3.1	Material and sample preparation	118
5.3	3.2	Methods	119
5.4	Res	ults and Discussion	120
5.4	4.1	Thickness of the TiO <sub>2</sub> layer	120
5.4	4.2	Crystal structure of the TiO <sub>2</sub> P before and after heating	120
5.4	4.3	Topography of the TiO <sub>2</sub> layer	121
5.4	4.4	Agglomeration of Au <sub>9</sub> and influence of the Cr <sub>2</sub> O <sub>3</sub> layer	122
5.5	Cor	nclusions	128
5.6	Ref	erences	129
Chapte	er 6:	Effect of TiO <sub>2</sub> Film Thickness on the Stability of Au <sub>9</sub> Clusters with a Ci	rOx layer
6.1	Abs	stract	135
6.2	Intr	oduction	136
6.3	Exp	perimental	137
6.3	3.1	Material and sample preparation	137
6.3	3.2	Methods	138
6.4	Res	ults and Discussion	138
6.4	4.1	Influence of the thickness of the TiO <sub>2</sub> films	138
6.4	4.2	Au <sub>9</sub> clusters on TiO <sub>2</sub> P and TiO <sub>2</sub> G; a probe for mobility during heating	141
6.4	4.3	Effect of the TiO <sub>2</sub> film thickness	
6.5	Cor	nclusions	147
6.6	Ref	erences	148
Chapte Particl		Suppression of Phosphine-Protected Au <sub>9</sub> Clusters Agglomeration or ing a Chromium Hydroxide Layer	
7.1		stract	
7.2		oduction	
7.3		perimental	
	3.1	Material and sample preparation	
7 3	3 2	Methods	155

7.4	Re	sults and Discussion	156
7.	4.1	Before heating	156
7.	4.2	After heating	160
7.	4.3	After photocatalysis	163
7.5	Co	onclusions	166
7.6	Re	ferences	168
Chapt	er 8:	Conclusions and Future work	173
8.1	Co	onclusions	174
8.2	Fut	ture Works	176
8.3	Re	ferences	178
Appen	dices	S	180
		A: Investigation of the Diffusion of Cr <sub>2</sub> O <sub>3</sub> into Different Phase	-
		3: Reduction and Diffusion of Cr-oxide Layer into P25, BaLa <sub>4</sub> Ti <sub>4</sub> O pon High-Temperature Annealing	
		C: Cr <sub>2</sub> O <sub>3</sub> Layer Inhibits Agglomeration of Phosphine-Protected	
		D: Effect of TiO <sub>2</sub> Film Thickness on the Stability of Au <sub>9</sub> Clusters w	•
		E: Suppression of Phosphine-Protected Au <sub>9</sub> Clusters Agglomera	

#### **Abstract**

The scientific community is researching alternative renewable and clean energy sources to shift from fossil fuels. The conversion of solar energy into useful chemical energy such as hydrogen production via photocatalysis is a promising process to contribute to these alternatives, with much effort being focused on the development of photocatalysts for photocatalysis. The deposition of noble metal nanocluster co-catalysts can modify the properties and improve the efficiency of photocatalysts. The use of noble metal nanoclusters consisting of a few atoms as co-catalysts has attracted considerable attention due to their unique electronic and catalytic properties. However, it is challenging to maintain the cluster co-catalysts' size due to the clusters' tendency to agglomerate to form larger particles and lose their cluster-like properties. Another challenge that co-catalysts face is the back reactions of water splitting such as water formation from hydrogen and oxygen on the co-catalysts.

An overlayer of thin metal oxide on a co-catalyst-modified photocatalyst plays a critical role in photocatalysis reactions by stabilising the co-catalysts and suppressing the back reactions. This thesis makes an original contribution to our knowledge on the chromium oxide layer formed onto photocatalysts and gold cluster-modified photocatalysts by performing physical, chemical, electronic and catalytic studies on this layer.

The stability of the CrO<sub>x</sub> layer photodeposited onto different crystal phases of TiO<sub>2</sub> films and P25, BaLa<sub>4</sub>Ti<sub>4</sub>O<sub>15</sub> and Al:SrTiO<sub>3</sub> particles with subsequent annealing at temperatures up to 600 °C was investigated (Please note that the layer is labelled "CrO<sub>x</sub>" until the nature of the Cr component is confirmed (vide infra)). After annealing, for TiO<sub>2</sub> films, CrO<sub>x</sub> layer diffuses into the amorphous and anatase phases of TiO<sub>2</sub> film but remains stable at the surface of the rutile phase. Moreover, for particles, CrO<sub>x</sub> mostly diffuses into P25, while for BaLa<sub>4</sub>Ti<sub>4</sub>O<sub>15</sub>, the degree of CrO<sub>x</sub> diffusion is less than that into P25. Interestingly, the CrO<sub>x</sub> layer is very stable on the surface of Al:SrTiO<sub>3</sub> particles. This diffusion is attributed to the strong metal–support interaction effect between CrO<sub>x</sub> and different photocatalysts. Moreover, some of the CrO<sub>x</sub> was reduced to metallic Cr after annealing but there was no observation of the high oxidation state of Cr. The particles' bulk and surface band gap structures were also investigated, along with the photocatalytic water splitting activity.

For the first time, chemically synthesised phosphine-protected gold clusters, Au<sub>9</sub>(PPh<sub>3</sub>)<sub>8</sub>(NO<sub>3</sub>)<sub>3</sub>, deposited onto RF-sputter deposited TiO<sub>2</sub> film are prevented from agglomeration after the removal of ligands. This effect is achieved by photodepositing the CrO<sub>x</sub> layer on the top of the clusters as a protective layer. Further, the influence of heat treatment on the surface roughness of two different thicknesses of RF-sputter deposited TiO<sub>2</sub> films and the effect this has on size-specific Au<sub>9</sub> clusters

deposited on the surface was also investigated. It is found that the high mobility of the thick TiO<sub>2</sub> film after heating leads to a significant agglomeration of the Au<sub>9</sub> clusters, even when protected by the CrO<sub>x</sub> layer. However, the thin TiO<sub>2</sub> film has much lower mobility when heated, resulting in non-agglomerated clusters with CrO<sub>x</sub> coverage.

In the last part of this thesis, the stability of  $Au_9$  clusters beneath a  $Cr(OH)_3$  layer onto  $SrTiO_3$  particles under conditions of photocatalytic water splitting (i.e., UV irradiation) was investigated. After a photocatalytic water splitting reaction for seven hours,  $Au_9$  clusters without the  $CrO_x$  layer were found to agglomerate into large particles, while the application of the  $CrO_x$  layer resulted in the inhibition of the agglomeration of  $Au_9$  clusters.

# **Declaration**

I certify that this thesis:

1. does not incorporate without acknowledgment any material previously submitted for a degree or diploma in any university

2. and the research within will not be submitted for any other future degree or diploma without the permission of Flinders University; and

3. to the best of my knowledge and belief, does not contain any material previously published or written by another person except where due reference is made in the text.

Signed	 	
Date		

# **Acknowledgements**

My first and foremost acknowledgment goes to Allah Almighty for giving me strength, blessing, and guidance throughout this PhD journey. After that, I have to begin my acknowledgements with my family, without them I would not have been able to accomplish my goals. My sincere gratitude to my whole family, especially my mother Sarah Alotabi for their encouragement, tolerant and support. The gratitude and love I have for you is endless. Thank you!

I would like to acknowledge Albaha University and Saudi Arabian Cultural Mission in Australia (SACM) for the financial scholarship support.

I would like to express my deepest gratitude to my primary supervisor Professor Gunther Andersson for his unparalleled support and guidance throughout this candidature. Under his wonderful supervision, we have had a weekly progress meeting, which I have enjoyed every second of it. I have learned from him how to do research and be an independent scientific researcher. It has been a fantastic experience to discuss ideas together and develop them to be completed projects ending to form this thesis. This PhD would not finish without his help and support. Thank you so much! I also would like to express my deepest appreciation to Professor Gregory Metha from The University of Adelaide for his continuous encouragement and feedback throughout my PhD. He has given me an opportunity with full support to work in his laboratory during my PhD. His support for my academic advancement was incredible, thank so much Prof. Greg for your support, time and feedbacks!

I am also grateful to Prof. David Lewis, Prof. Sarah Harmer and Prof. Mats Andersson for attending my PhD milestones and providing me with discussions on the research and progression of my PhD candidature. Thank you so much for your feedback and support.

Many thanks to Professor Yuichi Negishi from Tokyo University of Science for having me in his laboratory during my PhD. Special thanks to Dr. Bruce Cowie from the Australian Synchrotron for his excellent support at the Soft X-ray spectroscopy beamline. He had putting much in the effort to train and discuss the measurements and results with us during the visit and after. Also, I would like to acknowledge Mr. Jesse Daughtry his assistance in preparing the TiO<sub>2</sub> films that were used in this thesis. My thanks are also extended to Prof. Kazunari Domen for providing us with Al:SrTiO<sub>3</sub> samples used in this thesis.

Words cannot express my gratitude to my friends and colleagues for their support during this journey. Special thanks to Andersson's group: Dr. Benjamin Chambers, Dr. Yanting Yin, Dr. Hassan Alqahtani, Dr. Altaf Shamsaldeen, Dr. Herri Trilaksana, Dr. Liam Howard-Fabretto, Dr. Jesse

Daughtry, Dr. Amira Alghamdi, Dr. Anand Kumar, Dr. Bradley Kirk, Gowri Krishnan, Ahlam Alharbi, Sunita Adhikari, Anahita Motamedisade, Alex Griesser, Abdulaziz Almutairi, Yahya Alfayfi and Zuhur Alotaibi. I want also to express my gratitude to all my colleagues outside Andersson's group, especially Salah Alboaiji, Fayed Alrashaidi and Thaar Alharbi. I wish you all the best and hope to collaborate with you in the future.

I want to express my gratitude in particular to those friends who have supported me outside of the academic community. Thank you all for your support! I cannot list all friends' names here, but I want to give a special thanks to Turki Alsaeed for his constant generous support during my PhD.

## **List of Publications and Conference Presentations**

#### Peer-reviewed Journals

- 1) **Alotabi, A. S.**; Gibson, C. T.; Metha, G. F.; & Andersson, G. G. (**2021**). Investigation of the Diffusion of Cr<sub>2</sub>O<sub>3</sub> into Different Phases of TiO<sub>2</sub> upon Annealing. *ACS Applied Energy Materials*, 4(1), 322-330.
- 2) **Alotabi, A. S.**; Yin, Y.; Redaa, A.; Tesana, S.; Metha, G. F.; & Andersson, G. G. (**2021**). Cr<sub>2</sub>O<sub>3</sub> layer inhibits agglomeration of phosphine-protected Au<sub>9</sub> clusters on TiO<sub>2</sub> films. *Journal of Chemical Physics*, 155(16), [164702].
- 3) **Alotabi, A. S.**; Osborn, D. J.; Ozaki, S.; Kataoka, Y.; Negishi, Y.; Tesana, S.; Metha, G. F.; & Andersson, G. G. (2022). Suppression of phosphine-protected Au<sub>9</sub> cluster agglomeration on SrTiO<sub>3</sub> particles using a chromium hydroxide layer. *Materials Advances*, 2(8), 3620-3630
- 4) Alotabi, A. S.; Yin, Y.; Redaa, A.; Tesana, S.; Metha, G. F.; & Andersson, G. G. (2022). Effect of TiO<sub>2</sub> Film Thickness on the Stability of Au<sub>9</sub> Clusters with a CrO<sub>x</sub> Layer. *Nanomaterials*, 12(18), [3218].
- 5) Alotabi, A. S.; Small, T. D.; Yin Y.; Osborn, D.; Ozaki, S.; Kataoka, Y.; Negishi, Y. Domen K.; Teranishi, T.; Metha, G. F.; & Andersson, G. G (2023). Reduction and Diffusion of Cr-oxide Layer into P25 Particles, BaLa<sub>4</sub>Ti<sub>4</sub>O<sub>15</sub> and Al:SrTiO<sub>3</sub> upon High-Temperature Annealing. *ACS Applied Materials & Interfaces* 15, 14990-15003.
- 6) **Alotabi, A. S.**; Adnan, R. H.; Almutairi, A.M., Kawawaki, T.; Negishi, Y. Domen K.; Metha, G. F.; & Andersson, G. G. Metal Overlayers in Photocatalytic Overall Water Splitting: A Comprehensive Review of their Role in Suppressing Back Reactions. This manuscript is close to submission at the time of thesis submission.
- 7) Daughtry, J.; **Alotabi, A. S.**; Howard-Fabretto, L.; & Andersson, G. G. (**2021**). Composition and properties of RF-sputter deposited titanium dioxide thin films. *Nanoscale Advances*, 3(4), 1077-1086.
- 8) Adnan, R. H.; Madridejos, J. M. L., **Alotabi, A. S.**, Metha, G. F., & Andersson, G. G. (2022). A Review of State of the Art in Phosphine Ligated Gold Clusters and Application in Catalysis. *Advanced Science*, 9(15), 2105692.

- 9) Kawawaki, T., Kataoka, Y., Hirata, M., Akinaga, Y., Takahata, R., Wakamatsu, K., Fujiki, Y., Kataoka, M., Kikkawa, S., **Alotabi, A. S.**, Hossain, S., Osborn, D. J., Teranishi, T., Andersson, G. G., Metha, G. F., Yamazoe, S., & Negishi, Y. (2021). Creation of High-Performance Heterogeneous Photocatalysts by Controlling Ligand Desorption and Particle Size of Gold Nanocluster. *Angewandte Chemie International Edition*, 60(39), 21340-21350.
- 10) Alharbi, T. M. D., Elmas, S., **Alotabi, A. S.**, Andersson, M. R., & Raston, C. L. (2022). Continuous Flow Fabrication of MoS<sub>2</sub> Scrolls for Electrocatalytic Hydrogen Evolution. *ACS Sustainable Chemistry and Engineering*, 10(29), 9325-9333.
- 11) Wang. Z., Qin, S., Chen, F., Chen, S., Liu, D., Jiang, D., Zhang, P., Mota-Santiago, P., Hegh, D., Lynch, P., **Alotabi, A. S.**, Andersson, G. G. Howlett, P.C., Weiwei Lei, F. W., & Razal, J. M. Interfacial Modification of Lithium Metal Anode by Boron Nitride Nanosheets. (Submitted). The manuscript submitted for review to the *ACS Nano* at the time of thesis submission.
- 12) Motamedisade. A., Heydari, A., Osborn, D., **Alotabi, A. S.**, & Andersson, G. G. Au<sub>9</sub> clusters deposited as Co-Catalysts on S-Modified Mesoporous TiO<sub>2</sub> for Photocatalytic Degradation of Methyl Orange. (Submitted). The manuscript submitted for review to the *Applied Surface Science* at the time of thesis submission.
- 13) Adhikari. S., Gascooke, J., **Alotabi, A. S.**, & Andersson, G. G. Anchoring Modes of Ru-based N719 dye onto Titania Substrates. (Submitted). The manuscript submitted for review to the *The Journal of Physical Chemistry C* at the time of thesis submission.
- 14) Alrashaidi F.A, Rahpeim, S., Luo. X, Vimalanathan, K., **Alotabi, A. S**., Alharbi, T. M. D, Chen, X., Chen, D., Tang, Y., Gibson, C., Darwish, N, Li, Q., & Raston, C. L. Vortex Mediated Fabrication of Antimonene From Antimony Powder. (Submitted). The manuscript submitted for review to the *Chemical Communications* at the time of thesis submission.
- 15) Rahim, I.H., Yin, L.X., **Alotabi, A. S.**, Osborn, D., Andersson, G. G., Metha, G. F., & Adnan, R. H. (Submitted). Photocatalytic H<sub>2</sub>O<sub>2</sub> Production Over Phosphine-protected Au<sub>101</sub> Nanoclusters on WO<sub>3</sub>. This manuscript is close to submission at the time of thesis submission.
- 16) Krishnan, G., **Alotabi, A. S.**, O'Donnell, S., Maggard, P.A., Metha, G. F., & Andersson, G. G. Study of the valence electronic structure of the Sn(II) perovskites using photoelectron spectroscopy. This manuscript is close to submission at the time of thesis submission.

#### **Conference Presentations**

- 1) The 12th Asian Photochemistry Conference in Melbourne, November-2023, Oral Presentation.
- 2) The 10th International Conference on Advanced Materials and Nanotechnology in Rotorua, February-2023, Poster Presentation.
- 3) The 24th Australian Institute of Physics Congress in Adelaide, December-2022, Oral Presentation.
- 4) The Institute for Nanoscale Science & Technology Annual Conference in Adelaide, June-2022, Poster Presentation.
- 5) Australian Nuclear Science and Technology Organisation User Meeting Conference in Melbourne, November-2021, Oral and Poster Presentation.
- 6) The Institute for Nanoscale Science & Technology 10th Conference in Adelaide, June-2021, Poster Presentation
- 7) Asia-Pacific Solar Research Conference, November-2020, Oral Presentation.
- 8) Seminar at Tokyo University of Science in Tokyo, December-2019, Oral Presentation.
- 9) The 3rd Annual College of Science and Engineering Higher Degree by Research (HDR) Conference in Adelaide, November-2019, Poster Presentation.
- 10) The Institute for Nanoscale Science & Technology 9th Conference in Adelaide, June-2019, Poster Presentation

# **List of Figures**

- **Figure 1.1:** Schematic diagram of natural and artificial photosynthesis methods. Reproduced from reference<sup>5</sup>.
- **Figure 1.2:** Schematic of solar water splitting using particulate photocatalyst. Reproduced from reference<sup>11</sup>.
- *Figure 1.3:* Examples of semiconductor band gaps with reduction and oxidation potentials. Modified from reference<sup>5</sup>.
- *Figure 1.4:* Mechanism of water splitting over a NiO/La-doped NaTaO<sub>3</sub> photocatalyst. Reproduced from reference <sup>25</sup> originally published by<sup>24</sup>.
- **Figure 1.5:** Example of phase junction between anatase and rutile phase  $TiO_2$  for promoting photogenerated charge separation. Reproduced from reference  $^{28}$ .
- **Figure 1.6:** SEM images of (a) BiVO<sub>4</sub>; (b) Au/BiVO<sub>4</sub>; (c) Pt/BiVO<sub>4</sub>; (d) Ag/BiVO<sub>4</sub>; (e) MnO<sub>x</sub>/BiVO<sub>4</sub> and (f) PbO<sub>2</sub>/BiVO<sub>4</sub>. Modified from reference <sup>29</sup>.
- **Figure 1.7:** The crystal structure of  $TiO_2$  phases, (a) rutile phase, (b) brookite phase and (c) anatase phase. Modified from reference  $^{33}$ .
- **Figure 1.8:** (a) Schematic of  $1 \times 1$  m water splitting panel based on Al-doped SrTiO<sub>3</sub> powder with RhCrO<sub>x</sub> co-catalyst (b) image of a  $1 \times 1$  m Al-doped SrTiO<sub>3</sub> panel. Reproduced from reference <sup>46</sup>.
- **Figure 1.9:** (A) Effect of cluster size on water splitting activity using  $Au_n$ -BaLa<sub>4</sub> $Ti_4O_{15}$  and AuNP-BaLa<sub>4</sub> $Ti_4O_{15}$ . (B) Schematic of the agglomeration of  $Au_n$  on the BaLa<sub>4</sub> $Ti_4O_{15}$  depending on the size of the cluster. Modified from references <sup>57, 66</sup>.
- **Figure 1.10:** (a-c) STEM-HAADF images of Au<sub>9</sub> supported on TiO<sub>2</sub> clusters with different structures. Reproduced from reference <sup>80</sup>. (d) Dynamic motion of Au<sub>9</sub> covalently bonded to the surface of graphene. Reproduced from reference <sup>81</sup>..
- **Figure 1.11:** Au 4f peaks of TPP-ligated  $Au_x$  (x=8,9,11,101) clusters on  $TiO_2$  (a) untreated and (b) calcined at 200 °C. Reproduced from reference<sup>98</sup>...
- **Figure 1.12:** Time-dependent a) XANES and b) EXAFS spectra, (c) coordination number, (d) bond distance R, and (e) Debye-Waller factor for the Au-P/Cl and Au-Au coordination pairs extracted from EXAFS curve-fitting against reaction time. Reproduced from reference<sup>147</sup>.
- **Figure 1.13:** Possible reactions that could occur during a photocatalytic water splitting reaction over a photocatalyst modified with co-catalysts: (a)  $H_2$  evolution, (b)  $O_2$  evolution, (c) water formation from  $H_2$  and  $O_2$  (back reaction), and (d) oxygen photoreduction reaction. Reproduced from reference<sup>151</sup>.
- **Figure 1.14:** Schematic illustration the  $NiO_x/SrTiO_3$  photocatalyst's structure after various treatments. Reproduced from reference<sup>150</sup>.

- **Figure 1.15:** a) HR-TEM images of Rh/Cr<sub>2</sub>O<sub>3</sub>-loaded(Ga<sub>1-x</sub>Zn<sub>x</sub>)(N<sub>1-x</sub>O<sub>x</sub>), b) schematic reaction mechanism and c) time courses of overall water splitting on Rh/Cr<sub>2</sub>O<sub>3</sub> loaded (Ga<sub>1-x</sub>Zn<sub>x</sub>)(N<sub>1-x</sub>O<sub>x</sub>). Modified from reference<sup>155</sup>.
- **Figure 1.16:** Schematic of the new procedure of forming a  $Cr_2O_3$  layer using SMSI effect with a HR-TEM image of  $Au_{25}$ - $Cr_2O_3$ - $BaLa_4Ti_4O_{15}$ . Modified from reference <sup>151</sup>.
- **Figure 2.1:** Principle of a photoemission spectrometer with examples of XP spectra for different metals . Reproduced with permission from Frank Muller  $^3$ .
- **Figure 2.2:** A schematic illustration of the normal and AR-XPS techniques. Modified from  $reference^{12}$ .
- Figure 2.3: A picture of the ultra-high vacuum instrument at Flinders University containing XPS, MIES, UPS, and IPES.
- Figure 2.4: Images of the soft X-ray beamline at the Australian Synchrotron, Melbourne.
- Figure 2.5: Schematic illustration of Bragg's law.
- Figure 2.6: an image of the NICISS instrument at Flinders University.
- *Figure 3.1:* AR-XPS relative intensities of Titanium and Chromium for the aTiO<sub>2</sub>-Cr<sub>2</sub>O<sub>3</sub> sample.
- **Figure 3.2:** (A) Cr L-edge NEXAFS spectra of chromium metal and  $Cr_2O_3$  reference samples. (B) Cr 2p XP spectrum of chromium metal reference sample. (C) Cr L-edge NEXAFS spectra of  $Cr_2O_3$ ,  $CrO_2$  and  $CrO_3$  from reference  $Cr_2O_3$  (D) Cr L-edge  $Cr_2O_3$  and  $Cr_2O_3$  reference for comparison. It should be noted that the reference spectra for  $Cr_2O_3$  in panel  $Cr_2O_3$  in panel  $Cr_2O_3$  and  $Cr_2O_3$  reference same.
- **Figure 3.3:** O K-edge NEXAFS spectra of (A) (i) anatase, (ii) rutile, (iii)  $Cr_2O_3$ , (iv)  $CrO_2$  and (v)  $CrO_3$  from reference <sup>30</sup> (Reprinted from reference <sup>30</sup> with permission from Elsevier) and (B)  $Cr_2O_3$ ,  $aTiO_2$  and  $aTiO_2$ - $Cr_2O_3$ .
- **Figure 3.4:** XPS relative amount of Cr 2p to Ti 2p of Cr2O3 photodeposited onto the different phases of TiO2 after annealing at various temperatures.
- **Figure 3.5:** XPS ratio intensity of  $Cr\ 2p$  to  $Ti\ 2p$  of  $aTiO_2$ - $Cr_2O_3$  and subsequently annealed to 600 °C. Then, the sample was sputtered for various times.
- **Figure 3.6:** NEXAFS spectra of Cr L-edge of aTiO<sub>2</sub>-Cr<sub>2</sub>O<sub>3</sub> before and after heating to 300°C and 600°C. (The intensity of the 600°C spectrum corresponds to the right hand axis, which has a smaller range.)
- **Figure 3.7:** NEXAFS spectra of O K-edge of aTiO<sub>2</sub>-Cr<sub>2</sub>O<sub>3</sub> before and after annealing to 300°C and 600°C.
- Figure 3.8: AFM images of (A)  $aTiO_2$  and (B)  $aTiO_2$  after the photodeposition of  $Cr_2O_3$  layer.
- **Figure 3.9:** NICISS results of the  $aTiO_2$ ,  $Cr_2O_3$  and  $aTiO_2$ - $CrO_x$  samples after annealing at  $200^{\circ}$ C under UHV for 10 min to remove water and hydrocarbon from the surface.

- **Figure 4.1**: STEM-EDX elemental mapping of Cr, Ti and O with line analysis of Ti and Cr for P25- $Cr_2O_3$ .
- **Figure 4.2**: STEM-EDX elemental mapping of Cr, Ba, La, Ti and O with line analysis of BLTO-Cr(OH)<sub>3</sub>.
- **Figure 4.3**: STEM-EDX elemental mapping of Cr, Al, Sr, Ti and O with line analysis of Al: $SrTiO_3$ - $Cr_2O_3$ .
- **Figure 4.4**: Cr L-edge NEXAFS spectra of (a)  $Cr_2O_3$  and  $Cr(OH)_3$  reference samples (b) Cr-oxide photodeposited onto P25, BLTO and Al:SrTiO<sub>3</sub>. Cr 2p XP spectra of (c) P25-Cr<sub>2</sub>O<sub>3</sub> (d) BLTO-Cr(OH)<sub>3</sub> and (e) AlSrTiO<sub>3</sub>-Cr<sub>2</sub>O<sub>3</sub>.
- **Figure 4.5**: XPS relative intensity ratio of Cr 2p to Ti 2p of (a) P25-Cr<sub>2</sub>O<sub>3</sub>, (b) BLTO-Cr(OH)<sub>3</sub> and (c) Al:SrTiO<sub>3</sub>-Cr<sub>2</sub>O<sub>3</sub> annealed at various temperatures.
- **Figure 4.6**: (a) Cr L-edge NEXAFS spectra of P25-Cr<sub>2</sub>O<sub>3</sub>, BLTO-Cr<sub>2</sub>O<sub>3</sub> and Al:SrTiO<sub>3</sub>-Cr<sub>2</sub>O<sub>3</sub> after annealing at 600°C with Cr<sub>2</sub>O<sub>3</sub> reference spectrum. Cr 2p XP spectrum of (b) P25-Cr<sub>2</sub>O<sub>3</sub> (c) BLTO-Cr<sub>2</sub>O<sub>3</sub> and (d) AlSrTiO<sub>3</sub>-Cr<sub>2</sub>O<sub>3</sub> after annealing at 600°C.
- **Figure 4.7**: STEM-EDX elemental mapping of Cr, Ti and O with line analysis of Cr and Ti for P25- $Cr_2O_3$  after annealing at 600°C.
- **Figure 4.8**: STEM-EDX elemental mapping of Cr, Ba, La, Ti, and O with line analysis of Cr and Ti for BLTO-Cr<sub>2</sub>O<sub>3</sub> after annealing at 600°C.
- **Figure 4.9**: STEM-EDX elemental mapping and line analysis of Cr, Al, Sr, Ti and O for Al: $SrTiO_3$ - $Cr_2O_3$  after annealing at  $600^{\circ}C$ .
- **Figure 4.10**: The valence band and conduction band regions from UPS and IPES spectra of (a) P25,  $Cr_2O_3$ ,  $P25-Cr_2O_3$  and  $P25-Cr_2O_3$  after annealing at 600°C, (b) BLTO,  $Cr_2O_3$ , BLTO- $Cr_2O_3$  and BLTO- $Cr_2O_3$  after annealing at 600°C and (c) Al:SrTiO<sub>3</sub>,  $Cr_2O_3$ , Al:SrTiO<sub>3</sub>- $Cr_2O_3$  and Al:SrTiO<sub>3</sub>- $Cr_2O_3$  after annealing at 600°C with the cut-offs of valence band and conduction band.
- **Figure 4.11**: UPS reference spectra and weighting factors identified via SVD of (a,b) P25-Cr<sub>2</sub>O<sub>3</sub> after annealing at various temperatures (c,d) BLTO-Cr<sub>2</sub>O<sub>3</sub> after annealing at various temperatures (e,f) Al:SrTiO<sub>3</sub>-Cr<sub>2</sub>O<sub>3</sub> after annealing at various temperatures
- **Figure 4.12:** Kubelka-Munk Transformed UV-visible DRS spectra of (**a**) P25, P25-Cr<sub>2</sub>O<sub>3</sub> and P25-Cr<sub>2</sub>O<sub>3</sub> after annealing at 600°C, (**b**) BLTO, BLTO-Cr(OH)<sub>3</sub> and BLTO-Cr<sub>2</sub>O<sub>3</sub> after annealing at 600°C and (**c**) Al:SrTiO<sub>3</sub>, Al:SrTiO<sub>3</sub>-Cr<sub>2</sub>O<sub>3</sub> and Al:SrTiO<sub>3</sub>-Cr<sub>2</sub>O<sub>3</sub> after annealing at 600°C.
- **Figure 4.13**: The surface and bulk band gaps of  $Cr_2O_3$ , and  $(P25, BLTO, and Al:SrTiO_3)$  after the photodeposition of Cr-oxide layer and after annealing at  $600^{\circ}C$ .
- Figure 5.1: Cross-sectional SEM image of the  $TiO_2P$ . Arrows indicate the thickness of the  $TiO_2$  layer.
- **Figure 5.2:** XRD patterns of Si wafer,  $TiO_2P$  and  $TiO_2P$  after heating to 200 °C. The positions for diffraction peaks for anatase, rutile and brookite as well as Si are indicated.

- **Figure 5.3:** Synchrotron Au 4f XP spectra of the sample immersed into the 0.006 mM solution: **(A)**  $TiO_2P$ - $Au_9$  before heating, **(B)**  $TiO_2P$ - $Au_9$  after heating, **(C)**  $TiO_2P$ - $Au_9$ - $Cr_2O_3$  before heating and **(D)**  $TiO_2P$ - $Au_9$ - $Cr_2O_3$  after heating.
- **Figure 5.4:** Synchrotron Au 4f XP spectra of the sample immersed into the 0.6 mM solution: **(A)**  $TiO_2P$ -Au<sub>9</sub> before heating, **(B)**  $TiO_2P$ -Au<sub>9</sub> after heating, **(C)**  $TiO_2P$ -Au<sub>9</sub>-Cr<sub>2</sub>O<sub>3</sub> after heating.
- **Figure 5.5:** Summary of synchrotron XPS results of  $TiO_2P$ - $Au_9$  before and after heating of (A) Au  $4f_{7/2}$  peak positions and (B) relative HBP & LBP intensities, and  $TiO_2P$ - $Au_9$  after photodeposition of the  $Cr_2O_3$  layer and after heating with (C) position of  $Au 4f_{7/2}$  and (D) relative HBP & LBP intensities.
- **Figure 6.1:** Cross-section SEM images of the (A)  $TiO_2P^{26}$  and (B)  $TiO_2G$  layer.
- **Figure 6.2:** XRD patterns of the Si wafer, TiO<sub>2</sub>P, TiO<sub>2</sub>P after heating, TiO<sub>2</sub>G and TiO<sub>2</sub>G after heating to 200 °C. The positions of the diffraction peaks for anatase, rutile and brookite, as well as Si, are indicated using the standard XRD patterns (anatase PDF 01-075-1537, rutile PDF 01-071-4809, brookite PDF 04-007-0758 and Si PDF 00-013-0542).
- **Figure 6.3:** Surface morphology with the Ra and Rq values of (A)TiO<sub>2</sub>P before heating and (B) TiO<sub>2</sub>P after heating, (C)TiO<sub>2</sub>G before heating and (D) TiO<sub>2</sub>G after heating (area 16 x 16  $\mu$ m). Note that the scale bars are different.
- **Figure 6.4:** XPS results of  $TiO_2P$ - $Au_9$  for three different  $Au_9$  concentrations: (**A**) position of Au  $4f_{7/2}$  and (**B**) relative intensity of Au before and after heating.  $TiO_2P$ - $Au_9$ - $CrO_x$  (**C**) position of Au  $4f_{7/2}$  and (**D**) relative intensity of Au before and after photodeposition of  $CrO_x$  layer and after heating. Note that the vertical scales of (**B**,**D**) are different and that the samples in (**A**,**C**) are different but are prepared in the same manner.
- **Figure 6.5:** XPS results of Au<sub>9</sub> deposited on TiO<sub>2</sub>G for three different Au<sub>9</sub> concentrations: (A) position of Au  $4f_{7/2}$  and (B) relative intensity of Au before and after heating. TiO<sub>2</sub>G-Au<sub>9</sub> with CrO<sub>x</sub> layer: (C) position of Au  $4f_{7/2}$  and (D) relative intensity of Au before and after photodeposition of CrO<sub>x</sub> layer and after heating. Note that vertical scales of (B,D) are different and that the samples in (A,C) are different but are prepared in the same manner.
- **Figure 7.1:** XPS spectra of Au 4f of (A) Au<sub>9</sub> deposited on  $SrTiO_3$  and (B)  $SrTiO_3$ -Au<sub>9</sub> after photodeposition of a  $CrO_x$  layer.
- *Figure 7.2:* XPS Cr 2p spectrum of  $SrTiO_3$ -Au<sub>9</sub> after photodeposition of a  $CrO_x$  layer.
- **Figure 7.3:** (A) HAADF-STEM image with EDX elemental mapping of (B) Au and (C) Ti in  $SrTiO_3$ -Au<sub>9</sub> before heating and (D) line analyses of the Au signal.
- **Figure 7.4:** HAADF-STEM image with EDX elemental mapping and line analyses of the Cr, Au and Ti in SrTiO<sub>3</sub>-Au<sub>9</sub>-Cr(OH)<sub>3</sub>.
- Figure 7.5: XPS spectra of Au 4f after heating of (A) SrTiO<sub>3</sub>-Au<sub>9</sub> and (B) SrTiO<sub>3</sub>-Au<sub>9</sub>-CrO<sub>x</sub>.

- **Figure 7.6:** XPS spectra of  $Cr\ 2p$  of  $SrTiO_3$ - $Au_9$ - $Cr(OH)_3$  before heating and  $SrTiO_3$ - $Au_9$ - $CrO_x$  after heating with reference spectrum of  $Cr_2O_3$  and  $Cr(OH)_3$  (Figure E4 shows complete fitting to all components).
- **Figure 7.7:** H<sub>2</sub> evolution by overall photocatalytic water splitting of SrTiO<sub>3</sub>, SrTiO<sub>3</sub>-Au<sub>9</sub> and SrTiO<sub>3</sub>-Au<sub>9</sub>-Cr<sub>2</sub>O<sub>3</sub> (i.e. after heating to remove the ligands).
- Figure 7.8: XPS spectra of Au 4f after 7 h irradiation of (A) SrTiO<sub>3</sub>-Au<sub>9</sub> and (B) SrTiO<sub>3</sub>-Au<sub>9</sub>-CrO<sub>x</sub>.
- **Figure 7.9:** XPS spectra of Cr 2p of  $SrTiO_3$ - $Au_9$ - $Cr(OH)_3$  before heating,  $SrTiO_3$ - $Au_9$ - $Cr_2O_3$  after heating and  $SrTiO_3$ - $Au_9$ -CrOx after 7 h irradiation with reference spectrum of  $Cr_2O_3$  and  $Cr(OH)_3$  (Figure E7 shows complete fitting to all components).
- **Figure 7.10:** (A) HAADF-STEM image with EDX elemental mapping of (B) Au and (C) Ti in  $SrTiO_3$ -Au<sub>9</sub> after 7 h irradiation and (D) line analyses of the Au signal.
- Figure 7.11: (A) HAADF-STEM image with EDX elemental mapping of (B) Au, (C) Ti. Au and Cr, (D) Ti and (E) Cr in SrTiO<sub>3</sub>-Au<sub>9</sub>-Cr(OH)<sub>3</sub> after 7 h irradiation and (F) line analyses of the Au signal.

# **List of Tables**

- **Table 1.1:** Photocatalytic water splitting performance of 18-facet  $SrTiO_3$  nanocrystals with Pt and  $Co_3O_4$  co-catalysts deposited. Modified from reference  $^{51}$ .
- **Table 1.2:** BE of Au 4f<sub>7/2</sub> for different gold compounds and several gold-phosphine clusters reported up-to-date
- **Table 1.3:** One-step-excitation overall water splitting using overlayer to block the back reaction up to date
- **Table 1.4:** Overlayer procedure used with other photocatalytic reactions to block the back reaction (contact of  $O_2$  to co-catalyst).
- **Table 2.1:** Atomic sensitivity factors for X-ray source at  $54.7^{\circ}$  of elements were measured in this study.
- **Table 4.1:** Summary of the effect of annealing  $Cr_2O_3$  layer on various forms of  $TiO_2$ .
- **Table 5.1:** The average of Ra and Rq values of  $TiO_2P$  before and after heating.

# **Abbreviations**

Abbreviations		
AFM	Atomic force microscopy	
ALD	Atomic layer deposition	
AMMRF	Australian microscopy and microanalysis research facility	
ANFF	Australian national fabrication facility	
AQE	Apparent quantum efficiency	
AQY	Apparent quantum yield	
AR-XPS	Angle-resolved X-ray photoelectron spectroscopy	
BE	Binding energy	
BLTO	BaLa <sub>4</sub> Ti <sub>4</sub> O <sub>15</sub>	
EDAX	Energy-dispersive X-ray spectroscopy	
EXAFS	Extended X-ray absorption fine structure	
FWHM	Full width at half maximum	
HAADF	High-angle annular dark-field	
НВР	High binding peak	
HSA	Hemispherical analyser	
IPES	Inverse photoelectron spectroscopy	
LBP	Low binding peak	
LSCM	Laser scanning confocal microscope	
MIES	Metastable impact electron spectroscopy	
NC	Nanoclusters	
NEXAFS	Near-edge X-ray absorption fine structure	
NICISS	Neutral impact collision ion scattering spectroscopy	
NP	Nanoparticle	
ORR	Oxygen photoreduction reaction	
PPh <sub>3</sub>	Triphenylphosphine	
Ra	Arithmetic mean deviation	
RF	Radio frequency	
RF-TiO <sub>2</sub>	Radio frequency-sputter deposited titania	
Rq	Root mean square deviation	
SEM	Scanning electron spectroscopy	
SMSI	Strong metal–support interaction	

STEM	Scanning transmission electron microscopy
STH	Solar-to-hydrogen
SVD	Single value decomposition
Synchrotron XPS	Synchrotron X-ray photoelectron spectroscopy
TEM	Transmission electron microscopy
UHV	Ultra-high vacuum
UPS	Ultraviolet photoelectron spectroscopy
UV	Ultraviolet
XANES	X-ray absorption near edge structure
XAS	X-ray absorption spectroscopy
XPS	X-ray photoelectron spectroscopy
XRD	X-ray diffraction

# **Chapter 1:** Introduction

The "Characterisation of Gold Clusters" Section in this chapter is a reformatted version of the review with title of "A Review of State of the Art in Phosphine Ligated Gold Clusters and Application in Catalysis" published in *Advanced Science*, 2022, Vol. 9, Issue 15, Page 2105692. **DOI**: 10.1002/advs.202105692. Title.

# 1.1 Background

The world's population is growing continuously. Meanwhile, global energy consumption is anticipated to rise due to the increasing population <sup>1</sup>. Fossil fuels are currently used to generate energy worldwide. However, fossil fuel resources are limited and expected to be depleted with consumption growth <sup>1</sup>. Moreover, in the last few years, the planet has been experiencing the hottest temperatures on record due to the extensive use of fossil fuels, polluting the environment through liberated harmful gases <sup>2</sup>. This raises the demand to provide renewable, clean and environmental energy sources to replace fossil fuels.

Solar energy is one of the most intriguing renewable energy sources<sup>3</sup>. Energy harvested from the sun provides a promising path to meet global demands for clean renewable energy while reducing the impact on the environment. It is on human time scales an inexhaustible source of energy, abundant and widely distributed, which has an energy share to the earth of  $3\times10^{24}$  j year<sup>-1</sup> <sup>4</sup>. However, solar irradiation is not available the whole day on the earth, which is the intermittent nature of sunlight. Therefore, it is necessary to find ways to convert sunlight into fuels (or battery) that are easy to store and transport safely, and usable upon demand.

Photosynthesis is a natural method of generating fuels using solar energy from water and carbon dioxide in plants (Figure 1.1)<sup>5</sup>. This has motivated scientists to develop an artificial photosynthesis method to produce chemical fuel with photocatalyst utilising solar energy. Converting solar energy into chemical energy provides a beneficial way to efficiently store solar energy as sustainable energy carriers while minimising the environment's impact. One potential solar fuel from artificial photosynthesis is hydrogen, which is environmentally friendly and efficient energy that should be a substitute for fossil fuels<sup>6, 7</sup>. Hydrogen is one of the elements with the highest abundance in the universe. However, usually, hydrogen found on earth is in covalent bonds with others element as compounds, for example, water and hydrocarbons<sup>6</sup>. Water is the major resource of hydrogen, as the most available source in the earth. Combination of solar energy, water and an efficient photocatalyst can be a platform for hydrogen production using artificial photosynthesis process for photocatalytic water splitting to  $H_2$  and  $O_2$ <sup>5</sup>.

Honda and Fujishima were the first to use titanium oxide (TiO<sub>2</sub>) to split water into H<sub>2</sub> and O<sub>2</sub>.<sup>8</sup>. Since then, various research has been commenced to study how to employ semiconductor materials for photocatalytic water splitting<sup>9, 10</sup>. The investigations are focused on enhancing the performance of photocatalyst to produce hydrogen. Very recently, the highest solar-to-hydrogen (STH) efficiency of about 9.2% for the photocatalytic water splitting reaction was reported in 2023 using InGaN/GaN

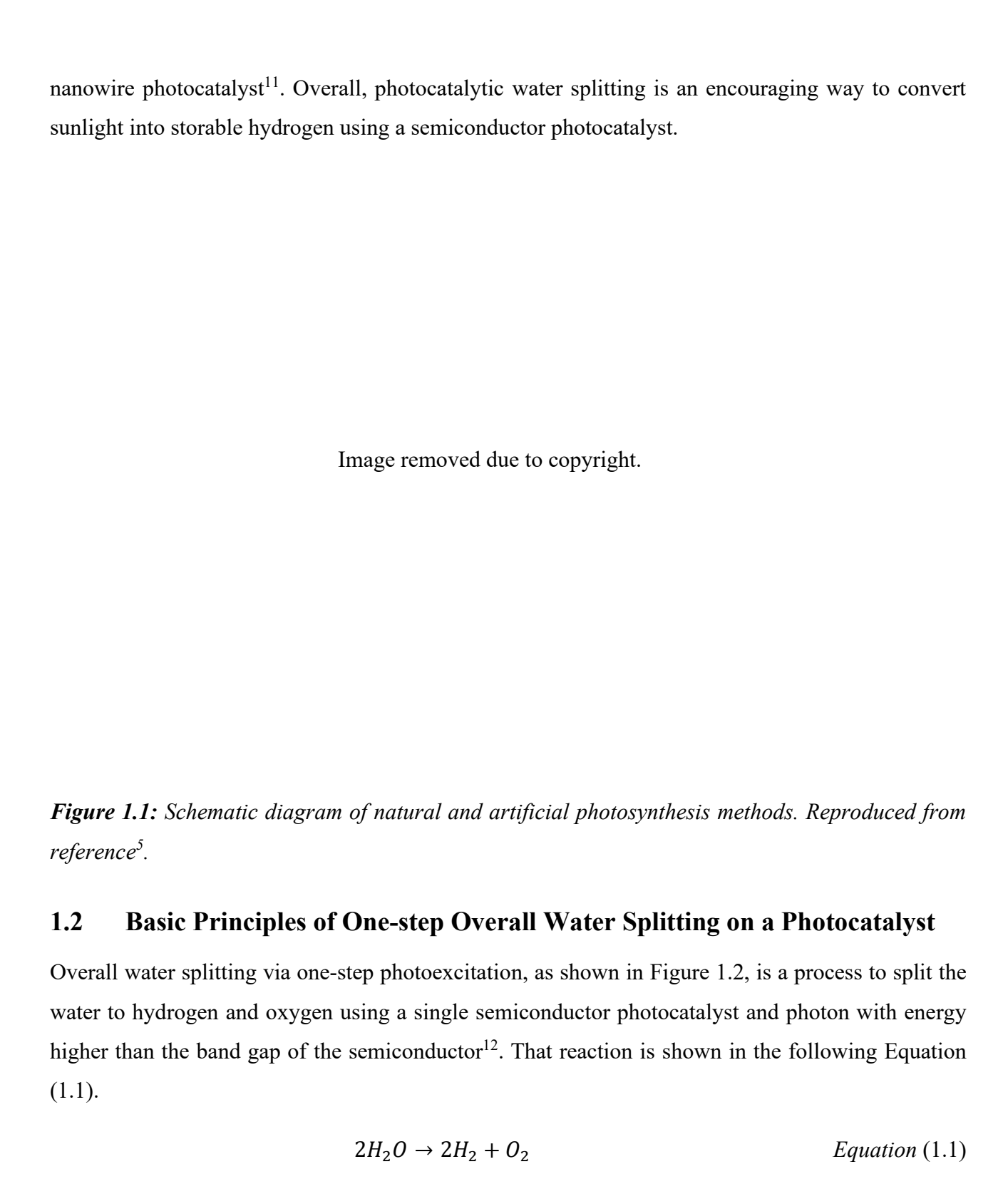


Image removed due to copyright.

Figure 1.2: Schematic of solar water splitting using particulate photocatalyst. Reproduced from  $reference^{12}$ .

The photocatalytic water splitting reaction involves three main steps as shown in Figure  $1.2^{12}$ . The first step is that the semiconductor absorbs photons with sufficient energy to overcome the band gap. This photon will excite an electron from the valence band to the conduction band, leaving a hole in the valence region. The generation mechanism of the electron-hole pair is continuous during irradiation. The second step is that the electrons and holes generated are separated and transferred to the photocatalyst surface. The third step is that  $H_2O$  is reduced by electron emission at the reduction side and oxidised by a hole at the oxidation side. Both sides are reckoned as the active surface side of the photocatalyst, which generates hydrogen and oxygen gas in the process, as shown in equations 1.2 and 1.3.

Hydrogen evolution reaction: 
$$4H^+ + 4e^- \rightarrow 2H_2$$
 Equation (1.2)

Oxygen evolution reaction: 
$$2H_2O + 4h^+ \rightarrow 4H^+ + O_2$$
 Equation (1.3)

The decomposition of H<sub>2</sub>O has a Gibbs free energy of 237.13 kJ/mol which equal to 1.23 eV photon energy required to drive water splitting<sup>12, 13</sup>. The photon energy, *E*, calculated using the Planck equation:

$$E = hv = \frac{hc}{\lambda}$$
 Equation (1.4)

Where h is Planck's constant, c is the speed of the light,  $\lambda$  is the wavelength, and v is the frequency of the photon. The water splitting reaction depends on the potential redox requirements of the reaction, wherein the conduction band of the semiconductor must be more negative than the reduction

potential of  $H^+/H_2$  energy level (0 V versus NHE, at pH = 0), whereas the valence band must be more positive than the oxidation potential of  $O_2/H_2O$  energy level (1.23 V versus NHE, at pH = 0), as shown in Figure 1.3, examples of semiconductor band gaps with reduction and oxidation potentials<sup>5</sup>. Thus, the bandgap of semiconductor should be greater than 1.23 eV with reduction and oxidation potential requirements to carry out photocatalytic water splitting. However, using sacrificial agents, only hydrogen evolution or oxygen evolution reactions can be occurred to generate hydrogen or oxygen in photocatalytic water splitting system.

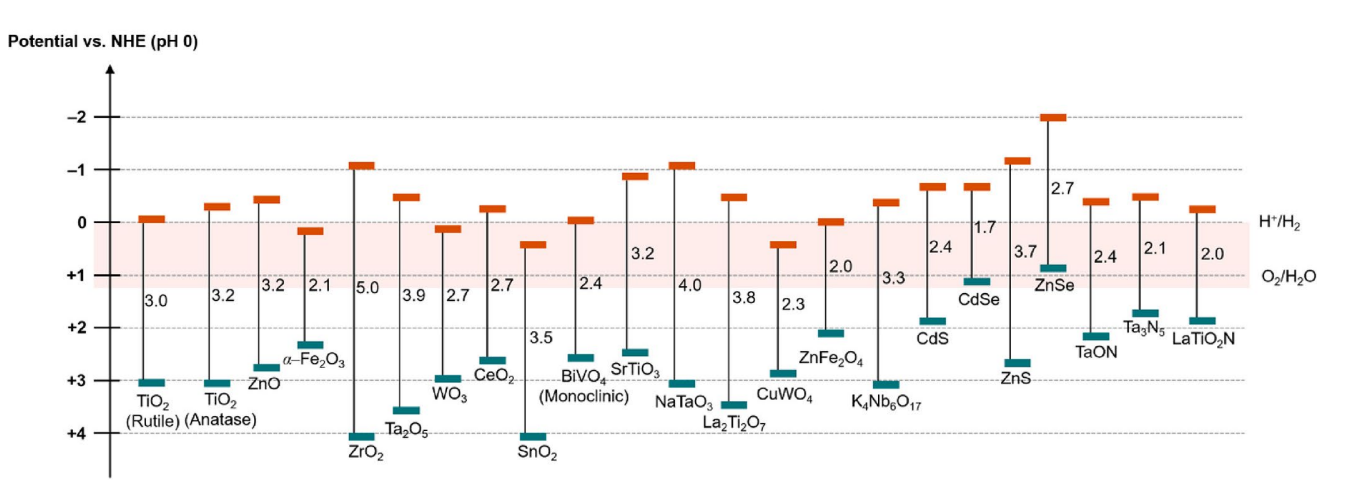


**Figure 1.3:** Examples of semiconductor band gaps with reduction and oxidation potentials. Modified from reference<sup>5</sup>.

The photocatalyst activities are usually reported as H<sub>2</sub> and O<sub>2</sub> evolution rates in photocatalytic water splitting using various irradiation sources. However, it is very complex to directly compare the H<sub>2</sub> and O<sub>2</sub> evolution rates of photocatalysts using different light sources and different photocatalytic reactors. Therefore, to compare the performance of different photocatalysts, more precise standards are required. The efficiency of the photocatalytic water splitting can be measured using the quantum yield (QY) (or quantum efficiency (QE)) and STH conversion efficiency<sup>14</sup>. QY, defined as the number of photons contributing to activity of the photocatalytic to the total number of absorbed photons. However, determining the number of photons absorbed by the particulate photocatalyst is impossible due to light transmission and scattering. Hence, the apparent quantum yield (AQY), or apparent quantum efficiency (AQE), is used, which is the ratio of the photoreaction rate measured in a specific time interval divided by the to the rate of incident photons during the same time interval at a specified wavelength. <sup>14-16</sup>. The AQY is shown in Equation (1.5):

$$AQY (hv) = \frac{nR}{I} \times 100\%$$
 Equation (1.5)

n is the number of electrons or holes involved in the photocatalytic reaction, R is the amount of molecular gas produced in a specific time, and I is the number of incident photons during the same

time interval <sup>10</sup>. The STH energy conversion efficiency is the practical standard to investigate the performance of photocatalysts, which can be determined from the following Equation (1.6):

$$STH = \frac{\text{output energy as } H_2}{\text{energy of incident solar light}} = \frac{R \times \Delta G}{P_{Sun} \times S} \times 100\%$$
 Equation (1.6)

Where R is the H<sub>2</sub> production rate during the water splitting reaction (mmol/s),  $\Delta G$  is the increase in the Gibbs free energy (kJ/mol),  $P_{sun}$  is the energy flux of sunlight at the ASTM-G173 AM 1.5 global tilt (100 mW cm<sup>2</sup>) and S is the area of the irradiated photocatalyst (cm<sup>2</sup>)<sup>14</sup>.

The AQY and STH of photocatalysts are being improved by studying and developing new photocatalysts modified with co-catalysts and metal oxide overlayers, which will be explained in the following sections.

## 1.3 Photocatalyst

#### 1.3.1 Light-Harvesting of Photocatalysts

Semiconductor photocatalysts are one of the most attractive areas of research currently<sup>17</sup>. The progress of different photocatalysts can be summarised in three periods, known as 'generations' 18. From about 1972 to 1980, the first generation focused on understanding the semiconductor-liquid interface under irradiation using monocrystalline semiconductor surfaces and investigating different types of semiconductors. In this period, the first use of the TiO<sub>2</sub> to decompose water into O<sub>2</sub> and H<sub>2</sub> in photoelectrochemical water splitting was reported<sup>8</sup>. Also, a preliminary study to demonstrate the photocatalytic water splitting process using TiO<sub>2</sub> and various titanates was reported during the same period<sup>12</sup>. From about 1980 to 2000, the second generation focused on polycrystalline semiconductors and modifying the semiconductors to perform photocatalytic water splitting under UV light<sup>12</sup>. From about 2000 to date, the third generation focused on nanotechnology in photocatalysis. Active semiconductors in photocatalytic water splitting have been developed and classified into two groups based on their electronic configuration: transition metal cations with d<sup>0</sup> electronic configurations (such as Ti<sup>4+</sup>, Zr<sup>4+</sup>, Nb<sup>5+</sup> and Ta<sup>5+</sup>) and typical metal cations with d<sup>10</sup> electronic configurations (such as Ga<sup>3+</sup>, In<sup>3+</sup>, Ge<sup>4+</sup> and Sn<sup>4+</sup>)<sup>12, 19</sup>. The light absorption has to be extended to the visible range to harness more sunlight for these semiconductors. Therefore, band engineering by adding foreign elements to d<sup>0</sup>-type or d<sup>10</sup>-type oxides can enhance the visible light absorption of metal oxide photocatalysts. The following sections summarise band engineering to narrow the band gap.

#### 1.3.2 Band Gap Engineering – Doping

Doping by incorporating foreign elements into semiconductors is a successful procedure for narrowing the Fermi level position within the band gap of photocatalysts to extend the optical absorption of wide band gap semiconductors to harness more sunlight<sup>5</sup>. This band gap engineering can result in improving the photocatalytic water splitting efficiency. Incorporating metal cations with ionic radii similar to the host ions can narrow the Fermi level position within the band gap by interacting with the valence or conduction bands of the host ions or by creating intra-band gap levels where donors are able to generate holes at the valence band and donate electrons to the conduction band<sup>20</sup>. In contrast, acceptors at the conduction band can accept an electron from the valence band. However, even though the doping strategy can generate active photocatalysts in the visible light range, it may also negatively affect photocatalysis. In some cases, the dopants can act as recombination centres of photogenerated electrons and holes thus decreasing photocatalytic activity<sup>21</sup>.

# 1.3.3 Photogenerated Charge Separation

The photocatalyst absorbs photons in response to illumination resulting in the generation of electronhole pairs in valence or conduction bands, respectively. Then, the photoinduced electrons and holes are separated and transferred from semiconductor's inside to the active sites on the surface for reduction and oxidation reactions, respectively<sup>22</sup>. Therefore, photocatalytic water splitting can be improved by enhancing the photogenerated charge separation efficiency<sup>19, 23</sup>. Recombination of photogenerated charge is one of the challenging issues in photocatalyst, where electrons tend to fall from the conduction band to the valence band, reducing the charge carrier<sup>5</sup>. Nevertheless, the trapping of a carrier in energy level close to the band edge can cause spatial electron–hole separation and lengthen the charge lifetime. Several procedures to separate photogenerated charge carriers have been explored for reducing electron–hole recombination and trapping in a photocatalyst<sup>22</sup>.

#### 1.3.3.1 Enhancement of Photogenerated Charge Separation

## 1.3.3.1.1 Particle Size and Morphology

The electron—hole recombination probability can be reduced by decreasing the photocatalyst particle size to increase the speed of the photogenerated charge separation to the active sites on the surface <sup>12,</sup> <sup>24</sup>. As an example, the photocatalytic activity of NaTaO<sub>3</sub> was enhanced due to doping with La<sup>25</sup>. The NiO/La-doped NaTaO<sub>3</sub> showed an AQY of 56% at 270 nm, which was 9 times higher than that gained from a NiO/nondoped NaTaO<sub>3</sub>, apparently because decreased particle size with higher crystallinity (Figure 1.4)<sup>25, 26</sup>. This catalyst's photogenerated electrons and holes efficiently migrated over small distances to reach the reaction sites on the surface rather than recombine. Doping of Ca, Sr and Ba also had a similar effect as the La doping on smaller particle sizes and improved photocatalytic activity under UV light<sup>27</sup>. However, it should be noted that the absorption of the incident light can be limited due to the tiny particle size.

Image removed due to copyright.

*Figure 1.4:* Mechanism of water splitting over a NiO/La-doped NaTaO<sub>3</sub> photocatalyst. Reproduced from reference  $^{26}$  originally published by  $^{25}$ .

#### 1.3.3.1.2 Crystalline Phases and Junctions

One way to reduce the probability of electron-hole recombination is the homojunction. Specifically, a homojunction is the interface region between two different phases with the same composition and it often facilitates charge separation. For example, P25, a commercial TiO<sub>2</sub> with a mixture of anatase and rutile phases, is a typical benchmark photocatalyst in photocatalytic reactions<sup>28</sup>. In anatase and rutile phases, a smooth path for photogenerated charge separation is provided between anatase and rutile phases due to the formation of phase junctions between the two phases (Figure 1.5)<sup>29</sup>. This phase junction is the main factor for the highly photocatalytic activity of the mixture of anatase and rutile phases<sup>29</sup>.

Image removed due to copyright.

**Figure 1.5:** Example of phase junction between anatase and rutile phase  $TiO_2$  for promoting photogenerated charge separation. Reproduced from reference <sup>29</sup>.

#### 1.3.3.1.3 Facet Control

The crystal surfaces of semiconductors play a vital role in photocatalytic performance. Spatial charge separation was found in several single crystals between exposed facets such as BiVO<sub>4</sub><sup>30-32</sup>. It has been

observed that the reduction deposition of noble metals such as Au, Pt and Au occur separately on the (010) facets. In contrast, the oxidation deposition of metal oxides such as MnO<sub>x</sub> and PbO<sub>2</sub> selectively takes place on (110) facets of BiVO<sub>4</sub> (Figure 1.6)<sup>30</sup>. This indicates that photogenerated charges are separated and distributed on [010] facet involving electrons and [110] facet involving holes, respectively. The BiVO<sub>4</sub> sample with a selective photodeposition of metallic Pt and MnO<sub>x</sub> particles on the [010] and [110] facets showed much higher photocatalytic activity than materials loaded using the impregnation method at random sites. This finding suggests that spatial charge separation can enhance photocatalytic performance to the greatest extent by selectively photodepositing the co-catalysts on the preferred reduction/oxidation reaction facets of the photocatalyst.

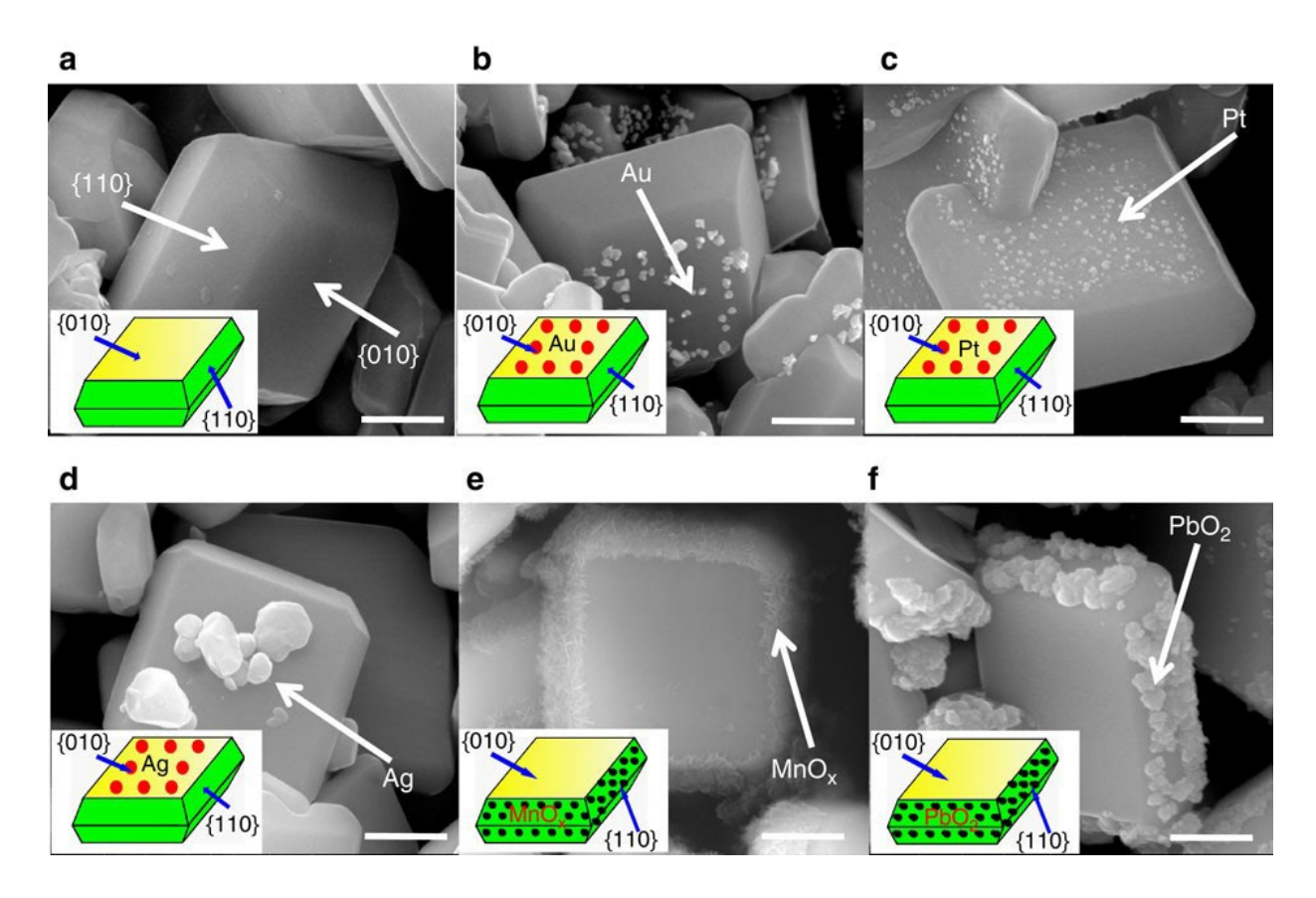


**Figure 1.6:** SEM images of (a) BiVO<sub>4</sub>; (b) Au/BiVO<sub>4</sub>; (c) Pt/BiVO<sub>4</sub>; (d) Ag/BiVO<sub>4</sub>; (e) MnO<sub>x</sub>/BiVO<sub>4</sub> and (f) PbO<sub>2</sub>/BiVO<sub>4</sub>. Modified from reference <sup>30</sup>.

# 1.4 Photocatalysts for water splitting

#### 1.4.1 Titanium Dioxide

TiO<sub>2</sub> is extensively used as a photocatalyst in various oxidation and reduction reactions on the active surface as a semiconductor. Owing to its great properties such as high catalytic efficiency, remarkable stability, and also durability, safety, and inexpensiveness, it is in high demand.<sup>33</sup>. Titanium dioxide has crystal phases of brookite, anatase and rutile. The crystal structures of the three phases of TiO<sub>2</sub> are shown in Figure 1.7<sup>34</sup>. The most stable phase is rutile. The brookite and anatase can be converted

to the rutile phase by providing appropriate heat treatment. The band gaps of rutile, anatase and brookite are 3.0, 3.2 and 2.9 eV, respectively. In photocatalysis applications, anatase is more effective than rutile and brookite because the conduction band location of anatase is more conducive to initiating conjugate reactions involving electrons<sup>33</sup>. In addition, the formation of the surface peroxide groups during a photooxidation reaction at anatase are very stable, in comparison to those formed at the surface of rutile<sup>33</sup>.

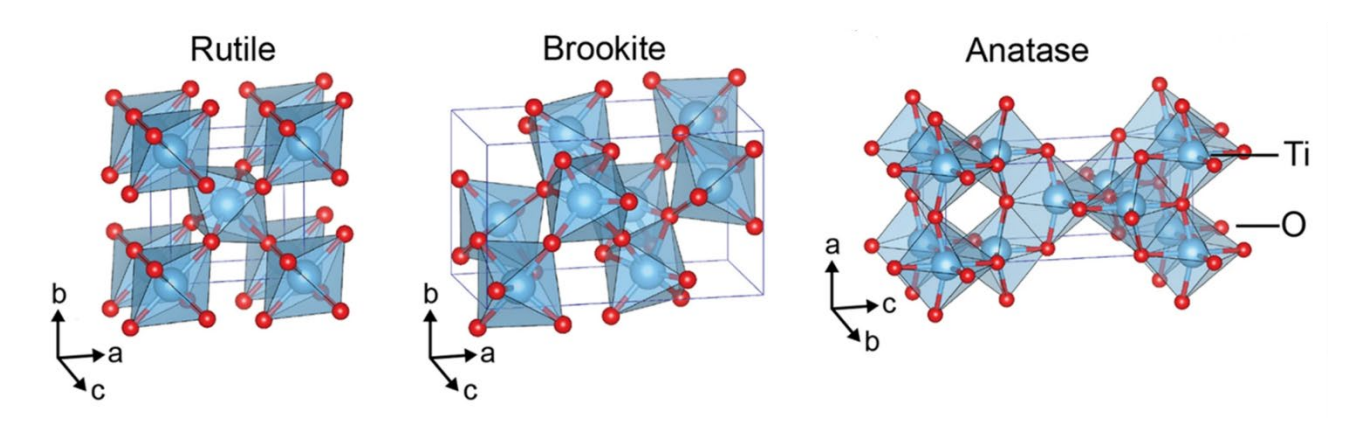


**Figure 1.7:** The crystal structure of  $TiO_2$  phases, (a) rutile phase, (b) brookite phase and (c) anatase phase. Modified from reference  $^{34}$ .

The physical and chemical properties of TiO<sub>2</sub> can be affected by how it is formed. TiO<sub>2</sub> can be formed in various forms such as film (atomically flat), thin nanosheets, nanotubes and nanoparticles<sup>35</sup>. TiO<sub>2</sub> film is helpful for surface imaging techniques, while the latter forms are helpful for transmission microscopy techniques. Numerous methods can be used to synthesise titania, including the sol-gel method<sup>36</sup>, chemical vapour deposition method<sup>37</sup>, microwave-assisted method, atomic layer deposition method<sup>38</sup> and radio frequency (RF) magnetron sputtering method<sup>39</sup>. Each of these methods will influence the size/thickness and geometry of the particles/film.

#### 1.4.2 Strontium Titanate

The perovskite oxides (ABO<sub>3</sub>) have many photocatalytic applications because of their structural and compositional flexibility, high thermal and chemical stability and outstanding photocatalytic activity<sup>20</sup>. For photocatalytic applications, titanate perovskites have been prepared with various morphologies such as mesoporous spheres, nanoparticles, and cubes<sup>20</sup>. Strontium titanate (SrTiO<sub>3</sub>) nanoparticles are promising metal oxide for photocatalytic water splitting due to the unique properties and long lifetime on e<sup>-</sup> and h<sup>+</sup> pairs with an indirect band gap of 3.2 eV in water redox potentials<sup>40</sup>. The O 2p orbitals make up the majority of the top of SrTiO<sub>3</sub> valence band, with contributions from Sr 5s and Ti 3d, while the Ti 3d orbitals consists manly the bottom of the conduction band<sup>41</sup>.

SrTiO<sub>3</sub> is UV light irradiation active only. However, the light absorption of SrTiO<sub>3</sub> can be enhanced by doping with elements such as Cr<sup>3+</sup>, Ga<sup>3+</sup>, Na<sup>+</sup> and Al<sup>3+ 42-45</sup>. This process introduces additional elements into the SrTiO<sub>3</sub> to tune and improve the optical, electronic and other physical properties of SrTiO<sub>3</sub>. Ma et al. have reported that transition metal such as Cu, Ni, Rh, Mn and Fe doped SrTiO<sub>3</sub> can be prepared by the hydrothermal synthesis method<sup>46</sup>. It has been found that Rh<sup>3+</sup> doped SrTiO<sub>3</sub> has the best activity for H<sub>2</sub> evolution under visible light, caused by Rh<sup>3+</sup> states narrowing the SrTiO<sub>3</sub> band gap and the visible light activity was enhanced.

Doping with aluminium has attracted more attention as it can improve the SrTiO<sub>3</sub> morphology and photocatalytic activity. For example, the activity of SrTiO<sub>3</sub> was enhanced due to flux-mediated doping of Al<sup>3+</sup> into SrTiO<sub>3</sub> by applying SrCl<sub>2</sub> flux treatment at 1100°C in an alumina crucible<sup>44</sup>. This resulted in overall water splitting with an AQE of 30% at 360 nm for RhCrO<sub>x</sub> loaded Al-doped SrTiO<sub>3</sub> due to the better doping and crystallinity of Al<sup>3+</sup> using crucibles. Al-doped SrTiO<sub>3</sub> with RhCrO<sub>x</sub> cocatalyst has also been used for large-scale photoreactors for photocatalytic water splitting reactions (Figure 1.8)<sup>47</sup>. The size of the photoreactor panel was 1 m<sup>2</sup> with a depth of 4 mm of the water layer, which provided an active water splitting reaction with 0.4 STH efficiencies. Further, applying MoO<sub>x</sub> on the surface of Al-doped SrTiO<sub>3</sub> increased the AQE to 69%, which is assumed due to be the modification of the chemical state of the RhCrO<sub>x</sub> co-catalyst and promotes H<sub>2</sub> evolution<sup>48</sup>. Very recently, it was found that the AQE during overall water splitting improved up to 96% by modification of Al-doped SrTiO<sub>3</sub> with the photodeposition of Rh/Cr<sub>2</sub>O<sub>3</sub> and CoOOH as hydrogen and oxygen evolution sites at different facets<sup>49</sup>. This, at wavelengths between 350 and 360 nm, is equivalent to an internal quantum efficiency of almost unity.

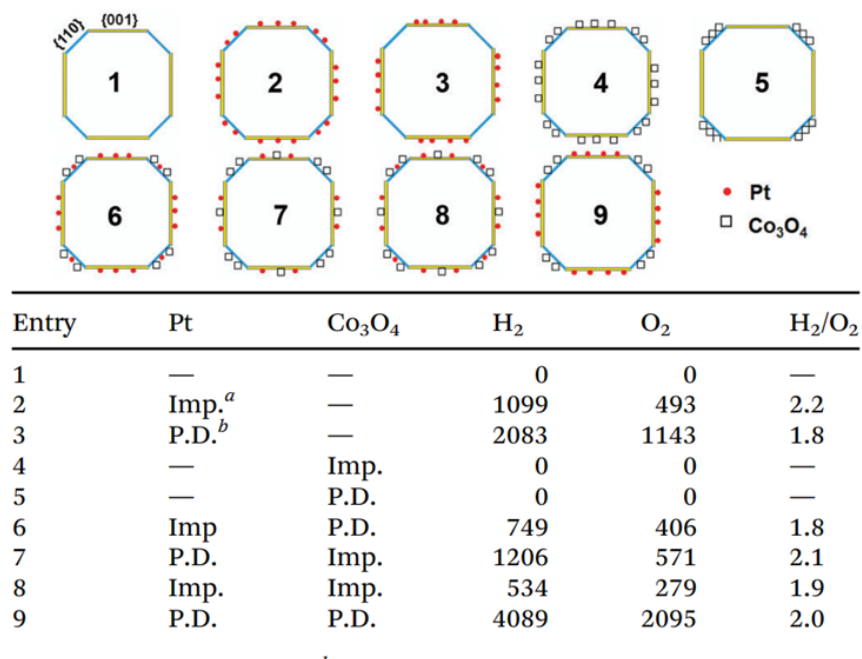
Image removed due to copyright.

**Figure 1.8:** (a) Schematic of  $1 \times 1$  m water splitting panel based on Al-doped SrTiO<sub>3</sub> powder with  $RhCrO_x$  co-catalyst (b) image of a  $1 \times 1$  m Al-doped SrTiO<sub>3</sub> panel. Reproduced from reference <sup>47</sup>.

# 1.5 Co-catalysts for photocatalytic water splitting

Cocatalysts provide the active sites of water splitting reactions, where reduction by electron emission at the reduction side and oxidation by a hole at the oxidation side, because most bare photocatalysts have negligible H<sub>2</sub> evolution activity. Co-catalysts are essential for photocatalytic water splitting because of their redox reaction function that helps to reduce the activation energy<sup>12, 50</sup>. As illustrated in Figure 1.2, the loaded co-catalysts extract photogenerated electrons and holes from the photocatalyst (step 2) and host active sites for H<sub>2</sub> and O<sub>2</sub> evolution (step 3). Therefore, the overall efficiency of a particular photocatalytic system depends on the loaded co-catalyst<sup>51</sup>. Moreover, the full function of the co-catalysts can be achieved by depositing the reduction and oxidation co-catalysts on the correct sites. The correct sites for co-catalysts on the photocatalyst are located on the anisotropic facets where the spatial separation of the photogenerated charges can be control. For example, in Table 1.1, the dual-cocatalysts were deposited selectively and randomly on the two types of SrTiO<sub>3</sub> nanocrystals for comparison. The Pt and Co<sub>3</sub>O<sub>4</sub> are deposited on the correct sites of 18facet SrTiO<sub>3</sub> nanocrystals with anisotropic facets exhibiting significantly enhanced overall photocatalytic water splitting compared to homogeneous co-catalysts deposition<sup>52</sup>. Also, it is essential to modify the photocatalyst with effective co-catalysts for H<sub>2</sub> and O<sub>2</sub> evolution to achieve the highest function of the system.

**Table 1.1:** Measured photocatalytic water splitting performance of 18-facet SrTiO<sub>3</sub> nanocrystals with Pt and Co<sub>3</sub>O<sub>4</sub> co-catalysts deposited. (Gas unit:  $\mu$ mol h-1 m-2.) Modified from reference <sup>52</sup>.



<sup>&</sup>lt;sup>a</sup> Impregnation method. <sup>b</sup> Photo-deposition method.

Several noble-metals have been studied as a co-catalyst in recent years such as Pt<sup>53, 54</sup>, Ag<sup>55</sup>, Pd<sup>54</sup>, and Au<sup>54</sup>. Au is an interesting noble-metal to use as a co-catalyst. Au is an inert substance in its bulk

nature. However, due to their unique physical, chemical, and crystallographic properties, Au nanoparticles (Au NPs) have the ability to modify surfaces as a co-catalyst<sup>56</sup>. Gold particles have gained attention in the last decade as an effective co-catalyst metal due to the interactions between surface plasmon resonance effect (SPR) and semiconductors<sup>57</sup>.

## 1.5.1 Gold Clusters as Co-catalysts

Smaller than Au NPs, gold nanoclusters (Au NCs) have the potential to modify surface properties to realize strong enhancements of photocatalytic processes. Au NCs consist of unique atomic structures that are dependent on the number of atoms in the Au NCs. The electronic structure, size and morphology of the Au NCs depend on the number of constituent atoms in an Au cluster<sup>58</sup>. Therefore, the photocatalytic activity of Au NCs modified surfaces can completely change with the addition or removal of one atom from a cluster<sup>59</sup>. In general, metal clusters are typically employed for the reasons listed below: A) Unlike a band, they have distinct electrical states. B) They have properties called fluxionality and structural isomerism, which make it simple to switch between configurations and aid in the attachment and dissociation of molecules. C) They also have more surface area in comparison to the amount of material used<sup>60-62</sup>.

Au NCs can be synthesised with protecting ligands to stabilise the cluster core and avoid agglomeration<sup>60</sup>. The physical, chemical, electronic, and optical properties largely depend on the gold–ligand interaction and bonding for ligated gold clusters<sup>62</sup>. Examples of ligated gold clusters are the thiolate-ligated gold<sup>63</sup>, alkynyl-ligated gold<sup>64</sup> and phosphine-ligated gold clusters<sup>62</sup>. Phosphine-ligated gold clusters have significantly different physical, chemical and structural properties than the thiolate-ligated and alkynyl-ligated gold clusters. For example, the gold–phosphine (Au–P) bonding is relatively weaker than to gold–sulfur (Au–S) bonding, advantageous for ligand removal and exchange or intercluster conversion of Au clusters<sup>62</sup>.

Supported Au NCs on photocatalysts are considered to improve the photocatalytic water splitting performance<sup>65</sup>. Kudo and co-workers published an example of improving photocatalytic water splitting using Au clusters<sup>66</sup>. They found that loading ultra-small Au clusters using Au<sub>25</sub> into BaLa<sub>4</sub>Ti<sub>4</sub>O<sub>15</sub> enhanced the photocatalytic water splitting activity by 2.6 times compared to BaLa<sub>4</sub>Ti<sub>4</sub>O<sub>15</sub> loaded with Au nanoparticles. The same group explored that loading other sizes of Au<sub>n</sub> NCs (n=10, 15, 18, 22, 25, 29, 33, 39) on BaLa<sub>4</sub>Ti<sub>4</sub>O<sub>15</sub> showed an increase the photocatalytic activity with decreasing Au<sub>n</sub> cluster sizes (Figure 1.9A)<sup>67</sup>. Moreover, it was found that it was crucial to use a very stable cluster as a precursor to achieve control of the Au<sub>n</sub> clusters loading onto BaLa<sub>4</sub>Ti<sub>4</sub>O<sub>15</sub> without agglomeration (Figure 1.9B). In another example, Au<sub>25</sub> clusters loaded onto SrTiO<sub>3</sub> have improved water splitting activity compared to Au NPs<sup>68</sup>.

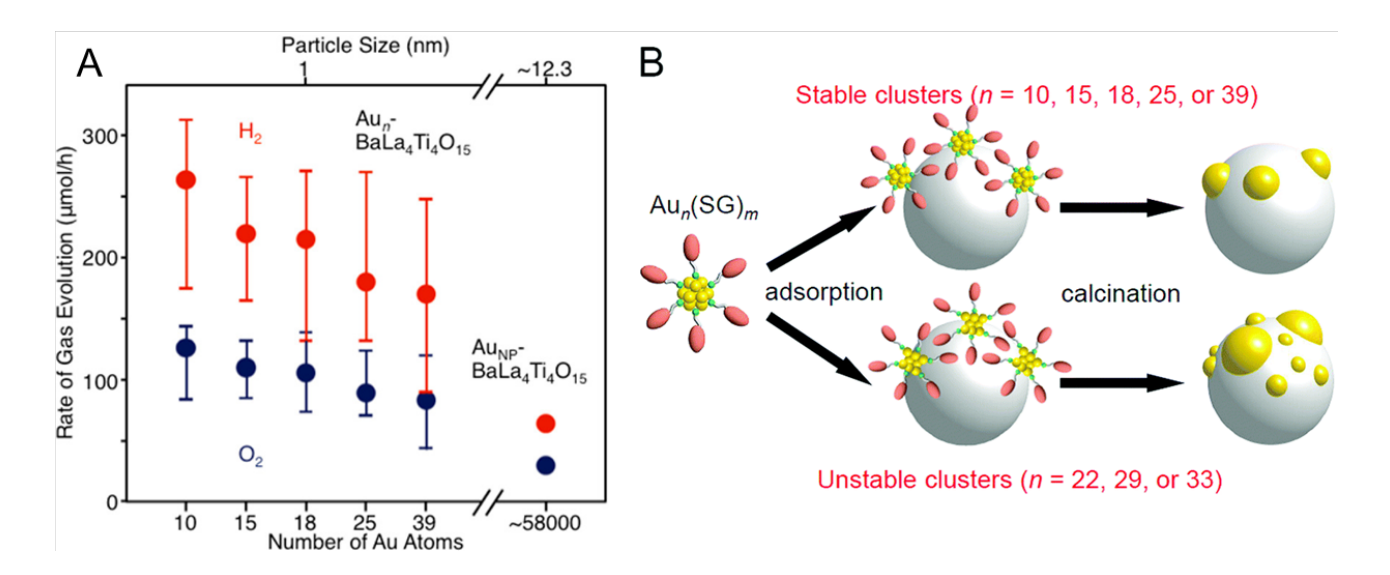


**Figure 1.9:** (A) Effect of cluster size on water splitting activity using  $Au_n$ -BaLa<sub>4</sub> $Ti_4O_{15}$  and AuNP-BaLa<sub>4</sub> $Ti_4O_{15}$ . (B) Schematic of the agglomeration of  $Au_n$  on the BaLa<sub>4</sub> $Ti_4O_{15}$  depending on the size of the cluster. Modified from references <sup>58, 67</sup>.

#### 1.5.1.1 Characterization of Gold Clusters

State-of-the-art characterization techniques are indispensable in studying the structural and fundamental properties of atomically-precise Au clusters. Previously, reliance on elemental analysis had led to an incorrect assignment of molecular formula for the pentagold cluster;<sup>69</sup> it was later corrected to be undecagold. Apparently, no single characterization method can provide complete and conclusive information about material properties and characteristics. Thus, very often multiple, complementary techniques are required to gain information about their structure and properties. Progress in gold-phosphine clusters has benefited from numerous characterization tools, including microscopy spectroscopy. This section discusses in detail several of the key techniques employed to characterize the size-dependent and unique properties of gold-phosphine clusters which enables our understanding of these properties.

#### 1.5.1.1.1 Electron microscopy

Progress of nanoscale science and technology is heavily dependent on state-of-the-art characterization techniques. Very often, a method by which one can directly 'see' nanoscale materials provides conclusive evidence of their existence compared to indirect methods - *seeing is believing*. Transmission electron microscopy (TEM) and scanning transmission electron microscopy (STEM) are widely used techniques for imaging an electron-transparent sample at the atomic scale. The difference between the two techniques is that STEM uses a small electron beam that is pre-focused before imaging the sample, while the large electron beam used for TEM is focussed after transmision through the sample.<sup>70</sup> The high-angle annular dark-field (HAADF) method in STEM is predicated on

detecting the incoherent scattering electrons, referred to as Z-contrast microscopy. STEM has higher resolution imaging and analytical capabilities due to the use of aberration correctors. Advances in aberration corrector electron optics allow direct imaging at the atomic level with high resolution beyond 50 pm.<sup>71</sup> Due to its high atomic number, gold can be easily imaged at high contrast using TEM. With aberration correction, imaging of Au clusters at the atomic resolution is now possible.<sup>72</sup> Information that can be obtained from TEM and STEM imaging includes particle size, shape, lattice fringe, crystallographic structure, defects and grain boundaries.

TEM images of Schmid's Au $_{55}$  cluster (the average formula is Au $_{55}$ (PPh $_3$ ) $_{12}$ Cl $_6$ )) revealed the particle size to be 1.4  $\pm$  0.4 nm. <sup>73, 74</sup> Initial assignments based on EXAFS attributed the Au core structure to have cuboctahedral geometry, <sup>75, 76</sup> however, an icosahedral structure was also suggested to be plausible by powder X-ray diffraction. <sup>77</sup> Recently, thorough and systematic studies using aberration-corrected STEM by Jian *et al.* discovered that Au $_{55}$  clusters contain both hybrid icosahedron-cuboctahedron and amorphous structures, resolving the contradictory studies previously reported. <sup>78</sup> Based on the intensity representing the number of clusters as a function of core size, the authors found that the four most intense peaks occurred at 41  $\pm$  2, 47  $\pm$  1.5, 50  $\pm$  1.5 and 54  $\pm$  1.5 Au atoms, with the last peak being assigned to Au $_{55}$ (PPh $_3$ ) $_{12}$ Cl $_6$ .

Fluxionality is the fast, dynamic intramolecular rearrangement of chemically equivalent configurations due to the stereochemical nonrigidity and low energy barrier between different configurations<sup>79</sup>. The fluxionality of Au clusters on surfaces renders precise structural determination difficult,<sup>79</sup> particularly because electron beams can affect the geometry and induce fluctuation between isomers.<sup>80</sup> Wang and Palmer observed that the structure of Au<sub>20</sub> clusters fluctuate between tetrahedral and disordered structures.<sup>80</sup> Deposition of Au clusters on surfaces also reduces the degree of freedom. A study by Al Qahtani *et al.* investigated the structure of Au<sub>9</sub>(PPh<sub>3</sub>)<sub>8</sub>(NO<sub>3</sub>)<sub>3</sub> clusters on TiO<sub>2</sub> nanosheets.<sup>81</sup> They observed three atomic configurations using STEM (Figure 1.10a-c); one three-dimensional structure and two pseudo-two-dimensional structures. The three-dimensional structure was attributed to Au<sub>9</sub> protected with ligands, while the pseudo-two-dimensional structures were attributed to de-ligated clusters with intrinsic fluxionality.

Image removed due to copyright.

**Figure 1.10:** (a-c) STEM-HAADF images of Au<sub>9</sub> supported on TiO<sub>2</sub> clusters with different structures. Reproduced from reference <sup>81</sup>. (d) Dynamic motion of Au<sub>9</sub> covalently bonded to the surface of graphene. Reproduced from reference <sup>82</sup>..

Rourke and co-workers used STEM to image Au<sub>9</sub>(PPh<sub>3</sub>)<sub>8</sub>(NO<sub>3</sub>)<sub>3</sub> clusters attached to sulfurfunctionalized graphene oxide (GOSH). <sup>82</sup> Time-dependent rotations of Au<sub>9</sub> cluster covalently bonded to the surface of GOSH are shown in Figure 1.10(d). This result shows the effect of the electron beam on a single Au<sub>9</sub> cluster inducing rotation of the cluster, without any lateral displacement, during the imaging. This also demonstrates that Au<sub>9</sub> clusters attached to GOSH are robustly bound even under the effect of an intense STEM electron beam.

## 1.5.1.1.2 Photoelectron spectroscopy

Photoelectron spectroscopy (PES) is an important and powerful tool to investigate the surface properties of materials down to a few nanometers in depth. The surface sensitivity of PES is due to the limitation of the emitted electron mean free path, where an electron excited by a photon will lose energy before leaving the surface to reach the detector. PES is classified into two energy regimes: X-ray photoelectron spectroscopy (XPS) and ultraviolet photoelectron spectroscopy (UPS).

### 1.5.1.1.2.1 X-ray Photoelectron Spectroscopy

XPS is a widely used technique to investigate the chemical composition and elemental concentration of a surface. The technique measures the kinetic energy of electrons emitted from the top layer (<5 nm) of the surface. 83 It is employed to determine the electronic structure, elemental composition and chemical environment of various elements present in the sample via the binding energy (BE), full width at half maximum (FWHM) and intensity of the corresponding elemental peak.

For gold, the core electrons usually analyzed in XPS originate from the Au 4f orbitals. The Au 4f doublet peak  $(4f_{7/2} \text{ and } 4f_{5/2})$  in an XPS spectrum arises due to the quantum mechanical nature of the spin-orbit coupling. For bulk gold, the literature standard BE of the Au  $4f_{7/2}$  peak is 84.0 eV with a separation of 3.67 eV to the Au  $4f_{5/2}$  peak.<sup>84, 85</sup> The BEs for Au clusters are significantly different from the bulk value. Such differences are attributed to the initial and final state effects, which strongly influence the peak position and FWHM.<sup>86</sup>

The initial state effect reflects the oxidation state of the metal. The BE is positively charged for oxidized metal due to the loss of charge to oxygen, which reduces the core state energy, leading to an increase in the electron BE.<sup>87,88</sup> The final state effect is due to the difficulty of the charged atom being relaxed by residual electrons following excitation by an X-ray beam.<sup>89</sup> When an electron is excited, the positively charge hole remains in a charged state for a finite time and the residual electrons redistribute to screen the positively charge hole.<sup>88,90</sup> The initial and final state effects lead to a shift towards a higher BE, referred to as a positive BE shift. Several examples using XPS to study the change in the chemical state of Au and Au cluster size are given below.<sup>91</sup>

Table 1.2 summarizes the BE of Au 4f<sub>7/2</sub> for different gold compounds and several atomically-precise gold-phosphine clusters reported to date. Upon formation of oxidized species such as Au<sup>+</sup> and Au<sup>3+</sup>, the Au 4f<sub>7/2</sub> peak shifts to 85–87 eV, depending on the composition of the gold compound, due to the initial state effect. <sup>92</sup> For this reason, XPS can be used to trace the formation of Au metal nanoparticles from Au precursors during the synthesis by measuring the change in the BE of the Au 4f peak. For example, Visco *et al.* probed the oxidation state of Au prepared by different synthetic methods and pre-treatment using XPS. <sup>93</sup> The authors found that thermal treatment under conditions such as vacuum, H<sub>2</sub>, and H<sub>2</sub> followed by O<sub>2</sub>, were required to transform gold hydroxide (from reaction of HAuCl<sub>4</sub> with OH<sup>-</sup>) into metallic gold (Au<sup>0</sup>) as manifested by the simultaneous decrease and increase of the Au<sup>3+</sup> and Au<sup>0</sup> peak areas, respectively.

**Table 1.2:** BE of Au 4f<sub>7/2</sub> for different gold compounds and several gold-phosphine clusters reported up-to-date

Compound	Au 4f <sub>7/2</sub> (eV)	Calibrated against	Excitation energy	Refs
Au metal	84.0	C 1s peak at 284.8 eV	Mg-Kα (1253.6 eV)	85
HAuCl <sub>4</sub>	87.3 – 87.6	C 1s peak at 285 eV	Al-Kα (1486.6 eV)	93
$Au_2O_3$	85.5 – 86.3	C 1s peak at 285 eV	Al-Kα (1486.6 eV)	93
AuCl	85.8 – 86.0	C 1s peak at 285 eV	Al-Kα (1486.6 eV)	93
Au(PPh <sub>3</sub> )Cl	85.3	No information provided	No information provided	94
Au(PPh <sub>3</sub> ) <sub>2</sub> Cl	85.6	No information provided	No information provided	94
Au(PPh <sub>3</sub> )NO <sub>3</sub>	84.9	C 1s peak at 284.6 eV	Mg-Kα (1253.6 eV)	95
Au <sub>5</sub> Cu <sub>6</sub> (Dppf) <sub>2</sub> (SAdm) <sub>6</sub> (BPh <sub>4</sub> )	84.7	No information provided	Al-Kα (1486.6 eV)	96
Au <sub>6</sub> (PPh <sub>3</sub> ) <sub>6</sub> (BF <sub>4</sub> ) <sub>2</sub>	84.7	C 1s peak at 284.7 eV	Mg-Kα (1253.6 eV)	97, 98
[Au <sub>8</sub> (PPh <sub>3</sub> ) <sub>7</sub> ] <sup>2+</sup>	85.2	No information provided	No information provided	94
Au <sub>8</sub> (PPh <sub>3</sub> ) <sub>8</sub> (NO <sub>3</sub> ) <sub>2</sub>	85.1	C 1s peak at 285 eV	Synchrotron (690 eV)	99, 100
Au <sub>8</sub> (TPPMS) <sub>x</sub> (NO <sub>3</sub> ) <sub>2</sub> with x=7,8	84.5	C 1s peak at 284.8 eV	Al-Kα 1486.6 eV)	101
Au <sub>9</sub> (PPh <sub>3</sub> ) <sub>8</sub> (NO <sub>3</sub> ) <sub>3</sub>	84.7 – 85.3	C 1s peak at 285 eV	Mg-Kα (1253.6 eV) Synchrotron (625 eV) Synchrotron (690 eV)	81, 99, 100, 102- 107
Au <sub>11</sub> (PPh <sub>3</sub> ) <sub>8</sub> Cl <sub>3</sub>	84.7	C 1s peak at 285 eV	Mg-Kα (1253.6 eV)	94, 99, 100
$Au_{11}(PPh_3)_7I_3$	84.5	No information provided	Mg-Kα (1253.6 eV)	108
Au <sub>13</sub> (dppe) <sub>5</sub> Cl <sub>2</sub> Cl <sub>3</sub>	85.1 – 85.6	C 1s peak at 285 eV	Mg-Kα (1253.6 eV)	109
$[Au_{13}(dppe)_5Cl_2]^{3+}$	84.4	C 1s peak at 284.8 eV	Al-Kα (1486.6 eV)	110
$Au_{13}Ag_{12}(PPh_3)_{10}Cl_8$	84.4	C 1s peak 284.6 eV	Al-Kα (1486.6 eV)	111
$[Au_{19}Cu_{30}(PPh_3)_6(C\equiv CPh)_{22}Cl_2](NO_3)_3$	84.3	C 1s peak at 284.6 eV	Al-Kα (1486.6 eV)	112
Au <sub>20</sub> (PP <sub>3</sub> ) <sub>4</sub> Cl <sub>4</sub>	84.3	C 1s peak at 284.6 eV	Al-Kα (1486.6 eV)	113
$[Au_{23}(PPh_3)_6(C \equiv CPh)_9](SbF_6)_2$	84.4	C 1s peak at 284.6 eV	Al-Kα (1486.6 eV)	114
$[Au_{24}(PPh_3)_4(C \equiv CPh)_{14}](SbF_6)_2$	84.5	C 1s peak at 284.6 eV	Al-Kα (1486.6 eV)	115
[Au <sub>24</sub> Pd(PPh <sub>3</sub> ) <sub>10</sub> (SR) <sub>5</sub> Cl <sub>2</sub> ]Cl	84.5	Ag 3d <sub>5/2</sub> peak at 367.9 eV	Mg-Kα (1253.6 eV)	116
$[Au_{25}(PPh_3)_{10}(SR)_5Cl_2](SbF_6)_2$	84.9	Ag 3d <sub>5/2</sub> peak at 367.9 eV	Mg-Kα (1253.6 eV)	116
Au <sub>25</sub> (PPh <sub>3</sub> ) <sub>10</sub> (SC <sub>12</sub> H <sub>25</sub> ) <sub>5</sub> Cl <sub>2</sub>	84.3	C 1s peak at 284.8 eV	Al-Kα (1486.6 eV)	117

$[Au_{32}(PPh_3)_8(dpa)_6](SbF_6)_2$	84.6	C 1s peak at 284.6 eV	Non-monochromatic Al- Kα	118
Au <sub>55</sub> (PPh <sub>3</sub> ) <sub>12</sub> Cl <sub>6</sub>	84.3	No information provided	Al-Kα (1486.6 eV)	119
Au <sub>55</sub> (PPh <sub>3</sub> ) <sub>12</sub> Cl <sub>6</sub>	85.1*	No information provided	Al-Kα (1486.6 eV)	120
Au <sub>101</sub> (PPh <sub>3</sub> ) <sub>21</sub> Cl <sub>5</sub>	83.8 – 83.7	C 1s peak at 285 eV	Mg-Kα (1253.6 eV) Synchrotron (690 eV)	99, 100, 121, 122

<sup>\*</sup>The binding energy published in ref. <sup>120</sup> for Au clusters is significantly different to other published binding energies for Au clusters of similar size, e.g. in refs. <sup>99, 100, 119</sup>.

The use of XPS is not limited to determining the chemical states and composition but can also be used to determine the relative size of Au clusters due to the final state effect. Haruta used the positive shift in the BE to assign small Au clusters as the most active sites in gold-based catalysts; at the time of that study, access to high-resolution TEM was extremely limited. Early XPS studies of phosphine-ligated Au clusters were performed and reported by Battistoni *et al.* 124, 125 The authors observed a general trend of positive BE shifts of the Au 4f<sub>7/2</sub> peak as the number of Au atoms in the cluster decreased. However, the interpretation of XPS spectra of Au clusters at that time attributed the variation to changes in the cluster geometry and ligand components. Similar contributions have been made by Van Attekum *et al.* using Au<sub>11</sub>, Au<sub>9</sub> and Au<sub>8</sub> clusters stabilized by triarylphosphine ligands. The authors showed that the BE of Au 4f peaks shifted to higher BE and the width (FWHM) broadens as the Au cluster size decreases.

An early XPS report of the final state effect on phosphine-stabilized Au clusters was done by Schmid and co-workers on Au<sub>55</sub>(PPh<sub>3</sub>)<sub>12</sub>Cl<sub>6</sub>. <sup>119</sup> The authors suggested that the Au 4f peak shifted to higher BE compared to bulk Au due to the final state effect, following what had been discussed in earlier publications. <sup>128, 129</sup> A number of other XPS studies on Au<sub>55</sub> can be found here. <sup>120, 130, 131</sup> However, several XPS studies have investigated the electronic structure of new phosphine-ligated Au clusters according to final state effect which differ from the interpretation of Schmid and co-workers for Au<sub>55</sub>(PPh<sub>3</sub>)<sub>12</sub>Cl<sub>6</sub>. These studies were performed on Au<sub>13</sub><sup>110</sup>, bimetallic Au/Ag<sup>132</sup>, Au<sub>5</sub>Cu<sub>6</sub><sup>96</sup> and Au<sub>8</sub><sup>133</sup> clusters, and all observed a shift in the BE of Au 4f<sub>7/2</sub> peak to higher BEs due to the formation of the small-sized clusters.

XPS studies have been performed on supported Au clusters to investigate the effect of supporting metal oxides on the clusters. In a study by Goodman and co-workers,  $Au_6(PPh_3)_6(BF_4)_2$  was deposited on a single crystal  $TiO_2(110)$  surface using a solution deposition method.<sup>98</sup> The XPS of Au  $4f_{7/2}$  peak experienced a shift of +0.4 eV after removal of phosphine ligands via electron-stimulated desorption. This shift was due to the size reduction of Au clusters, which was observed by scanning tunneling

microscopy (STM). The same group reported that different pre-treatment procedures of Au<sub>6</sub> deposited on TiO<sub>2</sub> particles had a profound influence on the stability of Au clusters on the surface of TiO<sub>2</sub>, which played a crucial role on CO oxidation activity.<sup>97</sup>

Recent studies by Anderson *et al.* utilized synchrotron XPS of Au<sub>8</sub>, Au<sub>9</sub>, Au<sub>11</sub> and Au<sub>101</sub> clusters supported on TiO<sub>2</sub>.<sup>99, 100</sup> Figure 1.11 shows the Au 4f spectra of untreated and calcined Au clusters. The authors concluded that a positive shift in the BE and an increase in the FWHM of Au 4f<sub>7/2</sub> peak were due to a decreasing number of Au atoms. Moreover, the as-deposited Au clusters were not affected by the TiO<sub>2</sub> substrate. However, calcination of the sample to remove the ligands lead to a degree of aggregation of Au clusters, as observed in the Au 4f spectra with two doublets of Au peaks. Al Qahtani *et al.* studied the aggregation of Au<sub>9</sub> on TiO<sub>2</sub> nanosheets and atomic layer deposition (ALD) TiO<sub>2</sub>.<sup>104, 105</sup> They demonstrated that the Au 4f<sub>7/2</sub> peak shifted to a lower BE after calcination due to aggregation of the Au<sub>9</sub> clusters. This finding was supported by other techniques such as atomic force microscopy (AFM) and STM. One XPS study by Ruzicka *et al.* applied several pre-treatment methods to TiO<sub>2</sub> before depositing Au<sub>9</sub> clusters to improve the Au cluster stability on the surface. They demonstrated that Au<sub>9</sub> aggregation could be prevented, even under calcination, via pre-treatment of the TiO<sub>2</sub> with H<sub>2</sub>SO<sub>4</sub>, by observing a slight shift of the Au 4f<sub>7/2</sub> peak to a higher BE after calcination.<sup>106</sup> Further reports of XPS studies performed to examine the electronic structure of gold-phosphine clusters by different groups are available here.<sup>102, 103, 109, 121, 134-137</sup>

Image removed due to copyright.

**Figure 1.11:** Au 4f peaks of TPP-ligated  $Au_x$  (x=8,9,11,101) clusters on  $TiO_2$  (a) untreated and (b) calcined at 200 °C. Reproduced from reference<sup>99</sup>..

In many cases, XPS is also useful to determine removal of phosphine ligands. Several XPS studies show that the P 2p peak shifts to higher BEs due to the removal of phosphine ligands from the Au core and subsequent surface oxidation upon calcination. 95, 97, 99, 100, 106, 109, 135 The use of XPS to study

phosphine-ligated Au clusters is not only limited to initial and final state effects. Ahmad *et al.* used XPS to estimate the concentration of Au on the surface of WO<sub>3</sub> deduced from the electron mean free path.<sup>138</sup>

## 1.5.1.1.2.2 Ultraviolet Photoelectron Spectroscopy

UPS is a technique to study the electronic properties of a solid sample surface to a depth of 2–3 nm. <sup>83</sup> It can be used to determine the valence band and the work function of a solid sample surface. It is an important technique to study the behaviour of phosphine-ligated Au clusters as clusters or metals. UPS has been employed to measure the electronic structure of individual phosphine-protected Au clusters. A study by Boyen *et al.* investigated the valence band structure of the Au<sub>55</sub>(PPh<sub>3</sub>)<sub>12</sub>Cl<sub>6</sub> cluster and compared it to Au<sub>55</sub> after removal of ligands by exposure to X-ray photons over a long period of time. <sup>131</sup> They concluded from the UPS valence band spectrum that Au<sub>55</sub>(PPh<sub>3</sub>)<sub>12</sub>Cl<sub>6</sub> has an insulating behaviour; however, after ligand removal the spectrum shifted towards the Fermi energy with a similar spectral profile to Au films. It was concluded that the Au<sub>55</sub> cluster exhibited metallic behaviour after ligand removal due to the large size of Au<sub>55</sub> (1.4 nm). Recent research performed on the [Au<sub>13</sub>(dppe)<sub>5</sub>Cl<sub>2</sub>]<sup>3+</sup> cluster determined that the valence band was 1.9 eV, which was confirmed by UV-visible spectroscopy and DFT simulations. <sup>110</sup>

# 1.5.1.1.2.3 Metastable Impact Electron Spectroscopy

Another powerful technique to measure the electronic structure is metastable impact electron spectroscopy (MIES) using metastable helium atoms (He\*). The great benefit of MIES is that it only measures the electronic structure of the outermost layer of a sample. This is due to the He\* deexcitation process that only occurs within a few Å of the surface, which leads to emission of an electron with kinetic energy that can be measured.

The first MIES study on Au clusters was performed on phosphine-ligated Au clusters supported on ALD TiO<sub>2</sub> and SiO<sub>2</sub> via dip-coating conditions and followed by heating to remove the ligands. The reaction between the phosphine-ligated Au clusters and the two substrates after removal of the ligands was investigated using MIES and synchrotron XPS. It was found that the phosphine ligands react with the oxygen atoms of TiO<sub>2</sub> after heating, leading to oxidation of the phosphine species. Non-agglomerated clusters were only found for samples deposited with a concentration between 0.02 and 0.75 mM. In contrast, on SiO<sub>2</sub> there was no sign of interaction between the phosphine ligands and substrate and the Au clusters were fully agglomerated to large nanoparticles after heating.

Krishnan *et al.* performed MIES studies on Au<sub>9</sub>(PPh<sub>3</sub>)<sub>8</sub>(NO<sub>3</sub>)<sub>3</sub> and Au<sub>13</sub>(dppe)<sub>5</sub>Cl<sub>2</sub>Cl<sub>3</sub> deposited with several concentrations onto defect-rich ALD TiO<sub>2</sub>. <sup>109, 135</sup>. It was found that the formation of defects at the surface of ALD TiO<sub>2</sub> strongly reduced the tendency of the Au clusters to agglomerate. A

singular value decomposition (SVD) algorithm was applied to analyze a series of MIE spectra and separate them into reference spectra. They found reference spectra that represent (i) titania and (ii) Au clusters attached to the surface for both Au<sub>9</sub> and Au<sub>13</sub> deposited on ALD TiO<sub>2</sub>. An interesting finding was that the reference spectrum for Au<sub>13</sub> shifted closer to the Fermi level compared to Au<sub>9</sub>. The authors suggested that the increase in the number of atoms forming the Au cluster from 9 to 13 leads to a shift of the electronic states towards the Fermi level.

## 1.5.1.1.3 X-ray Absorption Spectroscopy

X-ray absorption spectroscopy (XAS) is a widely used tool for determining the interatomic distance, metal-ligand bond length and average coordination number that are otherwise impossible to obtain for non-crystalline compounds. Absorption spectra are measured by X-ray excitation of a core electron to an unoccupied orbital in an atom. X-ray absorption spectra tend to exhibit a sharp increase in absorption, called an edge. This absorption peak at the edge corresponds to a transition from the core level to the unoccupied valence states of an atom, which are sensitive to the local environment.

XAS is divided into two parts: the lower energy region, known as X-ray absorption near edge structure (XANES), and the higher energy region, known as extended X-ray absorption fine structure (EXAFS). XANES has two edges: rising edge (high-energy edges) and pre-edge (low-energy edges). The result of low-energy edges is usually referred to as near-edge X-ray absorption fine structure (NEXAFS). XANES is commonly employed to probe the oxidation states, symmetry, coordination environment, and density of states (DOS) while EXAFS is used to determine local atomic structure including bond length, coordination number and type of ligands. The versatility of XAS is made possible by simultaneous measurements with other techniques such as UV-visible and infrared spectroscopy, and small-angle X-ray scattering. The Au L<sub>3</sub>-edge is typically used to record EXAFS and XANES spectra in the range of 11,880 and 12,000 eV.

In the absence of single crystals, EXAFS is a powerful tool to establish a plausible structure. This is particularly true for Schmid's Au<sub>55</sub> cluster where the power sample is amorphous and cannot be grown into single crystals due to decomposition. Early works to investigate the structure and bonding in Schmid's Au<sub>55</sub> cluster utilized XAS.<sup>75, 76, 140</sup>. A measurement using Au L<sub>3</sub>-edge EXAFS revealed shorter A-Au distances (2.76–2.78 Å) in Au<sub>55</sub>(PPh<sub>3</sub>)<sub>12</sub>Cl<sub>6</sub> than in bulk gold and a mean coordination number of seven, which suggested a cuboctahedral structure.<sup>76</sup> This finding is in contrast with the result from powder X-ray diffraction (XRD) that assigned an icosahedra structure to the same cluster. A later investigation that combined EXAFS, XANES and wide angle X-ray scattering (WAXS) revealed a face-centered cubic structure characteristic of bulk gold.<sup>141</sup> Marcus *et al.* performed

temperature-dependent EXAFS measurements on Au<sub>55</sub>(PPh<sub>3</sub>)<sub>12</sub>Cl<sub>6</sub> and found that the cluster had 40% less thermal vibration compared to bulk gold due to stiffening of the Au-Au bonds in the cluster.<sup>75</sup>.

Menard *et al.* provided evidence for the structure of highly monodisperse mixed-ligand  $Au_{13}(PPh_3)_4(SR)_2Cl_2$  and  $Au_{13}(PPh_3)_4(SR)_4$  clusters using XAS. <sup>142</sup> They attributed the  $Au_{13}$  structure to an icosahedral structure with a size of 0.8 nm as observed by STEM. Changes in the EXAFS and XANES spectral features can provide a signature for the structural transformation or evolution of clusters. For example, Li *et al.* observed an icosahedral-to-cuboctahedral structural transformation of  $Au_{13}$  clusters for the first time using a solvent-exchange method. <sup>143</sup> The Fourier-transformed  $k^2\chi(k)$  function in hexane showed a significant reduction of the Au-ligand peak amplitude, a reduction in coordination number from 0.9 to 0.4, and a marked increase in the Au-Au peak intensity. These results suggest that changing the solvent from ethanol to hexane leads to rapid thiolate desorption from the  $Au_{13}$  core and then rearrangement of the core to a cuboctahedral structure.

An *in situ* XAS experiment by Kilmartin *et al.* followed the removal of phosphine ligands from Au<sub>6</sub>(Ph<sub>2</sub>P-*o*-tolyl)<sub>6</sub>(NO<sub>3</sub>)<sub>2</sub> clusters at low temperature by organic hydrogen peroxide.<sup>144</sup> It was observed that after the addition of peroxide, the coordination number of Au-P decreased from 1.6 to ~0.35 and that of Au-Au increased from 3.5 to 8.7, suggesting removal of the ligands and the appearance of metallic gold. The authors concluded that the removal of the ligand had occurred gradually.

Doping of Au clusters with a transition metal atom can change the fluxional nature of Au clusters. For instance, structural isomerization of  $[Au_9(PPh_3)_8]^{3+}$  between the crown and the butterfly structures is inhibited by substituting the central Au atom of  $[Au_9(PPh_3)_8]^{3+}$  with a single Pd atom to produce a preferred AuPd<sub>8</sub> crown structure. This was demonstrated by analyzing the Debye–Waller factors of the radial and lateral Au–Au(Pd) bonds as a function of temperature using Fourier transformed-EXAFS. It was found that the bond strength for both the radial Au-Pd and lateral Au-Au bonds in PdAu<sub>8</sub> are stiffened compared to the Au–Au bonds in Au<sub>9</sub> due to the central Pd atom doping.

One XAS study by Liu *et al.* investigated the correlation between the electronic and geometric structure of Au<sub>25</sub>(PPh<sub>3</sub>)<sub>10</sub>(SR)<sub>5</sub>Cl<sub>2</sub> and Au<sub>25</sub>(SR)<sub>18</sub> clusters and their catalytic activity.<sup>146</sup> The authors found that the d-bond electrons of the clusters are affected by the variation of the ligands. It was suggested that the differences in the d-band unoccupied-state populations are correlated with the differences in catalytic activity and selectivity of these clusters. More recently, the ligand effect on the Au 5d electronic state in [Au<sub>9</sub>(PPh<sub>3</sub>)<sub>8</sub>]<sup>3+</sup> and [Au<sub>25</sub>(SC<sub>2</sub>H<sub>4</sub>Ph)<sub>18</sub>]<sup>-</sup> has been reported by Matsuyama *et al.*<sup>147</sup> The authors concluded that the interaction between the unoccupied 5d orbitals with the S/P

3s+3p orbitals lead to different peak positions in the XANES spectra of both clusters; the white-line peak of Au<sub>9</sub> is higher by 3 eV than that of Au<sub>25</sub>.

Etching of Au clusters is a process to synthesis polydisperse Au-ligand clusters by treating for a period in a reactant. Understanding the etching mechanism during the formation of Au clusters is central for rational design and synthesis of clusters in future. The research group of Wei reported a number of studies using *in situ* XAS to study the structure and composition of Au clusters during cluster formation. <sup>148-150</sup> The formation process of monodisperse Au<sub>13</sub>(L<sub>3</sub>)<sub>4</sub>Cl<sub>4</sub> with HCl etching of a polydisperse mixture was traced using *in situ* XAS. The XANES spectra in Figure 1.12a shows the white line peak at 11,926 eV, which emerges from the excitation of Au 2p<sub>3/2</sub> electrons to the unoccupied Au 5d state, is strengthened immediately after addition of HCl (0 to 0.5 h). This is assumed to be due to the charge transfer from Au atoms to the Cl<sup>-</sup> ligands. Figure 1.12b shows EXAFS spectra with the Au-ligand peak at 1.90 Å intensified and the Au-Au peaks at 2.36 and 2.88 Å decreased after the addition of HCl. This indicates the decomposition of the larger Au clusters into smaller intermediates. The changes in the XANES and EXAFS spectra continued over the reaction time but not as markedly as the first hour. The same group showed the formation process of monodisperse Au<sub>13</sub>(L<sub>3</sub>)<sub>2</sub>(SR)<sub>4</sub>Cl<sub>4</sub> (Au<sub>13</sub>) mixed-ligand clusters, <sup>150</sup> observing that the formation of Au<sub>13</sub> clusters occurred in three steps: etching, growth and rearrangement.

Image removed due to copyright.

**Figure 1.12:** Time-dependent a) XANES and b) EXAFS spectra, (c) coordination number, (d) bond distance R, and (e) Debye-Waller factor for the Au-P/Cl and Au-Au coordination pairs extracted from EXAFS curve-fitting against reaction time. Reproduced from reference<sup>148</sup>.

Several studies have used XAS to determine the change in size of supported clusters after removal of the ligands. <sup>95, 100, 136</sup> It has been demonstrated that the properties of the support play a crucial role in the stability of surface-supported gold phosphine clusters. Donoeva and co-workers demonstrated that thermal treatment of Au<sub>9</sub> clusters on Brønsted acidic supports such as carbon and SiO<sub>2</sub> leads to fragmentation into isolated Au-ligand species as manifested by the absence of an Au-Au bond in the EXAFS spectra. <sup>137</sup> In contrast, phosphine ligand migration from Au<sub>9</sub> clusters to CeO<sub>2</sub> was signified by the absence of an Au-P peak, which also resulted in the formation of an active catalyst.

# 1.5.2 Challenges in Co-catalysts

#### 1.5.2.1 Back Reactions

The nature of photocatalytic water splitting works using semiconductors modified with co-catalyst materials as H<sub>2</sub> or O<sub>2</sub> evolution sites has been explained. In particular, the H<sub>2</sub> evolution co-catalysts promote the hydrogen evolution reaction. Concurrently, it is active for inhibited reactions, including the oxygen photoreduction reaction (ORR) (Figure 1.13D) and water formation from H<sub>2</sub> and O<sub>2</sub> (Figure 1.13C), which affects the hydrogen generation rates<sup>5, 151</sup>. The ORR occurs on the co-catalysts during the water splitting reaction by reducing H<sup>+</sup> with O<sub>2</sub> to form water. In contrast, the water formation of H<sub>2</sub> and O<sub>2</sub> can take-place on the co-catalysts under dark condition. These inhibited reactions occur due to the close location of H<sub>2</sub> and O<sub>2</sub> evolution sites in photocatalytic systems. It should be noted that the inhibited reactions are also referred to in the literature as back reactions, reverse reactions and backward reactions. Enhancing the hydrogen evolution with concurrent blocking of the back reactions is challenging.

Image removed due to copyright.

**Figure 1.13:** Possible reactions that could occur during a photocatalytic water splitting reaction over a photocatalyst modified with co-catalysts: (a)  $H_2$  evolution, (b)  $O_2$  evolution, (c) water formation from  $H_2$  and  $O_2$  (back reaction), and (d) oxygen photoreduction reaction. Reproduced from reference<sup>152</sup>.

#### 1.5.2.2 Stability of Co-catalyst

The catalytic activity of a co-catalyst-modified photocatalyst depends on the nature of the co-catalyst. It has been discussed above how the size of the noble-metal co-catalyst play a critical role in photocatalytic water splitting activity. Thus, the size stability of noble-metal as co-catalyst-modified photocatalyst is essential to preserve the efficiency of photocatalytic activity. However, it has been reported that noble-metal NPs and NCs as co-catalyst-modified photocatalyst tends to agglomerate during the preparation treatment or photocatalysis process. For example, the Au<sub>8</sub>, Au<sub>25</sub> and Au<sub>24</sub>Pt alloy NCs modified photocatalysts were reported to aggregate during the calcination treatment to

remove the ligands<sup>66, 153, 154</sup>. Also, the same phenomenon was observed other sizes of Au<sub>n</sub> NCs (*n*= 22, 29, 33 and 39) on BaLa<sub>4</sub>Ti<sub>4</sub>O<sub>15</sub><sup>67</sup>. Furthermore, the agglomeration of clusters co-catalyst is largely observed during photocatalysis. For example, the size of Au<sub>25</sub> modified SrTiO<sub>3</sub> and BaLa<sub>4</sub>Ti<sub>4</sub>O<sub>15</sub> was increased after photocatalysis (10 h of irradiation) from 1.2 nm to 4.2 and 7.0 nm, respectively<sup>68</sup>. The agglomeration of clusters is assumed due to the weak interaction between the cluster and photocatalyst. Therefore, improving the stability of clusters co-catalyst-modified photocatalyst is of practical significance in photocatalysis applications to maintain the catalysis properties of the co-catalyst.

# 1.6 Metal Oxide Layers for Photocatalytic Water Splitting

### 1.6.1 Nickel Oxide Layer to Suppress Back Reactions

A successful strategy of blocking the back reactions on hydrogen evolution co-catalysts is using an overlayer metal oxide. Early discovery of suppression of back reactions using metal oxide layer was by Domen and co-workers in 1986<sup>155</sup>. They found that reducing NiO to metallic Ni and then reoxidising at 200°C will result in Ni–NiO core-shell structure (Figure 1.14). In Ni–NiO structure, during photocatalytic water splitting, the core receives electrons from the SrTiO<sub>3</sub> and acts as H<sub>2</sub> evolution sites, while the NiO layer suppresses O<sub>2</sub> from reaching the metallic Ni core and causing back reactions such as ORR and water formation.

Image removed due to copyright.

**Figure 1.14:** Schematic illustration the  $NiO_x/SrTiO_3$  photocatalyst's structure after various treatments. Reproduced from reference<sup>151</sup>.

## 1.6.2 Chromium Oxide Layer to Suppress Back Reactions

Ni–NiO structure has encouraged researchers to develop a technique to deposit metal oxide nanolayer onto various  $H_2$  evolution co-catalysts that prevents oxygen from reaching the co-catalysts and initiating back reactions. Maeda and co-workers reported the first formation of the  $Cr_2O_3$  layer onto

metallic Rh and other noble metals with a core-shell structure to block the back reactions  $^{156}$ . The  $Cr_2O_3$  layer is formed around metallic Rh with a thickness of 2 nm using the photodeposition method (Figure 1.15a). It was demonstrated that protons and the hydrogen molecules are permeable through the  $Cr_2O_3$  layer, but not the oxygen, which suppresses the back reactions that involve oxygen molecules on the metallic Rh (see Figure 1.15b) $^{156,157}$ . As a result, the Rh-loaded  $(Ga_{1-x}Zn_x)(N_{1-x}O_x)$  without  $Cr_2O_3$  was almost inactive for water splitting due to the back reactions, while a successful overall water splitting was observed with the  $Cr_2O_3$  layer (Figure 1.15c). In 2023, the highest STH efficiency for the overall photocatalytic water splitting reaction was reported using Rh/ $Cr_2O_3$  and  $Co_3O_4$  loaded InGaN/GaN nanowires $^{11}$ . The high efficiency here is attributed to the role of the  $Cr_2O_3$  layer in inhibiting back reactions.

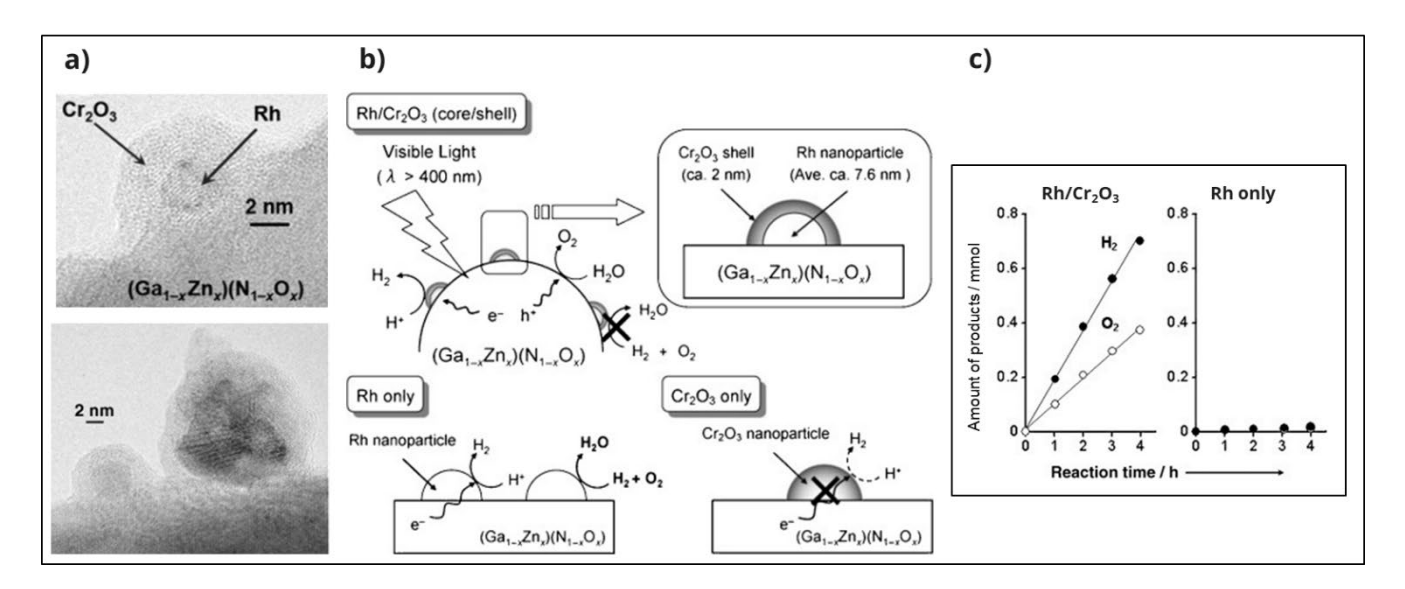


**Figure 1.15:** a) HR-TEM images of  $Rh/Cr_2O_3$ -loaded( $Ga_{1-x}Zn_x$ )( $N_{1-x}O_x$ ), b) schematic reaction mechanism and c) time courses of overall water splitting on  $Rh/Cr_2O_3$  loaded ( $Ga_{1-x}Zn_x$ )( $N_{1-x}O_x$ ). Modified from reference<sup>156</sup>.

The Cr<sub>2</sub>O<sub>3</sub> layer with core/shell structure has also promoted photocatalytic water splitting when photodeposited onto different co-catalyst materials such as platinum<sup>158</sup>, palladium<sup>159</sup>, iridium<sup>160</sup> and gold<sup>152</sup>. The promotion of the photocatalytic water splitting reaction was due to the suppression of back reactions on hydrogen evolution co-catalysts.

Recently, it was reported that the  $Cr_2O_3$  layer with Au cluster showed a remarkable improvement in photocatalytic activity using a new procedure of forming a  $Cr_2O_3$  shell on the Au clusters (Figure 1.16)<sup>152</sup>. In this procedure, the  $Cr_2O_3$  layer was first photodeposited onto  $BaLa_4Ti_4O_{15}$  and then  $Au_{25}$  clusters were adsorbed on the surface, followed by heating at  $300^{\circ}C$  under vacuum pressure. As a result, the  $Au_{25}$  was embedded into the  $Cr_2O_3$  layer during heating via the strong metal–support interaction (SMSI) effect (Figure 1.16c). The  $Au_{25}$ - $Cr_2O_3$ - $BaLa_4Ti_4O_{15}$  water splitting photocatalyst

was about 19 times higher than that without a  $Cr_2O_3$  shell. The improvement of the activity is induced by the suppression of the ORR using the  $Cr_2O_3$  layer. Further, the  $Cr_2O_3$  layer improved the photocatalytic activity and helped to stabilise the size of  $Au_{25}$  clusters after removing the thiolate ligands (see HR-TEM Figure 1.16)<sup>152</sup>.

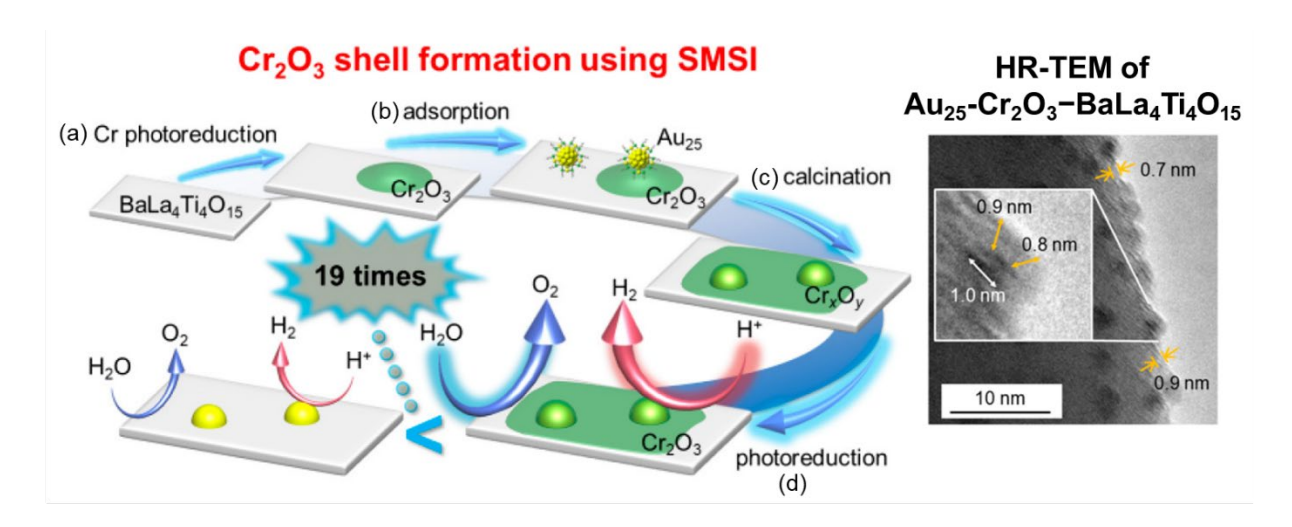


**Figure 1.16:** Schematic of the new procedure of forming a  $Cr_2O_3$  layer using SMSI effect with a HR-TEM image of  $Au_{25}$ - $Cr_2O_3$ - $BaLa_4Ti_4O_{15}$ . Modified from reference  $^{152}$ .

# 1.6.3 Other Metal Oxide Layers

In addition to the Cr<sub>2</sub>O<sub>3</sub> layer, other oxide layers have been developed to block the back reactions such as lanthanoid(III) oxide <sup>161</sup>, SiO<sub>2</sub> <sup>162</sup>, TiO<sub>2</sub> <sup>163</sup>, MoO<sub>x</sub> <sup>158</sup> and Ta<sub>2</sub>O<sub>5</sub> <sup>164</sup>. Table 1.3 summarises the oxide layers deposited onto photocatalysts for a one-step photoexcitation overall water splitting system to block the back reactions reported to date, including deposition method, thickness and structure of oxide layer and type of co-catalyst and photocatalyst.

Table 1.3: One-step-excitation overall water splitting using overlayer to block the back reaction up to date

Photocatalyst	Photocatalyst Deposition method of Co-catalyst		Overlayer Thickness		Deposition method of overlayer	Structure	Ref
$(Ga_{1-x}Zn_x)(N_{1-x}O_x)$	Photodeposition	Rh NPs Pd NPs Ir NPs Pt NPs	Cr <sub>2</sub> O <sub>3</sub>	1-2 nm	Photodeposition	Core/Shell	156, 157, 165- 169
$(Ga_{1-x}Zn_x)(N_{1-x}O_x)$	Adsorption	Rh NPs with sodium 3- mercapto-1- propanesulfonate ligands	Cr <sub>2</sub> O <sub>3</sub>	2 nm	Photodeposition	Core/Shell	170- 172
$(Ga_{1-x}Zn_x)(N_{1-x}O_x)$	Adsorption	Rh NPs with polyvinylpyrrolidone protected polymer	Cr <sub>2</sub> O <sub>3</sub>	2 nm	Photodeposition	Core/Shell	173
$(Ga_{1-x}Zn_x)(N_{1-x}O_x)$	Electroless deposition	Rh NPs	La-oxide Pr-oxide Sm-oxide Gd-oxide Dy-oxide Ce-oxide Eu-oxide	-	Electroless deposition	Layer	161
$(Ga_{1-x}Zn_x)(N_{1-x}O_x)$ Nanotubes	Photodeposition	Rh NPs	Cr <sub>2</sub> O <sub>3</sub>	-	Photodeposition	Core/Shell	174
$(Ga_{1-x}Zn_x)(N_{1-x}O_x)$	Atomic Layer Deposition (ALD)	Pd NPs	Cr <sub>2</sub> O <sub>3</sub>	-	Photodeposition	Core/Shell	159
$(Ga_{1-x}Zn_x)(N_{1-x}O_x)$ Reduced Graphene Oxide (RGO)	Photodeposition	Rh NPs	Cr <sub>2</sub> O <sub>3</sub>	-	Photodeposition	Core/Shell	175
BaLa <sub>4</sub> TiO <sub>15</sub>	Adsorption	Au <sub>25</sub> (SG) <sub>18</sub>	Cr <sub>2</sub> O <sub>3</sub>	0.7-0.9 nm	Photodeposition	Layer	152
BaLa <sub>4</sub> TiO <sub>15</sub>	Adsorption	Au <sub>25</sub> (PET) <sub>18-y</sub> (p-MBA) <sub>y</sub> Au <sub>24</sub> Pd(PET) <sub>18-y</sub> (p-MBA) <sub>y</sub> Au <sub>24</sub> Pt(PET) <sub>18-y</sub> (p-MBA) <sub>y</sub>	Cr <sub>2</sub> O <sub>3</sub>	1.25 nm	Photodeposition	Layer	153
BaLa <sub>4</sub> TiO <sub>15</sub>	Adsorption	Au <sub>25</sub> (PET) <sub>18</sub>	Cr <sub>2</sub> O <sub>3</sub>	-	Photodeposition	Layer	176
BaLa <sub>4</sub> TiO <sub>15</sub>	Adsorption	Rh-SG complex	Cr <sub>2</sub> O <sub>3</sub>	-	Photodeposition	Layer	177
Ba <sub>5</sub> Ta <sub>4</sub> O <sub>15</sub>	Photodeposition	Rh NPs	Cr <sub>2</sub> O <sub>3</sub>	2 -3 nm	Photodeposition	Core/Shell	178

Ba <sub>5</sub> Ta <sub>4</sub> O <sub>15</sub> nanofibers	Photodeposition	Rh NPs	Cr <sub>2</sub> O <sub>3</sub>	-	Photodeposition	Core/Shell	179, 180
Ba <sub>5</sub> Ta <sub>4</sub> O <sub>15</sub> -Ba <sub>3</sub> Ta <sub>5</sub> O <sub>15</sub> - BaTa <sub>2</sub> O <sub>6</sub> composites	Photodeposition	Rh NPs	Cr <sub>2</sub> O <sub>3</sub>	2 -3 nm	Photodeposition	Core/Shell	181, 182
Ba <sub>5</sub> Ta <sub>4</sub> O <sub>15</sub> -Ba <sub>3</sub> Ta <sub>5</sub> O <sub>15</sub> composite nanofibers	Photodeposition	Rh NPs	Cr <sub>2</sub> O <sub>3</sub>	-	Photodeposition	Core/Shell	183
Ba <sub>5</sub> Ta <sub>2</sub> Nb <sub>2</sub> O <sub>15</sub> nanofibers	Photodeposition	Rh NPs	Cr <sub>2</sub> O <sub>3</sub>	-	Photodeposition	Core/Shell	180
Ba <sub>5</sub> Ta <sub>4</sub> <b>Nb</b> <sub>2</sub> O <sub>15</sub> nanofibers	Photodeposition	Rh NPs	Cr <sub>2</sub> O <sub>3</sub>	-	Photodeposition	Core/Shell	180
BaTaO <sub>2</sub> N:Mg	Impregnation	Rh NPs Pt NPs	Cr <sub>2</sub> O <sub>3</sub>	-	Photodeposition	Core/Shell	184
BaTiO <sub>3</sub> /Au single crystal	Photodeposition	Rh NPs	Cr <sub>2</sub> O <sub>3</sub>	-	Photodeposition	Core/Shell	185
CaTaO₂N	Impregnation	Rh-Cr NPs	Metal oxyhydroxide - TiO <sub>2</sub>	-	Photodeposition	Layer	186
Ca <sub>2</sub> Nb <sub>2.99</sub> Rh <sub>0.01</sub> O <sub>10</sub> nanosheets	Solution	Rh single atom	NiO <sub>x</sub>	0.5 nm	Photodeposition	Layer	187
GaN nanowires	Photodeposition	Rh NPs	Cr <sub>2</sub> O <sub>3</sub>	-	Photodeposition	Core/Shell	188, 189
GaN:Mg nanowires	Photodeposition	Rh NPs	Cr <sub>2</sub> O <sub>3</sub>	-	Photodeposition	Core/Shell	190, 191
Ga <sub>2</sub> O <sub>3</sub>	Photodeposition	MoO <sub>x</sub>	Cr <sub>2</sub> O <sub>3</sub>	-	Photodeposition	Layer	192
$Ga_2O_3$	Photodeposition	Rh NPs	Cr <sub>2</sub> O <sub>3</sub>	-	Photodeposition	Core/Shell Partly covered <sup>193</sup>	193- 195
Ga <sub>2</sub> O <sub>3</sub> :Zn	Photodeposition	Rh NPs	Cr <sub>2</sub> O <sub>3</sub>	-	Photodeposition	Core/Shell	194
g-C <sub>3</sub> N <sub>4</sub>	Impregnation	Pt NPs	mixed alkali- metal-oxides - KO <sub>x</sub> - NaO <sub>x</sub> - LiO <sub>x</sub>	-	Impregnation	Core/Shell	196
InGaN/GaN nanowire	Photodeposition	Rh NPs	Cr <sub>2</sub> O <sub>3</sub>	2-3 nm	Photodeposition	Core/Shell	11, 197 198
In <sub>0.26</sub> Ga <sub>0.74</sub> N:Mg nanowire	Photodeposition	Rh NPs	Cr <sub>2</sub> O <sub>3</sub>	-	Photodeposition	Core/Shell	24
$LaMg_{1/3}Ta_{2/3}O_2N$	Impregnation	Rh-Cr NPs	Metal oxyhydroxide - TiO <sub>2</sub> - SiO <sub>2</sub>	-	Photodeposition	Layer	163, 199

$LaSc_{x}Ta_{1-x}O_{1+2x}N_{2-2x}$	Impregnation	Rh-Cr NPs	Metal oxyhydroxide - TiO <sub>2</sub>	-	Photodeposition	Layer	200
La <sub>0.02</sub> Na <sub>0.98</sub> TaO <sub>3</sub>	Impregnation	Pd NPs	NiO	0.3-1.8 nm	Impregnation	Core/Shell	201
SrTiO <sub>3</sub>	Impregnation	Pt NPS	MoO <sub>x</sub>	-	Photodeposition	Layer	158
SrTiO <sub>3</sub>	Impregnation	Au <sub>9</sub> (PPh <sub>3</sub> ) <sub>8</sub> (NO <sub>3</sub> ) <sub>3</sub>	CrO <sub>x</sub>	2 nm	Photodeposition	Layer	202
SrTiO <sub>3</sub>	Photodeposition	Pt NPs Cu NPs Au NPs Ag NPs Ir NPs Rh NPs Pd NPs	Cr <sub>2</sub> O <sub>3</sub>	3 nm	Photodeposition	Core/Shell for Au and Pd	203- 206
SrTiO <sub>3</sub>	Wet impregnation	Pt NPs	Cr <sub>2</sub> O <sub>3</sub>	2 nm	Photodeposition	Layer	207, 208
SrTiO <sub>3</sub>	Wet impregnation	Pt NPs	Microporous SiO <sub>2</sub>	7 nm	Photodeposition	Core/Shell	162
SrTiO <sub>3</sub> :Al	Wet impregnation	Rh NPs	Cr <sub>2</sub> O <sub>3</sub>	-	Photodeposition	Core/Shell	209
SrTiO <sub>3</sub> :Al	Photodeposition	Rh NPs	Cr <sub>2</sub> O <sub>3</sub>	-	Photodeposition	Core/Shell	49, 210- 212
SrTiO <sub>3</sub> :Al	Photodeposition	Pt NPs	Cr <sub>2</sub> O <sub>3</sub>	-	Photodeposition	Core/Shell	213
SrTiO <sub>3</sub> :Al	1- Liquid-phase adsorption 2- Impregnation 3- Photodeposition	PtRu alloy NPs	Cr <sub>2</sub> O <sub>3</sub>	-	Photodeposition	Core/Shell	214
SrTiO <sub>3</sub> :Al	Photodeposition- phosphorization	СоР	Cr <sub>2</sub> O <sub>3</sub>	-	Photodeposition	-	215
SrTiO <sub>3</sub> :Na	Impregnation	Rh NPs	Cr <sub>2</sub> O <sub>3</sub>	-	Photodeposition	Core/Shell	216
SrTiO3:La,Al	Photodeposition	Rh NPs	Cr <sub>2</sub> O <sub>3</sub>	-	Photodeposition	Core/Shell	217
SrTiO <sub>3</sub> :Sc	Impregnation	Rh <sub>2</sub> O <sub>3</sub>	Metal oxyhydroxide - TiO <sub>2</sub> - Nb <sub>2</sub> O <sub>5</sub> - Ta <sub>2</sub> O <sub>5</sub>	-	Photodeposition	Layer	164

Ta <sub>3</sub> N <sub>5</sub> /KTaO <sub>3</sub>	Photodeposition	Rh NPs Pt NPs Ir NPs Ru NPs	Cr <sub>2</sub> O <sub>3</sub>	-	Photodeposition	Core/Shell	160
TiO <sub>2</sub> (anatase)	Photodeposition	Rh NPs	Cr <sub>2</sub> O <sub>3</sub>	-	Photodeposition	Core/Shell	218
$Y_2Ti_2O_5S_2$	Photodeposition	Rh NPs	Cr <sub>2</sub> O <sub>3</sub>	-	Photodeposition	Core/Shell	219
ZrO <sub>2</sub> /TaON	Impregnation	RuO <sub>x</sub> NPs	Cr <sub>2</sub> O <sub>3</sub>	1-2 nm	Photodeposition	Core/Shell	220
Zr-TaON/Ta <sub>3</sub> N <sub>5</sub>	Impregnation	Ru NPs Rh NPs Pt NPs	Cr <sub>2</sub> O <sub>3</sub>	-	Photodeposition	Core/Shell	221

# 1.7 Applications of Metal Oxide Layers for Other Photocatalysis Reactions

The usage of oxide layers to prevent the inhibited reactions is not limited to overall photocatalytic water splitting reaction but is also applicable for other photocatalytic reactions. For example, Ag loaded Ga<sub>2</sub>O<sub>3</sub> is used for photocatalytic conversion of CO<sub>2</sub> into CO with H<sub>2</sub>O as an electron donor<sup>222-225</sup>. The Ag co-catalysts improve the reduction of CO<sub>2</sub> into CO, but it is also active for the back reaction, which is the oxidation of CO into CO<sub>2</sub>. The modification of the Cr<sub>2</sub>O<sub>3</sub> layer on the Ag co-catalyst has significantly enhanced the photocatalytic conversion of CO<sub>2</sub> into CO by suppressing the CO and O<sub>2</sub> to form into CO<sub>2</sub>. The Cr<sub>2</sub>O<sub>3</sub> layer has also been demonstrated to block the back reaction for other photocatalytic reactions by preventing the O<sub>2</sub> from reaching the co-catalyst<sup>226-228</sup>. Table 1.4 summarises the usage of oxide layers to block the back reaction in a one-step photoexcitation system for other photocatalytic reactions.

*Table 1.4:* Overlayer procedure used with other photocatalytic reactions to block the back reaction (contact of  $O_2$  to co-catalyst).

Photocatalyst	Deposition method of Co-catalyst	Co-catalyst	Overlayer	Deposition method of overlayer	Structure	Photocatalytic reaction	Ref
GaN nanowires	Photodeposition	Rh NPs	Cr <sub>2</sub> O <sub>3</sub>	Photodeposition	Core/Shell	Reduction of CO <sub>2</sub> to CH <sub>4</sub> and CO	229
g-C <sub>3</sub> N <sub>4</sub> nanosheets	Photodeposition	Pt NPs	CrO <sub>x</sub>	Photodeposition	Core/Shell	H <sub>2</sub> production from aqueous solutions containing different electron donors.	230
Ga <sub>2</sub> O <sub>3</sub>	Photodeposition	Ag NPs	Cr(OH) <sub>3</sub>	Photodeposition	Core/Shell	Reduction of CO <sub>2</sub> to CO	222- 225
Ga <sub>2</sub> O <sub>3</sub> :Ca	Photodeposition	Ag NPs	Cr(OH) <sub>3</sub>	Photodeposition	Core/Shell	Reduction of CO <sub>2</sub> to CO	231
AgTaO <sub>3</sub>	Impregnation	Rh NPs Pt NPs Ag NPs	CrO <sub>x</sub>	Photodeposition	Core/Shell	Reduction of CO <sub>2</sub> to CH <sub>4</sub> and CO	232
SrTiO <sub>3</sub>	Photodeposition	Rh NPs	Cr <sub>2</sub> O <sub>3</sub>	Photodeposition	Core/Shell	H <sub>2</sub> production with mineralization of 4-chlorophenol	226
$(Ga_{1-x}Zn_x)(N_{1-x}O_x)$ nanowires	Photodeposition	Rh NPs	Cr <sub>2</sub> O <sub>3</sub>	Photodeposition	Core/Shell	H <sub>2</sub> production using H <sub>2</sub> SO <sub>4</sub> aqueous solution	227
TiO <sub>2</sub>	Photodeposition	Au NPs	Cr <sub>2</sub> O <sub>3</sub>	Photodeposition	Core/Shell	Oxidation of carbon monoxide	233
Au/TiO <sub>2</sub> nanodumbell	Photodeposition	Pd NPs	Cr <sub>2</sub> O <sub>3</sub>	Photodeposition	Layer	O <sub>2</sub> production using Na <sub>2</sub> S <sub>2</sub> O <sub>8</sub>	228

# 1.8 Thesis Outline

Researching metal oxide overlayers on photocatalyst and co-catalyst-modified photocatalyst is paramount in developing an efficient photocatalyst that prevents back reactions and stabilises the photocatalysis reaction. Moreover, the application of a thin metal oxide layer on the top of a co-catalyst-modified photocatalyst is an interesting concept to inhibit the size increase of the co-catalyst. This thesis aims to perform physical, chemical, electronic and catalytic studies on the chromium oxide layer formed onto photocatalysts and Au cluster-modified photocatalysts.

This thesis comprises eight chapters, structured as follows. Chapter 2 describes the main experimental techniques used in this thesis and provides the details of the data analysis for each method. In Chapter 3, the first experimental study investigates the stability of the  $CrO_x$  layer onto different phases of  $TiO_2$  film upon annealing. Chapter 4 expands the stability investigation of  $CrO_x$  onto P25,  $BaLa_4Ti_4O_{15}$  and  $Al:SrTiO_3$  particles, along with electronic and catalytic studies. Chapter 5 focuses on the application of the  $CrO_x$  layer on the top of the phosphine-protected  $Au_9$  cluster-modified radio frequency (RF)-sputter deposited  $TiO_2$  film. Chapter 6 discusses the change in surface roughness upon heating two different thicknesses of RF-sputter deposited  $TiO_2$  films and its influence on the stability of  $Au_9$  clusters beneath a  $CrO_x$  layer. Chapter 7 focuses on the stability of phosphine-protected  $Au_9$  clusters on  $SrTiO_3$  particles with and without a  $CrO_x$  layer under a photocatalytic water splitting reaction. Chapter 8 concludes the thesis and provides directions for future research.

## 1.9 References

- 1. Schreck, M.; Niederberger, M., Photocatalytic Gas Phase Reactions. *Chemistry of Materials* **2019,** *31* (3), 597-618.
- 2. Siegmund, P.; Abermann, J.; Baddour, O.; Canadell, P.; Cazenave, A.; Derksen, C.; Garreau, A.; Howell, S.; Huss, M.; Isensee, K., The global climate in 2015–2019. *WMO* **2019**.
- 3. Lewis, N. S., Toward cost-effective solar energy use. *science* **2007**, *315* (5813), 798-801.
- 4. Tüysüz, H.; Chan, C. K.; Tüysüz, H., Solar energy for fuels. Springer: 2016.
- 5. Wang, Q.; Domen, K., Particulate Photocatalysts for Light-Driven Water Splitting: Mechanisms, Challenges, and Design Strategies. *Chemical Reviews* **2020**, *120* (2), 919-985.
- 6. Ibrahim, A. A., Hydrogen production from light hydrocarbons. InTech: 2018.
- 7. da Silva Veras, T.; Mozer, T. S.; da Costa Rubim Messeder dos Santos, D.; da Silva César, A., Hydrogen: Trends, production and characterization of the main process worldwide. *International Journal of Hydrogen Energy* **2017**, *42* (4), 2018-2033.
- 8. Fujishima, A.; Honda, K., Electrochemical photolysis of water at a semiconductor electrode. *Nature* **1972**, *238* (5358), 37-8.
- 9. Nadeem, M. A.; Khan, M. A.; Ziani, A. A.; Idriss, H., An Overview of the Photocatalytic Water Splitting over Suspended Particles. *Catalysts* **2021**, *11* (1).
- 10. Wang, Z.; Li, C.; Domen, K., Recent developments in heterogeneous photocatalysts for solar-driven overall water splitting. *Chemical Society Reviews* **2019**, *48* (7), 2109-2125.
- 11. Zhou, P.; Navid, I. A.; Ma, Y.; Xiao, Y.; Wang, P.; Ye, Z.; Zhou, B.; Sun, K.; Mi, Z., Solar-to-hydrogen efficiency of more than 9% in photocatalytic water splitting. *Nature* **2023**, *613* (7942), 66-70.
- 12. Chen, S.; Takata, T.; Domen, K., Particulate photocatalysts for overall water splitting. *Nature Reviews Materials* **2017**, *2*, 17050.
- 13. Li, X.; Yu, J.; Jaroniec, M.; Chen, X., Cocatalysts for Selective Photoreduction of CO2 into Solar Fuels. *Chemical Reviews* **2019**, *119* (6), 3962-4179.
- 14. Hisatomi, T.; Takanabe, K.; Domen, K., Photocatalytic Water-Splitting Reaction from Catalytic and Kinetic Perspectives. *Catalysis Letters* **2015**, *145* (1), 95-108.
- 15. Colmenares, J. C.; Xu, Y.-J., *Heterogeneous Photocatalysis*. Springer: Heidelberg: Green Chemistry and Sustainable Technology, 2016.
- 16. Melchionna, M.; Fornasiero, P., Updates on the Roadmap for Photocatalysis. *ACS Catalysis* **2020,** *10* (10), 5493-5501.
- 17. Yuan, L.; Geng, Z.; Xu, J.; Guo, F.; Han, C., Metal-Semiconductor Heterostructures for Photoredox Catalysis: Where Are We Now and Where Do We Go? *Advanced Functional Materials* **2021**, *31* (27), 2101103.
- 18. Singh, R.; Dutta, S., A review on H2 production through photocatalytic reactions using TiO2/TiO2-assisted catalysts. *Fuel* **2018**, *220*, 607-620.
- 19. Li, R.; Li, C., Chapter One Photocatalytic Water Splitting on Semiconductor-Based Photocatalysts. In *Advances in Catalysis*, Song, C., Ed. Academic Press: 2017; Vol. 60, pp 1-57.
- 20. Kumar, A.; Kumar, A.; Krishnan, V., Perovskite Oxide Based Materials for Energy and Environment-Oriented Photocatalysis. *ACS Catalysis* **2020**, *10* (17), 10253-10315.
- 21. Choi, W.; Termin, A.; Hoffmann, M. R., The Role of Metal Ion Dopants in Quantum-Sized TiO2: Correlation between Photoreactivity and Charge Carrier Recombination Dynamics. *The Journal of Physical Chemistry* **1994**, *98* (51), 13669-13679.
- 22. Yanagi, R.; Zhao, T.; Solanki, D.; Pan, Z.; Hu, S., Charge Separation in Photocatalysts: Mechanisms, Physical Parameters, and Design Principles. *ACS Energy Letters* **2022**, *7* (1), 432-452.
- 23. Marschall, R., Semiconductor Composites: Strategies for Enhancing Charge Carrier Separation to Improve Photocatalytic Activity. *Advanced Functional Materials* **2014**, *24* (17), 2421-2440.

- 24. Kibria, M. G.; Chowdhury, F. A.; Zhao, S.; AlOtaibi, B.; Trudeau, M. L.; Guo, H.; Mi, Z., Visible light-driven efficient overall water splitting using p-type metal-nitride nanowire arrays. *Nature Communications* **2015**, *6* (1), 6797.
- 25. Kato, H.; Asakura, K.; Kudo, A., Highly Efficient Water Splitting into H2 and O2 over Lanthanum-Doped NaTaO3 Photocatalysts with High Crystallinity and Surface Nanostructure. *Journal of the American Chemical Society* **2003**, *125* (10), 3082-3089.
- 26. Kudo, A.; Miseki, Y., Heterogeneous photocatalyst materials for water splitting. *Chemical Society Reviews* **2009**, *38* (1), 253-278.
- 27. Iwase, A.; Kato, H.; Okutomi, H.; Kudo, A., Formation of Surface Nano-step Structures and Improvement of Photocatalytic Activities of NaTaO3 by Doping of Alkaline Earth Metal Ions. *Chemistry Letters* **2004**, *33* (10), 1260-1261.
- 28. Zhang, J.; Li, M.; Feng, Z.; Chen, J.; Li, C., UV Raman Spectroscopic Study on TiO2. I. Phase Transformation at the Surface and in the Bulk. *The Journal of Physical Chemistry B* **2006**, *110* (2), 927-935.
- 29. Zhang, J.; Xu, Q.; Feng, Z.; Li, M.; Li, C., Importance of the Relationship between Surface Phases and Photocatalytic Activity of TiO2. *Angewandte Chemie International Edition* **2008**, *47* (9), 1766-1769.
- 30. Li, R.; Zhang, F.; Wang, D.; Yang, J.; Li, M.; Zhu, J.; Zhou, X.; Han, H.; Li, C., Spatial separation of photogenerated electrons and holes among {010} and {110} crystal facets of BiVO4. *Nature Communications* **2013**, *4* (1), 1432.
- 31. Li, R.; Han, H.; Zhang, F.; Wang, D.; Li, C., Highly efficient photocatalysts constructed by rational assembly of dual-cocatalysts separately on different facets of BiVO4. *Energy & Environmental Science* **2014**, *7* (4), 1369-1376.
- 32. Zhu, J.; Fan, F.; Chen, R.; An, H.; Feng, Z.; Li, C., Direct Imaging of Highly Anisotropic Photogenerated Charge Separations on Different Facets of a Single BiVO4 Photocatalyst. *Angewandte Chemie International Edition* **2015**, *54* (31), 9111-9114.
- 33. Zhao, J.; Yang, X., Photocatalytic oxidation for indoor air purification: a literature review. *Building and Environment* **2003**, *38* (5), 645-654.
- 34. Haggerty, J. E. S.; Schelhas, L. T.; Kitchaev, D. A.; Mangum, J. S.; Garten, L. M.; Sun, W.; Stone, K. H.; Perkins, J. D.; Toney, M. F.; Ceder, G.; Ginley, D. S.; Gorman, B. P.; Tate, J., High-fraction brookite films from amorphous precursors. *Scientific Reports* **2017**, *7* (1), 15232.
- 35. Wang, Y.; He, Y.; Lai, Q.; Fan, M., Review of the progress in preparing nano TiO2: An important environmental engineering material. *Journal of Environmental Sciences* **2014**, *26* (11), 2139-2177.
- 36. Brinker, C. J.; Harrington, M. S., Sol-gel Derived Antireflective Coatings for Silicon. *Solar Energy Materials* **1981**, *5* (2), 159-172.
- 37. Yeung, K. S.; Lam, Y. W., A Simple Chemical Vapour Deposition Method for Depositing Thin TiO2 Films. *Thin Solid Films* **1983**, *109* (2), 169-178.
- 38. Aarik, J.; Aidla, A.; Uustare, T.; Kukli, K.; Sammelselg, V.; Ritala, M.; Leskelä, M., Atomic Layer Deposition of TiO2 Thin Films from TiI4 and H2O. *Applied Surface Science* **2002**, *193* (1-4), 277-286.
- 39. Dakka, A.; Lafait, J.; Abd-Lefdil, M.; Sella, C., Optical Study of Titanium Dioxide Thin Films Prepared by RF Sputtering. *Moroccan Journal of Condensed Matter* **1999**, *2*.
- 40. van Benthem, K.; Elsässer, C.; French, R. H., Bulk electronic structure of SrTiO3: Experiment and theory. *Journal of Applied Physics* **2001**, *90* (12), 6156-6164.
- 41. Yohan, P.; Takashi, H.; Kazunari, D., 10 Progress in fundamental studies and practical applications of SrTiO3 photocatalysts to overall water splitting. In *Current Developments in Photocatalysis and Photocatalytic Materials*, Wang, X.; Anpo, M.; Fu, X., Eds. Elsevier: 2020; pp 141-157.
- 42. Sakata, Y.; Miyoshi, Y.; Maeda, T.; Ishikiriyama, K.; Yamazaki, Y.; Imamura, H.; Ham, Y.; Hisatomi, T.; Kubota, J.; Yamakata, A.; Domen, K., Photocatalytic property of metal ion added SrTiO3 to Overall H2O splitting. *Applied Catalysis A: General* **2016**, *521*, 227-232.

- 43. Takata, T.; Domen, K., Defect Engineering of Photocatalysts by Doping of Aliovalent Metal Cations for Efficient Water Splitting. *The Journal of Physical Chemistry C* **2009**, *113* (45), 19386-19388.
- 44. Ham, Y.; Hisatomi, T.; Goto, Y.; Moriya, Y.; Sakata, Y.; Yamakata, A.; Kubota, J.; Domen, K., Flux-mediated doping of SrTiO3 photocatalysts for efficient overall water splitting. *Journal of Materials Chemistry A* **2016**, *4* (8), 3027-3033.
- 45. Ishii, T.; Kato, H.; Kudo, A., H2 evolution from an aqueous methanol solution on SrTiO3 photocatalysts codoped with chromium and tantalum ions under visible light irradiation. *Journal of Photochemistry and Photobiology A: Chemistry* **2004**, *163* (1), 181-186.
- 46. Ma, X.; Cui, X.; Zhao, Z.; Melo, M. A.; Roberts, E. J.; Osterloh, F. E., Use of surface photovoltage spectroscopy to probe energy levels and charge carrier dynamics in transition metal (Ni, Cu, Fe, Mn, Rh) doped SrTiO3 photocatalysts for H2 evolution from water. *Journal of Materials Chemistry A* **2018**, *6* (14), 5774-5781.
- 47. Goto, Y.; Hisatomi, T.; Wang, Q.; Higashi, T.; Ishikiriyama, K.; Maeda, T.; Sakata, Y.; Okunaka, S.; Tokudome, H.; Katayama, M.; Akiyama, S.; Nishiyama, H.; Inoue, Y.; Takewaki, T.; Setoyama, T.; Minegishi, T.; Takata, T.; Yamada, T.; Domen, K., A Particulate Photocatalyst Water-Splitting Panel for Large-Scale Solar Hydrogen Generation. *Joule* **2018**, *2* (3), 509-520.
- 48. Chiang, T. H.; Lyu, H.; Hisatomi, T.; Goto, Y.; Takata, T.; Katayama, M.; Minegishi, T.; Domen, K., Efficient Photocatalytic Water Splitting Using Al-Doped SrTiO3 Coloaded with Molybdenum Oxide and Rhodium—Chromium Oxide. *ACS Catalysis* **2018**, *8* (4), 2782-2788.
- 49. Takata, T.; Jiang, J.; Sakata, Y.; Nakabayashi, M.; Shibata, N.; Nandal, V.; Seki, K.; Hisatomi, T.; Domen, K., Photocatalytic Water Splitting with a Quantum Efficiency of Almost Unity. *Nature* **2020**, *581* (7809), 411-414.
- 50. Xiao, N.; Li, S.; Li, X.; Ge, L.; Gao, Y.; Li, N., The roles and mechanism of cocatalysts in photocatalytic water splitting to produce hydrogen. *Chinese Journal of Catalysis* **2020**, *41* (4), 642-671.
- 51. Yang, J.; Wang, D.; Han, H.; Li, C., Roles of Cocatalysts in Photocatalysis and Photoelectrocatalysis. *Accounts of Chemical Research* **2013**, *46* (8), 1900-1909.
- 52. Mu, L.; Zhao, Y.; Li, A.; Wang, S.; Wang, Z.; Yang, J.; Wang, Y.; Liu, T.; Chen, R.; Zhu, J.; Fan, F.; Li, R.; Li, C., Enhancing charge separation on high symmetry SrTiO3 exposed with anisotropic facets for photocatalytic water splitting. *Energy & Environmental Science* **2016**, *9* (7), 2463-2469.
- 53. Liu, M.; Xia, P.; Zhang, L.; Cheng, B.; Yu, J., Enhanced Photocatalytic H2-Production Activity of g-C3N4 Nanosheets via Optimal Photodeposition of Pt as Cocatalyst. *ACS Sustainable Chemistry & Engineering* **2018**, *6* (8), 10472-10480.
- 54. Al-Azri, Z. H. N.; Chen, W.-T.; Chan, A.; Jovic, V.; Ina, T.; Idriss, H.; Waterhouse, G. I. N., The roles of metal co-catalysts and reaction media in photocatalytic hydrogen production: Performance evaluation of M/TiO2 photocatalysts (M=Pd, Pt, Au) in different alcohol–water mixtures. *Journal of Catalysis* **2015**, *329*, 355-367.
- 55. Cheah, A. J.; Chiu, W. S.; Khiew, P. S.; Nakajima, H.; Saisopa, T.; Songsiriritthigul, P.; Radiman, S.; Hamid, M. A. A., Facile synthesis of a Ag/MoS2 nanocomposite photocatalyst for enhanced visible-light driven hydrogen gas evolution. *Catalysis Science & Technology* **2015**, *5* (8), 4133-4143.
- 56. Meyer, R.; Lemire, C.; Shaikhutdinov, S. K.; Freund, H. J., Surface chemistry of catalysis by gold. *Gold Bulletin* **2004**, *37* (1), 72-124.
- 57. Tatsuma, T.; Nishi, H.; Ishida, T., Plasmon-induced charge separation: chemistry and wide applications. *Chemical Science* **2017**, *8* (5), 3325-3337.
- 58. Kawawaki, T.; Kataoka, Y.; Hirata, M.; Iwamatsu, Y.; Hossain, S.; Negishi, Y., Toward the creation of high-performance heterogeneous catalysts by controlled ligand desorption from atomically precise metal nanoclusters. *Nanoscale Horizons* **2021**, *6* (6), 409-448.

- 59. Lim, D.-C.; Hwang, C.-C.; Ganteför, G.; Kim, Y. D., Model Catalysts of Supported Au Nanoparticles and Mass-Selected Clusters. *Physical Chemistry Chemical Physics* **2010**, *12* (46), 15172-15180.
- 60. Jin, R.; Zeng, C.; Zhou, M.; Chen, Y., Atomically Precise Colloidal Metal Nanoclusters and Nanoparticles: Fundamentals and Opportunities. *Chemical Reviews* **2016**, *116* (18), 10346-10413.
- 61. Liu, L.; Corma, A., Metal Catalysts for Heterogeneous Catalysis: From Single Atoms to Nanoclusters and Nanoparticles. *Chemical Reviews* **2018**, *118* (10), 4981-5079.
- 62. Adnan, R. H.; Madridejos, J. M. L.; Alotabi, A. S.; Metha, G. F.; Andersson, G. G., A Review of State of the Art in Phosphine Ligated Gold Clusters and Application in Catalysis. *Advanced Science* **2022**, *9* (15), 2105692.
- 63. Kawawaki, T.; Ebina, A.; Hosokawa, Y.; Ozaki, S.; Suzuki, D.; Hossain, S.; Negishi, Y., Thiolate-Protected Metal Nanoclusters: Recent Development in Synthesis, Understanding of Reaction, and Application in Energy and Environmental Field. *Small* **2021**, *17* (27), 2005328.
- 64. Qin, Z.; Sharma, S.; Wan, C.-q.; Malola, S.; Xu, W.-w.; Häkkinen, H.; Li, G., A Homoleptic Alkynyl-Ligated [Au13Ag16L24]3— Cluster as a Catalytically Active Eight-Electron Superatom. *Angewandte Chemie International Edition* **2021**, *60* (2), 970-975.
- 65. Kawawaki, T.; Mori, Y.; Wakamatsu, K.; Ozaki, S.; Kawachi, M.; Hossain, S.; Negishi, Y., Controlled colloidal metal nanoparticles and nanoclusters: recent applications as cocatalysts for improving photocatalytic water-splitting activity. *Journal of Materials Chemistry A* **2020**, 8 (32), 16081-16113.
- 66. Negishi, Y.; Mizuno, M.; Hirayama, M.; Omatoi, M.; Takayama, T.; Iwase, A.; Kudo, A., Enhanced Photocatalytic Water Splitting by BaLa4Ti4O15 Loaded with ~1 nm Gold Nanoclusters Using Glutathione-protected Au25 Clusters. *Nanoscale* **2013**, *5* (16), 7188-7192.
- 67. Negishi, Y.; Matsuura, Y.; Tomizawa, R.; Kurashige, W.; Niihori, Y.; Takayama, T.; Iwase, A.; Kudo, A., Controlled Loading of Small Aun Clusters (n = 10–39) onto BaLa4Ti4O15 Photocatalysts: Toward an Understanding of Size Effect of Cocatalyst on Water-Splitting Photocatalytic Activity. *The Journal of Physical Chemistry C* **2015**, *119* (20), 11224-11232.
- 68. Kurashige, W.; Kumazawa, R.; Mori, Y.; Negishi, Y., Au25 cluster-loaded SrTiO3 water-splitting photocatalyst; preparation and elucidation of the effect of cocatalyst refinement on photocatalytic activity. *Journal of Materials and Applications* **2018**, *7* (1), 1-11.
- 69. Malatesta, L., Cluster compounds of gold. *Gold Bulletin* **1975**, 8 (2), 48-52.
- 70. Goldstein, J. I.; Newbury, D. E.; Michael, J. R.; Ritchie, N. W.; Scott, J. H. J.; Joy, D. C., *Scanning electron microscopy and X-ray microanalysis*. Springer: 2017.
- 71. Kisielowski, C.; Freitag, B.; Bischoff, M.; Van Lin, H.; Lazar, S.; Knippels, G.; Tiemeijer, P.; van der Stam, M.; von Harrach, S.; Stekelenburg, M., Detection of single atoms and buried defects in three dimensions by aberration-corrected electron microscope with 0.5-Å information limit. *Microscopy and Microanalysis* **2008**, *14* (5), 469.
- 72. Yamamoto, Y.; Arai, S.; Esaki, A.; Ohyama, J.; Satsuma, A.; Tanaka, N., Statistical distribution of single atoms and clusters of supported Au catalyst analyzed by global high-resolution HAADF-STEM observation with morphological image-processing operation. *Microscopy* **2014**, *63* (3), 209-218.
- 73. Rapoport, D. H.; Vogel, W.; Cölfen, H.; Schlögl, R., Ligand-Stabilized Metal Clusters: Reinvestigation of the Structure of "Au55[P(C6H5)3]12Cl6". *The Journal of Physical Chemistry B* **1997**, *101* (21), 4175-4183.
- 74. Schmid, G., The relevance of shape and size of Au55 clusters. *Chemical Society Reviews* **2008**, *37* (9), 1909-1930.
- 75. Marcus, M. A.; Andrews, M. P.; Zegenhagen, J.; Bommannavar, A. S.; Montano, P., Structure and vibrations of chemically produced Au55 clusters. *Physical Review B* **1990**, *42* (6), 3312-3316.
- 76. Fairbanks, M. C.; Benfield, R. E.; Newport, R. J.; Schmid, G., An exafs study of the cluster molecule Au55(PPh3)12Cl6. *Solid State Communications* **1990**, *73* (6), 431-436.

- 77. Vogel, W.; Rosner, B.; Tesche, B., Structural investigations of gold (Au55) organometallic complexes by x-ray powder diffraction and transmission electron microscopy. *The Journal of Physical Chemistry* **1993**, *97* (45), 11611-11616.
- 78. Jian, N.; Stapelfeldt, C.; Hu, K.-J.; Fröba, M.; Palmer, R. E., Hybrid atomic structure of the Schmid cluster Au55(PPh3)12Cl6 resolved by aberration-corrected STEM. *Nanoscale* **2015**, *7* (3), 885-888.
- 79. Li, Z.; Young, N.; Di Vece, M.; Palomba, S.; Palmer, R.; Bleloch, A.; Curley, B.; Johnston, R.; Jiang, J.; Yuan, J., Three-dimensional atomic-scale structure of size-selected gold nanoclusters. *Nature* **2008**, *451* (7174), 46-48.
- 80. Wang, Z.; Palmer, R., Direct atomic imaging and dynamical fluctuations of the tetrahedral Au 20 cluster. *Nanoscale* **2012**, *4* (16), 4947-4949.
- 81. Al Qahtani, H. S.; Kimoto, K.; Bennett, T.; Alvino, J. F.; Andersson, G. G.; Metha, G. F.; Golovko, V. B.; Sasaki, T.; Nakayama, T., Atomically resolved structure of ligand-protected Au9 clusters on TiO2 nanosheets using aberration-corrected STEM. *The Journal of Chemical Physics* **2016**, *144* (11), 114703.
- 82. Bosch-Navarro, C.; Laker, Z. P. L.; Thomas, H. R.; Marsden, A. J.; Sloan, J.; Wilson, N. R.; Rourke, J. P., Covalently Binding Atomically Designed Au9 Clusters to Chemically Modified Graphene. *Angewandte Chemie International Edition* **2015**, *54* (33), 9560-9563.
- 83. Seah, M. P.; Dench, W. A., Quantitative electron spectroscopy of surfaces: A standard data base for electron inelastic mean free paths in solids. *Surface and Interface Analysis* **1979**, *1* (1), 2-11.
- 84. Koslowski, B.; Boyen, H.-G.; Wilderotter, C.; Kästle, G.; Ziemann, P.; Wahrenberg, R.; Oelhafen, P., Oxidation of preferentially (1 1 1)-oriented Au films in an oxygen plasma investigated by scanning tunneling microscopy and photoelectron spectroscopy. *Surface science* **2001**, *475* (1-3), 1-10.
- 85. Moulder, J. F., Handbook of x-ray photoelectron spectroscopy: a reference book of standard data for use in x-ray photoelectron spectroscopy. *Handbook of x-ray photoelectron spectroscopy*: **1992**.
- 86. Howard, A.; Clark, D. N. S.; Mitchell, C. E. J.; Egdell, R. G.; Dhanak, V. R., Initial and final state effects in photoemission from Au nanoclusters on TiO2(110). *Surface Science* **2002**, *518* (3), 210-224.
- 87. Roberts, F. S.; Anderson, S. L.; Reber, A. C.; Khanna, S. N., Initial and Final State Effects in the Ultraviolet and X-ray Photoelectron Spectroscopy (UPS and XPS) of Size-Selected Pdn Clusters Supported on TiO2(110). *The Journal of Physical Chemistry C* **2015**, *119* (11), 6033-6046.
- 88. Borman, V.; Pushkin, M.; Tronin, V.; Troyan, V., Evolution of the Electronic Properties of Transition Metal Nanoclusters on Graphite Surface. *Journal of Experimental and Theoretical Physics* **2010**, *110*, 1005-1025.
- 89. Mason, M., Electronic structure of supported small metal clusters. *Physical review B* **1983**, 27 (2), 748.
- 90. Wertheim, G.; DiCenzo, S.; Youngquist, S., Unit charge on supported gold clusters in photoemission final state. *Physical review letters* **1983**, *51* (25), 2310.
- 91. Peters, S.; Peredkov, S.; Neeb, M.; Eberhardt, W.; Al-Hada, M., Size-dependent XPS spectra of small supported Au-clusters. *Surface Science* **2013**, *608*, 129-134.
- 92. Ono, L. K.; Roldan Cuenya, B., Formation and Thermal Stability of Au2O3 on Gold Nanoparticles: Size and Support Effects. *The Journal of Physical Chemistry C* **2008**, *112* (12), 4676-4686.
- 93. M. Visco, A.; Neri, F.; Neri, G.; Donato, A.; Milone, C.; Galvagno, S., X-ray photoelectron spectroscopy of Au/Fe2O3 catalysts. *Physical Chemistry Chemical Physics* **1999**, *1* (11), 2869-2873.
- 94. Huang, T.; Huang, L.; Jiang, Y.; Hu, F.; Sun, Z.; Pan, G.; Wei, S., Direct self-focusing synthesis of monodisperse [Au8(PPh3)7]2+ nanoclusters. *Dalton Transactions* **2017**, *46* (36), 12239-12244.

- 95. Kozlova, A. P.; Kozlov, A. I.; Sugiyama, S.; Matsui, Y.; Asakura, K.; Iwasawa, Y., Study of Gold Species in Iron-Oxide-Supported Gold Catalysts Derived from Gold-Phosphine Complex Au(PPh3)(NO3) and As-Precipitated Wet Fe(OH)3\*. *Journal of Catalysis* **1999**, *181* (1), 37-48.
- 96. Deng, H.; Bai, Y.; Zhou, M.; Bao, Y.; Jin, S.; Li, X.; Yu, H.; Zhu, M., Structure and Properties of Au5Cu6(Dppf)2(SAdm)6)(BPh4). *The Journal of Physical Chemistry C* **2020**, *124* (39), 21867-21873.
- 97. Choudhary, T.; Sivadinarayana, C.; Chusuei, C.; Datye, A.; Fackler Jr, J.; Goodman, D., CO oxidation on supported nano-Au catalysts synthesized from a [Au6 (PPh3) 6](BF4) 2 complex. *Journal of Catalysis* **2002**, *207* (2), 247-255.
- 98. Chusuei, C. C.; Lai, X.; Davis, K. A.; Bowers, E. K.; Fackler, J. P.; Goodman, D. W., A Nanoscale Model Catalyst Preparation: Solution Deposition of Phosphine-Stabilized Gold Clusters onto a Planar TiO2(110) Support. *Langmuir* **2001**, *17* (13), 4113-4117.
- 99. Anderson, D. P.; Alvino, J. F.; Gentleman, A.; Al Qahtani, H.; Thomsen, L.; Polson, M. I.; Metha, G. F.; Golovko, V. B.; Andersson, G. G., Chemically-Synthesised, Atomically-Precise Gold Clusters Deposited and Activated on Titania. *Physical chemistry chemical physics* **2013**, *15* (11), 3917-3929.
- 100. Anderson, D. P.; Adnan, R. H.; Alvino, J. F.; Shipper, O.; Donoeva, B.; Ruzicka, J.-Y.; Al Qahtani, H.; Harris, H. H.; Cowie, B.; Aitken, J. B., Chemically Synthesised Atomically Precise Gold Clusters Deposited and Activated on Titania. Part II. *Physical chemistry chemical physics* **2013**, *15* (35), 14806-14813.
- 101. Kollmannsberger, K. L.; Weger, K.; Kratky, T.; Günther, S.; Tomanec, O.; Warnan, J.; Fischer, R. A., From phosphine-stabilised towards naked Au8 clusters through ZIF-8 encapsulation. *Molecular Systems Design & Engineering* **2021**, *6* (11), 876-882.
- 102. Bennett, T.; Adnan, R. H.; Alvino, J. F.; Golovko, V.; Andersson, G. G.; Metha, G. F., Identification of the Vibrational Modes in the Far-Infrared Spectra of Ruthenium Carbonyl Clusters and the Effect of Gold Substitution. *Inorganic Chemistry* **2014**, *53* (9), 4340-4349.
- 103. Daughtry, J.; Andersson, G. G.; Metha, G. F.; Tesana, S.; Nakayama, T., Sub-monolayer Au9 cluster formation via pulsed nozzle cluster deposition. *Nanoscale Advances* **2020**, *2* (9), 4051-4061.
- 104. Al Qahtani, H. S.; Metha, G. F.; Walsh, R. B.; Golovko, V. B.; Andersson, G. G.; Nakayama, T., Aggregation Behavior of Ligand-Protected Au9 Clusters on Sputtered Atomic Layer Deposition TiO2. *The Journal of Physical Chemistry C* **2017**, *121* (20), 10781-10789.
- 105. Al Qahtani, H. S.; Higuchi, R.; Sasaki, T.; Alvino, J. F.; Metha, G. F.; Golovko, V. B.; Adnan, R.; Andersson, G. G.; Nakayama, T., Grouping and aggregation of ligand protected Au9 clusters on TiO2 nanosheets. *RSC Advances* **2016**, *6* (112), 110765-110774.
- 106. Ruzicka, J.-Y.; Abu Bakar, F.; Hoeck, C.; Adnan, R.; McNicoll, C.; Kemmitt, T.; Cowie, B. C.; Metha, G. F.; Andersson, G. G.; Golovko, V. B., Toward Control of Gold Cluster Aggregation on TiO2 via Surface Treatments. *The Journal of Physical Chemistry C* **2015**, *119* (43), 24465-24474.
- 107. Alotabi, A. S.; Yin, Y.; Redaa, A.; Tesana, S.; Metha, G. F.; Andersson, G. G., Cr2O3 layer inhibits agglomeration of phosphine-protected Au9 clusters on TiO2 films. *The Journal of Chemical Physics* **2021**, *155* (16), 164702.
- 108. Das, A. K.; Mukherjee, S.; R, S. S.; Nair, A. S.; Bhandary, S.; Chopra, D.; Sanyal, D.; Pathak, B.; Mandal, S., Defects Engineering on Ceria and C–C Coupling Reactions Using [Au11(PPh3)7I3] Nanocluster: A Combined Experimental and Theoretical Study. *ACS Nano* **2020**, *14* (12), 16681-16688.
- 109. Krishnan, G.; Eom, N.; Kirk, R. M.; Golovko, V. B.; Metha, G. F.; Andersson, G. G., Investigation of Phosphine Ligand Protected Au13 Clusters on Defect Rich Titania. *The Journal of Physical Chemistry C* **2019**, *123* (11), 6642-6649.
- 110. Zhang, J.; Zhou, Y.; Zheng, K.; Abroshan, H.; Kauffman, D. R.; Sun, J.; Li, G., Diphosphine-induced chiral propeller arrangement of gold nanoclusters for singlet oxygen photogeneration. *Nano Research* **2018**, *11* (11), 5787-5798.

- 111. Qin, Z.; Hu, S.; Han, W.; Li, Z.; Xu, W. W.; Zhang, J.; Li, G., Tailoring optical and photocatalytic properties by single-Ag-atom exchange in Au13Ag12(PPh3)10Cl8 nanoclusters. *Nano Research* **2022**, *15* (4), 2971-2976.
- 112. Wan, X.-K.; Cheng, X.-L.; Tang, Q.; Han, Y.-Z.; Hu, G.; Jiang, D.-e.; Wang, Q.-M., Atomically Precise Bimetallic Au19Cu30 Nanocluster with an Icosidodecahedral Cu30 Shell and an Alkynyl–Cu Interface. *Journal of the American Chemical Society* **2017**, *139* (28), 9451-9454.
- 113. Wan, X.-K.; Yuan, S.-F.; Lin, Z.-W.; Wang, Q.-M., A Chiral Gold Nanocluster Au20 Protected by Tetradentate Phosphine Ligands. *Angewandte Chemie International Edition* **2014**, *53* (11), 2923-2926.
- 114. Wan, X.-K.; Yuan, S.-F.; Tang, Q.; Jiang, D.-e.; Wang, Q.-M., Alkynyl-Protected Au23 Nanocluster: A 12-Electron System. *Angewandte Chemie International Edition* **2015**, *54* (20), 5977-5980.
- 115. Wan, X.-K.; Xu, W. W.; Yuan, S.-F.; Gao, Y.; Zeng, X.-C.; Wang, Q.-M., A Near-Infrared-Emissive Alkynyl-Protected Au24 Nanocluster. *Angewandte Chemie International Edition* **2015**, *54* (33), 9683-9686.
- 116. Nair, L. V.; Hossain, S.; Takagi, S.; Imai, Y.; Hu, G.; Wakayama, S.; Kumar, B.; Kurashige, W.; Jiang, D.-e.; Negishi, Y., Hetero-biicosahedral [Au24Pd(PPh3)10(SC2H4Ph)5Cl2]+ nanocluster: selective synthesis and optical and electrochemical properties. *Nanoscale* **2018**, *10* (40), 18969-18979.
- 117. Katsiev, K.; Lozova, N.; Wang, L.; Sai Krishna, K.; Li, R.; Mei, W.-N.; Skrabalak, S. E.; Kumar, C. S. S. R.; Losovyj, Y., The electronic structure of Au25 clusters: between discrete and continuous. *Nanoscale* **2016**, *8* (31), 14711-14715.
- 118. Yuan, S.-F.; Xu, C.-Q.; Li, J.; Wang, Q.-M., A Ligand-Protected Golden Fullerene: The Dipyridylamido Au328+ Nanocluster. *Angewandte Chemie International Edition* **2019**, *58* (18), 5906-5909.
- 119. Quinten, M.; Sander, I.; Steiner, P.; Kreibig, U.; Fauth, K.; Schmid, G., Photoemission on gold-55-clusters derived from gold-phosphine AuP (C 6 H 5) 3 Cl. Zeitschrift für Physik D Atoms, Molecules and Clusters 1991, 20 (1), 377-379.
- 120. Turner, M.; Golovko, V. B.; Vaughan, O. P. H.; Abdulkin, P.; Berenguer-Murcia, A.; Tikhov, M. S.; Johnson, B. F. G.; Lambert, R. M., Selective Oxidation with Dioxygen by Gold Nanoparticle Catalysts Derived from 55-atom Clusters. *Nature* **2008**, *454* (7207), 981-983.
- 121. Mousavi, H.; Yin, Y.; Howard-Fabretto, L.; Sharma, S. K.; Golovko, V.; Andersson, G. G.; Shearer, C. J.; Metha, G. F., Au101–rGO nanocomposite: immobilization of phosphine-protected gold nanoclusters on reduced graphene oxide without aggregation. *Nanoscale Advances* **2021**, *3* (5), 1422-1430.
- 122. Mousavi, H.; Yin, Y.; Sharma, S. K.; Gibson, C. T.; Golovko, V.; Andersson, G. G.; Shearer, C. J.; Metha, G. F., Factors Influencing Catalytic Activity of Size-Specific Triphenylphosphine-Ligated Gold Nanoclusters in the Electrocatalytic Hydrogen Evolution Reaction. *The Journal of Physical Chemistry C* **2022**, *126* (1), 246-260.
- 123. Haruta, M., Chance and necessity: my encounter with gold catalysts. *Angewandte Chemie International Edition* **2014**, *53* (1), 52-56.
- 124. Battistoni, C.; Mattogno, G.; Cariati, F.; Naldini, L.; Sgamellotti, A., XPS photoelectron spectra of cluster compounds of gold. *Inorganica Chimica Acta* 1977, 24, 207-210.
- 125. Battistoni, C.; Mattogno, G.; Zanoni, R.; Naldini, L., Characterisation of some gold clusters by X-ray photoelectron spectroscopy. *Journal of Electron Spectroscopy and Related Phenomena* **1982**, 28 (1), 23-31.
- 126. Levy, F.; ACRIVOS, J.; LIANG, W., Physics and Chemistry of materials with low-dimensional structures. Reidel, Dordrecht: 1977.
- 127. Van Attekum, P. M. T. M.; Van der Velden, J. W. A.; Trooster, J. M., X-ray photoelectron spectroscopy study of gold cluster and gold(I) phosphine compounds. *Inorganic Chemistry* **1980**, *19* (3), 701-704.

- 128. Wertheim, G. K.; Kwo, J.; Teo, B. K.; Keating, K. A., XPS study of bonding in ligated Au clusters. *Solid State Communications* **1985**, *55* (4), 357-361.
- 129. Arfelli, M.; Battistoni, C.; Mattogno, G.; Mingos, D. M. P., X-ray photoelectron spectroscopic evidence for the electrophilic character of the AuL fragment in the cluster compound (Pt3Au(μ2-Co) 3L4)PF6. *Journal of Electron Spectroscopy and Related Phenomena* **1989**, 49 (2), 273-277.
- 130. Boyen, H.-G.; Kästle, G.; Weigl, F.; Koslowski, B.; Dietrich, C.; Ziemann, P.; Spatz, J. P.; Riethmüller, S.; Hartmann, C.; Möller, M., Oxidation-resistant gold-55 clusters. *Science* **2002**, 297 (5586), 1533-1536.
- 131. Boyen, H. G.; Kästle, G.; Weigl, F.; Ziemann, P.; Schmid, G.; Garnier, M. G.; Oelhafen, P., Chemically Induced Metal-to-Insulator Transition in Au55 Clusters: Effect of Stabilizing Ligands on the Electronic Properties of Nanoparticles. *Physical Review Letters* **2001**, *87* (27), 276401.
- 132. Mishra, D.; Wang, S.; Jin, Z.; Xin, Y.; Lochner, E.; Mattoussi, H., Highly fluorescent hybrid Au/Ag nanoclusters stabilized with poly(ethylene glycol)- and zwitterion-modified thiolate ligands. *Physical Chemistry Chemical Physics* **2019**, *21* (38), 21317-21328.
- 133. Li, S. H.; Liu, X.; Hu, W.; Chen, M.; Zhu, Y., An Au8 Cluster Fortified by Four Ferrocenes. *The Journal of Physical Chemistry A* **2020**, *124* (29), 6061-6067.
- 134. Bennett, T.; Adnan, R. H.; Alvino, J. F.; Kler, R.; Golovko, V. B.; Metha, G. F.; Andersson, G. G., Effect of Gold Nanoclusters on the Production of Ti3+ Defect Sites in Titanium Dioxide Nanoparticles under Ultraviolet and Soft X-ray Radiation. *The Journal of Physical Chemistry C* **2015**, *119* (20), 11171-11177.
- 135. Krishnan, G.; Al Qahtani, H. S.; Li, J.; Yin, Y.; Eom, N.; Golovko, V. B.; Metha, G. F.; Andersson, G. G., Investigation of Ligand-Stabilized Gold Clusters on Defect-Rich Titania. *The Journal of Physical Chemistry C* **2017**, *121* (50), 28007-28016.
- 136. Wu, Q.; Cen, J.; Zhao, Y.; Tong, X.; Li, Y.; Frenkel, A. I.; Zhao, S.; Orlov, A., A comprehensive study of catalytic, morphological and electronic properties of ligand-protected gold nanoclusters using XPS, STM, XAFS, and TPD techniques. *Physical Chemistry Chemical Physics* **2018**, *20* (3), 1497-1503.
- 137. Longo, A.; de Boed, E. J. J.; Mammen, N.; van der Linden, M.; Honkala, K.; Häkkinen, H.; de Jongh, P. E.; Donoeva, B., Towards Atomically Precise Supported Catalysts from Monolayer-Protected Clusters: The Critical Role of the Support. *Chemistry A European Journal* **2020**, *26* (31), 7051-7058.
- 138. Ahmad, M. Z.; Golovko, V. B.; Adnan, R. H.; Abu Bakar, F.; Ruzicka, J.-Y.; Anderson, D. P.; Anderson, G. G.; Wlodarski, W., Hydrogen sensing using gold nanoclusters supported on tungsten trioxide thin films. *International Journal of Hydrogen Energy* **2013**, *38* (29), 12865-12877.
- 139. Andersson, G. G.; Golovko, V. B.; Alvino, J. F.; Bennett, T.; Wrede, O.; Mejia, S. M.; Al Qahtani, H. S.; Adnan, R.; Gunby, N.; Anderson, D. P., Phosphine-stabilised Au9 Clusters Interacting with Titania and Silica Surfaces: The First Evidence for the Density of States Signature of the Support-immobilised Cluster. *The Journal of chemical physics* **2014**, *141* (1), 014702.
- 140. Cluskey, P. D.; Newport, R. J.; Benfield, R. E.; Gurman, S. J.; Schmid, G., An EXAFS study of some gold and palladium cluster compounds. *Zeitschrift für Physik D Atoms, Molecules and Clusters* **1993**, *26* (1), 8-11.
- 141. Benfield, R. E.; Grandjean, D.; Kröll, M.; Pugin, R.; Sawitowski, T.; Schmid, G., Structure and Bonding of Gold Metal Clusters, Colloids, and Nanowires Studied by EXAFS, XANES, and WAXS. *The Journal of Physical Chemistry B* **2001**, *105* (10), 1961-1970.
- 142. Menard, L. D.; Xu, H.; Gao, S.-P.; Twesten, R. D.; Harper, A. S.; Song, Y.; Wang, G.; Douglas, A. D.; Yang, J. C.; Frenkel, A. I.; Murray, R. W.; Nuzzo, R. G., Metal Core Bonding Motifs of Monodisperse Icosahedral Au13 and Larger Au Monolayer-Protected Clusters As Revealed by X-ray Absorption Spectroscopy and Transmission Electron Microscopy. *The Journal of Physical Chemistry B* **2006**, *110* (30), 14564-14573.
- 143. Li, Y.; Cheng, H.; Yao, T.; Sun, Z.; Yan, W.; Jiang, Y.; Xie, Y.; Sun, Y.; Huang, Y.; Liu, S.; Zhang, J.; Xie, Y.; Hu, T.; Yang, L.; Wu, Z.; Wei, S., Hexane-Driven Icosahedral to

- Cuboctahedral Structure Transformation of Gold Nanoclusters. *Journal of the American Chemical Society* **2012**, *134* (43), 17997-18003.
- 144. Kilmartin, J.; Sarip, R.; Grau-Crespo, R.; Di Tommaso, D.; Hogarth, G.; Prestipino, C.; Sankar, G., Following the Creation of Active Gold Nanocatalysts from Phosphine-Stabilized Molecular Clusters. *ACS Catalysis* **2012**, *2* (6), 957-963.
- 145. Yamazoe, S.; Matsuo, S.; Muramatsu, S.; Takano, S.; Nitta, K.; Tsukuda, T., Suppressing Isomerization of Phosphine-Protected Au9 Cluster by Bond Stiffening Induced by a Single Pd Atom Substitution. *Inorganic Chemistry* **2017**, *56* (14), 8319-8325.
- 146. Liu, J.; Krishna, K. S.; Losovyj, Y. B.; Chattopadhyay, S.; Lozova, N.; Miller, J. T.; Spivey, J. J.; Kumar, C. S. S. R., Ligand-Stabilized and Atomically Precise Gold Nanocluster Catalysis: A Case Study for Correlating Fundamental Electronic Properties with Catalysis. *Chemistry A European Journal* **2013**, *19* (31), 10201-10208.
- 147. Matsuyama, T.; Hirayama, J.; Fujiki, Y.; Kikkawa, S.; Kurashige, W.; Asakura, H.; Kawamura, N.; Negishi, Y.; Nakatani, N.; Hatada, K.; Ota, F.; Yamazoe, S., Effect of Ligand on the Electronic State of Gold in Ligand-Protected Gold Clusters Elucidated by X-ray Absorption Spectroscopy. *The Journal of Physical Chemistry C* **2021**, *125* (5), 3143-3149.
- 148. Yang, L.; Cheng, H.; Jiang, Y.; Huang, T.; Bao, J.; Sun, Z.; Jiang, Z.; Ma, J.; Sun, F.; Liu, Q.; Yao, T.; Deng, H.; Wang, S.; Zhu, M.; Wei, S., In situ studies on controlling an atomically-accurate formation process of gold nanoclusters. *Nanoscale* **2015**, *7* (34), 14452-14459.
- 149. Bao, J.; Yang, L.; Liu, W.; Huang, Y.; Huang, T.; Cao, Y.; Yao, T.; Sun, Z.; Wei, S., Combined spectroscopic study on the growth mechanism of Diphosphine-stabilized Gold Nanoclusters. *Journal of Physics: Conference Series* **2016**, *712*, 012108.
- 150. Yang, L.; Huang, T.; Liu, W.; Bao, J.; Huang, Y.; Cao, Y.; Yao, T.; Sun, Z.; Wei, S. In *XAFS studies of monodisperse Au nanoclusters formation in the etching process*, Journal of Physics: Conference Series, IOP Publishing: 2016; p 012035.
- 151. Pan, Z.; Hisatomi, T.; Domen, K., Chapter 10 Applications of Metal Oxide Layers on Particulate Photocatalysts for Water Splitting. In *Ultrathin Oxide Layers for Solar and Electrocatalytic Systems*, The Royal Society of Chemistry: 2022; pp 265-297.
- 152. Kurashige, W.; Kumazawa, R.; Ishii, D.; Hayashi, R.; Niihori, Y.; Hossain, S.; Nair, L. V.; Takayama, T.; Iwase, A.; Yamazoe, S.; Tsukuda, T.; Kudo, A.; Negishi, Y., Au25-Loaded BaLa4Ti4O15 Water-Splitting Photocatalyst with Enhanced Activity and Durability Produced Using New Chromium Oxide Shell Formation Method. *The Journal of Physical Chemistry C* **2018**, *122* (25), 13669-13681.
- 153. Kurashige, W.; Hayashi, R.; Wakamatsu, K.; Kataoka, Y.; Hossain, S.; Iwase, A.; Kudo, A.; Yamazoe, S.; Negishi, Y., Atomic-Level Understanding of the Effect of Heteroatom Doping of the Cocatalyst on Water-Splitting Activity in AuPd or AuPt Alloy Cluster-Loaded BaLa4Ti4O15. *ACS Applied Energy Materials* **2019**, *2* (6), 4175-4187.
- 154. Adnan, R. H.; Golovko, V. B., Benzyl Alcohol Oxidation Using Gold Catalysts Derived from Au8 Clusters on TiO2. *Catalysis Letters* **2019**, *149* (2), 449-455.
- 155. Domen, K.; Kudo, A.; Onishi, T.; Kosugi, N.; Kuroda, H., Photocatalytic decomposition of water into hydrogen and oxygen over nickel(II) oxide-strontium titanate (SrTiO3) powder. 1. Structure of the catalysts. *The Journal of Physical Chemistry* **1986**, *90* (2), 292-295.
- 156. Maeda, K.; Teramura, K.; Lu, D.; Saito, N.; Inoue, Y.; Domen, K., Noble-Metal/Cr2O3 Core/Shell Nanoparticles as a Cocatalyst for Photocatalytic Overall Water Splitting. *Angewandte Chemie International Edition* **2006**, *45* (46), 7806-7809.
- 157. Maeda, K.; Teramura, K.; Lu, D.; Saito, N.; Inoue, Y.; Domen, K., Roles of Rh/Cr2O3 (Core/Shell) Nanoparticles Photodeposited on Visible-Light-Responsive (Ga1-xZnx)(N1-xOx) Solid Solutions in Photocatalytic Overall Water Splitting. *The Journal of Physical Chemistry C* **2007**, *111* (20), 7554-7560.
- 158. Garcia-Esparza, A. T.; Shinagawa, T.; Ould-Chikh, S.; Qureshi, M.; Peng, X.; Wei, N.; Anjum, D. H.; Clo, A.; Weng, T.-C.; Nordlund, D.; Sokaras, D.; Kubota, J.; Domen, K.; Takanabe,

- K., An Oxygen-Insensitive Hydrogen Evolution Catalyst Coated by a Molybdenum-Based Layer for Overall Water Splitting. *Angewandte Chemie International Edition* **2017**, *56* (21), 5780-5784.
- 159. Li, Z.; Zhang, F.; Han, J.; Zhu, J.; Li, M.; Zhang, B.; Fan, W.; Lu, J.; Li, C., Using Pd as a Cocatalyst on GaN–ZnO Solid Solution for Visible-Light-Driven Overall Water Splitting. *Catalysis Letters* **2018**, *148* (3), 933-939.
- 160. Wang, Z.; Inoue, Y.; Hisatomi, T.; Ishikawa, R.; Wang, Q.; Takata, T.; Chen, S.; Shibata, N.; Ikuhara, Y.; Domen, K., Overall water splitting by Ta3N5 nanorod single crystals grown on the edges of KTaO3 particles. *Nature Catalysis* **2018**, *I* (10), 756-763.
- 161. Yoshida, M.; Maeda, K.; Lu, D.; Kubota, J.; Domen, K., Lanthanoid Oxide Layers on Rhodium-Loaded (Ga1–xZnx)(N1–xOx) Photocatalyst as a Modifier for Overall Water Splitting under Visible-Light Irradiation. *The Journal of Physical Chemistry C* **2013**, *117* (27), 14000-14006.
- 162. Bau, J. A.; Takanabe, K., Ultrathin Microporous SiO2 Membranes Photodeposited on Hydrogen Evolving Catalysts Enabling Overall Water Splitting. *ACS Catalysis* **2017**, *7* (11), 7931-7940.
- 163. Pan, C.; Takata, T.; Nakabayashi, M.; Matsumoto, T.; Shibata, N.; Ikuhara, Y.; Domen, K., A Complex Perovskite-Type Oxynitride: The First Photocatalyst for Water Splitting Operable at up to 600 nm. *Angewandte Chemie International Edition* **2015**, *54* (10), 2955-2959.
- 164. Takata, T.; Pan, C.; Nakabayashi, M.; Shibata, N.; Domen, K., Fabrication of a Core–Shell-Type Photocatalyst via Photodeposition of Group IV and V Transition Metal Oxyhydroxides: An Effective Surface Modification Method for Overall Water Splitting. *Journal of the American Chemical Society* **2015**, *137* (30), 9627-9634.
- 165. Maeda, K.; Xiong, A.; Yoshinaga, T.; Ikeda, T.; Sakamoto, N.; Hisatomi, T.; Takashima, M.; Lu, D.; Kanehara, M.; Setoyama, T.; Teranishi, T.; Domen, K., Photocatalytic Overall Water Splitting Promoted by Two Different Cocatalysts for Hydrogen and Oxygen Evolution under Visible Light. *Angewandte Chemie International Edition* **2010**, *49* (24), 4096-4099.
- 166. Dionigi, F.; Vesborg, P. C. K.; Pedersen, T.; Hansen, O.; Dahl, S.; Xiong, A.; Maeda, K.; Domen, K.; Chorkendorff, I., Suppression of the water splitting back reaction on GaN:ZnO photocatalysts loaded with core/shell cocatalysts, investigated using a μ-reactor. *Journal of Catalysis* **2012**, *292*, 26-31.
- 167. Xiong, A.; Yoshinaga, T.; Ikeda, T.; Takashima, M.; Hisatomi, T.; Maeda, K.; Setoyama, T.; Teranishi, T.; Domen, K., Effect of Hydrogen and Oxygen Evolution Cocatalysts on Photocatalytic Activity of GaN:ZnO. *European Journal of Inorganic Chemistry* **2014**, *2014* (4), 767-772.
- 168. Berto, T. F.; Sanwald, K. E.; Byers, J. P.; Browning, N. D.; Gutiérrez, O. Y.; Lercher, J. A., Enabling Overall Water Splitting on Photocatalysts by CO-Covered Noble Metal Co-catalysts. *The Journal of Physical Chemistry Letters* **2016**, *7* (21), 4358-4362.
- 169. Maeda, K.; Lu, D.; Teramura, K.; Domen, K., Simultaneous photodeposition of rhodium–chromium nanoparticles on a semiconductor powder: structural characterization and application to photocatalytic overall water splitting. *Energy & Environmental Science* **2010**, *3* (4), 470-477.
- 170. Sakamoto, N.; Ohtsuka, H.; Ikeda, T.; Maeda, K.; Lu, D.; Kanehara, M.; Teramura, K.; Teranishi, T.; Domen, K., Highly Dispersed Noble-metal/Chromia (Core/Shell) Nanoparticles as Efficient Hydrogen Evolution Promoters for Photocatalytic Overall Water Splitting under Visible Light. *Nanoscale* **2009**, *I* (1), 106-109.
- 171. Maeda, K.; Sakamoto, N.; Ikeda, T.; Ohtsuka, H.; Xiong, A.; Lu, D.; Kanehara, M.; Teranishi, T.; Domen, K., Preparation of Core–Shell-Structured Nanoparticles (with a Noble-Metal or Metal Oxide Core and a Chromia Shell) and Their Application in Water Splitting by Means of Visible Light. *Chemistry A European Journal* **2010**, *16* (26), 7750-7759.
- 172. Ohno, T.; Bai, L.; Hisatomi, T.; Maeda, K.; Domen, K., Photocatalytic Water Splitting Using Modified GaN:ZnO Solid Solution under Visible Light: Long-Time Operation and Regeneration of Activity. *Journal of the American Chemical Society* **2012**, *134* (19), 8254-8259.

- 173. Ikeda, T.; Xiong, A.; Yoshinaga, T.; Maeda, K.; Domen, K.; Teranishi, T., Polyol Synthesis of Size-Controlled Rh Nanoparticles and Their Application to Photocatalytic Overall Water Splitting under Visible Light. *The Journal of Physical Chemistry C* **2013**, *117* (6), 2467-2473.
- 174. Hahn, C.; Fardy, M. A.; Nguyen, C.; Natera-Comte, M.; Andrews, S. C.; Yang, P., Synthesis and Photocatalytic Properties of Single Crystalline (Ga1-xZnx)(N1-xOx) Nanotubes. *Israel Journal of Chemistry* **2012**, *52* (11-12), 1111-1117.
- 175. Adeli, B.; Taghipour, F., Reduced Graphene Oxide Composite of Gallium Zinc Oxynitride Photocatalyst with Improved Activity for Overall Water Splitting. *Chemical Engineering & Technology* **2016**, *39* (1), 142-148.
- 176. Kawawaki, T.; Kataoka, Y.; Hirata, M.; Akinaga, Y.; Takahata, R.; Wakamatsu, K.; Fujiki, Y.; Kataoka, M.; Kikkawa, S.; Alotabi, A. S.; Hossain, S.; Osborn, D. J.; Teranishi, T.; Andersson, G. G.; Metha, G. F.; Yamazoe, S.; Negishi, Y., Creation of High-Performance Heterogeneous Photocatalysts by Controlling Ligand Desorption and Particle Size of Gold Nanocluster. *Angewandte Chemie International Edition* **2021**, *60* (39), 21340-21350.
- 177. Kurashige, W.; Mori, Y.; Ozaki, S.; Kawachi, M.; Hossain, S.; Kawawaki, T.; Shearer, C. J.; Iwase, A.; Metha, G. F.; Yamazoe, S.; Kudo, A.; Negishi, Y., Activation of Water-Splitting Photocatalysts by Loading with Ultrafine Rh–Cr Mixed-Oxide Cocatalyst Nanoparticles. *Angewandte Chemie International Edition* **2020**, *59* (18), 7076-7082.
- 178. Soldat, J.; Busser, G. W.; Muhler, M.; Wark, M., Cr2O3 Nanoparticles on Ba5Ta4O15 as a Noble-Metal-Free Oxygen Evolution Co-Catalyst for Photocatalytic Overall Water Splitting. *ChemCatChem* **2016**, *8* (1), 153-156.
- 179. Bloesser, A.; Voepel, P.; Loeh, M. O.; Beyer, A.; Volz, K.; Marschall, R., Tailoring the diameter of electrospun layered perovskite nanofibers for photocatalytic water splitting. *Journal of Materials Chemistry A* **2018**, *6* (5), 1971-1978.
- 180. Hildebrandt, N. C.; Soldat, J.; Marschall, R., Layered Perovskite Nanofibers via Electrospinning for Overall Water Splitting. *Small* **2015**, *11* (17), 2051-2057.
- 181. Soldat, J.; Marschall, R.; Wark, M., Improved overall water splitting with barium tantalate mixed oxide composites. *Chemical Science* **2014**, *5* (10), 3746-3752.
- 182. Hofmann, A.; Weiss, M.; Marschall, R., Fast low temperature synthesis of layered perovskite heterojunctions for overall water splitting. *Journal of Physics: Energy* **2020**, *3* (1), 014002.
- 183. Bloesser, A.; Marschall, R., Layered Perovskite Nanofiber Heterojunctions with Tailored Diameter to Enhance Photocatalytic Water Splitting Performance. *ACS Applied Energy Materials* **2018**, *I* (6), 2520-2525.
- 184. Li, H.; Xiao, J.; Vequizo, J. J. M.; Hisatomi, T.; Nakabayashi, M.; Pan, Z.; Shibata, N.; Yamakata, A.; Takata, T.; Domen, K., One-Step Excitation Overall Water Splitting over a Modified Mg-Doped BaTaO2N Photocatalyst. *ACS Catalysis* **2022**, *12* (16), 10179-10185.
- 185. Liu, Y.; Zhang, M.; Wang, Z.; He, J.; Zhang, J.; Ye, S.; Wang, X.; Li, D.; Yin, H.; Zhu, Q.; Jing, H.; Weng, Y.; Pan, F.; Chen, R.; Li, C.; Fan, F., Bipolar charge collecting structure enables overall water splitting on ferroelectric photocatalysts. *Nature Communications* **2022**, *13* (1), 4245.
- 186. Xu, J.; Pan, C.; Takata, T.; Domen, K., Photocatalytic overall water splitting on the perovskite-type transition metal oxynitride CaTaO2N under visible light irradiation. *Chemical Communications* **2015**, *51* (33), 7191-7194.
- 187. Hsu, C.-W.; Awaya, K.; Tsushida, M.; Miyano, T.; Koinuma, M.; Ida, S., Water Splitting Using a Photocatalyst with Single-Atom Reaction Sites. *The Journal of Physical Chemistry C* **2020**, *124* (38), 20846-20853.
- 188. Wang, D.; Pierre, A.; Kibria, M. G.; Cui, K.; Han, X.; Bevan, K. H.; Guo, H.; Paradis, S.; Hakima, A.-R.; Mi, Z., Wafer-Level Photocatalytic Water Splitting on GaN Nanowire Arrays Grown by Molecular Beam Epitaxy. *Nano Letters* **2011**, *11* (6), 2353-2357.
- 189. Doughty, R. M.; Chowdhury, F. A.; Mi, Z.; Osterloh, F. E., Surface photovoltage spectroscopy observes junctions and carrier separation in gallium nitride nanowire arrays for overall water-splitting. *The Journal of Chemical Physics* **2020**, *153* (14), 144707.

- 190. Kibria, M. G.; Zhao, S.; Chowdhury, F. A.; Wang, Q.; Nguyen, H. P. T.; Trudeau, M. L.; Guo, H.; Mi, Z., Tuning the surface Fermi level on p-type gallium nitride nanowires for efficient overall water splitting. *Nature Communications* **2014**, *5* (1), 3825.
- 191. Kibria, M. G.; Chowdhury, F. A.; Zhao, S.; Trudeau, M. L.; Guo, H.; Mi, Z., Defect-engineered GaN:Mg nanowire arrays for overall water splitting under violet light. *Applied Physics Letters* **2015**, *106* (11), 113105.
- 192. Busser, G. W.; Mei, B.; Weide, P.; Vesborg, P. C. K.; Stührenberg, K.; Bauer, M.; Huang, X.; Willinger, M.-G.; Chorkendorff, I.; Schlögl, R.; Muhler, M., Cocatalyst Designing: A Regenerable Molybdenum-Containing Ternary Cocatalyst System for Efficient Photocatalytic Water Splitting. *ACS Catalysis* **2015**, *5* (9), 5530-5539.
- 193. Qian Ding; Tao Chen; Zheng Li; Zhaochi Feng; Wang, X., Time-resolved infrared spectroscopic investigation of Ga2O3 photocatalysts loaded with Cr2O3-Rh cocatalysts for photocatalytic water splitting. *Chinese Journal of Catalysis* **2021**, *42* (5), 808-816.
- 194. Busser, G. W.; Mei, B.; Muhler, M., Optimizing the Deposition of Hydrogen Evolution Sites on Suspended Semiconductor Particles using On-Line Photocatalytic Reforming of Aqueous Methanol Solutions. *ChemSusChem* **2012**, *5* (11), 2200-2206.
- 195. Lukic, S.; Menze, J.; Weide, P.; Busser, G. W.; Winterer, M.; Muhler, M., Decoupling the Effects of High Crystallinity and Surface Area on the Photocatalytic Overall Water Splitting over β-Ga2O3 Nanoparticles by Chemical Vapor Synthesis. *ChemSusChem* **2017**, *10* (21), 4190-4197.
- 196. Zeng, Z.; Quan, X.; Yu, H.; Chen, S.; Choi, W.; Kim, B.; Zhang, S., Alkali-metal-oxides coated ultrasmall Pt sub-nanoparticles loading on intercalated carbon nitride: Enhanced charge interlayer transportation and suppressed backwark reaction for overall water splitting. *Journal of Catalysis* **2019**, *377*, 72-80.
- 197. Pu, Y.-C.; Kibria, M. G.; Mi, Z.; Zhang, J. Z., Ultrafast Exciton Dynamics in InGaN/GaN and Rh/Cr2O3 Nanoparticle-Decorated InGaN/GaN Nanowires. *The Journal of Physical Chemistry Letters* **2015**, *6* (13), 2649-2656.
- 198. Kibria, M. G.; Nguyen, H. P. T.; Cui, K.; Zhao, S.; Liu, D.; Guo, H.; Trudeau, M. L.; Paradis, S.; Hakima, A.-R.; Mi, Z., One-Step Overall Water Splitting under Visible Light Using Multiband InGaN/GaN Nanowire Heterostructures. *ACS Nano* **2013**, *7* (9), 7886-7893.
- 199. Pan, C.; Takata, T.; Domen, K., Overall Water Splitting on the Transition-Metal Oxynitride Photocatalyst LaMg1/3Ta2/3O2N over a Large Portion of the Visible-Light Spectrum. *Chemistry A European Journal* **2016**, *22* (5), 1854-1862.
- 200. Pan, C.; Takata, T.; Kumamoto, K.; Khine Ma, S. S.; Ueda, K.; Minegishi, T.; Nakabayashi, M.; Matsumoto, T.; Shibata, N.; Ikuhara, Y.; Domen, K., Band engineering of perovskite-type transition metal oxynitrides for photocatalytic overall water splitting. *Journal of Materials Chemistry A* **2016**, *4* (12), 4544-4552.
- 201. Husin, H.; Su, W.-N.; Pan, C.-J.; Liu, J.-Y.; Rick, J.; Yang, S.-C.; Chuang, W.-T.; Sheu, H.-S.; Hwang, B.-J., Pd/NiO core/shell nanoparticles on La0. 02Na0. 98TaO3 catalyst for hydrogen evolution from water and aqueous methanol solution. *International journal of hydrogen energy* **2013**, *38* (31), 13529-13540.
- 202. Alotabi, A. S.; Osborn, D. J.; Ozaki, S.; Kataoka, Y.; Negishi, Y.; Tesana, S.; Metha, G. F.; Andersson, G. G., Suppression of phosphine-protected Au9 cluster agglomeration on SrTiO3 particles using a chromium hydroxide layer. *Materials Advances* **2022**, *3* (8), 3620-3630.
- 203. Kanazawa, T.; Maeda, K., Light-Induced Synthesis of Heterojunctioned Nanoparticles on a Semiconductor as Durable Cocatalysts for Hydrogen Evolution. *ACS Applied Materials & Interfaces* **2016**, *8* (11), 7165-7172.
- 204. Kanazawa, T.; Nozawa, S.; Lu, D.; Maeda, K., Structure and Photocatalytic Activity of PdCrOx Cocatalyst on SrTiO3 for Overall Water Splitting. *Catalysts* **2019**, *9* (1).
- 205. Yoshinaga, T.; Saruyama, M.; Xiong, A.; Ham, Y.; Kuang, Y.; Niishiro, R.; Akiyama, S.; Sakamoto, M.; Hisatomi, T.; Domen, K.; Teranishi, T., Boosting photocatalytic overall water splitting by Co doping into Mn3O4 nanoparticles as oxygen evolution cocatalysts. *Nanoscale* **2018**, *10* (22), 10420-10427.

- 206. Kanazawa, T.; Lu, D.; Maeda, K., Photochemical Synthesis of Fe(III)—Cr(III) Mixed Oxide Nanoparticles on Strontium Titanate Powder and Their Application as Water Oxidation Cocatalysts. *Chemistry Letters* **2016**, *45* (8), 967-969.
- 207. Qureshi, M.; Shinagawa, T.; Tsiapis, N.; Takanabe, K., Exclusive Hydrogen Generation by Electrocatalysts Coated with an Amorphous Chromium-Based Layer Achieving Efficient Overall Water Splitting. *ACS Sustainable Chemistry & Engineering* **2017**, *5* (9), 8079-8088.
- 208. Qureshi, M.; Garcia-Esparza, A. T.; Shinagawa, T.; Sautet, P.; Le Bahers, T.; Takanabe, K., Contribution of electrolyte in nanoscale electrolysis of pure and buffered water by particulate photocatalysis. *Sustainable Energy & Fuels* **2018**, *2* (9), 2044-2052.
- 209. Sanwald, K. E.; Berto, T. F.; Jentys, A.; Camaioni, D. M.; Gutiérrez, O. Y.; Lercher, J. A., Kinetic Coupling of Water Splitting and Photoreforming on SrTiO3-Based Photocatalysts. *ACS Catalysis* **2018**, *8* (4), 2902-2913.
- 210. Su, Z.; Fang, F.; Li, X.; Han, W.; Liu, X.; Chang, K., Synergistic surface oxygen defect and bulk Ti3+ defect engineering on SrTiO3 for enhancing photocatalytic overall water splitting. *Journal of Colloid and Interface Science* **2022**, *626*, 662-673.
- 211. Su, Z.; Fang, F.; Liu, S.; Wang, N.; Wan, Y.; Guo, D.; Han, W.; Chang, K., Size-dependent Al-doped SrTiO3 affecting solar-driven overall water splitting. *Catalysis Science & Technology* **2022**, *12* (16), 5003-5008.
- 212. Fang, F.; Xu, R.; Su, Z.; Li, J.; Sun, R.; Guo, D.; Chang, K., Insight of SrCl2 as an Appropriate Flux Medium in Synthesizing Al-Doped SrTiO3 Photocatalyst for Overall Water Splitting. *Catalysis Letters* **2022**.
- 213. Nakabayashi, M.; Takata, T.; Shibata, N.; Domen, K., Nanostructural Analysis of SrTiO3:Al Photocatalyst Dispersed with Pt/Cr2O3/CoOOH Cocatalysts by Electron Microscopy. *Chemistry Letters* **2022**, *51* (10), 978-981.
- 214. Pelicano, C. M.; Saruyama, M.; Takahata, R.; Sato, R.; Kitahama, Y.; Matsuzaki, H.; Yamada, T.; Hisatomi, T.; Domen, K.; Teranishi, T., Bimetallic Synergy in Ultrafine Cocatalyst Alloy Nanoparticles for Efficient Photocatalytic Water Splitting. *Advanced Functional Materials* **2022**, *32* (31), 2202987.
- 215. Zong, S.; Tian, L.; Guan, X.; Cheng, C.; Shi, J.; Guo, L., Photocatalytic overall water splitting without noble-metal: Decorating CoP on Al-doped SrTiO3. *Journal of Colloid and Interface Science* **2022**, *606*, 491-499.
- 216. Takanabe, K.; Domen, K., Preparation of Inorganic Photocatalytic Materials for Overall Water Splitting. *ChemCatChem* **2012**, *4* (10), 1485-1497.
- 217. Qin, Y.; Fang, F.; Xie, Z.; Lin, H.; Zhang, K.; Yu, X.; Chang, K., La, Al-Codoped SrTiO3 as a Photocatalyst in Overall Water Splitting: Significant Surface Engineering Effects on Defect Engineering. *ACS Catalysis* **2021**, *11* (18), 11429-11439.
- 218. Sudrajat, H.; Babel, S.; Hartuti, S.; Phanthuwongpakdee, J.; Laohhasurayotin, K.; Nguyen, T. K.; Tong, H. D., Origin of the overall water splitting activity over Rh/Cr2O3@ anatase TiO2 following UV-pretreatment. *International Journal of Hydrogen Energy* **2021**, *46* (61), 31228-31238.
- 219. Wang, Q.; Nakabayashi, M.; Hisatomi, T.; Sun, S.; Akiyama, S.; Wang, Z.; Pan, Z.; Xiao, X.; Watanabe, T.; Yamada, T.; Shibata, N.; Takata, T.; Domen, K., Oxysulfide photocatalyst for visible-light-driven overall water splitting. *Nature Materials* **2019**, *18* (8), 827-832.
- 220. Maeda, K.; Lu, D.; Domen, K., Direct Water Splitting into Hydrogen and Oxygen under Visible Light by using Modified TaON Photocatalysts with d0 Electronic Configuration. *Chemistry A European Journal* **2013**, *19* (16), 4986-4991.
- 221. Xiao, J.; Nishimae, S.; Vequizo, J. J. M.; Nakabayashi, M.; Hisatomi, T.; Li, H.; Lin, L.; Shibata, N.; Yamakata, A.; Inoue, Y.; Domen, K., Enhanced Overall Water Splitting by a Zirconium-Doped TaON-Based Photocatalyst. *Angewandte Chemie International Edition* **2022**, *61* (17), e202116573.
- 222. Pang, R.; Teramura, K.; Tatsumi, H.; Asakura, H.; Hosokawa, S.; Tanaka, T., Modification of Ga2O3 by an Ag-Cr core-shell cocatalyst enhances photocatalytic CO evolution for the conversion of CO2 by H2O. *Chemical Communications* **2018**, *54* (9), 1053-1056.

- 223. Pang, R.; Teramura, K.; Asakura, H.; Hosokawa, S.; Tanaka, T., Effect of Thickness of Chromium Hydroxide Layer on Ag Cocatalyst Surface for Highly Selective Photocatalytic Conversion of CO2 by H2O. ACS Sustainable Chemistry & Engineering 2019, 7 (2), 2083-2090.
- 224. Pang, R.; Teramura, K.; Asakura, H.; Hosokawa, S.; Tanaka, T., Effect of Cr Species on Photocatalytic Stability during the Conversion of CO2 by H2O. *The Journal of Physical Chemistry C* **2019**, *123* (5), 2894-2899.
- 225. Pang, R.; Teramura, K.; Tanaka, T., 12 Photocatalytic conversion of CO2 by H2O over heterogeneous photocatalysts. In *Current Developments in Photocatalysis and Photocatalytic Materials*, Wang, X.; Anpo, M.; Fu, X., Eds. Elsevier: 2020; pp 179-190.
- 226. Cho, Y.-J.; Moon, G.-h.; Kanazawa, T.; Maeda, K.; Choi, W., Selective dual-purpose photocatalysis for simultaneous H2 evolution and mineralization of organic compounds enabled by a Cr2O3 barrier layer coated on Rh/SrTiO3. *Chemical Communications* **2016**, *52* (62), 9636-9639.
- 227. Zhang, K.; Chen, T.; Abbas, Y.; Jan, S. U.; Zhou, Z.; Chu, S.; Xie, G.; Ullah, S.; Akram, M. Z.; Zhang, J.; Xuan, Y.; Gong, J. R., Atomic arrangement matters: band-gap variation in composition-tunable (Ga1–xZnx)(N1–xOx) nanowires. *Matter* **2021**, *4* (3), 1054-1071.
- 228. Ha, H. D.; Yan, C.; Katsoukis, G.; Kamat, G. A.; Moreno-Hernandez, I. A.; Frei, H.; Alivisatos, A. P., Precise Colloidal Plasmonic Photocatalysts Constructed by Multistep Photodepositions. *Nano Letters* **2020**, *20* (12), 8661-8667.
- 229. AlOtaibi, B.; Fan, S.; Wang, D.; Ye, J.; Mi, Z., Wafer-Level Artificial Photosynthesis for CO2 Reduction into CH4 and CO Using GaN Nanowires. *ACS Catalysis* **2015**, *5* (9), 5342-5348.
- 230. Nishioka, S.; Shibata, K.; Miseki, Y.; Sayama, K.; Maeda, K., Visible-light-driven nonsacrificial hydrogen evolution by modified carbon nitride photocatalysts. *Chinese Journal of Catalysis* **2022**, *43* (9), 2316-2320.
- 231. Pang, R.; Teramura, K.; Morishita, M.; Asakura, H.; Hosokawa, S.; Tanaka, T., Enhanced CO evolution for photocatalytic conversion of CO2 by H2O over Ca modified Ga2O3. *Communications Chemistry* **2020**, *3* (1), 137.
- 232. Guo, Q.; Xu, J.; Luo, Y.; Yang, Y.; Wang, Z.; He, H., Cocatalyst Modification of AgTaO3 Photocatalyst for Conversion of Carbon Dioxide with Water. *The Journal of Physical Chemistry C* **2021**, *125* (48), 26389-26397.
- 233. Chen, J.; Huang, F.; Wang, Q.; Huang, Y.; Ye, X.; Zheng, F.; Li, S., Ultrastable titania-supported Au nanoparticles covered by chromia via photo-induced strategy for low-temperature CO oxidation. *Catalysis Communications* **2021**, *149*, 106199.

# **Chapter 2:** Experimental Techniques

# 2.1 X-ray Photoelectron Spectroscopy

X-ray photoelectron spectroscopy (XPS) technique is used to analyse the elemental chemical composition of the sample surface. This technique is performed by irradiating a sample using monoenergetic soft X-rays with sufficient energy that allows electrons to be excited from the core level of the elements composing the sample  $^{1,2}$ . The excitation energy of the X-rays could be from different sources of radiation, such as 1,486.7 eV for Al K $\alpha$  or 1,253.6 eV for Mg K $\alpha$ . The probing depth of XPS is  $\sim$ 5 nm, making XPS a surface-sensitive quantitative technique because only those electrons emitted from the surface are detected. The surface sensitivity is due to the electron mean free path, the average distance electrons in a sample surface can move before losing their energy due to collisions through the sample. The electron spectrometer measures the kinetic energy of the electrons by a detector such as a hemispherical analyser (HSA) placed in an ultra-high vacuum. Equation (2.1) shows how the binding energy can be calculated from the kinetic energy of the emitted electron using the photoelectric equation:

$$BE = hv - KE - \phi s$$
 Equation (2.1)

The BE is the binding energy of the atomic orbital from which the electron originates, hv is the energy of the photon, KE is the kinetic energy of the emitted electron and  $\phi s$  is the spectrometer work function (constant)<sup>2</sup>. Figure 2.1 shows a schematic illustration of the XPS principle with examples of XPS spectra.

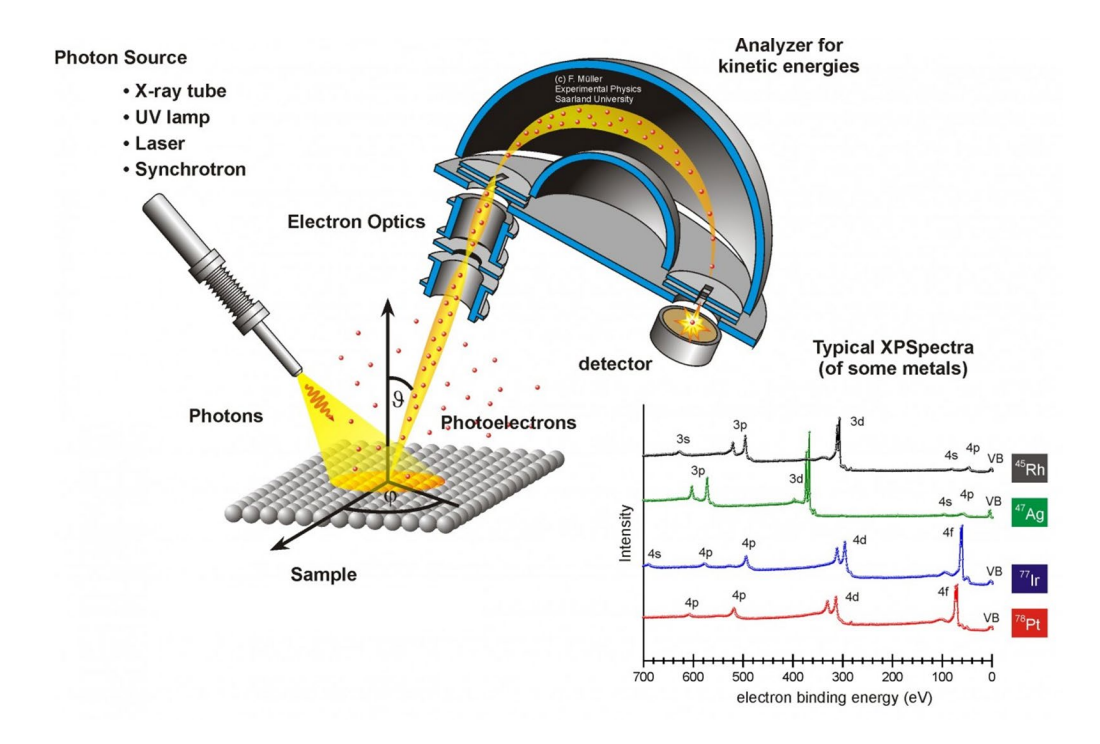


**Figure 2.1:** Principle of a photoemission spectrometer with examples of XP spectra for different metals . Reproduced with permission from Frank Muller  $^3$ .

An X-ray photoelectron spectrometer produces a spectrum of electron intensity versus binding energy. Peaks are shown at specific binding energies corresponding to a particular element present in a sample. The name of these peaks is based on the core electron that contributed to the peak; for example, the chromium 2p peak is a result of the photoelectric ejection of a 2p core electron in a chromium atom. The chemical composition of a surface sample is obtained by determining the respective contribution of every peak area and normalising the area with the respective atomic sensitive factor<sup>2, 4</sup>. The acquired spectrum of a sample sometimes shows a feature of charging during the scan, which will shift the XPS peaks to the higher binding energy, so calibration is required. The C-C 1s binding peak at 285 eV is used to calibrate the energy scale for all spectra<sup>2, 5</sup>.

An element's actual binding energy is dependent on the elemental identification and the local electronic and chemical environment, for example, the charging and oxidation of elements. Such changes influence the peak position and full width at half maximum (FWHM) are attributed to the initial and final state effects<sup>6, 7</sup>. A detailed description of initial and final state effects summarises the binding energies of Au  $4f_{7/2}$  for different Au compounds and several Au–P clusters reported to date are discussed in Chapter 1 (Section 1.5.1.1.2.1).

# Depth profiling with XPS

XPS can also be performed at different angles from the sample surface normal to the detector path to measure the concentration depth profiles. This technique is called angle-resolved X-ray photoelectron spectroscopy (AR-XPS). Due to the constant electron mean free path, the depth from which electrons can be detected changes with the angle of observation<sup>8</sup>. The distance for the electron emitted from an atom to travel and pass through the surface is longer with the larger the angle of observation. A species is enriched at the surface in case the intensity in an AR-XPS experiment increases with an increasing angle of observation. We used 60° as the maximum angle of observation to avoid the elastic scattering photoelectron effects within the sample, which affect the XPS signal<sup>9-11</sup>. Figure 2.2 illustrates the normal XPS and AR-XPS techniques.

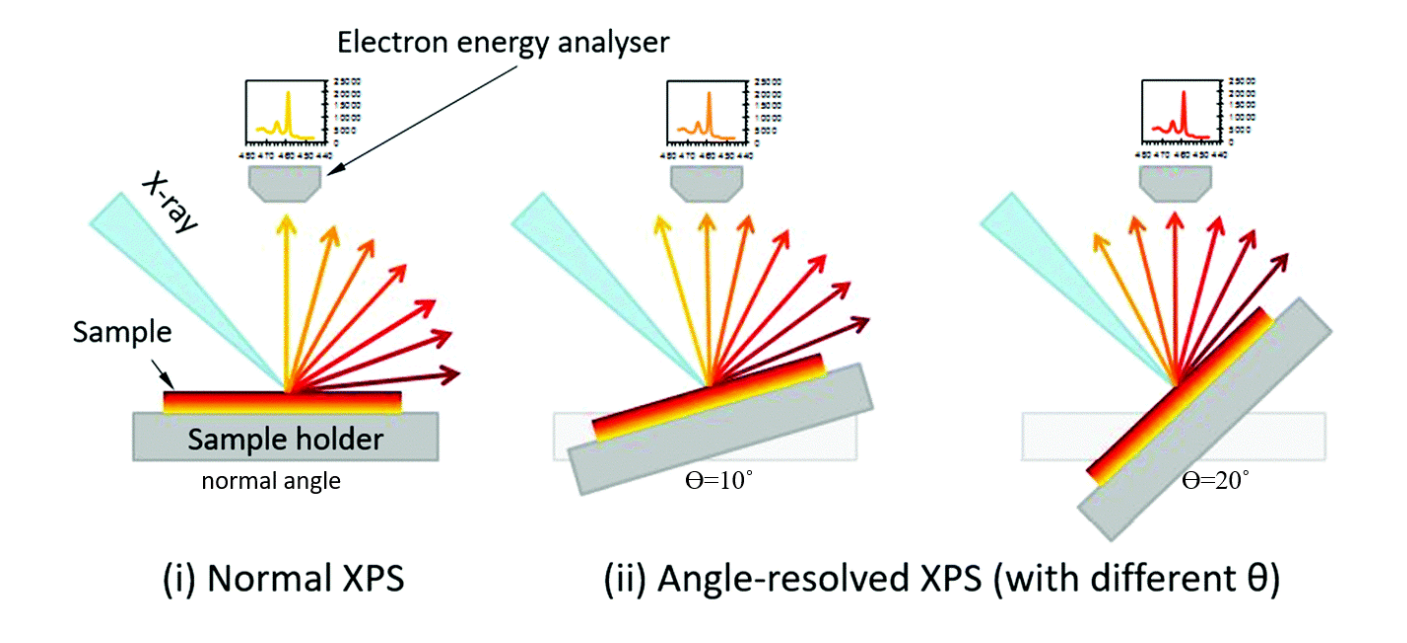


**Figure 2.2:** A schematic illustration of the normal and AR-XPS techniques. Modified from  $reference^{12}$ .

### Data Analysis

In this study, two XPS techniques were used with different X-ray sources. The first XPS at Flinders University used a non-monochromatic X-ray source with a Mg anode (12 kV–200 W, Kα line with an excitation energy of 1,253.6 eV) as X-ray irradiation to excite the photoelectric effect. A picture of the ultra-high vacuum instrument at Flinders University containing XPS is shown in Figure 2.3. The kinetic energy of the electrons emitted from the samples was analysed with a SPECS PHOIBOS-HSA 3500 hemispherical analyser with a pass energy of 10 eV at a base pressure of a few 10<sup>-10</sup> mbar. The angle between the X-ray source and the analyser is 54.7°. The second XPS technique used in this thesis is synchrotron XPS, which was undertaken at the soft X-ray beamline at the Australian Synchrotron (pictures of beamline are shown in Figure 2.4). The X-ray beam at the Australian Synchrotron has high intensity and tunability, which make it a powerful technique to characterise nanostructures and allow us to track small changes accurately<sup>13, 14</sup>. The SPECS PHOIBOS 150 hemispherical electron analyser was used with controllable photon energy to avoid overlapping satellite peaks with the peaks of interest.

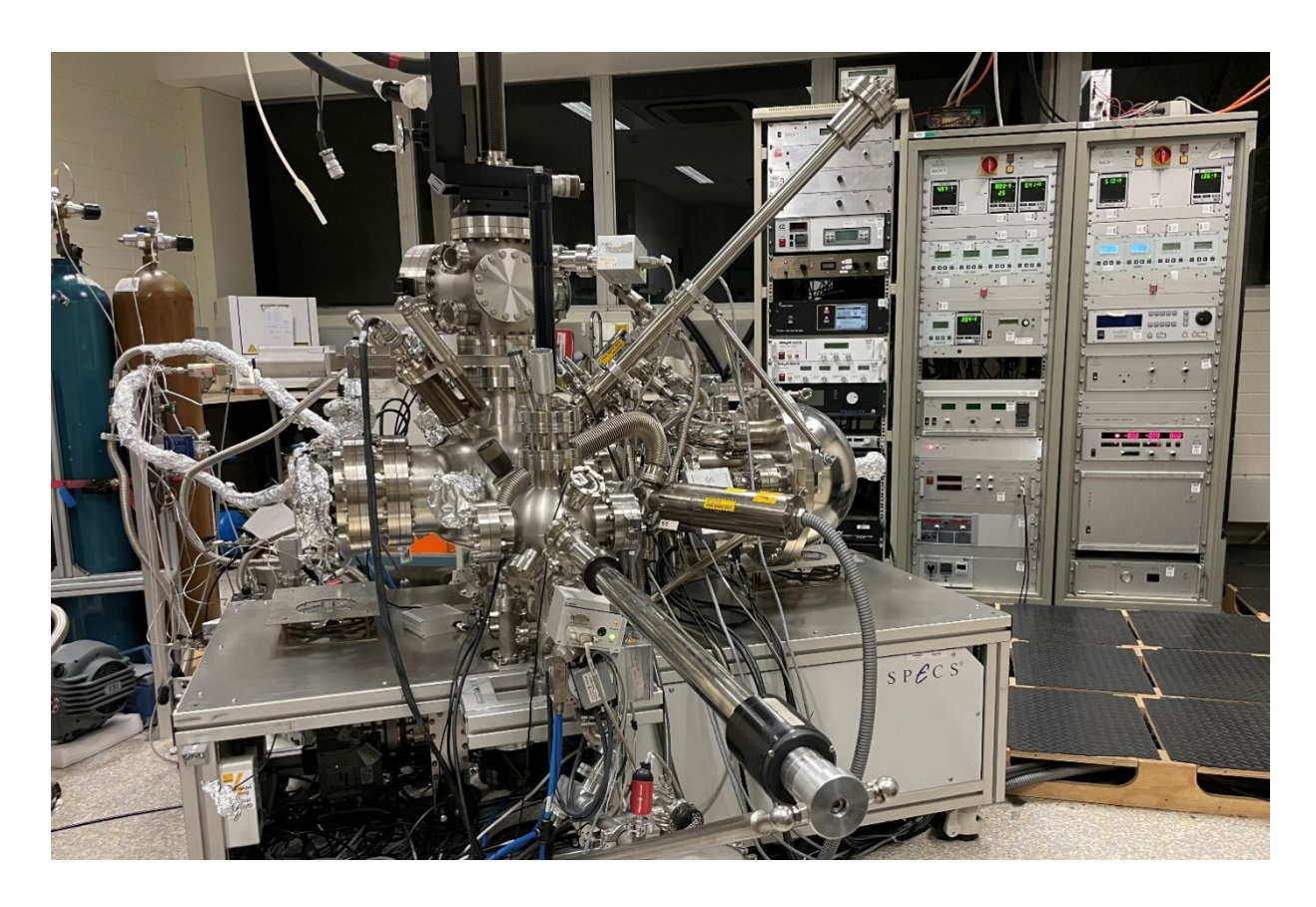


**Figure 2.3:** A picture of the ultra-high vacuum instrument at Flinders University containing XPS, MIES, UPS, and IPES.

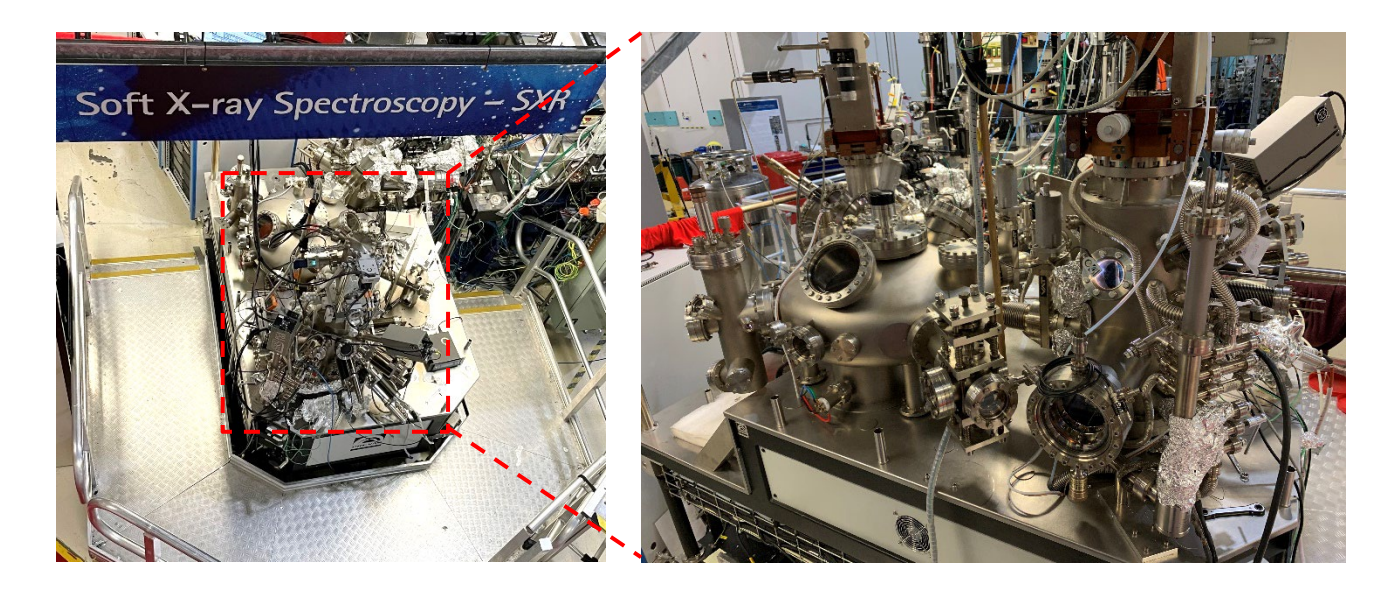


Figure 2.4: Images of the soft X-ray beamline at the Australian Synchrotron, Melbourne.

Survey scans at 40 eV pass energy at a step size of 0.5 eV were measured first, followed by high-resolution scans for both XPS techniques used in this study. The peak areas were used to calculate the relative elemental concentrations while considering the XPS sensitivity factor<sup>4</sup>. The calculation of the peak intensity of each element is done using Equation (2.2):

$$Intensity = \frac{Peak\ Area\ of\ Element}{Atomic\ Sensitivity\ Factor\ of\ Element} \qquad \qquad Equation\ (2.2)$$

Table 2.1 shows the atomic sensitivity factors that were used in this study to calculate the peak intensity.

**Table 2.1:** Atomic sensitivity factors for Mg X-ray source at 54.7° of elements were measured in this study.

Element	Line	Atomic sensitivity factors
C	1s	0.296
0	1s	0.711
Al	2p	0.234
Si	2p	0.339
P	2p	0.486
Ti	2p	2.001
Cr	2p	2.427
Sr	3d	1.843
Au	4f	6.250
Ba	3d	12.448
La	3d	9.122

The total intensity for all elements can be used to determine the atomic ratio using Equation (2.3):

$$Percentage\ Composition = \frac{Intensity\ for\ Each\ Element}{Total\ Intensity\ for\ All\ Elements} \times\ 100 \qquad Equation\ (2.3)$$

# 2.2 Ultraviolet Photoelectron Spectroscopy

Ultraviolet photoelectron spectroscopy (UPS)'s operation principle is very similar to XPS; the only difference is the energy excitation for the photoelectric effect. UPS uses energies in the range of 0–100 eV (usually the He I (21.2 eV) or the He II line (40.8 eV)), while in XPS, usually, the photon energy is higher than 1,000 eV<sup>15</sup>. UPS is a technique to emit electrons from the valence structure of a sample with a probing depth up to ~3 nm into the sample, making UPS very surface sensitive. The sample's valence electron and work function can be determined using the UPS<sup>16</sup>. The study of valence electrons is a substantial advantage to understanding the electronic properties of a sample surface<sup>17</sup>. The application of the UPS technique on supported Au clusters is discussed in Chapter 1 (Section 1.5.1.1.2.2).

#### Data Analysis

In this study, UPS experiments were performed using helium discharge lamp producing UV light with an excitation energy of 21.218 eV in the ultra-high vacuum (10<sup>-10</sup> mbar) chamber. The ejected electrons were detected using a SPECS PHOIBOS-HSA 3500 hemispherical analyser (Berlin, Germany). Singular value decomposition (SVD) algorithm was employed to analyse series of UPS spectra and identify similar components within a set of data<sup>18</sup>. The SVD algorithm works in two steps. In the first step, the measured spectra is used as matrices to determine how many basic spectra we need to recreate a set of collected spectra. These basic spectra are not referral to real substances but are important mathematically. In a second procedure, the basic spectra are transformed into meaningful reference spectra. This procedure has two boundary conditions which resulting in reference spectra should have only positive values and it must accurately represent the entire collection of measured spectra.

$$S_i = \sum_n a_n S_n^r$$
 Equation (2.4)

The  $S_i$ : the measures spectra,  $S_n^r$ : the reference spectra and  $a_n$ : the weighting factors that used in the fitting procedure. The total of the weighting factors must be equal or close to one  $(\sum_n a_n \approx 1)$ , allowing for a small margin of error of about 0.1. SVD was carried out using a solver procedure within Microsoft Excel.

# 2.3 Near-Edge X-ray Absorption Fine Structure

Near-edge x-ray absorption fine structure (NEXAFS) is a type of X-ray absorption spectroscopy (XAS) technique, which was previously discussed in Chapter 1 (Section 1.5.1.1.3). Briefly, NEXAFS is sensitive to the bonding environment formed around the absorbing atom<sup>19</sup>. NEXAFS is usually used as a fingerprint for identifying the chemical state of a specific element.

# Data Analysis

NEXAFS is used in the present study to investigate the chemical state of Cr and O. It was recorded using the soft X-ray spectroscopy beamline at the Australian Synchrotron<sup>20</sup>. NEXAFS spectra were recorded at the Cr L-edge (570–600 eV), O K-edge (520–565 eV) and Ti L-edge (450–475 eV). The NEXAFS data were processed using the Quick AS NEXAFS Tool<sup>21</sup>. NEXAFS spectra were calibrated using the reference foils of Cr for Cr L-edge, Mn for O K-edge and Ti for Ti L-edge.

# 2.4 X-ray Diffraction

X-ray diffraction (XRD) is an analytical technique used to study the crystalline and phase structure of material<sup>22</sup>. The characterised material can be in the form of powder or thin film. XRD pattern is obtained by irradiating the sample surface at different angles with X-ray radiation generated by a

cathode ray tube using a monochromatic X-ray resource. The X-ray diffracted at an angle is detected and interpreted by Bragg's law, as observed in Equation  $(2.5)^{23}$ :

$$n\lambda = 2d \sin \theta$$
 Equation (2.5)

The  $\lambda$  is the wavelength of the X-ray, n is an integer, d is the distance of the crystal layers  $\theta$  is the diffraction angle (the angle between the incident and outgoing X-ray beams, which is equal to  $2\theta$ , as shown in Figure 2.5).

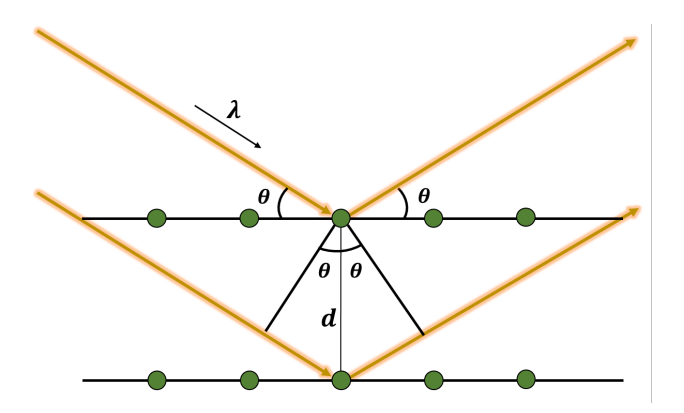


Figure 2.5: Schematic illustration of Bragg's law.

The scattered X-rays are then recorded, processed and counted. All potential diffraction peaks can be determined by scanning the sample over various angles. Identifying the unknown materials is possible by converting the diffraction peaks to d-spacings, as each mineral has a unique set of d-spacings. This identification is achieved by matching these d-spacings with standard reference patterns<sup>24</sup>.

#### Data Analysis

XRD patterns were recorded using a Bruker D8 Advance apparatus operating with a Co-K $\alpha$  ( $\lambda$  = 1.789 Å) irradiation source at 35 kV and 28 mA and processed using DIFFRAC.WIZARD software. The XRD patterns were recorded over a different 2 $\theta$  range between of 20 $^{\circ}$  to 80 $^{\circ}$ .

# 2.5 Neutral Impact Collision Ion Scattering Spectroscopy

Neutral Impact Collision Ion Scattering Spectroscopy (NICISS) is a technique that can provide information on the composition and the concentration depth profiles of elements (in non-crystalline samples) on the surface of a material when projectile ions interact with a target atom in the sample<sup>25</sup> at a depth of about 20–30 nm<sup>26</sup>. Further characterisation, such as the crystalline structure of the target sample, can be made by in-depth analysis.

NICISS typically involves directing a pulsed beam of inert gas ions, for example, helium ions (He+) at low energy ( $\approx$  3 keV), onto a sample<sup>27</sup>. As the ions travel to the sample surface, they have a chance

to be neutralised and continue penetration through the sample until they collide with an atom. Then, the He atoms neutralised are backscattered. The backscattered projectiles are detected by microchannel plates to produce the time-of-flight (TOF) spectrum. The kinetic energy of the backscattered projectiles is determined by their TOF from the target atom to the detector. During the backscattering process, the projectiles lose energy in an amount proportional to the mass of the element on target. The energy loss can be calculated from their primary energy and backscattered kinetic energy. In this case, the atomic mass of the target sample can be determined, and the element can be identified.

In analysing data from the NICISS spectrum, two types of energy loss need to be considered. Inelastic energy loss has to be considered for determining the backscattered projectile's energy as well as the inelastic energy loss due to small-angle scattering forms part of the continuous energy loss of the projectiles that pass through the material and depends on the energy loss straggling and stopping power of the section, as this has been determined previously<sup>28, 29</sup>. By combining the two mechanisms, a distribution of the element on the scale of a certain depth into the sample bulk is accomplished.

### Data Analysis

A picture of NICISS instrument at Flinders University is shown in Figure 2.6 This study used helium ions as projectiles with a kinetic energy of 3 keV. The TOF spectrum was recorded at a base pressure of 1  $\times$  10<sup>-7</sup> mbar. The size of the sample is 1 cm<sup>2</sup>.

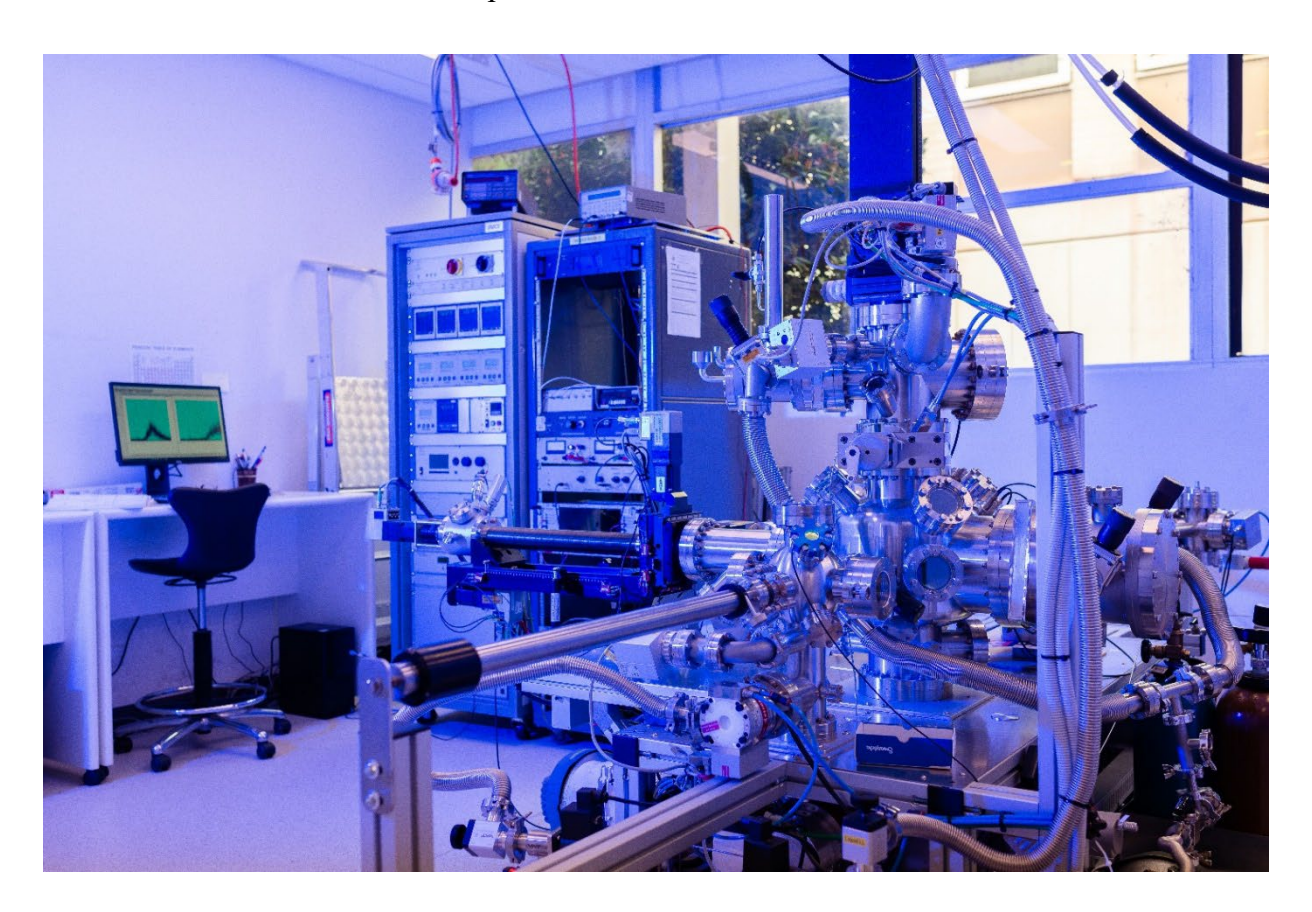


*Figure 2.6:* an image of the NICISS instrument at Flinders University.

# 2.6 Scanning Electron Microscopy

Scanning electron microscopy (SEM) is an electron microscope technique that scans the surface of a solid sample using high-energy electrons to produce a variety of signals. A two-dimensional image is made from the collected signals over an area of the surface sample. These signals hold information about the sample surface's external topography and chemical composition. The chemical composition of a spot size of a few micrometres can be determined using the energy-dispersive X-ray spectroscopy (EDAX) detector. The EDAX technique detects X-rays generated from the surface sample during the scanning with high-energy electrons to characterise the elemental composition and create element maps of a scanned area.

# Data Analysis

SEM detection was performed on an FEI Inspect F50 microscope using an electron energy of 15 kV with a resolution of up to 1 μm for better observation of the Z-contrast. The TiO<sub>2</sub> layer thickness was determined by combining the SEM imaging of the cross-section of the samples in combination with energy disperse X-ray spectroscopy (EDAX).

# 2.7 Atomic Force Microscopy

Atomic force microscopy (AFM) is an imaging technique used to obtain an image of surface topography and other information from a sample at a high resolution. AFM instrument consists of a laser source, a position-sensitive detector, a piezoelectric manipulator and a cantilever with a tip attached at the end. The AFM image is created by detecting the reflected light from the laser projected onto the cantilever's backside using a position-sensitive detector. The tip is raster horizontally scanned over the surface following the topography, making a topographic image. The information obtained from the interaction of a tip with the sample surface can be a simple physical topography or diversified as measurements of chemical or physical properties of the material<sup>30</sup>.

### Data Analysis

In this thesis, AFM images were acquired using a Bruker Multimode 8 AFM with a Nanoscope V controller using tapping mode in air, with all parameters including set-point, scan rate and feedback gains adjusted to optimize image quality. The AFM probes used were Mikromasch HQ:NSC15 Si probes with a nominal spring constant of 40 N m<sup>-1</sup> and a nominal tip diameter of 16 nm. The scanner was calibrated in x, y and z directions using silicon calibration grid (Bruker model numbers VGRP: 10 μm pitch, 180 nm depth, PG: 1 μm pitch, 110 nm depth). All analysis of AFM images was performed using Nanoscope analysis software version 1.4. Presented AFM topography images have been flattened and the average roughness, Ra, of each image was determined using the roughness analysis function in the Nanoscope analysis software.

# 2.8 Laser Scanning Confocal Microscope

Laser scanning confocal microscope (LSCM) is fast, non-contact, non-destructive and open to the atmosphere technique to characterise the three-dimensional nano-level surface topography. It uses a point laser illumination scanning across a sample to provide a high-resolution measurement of surface roughness, steps and other features. LSCM can detect steps in the nanometre range.

### Data Analysis

In this study, the surface roughness of TiO<sub>2</sub> films was measured at Adelaide Microscopy, University of Adelaide, using a laser scanning confocal microscope (Olympus LEXT OLS5000-SAF 3D LSCM) with 100x/0.80NA and 50x/0.60NA LEXT objective lenses. The arithmetic mean deviation (Ra) and root mean square deviation (Rq) values were determined using the Olympus Data Analysis application software.

# 2.9 Scanning Transmission Electron Microscopy

Scanning transmission electron microscopy (STEM) technique was introduced previously in more detail, including examples about the uses of STEM to study gold clusters, in Chapter 1 (Section 1.5.1.1.1).

## Data Analysis

STEM is applied to determine the size and distribution of the deposited Au clusters and thickness of the CrO<sub>x</sub> overlayer. STEM was applied with a high-angle annular dark-field (HAADF) detector (FEI Titan Themis 80-200). The STEM measurements were operated at 200 kV with a HAADF collection angle greater than 50 mrad. The energy-dispersive X-ray spectroscopy (EDS) elemental maps was employed with STEM-HAADF to determine the elemental distribution. STEM-EDS elemental maps obtained at a resolution up to 1 nm. The Velox<sup>TM</sup> software was used to process elemental maps data.

# 2.10 References

- 1. Reinert, F.; Hüfner, S., Photoemission spectroscopy—from early days to recent applications. *New Journal of Physics* **2005**, *7*, 97-97.
- 2. Moulder, J. F., Handbook of x-ray photoelectron spectroscopy: a reference book of standard data for use in x-ray photoelectron spectroscopy. *Handbook of x-ray photoelectron spectroscopy*: **1992**.
- 3. Müller, F. Epitaktisches Wachstum von Graphen und Boronitren auf Übergangsmetallen. Habilitation Thesis, Saarland University, 2014.
- 4. Band, I. M.; Kharitonov, Y. I.; Trzhaskovskaya, M. B., Photoionization cross sections and photoelectron angular distributions for x-ray line energies in the range 0.132-4.509 keV targets:  $1 \le Z \le 100$ . Atomic Data and Nuclear Data Tables **1979**, 23 (5), 443-505.
- 5. Briggs, D., Practical surface analysis. *Auger and X-Ray Photoelecton Spectroscory* **1990,** *I*, 151-152.
- 6. Roberts, F. S.; Anderson, S. L.; Reber, A. C.; Khanna, S. N., Initial and Final State Effects in the Ultraviolet and X-ray Photoelectron Spectroscopy (UPS and XPS) of Size-Selected Pdn Clusters Supported on TiO2(110). *The Journal of Physical Chemistry C* **2015**, *119* (11), 6033-6046.
- 7. Anderson, D. P.; Adnan, R. H.; Alvino, J. F.; Shipper, O.; Donoeva, B.; Ruzicka, J.-Y.; Al Qahtani, H.; Harris, H. H.; Cowie, B.; Aitken, J. B., Chemically Synthesised Atomically Precise Gold Clusters Deposited and Activated on Titania. Part II. *Physical chemistry chemical physics* **2013**, *15* (35), 14806-14813.
- 8. Seah, M. P.; Dench, W. A., Quantitative electron spectroscopy of surfaces: A standard data base for electron inelastic mean free paths in solids. *Surface and Interface Analysis* **1979**, *1* (1), 2-11.
- 9. Eschen, F.; Morgner, H.; Vogt, J., Vibrational excitations in electron energy loss spectroscopy of liquids. *Journal of Electron Spectroscopy and Related Phenomena* **1996**, 82 (3), 145-150.
- 10. Alharbi, T. M. D.; Andersson, G. G., Ordering in Surfactant Foam Films Transferred onto Hydrophilic and Hydrophobic Substrates. *The Journal of Physical Chemistry C* **2017**, *121* (46), 25967-25977.
- 11. Baschenko, O.; Bökman, F.; Bohman, O.; Siegbahn, H., Distribution of ions in subsurface layers of liquid solutions studied by ARXPS. *Journal of electron spectroscopy and related phenomena* **1993**, *62* (4), 317-334.
- 12. Azadmanjiri, J.; Wang, J.; Berndt, C. C.; Kapoor, A.; Zhu, D. M.; Ang, A. S. M.; Srivastava, V. K., Influence of charged defects on the interfacial bonding strength of tantalum- and silver-doped nanograined TiO2. *Physical Chemistry Chemical Physics* **2017**, *19* (19), 11881-11891.
- 13. Rosseel, T.; Carlson, T.; Negri, R.; Beall, C.; Taylor, J. Synchrotron radiation as a source for quantitative XPS: advantages and consequences; Oak Ridge National Lab.: 1986.
- 14. Lagomarsino, S.; Cedola, A., X-ray microscopy and nanodiffraction. *Encyclopedia of nanoscience and nanotechnology* **2004**, *10*, 681-710.
- 15. Hüfner, S., *Photoelectron spectroscopy: principles and applications*. Third Revised and Enlarged Edition ed.; Springer Science & Business Media: 2003; Vol. 82.
- 16. Schmerl, N. M.; Khodakov, D. A.; Stapleton, A. J.; Ellis, A. V.; Andersson, G. G., Valence band structure of PDMS surface and a blend with MWCNTs: A UPS and MIES study of an insulating polymer. *Applied Surface Science* **2015**, *353*, 693-699.
- 17. Moruzzi, V. L.; Janak, J. F.; Williams, A. R., Calculated electronic properties of metals. Elsevier: 2013.
- 18. Krischok, S.; Höfft, O.; Günster, J.; Stultz, J.; Goodman, D. W.; Kempter, V., H2O interaction with bare and Li-precovered TiO2: studies with electron spectroscopies (MIES and UPS(HeI and II)). *Surface Science* **2001**, *495* (1), 8-18.
- 19. Bianconi, A.; Inoccia, L.; Stipcich, S., *EXAFS and Near Edge Structure: Proceedings of the International Conference Frascati, Italy, September 13–17, 1982.* Springer Science & Business Media: Springer Berlin Heidelberg, 2012; Vol. 27.

- 20. Cowie, B. C. C.; Tadich, A.; Thomsen, L., The Current Performance of the Wide Range (90–2500 eV) Soft X-ray Beamline at the Australian Synchrotron. *AIP Conference Proceedings* **2010**, *1234* (1), 307-310.
- 21. Gann, E.; McNeill, C. R.; Tadich, A.; Cowie, B. C. C.; Thomsen, L., Quick AS NEXAFS Tool (QANT): a program for NEXAFS loading and analysis developed at the Australian Synchrotron. *Journal of Synchrotron Radiation* **2016**, *23* (1), 374-380.
- 22. Dinnebier, R. E.; Billinge, S. J., *Powder diffraction: theory and practice*. Royal society of chemistry: 2008.
- 23. Bragg, W. H.; Bragg, W. L., The reflection of X-rays by crystals. *Proceedings of the Royal Society of London. Series A, Containing Papers of a Mathematical and Physical Character* **1913,** 88 (605), 428-438.
- 24. Moecher, D. P., Characterization and Identification of Mineral Unknowns: A Mineralogy Term Project. *Journal of Geoscience Education* **2004**, *52* (1), 5-9.
- 25. Andersson, G.; Ridings, C., Ion Scattering Studies of Molecular Structure at Liquid Surfaces with Applications in Industrial and Biological Systems. *Chemical Reviews* **2014**, *114* (17), 8361-8387.
- 26. Alharbi, A. R. M.; Andersson, J. M.; Köper, I.; Andersson, G. G., Investigating the Structure of Self-Assembled Monolayers Related to Biological Cell Membranes. *Langmuir* **2019**, *35* (44), 14213-14221.
- 27. Ridings, C.; Lockett, V.; Andersson, G., Comparing the charge distribution along the surface normal in the [C6mim]+ ionic liquid with different anions. *Colloids and Surfaces A: Physicochemical and Engineering Aspects* **2012**, *413*, 149-153.
- 28. Andersson, G.; Morgner, H., Determining the stopping power of low energy helium in alkanethiolates with Neutral Impact Collision Ion Scattering Spectroscopy (NICISS). *Nuclear Instruments and Methods in Physics Research Section B: Beam Interactions with Materials and Atoms* **1999**, *155* (4), 357-368.
- 29. Andersson, G.; Morgner, H., Impact collision ion scattering spectroscopy (ICISS) and neutral impact collision ion scattering spectroscopy (NICISS) at surfaces of organic liquids. *Surface Science* **1998**, *405* (1), 138-151.
- 30. Bowen, W. R.; Hilal, N., *Atomic Force Microscopy in Process Engineering: An Introduction to AFM for Improved Processes and Products*. Elsevier Science: 2009.

# Chapter 3: Investigation of the Diffusion of Cr<sub>2</sub>O<sub>3</sub> into Different Phases of TiO<sub>2</sub> upon Annealing

This chapter is a reformatted version of the paper published in *ACS Applied Energy Materials*, 2021, Vol. 4, Issue 1, Page 322-330. **DOI**: 10.1021/acsaem.0c02270

# Author Contribution:

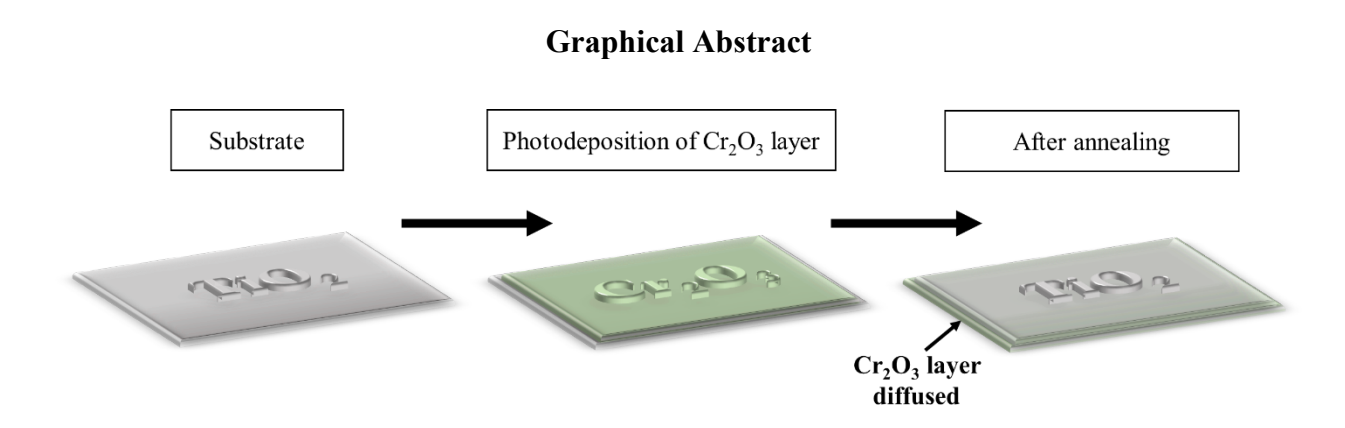
Abdulrahman Alotabi: Designed and performed experiments, data analysis and interpretation, and prepared the manuscript for publication.

Christopher Gibson: Performed AFM measurements and analysis on samples prepared by AA Gregory Metha: Intellectual contribution in revision of manuscript.

Gunther Andersson: Intellectual contribution in conceptualising experiments, data interpretation & revision of manuscript.

# 3.1 Abstract

Chromium oxide (Cr<sub>2</sub>O<sub>3</sub>) can be used as a protective layer for photocatalysts to improve photocatalytic water splitting activity and is commonly photodeposited. However, it is not known how the conditions of the Cr<sub>2</sub>O<sub>3</sub> formation affect the formation of the protective layer and potential diffusion into the substate onto which the Cr<sub>2</sub>O<sub>3</sub> has been deposited. We have investigated the stability of Cr<sub>2</sub>O<sub>3</sub> photodeposited onto the surface of different crystal phases of TiO<sub>2</sub> with subsequent annealing at a range of temperatures up to 600 °C. X-ray photoelectron spectroscopy and synchrotron near-edge X-ray absorption fine structure were used to analyse the chemical composition of the sample, Neutral impact collision ion scattering spectroscopy was used to study the concentration depth profile of the elements in the sample and atomic force microscopy was used to investigate the morphology of the surface. Under annealing conditions, the Cr<sub>2</sub>O<sub>3</sub> layer diffuses into the amorphous and anatase phases of TiO<sub>2</sub> but remains at the surface of the rutile phase. This finding is attributed to differences in surface energy with Cr<sub>2</sub>O<sub>3</sub> being higher in surface energy than the amorphous and anatase phases of TiO<sub>2</sub> but lower in surface energy than the rutile phase of TiO<sub>2</sub>. Reduction of Cr<sub>2</sub>O<sub>3</sub> to Cr metal was observed after annealing with no observation of the formation of higher oxidised forms of chromium oxide like CrO<sub>2</sub> and CrO<sub>3</sub>. These findings are of general interest to researchers utilising a protective overlayer to augment photocatalytic water splitting.



# 3.2 Introduction

The world is currently facing the issue of global warming and associated problems, the leading cause of which is fossil fuels <sup>1, 2</sup>. Due to its physical and chemical properties, hydrogen is a suitable substitute renewable energy source for fossil fuels as a transportation fuel and an energy carrier <sup>1, 3</sup>. Hydrogen found on earth is usually part of chemical compounds, for instance, hydrocarbons and water. Many methods exist to produce hydrogen <sup>1</sup>, including renewable and non-renewable methods.

Photocatalytic water splitting is a method for producing hydrogen using solar energy. This process produces hydrogen by splitting water into hydrogen and oxygen using semiconductor materials as photocatalysts and has been improved using noble metals as co-catalysts <sup>4-7</sup>. However, noble metals also encourage the reverse reaction of the hydrogen and oxygen, resulting from water splitting, decreasing the efficiency of the photocatalytic water splitting. Therefore, it is desirable to develop methods for suppressing the reverse reaction.

Domen and co-workers established that the oxygen reverse reaction could be blocked using chromium (III) oxide  $(Cr_2O_3)$  overlayers after the photodeposition of rhodium nanoparticles onto  $(Ga_{1-x}Zn_x)(N_{1-x}O_x)$ . The  $Cr_2O_3$  layer increases efficiency by preventing the oxygen from reaching the substrate surface and recombining as water. This is due to the permeability of protons and evolved  $H_2$ , but not  $O_2$ , through the  $Cr_2O_3$  layer. <sup>8-16</sup> There is evidence that through this mechanism,  $Cr_2O_3$  overlayers deposited onto the photocatalyst substrate leads to an enhancement of the photocatalytic water splitting activity <sup>8-20</sup>.

Cr<sub>2</sub>O<sub>3</sub> layer functionality has been explored in electrocatalytic and photocatalytic systems using a platinum disk electrode and platinum nanoparticles deposited onto SrTiO<sub>3</sub> with a variety of redox species by Qureshi and co-workers. <sup>21</sup>. It has been found that using the Cr<sub>2</sub>O<sub>3</sub> layer with both systems improves the hydrogen evolution reaction, even in the presence of redox species.

A remarkable improvement of photocatalytic water splitting activity was recently reported by Negishi and co-workers using a Cr<sub>2</sub>O<sub>3</sub> layer over Au<sub>25</sub>-loaded BaLa<sub>4</sub>Ti<sub>4</sub>O<sub>15</sub> (BLTO) <sup>22</sup>. The Au clusters were deposited as a co-catalyst after the photodeposition of the Cr<sub>2</sub>O<sub>3</sub> layer, followed by calcination in vacuum to migrate the clusters between the Cr<sub>2</sub>O<sub>3</sub> layer and the BLTO substrate according to the strong metal-support interaction (SMSI) mechanism. The authors considered that the migration occurs due to the high surface energy of Au clusters. They found that the Cr<sub>2</sub>O<sub>3</sub> layer enhanced the stability of the Au clusters and improved the photocatalytic water splitting activity to 19 times greater than that of Au<sub>25</sub>–BaLa<sub>4</sub>Ti<sub>4</sub>O<sub>15</sub> without a Cr<sub>2</sub>O<sub>3</sub> layer <sup>22</sup>. It should be noted that the SMSI method is a process occurs by thermally treating reducible where heating the samples increases the mobility of

the species forming the sample and can lead to diffusion. The degree of diffusion from the surface to the bulk is given by the relative surface energies of the substances. The lower the surface energy of a substance, the higher its tendency to diffuse to and cover the surface. The SMSI was discovered by Tauster et al, in 1978<sup>33, 34</sup>.

Photodeposition was applied in the above studies to deposit the Cr<sub>2</sub>O<sub>3</sub> layer onto the substrate. Photodeposition is based on light-induced electrochemistry, which involves oxidation and reduction at the surface of metal oxide. This deposition mechanism can be achieved by the illumination of a semiconductor immersed into an aqueous solution of Cr<sub>2</sub>O<sub>3</sub> with photon energy greater than the band gap of the substrate to excite electrons from the valence band to the conduction band, leaving a hole in the valence band. The reduction will occur by the electron acceptor at the conduction band, and the oxidation will occur by the electron donor at the valence band <sup>23</sup>. In the case of the Cr<sub>2</sub>O<sub>3</sub> layer, K<sub>2</sub>CrO<sub>4</sub> using Cr (VI) cations is used as a source for photodeposited Cr<sub>2</sub>O<sub>3</sub> on the surface of metal oxides<sup>24, 25</sup>.

Understanding the Cr<sub>2</sub>O<sub>3</sub> overlayer stability at elevated temperatures on metal oxides is a prerequisite for assessing its suitability and role for the protection function of the overlayer because heating of the samples is applied in the preparation of the photocatalyst. The purpose of this work is to investigate the diffusion and chemical composition of the Cr<sub>2</sub>O<sub>3</sub> photodeposited layer on TiO<sub>2</sub> as a function of parameters which are relevant for the process of depositing Cr<sub>2</sub>O<sub>3</sub> overlayer. The parameters are (i) the heating temperature of the samples after depositing the Cr<sub>2</sub>O<sub>3</sub> overlayer and (ii) the crystal phase of the TiO<sub>2</sub> substrate. The Cr<sub>2</sub>O<sub>3</sub> deposition and heating procedure was applied using different crystal phases of TiO<sub>2</sub> (amorphous, anatase and anatase:rutile) to investigate how the diffusion of Cr<sub>2</sub>O<sub>3</sub> depends on the surface energies of different crystal phases of TiO<sub>2</sub>.

The surface of the sample was characterised using the highly surface-sensitive technique of X-ray photoelectron spectroscopy (XPS). Near-edge X-ray absorption fine structure (NEXAFS) is a powerful technique providing direct information using a synchrotron X-ray source and was used to study the oxidation state and local chemical environment. Neutral impact collision ion scattering spectroscopy (NICISS) was used to investigate the concentration depth profile of the elements in the sample. Atomic force microscopy (AFM) was used to provide information on the topography and average roughness of the sample surfaces.

# 3.3 Experimental

#### 3.3.1 Material and sample preparation

Preparation of TiO<sub>2</sub> thin films

A precursor  $TiO_2$  film was prepared by a high vacuum radio frequency (RF) magnetron sputtering device (HHV/Edwards TF500 sputter coater). The  $TiO_2$  film was deposited on a silicon wafer by sputtering a target of ceramic  $TiO_2$  using  $Ar^+$ . The thickness of the  $TiO_2$  was approximately  $82 \pm 5$  nm as determined by cross–section scanning electron microscopy (see Figure A1). The crystal phase of the deposited  $TiO_2$  film was amorphous. The wafer was cut into 1 cm x 1 cm samples for photodeposition of the  $Cr_2O_3$  layer.

The conversion of TiO<sub>2</sub> into its two main phases can be achieved through heating. The phase structure of the TiO<sub>2</sub> was determined using X-ray diffraction (Figure A2). The anatase crystal phase was obtained by heating the sample in air for 3 hours at 900 °C with a heating rate of 10.2 °C/min, while a mixed phase of anatase:rutile was made by heating the sample in air for 18 hours at 1100 °C. The mixed phase was estimated to be 50:50 anatase and rutile according to the intensity of the main peaks in XRD of anatase and rutile (Figure A2). The average crystalline domain size of anatase was 6.6 nm and rutile 7.6 nm. These were obtained from the broadening of anatase and rutile main peaks (Figure A3). The different TiO<sub>2</sub> samples are hereafter referred to as (i) aTiO<sub>2</sub> (i.e. amorphous titania), (ii) anatase and (iii) anatase:rutile. Note that the density of amorphous, anatase and rutile is 2.9-3.8 g/cm<sup>3</sup>, 3.78 g/cm<sup>3</sup> and 4.23 g/cm<sup>3</sup>.

# Photodeposition of Cr<sub>2</sub>O<sub>3</sub> layer

Chromium metal (Cr target 99.9%, Quorum Technologies), Chromium oxide ( $Cr_2O_3$  99%, BDH) and potassium chromate ( $K_2CrO_4 \ge 99\%$ , Sigma-Aldrich) were used as obtained. The photodeposition procedure is summarised in Figure A4. The  $K_2CrO_4$  solution was prepared using deionised water with a concentration of 0.5 mM. The  $TiO_2$  sample (1 cm x 1 cm) was immersed in 1 mL of  $K_2CrO_4$  solution and irradiated for 1h. The illumination source was a UV LED at 365 nm (Vishay, VLMU3510-365-130) with a radiant power of 690 mW at a distance of  $\sim$ 1 cm from the sample. Subsequent to the  $K_2CrO_4$  solution exposure, the sample was rinsed with deionised water and dried using nitrogen gas. These samples are hereafter referred to as (i)  $aTiO_2-Cr_2O_3$ , (ii) anatase- $Cr_2O_3$  and (iii) anatase:rutile- $Cr_2O_3$ .

#### Heat treatment

The heat treatment was applied to all titania samples at ultrahigh vacuum ( $10^{-8}$  mbar) for 10 min at various temperatures (200 °C, 300 °C, 400 °C, 500 °C and 600 °C) with a total of 50 min annealing for each sample with an average heating rate of ~ 20 °C/min. The XPS measurements were applied between each temperature using the same sample. Further, to investigate the diffusion of  $Cr_2O_3$  layer, the amorphous crystal phase was sputtered using Argon gas to remove atoms from the surface for 30 min, 60 min, 90 min and 120 min with an energy of 3 keV at sputter dose of  $1.2 \times 10^{+15}$  ions/cm<sup>2</sup> for

each 30 minute period. Note that the sample was exposed to atmosphere after annealing. XPS was recorded after each sputtering period using the same sample.

#### 3.3.2 Methods

# X-ray Photoelectron Spectroscopy

Experimental details for X-ray photoelectron spectroscopy (XPS) and angle-resolved X-ray photoelectron spectroscopy (AR-XPS) are discussed in Section 2.1. In this chapter, the calibration of the energy scale of the XPS spectra is described in the appendix section after Figure A5.

# Synchrotron X-ray Photoelectron Spectroscopy

Experimental details for Synchrotron X-ray Photoelectron Spectroscopy (Synchrotron XPS) are discussed in Section 2.1. In this chapter, Synchrotron XPS was undertaken at the soft X-ray beamline at the Australian Synchrotron with a photon energy of 750 eV. The X-ray beam was adjusted to yield an irradiation spot size of ca.  $320\times320~\mu\text{m}$ . High-resolution XPS spectra of C 1s, O 1s, Ti 2p, Cr 2p and Au 4f were recorded with a pass energy of 10 eV. The C 1s peak position at 285 eV was used to calibrate all spectra to correct for charging effects. The photon energy was calibrated by measuring the Au 4f (84 eV) peak position.

# Near-Edge X-ray Absorption Fine Structure

Experimental details for near-edge X-ray absorption fine structure (NEXAFS) are discussed in Section 2.3. In this chapter, it was used in the present study to investigate the chemical state of Cr on the samples.

### Neutral Impact Collision Ion Scattering Spectroscopy

Experimental details for neutral impact collision ion scattering spectroscopy (NICISS) are discussed in Section 2.5.

### Atomic Force Microscopy

Experimental details for atomic force microscopy (AFM) are discussed in Section 2.7. AFM is used to study the topography of a sample surface after the photodeposition of the chromium oxide layer.

### X-ray Diffraction

Experimental details for X-ray diffraction (XRD) are discussed in Section 2.4.

# Scanning Electron Microscopy

Experimental details for scanning electron microscopy (SEM) are discussed in Section 2.6. SEM measurement was performed to analyse the thickness of  $TiO_2$  film using an electron energy of 10 kV with a magnification of up to x120,000.

### Ultraviolet Photoelectron Spectroscopy

Experimental details for ultraviolet photoelectron spectroscopy (UPS) are discussed in Section 2.2.

### 3.4 Results and Discussion

# 3.4.1 Room temperature studies

High resolution XPS spectra of Cr, Ti, C and O are shown in Figures A6 and A7 and the binding energies are listed in Table A1. Below Table A1, the calibration of the binding energies is described. Briefly, the elements Cr, Ti, C and O were identified: Cr is assigned to Cr<sub>2</sub>O<sub>3</sub>, Ti assigned to TiO<sub>2</sub>, C is assigned to adventitious hydrocarbons and O assigned to TiO<sub>2</sub> and Cr<sub>2</sub>O<sub>3</sub>. AR-XPS was used to confirm the formation of Cr at the surface of aTiO<sub>2</sub> pre-annealing. Figure 3.1 shows the relative intensities of Ti and Cr of aTiO<sub>2</sub>-Cr<sub>2</sub>O<sub>3</sub> for the AR-XPS measurements for six different angles (normal 0°, 30°, 40°, 45°, 50° and 60°). It can be seen that the Ti intensity decreases with an increasing angle of observation while the Cr intensity increases, meaning that the Cr content is increased at the surface and forms a layer covering the aTiO<sub>2</sub>. The Ti 2p and Cr 2p spectra at each angle are shown in Figure A8 in the appendix information.

AR-XPS can be used to determine the layer thicknesses  $^{26}$ . Eschen et al. have described the procedure in detail in  $^{27}$ . The concentration depth profile of  $aTiO_2$ - $Cr_2O_3$  are showing in Figure A9. The depth profile measurement interpreted that the thickness of Cr is  $\sim 11$  Å (1.1 nm) (see Figure A9 for more information).

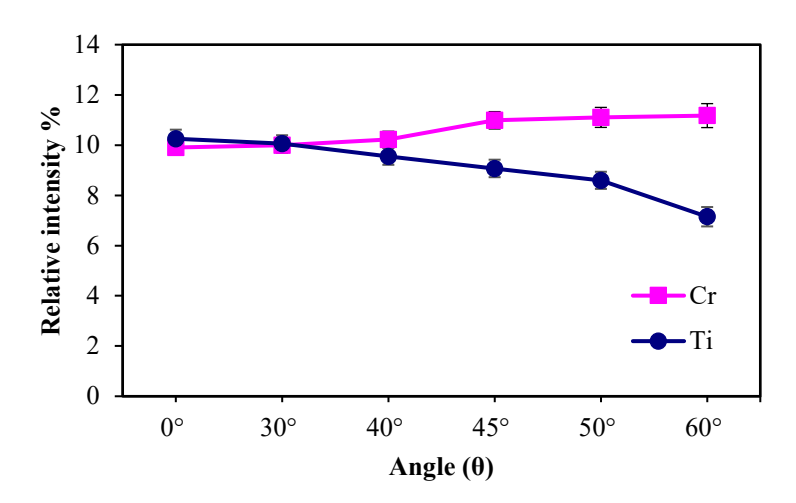


*Figure 3.1*: AR-XPS relative intensities of Titanium and Chromium for the aTiO<sub>2</sub>-Cr<sub>2</sub>O<sub>3</sub> sample.

NEXAFS was used in the present study to investigate the chemical state of Cr on the samples. NEXAFS Cr L-edge spectra are shown in Figures 3.2A, 3.2C and 3.2D. The Cr L-edge spectra show

two strong absorption edges: the Cr  $L_3$ -edge at the low energy ( $\sim$ 578 eV) and Cr  $L_2$ -edge at the high energy ( $\sim$ 586 eV).

Chromium metal sample was used here to determine metallic Cr L-edge spectrum in NEXAFS. The metallic Cr and Cr<sub>2</sub>O<sub>3</sub> spectra appear in Figure 3.2A with three different features for the metallic Cr spectrum. The first feature is that the Cr L<sub>3</sub>-edge of the metallic Cr spectrum starts before 575 eV, while the Cr<sub>2</sub>O<sub>3</sub> spectrum starts after 575 eV. The second feature is that the Cr L<sub>3,2</sub>-edges of the metallic Cr spectrum have fewer sharp peaks comparing to the Cr L<sub>3,2</sub>-edges of the Cr<sub>2</sub>O<sub>3</sub> spectrum. These peaks are indicated with black arrows in the figure. Note that the peak at 576.5 eV becomes a shoulder in the Cr metal spectrum. The third feature appears at the photon energy of 584 eV, which is an interference of a small peak on the tail of Cr L<sub>2</sub>-edge. This peak is also indicated by a black arrow in the figure. These features are essential for distinguishing the difference between metallic Cr and Cr<sub>2</sub>O<sub>3</sub> in Cr L<sub>3,2</sub>-edge spectra.

Figure 3.2B shows the Cr 2p XPS spectrum of the metallic Cr reference sample. The two peaks in the spectrum indicate that the metallic Cr reference sample also contains  $Cr_2O_3$  (30:70). Note that this XPS ratio depends on the depth profile of XPS, which would be different for NEXAFS. The metallic Cr sample contains  $Cr_2O_3$  at the surface due to the exposure to the air. When Cr atoms at the surface come into contact with oxygen molecules from the air, the surface atoms oxidise to form an oxide layer  $^{28}$ . Therefore, XPS spectrum of the metallic Cr reference sample demonstrates this as a mixture of Cr and  $Cr_2O_3$ . Thus, the NEXAFS spectrum of the metallic Cr reference sample should be considers as mixture of Cr and  $Cr_2O_3$ .

In Figure 3.2C  $^{29}$ , reference spectra of the Cr L<sub>2,3</sub>-edges of Cr<sub>2</sub>O<sub>3</sub>, CrO<sub>2</sub> and CrO<sub>3</sub> can be found, which can be used as fingerprints of the chemical state of Cr. It can be seen that both references spectra have different lineshapes. This can be seen clearly in the Cr L<sub>3</sub>-edge for CrO<sub>2</sub> and CrO<sub>3</sub> where the main peak shifts to high energy with a high oxidation state.

Figure 3.2D shows the Cr L-edge spectra of  $Cr_2O_3$  and  $aTiO_2-Cr_2O_3$ , which both have the same lineshape. This demonstrates that the chemical state of Cr photodeposited onto  $aTiO_2$  is chromium (III) oxide  $(Cr_2O_3)$ . Also, the chemical state of Cr on the various substrates (anatase and anatase:rutile) was the same as evident from XPS (see Figure A10).

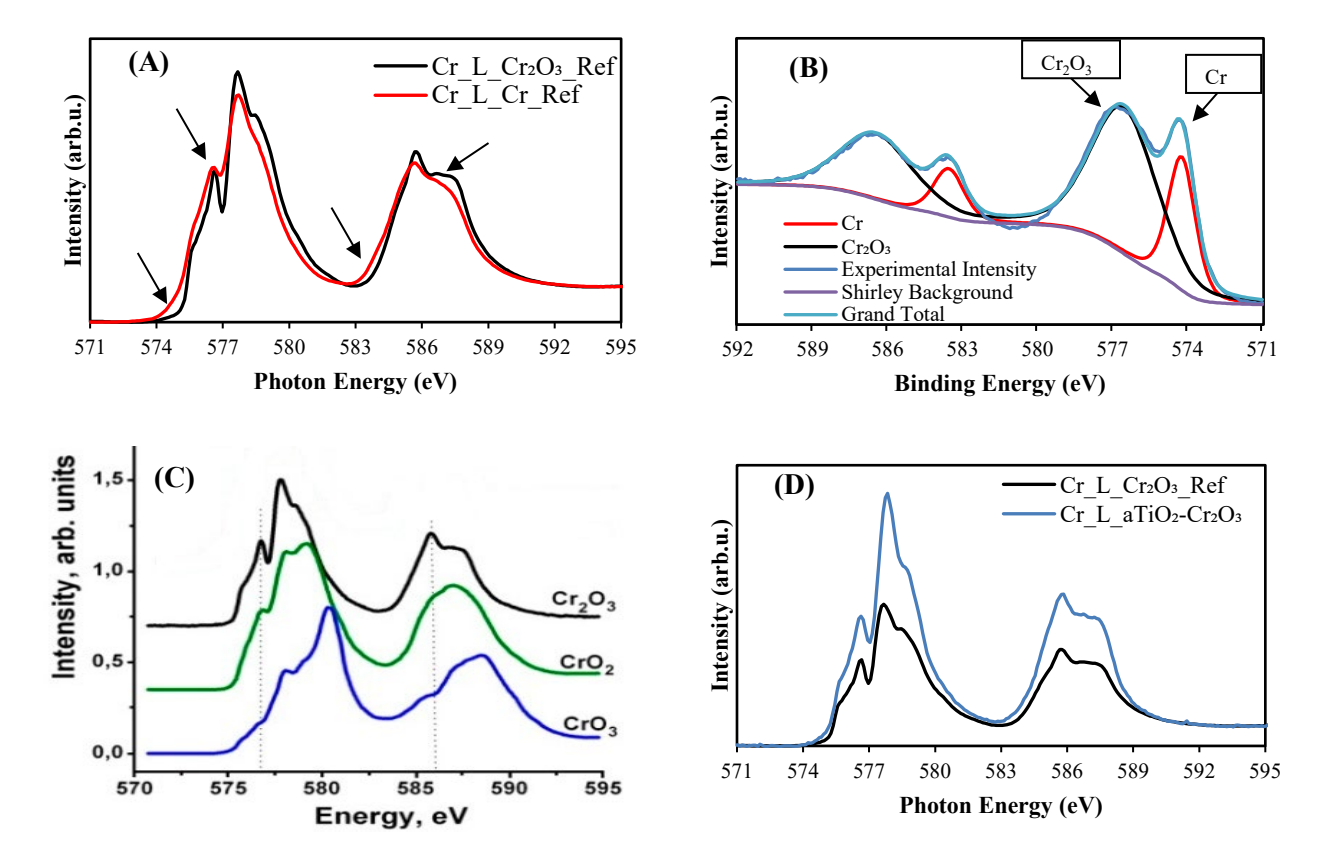


**Figure 3.2**: (A) Cr L-edge NEXAFS spectra of chromium metal and  $Cr_2O_3$  reference samples. (B) Cr 2p XPS spectrum of chromium metal reference sample. (C) Cr L-edge NEXAFS spectra of  $Cr_2O_3$ ,  $CrO_2$  and  $CrO_3$  from reference  $^{29}$ , (D) Cr L-edge NEXAFS spectra of  $aTiO_2$ - $Cr_2O_3$  and  $Cr_2O_3$  reference for comparison. It should be noted that the reference spectra for  $Cr_2O_3$  in panel A, C and D are the same.

Figure 3.3A shows the previously reported O K-edge spectra of Cr<sub>2</sub>O<sub>3</sub>, CrO<sub>2</sub>, CrO<sub>3</sub>, anatase and rutile <sup>30</sup>. It can be seen that the CrO<sub>2</sub> and CrO<sub>3</sub> spectra main peaks are observed at 528 eV and 529 eV, while the Cr<sub>2</sub>O<sub>3</sub> spectrum main peak is observed at 532 eV. These main peaks can be used as fingerprints to indicate the oxidation state of Cr in the NEXAFS O K-edge spectrum. Anatase and rutile have different fingerprints in NEXAFS and are related to different oxidation states of Cr, which are the two main peaks observed in the spectra at 531 eV and 533 eV.

Figure 3.3B shows the O K-edge spectra of aTiO<sub>2</sub>, Cr<sub>2</sub>O<sub>3</sub> and aTiO<sub>2</sub>-Cr<sub>2</sub>O<sub>3</sub>. Note that the Cr<sub>2</sub>O<sub>3</sub> spectrum shows a small peak at 529 eV, which is assumed to be a small amount of contamination with CrO<sub>3</sub> in the sample. The O K-edge spectrum of aTiO<sub>2</sub>-Cr<sub>2</sub>O<sub>3</sub> has the combined lineshape of the aTiO<sub>2</sub> and Cr<sub>2</sub>O<sub>3</sub> spectra with no features of CrO<sub>2</sub> or CrO<sub>3</sub> observed.

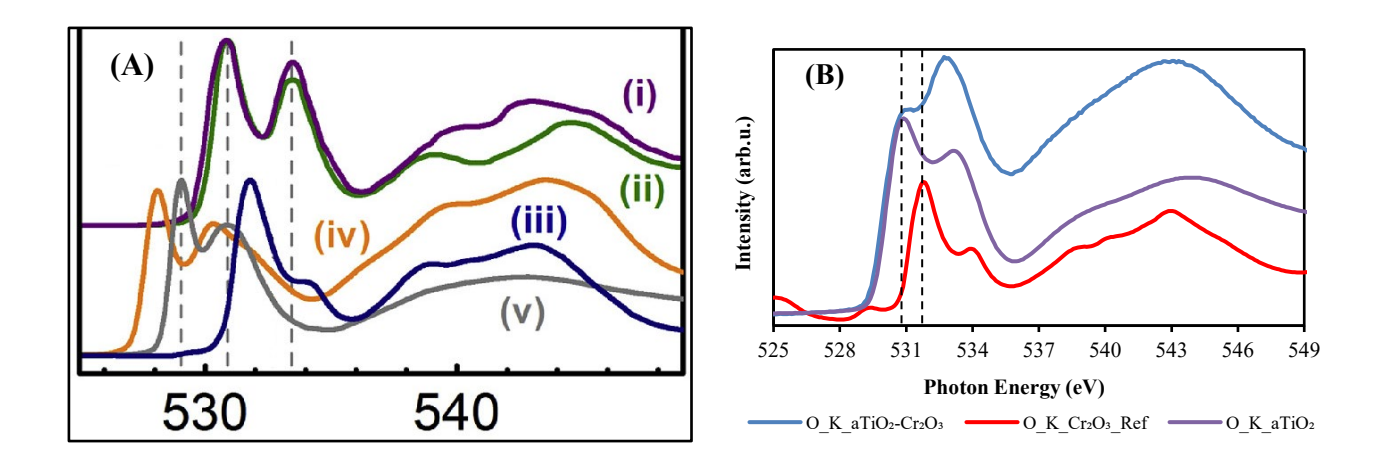


**Figure 3.3**: O K-edge NEXAFS spectra of (A) (i) anatase, (ii) rutile, (iii)  $Cr_2O_3$ , (iv)  $CrO_2$  and (v)  $CrO_3$  from reference <sup>30</sup> (Reprinted from reference <sup>30</sup> with permission from Elsevier) and (B)  $Cr_2O_3$ ,  $aTiO_2$  and  $aTiO_2$ - $Cr_2O_3$ .

# 3.4.2 Annealing studies

Figure 3.4 shows the relative amount of Cr<sub>2</sub>O<sub>3</sub> and TiO<sub>2</sub> from XPS measurements at different annealing temperatures for photodeposited Cr<sub>2</sub>O<sub>3</sub> on the different phases of TiO<sub>2</sub>. Note that the Cr 2p had to be fitted by taking the Ti 2s energy loss peak into consideration because it occurs in the same spectral region (see Figure A11 for more information and accompanying text). The Cr 2p and Ti 2p spectra of aTiO<sub>2</sub>-Cr<sub>2</sub>O<sub>3</sub>, anatase-Cr<sub>2</sub>O<sub>3</sub> and anatase:rutile-Cr<sub>2</sub>O<sub>3</sub> as a function of annealing temperature are shown in Figure A6. The peak position of Cr 2p<sub>3/2</sub> and Ti 2p<sub>3/2</sub> of aTiO<sub>2</sub>-Cr<sub>2</sub>O<sub>3</sub>, anatase-Cr<sub>2</sub>O<sub>3</sub> and anatase:rutile-Cr<sub>2</sub>O<sub>3</sub> samples as a function of annealing temperature are shown in Table A1.

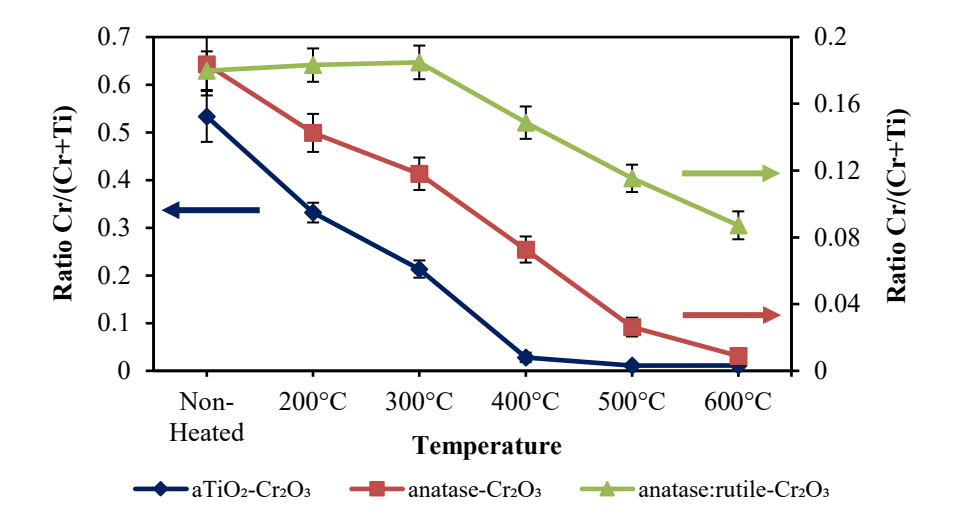


**Figure 3.4**: XPS relative amount of  $Cr\ 2p$  to  $Ti\ 2p$  of  $Cr_2O_3$  photodeposited onto the different phases of  $TiO_2$  after annealing at various temperatures.

For the aTiO<sub>2</sub>-Cr<sub>2</sub>O<sub>3</sub> sample, it is observed that the relative amount of Cr<sub>2</sub>O<sub>3</sub> decreases when heated. When the sample was heated to 300 °C, Cr<sub>2</sub>O<sub>3</sub> ratio dropped to 60% of that of the non-heated sample. When the sample was heated to 400 °C, over 90% of the Cr<sub>2</sub>O<sub>3</sub> intensity was lost. The Cr<sub>2</sub>O<sub>3</sub> peak mostly disappeared at a temperature of 600 °C. For the anatase-Cr<sub>2</sub>O<sub>3</sub> sample, the Cr<sub>2</sub>O<sub>3</sub> behaved similarly under annealing treatment; decreasing by around 25% after annealing to 300 °C. When the sample was heated to 400 °C, Cr<sub>2</sub>O<sub>3</sub> ratio had decreased by 50% and most of the Cr<sub>2</sub>O<sub>3</sub> disappeared when heated at 600 °C. For both the anatase and aTiO<sub>2</sub> substrate, the Cr<sub>2</sub>O<sub>3</sub> ratio mostly disappeared after annealing at 600 °C. However, the slope of the Cr<sub>2</sub>O<sub>3</sub> ratio with respect to annealing temperature, specifically between 200-600 °C, is less steep for anatase compared to the amorphous titania sample.

For the anatase:rutile-Cr<sub>2</sub>O<sub>3</sub> sample, it can be seen that the relative amount of Cr remained approximately constant within error bars when the sample was heated to 300 °C. It should be noted that the intensity ratios for this sample could be influenced by the removal of hydrocarbons and water from the surface by heating, which increases the signal of the elements present at the surface <sup>31</sup>. Note that the aTiO<sub>2</sub>-Cr<sub>2</sub>O<sub>3</sub> and anatase-Cr<sub>2</sub>O<sub>3</sub> samples probably have the same effect but the decrease of Cr<sub>2</sub>O<sub>3</sub> intensities for both samples is much stronger with increasing temperature. However, when the sample was heated to 400 °C, the relative amount of Cr decreased. When the sample was heated to 600 °C, Cr ratio dropped to almost 50%. The decrease of Cr<sub>2</sub>O<sub>3</sub> also occurs in the sample with the mixed anatase:rutile phase of TiO<sub>2</sub>. However, the decrease is less strong than on the amorphous and anatase titania.

It is unlikely that the decrease in Cr ratio is related to evaporation since according to Gulbransen, Cr<sub>2</sub>O<sub>3</sub> does not evaporate significantly until temperatures above 816 °C <sup>32</sup>. Moreover, when annealing the samples to 600 °C, the decrease did not occur equally for all substrates. Nearly 50% of relative amount of Cr remained for the anatase:rutile substrate.

Therefore, it is proposed that the decrease of Cr ratio is due to diffusion into the TiO<sub>2</sub> substrates by varying degrees. Heating the samples increases the mobility of the species forming the sample and can lead to diffusion. The degree of diffusion from the surface to the bulk is given by the relative surface energies of the substances. The lower the surface energy of a substance, the higher its tendency to diffuse to and cover the surface <sup>33, 34</sup>. This process is attributed to the strong metal-support interaction (SMSI) <sup>35, 36</sup>. It should be noted that diffusion to cover the surface can be either lateral across the surface or along the surface normal.

The surface energy of rutile is  $2.22 \pm 0.07 \text{ J/m}^2$ , and that of anatase is  $0.95 \pm 0.07 \text{ J/m}^2$  <sup>37</sup>. There is no experimental data for the surface energy of amorphous TiO<sub>2</sub> But it should have a relatively low surface energy because it has a less dense structure than anatase <sup>38</sup>. The surface energy of Cr<sub>2</sub>O<sub>3</sub> is

reported to be 1.60 J/m<sup>2</sup> <sup>39</sup>; higher than the amorphous and anatase surface energies but lower than the rutile surface energy. Therefore, upon annealing, the Cr<sub>2</sub>O<sub>3</sub> diffuses into the amorphous and anatase phases with lower surface energy. However, the Cr<sub>2</sub>O<sub>3</sub> remains on top of the rutile phase because it has higher surface energy than that of the Cr<sub>2</sub>O<sub>3</sub>. In the case of the mixed anatase:rutile phases, the sample contains separate domains, of anatase and rutile as evident through AFM and SEM images in reference<sup>40</sup>. Therefore, it is likely that Cr<sub>2</sub>O<sub>3</sub> has diffused into anatase but not into rutile. It should be noted that diffusion of Cr<sub>2</sub>O<sub>3</sub> into the metal oxide substrate driven by surface energy is not significantly affected whether the sample is exposed to air or vacuum. The diffusion process and the result of the diffusion process such as the concentration depth profiles of the constituents, could, however, be different between vacuum and air.

According to the above discussion, the stability of the  $Cr_2O_3$  at the surface of the different phases of  $TiO_2$  after annealing is strongly dependent on the surface energy of the phase of the  $TiO_2$ .

To further investigate the diffusion effect, the aTiO<sub>2</sub>-Cr<sub>2</sub>O<sub>3</sub> sample was sputtered with Ar<sup>+</sup> under UHV for various lengths of time to remove atoms from the surface and the XPS spectra recorded. The ratio intensity of the Cr to Ti after sputtering is shown in Figure 3.5. It can be seen that the Cr to Ti ratio increases with increasing sputter dose. These changes demonstrate the diffusion of Cr<sub>2</sub>O<sub>3</sub> into TiO<sub>2</sub>; the removal of surface TiO<sub>2</sub> atoms leads to an increase of the Cr<sub>2</sub>O<sub>3</sub> signal. The formation of Ti<sup>3+</sup> is observed after sputtering but is not relevant for investigating the change in relative intensity of Cr and Ti upon sputtering. This is further explained in the appendix section (Figure A12).

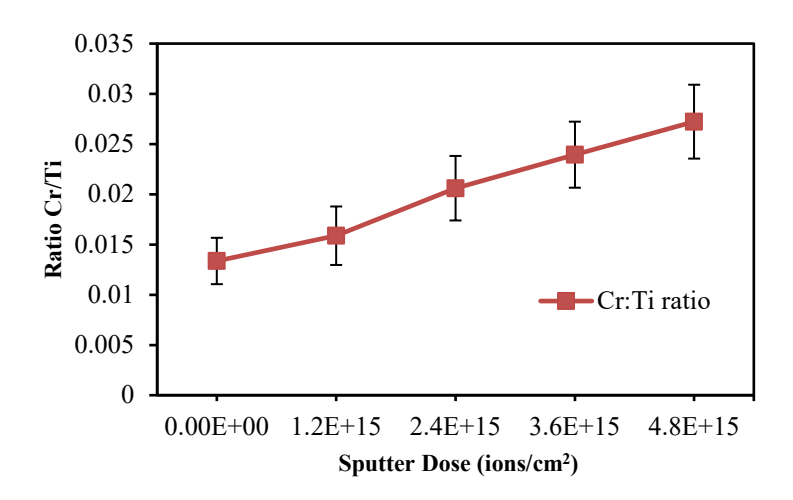


**Figure 3.5**: XPS ratio intensity of  $Cr\ 2p$  to  $Ti\ 2p$  of  $aTiO_2$ - $Cr_2O_3$  and subsequently annealed to 600 °C. Then, the sample was sputtered for various times.

Figure 3.6 shows the Cr L-edge of aTiO<sub>2</sub>-Cr<sub>2</sub>O<sub>3</sub> before and after annealing to 300°C and 600°C. It can be seen that the Cr L-edge spectrum of aTiO<sub>2</sub>-Cr<sub>2</sub>O<sub>3</sub> shifts to lower energy after annealing at

300°C and then shifts further at 600°C. This shift of the spectrum to lower energy is interpreted as a reduction of Cr<sub>2</sub>O<sub>3</sub>. This is clearly seen by comparison with the Cr metallic reference spectrum in Figure 3.2A. The aTiO<sub>2</sub>-Cr<sub>2</sub>O<sub>3</sub>-300°C spectrum has features of the metallic Cr spectrum, which are considered as a mixture of Cr and Cr<sub>2</sub>O<sub>3</sub> (see Figure 3.2A). The changes in features—the start of the spectrum before 575 eV, a decrease in sharpness of the peaks, the loss in minimum at 577 eV and appearance of the small peak at 584 eV—confirm that some of the Cr<sub>2</sub>O<sub>3</sub> was reduced to Cr metal by annealing. It is important to note that no features of CrO<sub>2</sub> or CrO<sub>3</sub> appear in the spectrum (Figure 3.2C). The Cr L-edge spectrum of aTiO<sub>2</sub>-Cr<sub>2</sub>O<sub>3</sub> annealed to 600°C shows more noise because of the diffusion of Cr<sub>2</sub>O<sub>3</sub> into aTiO<sub>2</sub>, which decreases the signal of Cr due to the reduced concentration of Cr in the surface region. Even so, the spectrum has a similar lineshape to that of the 300°C spectrum and shows even further that some of the Cr<sub>2</sub>O<sub>3</sub> is reduced to Cr metal. The synchrotron XPS spectra of Cr 2p shows a peak at low energy which is related to Cr metal (Figure A13). Metallic Cr can also be seen in Figure A6 but is less obvious due to the larger S/N ratio in these spectra. Again, no features of CrO<sub>2</sub> or CrO<sub>3</sub> appear in the Cr L-edge spectrum. Note that the NEXAFS has not been applied to other substrates (anatase and anatase:rutile) after annealing. However, we assume that the chemical changes of Cr<sub>2</sub>O<sub>3</sub> upon annealing is the same for all substrates. The reduced Cr is not observed in XRD, most likely because the total volume affected by the diffusion is too small to be visible (Figure A14). We have no information where the reduced Cr is positioned in the samples; the reduced Cr could cover the surface or reside as particles below the surface. It should be noted that a small amount of Ti<sup>3+</sup> is formed when heating the samples to 600°C (see Figure A13).

Above, it is argued that the diffusion of  $Cr_2O_3$  is driven by surface energy. This has to be considered in conjunction with the observation of metallic Cr. It needs to be emphasised that the argument that surface energy is the driving force for the diffusion of  $Cr_2O_3$  (including the reduced parts of  $Cr_2O_3$ ) into amorphous and anatase form of  $TiO_2$  does not mean that the diffusing process is independent of whether reducing or oxidising conditions prevail (i.e. heating under vacuum or in air) as discussed above. Thus, the diffusion of the metallic Cr could also be described with the SMSI concept given that the surface energy of Cr is  $1.9 \text{ J/m}^2$  and thus higher than that of anatase.

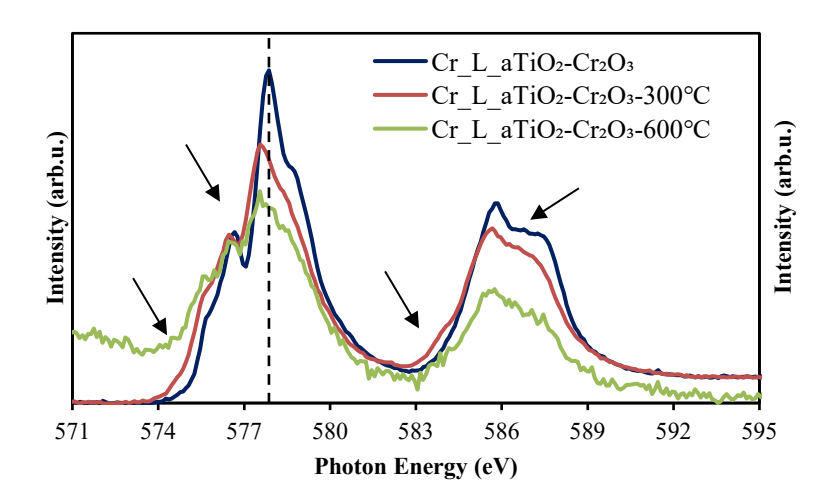


**Figure 3.6**: NEXAFS spectra of Cr L-edge of aTiO<sub>2</sub>-Cr<sub>2</sub>O<sub>3</sub> before and after heating to 300°C and 600°C. (The intensity of the 600°C spectrum corresponds to the right hand axis, which has a smaller range.)

Figure 3.7 shows the O K-edge spectra of aTiO<sub>2</sub>-Cr<sub>2</sub>O<sub>3</sub> before and after annealing to 300°C and 600°C. The spectrum edge does not shift upon annealing (see Figure 3.3A), confirming no presence of CrO<sub>2</sub> or CrO<sub>3</sub>. Moreover, the aTiO<sub>2</sub>-Cr<sub>2</sub>O<sub>3</sub>-600°C spectrum has a similar profile to that of the aTiO<sub>2</sub> due to the diffusion of Cr<sub>2</sub>O<sub>3</sub> into TiO<sub>2</sub> after annealing (see Figure 3.3B).

The NEXAFS spectra of Cr L-edge and O K-edge in Figures 3.6 and 3.7 emphasises no presence of CrO<sub>2</sub> or CrO<sub>3</sub> in the sample after annealing. Furthermore, the Cr L-edge spectra confirm that some of the Cr<sub>2</sub>O<sub>3</sub> was reduced to metallic Cr during the annealing.

The question arises whether the  $Cr_2O_3$  incorporates into the  $TiO_2$  upon diffusion and as a consequence results in doping of the  $TiO_2$ . We have measured UV-photoelectron spectroscopy of the  $aTiO_2$  and  $aTiO_2$ - $Cr_2O_3$  samples heated up to  $600^{\circ}C$ , which are shown in the appendix section in Figure A15. The valence band cut-off for both samples is the same, thus there is no significant doping of the  $TiO_2$  happening upon diffusion of the  $Cr_2O_3$ .

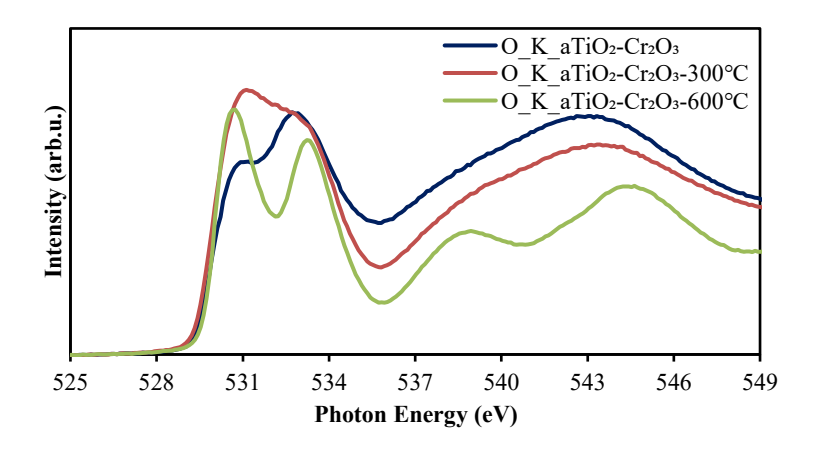


**Figure 3.7**: NEXAFS spectra of O K-edge of aTiO<sub>2</sub>-Cr<sub>2</sub>O<sub>3</sub> before and after annealing to 300°C and 600°C.

# 3.4.3 Surface morphology studies

AFM was used to investigate the topography of the aTiO<sub>2</sub> surface before and after the photodeposition of  $Cr_2O_3$ . Figures 3.8A and B are example AFM height images and show the topography of the aTiO<sub>2</sub> surface before and after the photodeposition of  $Cr_2O_3$  respectively. More images are shown in Figure A15 in the appendix information. The Ra of the images acquired on the aTiO<sub>2</sub> surface was  $1.1\pm0.03$  nm and the Ra for the aTiO<sub>2</sub> surface after  $Cr_2O_3$  deposition was  $1.16\pm0.17$  nm. It can be observed on the aTiO<sub>2</sub>- $Cr_2O_3$  images (Figures 3.8B, A16D-F) that there are a small number of particles, between 20 to 100 nm in height, that are responsible for producing the increased error in the Ra value for the aTiO<sub>2</sub>- $Cr_2O_3$  surface. The origin of the bigger particles is not known, however, only a small amount was found on the samples. Roughness analysis of aTiO<sub>2</sub>- $Cr_2O_3$  surfaces was also performed by excluding the particles between 20 to 100 nm in height on each AFM image and revealed an Ra =  $0.94\pm0.04$  nm. While a small decrease this does indicate a measurable change and is compatible with the formation of a closed  $Cr_2O_3$  layer, rather than islands on the aTiO<sub>2</sub> surface.

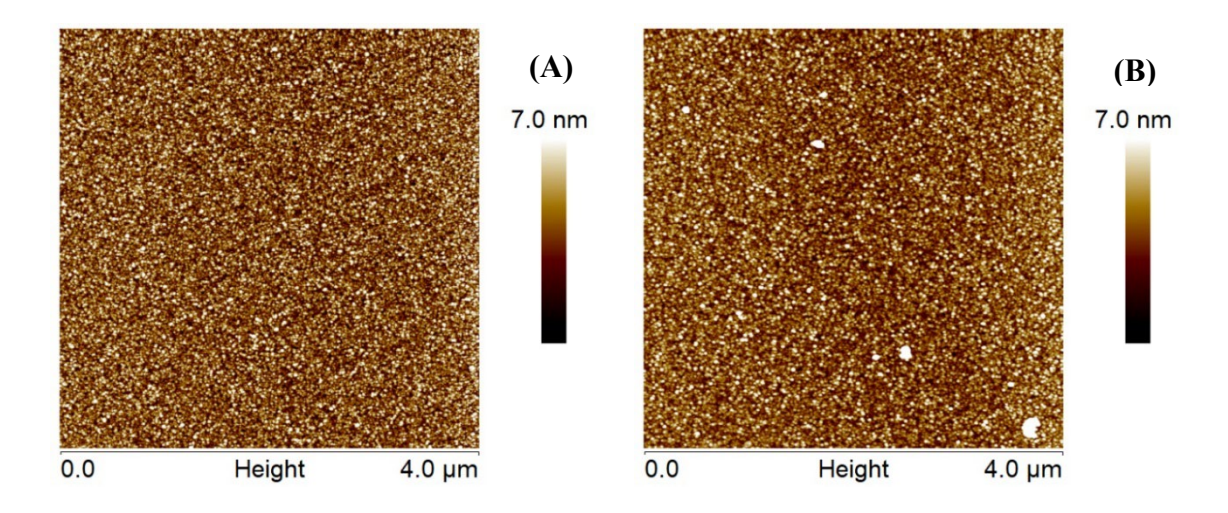


**Figure 3.8**: AFM images of (A)  $aTiO_2$  and (B)  $aTiO_2$  after the photodeposition of  $Cr_2O_3$  layer.

NICISS was used to investigate the concentration depth profile of the Cr<sub>2</sub>O<sub>3</sub> at the surface. Figure 3.9 shows that the NICISS spectra of TiO<sub>2</sub>, Cr<sub>2</sub>O<sub>3</sub> and aTiO<sub>2</sub>-CrO<sub>x</sub>. Note that all the samples were heated to 200 °C under UHV for 10 min to remove water and hydrocarbon from the surface for better depth resolution at the surface. Annealing the aTiO2-Cr2O3 sample to 200 °C causes a change in the concentration and chemical state of Cr<sub>2</sub>O<sub>3</sub> at the surface (see Figures 3.4 and 3.7). However, we do not know the exact ratio between Cr and Cr2O3. Therefore, the sample is here referred to as aTiO2-CrO<sub>x</sub>. The spectra in Figure 3.9 show onsets at specific energies with the onsets having various gradients. The position of the onset is determined by the mass of the element representing the step<sup>42</sup>. Cr is heavier than Ti and thus the onset of the step for Cr of the Cr<sub>2</sub>O<sub>3</sub> sample is at a higher binding energy than that of Ti of the TiO<sub>2</sub> sample. The onset of the Cr step can be found at 1270 eV and the onset of the Ti step at 1240 eV. The slope of the onset of the steps is determined by the energy resolution of the method and how clean the surface is. Small amounts of residual surface contamination will lead to a more shallow onset<sup>43</sup>. Metal oxides usually have adventitious hydrocarbons or water present at the surface even after heating to 200 °C<sup>31</sup>. It can be seen that the slope of the onset of Cr and Ti is similar and thus the coverage with residual hydrocarbons and water is similar. The onset of the step for aTiO<sub>2</sub>-Cr<sub>2</sub>O<sub>3</sub> is at the same binding energy as the onset of the Cr step at 1270 eV. Towards lower kinetic energies the slope of the step is shallower for aTiO<sub>2</sub>-Cr<sub>2</sub>O<sub>3</sub>. Around 1190 eV a change in slope of the onset can be identified. The change in slope is caused by the finite thickness of the CrO<sub>x</sub> layer deposited on the TiO<sub>2</sub>. A similar shape of a NICISS spectrum was found for thin ALD TiO<sub>2</sub> layers on Si substrates<sup>44</sup>. In Fig. 2 in <sup>44</sup> a clear minimum can be identified. The reason that in the present case such a minimum cannot be identified is that the difference in atomic mass between Cr and Ti is much smaller than between Ti and Si. This interpretation of the NICIS spectra means that the Cr2O3 forms a layer on the aTiO2 upon photodeposition and are compatible with the XPS spectra of the same type of sample.

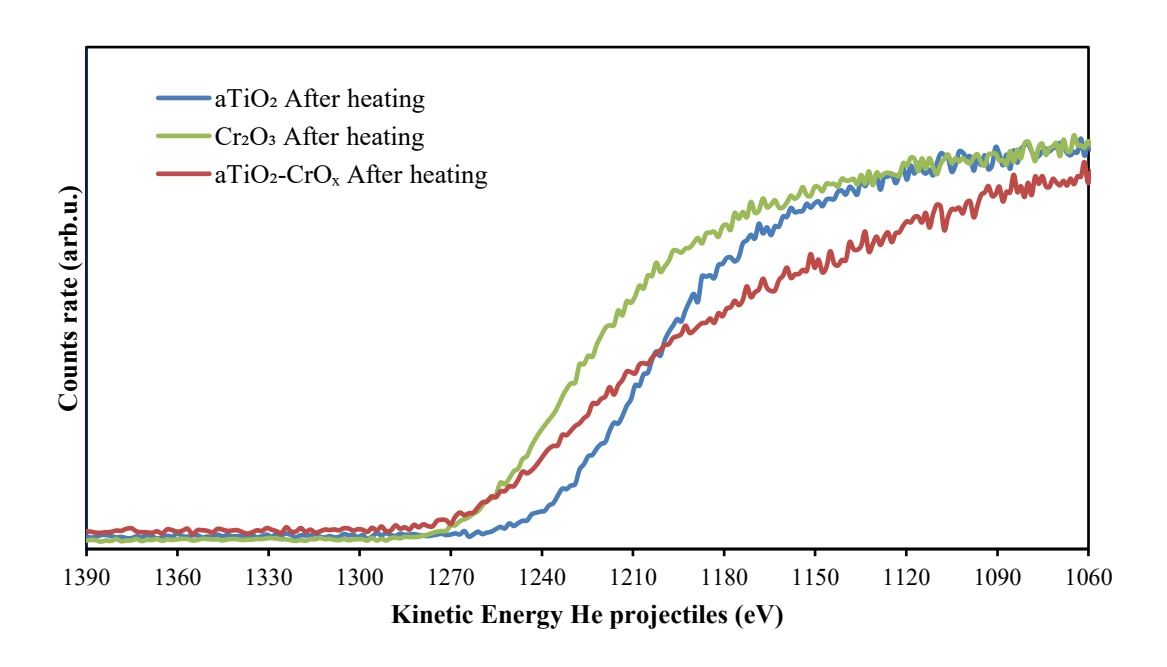


**Figure 3.9**: NICISS results of the  $aTiO_2$ ,  $Cr_2O_3$  and  $aTiO_2$ - $CrO_x$  samples after annealing at 200°C under UHV for 10 min to remove water and hydrocarbon from the surface.

# 3.5 Conclusions

AR-XPS, AFM and NICISS confirmed the photodeposition of Cr as a layer onto TiO<sub>2</sub>. The chemical state of the Cr layer was investigated using XPS and NEXAFS and confirmed as Cr<sub>2</sub>O<sub>3</sub>. Under annealing conditions, it was observed with XPS that Cr<sub>2</sub>O<sub>3</sub> diffused into all samples but that the degree of diffusion depends on the crystal phase of the TiO<sub>2</sub>. Cr<sub>2</sub>O<sub>3</sub> diffuses after annealing at 300°C and 600°C under vacuum into the amorphous and anatase phases but remains, at least partially, on the surface of the rutile phase. The degree of diffusion is attributed to the differences in surface energy between Cr<sub>2</sub>O<sub>3</sub> and the different crystal phases of titania. NEXAFS proved that some of the Cr<sub>2</sub>O<sub>3</sub> was reduced to Cr metal on amorphous TiO<sub>2</sub> by annealing to 300°C and up to 600 °C under vacuum, with no observation of CrO<sub>2</sub> or CrO<sub>3</sub>. A crucial finding of the present work is that the stability of the Cr<sub>2</sub>O<sub>3</sub> layer on the TiO<sub>2</sub> surface under annealing depends on the surface energy of TiO<sub>2</sub>, which varies depending on the TiO<sub>2</sub> crystal phase.

# 3.6 References

- 1. Dincer, I.; S. Joshi, A., Solar Based Hydrogen Production Systems. *Springer New York* **2013**.
- 2. Colmenares, J. C.; Xu, Y.-J., *Heterogeneous Photocatalysis*. Springer: Heidelberg: Green Chemistry and Sustainable Technology, 2016.
- 3. Wang, Z.; Li, C.; Domen, K., Recent developments in heterogeneous photocatalysts for solar-driven overall water splitting. *Chemical Society Reviews* **2019**, *48* (7), 2109-2125.
- 4. Negishi, Y.; Mizuno, M.; Hirayama, M.; Omatoi, M.; Takayama, T.; Iwase, A.; Kudo, A., Enhanced Photocatalytic Water Splitting by BaLa4Ti4O15 Loaded with ~1 nm Gold Nanoclusters Using Glutathione-protected Au25 Clusters. *Nanoscale* **2013**, *5* (16), 7188-7192.
- 5. Yoshida, M.; Maeda, K.; Lu, D.; Kubota, J.; Domen, K., Lanthanoid Oxide Layers on Rhodium-Loaded (Ga1–xZnx)(N1–xOx) Photocatalyst as a Modifier for Overall Water Splitting under Visible-Light Irradiation. *The Journal of Physical Chemistry C* **2013**, *117* (27), 14000-14006.
- 6. Garcia-Esparza, A. T.; Shinagawa, T.; Ould-Chikh, S.; Qureshi, M.; Peng, X.; Wei, N.; Anjum, D. H.; Clo, A.; Weng, T.-C.; Nordlund, D.; Sokaras, D.; Kubota, J.; Domen, K.; Takanabe, K., An Oxygen-Insensitive Hydrogen Evolution Catalyst Coated by a Molybdenum-Based Layer for Overall Water Splitting. *Angewandte Chemie International Edition* **2017**, *56* (21), 5780-5784.
- 7. Chen, S.; Takata, T.; Domen, K., Particulate photocatalysts for overall water splitting. *Nature Reviews Materials* **2017**, *2*, 17050.
- 8. Maeda, K.; Teramura, K.; Lu, D.; Saito, N.; Inoue, Y.; Domen, K., Roles of Rh/Cr2O3 (Core/Shell) Nanoparticles Photodeposited on Visible-Light-Responsive (Ga1-xZnx)(N1-xOx) Solid Solutions in Photocatalytic Overall Water Splitting. *The Journal of Physical Chemistry C* **2007**, *111* (20), 7554-7560.
- 9. Maeda, K.; Teramura, K.; Lu, D.; Saito, N.; Inoue, Y.; Domen, K., Noble-Metal/Cr2O3 Core/Shell Nanoparticles as a Cocatalyst for Photocatalytic Overall Water Splitting. *Angewandte Chemie International Edition* **2006**, *45* (46), 7806-7809.
- 10. Yoshida, M.; Takanabe, K.; Maeda, K.; Ishikawa, A.; Kubota, J.; Sakata, Y.; Ikezawa, Y.; Domen, K., Role and Function of Noble-Metal/Cr-Layer Core/Shell Structure Cocatalysts for Photocatalytic Overall Water Splitting Studied by Model Electrodes. *The Journal of Physical Chemistry C* **2009**, *113* (23), 10151-10157.
- 11. Maeda, K.; Domen, K., Photocatalytic Water Splitting: Recent Progress and Future Challenges. *The Journal of Physical Chemistry Letters* **2010**, *I* (18), 2655-2661.
- 12. Sakamoto, N.; Ohtsuka, H.; Ikeda, T.; Maeda, K.; Lu, D.; Kanehara, M.; Teramura, K.; Teranishi, T.; Domen, K., Highly Dispersed Noble-metal/Chromia (Core/Shell) Nanoparticles as Efficient Hydrogen Evolution Promoters for Photocatalytic Overall Water Splitting under Visible Light. *Nanoscale* **2009**, *I* (1), 106-109.
- 13. Maeda, K.; Sakamoto, N.; Ikeda, T.; Ohtsuka, H.; Xiong, A.; Lu, D.; Kanehara, M.; Teranishi, T.; Domen, K., Preparation of Core–Shell-Structured Nanoparticles (with a Noble-Metal or Metal Oxide Core and a Chromia Shell) and Their Application in Water Splitting by Means of Visible Light. *Chemistry A European Journal* **2010**, *16* (26), 7750-7759.
- 14. Maeda, K.; Xiong, A.; Yoshinaga, T.; Ikeda, T.; Sakamoto, N.; Hisatomi, T.; Takashima, M.; Lu, D.; Kanehara, M.; Setoyama, T.; Teranishi, T.; Domen, K., Photocatalytic Overall Water Splitting Promoted by Two Different Cocatalysts for Hydrogen and Oxygen Evolution under Visible Light. *Angewandte Chemie International Edition* **2010**, *49* (24), 4096-4099.
- 15. Maeda, K.; Lu, D.; Domen, K., Direct Water Splitting into Hydrogen and Oxygen under Visible Light by using Modified TaON Photocatalysts with d0 Electronic Configuration. *Chemistry A European Journal* **2013**, *19* (16), 4986-4991.
- 16. Takata, T.; Jiang, J.; Sakata, Y.; Nakabayashi, M.; Shibata, N.; Nandal, V.; Seki, K.; Hisatomi, T.; Domen, K., Photocatalytic Water Splitting with a Quantum Efficiency of Almost Unity. *Nature* **2020**, *581* (7809), 411-414.

- 17. Chiang, T. H.; Lyu, H.; Hisatomi, T.; Goto, Y.; Takata, T.; Katayama, M.; Minegishi, T.; Domen, K., Efficient Photocatalytic Water Splitting Using Al-Doped SrTiO3 Coloaded with Molybdenum Oxide and Rhodium-Chromium Oxide. *ACS Catalysis* **2018**, *8* (4), 2782-2788.
- 18. Sun, S.; Hisatomi, T.; Wang, Q.; Chen, S.; Ma, G.; Liu, J.; Nandy, S.; Minegishi, T.; Katayama, M.; Domen, K., Efficient Redox-Mediator-Free Z-Scheme Water Splitting Employing Oxysulfide Photocatalysts under Visible Light. *ACS Catalysis* **2018**, *8* (3), 1690-1696.
- 19. Phivilay, S. P.; Roberts, C. A.; Gamalski, A. D.; Stach, E. A.; Zhang, S.; Nguyen, L.; Tang, Y.; Xiong, A.; Puretzky, A. A.; Tao, F. F.; Domen, K.; Wachs, I. E., Anatomy of a Visible Light Activated Photocatalyst for Water Splitting. *ACS Catalysis* **2018**, *8* (7), 6650-6658.
- 20. Pan, Z.; Hisatomi, T.; Wang, Q.; Chen, S.; Nakabayashi, M.; Shibata, N.; Pan, C.; Takata, T.; Katayama, M.; Minegishi, T.; Kudo, A.; Domen, K., Photocatalyst Sheets Composed of Particulate LaMg1/3Ta2/3O2N and Mo-Doped BiVO4 for Z-Scheme Water Splitting under Visible Light. *ACS Catalysis* **2016**, *6* (10), 7188-7196.
- 21. Qureshi, M.; Shinagawa, T.; Tsiapis, N.; Takanabe, K., Exclusive Hydrogen Generation by Electrocatalysts Coated with an Amorphous Chromium-Based Layer Achieving Efficient Overall Water Splitting. *ACS Sustainable Chemistry & Engineering* **2017**, *5* (9), 8079-8088.
- 22. Kurashige, W.; Kumazawa, R.; Ishii, D.; Hayashi, R.; Niihori, Y.; Hossain, S.; Nair, L. V.; Takayama, T.; Iwase, A.; Yamazoe, S.; Tsukuda, T.; Kudo, A.; Negishi, Y., Au25-Loaded BaLa4Ti4O15 Water-Splitting Photocatalyst with Enhanced Activity and Durability Produced Using New Chromium Oxide Shell Formation Method. *The Journal of Physical Chemistry C* **2018**, *122* (25), 13669-13681.
- 23. Wenderich, K.; Mul, G., Methods, Mechanism, and Applications of Photodeposition in Photocatalysis: A Review. *Chemical Reviews* **2016**, *116* (23), 14587-14619.
- 24. Sanwald, K. E.; Berto, T. F.; Jentys, A.; Camaioni, D. M.; Gutiérrez, O. Y.; Lercher, J. A., Kinetic Coupling of Water Splitting and Photoreforming on SrTiO3-Based Photocatalysts. *ACS Catalysis* **2018**, *8* (4), 2902-2913.
- 25. AlOtaibi, B.; Fan, S.; Wang, D.; Ye, J.; Mi, Z., Wafer-Level Artificial Photosynthesis for CO2 Reduction into CH4 and CO Using GaN Nanowires. *ACS Catalysis* **2015**, *5* (9), 5342-5348.
- 26. Wang, C.; Andersson, G. G., Measuring concentration depth profiles at liquid surfaces: Comparing angle resolved X-ray photoelectron spectroscopy and neutral impact collision scattering spectroscopy. *Surface Science* **2011**, *605* (9), 889-897.
- 27. Eschen, F.; Heyerhoff, M.; Morgner, H.; Vogt, J., The concentration-depth profile at the surface of a solution of tetrabutylammonium iodide in formamide, based on angle-resolved photoelectron spectroscopy. *Journal of Physics: Condensed Matter* **1995**, 7 (10), 1961-1978.
- 28. Thurner, G.; Holloway, P. H., Oxidation of Polycrystalline Chromium between 30° C and 400° C. *Acta Physica Polonica A* **1992**, *81* (2), 273-283.
- 29. Sivkov, D.; Petrova, O.; Mingaleva, A.; Ob'edkov, A.; Kaverin, B.; Gusev, S.; Vilkov, I.; Isaenko, S.; Bogachuk, D.; Skandakov, R.; Sivkov, V.; Nekipelov, S., The Structure and Chemical Composition of the Cr and Fe Pyrolytic Coatings on the MWCNTs' Surface According to NEXAFS and XPS Spectroscopy. *Nanomaterials (Basel)* **2020**, *10* (2), 374.
- 30. Gago, R.; Prucnal, S.; Pérez-Casero, R.; Caretti, I.; Jiménez, I.; Lungwitz, F.; Cornelius, S., Structural impact of chromium incorporation in as-grown and flash-lamp-annealed sputter deposited titanium oxide films. *Journal of Alloys and Compounds* **2017**, *729*, 438-445.
- 31. Krishnan, G.; Al Qahtani, H. S.; Li, J.; Yin, Y.; Eom, N.; Golovko, V. B.; Metha, G. F.; Andersson, G. G., Investigation of Ligand-Stabilized Gold Clusters on Defect-Rich Titania. *The Journal of Physical Chemistry C* **2017**, *121* (50), 28007-28016.
- 32. Gulbransen, E. A.; Andrew, K. F., A Preliminary Study of the Oxidation and Vapor Pressure of Chromium. *Journal of The Electrochemical Society* **1952**, *99* (10), 402-406.
- 33. Fu, Q.; Wagner, T.; Olliges, S.; Carstanjen, H.-D., Metal-Oxide Interfacial Reactions: Encapsulation of Pd on TiO2 (110). *The Journal of Physical Chemistry B* **2005**, *109* (2), 944-951.
- 34. Fu, Q.; Wagner, T., Interaction of nanostructured metal overlayers with oxide surfaces. *Surface Science Reports* **2007**, *62* (11), 431-498.

- 35. Tauster, S. J., Strong metal-support interactions. *Accounts of Chemical Research* **1987**, *20* (11), 389-394.
- 36. Wu, P.; Tan, S.; Moon, J.; Yan, Z.; Fung, V.; Li, N.; Yang, S.-Z.; Cheng, Y.; Abney, C. W.; Wu, Z.; Savara, A.; Momen, A. M.; Jiang, D.-e.; Su, D.; Li, H.; Zhu, W.; Dai, S.; Zhu, H., Harnessing strong metal—support interactions via a reverse route. *Nature Communications* **2020**, *11* (1), 3042.
- 37. da Silva, A. L.; Hotza, D.; Castro, R. H. R., Surface energy effects on the stability of anatase and rutile nanocrystals: A predictive diagram for Nb2O5-doped-TiO2. *Applied Surface Science* **2017**, *393*, 103-109.
- 38. Prasai, B.; Cai, B.; Underwood, M. K.; Lewis, J. P.; Drabold, D. A., Properties of amorphous and crystalline titanium dioxide from first principles. *Journal of Materials Science* **2012**, *47* (21), 7515-7521.
- 39. Rohr, F.; Bäumer, M.; Freund, H. J.; Mejias, J. A.; Staemmler, V.; Müller, S.; Hammer, L.; Heinz, K., Strong relaxations at the Cr2O3(0001) surface as determined via low-energy electron diffraction and molecular dynamics simulations. *Surface Science* **1997**, *372* (1), L291-L297.
- 40. Daughtry, J.; Alotabi, A. S.; Howard-Fabretto, L.; Andersson, G. G., Composition and Properties of RF-Sputter Deposited Titanium Dioxide Thin Films. *Nanoscale Advances* **2021**, *3* (4), 1077-1086.
- 41. Mezey, L. Z.; Giber, J., The Surface Free Energies of Solid Chemical Elements: Calculation from Internal Free Enthalpies of Atomization. *Japanese Journal of Applied Physics* **1982**, *21* (Part 1, No. 11), 1569-1571.
- 42. Andersson, G.; Morgner, H., Impact collision ion scattering spectroscopy (ICISS) and neutral impact collision ion scattering spectroscopy (NICISS) at surfaces of organic liquids. *Surface Science* **1998**, *405* (1), 138-151.
- 43. Andersson, G.; Morgner, H., Determining the stopping power of low energy helium in alkanethiolates with Neutral Impact Collision Ion Scattering Spectroscopy (NICISS). *Nuclear Instruments and Methods in Physics Research Section B: Beam Interactions with Materials and Atoms* **1999**, *155* (4), 357-368.
- 44. Ellis-Gibbings, L.; Johansson, V.; Walsh, R. B.; Kloo, L.; Quinton, J. S.; Andersson, G. G., Formation of N719 Dye Multilayers on Dye Sensitized Solar Cell Photoelectrode Surfaces Investigated by Direct Determination of Element Concentration Depth Profiles. *Langmuir* **2012**, *28* (25), 9431-9439.

# Chapter 4: Reduction and Diffusion of Cr-oxide Layer into P25, BaLa<sub>4</sub>Ti<sub>4</sub>O<sub>15</sub> and Al:SrTiO<sub>3</sub> Particles upon High-Temperature Annealing

Abdulrahman S. Alotabi, Thomas D. Small, Yanting Yin, D. J. Osborn, Shuhei Ozaki, Yuki Kataoka, Yuichi Negishi, Kazunari Domen, Gregory F. Metha and Gunther G. Andersson

This chapter is a reformatted version of the manuscript under review at the time of thesis submission.

### Author Contribution:

Abdulrahman S Alotabi: Designed and performed experiments, data analysis and interpretation, and prepared the manuscript for publication.

Thomas D. Small: Contributed to measurements and analysis of photocatalysis and DRS data.

Yanting Yin: Performed IPES measurements on samples prepared by A.S.A.

D. J. Osborn: Performed EDX-STEM data analysis.

Shuhei Ozaki & Yuki Kataoka: Synthesised BaLa<sub>4</sub>Ti<sub>4</sub>O<sub>15</sub>-Cr(OH)<sub>3</sub> for this project.

Yuichi Negishi & Kazunari Domen: Intellectual contribution in revision of manuscript.

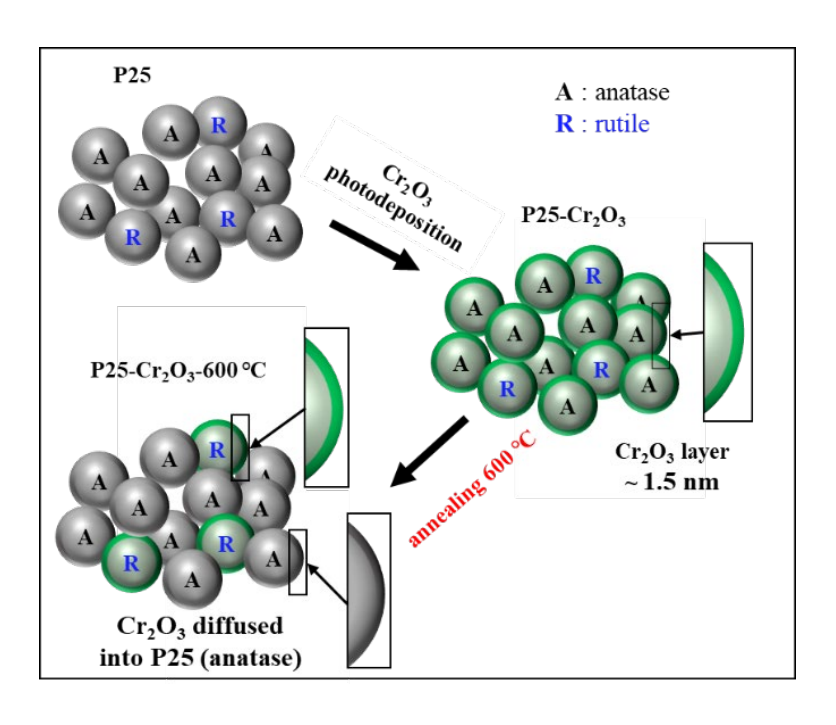
Gregory F Metha: Intellectual contribution in conceptualising experiments and revision of manuscript.

Gunther G Andersson: Intellectual contribution in conceptualising experiments, data interpretation & revision of manuscript.

## 4.1 Abstract

Chromium oxide (Cr<sub>2</sub>O<sub>3</sub>) is a beneficial metal oxide used to prevent the backward reaction in photocatalytic water splitting. The purpose of this study is to investigate the stability, oxidation state, and the bulk and surface electronic structure of Cr-oxide photodeposited onto P25, BaLa<sub>4</sub>Ti<sub>4</sub>O<sub>15</sub>, and Al:SrTiO<sub>3</sub> particles as a function of the annealing process. The oxidation state of Cr-oxide layer as deposited is found to be Cr<sub>2</sub>O<sub>3</sub> on the surface of P25 and Al:SrTiO<sub>3</sub> particles and Cr(OH)<sub>3</sub> on BLTO. After annealing at 600 °C, for P25, the Cr<sub>2</sub>O<sub>3</sub> layer diffuses into the anatase phase but remains at the surface of the rutile phase. For BaLa<sub>4</sub>Ti<sub>4</sub>O<sub>15</sub>, Cr(OH)<sub>3</sub> converts to Cr<sub>2</sub>O<sub>3</sub> upon annealing and diffuses slightly into the particles. However, for Al:SrTiO<sub>3</sub>, the Cr<sub>2</sub>O<sub>3</sub> remains stable at the surface of the particles. The diffusion here is due to the strong metal—support interaction effect. In addition, some of the Cr<sub>2</sub>O<sub>3</sub> on the P25, BaLa<sub>4</sub>Ti<sub>4</sub>O<sub>15</sub> and Al:SrTiO<sub>3</sub> particles is reduced to metallic Cr after annealing but there was no observation of the formation of CrO<sub>2</sub> or CrO<sub>3</sub>. The effect of Cr<sub>2</sub>O<sub>3</sub> formation and diffusion into the bulk on the surface and bulk band gaps and the change of the structure are investigated with electronic spectroscopy, electron diffraction, DRS and high-resolution imaging. The implications of the stability and diffusion of Cr<sub>2</sub>O<sub>3</sub> overlayers on P25, BaLa<sub>4</sub>Ti<sub>4</sub>O<sub>15</sub>, and Al:SrTiO<sub>3</sub> for photocatalytic water splitting are discussed.

### **Graphical Abstract**



## 4.2 Introduction

Human society requires a sustainable and renewable energy source to substitute for fossil fuels. Hydrogen (H<sub>2</sub>) produced from renewable energy sources can be used as fuels that do not contribute to CO<sub>2</sub> emissions<sup>1</sup>. Amongst the technologies for renewable H<sub>2</sub> production, photocatalytic water splitting is a promising technique to split water into H<sub>2</sub> and O<sub>2</sub> using semiconductor particles as photocatalysts<sup>2-6</sup>. The structural and electronic properties of photocatalyst semiconductors play a major role in determining photocatalytic activity<sup>7, 8</sup>. For example, SrTiO<sub>3</sub> doped with Al<sup>3+</sup> (Al:SrTiO<sub>3</sub>) is one of the most efficient photocatalysts for water splitting<sup>9-14</sup>. Recently, Osterloh and co-workers reported an electronic structure investigation of Al:SrTiO<sub>3</sub>, showing that Al<sup>3+</sup> reduces the Ti<sup>3+</sup> concentration in SrTiO<sub>3</sub>, which shifts the Fermi level to lower energy<sup>15</sup>. This makes the compound less of an n-type semiconductor, resulting in improved photocatalytic activity.

Co-catalysts make a significant contribution to promoting efficient photocatalytic water splitting <sup>16, 17</sup>. The co-catalyst reduces the overpotential barrier needed to suppress the electron-hole recombination in a semiconductor and act as active sites for the water splitting reaction <sup>18-20</sup>. However, the co-catalyst also can function to suppress the H<sub>2</sub> and O<sub>2</sub> recombination reaction back to H<sub>2</sub>O (backward reaction)<sup>21</sup>. One such example is that mixed transition metal oxides lead to improved overall water splitting by blocking the backward reaction<sup>22-25</sup>. For example, GaN:ZnO loaded with Rh<sub>2-y</sub>Cr<sub>y</sub>O<sub>3</sub> has higher photocatalytic activity than that loaded with RuO<sub>2</sub> due to the ability of Rh<sub>2-y</sub>Cr<sub>y</sub>O<sub>3</sub> to evolve H<sub>2</sub> and O<sub>2</sub> with inactivity for the backward reaction<sup>22-25</sup>. Domen and co-workers have developed a new way to use Cr<sub>2</sub>O<sub>3</sub> with noble metal particles as core/shell nanostructures (Rh/Cr<sub>2</sub>O<sub>3</sub>) on GaN:ZnO<sup>26-32</sup>. It was confirmed that the Cr<sub>2</sub>O<sub>3</sub> shells suppresses water formation on Rh nanoparticles, which is an effective approach to improve photocatalytic water splitting activity.

It has also been demonstrated that the photodeposition of a Cr<sub>2</sub>O<sub>3</sub> layer (with a thickness of 0.7 – 1.3 nm) can enhance the stability of Au nanoclusters (~1 nm in size) on BaLa<sub>4</sub>Ti<sub>4</sub>O<sub>15</sub> (BLTO) and suppress the backward reaction, thereby improving photocatalytic water splitting activity<sup>33-35</sup>. Recently, it was demonstrated that this Cr-oxide layer exists as amorphous chromium hydroxide (Cr(OH)<sub>3</sub>)<sup>35</sup>. The stability of Au nanoclusters was achieved by adsorption of Au nanoclusters onto BLTO-Cr(OH)<sub>3</sub> followed by calcination to diffuse the Au nanoclusters between the Cr-oxide layer and BLTO due to the high surface energy of Au nanoclusters<sup>33,35</sup>. Also, Negishi and co-workers have reported that calcination of Rh–SG complexes adsorbed on BLTO-Cr(OH)<sub>3</sub> layer produces mixed oxide particles of Rh and Cr with a size of ~1.3 nm<sup>34</sup>. The resulting BLTO-Rh<sub>2-x</sub>Cr<sub>x</sub>O<sub>3</sub> significantly improved the efficiency of photocatalytic water splitting activity.

The above listed examples show that Cr<sub>2</sub>O<sub>3</sub> is a beneficial metal oxide for photocatalytic water splitting. Therefore, as a step towards improving the efficiency of photocatalytic water splitting, studying the stability and electronic structure properties of the Cr<sub>2</sub>O<sub>3</sub> layer on a photocatalyst particle under annealing is necessary due to the requirement of heating for preparation of a photocatalyst. This study aims to determine the stability, chemical composition, and the bulk and surface electronic structure of Cr-oxide overlayers photodeposited onto P25, BLTO and Al:SrTiO<sub>3</sub> particles as a function of the annealing process. P25 has a mixture of anatase and rutile phases, which benefits investigation of Cr<sub>2</sub>O<sub>3</sub> stability in relation to surface energies for different crystalline particles of TiO<sub>2</sub>. The influence of the annealing on the surface and bulk band gaps of the photocatalysts is examined. Photocatalytic water splitting activity of these photocatalysts was also investigated.

# 4.3 Experimental

### 4.3.1 Material and Sample Preparation

## Preparation of P25-Cr<sub>2</sub>O<sub>3</sub>

Photodeposition method was used to deposit Cr<sub>2</sub>O<sub>3</sub> onto P25 particles (Evonik Degussa GmbH, Sigma-Aldrich, Australia) by dispersing 45 mg of P25 with size of 20 nm in 25 mL of K<sub>2</sub>CrO<sub>4</sub> solution with a concentration of 0.5 mM. The K<sub>2</sub>CrO<sub>4</sub> solution was prepared using deionised water. The K<sub>2</sub>CrO<sub>4</sub>-P25 suspension was irradiated using a UV LED (365 nm) with a radiant power of 690 mW (Vishay, VLMU3510-365-130). The distance between the UV LED and suspension surface was ~9 cm. Irradiation was applied under continuous stirring of the suspension in a beaker with the size of 50 mL for a duration of 12 hours in air. The photodeposition procedure is summarised in Figure B1. The green P25-Cr<sub>2</sub>O<sub>3</sub> powder was collected using a centrifuge and washed with water. ICP-MS analyses determined that 97% of available Cr was deposited onto the P25 particles. The P25-Cr<sub>2</sub>O<sub>3</sub> powder drop casted onto Si wafer for characterisation.

### Preparation of BaLa<sub>4</sub>Ti<sub>4</sub>O<sub>15</sub>(BLTO)-Cr(OH)<sub>3</sub>

BLTO-Cr(OH)<sub>3</sub> was obtained by photodeposition of a Cr<sub>2</sub>O<sub>3</sub> layer onto BLTO using a previously reported procedure<sup>33</sup>. First, 650 mg of BLTO with size range 4–10 μm was added to 350 mL of an aqueous K<sub>2</sub>CrO<sub>4</sub> solution in a quartz cell. The mixing ratio of K<sub>2</sub>CrO<sub>4</sub> to BaLa<sub>4</sub>Ti<sub>4</sub>O<sub>15</sub> was 0.5 wt% Cr. The mixture was stirred under Ar flowing for one hour to ensure complete removal of air with Ar. Subsequently, the solution was irradiated with a high-pressure Hg lamp (400 W) under an Ar flow of 30 mL/min for one hour. The BLTO-Cr(OH)<sub>3</sub> powder was collected from centrifugation and washed with water three times. The ICP-MS analyses showed that ~100% of available Cr was adsorbed onto the BLTO. The BLTO-Cr(OH)<sub>3</sub> powder drop casted onto Si wafer for characterisation.

## Preparation of Al:SrTiO<sub>3</sub>-Cr<sub>2</sub>O<sub>3</sub>

Al:SrTiO<sub>3</sub> was synthesised using a flux method (previously reported in detail<sup>9</sup>). SrTiO<sub>3</sub> (Wako), Al<sub>2</sub>O<sub>3</sub> nanopowder (Aldrich) and SrCl<sub>2</sub> (Kanto) were mixed with a molar ratio of (1:0.02:10) and heated at 1150°C for 10 hours in air. The obtained Al:SrTiO<sub>3</sub> with size range 0.2–3 μm was washed three times with deionised water. Cr<sub>2</sub>O<sub>3</sub> was loaded onto Al:SrTiO<sub>3</sub> using the same procedure described above for P25-Cr<sub>2</sub>O<sub>3</sub>. Al:SrTiO<sub>3</sub> (45 mg) was dispersed in 25 mL of K<sub>2</sub>CrO<sub>4</sub> solution (0.5 mM) and irradiated for 12 hours. Al:SrTiO<sub>3</sub>-Cr<sub>2</sub>O<sub>3</sub> powder was collected using a centrifuge and washed with water. ICP-MS analyses determined that ~22% of available Cr was deposited onto the Al:SrTiO<sub>3</sub> particles. The Al:SrTiO<sub>3</sub>-Cr<sub>2</sub>O<sub>3</sub> powder drop casted onto Si wafer for characterisation.

### Annealing treatment

All samples (P25-Cr<sub>2</sub>O<sub>3</sub>, BLTO-Cr(OH)<sub>3</sub> and Al:SrTiO<sub>3</sub>-Cr<sub>2</sub>O<sub>3</sub>) were annealed under ultrahigh vacuum (1 × 10<sup>-8</sup> mbar) for 10 minutes at each temperature. For XPS measurements, samples were annealed for 10 minutes at each temperature (200, 300, 400, 500 and 600 °C) with a total annealing time of 50 minutes for each sample. All XPS measurements were undertaken at each temperature using the same sample without exposed the sample to air. For NEXAFS measurement, all samples were annealed at 600 °C for 10 minutes and the measurements were applied without exposed the sample to air.

#### 4.3.2 Methods

### Scanning Transmission Electron Microscopy

Experimental details for Scanning transmission electron microscopy (STEM) are discussed in Section 2.9. In this chapter, elemental maps were obtained using STEM up to a magnification of 1 nm.

### Synchrotron X-ray Photoelectron Spectroscopy

Experimental details for Synchrotron X-ray Photoelectron Spectroscopy (Synchrotron XPS) are discussed in Section 2.1. In this chapter, Synchrotron XPS spectra were collected at the Australian Synchrotron using a photon energy of 1000 eV. The X-ray beam spot size was close to  $320\times320\,\mu\text{m}$ . High-resolution XPS spectra of C 1s, O 1s, Ti 2p, Cr 2p, Ba 3d, La 3d and Au 4f were recorded with a pass energy of 10 eV. The Au 4f peak position at 84 eV was used for synchrotron XPS measurements to calibrate the excitation photon energy of all spectra. More details are provided in reference<sup>36,37</sup>.

### Near Edge X-ray Absorption Fine Structure

Experimental details for near-edge X-ray absorption fine structure (NEXAFS) are discussed in Section 2.3.

## X-ray Diffraction

Experimental details for X-ray diffraction (XRD) are discussed in Section 2.4.

## Ultraviolet Photoelectron Spectroscopy

Experimental details for ultraviolet photoelectron spectroscopy (UPS) are discussed in Section 2.2. The Single Value Decomposition (SVD) algorithm has been used on the valence electron region of the UPS spectra after annealing at various temperatures with reference spectra of substances to determine the components forming the measured UPS spectra. The details of the SVD algorithm can be found elsewhere<sup>38</sup>.

# Inverse Photoelectron Spectroscopy

Inverse photoelectron spectroscopy (IPES) relies on a reversed mechanism of photoelectron emission. It was employed to determine the surface energy of the conduction band at the sample surface. This technique works by directing electrons, generated using a BaO filament, onto the surface of the sample. These electrons transition into unoccupied states below kinetic energy, and synchronous recombination occurs, releasing photons. A Geiger Müller photon detector was utilised for photon detection.

## X-ray Photoelectron Spectroscopy

Experimental details for X-ray photoelectron spectroscopy (XPS) are discussed in Section 2.1. In this chapter, the spectra were calibrated using the C 1s peak set to 285 eV.

### 4.4 Results and Discussion

## 4.4.1 Cr-oxide layer on P25, BLTO and Al:SrTiO<sub>3</sub> particles – as deposited

STEM-EDX elemental mapping of Cr, Ti and O for P25-Cr<sub>2</sub>O<sub>3</sub> are shown in Figure 4.1. The elemental mapping of a whole P25 particle shows that the entire particle is covered with a Cr-oxide layer. Figure B2 shows a close elemental mapping with line analysis at the edge of the P25-Cr<sub>2</sub>O<sub>3</sub> particle. The line analysis indicates that the thickness of the Cr-oxide layer is 1.2 - 1.5 nm.

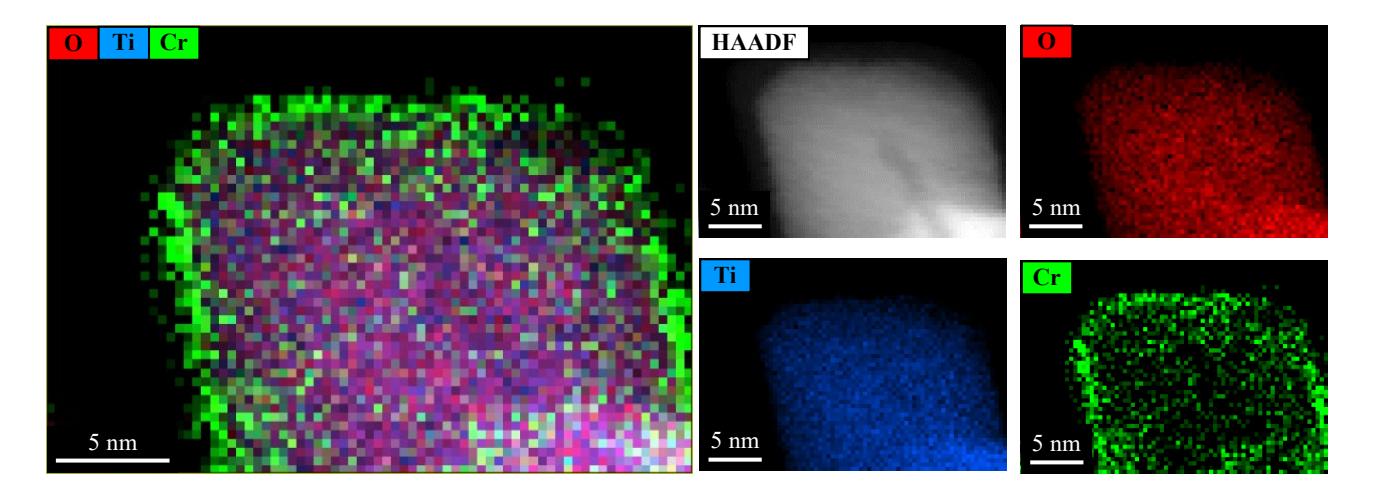


**Figure 4.1**: STEM-EDX elemental mapping of Cr, Ti and O for a P25-Cr<sub>2</sub>O<sub>3</sub> particle before annealing.

Figure 4.2 shows the STEM-EDX elemental mapping for BLTO-Cr(OH)<sub>3</sub> with line analysis of Cr and Ti. The mapping and line analysis demonstrate that a Cr-oxide layer has formed and is evenly distributed on the surface of the BLTO with a thickness of 1.4 nm.

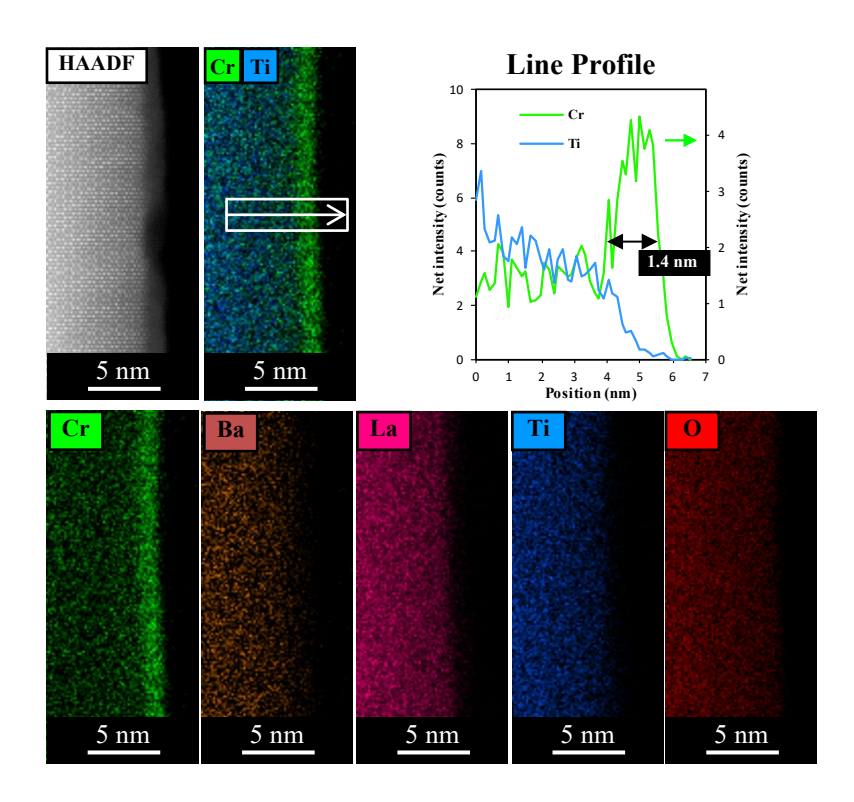


**Figure 4.2**: STEM-EDX elemental mapping of Cr, Ba, La, Ti and O with line analysis of BLTO-Cr(OH)<sub>3</sub>.

Figure 4.3 shows STEM-EDX elemental mapping of Cr, Al, Sr, Ti and O and the line profiles for the Al:SrTiO<sub>3</sub>-Cr<sub>2</sub>O<sub>3</sub> sample. The elemental mapping clearly shows that Cr-oxide is present on the

surface of the Al:SrTiO<sub>3</sub>. The line profile shows that Cr-oxide forms a layer on the surface with a thickness of 1.7 nm.

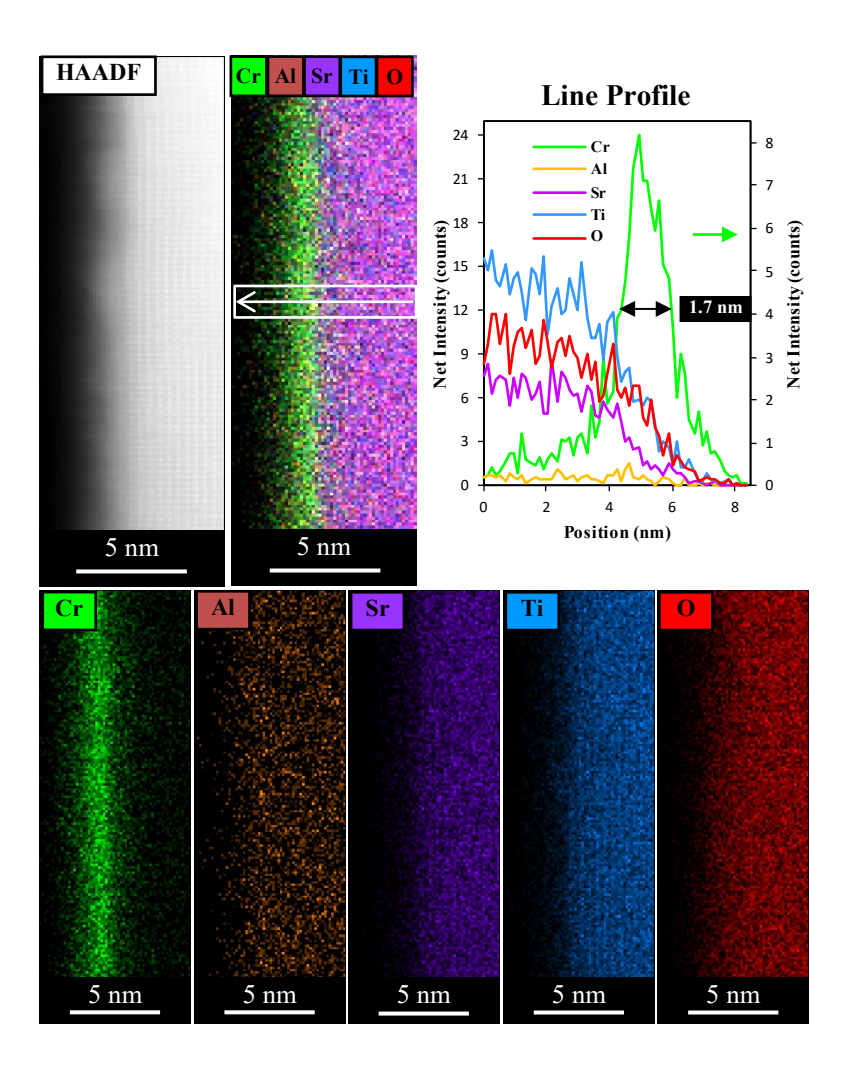


**Figure 4.3**: STEM-EDX elemental mapping of Cr, Al, Sr, Ti and O with line analysis of Al:SrTiO<sub>3</sub>- $Cr_2O_3$ .

The NEXAFS Cr L-edge spectrum has two strong absorption edges, at 578 eV (L<sub>3</sub>) and 586 eV (L<sub>2</sub>), as shown in Figures 4.4a and 4.4b. Figure 4.4a shows the Cr L-edge spectra of Cr<sub>2</sub>O<sub>3</sub> and Cr(OH)<sub>3</sub> reference samples (see Figure B3 for more details of different oxidation state features in the Cr L-edge spectrum). In the Cr L<sub>3</sub>-edge spectrum of Cr<sub>2</sub>O<sub>3</sub> two main peaks appear at 576.6 and 577.6 eV, while these peaks appear at higher photon energy (576.7 and 577.9 eV) with sharper features for Cr(OH)<sub>3</sub>. These features can be used to distinguish between Cr<sub>2</sub>O<sub>3</sub> and Cr(OH)<sub>3</sub> even though Cr<sub>2</sub>O<sub>3</sub> and Cr(OH)<sub>3</sub> have the same 3+ oxidation state. The Cr L-edge spectra of Cr-oxide photodeposited onto P25, BLTO and Al:SrTiO<sub>3</sub> are shown in Figure 4.4b. The Cr L-edge spectra of P25-Cr<sub>2</sub>O<sub>3</sub> and Al:SrTiO<sub>3</sub>-Cr<sub>2</sub>O<sub>3</sub> have the same lineshape as that of the Cr<sub>2</sub>O<sub>3</sub> reference spectrum, which confirms that the chemical state of the Cr-oxide layer deposited on P25 and Al:SrTiO<sub>3</sub> is consistent with Cr<sub>2</sub>O<sub>3</sub>. However, the Cr L-edge spectrum of BLTO-Cr(OH)<sub>3</sub> has the same features as Cr(OH)<sub>3</sub>, indicating

that the chemical state of Cr-oxide layer on BLTO is different from P25 and Al:SrTiO<sub>3</sub>. It should be noted that the Cr L-edge spectra of all samples bare no features of the CrO<sub>2</sub> and CrO<sub>3</sub> spectra (Figure B3). This interpretation is confirmed by XPS, which shows the Cr 2p<sub>3/2</sub> peaks at 577.2 and 577.5 eV<sup>39,40</sup>, which corresponds to Cr<sub>2</sub>O<sub>3</sub> and Cr(OH)<sub>3</sub> (Figures 4.4c–e). Note that the XPS fitting includes a broad peak around 579 eV, which corresponds to an energy loss peak from Ti 2s that occurs in the Cr 2p region. This peak was fitted using a related factor described in our previous work<sup>41</sup>. This peak has also been identified elsewhere<sup>42</sup>.

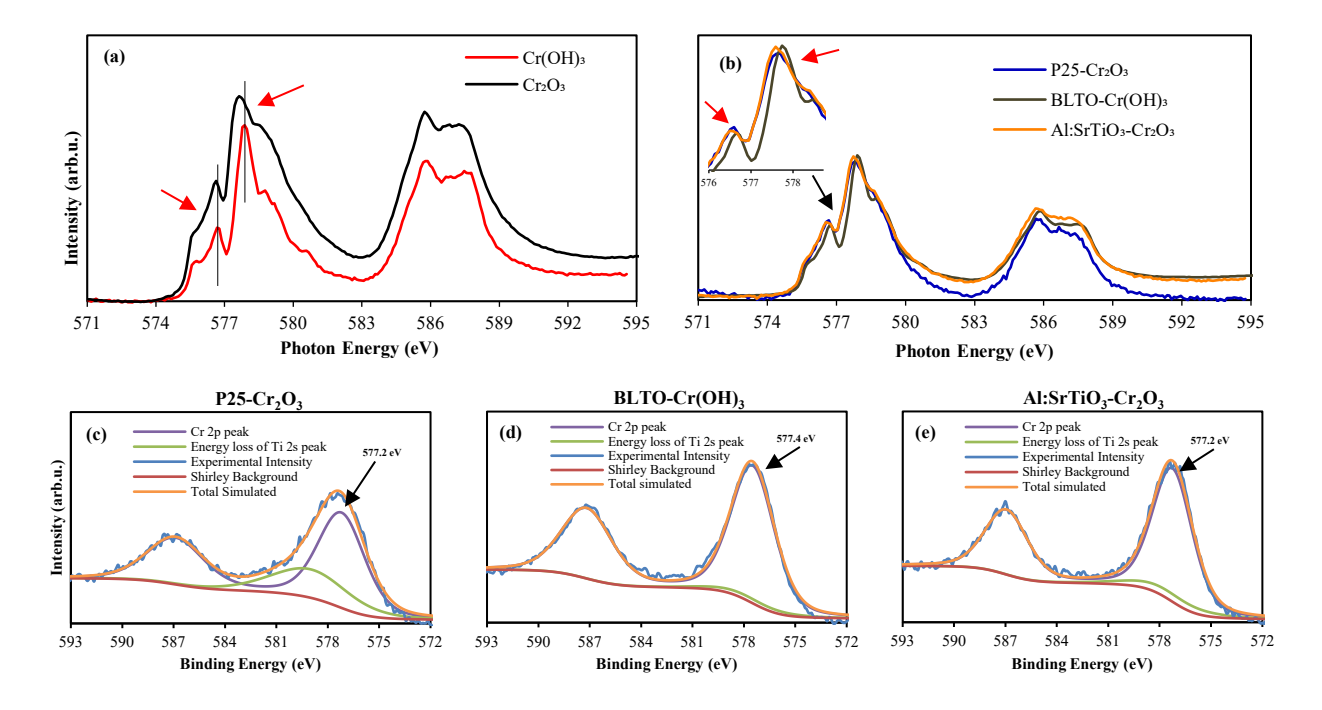


**Figure 4.4**:Cr L-edge NEXAFS spectra of **(a)**  $Cr_2O_3$  and  $Cr(OH)_3$  reference samples **(b)** Cr-oxide photodeposited onto P25, BLTO and Al:SrTiO<sub>3</sub>. Cr 2p XP spectra of **(c)** P25-Cr<sub>2</sub>O<sub>3</sub> **(d)** BLTO- $Cr(OH)_3$  and **(e)** AlSrTiO<sub>3</sub>-Cr<sub>2</sub>O<sub>3</sub>.

### 4.4.2 Cr-oxide layer on P25, BLTO and Al:SrTiO<sub>3</sub> particles – after annealing

The XPS intensity ratio of the total Cr to Ti peaks for P25-Cr<sub>2</sub>O<sub>3</sub>, BLTO-Cr(OH)<sub>3</sub> and Al:SrTiO<sub>3</sub>-Cr<sub>2</sub>O<sub>3</sub> samples after annealing at various temperatures is plotted in Figure 4.5. For the P25-Cr<sub>2</sub>O<sub>3</sub> sample (Figure 4.5a), it is observed that the relative intensity Cr:Ti ratio decreases from 0.20 to 0.05 as the annealing temperature increases to 600°C, a decrease of Cr intensity by ~80%. For the BLTO-Cr(OH)<sub>3</sub> sample (Figure 4.5b), the Cr:Ti ratio is 2 for the unheated sample and decreases slightly with heating. After annealing at 600°C, the Cr:Ti ratio decreases to 1.4, an overall decrease of ~30% compared to the unheated sample. The intensity ratios La:Ti and Ba:Ti for BLTO-Cr(OH)<sub>3</sub> are unchanged with annealing, as shown in Figures B5a-c, indicating no change in the overall perovskite structure. Note that the Cr 2p<sub>3/2</sub> peak is shifted to 577.0 eV after annealing at 200°C (see Figure B5d), indicating that Cr-oxide layer on BLTO is mainly composed of Cr<sub>2</sub>O<sub>3</sub> after annealing, i.e. has changed

from Cr(OH)<sub>3</sub> to Cr<sub>2</sub>O<sub>3</sub> due to annealing (hereafter referred to as BLTO-Cr<sub>2</sub>O<sub>3</sub>). For the Al:SrTiO<sub>3</sub>-Cr<sub>2</sub>O<sub>3</sub> sample, the Cr:Ti ratio after annealing remains relatively constant at ~0.85, which is very different from the P25 and BLTO samples. Note that the same treatment was applied to a sample of non-Al doped SrTiO<sub>3</sub>, which also shows a stable Cr:Ti ratio after annealing (Figure B5).

It is suggested that the decrease of the Cr:Ti ratio is due to the strong metal-support interaction (SMSI) effect, where heating increases the mobility of the species, which can result in diffusion and encapsulation<sup>43</sup>. The amount of diffusion depends on the differences in surface energy of the substances<sup>41</sup>. SMSI describes the segregation of a metal into the supporting substrate and has been widely used in encapsulation of noble metal where it has demonstrated effects in photocatalytic applications such as improvement of charge transfer<sup>44</sup> and stabilisation of metal clusters<sup>45</sup>.

It is known that TiO<sub>2</sub> has three crystal phases: anatase, brookite, and rutile. Different phases have different surface energies<sup>46</sup>. To better understand the diffusion of Cr<sub>2</sub>O<sub>3</sub> into P25, an XRD analysis of P25 was performed. Figure B6 shows the XRD pattern of P25 with a rough estimation based on the relative intensities of the anatase (85%) and rutile (15%) composition of P25. This ratio is approximately in agreement with that previously reported<sup>47</sup>. The 15% rutile in P25 is close to the proportion of Cr to Ti ratio retained after annealing to 600°C (Figure 4.5a).

The surface energy of anatase is reported to be  $0.95 \pm 0.07$  J/m<sup>246</sup>,  $Cr_2O_3$  is 1.60 J/m<sup>248</sup> and rutile is  $2.22 \pm 0.07$  J/m<sup>246</sup>. Thus, the surface energy of  $Cr_2O_3$  is higher than the anatase but lower than the rutile. Therefore, based on differences in surface energy, the decrease of the Cr:Ti ratio of  $P25-Cr_2O_3$  after annealing can be ascribed to the diffusion of  $Cr_2O_3$  into the anatase component of P25 but not rutile (Scheme 4.1a). For the BLTO- $Cr_2O_3$  sample, the diffusion of  $Cr_2O_3$  into BLTO is less than the anatase particles. There are no experimental data for the surface energy of BLTO, however, it is assumed that the difference in surface energy is the likely reason for the diffusion (Scheme 4.1b). For the Al:SrTiO<sub>3</sub>- $Cr_2O_3$  sample, the Cr:Ti ratio for after annealing is stable. SrTiO<sub>3</sub> has a surface energy of 2.85 J/m<sup>249</sup>. Unfortunately, there are no experimental data for the surface energy of Al:SrTiO<sub>3</sub>, however, it is assumed that their surface energies are similar. As argued above, this higher surface energy than  $Cr_2O_3$  (1.60 J/m<sup>2</sup>)<sup>48</sup> is the reason for the lack of  $Cr_2O_3$  diffusion (Scheme 4.1c). Note that  $Cr_2O_3$  was also found to be stable on non-Al doped SrTiO<sub>3</sub> (Figure B5). These results are in agreement with our previous report showing that  $Cr_2O_3$  layer diffuse into a substance with lower surface energy upon annealing <sup>41</sup>.

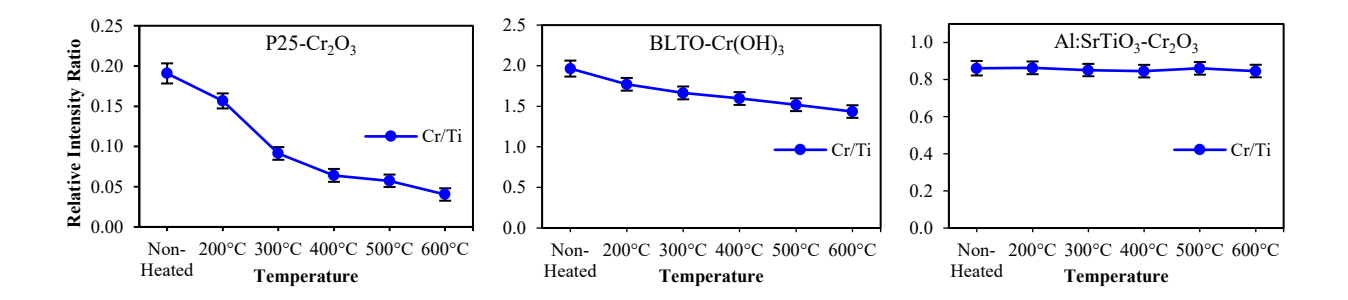
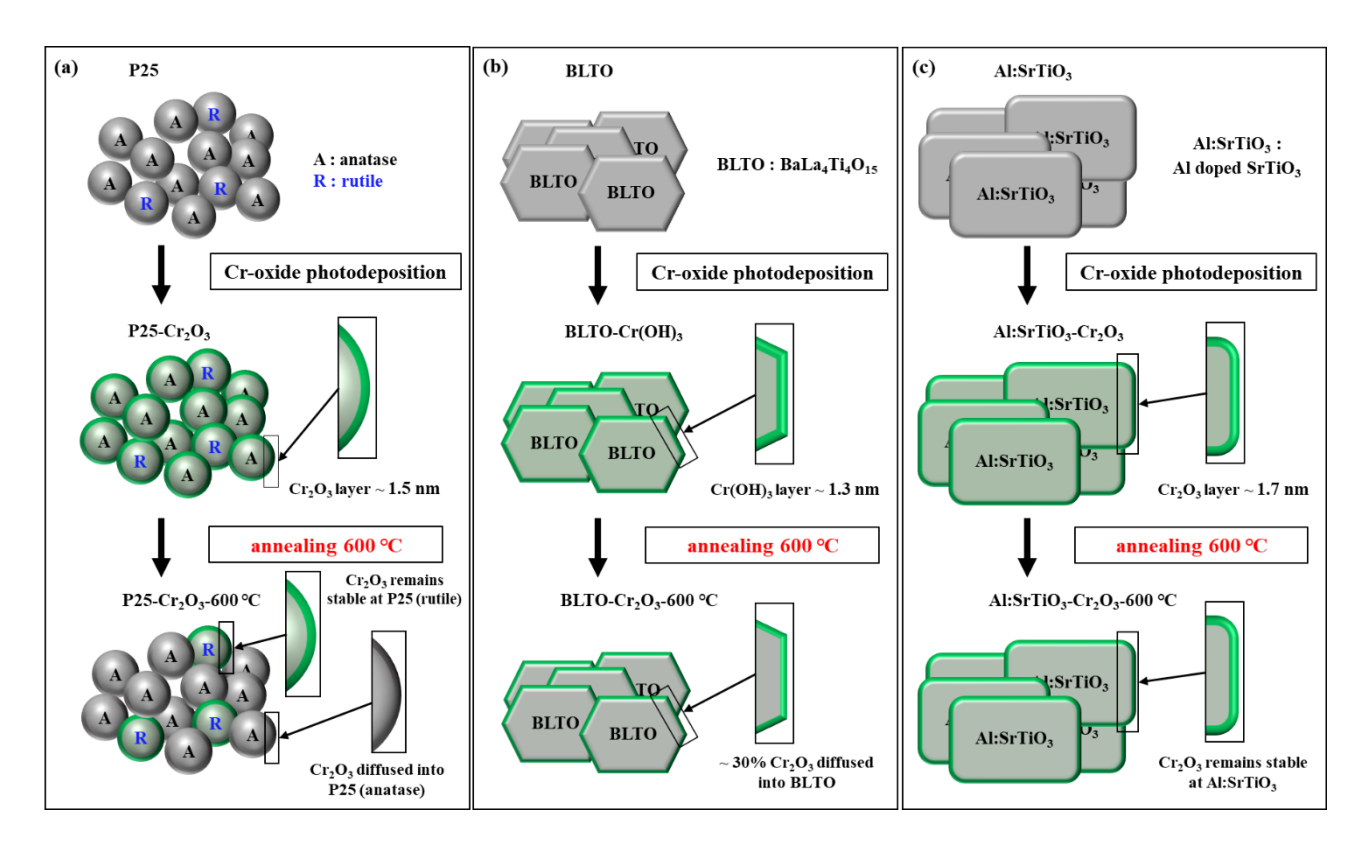


**Figure 4.5**: XPS relative intensity ratio of Cr 2p to Ti 2p of (a) P25-Cr<sub>2</sub>O<sub>3</sub>, (b) BLTO-Cr(OH)<sub>3</sub> and (c) Al:SrTiO<sub>3</sub>-Cr<sub>2</sub>O<sub>3</sub> annealed at various temperatures.



**Scheme 4.1**: Schematic illustration of experimental procedure of (a) P25, (b) BLTO and (c) Al:SrTiO<sub>3</sub> after photodeposition of Cr-oxide layer and after annealing 600°C

Figure 4.6a shows the Cr L-edge spectra of P25-Cr<sub>2</sub>O<sub>3</sub>, BLTO-Cr<sub>2</sub>O<sub>3</sub> and Al:SrTiO<sub>3</sub>-Cr<sub>2</sub>O<sub>3</sub> after annealing at 600°C with the Cr<sub>2</sub>O<sub>3</sub> reference spectrum for comparison. It should be noted that the Cr L-edge spectrum of P25 is at a lower intensity and noisy due to the large diffusion of Cr<sub>2</sub>O<sub>3</sub> into P25. These spectra after annealing have the metallic Cr features indicated by black arrows in Figure 4.6a: the onset of the spectrum before 575 eV (at around 574 eV), broad peaks and a small peak in the tail of the Cr L<sub>2</sub>-edge (at 584 eV). These features are further described in Figure B7. The Cr L-edge spectrum of P25-Cr<sub>2</sub>O<sub>3</sub>, BLTO-Cr<sub>2</sub>O<sub>3</sub> and Al:SrTiO<sub>3</sub>-Cr<sub>2</sub>O<sub>3</sub> after annealing confirmed that some Cr<sub>2</sub>O<sub>3</sub> was reduced to Cr metal.

Figures 4.6b–d show the XPS spectra of Cr 2p of P25-Cr<sub>2</sub>O<sub>3</sub>, BLTO-Cr<sub>2</sub>O<sub>3</sub> and Al:SrTiO<sub>3</sub>-Cr<sub>2</sub>O<sub>3</sub> after annealing at 600°C. The Cr 2p spectra for all three samples exhibit new spin-orbit peaks at 574.4–575.0 eV, corresponding to metallic Cr <sup>50, 51</sup>. The Cr 2p spectra agree with the finding from the NEXAFS Cr L-edge spectra of P25-Cr<sub>2</sub>O<sub>3</sub>, BLTO-Cr<sub>2</sub>O<sub>3</sub> and Al:SrTiO<sub>3</sub>-Cr<sub>2</sub>O<sub>3</sub> that, after annealing, some Cr<sub>2</sub>O<sub>3</sub> is reduced to Cr metal. Note that the Cr 2p XPS spectra was also applied to a sample of non-Al doped SrTiO<sub>3</sub>, which shows the reduction of some Cr<sub>2</sub>O<sub>3</sub> to Cr metal (Figure B8).

The NEXAFS O K-edge reference spectra of anatase, rutile, Cr<sub>2</sub>O<sub>3</sub>, CrO<sub>2</sub> and CrO<sub>3</sub> and spectra of P25, BLTO and Al:SrTiO<sub>3</sub> before photodeposition of Cr-oxide, and before and after annealing at 600°C are shown in Figure B9. These spectra provide further evidence that there is no presence of CrO<sub>2</sub> or CrO<sub>3</sub> species in P25-Cr<sub>2</sub>O<sub>3</sub>, BLTO-Cr<sub>2</sub>O<sub>3</sub> and Al:SrTiO<sub>3</sub>-Cr<sub>2</sub>O<sub>3</sub> after annealing at 600°C. See Figure B9 for more details.

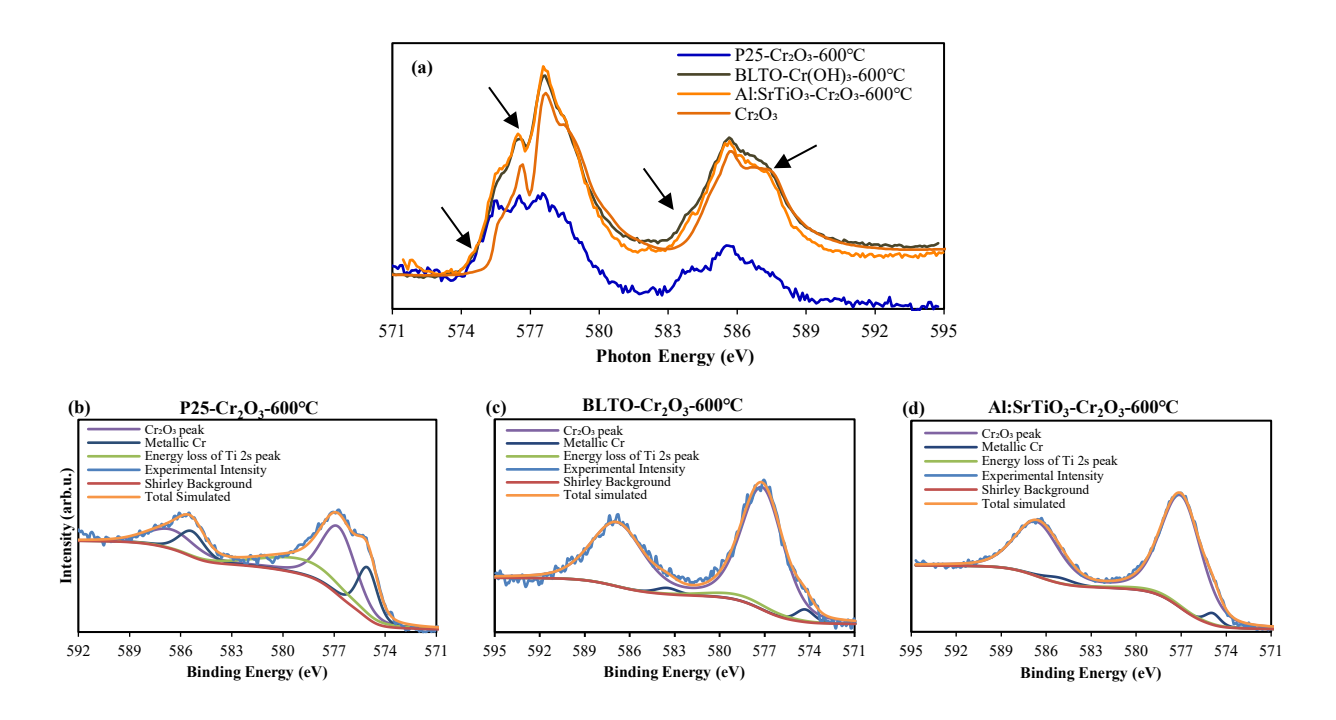


**Figure 4.6**: (a) Cr L-edge NEXAFS spectra of P25- $Cr_2O_3$ , BLTO- $Cr_2O_3$  and  $Al:SrTiO_3$ - $Cr_2O_3$  after annealing at  $600^{\circ}C$  with  $Cr_2O_3$  reference spectrum. Cr 2p XP spectrum of (b) P25- $Cr_2O_3$  (c) BLTO- $Cr_2O_3$  and (d)  $AlSrTiO_3$ - $Cr_2O_3$  after annealing at  $600^{\circ}C$ .

Figure 4.7 shows STEM-EDX elemental mapping with line analysis of Cr, Ti, and O for the P25-Cr<sub>2</sub>O<sub>3</sub> sample after annealing to 600°C. In comparison to Figure 4.1, the elemental mapping and line profile at the interface of half an entire P25 particle after annealing clearly shows that the Cr<sub>2</sub>O<sub>3</sub> layer has diffused into the P25 particle; however, line profile A still shows a high intensity of Cr at the edge of the P25 particle, which indicates that not all the Cr on the surface has diffused into P25, consistent with the XPS results. Moreover, Figure B10 shows a significant amount of Cr appears in the inner

part of the P25 particle due to the diffusion of Cr<sub>2</sub>O<sub>3</sub>. Figure B11 shows further evidence from STEM images that Cr<sub>2</sub>O<sub>3</sub> diffuses into anatase particles but remain on the surface of rutile particles.

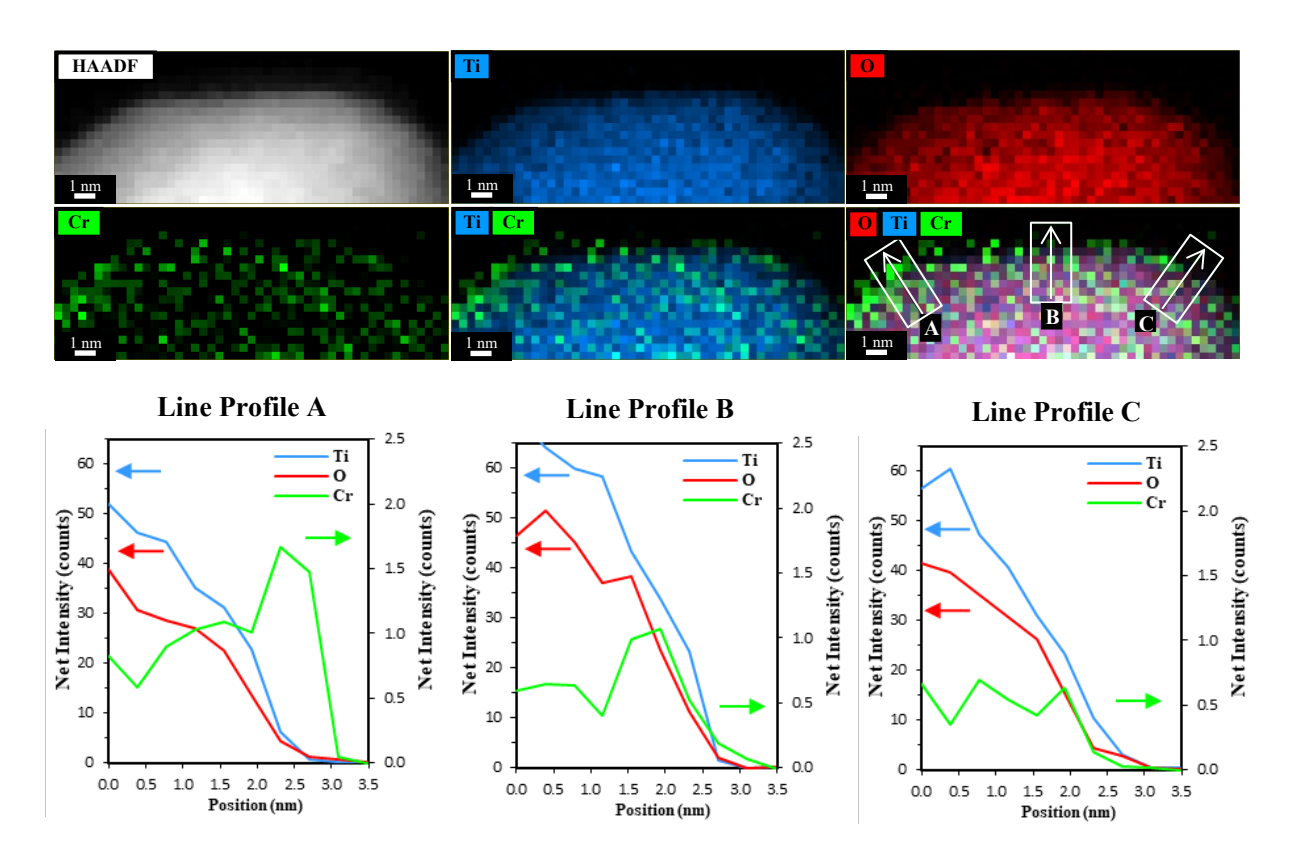


**Figure 4.7**: STEM-EDX elemental mapping with line analysis of Cr, Ti and O of P25-Cr<sub>2</sub>O<sub>3</sub> after annealing at 600°C.

STEM-EDX elemental mapping of Cr, Ba, La, Ti, and O for BLTO-Cr<sub>2</sub>O<sub>3</sub> after annealing at 600°C are shown in Figure 4.8 with line analysis for Cr and Ti. The line analysis shows that Cr layer has a thickness of 1.4 nm with more intensity of Cr through the surface (indicated by the black arrow in the line profile of Figure 4.8). Also, the EDX elemental mapping demonstrates that the Cr layer is unevenly distributed on the surface of the BLTO compared with BLTO-Cr(OH)<sub>3</sub> before annealing in Figure 4.2. The STEM-EDX results indicates further evidence that the Cr<sub>2</sub>O<sub>3</sub> layer has diffused to a small degree into BLTO during annealing.

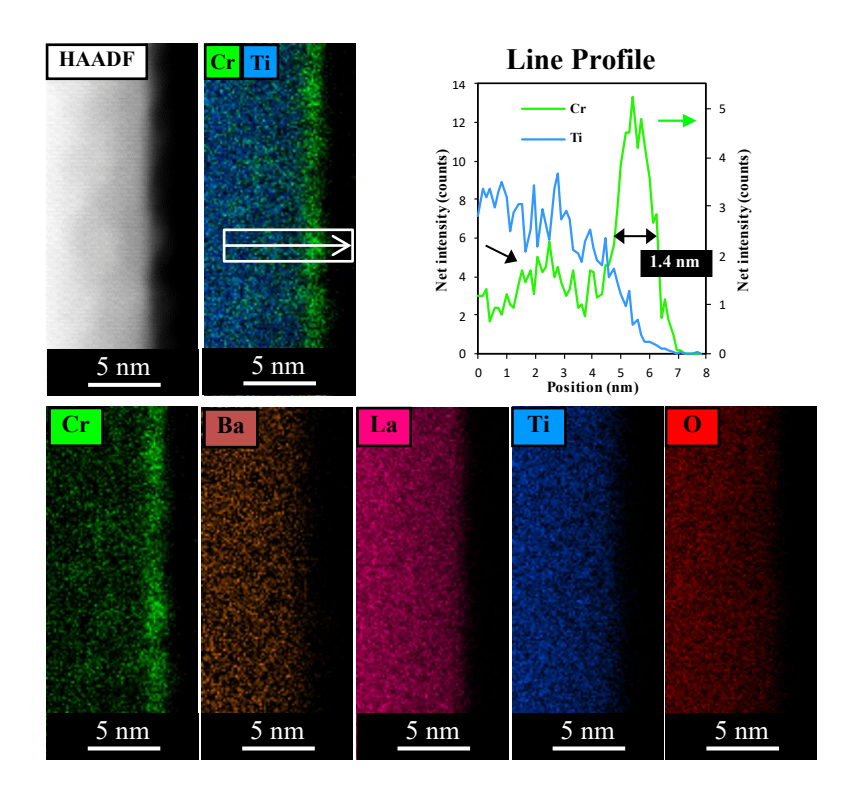


**Figure 4.8**: STEM-EDX elemental mapping of Cr, Ba, La, Ti, and O with line analysis of Cr and Ti for BLTO-Cr<sub>2</sub>O<sub>3</sub> after annealing at 600°C.

Figure 4.9 shows STEM-EDX elemental mapping of Cr, Al, Sr, Ti and O and the line profiles for the Al:SrTiO<sub>3</sub>-Cr<sub>2</sub>O<sub>3</sub> after annealing at 600°C. Interestingly, the Cr<sub>2</sub>O<sub>3</sub> layer is observed covering the surface of the Al:SrTiO<sub>3</sub> with a thickness of 1.7 nm, which is similar to the result shown in Figure 4.3 before annealing. These STEM-EDX results are in agreement with XPS data that Cr<sub>2</sub>O<sub>3</sub> layer is very stable on Al:SrTiO<sub>3</sub>.

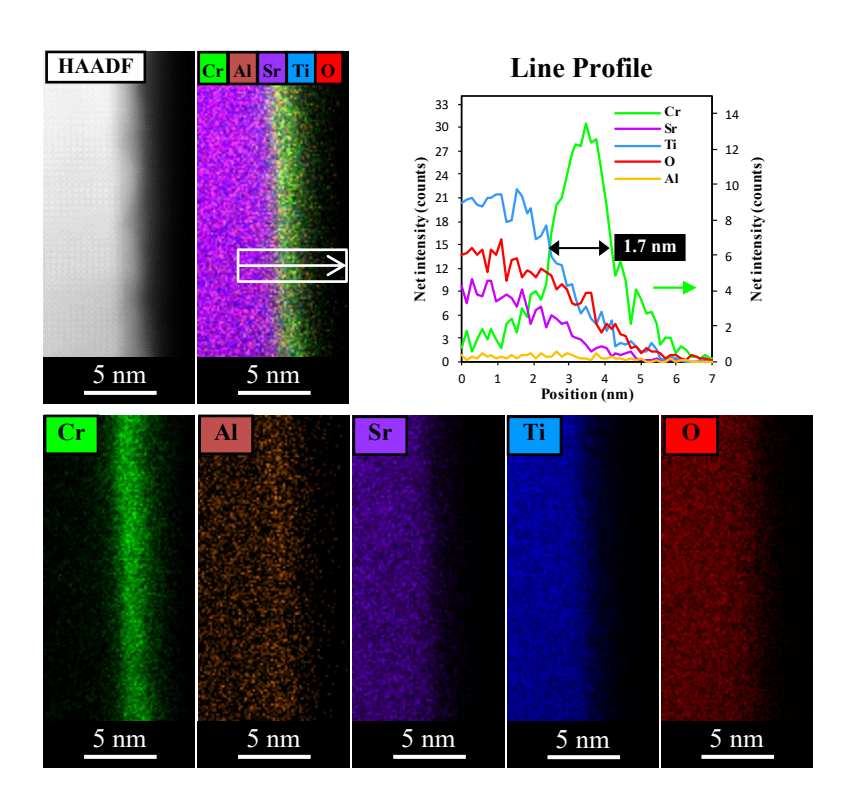


**Figure 4.9**: STEM-EDX elemental mapping and line analysis of Cr, Al, Sr, Ti and O for Al: $SrTiO_3$ - $Cr_2O_3$  after annealing at  $600^{\circ}C$ .

## 4.4.3 Change of surface electronic properties upon annealing

UPS and IPES were applied to investigate the electronic structure at the surface. Figure 4.10a shows the valence band and conduction band cut-offs for the P25,  $Cr_2O_3$ , P25- $Cr_2O_3$  and P25- $Cr_2O_3$ -600°C samples. The valence band and conduction band cut-offs for P25 are  $3.3 \pm 0.1$  eV and  $-0.3 \pm 0.1$  eV, respectively. The surface band gap of P25 is  $3.6 \pm 0.2$  eV, which is the difference between the UPS valence band and IPES conduction band cut-offs.  $Cr_2O_3$  has a lower surface band gap  $(1.7 \pm 0.2 \text{ eV})$  compared to P25 which is driven by its low energy valence band at  $1.3 \pm 0.1$  eV. P25- $Cr_2O_3$  shows a similar valence band cut-off as  $Cr_2O_3$  with the conduction band cut-off at  $-0.2 \pm 0.1$  eV, which makes the surface band gap  $1.5 \pm 0.2$  eV. The reason for the decrease of the surface band gap here is due to the contribution of electronic states from  $Cr_2O_3$  in the P25- $Cr_2O_3$  valence band region. After annealing at 600°C, the band structure of P25- $Cr_2O_3$  reverts back to unadulterated P25, showing a valence band cut-off at  $3.2 \pm 0.1$  eV and conduction band cut-off at  $-0.0 \pm 0.1$  eV. The change observed after annealing is clearly due to the diffusion of  $Cr_2O_3$  into P25, causing a loss in the contribution from  $Cr_2O_3$  electronic states. The decrease of the conduction band cut-off of P25- $Cr_2O_3$ -600°C is possibly due to the new contribution of Cr metal that was reduced from  $Cr_2O_3$  after annealing.

Figure 4.10b shows the valence band and conduction band regions with cut-offs for the BLTO,  $Cr_2O_3$ , BLTO- $Cr_2O_3$  and BLTO- $Cr_2O_3$ -600°C samples. The valence band and conduction band cut-offs of BLTO are  $3.2 \pm 0.1$  eV and  $-1.0 \pm 0.1$  eV, with a surface band gap of  $4.2 \pm 0.2$  eV. Both the BLTO-

 $Cr_2O_3$  and BLTO- $Cr_2O_3$ -600°C samples have similar valence band cut-offs to  $Cr_2O_3$  (1.2 ± 0.1 eV and 1.4 ± 0.1 eV, respectively) with a higher conduction band cut-off at -0.7 ± 0.1 eV. Note that the conduction band for these samples have minor electronic states at -0.5 ± 0.1 eV, which can be a feature of  $Cr_2O_3$  contribution within conduction band because  $Cr_2O_3$  conduction band cut-off has appeared at 0.4 eV. Thus, it is concluded that photodeposition of  $Cr_2O_3$  on BLTO introduces electronic states of  $Cr_2O_3$  within the BLTO surface band gap that remain upon annealing.

Figure 4.10c shows that Al:SrTiO<sub>3</sub> has a surface band gap of  $3.3 \pm 0.2$  eV, with the valence band and conduction band cut-offs at  $2.9 \pm 0.1$  eV and  $0.4 \pm 0.1$  eV, respectively. Similar to P25 and BLTO, photodeposition of Cr<sub>2</sub>O<sub>3</sub> onto Al:SrTiO<sub>3</sub> introduces electronic states of Cr<sub>2</sub>O<sub>3</sub>, which reduces the band gap to  $1.6 \pm 0.1$  eV. After annealing, the conduction band increases to  $0.8 \pm 0.1$  eV, resulting in an increased band gap of  $2.2 \pm 0.2$  eV.

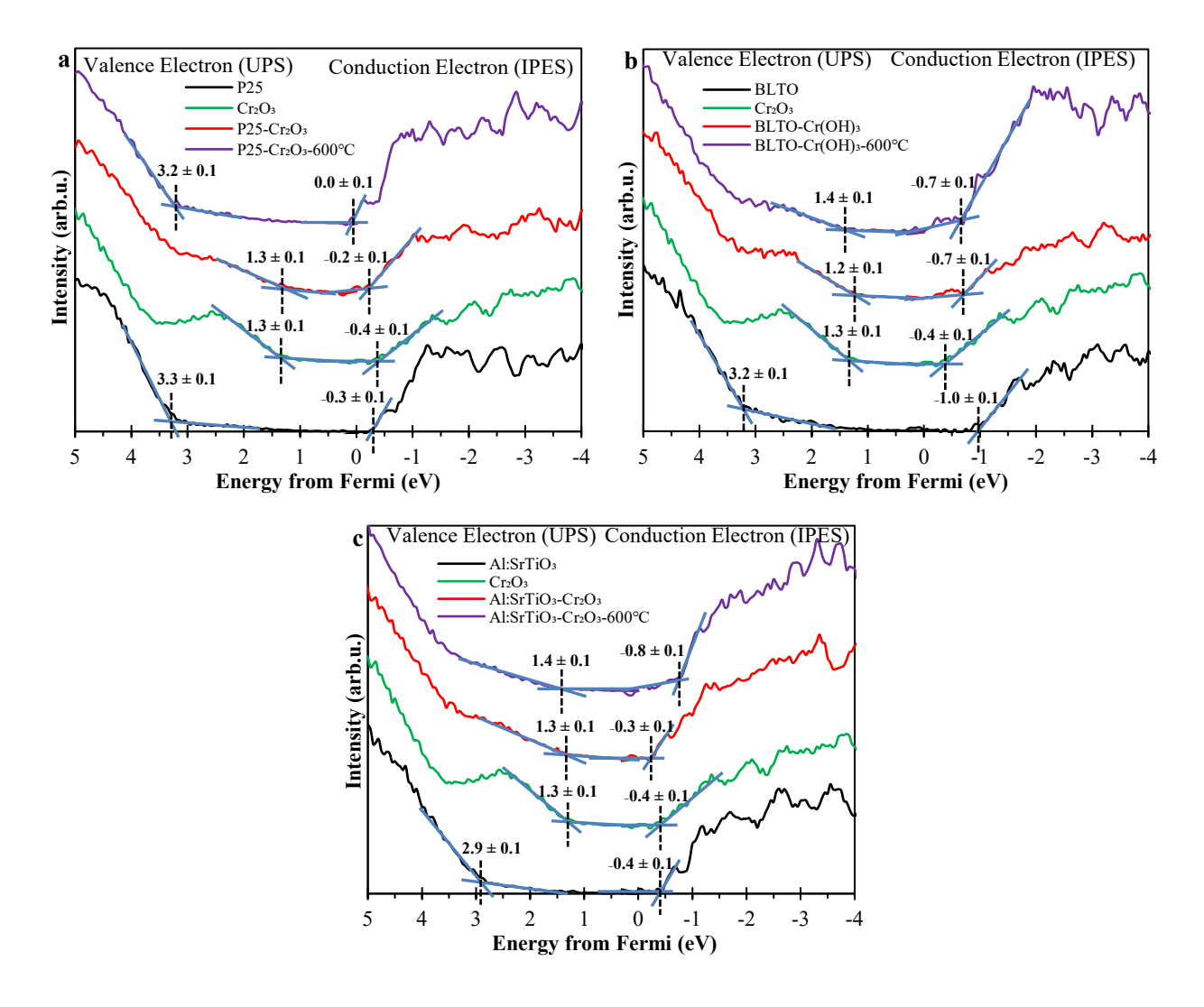
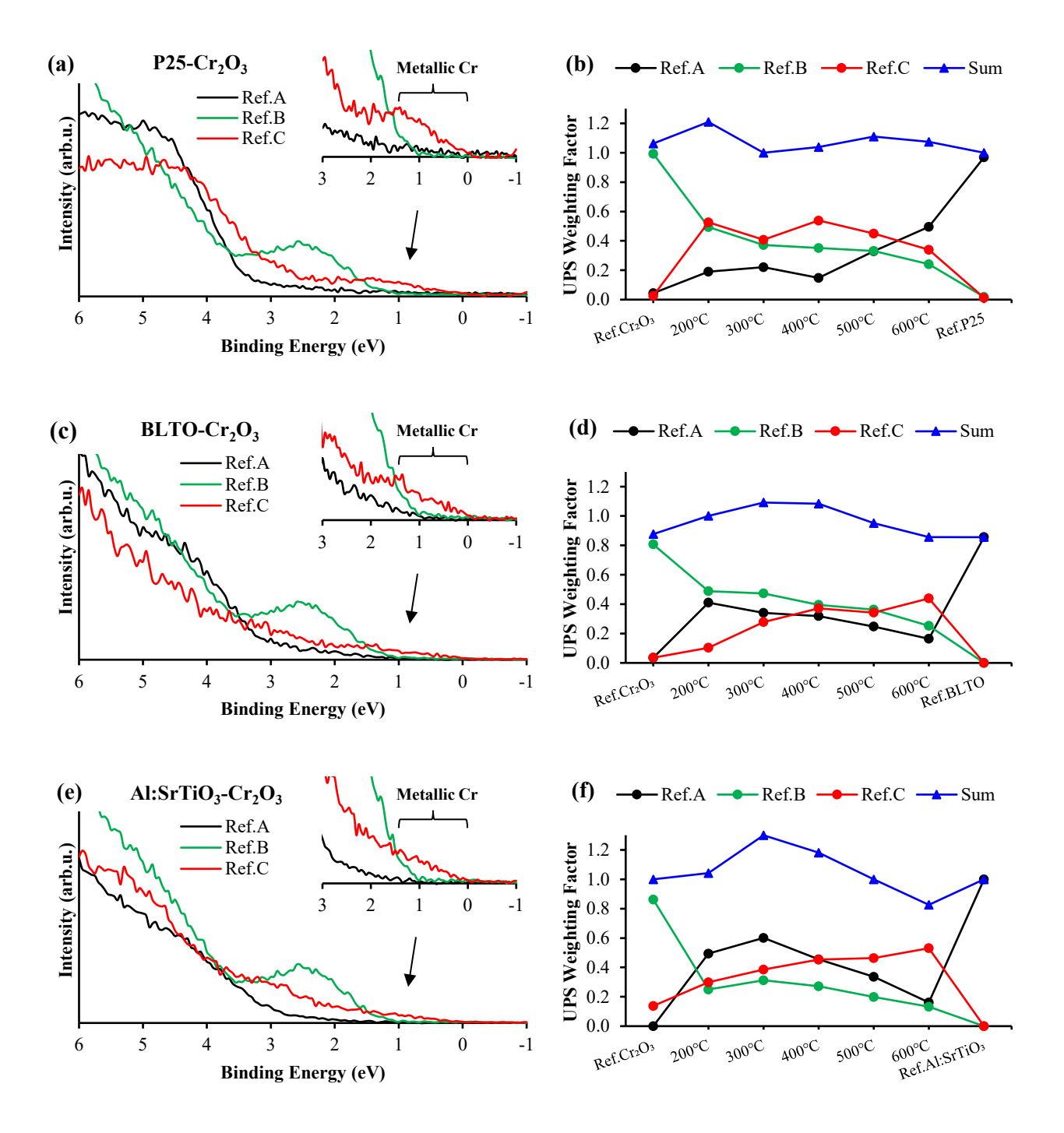


Figure 4.10: The valence band and conduction band regions from UPS and IPES spectra of (a) P25, Cr<sub>2</sub>O<sub>3</sub>, P25-Cr<sub>2</sub>O<sub>3</sub> and P25-Cr<sub>2</sub>O<sub>3</sub> after annealing at 600°C, (b) BLTO, Cr<sub>2</sub>O<sub>3</sub>, BLTO-Cr<sub>2</sub>O<sub>3</sub> and BLTO-Cr<sub>2</sub>O<sub>3</sub> after annealing at 600°C and (c) Al:SrTiO<sub>3</sub>, Cr<sub>2</sub>O<sub>3</sub>, Al:SrTiO<sub>3</sub>-Cr<sub>2</sub>O<sub>3</sub> and Al:SrTiO<sub>3</sub>-Cr<sub>2</sub>O<sub>3</sub> after annealing at 600°C with the cut-offs of valence band and conduction band. (All the samples were heated to 100°C to clean the surface and avoid any chance of charging during the measurements.)

Singular value decomposition (SVD) is applied to evaluate a series of data and identify similar components within a set of data. The SVD algorithm has been used here to determine the components forming measured UPS spectra by fitting a series of UPS spectra as a linear combination of reference spectra. All the pristine UPS spectra that were used to analyse the SVD can be found in Figure B12. Figures 4.11a and 4.11b shows the UPS reference spectra identified via SVD on the UPS spectrum of P25-Cr<sub>2</sub>O<sub>3</sub>. Three contributing reference spectra with varying weightings at each annealing temperature are identified; Ref.A, Ref.B and Ref.C. The Ref.A and Ref.B spectra have a same line shape as P25 and Cr<sub>2</sub>O<sub>3</sub> (Figure B13a). The new spectrum (Ref.C) only appears for P25-Cr<sub>2</sub>O<sub>3</sub> after annealing (200 to 600°C) with states close to the Fermi edge suggesting a metallic feature (inset of

Figure 4.11a). This spectrum is thus identified as Cr metal. The weighting factor of P25 (Ref.A) increases as the annealing temperature increases with a concurrent decrease in the weighting factor of Cr<sub>2</sub>O<sub>3</sub> (Ref.B). This agrees with the early finding from XPS and STEM that Cr<sub>2</sub>O<sub>3</sub> has diffused into P25 upon annealing. The weighting factor of Cr metal (Ref.C) stays relatively constant during annealing. However, Figure B12a shows the UPS spectra during annealing (200 to 600°C) with an increase of intensity close to the Fermi edge, which indicates that the Cr metal state increases slightly during annealing. The UPS valence electronic structure study of P25-Cr<sub>2</sub>O<sub>3</sub> after annealing at various temperatures agrees with the NEXAFS and XPS data that after annealing of P25-Cr<sub>2</sub>O<sub>3</sub> some of the Cr<sub>2</sub>O<sub>3</sub> layer is reduced to Cr metal. This is direct evidence of the contribution of reduced metallic Cr in the valence electronic band of P25-Cr<sub>2</sub>O<sub>3</sub>.

Figures 4.11c—f show the UPS reference spectra identified via SVD of BLTO-Cr<sub>2</sub>O<sub>3</sub> and Al:SrTiO<sub>3</sub>-Cr<sub>2</sub>O<sub>3</sub> with the weighting factors for the reference spectra. Three reference spectra are identified for the UPS spectra of both BLTO-Cr<sub>2</sub>O<sub>3</sub> and Al:SrTiO<sub>3</sub>-Cr<sub>2</sub>O<sub>3</sub>, as seen in Figures 4.11c and 4.11e. Ref.A represents BLTO and Al:SrTiO<sub>3</sub>, while Ref.B in both cases represents Cr<sub>2</sub>O<sub>3</sub> (see Figures B13a and B13b). In both cases Ref.C is similar to the third reference spectrum identified for P25-Cr<sub>2</sub>O<sub>3</sub> as a Cr metal reference spectrum. The weighting factors of Ref.A (BLTO and Al:SrTiO<sub>3</sub>) and Ref.B (Cr<sub>2</sub>O<sub>3</sub>) show a relatively constant decrease as the annealing temperature increases. Within uncertainty, it is not clear whether the substrate intensities really do decrease for these samples. However, it was observed with XPS that the substrate intensities increased for BLTO due to the diffusion of CrO<sub>x</sub> but remained stable for Al:SrTiO<sub>3</sub>. The weighting factor of Ref.C (Cr metal) increases constantly with the increase of the annealing temperature for both samples. Figure B12b and B12c clearly shows the Cr metal feature close to the Fermi edge, which increased during annealing. This agrees with the NEXAFS and XPS data that some of the Cr<sub>2</sub>O<sub>3</sub> layer is reduced to Cr metal after annealing, which is direct evidence of the contribution of reduced metallic Cr in the valence electronic structure of BLTO-Cr<sub>2</sub>O<sub>3</sub> and Al:SrTiO<sub>3</sub>-Cr<sub>2</sub>O<sub>3</sub>.



**Figure 4.11**: UPS reference spectra and weighting factors identified via SVD of (a,b) P25-Cr<sub>2</sub>O<sub>3</sub> after annealing at various temperatures (c,d) BLTO-Cr<sub>2</sub>O<sub>3</sub> after annealing at various temperatures (e,f) Al:SrTiO<sub>3</sub>-Cr<sub>2</sub>O<sub>3</sub> after annealing at various temperatures

## 4.4.4 Change of bulk electronic properties upon annealing

Figure 4.12 shows the absorption measurements using diffuse reflectance spectroscopy (DRS) of the three photocatalysts before and after Cr-oxide deposition and after annealing. The as-deposited BLTO-Cr(OH)<sub>3</sub> sample contains two peaks at lower energy. This feature replicates the two peaks from 1.6 to 3.2 eV in pure Cr<sub>2</sub>O<sub>3</sub>, indicating the presence of undoped Cr<sub>2</sub>O<sub>3</sub> on the photocatalyst surface (see Figure B14). This feature is also present for the as-deposited P25 and Al:SrTiO<sub>3</sub> samples,

however, only the first peak (cresting at ca. 2.0 eV) is distinct, likely because the bulk band gap for these two materials begins at a lower energy than BLTO. On the other hand, these differences could also be due to Cr<sub>2</sub>O<sub>3</sub> being differently incorporated by each of the semiconductors.

After annealing, none of the annealed photocatalysts display these Cr<sub>2</sub>O<sub>3</sub>-like twin peaks. However, in comparison with their bare counterparts, a prominent absorption tail appears at lower energies (although it is less prominent for Al:SrTiO<sub>3</sub>). This is typical for photocatalysts which have been doped or surface modified.<sup>52</sup> This, in conjunction with the change in the shape of the absorption tail and sample colour before and after annealing (see Figure B15), indicates that annealing causes some electronic change due to doping with Cr<sub>2</sub>O<sub>3</sub>. Note that the less prominent absorption tail for Al:SrTiO<sub>3</sub>, compared to P25 and BLTO, potentially indicates lower doping levels. Although, Cr<sub>2</sub>O<sub>3</sub>-doping both before and after annealing the samples does not appear to narrow the bulk bandgap of the bulk material (see Table B1 and Figure B16). Instead the Cr<sub>2</sub>O<sub>3</sub>-doping is only responsible for the absorption tail.<sup>52</sup>

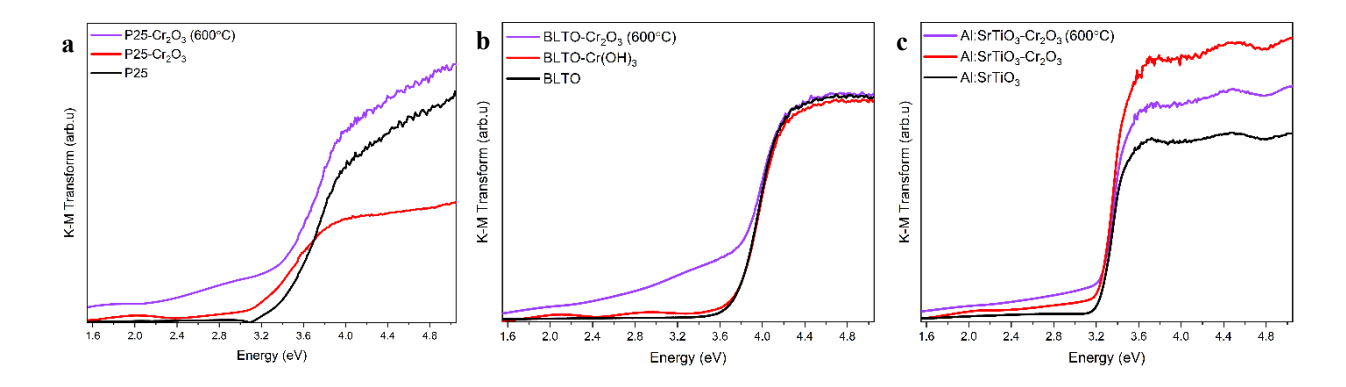


**Figure 4.12:** Kubelka-Munk Transformed UV-visible DRS spectra of (**a**) P25, P25-Cr<sub>2</sub>O<sub>3</sub> and P25-Cr<sub>2</sub>O<sub>3</sub> after annealing at 600°C, (**b**) BLTO, BLTO-Cr(OH)<sub>3</sub> and BLTO-Cr<sub>2</sub>O<sub>3</sub> after annealing at 600°C and (**c**) Al:SrTiO<sub>3</sub>-Cr<sub>2</sub>O<sub>3</sub> and Al:SrTiO<sub>3</sub>-Cr<sub>2</sub>O<sub>3</sub> after annealing at 600°C.

### 4.4.5 Photocatalytic water splitting

Figure 4.13 summarises the surface and bulk band gaps obtained from UPS, IPES and DRS of all the photocatalysts. The differences in the surface band gaps and the shape of the absorption spectra due to the photodeposition and diffusion of Cr-oxide could be an advantage in the improvement of light absorption and photogenerated electron—hole pairs at the surface and contribute to for photocatalytic water splitting activity. Photocatalytic water splitting was performed with two light sources (405 and 365 nm) on P25 and BLTO as they have shown various degrees of Cr-oxide diffusion (see Table B2). Both samples after treatments show no H<sub>2</sub> production using the visible light source. Using the UV light source and with the modification of the photocatalysts with 1 wt % Pt nanoparticles as co-catalyst, only P25 showed H<sub>2</sub> production. It is observed that photodeposition of Cr-oxide decreases

the H<sub>2</sub> production compared to plain P25. After annealing, the activity has increased slightly but remains lower than unadulterated P25. From the photocatalytic water splitting tests of P25 and BLTO, it is observed that the change of the surface band gap and the shape of the absorption spectra due to the diffusion of Cr-oxide layer does not contribute to photocatalytic activity.

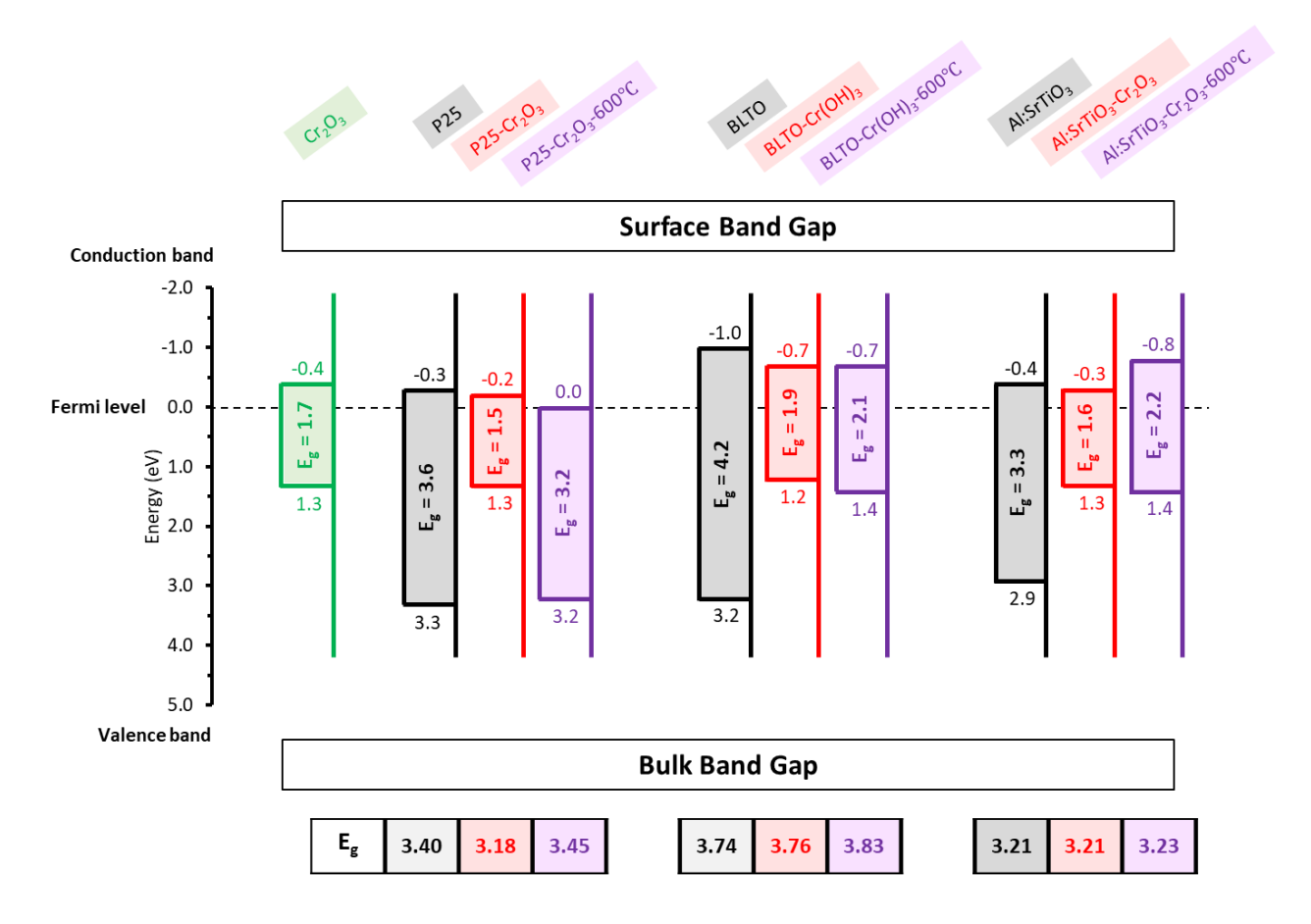


**Figure 4.13**: The surface and bulk band gaps of  $Cr_2O_3$ , and  $(P25, BLTO, and Al:SrTiO_3)$  after the photodeposition of Cr-oxide layer and after annealing at  $600^{\circ}C$ .

As discussed above,  $Cr_2O_3$  layers deposited onto metal oxide are beneficial for photocatalytic water splitting by blocking the backward reaction. Table 4.1 summarises the effect of annealing of  $Cr_2O_3$  layers photodeposited onto various substrates, including results from our previous study on films. The findings presented herein demonstrate that the  $Cr_2O_3$  layer remains stable at the surface of rutile and Al:SrTiO<sub>3</sub> but not for anatase and BLTO. This provides understanding on the suitability of different substrates to deposit  $Cr_2O_3$  layers to produce robust photocatalysts for water splitting and in preventing the  $H_2$  and  $O_2$  back reaction back to form  $H_2O$ .

**Table 4.1:** Summary of the effect of annealing  $Cr_2O_3$  layer on various forms of  $TiO_2$ .

Substrate		Amorphous film	Anatase film <sup>41</sup>	50:50 anatase:rutile film	P25*	Al:SrTiO <sub>3</sub>	BLTO
Surface energy (J/m <sup>2</sup> )		< 0.95	0.95	Anatase: 0.95 Rutile: 2.22	Anatase: 0.95 Rutile: 2.22	SrTiO <sub>3</sub> : 2.85 Al:SrTiO <sub>3</sub> : -	-
Deposition method		Photo-deposition	Photo-deposition	Photo-deposition	Photo-deposition	Photo-deposition	Photo-deposition
Cr formation on the surface as deposited		Layer	Layer	Layer	Layer	Layer	Layer <sup>33</sup>
	Before annealing	Cr <sub>2</sub> O <sub>3</sub>	Cr <sub>2</sub> O <sub>3</sub>	Cr <sub>2</sub> O <sub>3</sub>	Cr <sub>2</sub> O <sub>3</sub>	Cr <sub>2</sub> O <sub>3</sub>	Cr(OH) <sub>3</sub>
Chemical state of Cr <sub>2</sub> O <sub>3</sub> layer	After annealing	Some Cr <sub>2</sub> O <sub>3</sub> reduced to metallic Cr and no appearance of CrO <sub>2</sub> or CrO <sub>3</sub>	Some Cr <sub>2</sub> O <sub>3</sub> reduced to metallic Cr	Some Cr <sub>2</sub> O <sub>3</sub> reduced to metallic Cr	Some Cr <sub>2</sub> O <sub>3</sub> reduced to metallic Cr and no appearance of CrO <sub>2</sub> or CrO <sub>3</sub>	Some Cr <sub>2</sub> O <sub>3</sub> reduced to metallic Cr and no appearance of CrO <sub>2</sub> or CrO <sub>3</sub>	Some Cr <sub>2</sub> O <sub>3</sub> reduced to metallic Cr and no appearance of CrO <sub>2</sub> or CrO <sub>3</sub>
Stability of Cr <sub>2</sub> O <sub>3</sub> layer after annealing		Cr <sub>2</sub> O <sub>3</sub> layer diffused	Cr <sub>2</sub> O <sub>3</sub> layer diffused	50% of Cr <sub>2</sub> O <sub>3</sub> layer diffused	Cr <sub>2</sub> O <sub>3</sub> layer diffused into anatase particles but remained on rutile particles	No diffusion of Cr <sub>2</sub> O <sub>3</sub> layer	~30% of Cr <sub>2</sub> O <sub>3</sub> layer diffused
Scheme		After photodeposition  Cr <sub>2</sub> O <sub>3</sub> layer  amorphous TiO <sub>2</sub> annealing  metallic Cr and  Cr <sub>2</sub> O <sub>3</sub> amorphous TiO <sub>2</sub> Cr <sub>2</sub> O <sub>3</sub> diffused	After photodeposition  Cr <sub>2</sub> O <sub>3</sub> layer  anatase phase  annealing  metallic Cr and  Cr <sub>2</sub> O <sub>3</sub> anatase phase  Cr <sub>2</sub> O <sub>3</sub> diffused	After photodeposition  Cr <sub>2</sub> O <sub>3</sub> layer  rutile and anatase  annealing  metallic Cr and Cr <sub>2</sub> O <sub>3</sub> rutile and anatase  Cr <sub>2</sub> O <sub>3</sub> diffused	After photodeposition  Cr <sub>2</sub> O <sub>3</sub> layer  P25  annealing  metallic Cr and  Cr <sub>2</sub> O <sub>3</sub> P25  80% of Cr <sub>2</sub> O <sub>3</sub> diffused	After photodeposition  Cr <sub>2</sub> O <sub>3</sub> layer  Al:SrTiO <sub>3</sub> annealing  metallic Cr and  Cr <sub>2</sub> O <sub>3</sub> CCO layer  Al:SrTiO <sub>3</sub>	After photodeposition  Cr(OH)s layer  BLTO  annealing  metallic Cr  and Cr <sub>2</sub> O <sub>3</sub> BLTO  30% of Cr <sub>2</sub> O <sub>3</sub> diffused

<sup>\*</sup>P25 contains 85% anatase and 15% rutile particles.

## 4.5 Conclusions

Cr-oxide was photodeposited as a layer onto P25, BLTO and Al:SrTiO<sub>3</sub> particles. The chemical nature of the layers was found to be Cr<sub>2</sub>O<sub>3</sub> and Cr(OH)<sub>3</sub> based on NEXAFS and XPS. STEM-EDX elemental mapping showed a Cr-oxide layer formed a coating with thickness 1.2 - 1.7 nm on the three photocatalyst particles. Annealing of P25-Cr<sub>2</sub>O<sub>3</sub> up to 600°C causes diffusion of Cr<sub>2</sub>O<sub>3</sub> into the anatase fraction of P25 but not into the rutile fraction. For BLTO and Al:SrTiO<sub>3</sub>, after annealing, the Cr<sub>2</sub>O<sub>3</sub> layer diffused to a small degree into BLTO particles but was stable on the surface of Al:SrTiO<sub>3</sub> particles. This diffusion effect is attributed to differences in the surface energy between Cr<sub>2</sub>O<sub>3</sub> and the respective substrate, according to the SMSI effect. NEXAFS, XPS and UPS confirmed that the Cr<sub>2</sub>O<sub>3</sub> layer on the P25, BLTO and Al:SrTiO<sub>3</sub> surfaces was reduced to metallic Cr after annealing with no presence of CrO<sub>2</sub> or CrO<sub>3</sub> found on the surface. The formation and diffusion of Cr<sub>2</sub>O<sub>3</sub> was found to influence the surface and bulk band gaps by narrowing the band gap and introducing an absorption tail at lower energies of the bulk band gap. It was confirmed that the changes in the surface and bulk band gaps do not contribute to improved photocatalytic activity. The deep understanding of the stability, oxidation state and electronic structure of Cr-oxide layer on photocatalyst particles under annealing are essential for overlayer applications in photocatalytic water splitting.

## 4.6 References

- 1. Fujishima, A.; Honda, K., Electrochemical photolysis of water at a semiconductor electrode. *Nature* **1972**, *238* (5358), 37-8.
- 2. Lee, J. S., Photocatalytic Water Splitting Under Visible Light with Particulate Semiconductor Catalysts. *Catalysis Surveys from Asia* **2005**, *9* (4), 217-227.
- 3. Abe, R., Development of a New System for Photocatalytic Water Splitting into H2 and O2 under Visible Light Irradiation. *Bulletin of the Chemical Society of Japan* **2011**, *84* (10), 1000-1030.
- 4. Maeda, K., Z-Scheme Water Splitting Using Two Different Semiconductor Photocatalysts. *ACS Catalysis* **2013**, *3* (7), 1486-1503.
- 5. Kudo, A.; Miseki, Y., Heterogeneous photocatalyst materials for water splitting. *Chemical Society Reviews* **2009**, *38* (1), 253-278.
- 6. Maeda, K., (Oxy)nitrides with d0-electronic configuration as photocatalysts and photoanodes that operate under a wide range of visible light for overall water splitting. *Physical Chemistry Chemical Physics* **2013**, *15* (26), 10537-10548.
- 7. Takata, T.; Domen, K., Defect Engineering of Photocatalysts by Doping of Aliovalent Metal Cations for Efficient Water Splitting. *The Journal of Physical Chemistry C* **2009**, *113* (45), 19386-19388.
- 8. Maeda, K., Photocatalytic water splitting using semiconductor particles: History and recent developments. *Journal of Photochemistry and Photobiology C: Photochemistry Reviews* **2011,** *12* (4), 237-268.
- 9. Ham, Y.; Hisatomi, T.; Goto, Y.; Moriya, Y.; Sakata, Y.; Yamakata, A.; Kubota, J.; Domen, K., Flux-mediated doping of SrTiO3 photocatalysts for efficient overall water splitting. *Journal of Materials Chemistry A* **2016**, *4* (8), 3027-3033.
- 10. Lyu, H.; Hisatomi, T.; Goto, Y.; Yoshida, M.; Higashi, T.; Katayama, M.; Takata, T.; Minegishi, T.; Nishiyama, H.; Yamada, T.; Sakata, Y.; Asakura, K.; Domen, K., An Al-doped SrTiO3 photocatalyst maintaining sunlight-driven overall water splitting activity for over 1000 h of constant illumination. *Chemical Science* **2019**, *10* (11), 3196-3201.
- 11. Wang, S.; Teramura, K.; Hisatomi, T.; Domen, K.; Asakura, H.; Hosokawa, S.; Tanaka, T., Effective Driving of Ag-Loaded and Al-Doped SrTiO3 under Irradiation at  $\lambda > 300$  nm for the Photocatalytic Conversion of CO2 by H2O. ACS Applied Energy Materials **2020**, *3* (2), 1468-1475.
- 12. Chiang, T. H.; Lyu, H.; Hisatomi, T.; Goto, Y.; Takata, T.; Katayama, M.; Minegishi, T.; Domen, K., Efficient Photocatalytic Water Splitting Using Al-Doped SrTiO3 Coloaded with Molybdenum Oxide and Rhodium—Chromium Oxide. *ACS Catalysis* **2018**, *8* (4), 2782-2788.
- 13. Goto, Y.; Hisatomi, T.; Wang, Q.; Higashi, T.; Ishikiriyama, K.; Maeda, T.; Sakata, Y.; Okunaka, S.; Tokudome, H.; Katayama, M.; Akiyama, S.; Nishiyama, H.; Inoue, Y.; Takewaki, T.; Setoyama, T.; Minegishi, T.; Takata, T.; Yamada, T.; Domen, K., A Particulate Photocatalyst Water-Splitting Panel for Large-Scale Solar Hydrogen Generation. *Joule* **2018**, *2* (3), 509-520.
- 14. Takata, T.; Jiang, J.; Sakata, Y.; Nakabayashi, M.; Shibata, N.; Nandal, V.; Seki, K.; Hisatomi, T.; Domen, K., Photocatalytic Water Splitting with a Quantum Efficiency of Almost Unity. *Nature* **2020**, *581* (7809), 411-414.
- 15. Zhao, Z.; Goncalves, R. V.; Barman, S. K.; Willard, E. J.; Byle, E.; Perry, R.; Wu, Z.; Huda, M. N.; Moulé, A. J.; Osterloh, F. E., Electronic structure basis for enhanced overall water splitting photocatalysis with aluminum doped SrTiO3 in natural sunlight. *Energy & Environmental Science* **2019**, *12* (4), 1385-1395.
- 16. Maeda, K.; Domen, K., Development of Novel Photocatalyst and Cocatalyst Materials for Water Splitting under Visible Light. *Bulletin of the Chemical Society of Japan* **2016**, *89* (6), 627-648.
- 17. Negishi, Y.; Mizuno, M.; Hirayama, M.; Omatoi, M.; Takayama, T.; Iwase, A.; Kudo, A., Enhanced Photocatalytic Water Splitting by BaLa4Ti4O15 Loaded with ~1 nm Gold Nanoclusters Using Glutathione-protected Au25 Clusters. *Nanoscale* **2013**, *5* (16), 7188-7192.
- 18. Chen, S.; Takata, T.; Domen, K., Particulate photocatalysts for overall water splitting. *Nature Reviews Materials* **2017**, *2*, 17050.

- 19. Narayanan, H.; Viswanathan, B.; Krishnamurthy, K. R.; Nair, H., Chapter 12 Hydrogen from photo-electrocatalytic water splitting. In *Solar Hydrogen Production*, Calise, F.; D'Accadia, M. D.; Santarelli, M.; Lanzini, A.; Ferrero, D., Eds. Academic Press: 2019; pp 419-486.
- 20. Bai, S.; Yin, W.; Wang, L.; Li, Z.; Xiong, Y., Surface and interface design in cocatalysts for photocatalytic water splitting and CO2 reduction. *RSC Advances* **2016**, *6* (62), 57446-57463.
- 21. Sato, S.; White, J. M., Photodecomposition of water over Pt/TiO2 catalysts. *Chemical Physics Letters* **1980**, 72 (1), 83-86.
- 22. Maeda, K.; Teramura, K.; Lu, D.; Takata, T.; Saito, N.; Inoue, Y.; Domen, K., Photocatalyst Releasing Hydrogen from Water. *Nature* **2006**, *440* (7082), 295-295.
- 23. Maeda, K.; Teramura, K.; Masuda, H.; Takata, T.; Saito, N.; Inoue, Y.; Domen, K., Efficient Overall Water Splitting under Visible-Light Irradiation on (Ga1-xZnx)(N1-xOx) Dispersed with Rh–Cr Mixed-Oxide Nanoparticles: Effect of Reaction Conditions on Photocatalytic Activity. *The Journal of Physical Chemistry B* **2006**, *110* (26), 13107-13112.
- 24. Maeda, K.; Teramura, K.; Saito, N.; Inoue, Y.; Domen, K., Improvement of photocatalytic activity of (Ga1-xZnx)(N1-xOx) solid solution for overall water splitting by co-loading Cr and another transition metal. *Journal of Catalysis* **2006**, *243* (2), 303-308.
- 25. Maeda, K.; Teramura, K.; Lu, D.; Takata, T.; Saito, N.; Inoue, Y.; Domen, K., Characterization of Rh–Cr Mixed-Oxide Nanoparticles Dispersed on (Ga1-xZnx)(N1-xOx) as a Cocatalyst for Visible-Light-Driven Overall Water Splitting. *The Journal of Physical Chemistry B* **2006**, *110* (28), 13753-13758.
- 26. Maeda, K.; Teramura, K.; Lu, D.; Saito, N.; Inoue, Y.; Domen, K., Noble-Metal/Cr2O3 Core/Shell Nanoparticles as a Cocatalyst for Photocatalytic Overall Water Splitting. *Angewandte Chemie International Edition* **2006**, *45* (46), 7806-7809.
- 27. Maeda, K.; Teramura, K.; Lu, D.; Saito, N.; Inoue, Y.; Domen, K., Roles of Rh/Cr2O3 (Core/Shell) Nanoparticles Photodeposited on Visible-Light-Responsive (Ga1-xZnx)(N1-xOx) Solid Solutions in Photocatalytic Overall Water Splitting. *The Journal of Physical Chemistry C* **2007**, *111* (20), 7554-7560.
- 28. Yoshida, M.; Takanabe, K.; Maeda, K.; Ishikawa, A.; Kubota, J.; Sakata, Y.; Ikezawa, Y.; Domen, K., Role and Function of Noble-Metal/Cr-Layer Core/Shell Structure Cocatalysts for Photocatalytic Overall Water Splitting Studied by Model Electrodes. *The Journal of Physical Chemistry C* **2009**, *113* (23), 10151-10157.
- 29. Maeda, K.; Domen, K., Photocatalytic Water Splitting: Recent Progress and Future Challenges. *The Journal of Physical Chemistry Letters* **2010**, *1* (18), 2655-2661.
- 30. Sakamoto, N.; Ohtsuka, H.; Ikeda, T.; Maeda, K.; Lu, D.; Kanehara, M.; Teramura, K.; Teranishi, T.; Domen, K., Highly Dispersed Noble-metal/Chromia (Core/Shell) Nanoparticles as Efficient Hydrogen Evolution Promoters for Photocatalytic Overall Water Splitting under Visible Light. *Nanoscale* **2009**, *1* (1), 106-109.
- 31. Maeda, K.; Sakamoto, N.; Ikeda, T.; Ohtsuka, H.; Xiong, A.; Lu, D.; Kanehara, M.; Teranishi, T.; Domen, K., Preparation of Core–Shell-Structured Nanoparticles (with a Noble-Metal or Metal Oxide Core and a Chromia Shell) and Their Application in Water Splitting by Means of Visible Light. *Chemistry A European Journal* **2010**, *16* (26), 7750-7759.
- 32. Maeda, K.; Xiong, A.; Yoshinaga, T.; Ikeda, T.; Sakamoto, N.; Hisatomi, T.; Takashima, M.; Lu, D.; Kanehara, M.; Setoyama, T.; Teranishi, T.; Domen, K., Photocatalytic Overall Water Splitting Promoted by Two Different Cocatalysts for Hydrogen and Oxygen Evolution under Visible Light. *Angewandte Chemie International Edition* **2010**, *49* (24), 4096-4099.
- 33. Kurashige, W.; Kumazawa, R.; Ishii, D.; Hayashi, R.; Niihori, Y.; Hossain, S.; Nair, L. V.; Takayama, T.; Iwase, A.; Yamazoe, S.; Tsukuda, T.; Kudo, A.; Negishi, Y., Au25-Loaded BaLa4Ti4O15 Water-Splitting Photocatalyst with Enhanced Activity and Durability Produced Using New Chromium Oxide Shell Formation Method. *The Journal of Physical Chemistry C* **2018**, *122* (25), 13669-13681.
- 34. Kurashige, W.; Mori, Y.; Ozaki, S.; Kawachi, M.; Hossain, S.; Kawawaki, T.; Shearer, C. J.; Iwase, A.; Metha, G. F.; Yamazoe, S.; Kudo, A.; Negishi, Y., Activation of Water-Splitting

- Photocatalysts by Loading with Ultrafine Rh–Cr Mixed-Oxide Cocatalyst Nanoparticles. *Angewandte Chemie International Edition* **2020**, *59* (18), 7076-7082.
- 35. Kawawaki, T.; Kataoka, Y.; Hirata, M.; Akinaga, Y.; Takahata, R.; Wakamatsu, K.; Fujiki, Y.; Kataoka, M.; Kikkawa, S.; Alotabi, A. S.; Hossain, S.; Osborn, D. J.; Teranishi, T.; Andersson, G. G.; Metha, G. F.; Yamazoe, S.; Negishi, Y., Creation of High-Performance Heterogeneous Photocatalysts by Controlling Ligand Desorption and Particle Size of Gold Nanocluster. *Angewandte Chemie International Edition* **2021**, *60* (39), 21340-21350.
- 36. Anderson, D. P.; Alvino, J. F.; Gentleman, A.; Al Qahtani, H.; Thomsen, L.; Polson, M. I.; Metha, G. F.; Golovko, V. B.; Andersson, G. G., Chemically-Synthesised, Atomically-Precise Gold Clusters Deposited and Activated on Titania. *Physical chemistry chemical physics* **2013**, *15* (11), 3917-3929.
- 37. Anderson, D. P.; Adnan, R. H.; Alvino, J. F.; Shipper, O.; Donoeva, B.; Ruzicka, J.-Y.; Al Qahtani, H.; Harris, H. H.; Cowie, B.; Aitken, J. B., Chemically Synthesised Atomically Precise Gold Clusters Deposited and Activated on Titania. Part II. *Physical chemistry chemical physics* **2013**, *15* (35), 14806-14813.
- 38. Krischok, S.; Höfft, O.; Günster, J.; Stultz, J.; Goodman, D. W.; Kempter, V., H2O interaction with bare and Li-precovered TiO2: studies with electron spectroscopies (MIES and UPS(HeI and II)). *Surface Science* **2001**, *495* (1), 8-18.
- 39. Biesinger, M. C.; Brown, C.; Mycroft, J. R.; Davidson, R. D.; McIntyre, N. S., X-ray photoelectron spectroscopy studies of chromium compounds. *Surface and Interface Analysis* **2004**, *36* (12), 1550-1563.
- 40. Jianjun, W.; Qunji, X., Effects of synthetic additives on the friction and wear properties of a Cr2O3 coating. *Wear* **1994**, *176* (2), 213-216.
- 41. Alotabi, A. S.; Gibson, C. T.; Metha, G. F.; Andersson, G. G., Investigation of the Diffusion of Cr2O3 into Different Phases of TiO2 upon Annealing. *ACS Applied Energy Materials* **2021**, *4* (1), 322-330.
- 42. Trenczek-Zajac, A.; Radecka, M.; Jasinski, M.; Michalow, K. A.; Rekas, M.; Kusior, E.; Zakrzewska, K.; Heel, A.; Graule, T.; Kowalski, K., Influence of Cr on structural and optical properties of TiO2:Cr nanopowders prepared by flame spray synthesis. *Journal of Power Sources* **2009**, *194* (1), 104-111.
- 43. Pan, C.-J.; Tsai, M.-C.; Su, W.-N.; Rick, J.; Akalework, N. G.; Agegnehu, A. K.; Cheng, S.-Y.; Hwang, B.-J., Tuning/exploiting Strong Metal-Support Interaction (SMSI) in Heterogeneous Catalysis. *Journal of the Taiwan Institute of Chemical Engineers* **2017**, *74*, 154-186.
- 44. Setvin, M.; Hao, X.; Daniel, B.; Pavelec, J.; Novotny, Z.; Parkinson, G. S.; Schmid, M.; Kresse, G.; Franchini, C.; Diebold, U., Charge Trapping at the Step Edges of TiO2 Anatase (101). *Angewandte Chemie International Edition* **2014**, *53* (18), 4714-4716.
- 45. Wan, J.; Chen, W.; Jia, C.; Zheng, L.; Dong, J.; Zheng, X.; Wang, Y.; Yan, W.; Chen, C.; Peng, Q.; Wang, D.; Li, Y., Defect Effects on TiO2 Nanosheets: Stabilizing Single Atomic Site Au and Promoting Catalytic Properties. *Advanced Materials* **2018**, *30* (11), 1705369.
- 46. da Silva, A. L.; Hotza, D.; Castro, R. H. R., Surface energy effects on the stability of anatase and rutile nanocrystals: A predictive diagram for Nb2O5-doped-TiO2. *Applied Surface Science* **2017**, *393*, 103-109.
- 47. Ohtani, B.; Prieto-Mahaney, O. O.; Li, D.; Abe, R., What is Degussa (Evonik) P25? Crystalline composition analysis, reconstruction from isolated pure particles and photocatalytic activity test. *Journal of Photochemistry and Photobiology A: Chemistry* **2010**, *216* (2), 179-182.
- 48. Rohr, F.; Bäumer, M.; Freund, H. J.; Mejias, J. A.; Staemmler, V.; Müller, S.; Hammer, L.; Heinz, K., Strong relaxations at the Cr2O3(0001) surface as determined via low-energy electron diffraction and molecular dynamics simulations. *Surface Science* **1997**, *372* (1), L291-L297.
- 49. Sahu, S. K.; Maram, P. S.; Navrotsky, A., Thermodynamics of Nanoscale Calcium and Strontium Titanate Perovskites. *Journal of the American Ceramic Society* **2013**, *96* (11), 3670-3676.

- 50. Choi, K.; Lee, S.; Park, J. O.; Park, J.-A.; Cho, S.-H.; Lee, S. Y.; Lee, J. H.; Choi, J.-W., Chromium removal from aqueous solution by a PEI-silica nanocomposite. *Scientific Reports* **2018**, *8* (1), 1438.
- 51. Idczak, K.; Idczak, R., Investigation of Surface Segregation in Fe-Cr-Si Alloys by XPS. *Metallurgical and Materials Transactions A* **2020,** *51* (6), 3076-3089.
- 52. Makuła, P.; Pacia, M.; Macyk, W., How To Correctly Determine the Band Gap Energy of Modified Semiconductor Photocatalysts Based on UV–Vis Spectra. *The Journal of Physical Chemistry Letters* **2018**, *9* (23), 6814-6817.

# Chapter 5: Cr<sub>2</sub>O<sub>3</sub> Layer Inhibits Agglomeration of Phosphine-Protected Au<sub>9</sub> Clusters on TiO<sub>2</sub> Films

Abdulrahman S. Alotabi, Yanting Yin, Ahmad Redaa, Siriluck Tesana, Gregory F. Metha and Gunther G. Andersson

This chapter is a reformatted version of the paper published in *The Journal of Chemical Physics*, 2021, Vol. 155, Issue 61, Page 164702. **DOI**: 10.1063/5.0059912

### Author Contribution:

Abdulrahman S Alotabi: Designed and performed experiments, data analysis and interpretation, and prepared the manuscript for publication.

Yanting Yin: Performed cross-section SEM measurements on samples prepared by A.S.A and contributed to revision of manuscript.

Ahmad Redaa: Performed LSCM measurements on samples prepared by A.S.A

Siriluck Tesana: Synthesised Au<sub>9</sub>(PPh<sub>3</sub>)<sub>8</sub>(NO<sub>3</sub>)<sub>3</sub> clusters for this project.

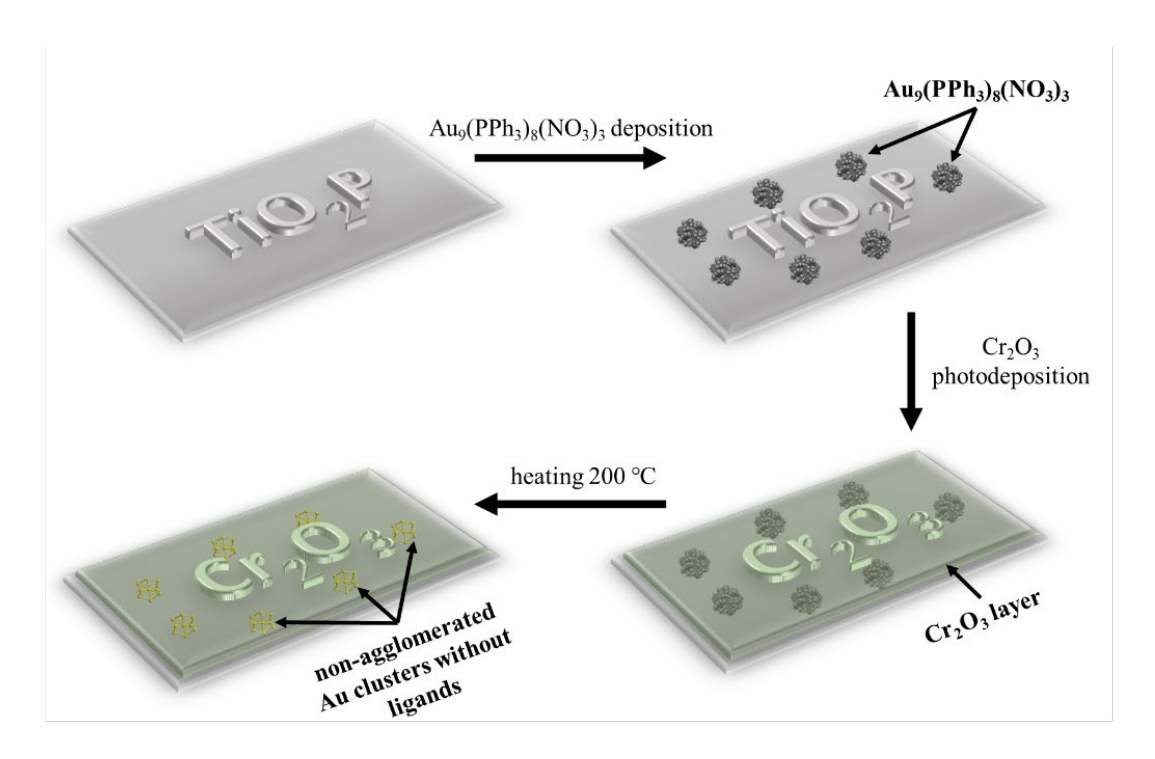
*Gregory F Metha: Intellectual contribution in revision of manuscript.* 

Gunther G Andersson: Intellectual contribution in conceptualising experiments, data interpretation & revision of manuscript

## 5.1 Abstract

The properties of semiconductor surfaces can be modified by the deposition of metal clusters consisting of a few atoms. The properties of metal clusters and of cluster-modified surfaces depend on the number of atoms forming the clusters. Deposition of clusters with a monodisperse size distribution thus allows tailoring of the surface properties for technical applications. However, it is a challenge to retain the size of the clusters after their deposition due to the tendency of the clusters to agglomerate. The agglomeration can be inhibited by covering the metal cluster modified surface with a thin metal oxide overlayer. In the present work, phosphine-protected Au clusters, Au<sub>9</sub>(PPh<sub>3</sub>)<sub>8</sub>(NO<sub>3</sub>)<sub>3</sub>, were deposited onto RF-sputter deposited TiO<sub>2</sub> films and subsequently covered with a Cr<sub>2</sub>O<sub>3</sub> film only a few monolayers thick. The samples were then heated to 200 °C to remove the phosphine ligands, which is a lower temperature than that required to remove thiolate ligands from Au clusters. It was found that the Cr<sub>2</sub>O<sub>3</sub> covering layer inhibited cluster agglomeration at an Au cluster coverage of 0.6% of a monolayer. When no protecting Cr<sub>2</sub>O<sub>3</sub> layer was present, the clusters were found to agglomerate to a large degree on the TiO<sub>2</sub> surface.

# **Graphical Abstract**



## 5.2 Introduction

Gold nanoclusters (Au<sub>n</sub>) are smaller than gold nanoparticles, generally less than 2 nm, and are formed by a specific number of Au atoms. Au<sub>n</sub> clusters deposited onto suitable substrates can be used as co-catalysts for various reactions, amongst them photocatalytic water splitting<sup>1-3</sup>. Au<sub>n</sub> clusters, as opposed to Au nanoparticles, are used due to their specific electronic states, fluxionality and structural isomerism<sup>4-6</sup>. The catalytic activity of supported, size-specific Au<sub>n</sub> clusters is known to depend on the number of atoms forming the cluster and its resultant electronic structure<sup>7-9</sup>. Thus, changing one atom in a cluster can result in a different catalytic activity<sup>2, 10</sup>. Therefore, in order to retain the properties of the modified surface, the Au<sub>n</sub> cluster size needs to be preserved from agglomeration to form Au nanoparticles. However, inhibiting the agglomeration of Au<sub>n</sub> clusters deposited onto a metal oxide surface is a major challenge<sup>6, 11, 12</sup>. Non-agglomerated clusters are relevant for developing catalysts<sup>13, 14</sup>.

Reducing agglomeration of co-catalysts deposited on a surface has been demonstrated by covering the co-catalyst with a metal oxide overlayer. For example, chromium oxide (Cr<sub>2</sub>O<sub>3</sub>) layer has been used to improve the stability of rhodium nanoparticles<sup>15</sup>, gold clusters<sup>16, 17</sup> and alloy clusters<sup>18</sup> but do not completely inhibit the agglomeration. The Cr<sub>2</sub>O<sub>3</sub> can form with various structures, such as core/shell nanostructures<sup>15, 19-21</sup> and overlayers<sup>14, 16, 18</sup>.

In addition, the  $Cr_2O_3$  overlayer is also beneficial to improve water splitting photocatalytic activity by preventing the reverse, oxygen photoreduction reaction  $(ORR)^{14,\ 22-31}$ . This reverse reaction is stymied by keeping the co-catalyst site free from oxygen atoms but not hydrogen, which can permeate through the  $Cr_2O_3$  overlayer<sup>27, 32</sup>. Other metal oxide overlayers such as  $SiO_2^{33}$ ,  $MoO_x^{34}$ ,  $TiO_2^{35}$  and lanthanoid oxide<sup>36</sup> have also been reported to be active in suppressing the reverse reaction.

Negishi and co-workers have developed a method to avoid agglomeration of thiolate-protected Au<sub>25</sub> using Cr<sub>2</sub>O<sub>3</sub> layers<sup>16, 17</sup>. The photodeposition of the Cr<sub>2</sub>O<sub>3</sub> layer was undertaken *before* the Au<sub>25</sub>(SG)<sub>18</sub> was adsorbed onto the BaLa<sub>4</sub>Ti<sub>4</sub>O<sub>15</sub> substrate. The sample was then calcined at 300 °C for two hours to remove the thiolate ligands, which also drives migration of the clusters into or below the Cr<sub>2</sub>O<sub>3</sub> layer. Addition of the Cr<sub>2</sub>O<sub>3</sub> overlayer improved the water splitting efficiency by 19-fold for Au<sub>25</sub>-Cr<sub>2</sub>O<sub>3</sub>-BaLa<sub>4</sub>Ti<sub>4</sub>O<sub>15</sub> due to the suppression of the reverse reaction, and increased the lifetime of the thiolate-protected Au clusters<sup>16</sup>. Notably, heating to 300 °C is not possible for phosphine-protected Au clusters because the clusters would agglomerate before the Cr<sub>2</sub>O<sub>3</sub> layer had formed over the clusters; the authors reported that photodeposition of the Cr<sub>2</sub>O<sub>3</sub> layer *after* the Au<sub>25</sub>-BaLa<sub>4</sub>Ti<sub>4</sub>O<sub>15</sub> substrate was formed could not be achieved<sup>11</sup>. To date, no experimental data are available on

stabilising a Au cluster-modified surface by depositing a protective Cr<sub>2</sub>O<sub>3</sub> layer on top of the Au clusters.

Protecting clusters from agglomeration with overlayers has been reported before but with much thicker layers, ranging from a few to many nms<sup>6, 37</sup>. For photocatalytic applications, it is necessary to keep the Cr<sub>2</sub>O<sub>3</sub> overlayer to a few monolayers<sup>15, 19</sup>. The aim of this work is to investigate whether a few monolayer thick Cr<sub>2</sub>O<sub>3</sub> layer photodeposited directly onto phosphine-protected Au clusters on a TiO<sub>2</sub> surface can inhibit the agglomeration of the Au clusters. The deposition of the Cr<sub>2</sub>O<sub>3</sub> layer on top of the phosphine-protected Au cluster has been chosen because the method developed by Negishi and co-workers described above<sup>16</sup> is not suitable for phosphine-protected Au clusters because of the required temperature; the phosphine-protected Au clusters require only heating to 200 °C for ten minutes to remove the ligands<sup>11</sup>.

In this work, chemically synthesised phosphine-protected gold clusters Au<sub>9</sub>(PPh<sub>3</sub>)<sub>8</sub>(NO<sub>3</sub>)<sub>3</sub> (hereafter referred to as Au<sub>9</sub>) are deposited onto a RF-sputter deposited TiO<sub>2</sub> film followed by photodeposition of the Cr<sub>2</sub>O<sub>3</sub> layer. The size of the Au<sub>9</sub> clusters on the TiO<sub>2</sub> film, with and without the Cr<sub>2</sub>O<sub>3</sub> layer, was investigated and the role of the Cr<sub>2</sub>O<sub>3</sub> layer determined. The effect of transforming the TiO<sub>2</sub> film from amorphous to anatase during heat treatment on the topography of the surface of the TiO<sub>2</sub> film is also investigated. Synchrotron X-ray photoelectron spectroscopy (XPS) was applied to study the chemical composition and size of the phosphine-protected Au<sub>9</sub>. The characterisation of the thickness of the TiO<sub>2</sub> film was analysed using scanning electron microscopy (SEM). X-ray diffraction (XRD) was used to determine the crystallinity of the TiO<sub>2</sub> film. A laser scanning confocal microscope (LSCM) generated 3D images to characterise the surface topography of the TiO<sub>2</sub> film.

# 5.3 Experimental

### 5.3.1 Material and sample preparation

## Preparation of TiO2 thin film

TiO<sub>2</sub> films were prepared by the radio frequency (RF) magnetron sputtering method<sup>38</sup> onto a p-type silicon wafer substrate using a high vacuum sputtering system (HHV/Edwards TF500 sputter coater). The substrate was cleaned using ethanol and acetone and then dried in a stream of dry nitrogen. The TiO<sub>2</sub> film was deposited by sputtering the TiO<sub>2</sub> target using Ar<sup>+</sup> with a sputtering power of 500 W. The pressure of the sputter deposition chamber was  $2 \times 10^{-5}$  mbar. During sputtering, the flow rate of argon gas was 5 sccm with a distance between the substrate and the target of ~14 cm. The deposition process resulted in the formation of a TiO<sub>2</sub> film on the Si wafer with a native oxide layer. The TiO<sub>2</sub>/Si wafer had a purple surface colour (see Figure C1), hence it is referred to throughout as TiO<sub>2</sub>P. The wafer was cut into  $1 \times 1$  cm pieces and used without further treatment.

## Deposition of phosphine-protected Au<sub>9</sub> clusters

Au<sub>9</sub> was synthesised using the procedure reported previously<sup>39</sup> and was deposited by immersing the TiO<sub>2</sub> samples into 2 mL of Au<sub>9</sub> methanol solutions for 30 min at two different concentrations (0.006 and 0.6 mM). The samples were then rinsed briefly with methanol before being dried in a stream of dry nitrogen. The samples are hereafter referred to as TiO<sub>2</sub>P-Au<sub>9</sub>.

### Photodeposition of Cr<sub>2</sub>O<sub>3</sub> layer

Potassium chromate ( $K_2CrO_4$ ;  $\geq 99\%$ , Sigma-Aldrich) was used as obtained to prepare a  $K_2CrO_4$  solution (0.5 mM) with deionised water. The  $TiO_2P$ -Au<sub>9</sub> sample was immersed in 1 mL of  $K_2CrO_4$  solution and irradiated using a UV LED source (Vishay, VLMU3510-365-130) for 1h. The radiant power of the UV source was 690 mW at a wavelength of 365 nm. The distance between the sample and the UV source was ~1 cm. After irradiation, the sample was washed with deionised water and dried utilising nitrogen gas.

### Heat treatment

All samples were heated under ultrahigh vacuum ( $1 \times 10^{-8}$  mbar) at 200 °C for 10 min. XPS spectra were recorded immediately after heating.

### Sample preparation for Synchrotron XPS analysis

Samples were prepared approximately one week prior to the Synchrotron experiments and immediately stored in a freezer. Samples were subsequently exposed to room temperature for ~12 hours during travel to the Synchrotron (i.e. Adelaide to Melbourne) but were kept in the dark. Any possible effects from this are considered below.

### 5.3.2 Methods

### Scanning Electron Microscopy

Experimental details for Scanning electron microscopy (SEM) and energy disperse X-ray spectroscopy (EDAX) are discussed in Section 2.6. The TiO<sub>2</sub> layer thickness was determined by combining the SEM imaging of the cross-section of the samples in combination with EDAX.

### X-ray Diffraction

Experimental details for X-ray diffraction (XRD) are discussed in Section 2.4. In this chapter, XRD was used to study the crystalline and phase structure of the TiO<sub>2</sub> film.

### Laser Scanning Confocal Microscope

Experimental details for laser scanning confocal microscope (LSCM) are discussed in Section 2.8. Briefly, this technique was applied to investigate the phase transformation of TiO<sub>2</sub> (i.e. surface topography) after heating.

### Synchrotron X-ray Photoelectron Spectroscopy

Experimental details for Synchrotron X-ray Photoelectron Spectroscopy (Synchrotron XPS) are discussed in Section 2.1. Synchrotron XPS spectra were recorded at the soft X-ray beamline at the Australian synchrotron. In this chapter, the X-ray photon energy was used is 750 eV. The spot size of the X-ray beam was ca.  $320\times320~\mu\text{m}$ . High-resolution XPS spectra were recorded for C 1s, O 1s, P 2p, Si 2p, Ti 2p, Cr 2p and Au 4f with a pass energy of 20 eV. The position of the C 1s peak for C-C sp3 carbon was set to 285 eV for calibrating the energy scale for all spectra to correct for charging effects.

## Near Edge X-ray Absorption Fine Structure

Experimental details for near edge X-ray absorption fine structure (NEXAFS) are discussed in Section 2.3.

### 5.4 Results and Discussion

## 5.4.1 Thickness of the TiO<sub>2</sub> layer

The  $TiO_2$  substrate properties will be first considered before addressing the influence of the  $Cr_2O_3$  layer on the  $Au_9$  clusters deposited onto  $TiO_2$ . Figure 5.1 shows a cross-section SEM image of  $TiO_2P$  with line measurement of the thickness of the  $TiO_2$  film a various points. Cross-section SEM-EDAX elemental maps of Ti, O and Si of  $TiO_2P$  at the same image spots are shown in Figure C2. The SEM image and SEM-EDAX elemental maps confirm that the thickness of the  $TiO_2$  film on the  $TiO_2P$  is  $\sim 400$  nm.

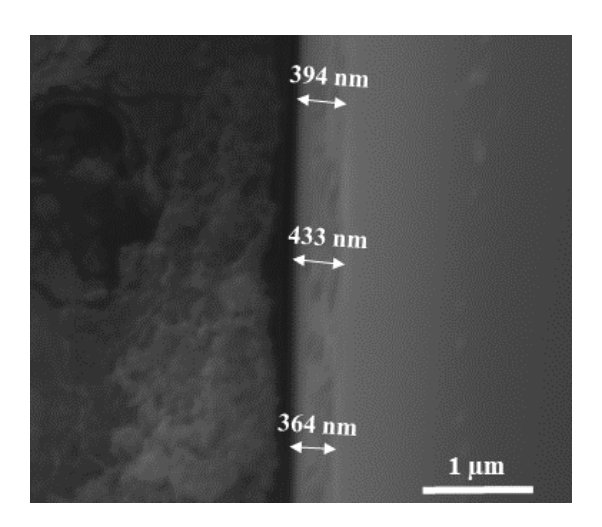


*Figure 5.1*: Cross-sectional SEM image of the  $TiO_2P$ . Arrows indicate the thickness of the  $TiO_2$  layer.

## 5.4.2 Crystal structure of the TiO<sub>2</sub>P before and after heating

The crystal structure of the TiO<sub>2</sub> film was investigated because it is known that it can change with heating, which could affect the stability of the Au clusters deposited onto the TiO<sub>2</sub> film and

subsequently covered with a Cr<sub>2</sub>O<sub>3</sub> layer. In Figure 5.2, the XRD patterns of the Si wafer with TiO<sub>2</sub>P before and after heating at 200°C for 10 min are shown. (Note: this is the same temperature and duration that is applied after deposition of the phosphine-protected Au<sub>9</sub> and Cr<sub>2</sub>O<sub>3</sub> overlayer to remove triphenylphosphine (PPh<sub>3</sub>) ligands.) The TiO<sub>2</sub>P before heating shows no diffraction peaks, in particular no peaks for anatase, rutile or brookite crystal phases are detected<sup>40</sup>. This shows that the as prepared TiO<sub>2</sub>P film has an amorphous crystal structure. After heating, the crystal structure of TiO<sub>2</sub>P changes to the anatase phase.

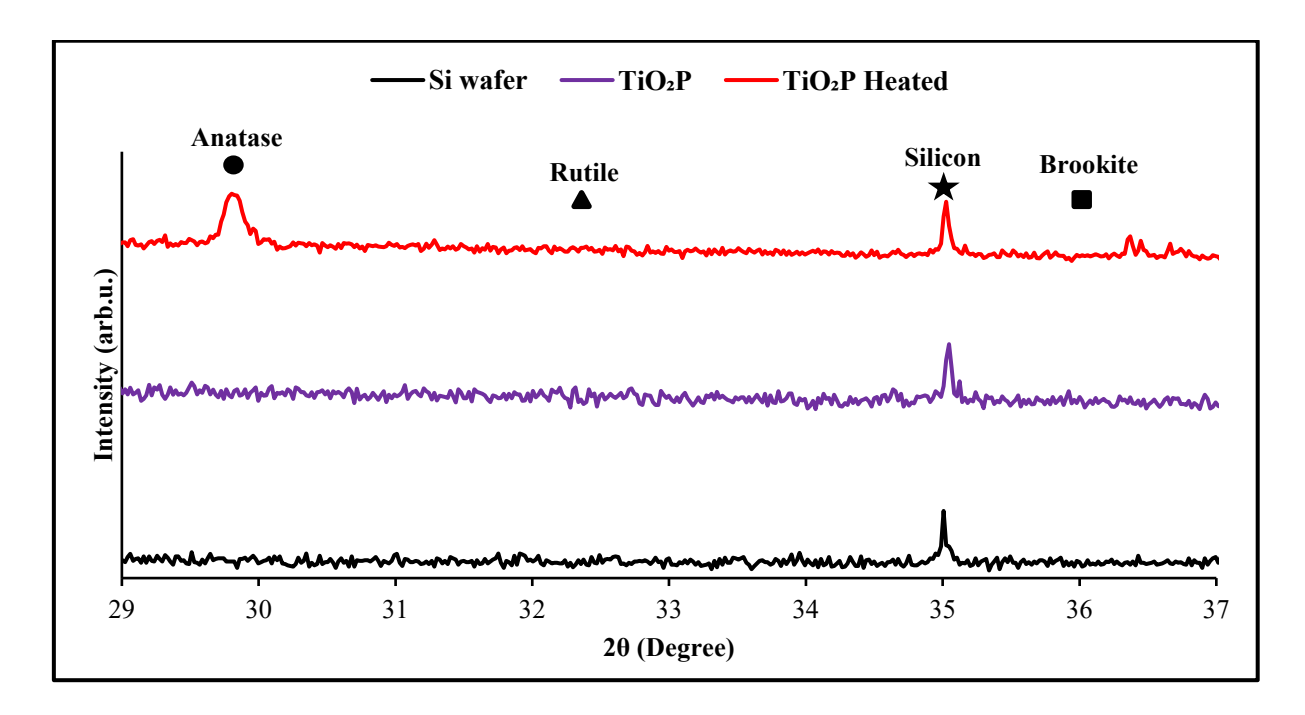


**Figure 5.2**: XRD patterns of Si wafer, TiO<sub>2</sub>P and TiO<sub>2</sub>P after heating to 200 °C. The positions for diffraction peaks for anatase, rutile and brookite as well as Si are indicated.

## 5.4.3 Topography of the TiO<sub>2</sub> layer

The surface topography of the  $TiO_2P$  film before and after heating has been investigated with LSCM. The surface topography of  $TiO_2P$  before and after heating is measured using surface laser imaging over an area of  $16 \times 16 \mu m$  (see Figure C3). The 3D profiles are displayed in Figure C4. As shown in Table 5.1, the average Ra and Rq values of the  $TiO_2P$  image before heating are 0.61 nm and 0.76 nm, respectively, and become 1.04 nm and 1.34 nm after heating. Similar changes in the Ra and Rq values were observed imaging over a larger area of  $595 \times 595 \mu m$  (see Figure C5).

**Table 5.1**: The average of Ra and Rq values of  $TiO_2P$  before and after heating.

	Before heating	After heating					
TiO₂P							
Ra (nm)	0.61	1.04					
Rq (nm)	0.76	1.34					

The observed changes to the surface topography of TiO<sub>2</sub>P heating is consistent with transformation of the TiO<sub>2</sub> film from amorphous to anatase and is consistent with previous reports<sup>41-43</sup>.

## 5.4.4 Agglomeration of Au<sub>9</sub> and influence of the Cr<sub>2</sub>O<sub>3</sub> layer

An analysis of the Cr<sub>2</sub>O<sub>3</sub> layer will now be presented and its effect on phosphine-protected Au<sub>9</sub> clusters deposited onto TiO<sub>2</sub>P addressed. Figures 5.3 and 5.4 shows Au spectra of TiO<sub>2</sub>P-Au<sub>9</sub> at two concentrations (0.006 mM and 0.6 mM) before and after heating, both without and with the Cr<sub>2</sub>O<sub>3</sub> layer covering the phosphine-protected Au clusters using Synchrotron XPS. A summary of the peak positions and full-width-half-maximum (FWHM) is presented in Table C1 and full elemental composition analyses are presented in Tables C2, C3, C4 and C5. For both the 0.006 mM and 0.6 mM samples, the Au coverage is estimated based on the relative intensity of Au to be around 0.6% and 60% of a monolayer, respectively. We will first consider the results of the 0.006 mM sample without  $Cr_2O_3$  layer. Before heating, the Au spectrum can be fitted with two 4f doublet ( $4f_{7/2}$  and  $4f_{5/2}$ ) peaks (see Figure 5.3A). These peaks are referred to as the high binding peak (HBP) and low binding peak (LBP), which are found at  $85.3 \pm 0.2$  eV and  $84.1 \pm 0.2$  eV with FWHM of  $1.7 \pm 0.2$  eV and  $1.0 \pm 0.2$  eV, respectively. The XPS Au peak position and FWHM can be used to determine the size of the phosphine-protected Au clusters due to the final state effect<sup>44-48</sup>. A higher binding energy and FWHM is interpreted as smaller clusters, while the shift to lower binding energy with decrease of the FWHM is interpreted as an increase in cluster size (agglomeration). This interpretation of XPS data has been corroborated by correlating XPS data with other techniques such as scanning transmission electron microscopy<sup>47</sup> and atomic force microscopy<sup>48</sup>. Previous research on similar systems showed non-agglomerated, phosphine-protected Au<sub>9</sub> clusters at a binding energy of 84.8 – 85 eV (HBP) and FWHM of 1.5 - 1.9 eV, with a shift to 84 eV (LBP) and FWHM of 0.9 - 1.1 eV following agglomeration of the clusters 44-46, 48, 49. For the unheated 0.006 mM sample without Cr<sub>2</sub>O<sub>3</sub> layer, 83% of the Au spectrum intensity is at the HBP position and 17% is at the LBP position. After heating, the Au spectrum was similarly fitted with HBP (85.3  $\pm$  0.2 eV, FWHM of 1.5  $\pm$  0.2 eV) and LBP  $(84.3 \pm 0.2 \text{ eV}, \text{ FWHM of } 1.1 \pm 0.2 \text{ eV})$  peaks, indicating that 55% of Au clusters remain nonagglomerated and 45% are agglomerated (see Scheme 5.1A).

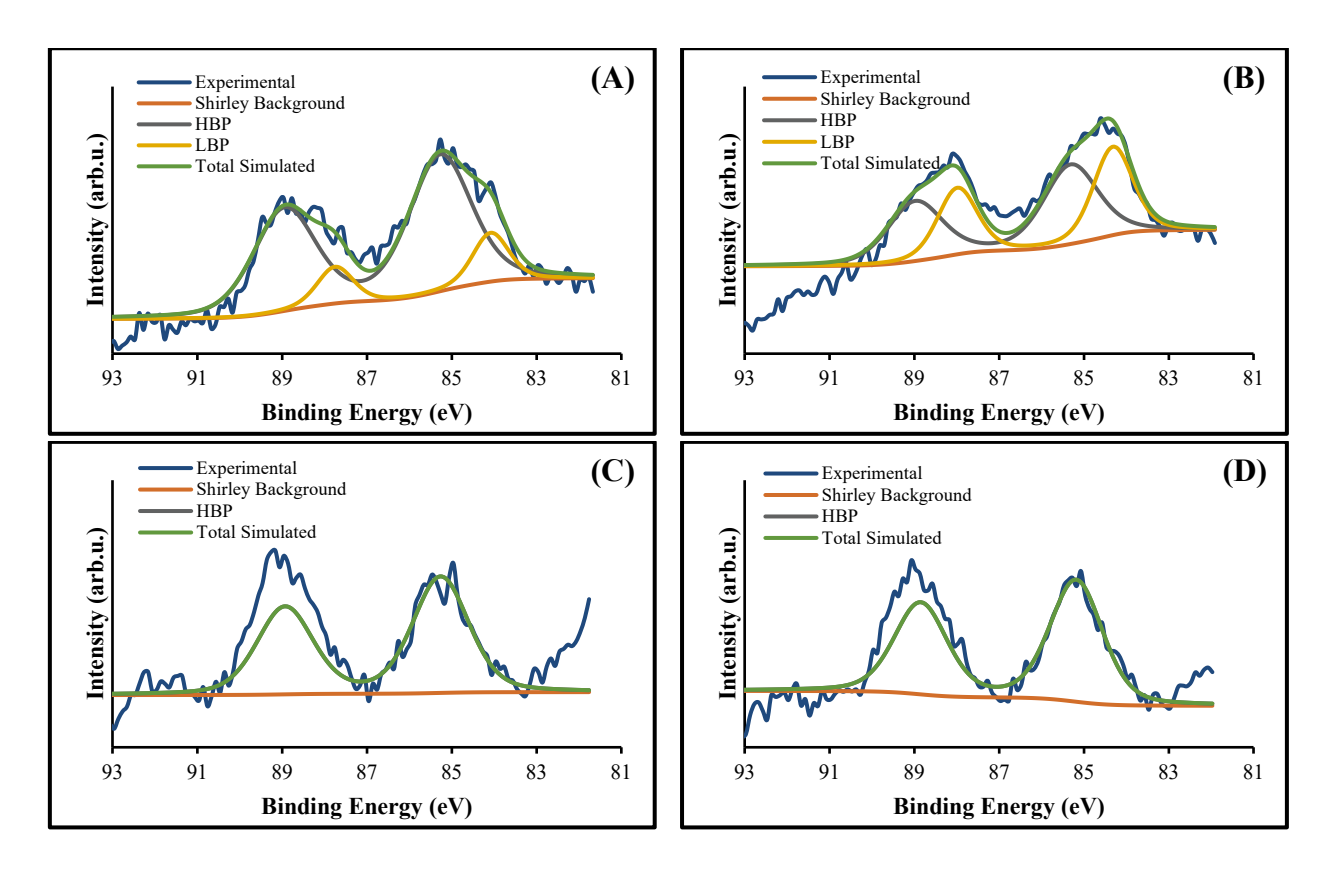


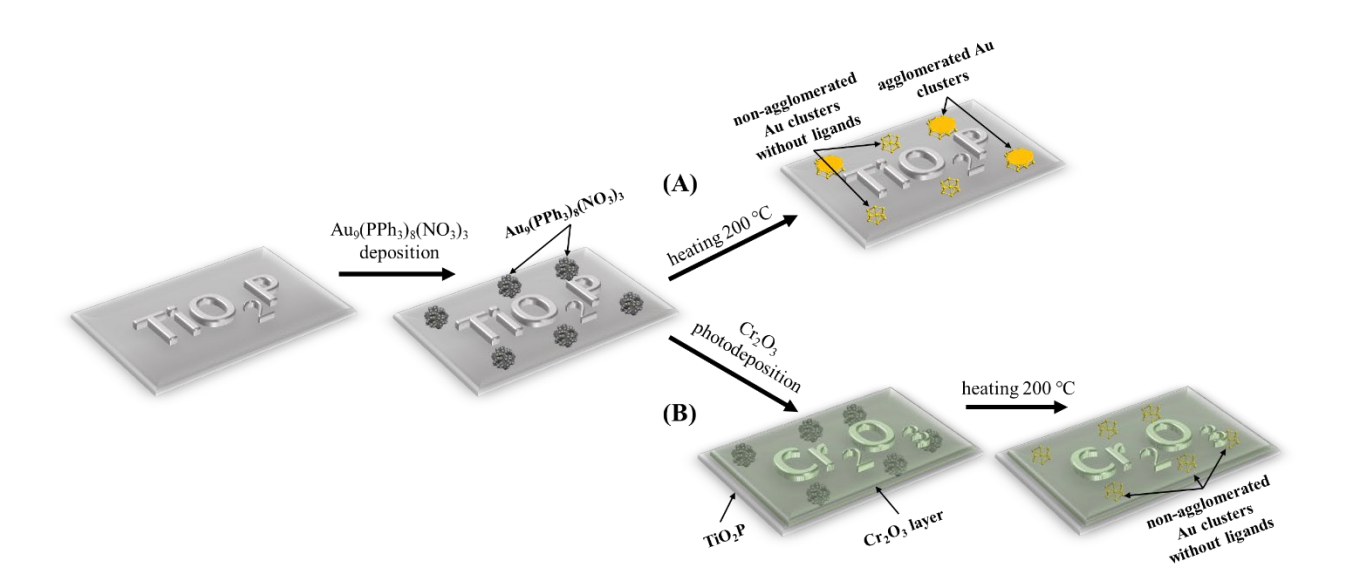
**Figure 5.3:** Synchrotron Au 4f XPS spectra of the sample immersed into the 0.006 mM solution: **(A)**  $TiO_2P$ - $Au_9$  before heating, **(B)**  $TiO_2P$ - $Au_9$  after heating, **(C)**  $TiO_2P$ - $Au_9$ - $Cr_2O_3$  before heating and **(D)**  $TiO_2P$ - $Au_9$ - $Cr_2O_3$  after heating.

After application of the  $Cr_2O_3$  layer but before heating, the Au 4f spectrum was fitted with only one doublet peak (Figures 5.3C and 5.3D). Note that the Au  $4f_{5/2}$  spin-orbit component in Figures 5.3C and 5.3D is larger in intensity than the fitted peak due to overlapping of the energy loss peak of the Cr 3s peak at ~88.6 eV (see Figure C6 for further information). The  $4f_{7/2}$  Au peak was found at the HBP position of  $85.3 \pm 0.2$  eV with FWHM of  $1.6 \pm 0.2$  eV (Figure 5.3C), indicating that all the clusters are non-agglomerated. After heating, the Au peak is unmoved at  $85.2 \pm 0.2$  eV with FWHM of  $1.5 \pm 0.2$  eV (Figure 5.3D), attributable to 100% non-agglomerated clusters  $^{48}$ . This interpretation of the Au peak position is based on the final state effect for Au clusters *without* a  $Cr_2O_3$  overlayer. We assume that the interaction between Au clusters and  $Cr_2O_3$  is similar to the interaction with  $TiO_2$  and thus the interpretation of the final state effect can be based on previous results of Au clusters deposited onto  $TiO_2$ . It is important to note that the structure of Au clusters core will change when the ligands are removed as has been demonstrated by Al Qahtani et al. for Au clusters deposited onto  $TiO_2$  nanosheets  $^{47}$ .

The synchrotron XPS Cr 2p spectra for  $TiO_2P$ -Au<sub>9</sub>-Cr<sub>2</sub>O<sub>3</sub> before and after heating are shown in Figure C7. The Cr  $2p_{3/2}$  peak appears at 577.1  $\pm 0.2$  eV, which corresponds to  $Cr_2O_3^{50}$ . This is confirmed by near edge X-ray absorption fine structure (NEXAFS) experiments, which shows the Cr L-edge

spectra for TiO<sub>2</sub>P-Au<sub>9</sub>-Cr<sub>2</sub>O<sub>3</sub> have the same lineshape as a Cr<sub>2</sub>O<sub>3</sub> reference spectrum (Figure C8). We have previously confirmed that Cr<sub>2</sub>O<sub>3</sub> forms a layer on the TiO<sub>2</sub> film with a thickness of 1.1 nm using the photodeposition method with the same parameters as reported here<sup>51</sup>. Tables C3 and C5 show the XPS ratio intensity of Au 4f to Ti 2p without and with the Cr<sub>2</sub>O<sub>3</sub> layer for TiO<sub>2</sub>P-Au<sub>9</sub> (0.006 mM and 0.6 mM). It is observed that the Au to Ti ratio decreases after the photodeposition of Cr<sub>2</sub>O<sub>3</sub> for TiO<sub>2</sub>P-Au<sub>9</sub> in the high concentration (0.6 mM) sample. This demonstrates that Cr<sub>2</sub>O<sub>3</sub> most likely has a slight preference to cover the Au clusters rather than the TiO<sub>2</sub> film. However, this is hard to confirm at low concentration (0.006 mM) due to the low intensity of the Au 4f XPS peak.

The comparison of the results between the samples with and without  $Cr_2O_3$  show that the presence of a 1.1 nm layer over the phosphine-protected Au clusters completely blocks agglomeration of the Au<sub>9</sub> clusters on the surface of  $TiO_2P$ , even with heating to 200 °C (see Scheme 5.1B). It is important to note that these Synchrotron XPS measurements were done one week after the deposition of Au<sub>9</sub> and subsequent photodeposition of the  $Cr_2O_3$  layer. Therefore, the 17% of clusters observed to be agglomerated without the  $Cr_2O_3$  layer may be due to "ageing", causing the size of the clusters to increase<sup>52</sup>.



**Scheme 5.1:** Schematic illustration of experimental procedure for the  $TiO_2P$  sample with the low concentrations (0.006 mM). (A)  $TiO_2P$ - $Au_9$  after the deposition of  $Au_9$  and after heating. (B)  $TiO_2P$ - $Au_9$ - $Cr_2O_3$  after  $Au_9$  deposition, photodeposition of  $Cr_2O_3$  layer and after heating (the clusters are covered by the overlayer).

From the relative intensity of Au in the XPS spectra it can be estimated that the coverage of Au clusters for the 0.006 mM sample is around 0.6% of a monolayer. Assuming that the Au cluster after removal of the ligands forms a flat structure on the surface<sup>53</sup> with an interatomic distance 2.7 Å, it

can be assumed that the average distance between two Au<sub>9</sub> clusters on the surface is about 20 nm. At this average distance, it can be concluded that agglomeration of the Au clusters after heating occurs rarely, if at all.

The P 2p spectra for the 0.006 mM sample without and with a  $Cr_2O_3$  layer are shown in Figure C9. The P  $2p_{3/2}$  peaks are found at  $134 \pm 0.2$  eV, which corresponds to oxidised P most likely attached to the  $TiO_2$  substrate as previously described<sup>45, 48, 49</sup>

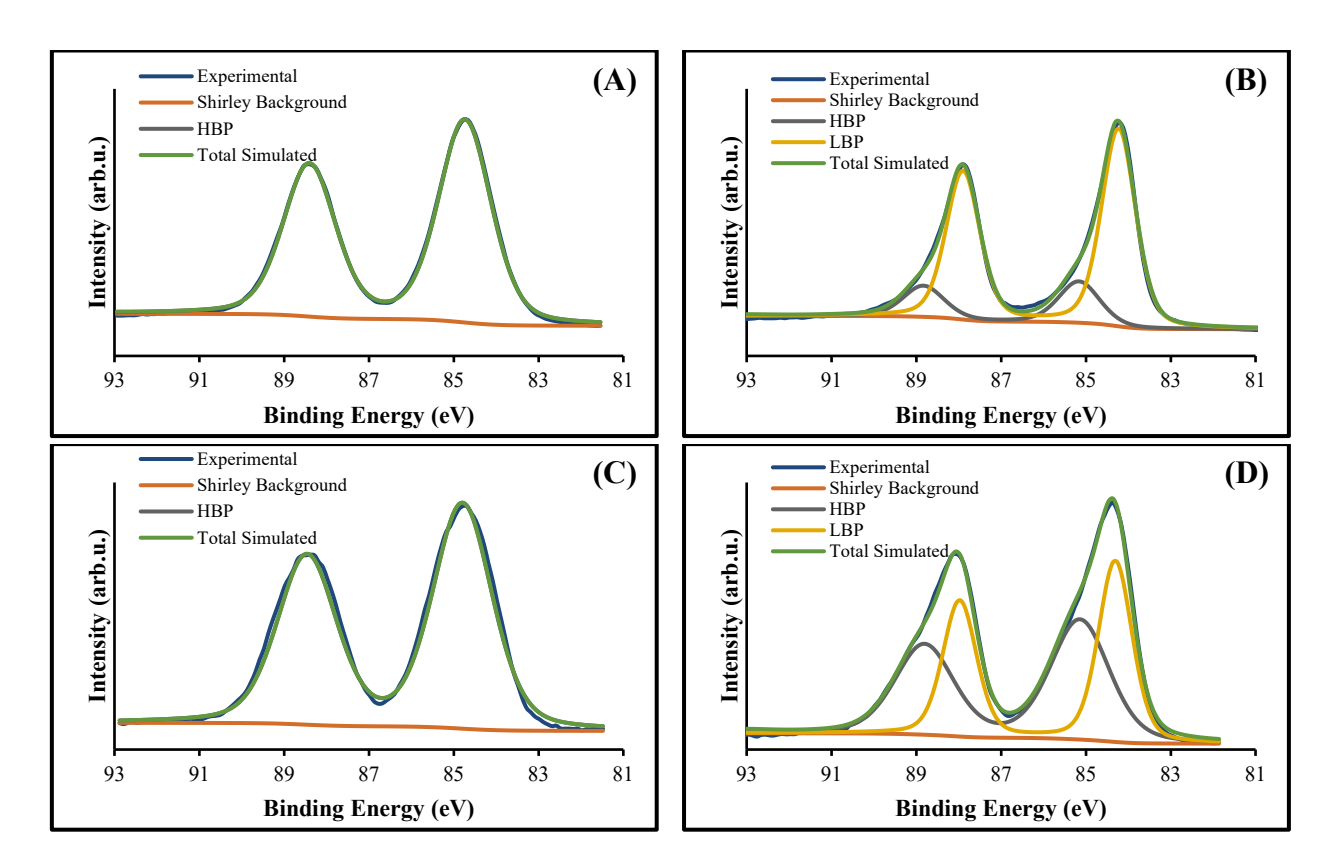


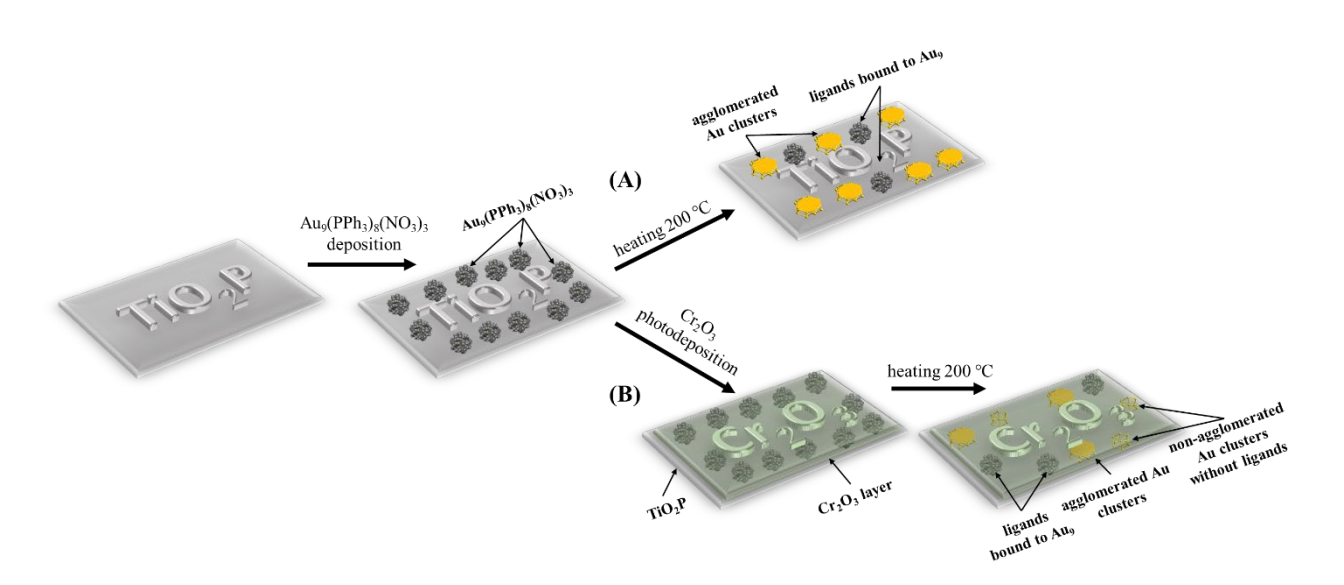
**Figure 5.4:** Synchrotron Au 4f XPS spectra of the sample immersed into the 0.6 mM solution: **(A)**  $TiO_2P$ -Au<sub>9</sub> before heating, **(B)**  $TiO_2P$ -Au<sub>9</sub> after heating, **(C)**  $TiO_2P$ -Au<sub>9</sub>-Cr<sub>2</sub>O<sub>3</sub> before heating and **(D)**  $TiO_2P$ -Au<sub>9</sub>-Cr<sub>2</sub>O<sub>3</sub> after heating.

The Au 4f spectra of the 0.6 mM  $TiO_2P$ -Au<sub>9</sub> and  $TiO_2P$ -Au<sub>9</sub>-Cr<sub>2</sub>O<sub>3</sub> samples are shown in Figure 5.4. The spectrum of the  $TiO_2P$ -Au<sub>9</sub> sample before heating was fitted with a single doublet peak at  $84.7 \pm 0.1$  eV with FWHM of  $1.5 \pm 0.2$  eV (Figure 5.4A), which is within the range of peak positions and FWHM found for the HPB of Au<sub>9</sub> clusters<sup>48, 49</sup>. After heating, the Au spectrum (Figure 5.4B) was fitted with 20% Au clusters at the HBP ( $85.2 \pm 0.1$  eV with FWHM of  $1.1 \pm 0.2$  eV) and 80% agglomerated clusters at the LBP ( $84.2 \pm 0.1$  eV with FWHM of  $1.0 \pm 0.2$  eV).

The Au 4f spectrum of the 0.6 mM  $TiO_2P$ -Au<sub>9</sub>-Cr<sub>2</sub>O<sub>3</sub> sample before heating was fitted with a single doublet with the Au  $4f_{7/2}$  peak at  $84.8 \pm 0.1$  eV with FWHM of  $1.7 \pm 0.2$  eV, which relates to the peak position of non-agglomerated clusters (Figure 5.4C). The Au 4f spectrum of the  $TiO_2P$ -Au<sub>9</sub>-Cr<sub>2</sub>O<sub>3</sub>

sample after heating shows a contribution of 53% Au clusters at the HBP at  $85.3 \pm 0.1$  eV with FWHM of  $1.6 \pm 0.2$  eV and 47% agglomerated clusters at the LBP at  $84.3 \pm 0.1$  eV with FWHM of  $0.9 \pm 0.2$  eV (Figure 5.4D).

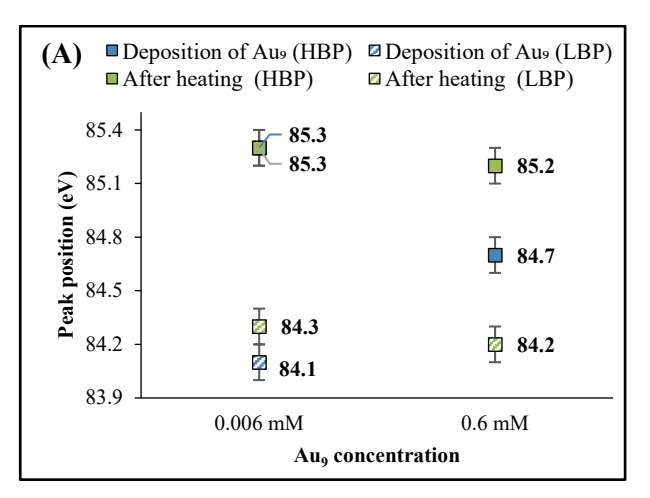
The P 2p spectra of the sample with 0.6 mM for  $TiO_2P$ -Au<sub>9</sub> and  $TiO_2P$ -Au<sub>9</sub>-Cr<sub>2</sub>O<sub>3</sub> are shown in Figure C10. The P 2p spectrum for  $TiO_2P$ -Au<sub>9</sub> after heating shows that 22% of the P peak intensity remains at  $131.6 \pm 0.1$  eV (Figure C10B). This peak position corresponds to the PPh<sub>3</sub> ligands bound to Au<sub>9</sub> clusters, indicating that 22% of PPh<sub>3</sub> ligands have not been removed, which is close to the percentage of Au clusters that remain stable on the surface after heating. This suggests that the amount of non-agglomerated Au clusters for  $TiO_2P$ -Au<sub>9</sub> after heating are still protected by PPh<sub>3</sub> ligands (see Scheme 5.2A). Similarly, the P 2p spectrum for  $TiO_2P$ -Au<sub>9</sub>-Cr<sub>2</sub>O<sub>3</sub> after heating also shows that 25% of the P peak intensity remains at  $131.7 \pm 0.1$  eV but with twice the fraction of non-agglomerated Au clusters (53%). This indicates that approximately half of the PPh<sub>3</sub> ligands have been removed from the non-agglomerated Au clusters on the surface in the presence of the Cr<sub>2</sub>O<sub>3</sub> layer (see Scheme 5.2B). This result also suggests that Cr<sub>2</sub>O<sub>3</sub> in some way displaces the PPh<sub>3</sub> ligands during the heating treatment and protects the clusters from agglomeration. At this stage it is not clear how the ligands are removed despite the presence of the Cr<sub>2</sub>O<sub>3</sub> layer and is currently the subject of further investigation.

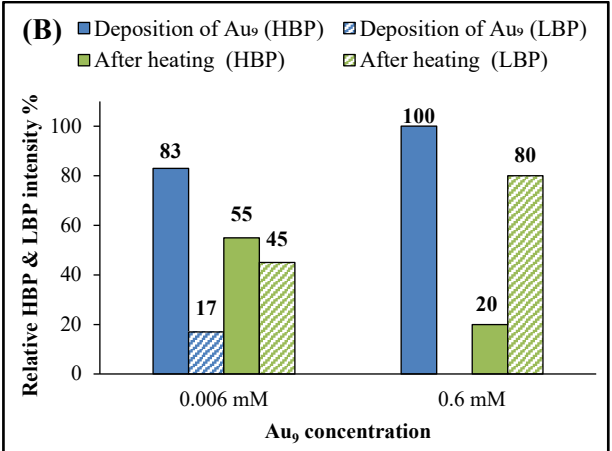


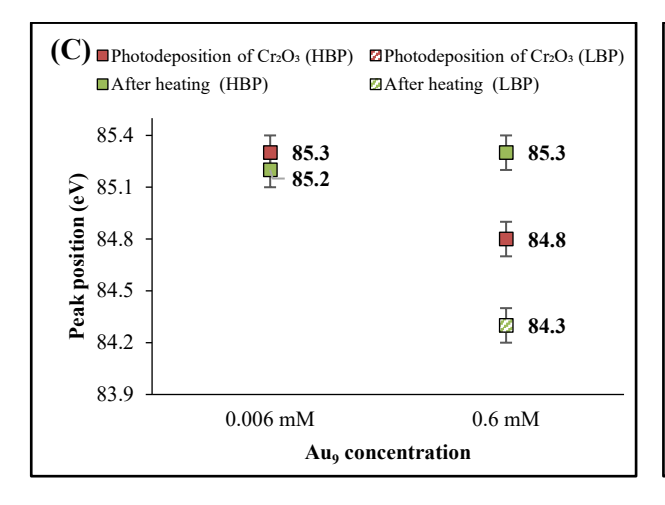
**Scheme 5.2:** Schematic illustration of experimental procedure for the  $TiO_2P$  sample with the high concentrations (0.6 mM). (A)  $TiO_2P$ -Au<sub>9</sub> after the deposition of Au<sub>9</sub> and after heating. (B)  $TiO_2P$ -Au<sub>9</sub>-Cr<sub>2</sub>O<sub>3</sub> after Au<sub>9</sub> deposition, photodeposition of Cr<sub>2</sub>O<sub>3</sub> layer and after heating (the clusters are covered by the overlayer).

Overall, the results for the 0.6 mM sample demonstrate that the Cr<sub>2</sub>O<sub>3</sub> layer improves the resistance of the phosphine-protected Au clusters to agglomerate, even with an extensive loading of Au clusters.

Based on the same assumption outlined above, the average distance between the Au clusters on the surface is 2 nm, approximately two to three times the diameter of an individual Au<sub>9</sub> cluster. From the XPS results, it can be concluded that at this average distance heating induces agglomeration for approximately 50% of the Au clusters with a Cr<sub>2</sub>O<sub>3</sub> layer.







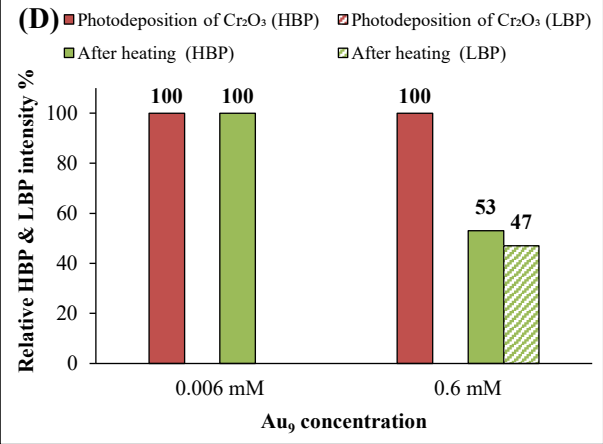


**Figure 5.5**: Summary of synchrotron XPS results of  $TiO_2P$ - $Au_9$  before and after heating of (A)  $Au_1$   $4f_{7/2}$  peak positions and (B) relative HBP & LBP intensities, and  $TiO_2P$ - $Au_9$  after photodeposition of the  $Cr_2O_3$  layer and after heating with (C) position of  $Au_1$   $4f_{7/2}$  and (D) relative HBP & LBP intensities.

Figure 5.5 shows a summary of the  $4f_{7/2}$  peak positions of  $TiO_2P$ -Au<sub>9</sub> at two concentrations (0.006 mM and 0.6 mM) before and after heating, both without and with the  $Cr_2O_3$  layer covering the phosphine-protected Au clusters. The  $Cr_2O_3$  overlayer is clearly effective at stopping agglomeration. The question arises whether the Au cluster, when covered with the  $Cr_2O_3$  layer, can still be accessed by molecules adsorbing to the sample surface and thus could still function as a catalyst. Based on the photocatalysis results reported by Negishi and co-workers,  $^{16}$  a  $Cr_2O_3$  overlayer has a beneficial effect by suppressing the reverse photocatalytic water-splitting reaction, and thus improve efficiency, for thiolate-protected  $Au_{25}$  clusters  $^{22-29}$ . In our case with phosphine-protected  $Au_9$  clusters covered with the 1.1 nm thick  $Cr_2O_3$  layer, it is likely that the clusters are still accessible to act as catalytic sites in,

for example, photocatalytic water splitting. However, such an effect on photocatalysis is still to be tested for phosphine-protected Au<sub>9</sub> clusters.

# 5.5 Conclusions

Cr<sub>2</sub>O<sub>3</sub> layers were photodeposited onto RF sputter coated TiO<sub>2</sub> (~400 nm thick) after deposition of phosphine-protected Au<sub>9</sub> clusters. A 1.1 nm thick layer of Cr<sub>2</sub>O<sub>3</sub> photodeposited over the TiO<sub>2</sub>-Au<sub>9</sub> substrate was found to inhibit the agglomeration of the Au clusters after heating due to the formation of a protective overlayer. An average distance between the Au clusters of 2 nm (two to three times the Au<sub>9</sub> diameter) results in the agglomeration of ~50% of the clusters, whereas an average separation of 20 nm leads to negligible agglomeration. A large fraction of the phosphine ligands is removed from the Au clusters during heating to 200°C. Our results show that Cr<sub>2</sub>O<sub>3</sub> layer can be applied before removal of the phosphine ligands for the purpose of protecting the Au clusters from agglomeration. Overall, this work provides a potential and novel use of Cr<sub>2</sub>O<sub>3</sub> for stabilising phosphine-protected Au clusters on TiO<sub>2</sub>. Notably, while this work was performed with TiO<sub>2</sub> as substrate, it could also be applied to a range of other metal oxide substrates. Au clusters with phosphine ligands require a lower temperature for removing the ligands than thiolate protected clusters, which is an advantage for the phosphine-protected clusters in avoiding cluster agglomeration during the ligand removal process.

# 5.6 References

- 1. Negishi, Y.; Mizuno, M.; Hirayama, M.; Omatoi, M.; Takayama, T.; Iwase, A.; Kudo, A., Enhanced Photocatalytic Water Splitting by BaLa4Ti4O15 Loaded with ~1 nm Gold Nanoclusters Using Glutathione-protected Au25 Clusters. *Nanoscale* **2013**, *5* (16), 7188-7192.
- 2. Negishi, Y.; Matsuura, Y.; Tomizawa, R.; Kurashige, W.; Niihori, Y.; Takayama, T.; Iwase, A.; Kudo, A., Controlled Loading of Small Aun Clusters (n = 10–39) onto BaLa4Ti4O15 Photocatalysts: Toward an Understanding of Size Effect of Cocatalyst on Water-Splitting Photocatalytic Activity. *The Journal of Physical Chemistry C* **2015**, *119* (20), 11224-11232.
- 3. Wang, C.; Lv, P.; Xue, D.; Cai, Y.; Yan, X.; Xu, L.; Fang, J.; Yang, Y., Zero-Dimensional/Two-Dimensional Au25(Cys)18 Nanoclusters/g-C3N4 Nanosheets Composites for Enhanced Photocatalytic Hydrogen Production under Visible Light. *ACS Sustainable Chemistry & Engineering* **2018**, *6* (7), 8447-8457.
- 4. Alvino, J. F.; Bennett, T.; Anderson, D.; Donoeva, B.; Ovoshchnikov, D.; Adnan, R. H.; Appadoo, D.; Golovko, V.; Andersson, G.; Metha, G. F., Far-infrared Absorption Spectra of Synthetically-Prepared, Ligated Metal Clusters with Au6, Au8, Au9 and Au6Pd Metal Cores. *RSC Advances* **2013**, *3* (44), 22140-22149.
- 5. Borman, V.; Pushkin, M.; Tronin, V.; Troyan, V., Evolution of the Electronic Properties of Transition Metal Nanoclusters on Graphite Surface. *Journal of Experimental and Theoretical Physics* **2010**, *110*, 1005-1025.
- 6. Sudheeshkumar, V.; Sulaiman, K. O.; Scott, R. W. J., Activation of atom-precise clusters for catalysis. *Nanoscale Advances* **2020**, *2* (1), 55-69.
- 7. Valden, M.; Lai, X.; Goodman, D. W., Onset of Catalytic Activity of Gold Clusters on Titania with the Appearance of Nonmetallic Properties. *Science* **1998**, *281* (5383), 1647.
- 8. Turner, M.; Golovko, V. B.; Vaughan, O. P. H.; Abdulkin, P.; Berenguer-Murcia, A.; Tikhov, M. S.; Johnson, B. F. G.; Lambert, R. M., Selective Oxidation with Dioxygen by Gold Nanoparticle Catalysts Derived from 55-atom Clusters. *Nature* **2008**, *454* (7207), 981-983.
- 9. Liu, L.; Corma, A., Metal Catalysts for Heterogeneous Catalysis: From Single Atoms to Nanoclusters and Nanoparticles. *Chemical Reviews* **2018**, *118* (10), 4981-5079.
- 10. Lim, D.-C.; Hwang, C.-C.; Ganteför, G.; Kim, Y. D., Model Catalysts of Supported Au Nanoparticles and Mass-Selected Clusters. *Physical Chemistry Chemical Physics* **2010**, *12* (46), 15172-15180.
- 11. Andersson, G. G.; Golovko, V. B.; Alvino, J. F.; Bennett, T.; Wrede, O.; Mejia, S. M.; Al Qahtani, H. S.; Adnan, R.; Gunby, N.; Anderson, D. P., Phosphine-stabilised Au9 Clusters Interacting with Titania and Silica Surfaces: The First Evidence for the Density of States Signature of the Support-immobilised Cluster. *The Journal of chemical physics* **2014**, *141* (1), 014702.
- 12. Howard-Fabretto, L.; Andersson, G. G., Metal Clusters on Semiconductor Surfaces and Application in Catalysis with a Focus on Au and Ru. *Advanced Materials* **2020**, *32* (18), 1904122.
- 13. Kurashige, W.; Mori, Y.; Ozaki, S.; Kawachi, M.; Hossain, S.; Kawawaki, T.; Shearer, C. J.; Iwase, A.; Metha, G. F.; Yamazoe, S.; Kudo, A.; Negishi, Y., Activation of Water-Splitting Photocatalysts by Loading with Ultrafine Rh–Cr Mixed-Oxide Cocatalyst Nanoparticles. *Angewandte Chemie International Edition* **2020**, *59* (18), 7076-7082.
- 14. Qureshi, M.; Shinagawa, T.; Tsiapis, N.; Takanabe, K., Exclusive Hydrogen Generation by Electrocatalysts Coated with an Amorphous Chromium-Based Layer Achieving Efficient Overall Water Splitting. *ACS Sustainable Chemistry & Engineering* **2017**, *5* (9), 8079-8088.
- 15. Sakamoto, N.; Ohtsuka, H.; Ikeda, T.; Maeda, K.; Lu, D.; Kanehara, M.; Teramura, K.; Teranishi, T.; Domen, K., Highly Dispersed Noble-metal/Chromia (Core/Shell) Nanoparticles as Efficient Hydrogen Evolution Promoters for Photocatalytic Overall Water Splitting under Visible Light. *Nanoscale* **2009**, *1* (1), 106-109.
- 16. Kurashige, W.; Kumazawa, R.; Ishii, D.; Hayashi, R.; Niihori, Y.; Hossain, S.; Nair, L. V.; Takayama, T.; Iwase, A.; Yamazoe, S.; Tsukuda, T.; Kudo, A.; Negishi, Y., Au25-Loaded BaLa4Ti4O15 Water-Splitting Photocatalyst with Enhanced Activity and Durability Produced Using

- New Chromium Oxide Shell Formation Method. *The Journal of Physical Chemistry C* **2018**, *122* (25), 13669-13681.
- 17. Kawawaki, T.; Kataoka, Y.; Hirata, M.; Akinaga, Y.; Takahata, R.; Wakamatsu, K.; Fujiki, Y.; Kataoka, M.; Kikkawa, S.; Alotabi, A. S.; Hossain, S.; Osborn, D. J.; Teranishi, T.; Andersson, G. G.; Metha, G. F.; Yamazoe, S.; Negishi, Y., Creation of High-Performance Heterogeneous Photocatalysts by Controlling Ligand Desorption and Particle Size of Gold Nanocluster. *Angewandte Chemie International Edition* **2021**, *60* (39), 21340-21350.
- 18. Kurashige, W.; Hayashi, R.; Wakamatsu, K.; Kataoka, Y.; Hossain, S.; Iwase, A.; Kudo, A.; Yamazoe, S.; Negishi, Y., Atomic-Level Understanding of the Effect of Heteroatom Doping of the Cocatalyst on Water-Splitting Activity in AuPd or AuPt Alloy Cluster-Loaded BaLa4Ti4O15. *ACS Applied Energy Materials* **2019**, *2* (6), 4175-4187.
- 19. Maeda, K.; Teramura, K.; Lu, D.; Saito, N.; Inoue, Y.; Domen, K., Roles of Rh/Cr2O3 (Core/Shell) Nanoparticles Photodeposited on Visible-Light-Responsive (Ga1-xZnx)(N1-xOx) Solid Solutions in Photocatalytic Overall Water Splitting. *The Journal of Physical Chemistry C* **2007**, *111* (20), 7554-7560.
- 20. Yoshida, M.; Takanabe, K.; Maeda, K.; Ishikawa, A.; Kubota, J.; Sakata, Y.; Ikezawa, Y.; Domen, K., Role and Function of Noble-Metal/Cr-Layer Core/Shell Structure Cocatalysts for Photocatalytic Overall Water Splitting Studied by Model Electrodes. *The Journal of Physical Chemistry C* **2009**, *113* (23), 10151-10157.
- 21. Maeda, K.; Sakamoto, N.; Ikeda, T.; Ohtsuka, H.; Xiong, A.; Lu, D.; Kanehara, M.; Teranishi, T.; Domen, K., Preparation of Core–Shell-Structured Nanoparticles (with a Noble-Metal or Metal Oxide Core and a Chromia Shell) and Their Application in Water Splitting by Means of Visible Light. *Chemistry A European Journal* **2010**, *16* (26), 7750-7759.
- 22. Maeda, K.; Teramura, K.; Lu, D.; Takata, T.; Saito, N.; Inoue, Y.; Domen, K., Photocatalyst Releasing Hydrogen from Water. *Nature* **2006**, *440* (7082), 295-295.
- 23. Maeda, K.; Teramura, K.; Masuda, H.; Takata, T.; Saito, N.; Inoue, Y.; Domen, K., Efficient Overall Water Splitting under Visible-Light Irradiation on (Ga1-xZnx)(N1-xOx) Dispersed with Rh–Cr Mixed-Oxide Nanoparticles: Effect of Reaction Conditions on Photocatalytic Activity. *The Journal of Physical Chemistry B* **2006**, *110* (26), 13107-13112.
- 24. Maeda, K.; Teramura, K.; Lu, D.; Takata, T.; Saito, N.; Inoue, Y.; Domen, K., Characterization of Rh–Cr Mixed-Oxide Nanoparticles Dispersed on (Ga1-xZnx)(N1-xOx) as a Cocatalyst for Visible-Light-Driven Overall Water Splitting. *The Journal of Physical Chemistry B* **2006**, *110* (28), 13753-13758.
- 25. Maeda, K.; Xiong, A.; Yoshinaga, T.; Ikeda, T.; Sakamoto, N.; Hisatomi, T.; Takashima, M.; Lu, D.; Kanehara, M.; Setoyama, T.; Teranishi, T.; Domen, K., Photocatalytic Overall Water Splitting Promoted by Two Different Cocatalysts for Hydrogen and Oxygen Evolution under Visible Light. *Angewandte Chemie International Edition* **2010**, *49* (24), 4096-4099.
- 26. Takata, T.; Jiang, J.; Sakata, Y.; Nakabayashi, M.; Shibata, N.; Nandal, V.; Seki, K.; Hisatomi, T.; Domen, K., Photocatalytic Water Splitting with a Quantum Efficiency of Almost Unity. *Nature* **2020**, *581* (7809), 411-414.
- 27. Maeda, K.; Lu, D.; Domen, K., Direct Water Splitting into Hydrogen and Oxygen under Visible Light by using Modified TaON Photocatalysts with d0 Electronic Configuration. *Chemistry A European Journal* **2013**, *19* (16), 4986-4991.
- 28. Maeda, K.; Domen, K., Photocatalytic Water Splitting: Recent Progress and Future Challenges. *The Journal of Physical Chemistry Letters* **2010**, *I* (18), 2655-2661.
- 29. Soldat, J.; Busser, G. W.; Muhler, M.; Wark, M., Cr2O3 Nanoparticles on Ba5Ta4O15 as a Noble-Metal-Free Oxygen Evolution Co-Catalyst for Photocatalytic Overall Water Splitting. *ChemCatChem* **2016**, *8* (1), 153-156.
- 30. Sanwald, K. E.; Berto, T. F.; Jentys, A.; Camaioni, D. M.; Gutiérrez, O. Y.; Lercher, J. A., Kinetic Coupling of Water Splitting and Photoreforming on SrTiO3-Based Photocatalysts. *ACS Catalysis* **2018**, *8* (4), 2902-2913.

- 31. Li, Z.; Zhang, F.; Han, J.; Zhu, J.; Li, M.; Zhang, B.; Fan, W.; Lu, J.; Li, C., Using Pd as a Cocatalyst on GaN–ZnO Solid Solution for Visible-Light-Driven Overall Water Splitting. *Catalysis Letters* **2018**, *148* (3), 933-939.
- 32. Wang, Q.; Nakabayashi, M.; Hisatomi, T.; Sun, S.; Akiyama, S.; Wang, Z.; Pan, Z.; Xiao, X.; Watanabe, T.; Yamada, T.; Shibata, N.; Takata, T.; Domen, K., Oxysulfide photocatalyst for visible-light-driven overall water splitting. *Nature Materials* **2019**, *18* (8), 827-832.
- 33. Bau, J. A.; Takanabe, K., Ultrathin Microporous SiO2 Membranes Photodeposited on Hydrogen Evolving Catalysts Enabling Overall Water Splitting. *ACS Catalysis* **2017**, *7* (11), 7931-7940.
- 34. Garcia-Esparza, A. T.; Shinagawa, T.; Ould-Chikh, S.; Qureshi, M.; Peng, X.; Wei, N.; Anjum, D. H.; Clo, A.; Weng, T.-C.; Nordlund, D.; Sokaras, D.; Kubota, J.; Domen, K.; Takanabe, K., An Oxygen-Insensitive Hydrogen Evolution Catalyst Coated by a Molybdenum-Based Layer for Overall Water Splitting. *Angewandte Chemie International Edition* **2017**, *56* (21), 5780-5784.
- 35. Takata, T.; Pan, C.; Nakabayashi, M.; Shibata, N.; Domen, K., Fabrication of a Core–Shell-Type Photocatalyst via Photodeposition of Group IV and V Transition Metal Oxyhydroxides: An Effective Surface Modification Method for Overall Water Splitting. *Journal of the American Chemical Society* **2015**, *137* (30), 9627-9634.
- 36. Yoshida, M.; Maeda, K.; Lu, D.; Kubota, J.; Domen, K., Lanthanoid Oxide Layers on Rhodium-Loaded (Ga1–xZnx)(N1–xOx) Photocatalyst as a Modifier for Overall Water Splitting under Visible-Light Irradiation. *The Journal of Physical Chemistry C* **2013**, *117* (27), 14000-14006.
- 37. Lu, J.; Fu, B.; Kung, M. C.; Xiao, G.; Elam, J. W.; Kung, H. H.; Stair, P. C., Coking-and sintering-resistant palladium catalysts achieved through atomic layer deposition. *Science* **2012**, *335* (6073), 1205-1208.
- 38. Daughtry, J.; Alotabi, A. S.; Howard-Fabretto, L.; Andersson, G. G., Composition and Properties of RF-Sputter Deposited Titanium Dioxide Thin Films. *Nanoscale Advances* **2021**, *3* (4), 1077-1086.
- 39. Wen, F.; Englert, U.; Gutrath, B.; Simon, U., Crystal Structure, Electrochemical and Optical Properties of [Au9(PPh3)8](NO3)3. *European Journal of Inorganic Chemistry* **2008**, *2008* (1), 106-111.
- 40. Ali, S.; Granbohm, H.; Lahtinen, J.; Hannula, S.-P., Titania Nanotubes Prepared by Rapid Breakdown Anodization for Photocatalytic Decolorization of Organic Dyes under UV and Natural Solar Light. *Nanoscale Research Letters* **2018**, *13* (1), 179.
- 41. Çörekçi, Ş.; Kizilkaya, K.; Asar, T.; Öztürk, M.; Çakmak, M.; Ozcelik, S., Effects of Thermal Annealing and Film Thickness on the Structural and Morphological Properties of Titanium Dioxide Films. *Acta Physica Polonica A* **2012**, *121*.
- 42. Chandra Sekhar, M.; Kondaiah, P.; Jagadeesh Chandra, S. V.; Mohan Rao, G.; Uthanna, S., Substrate temperature influenced physical properties of silicon MOS devices with TiO2 gate dielectric. *Surface and Interface Analysis* **2012**, *44* (9), 1299-1304.
- 43. Meng, F.; Xiao, L.; Sun, Z., Thermo-induced hydrophilicity of nano-TiO2 thin films prepared by RF magnetron sputtering. *Journal of Alloys and Compounds* **2009**, *485* (1), 848-852.
- 44. Anderson, D. P.; Alvino, J. F.; Gentleman, A.; Al Qahtani, H.; Thomsen, L.; Polson, M. I.; Metha, G. F.; Golovko, V. B.; Andersson, G. G., Chemically-Synthesised, Atomically-Precise Gold Clusters Deposited and Activated on Titania. *Physical chemistry chemical physics* **2013**, *15* (11), 3917-3929.
- 45. Anderson, D. P.; Adnan, R. H.; Alvino, J. F.; Shipper, O.; Donoeva, B.; Ruzicka, J.-Y.; Al Qahtani, H.; Harris, H. H.; Cowie, B.; Aitken, J. B., Chemically Synthesised Atomically Precise Gold Clusters Deposited and Activated on Titania. Part II. *Physical chemistry chemical physics* **2013**, *15* (35), 14806-14813.
- 46. Ruzicka, J.-Y.; Abu Bakar, F.; Hoeck, C.; Adnan, R.; McNicoll, C.; Kemmitt, T.; Cowie, B. C.; Metha, G. F.; Andersson, G. G.; Golovko, V. B., Toward Control of Gold Cluster Aggregation on TiO2 via Surface Treatments. *The Journal of Physical Chemistry C* **2015**, *119* (43), 24465-24474.

- 47. Al Qahtani, H. S.; Kimoto, K.; Bennett, T.; Alvino, J. F.; Andersson, G. G.; Metha, G. F.; Golovko, V. B.; Sasaki, T.; Nakayama, T., Atomically resolved structure of ligand-protected Au9 clusters on TiO2 nanosheets using aberration-corrected STEM. *The Journal of Chemical Physics* **2016**, *144* (11), 114703.
- 48. Al Qahtani, H. S.; Metha, G. F.; Walsh, R. B.; Golovko, V. B.; Andersson, G. G.; Nakayama, T., Aggregation Behavior of Ligand-Protected Au9 Clusters on Sputtered Atomic Layer Deposition TiO2. *The Journal of Physical Chemistry C* **2017**, *121* (20), 10781-10789.
- 49. Krishnan, G.; Al Qahtani, H. S.; Li, J.; Yin, Y.; Eom, N.; Golovko, V. B.; Metha, G. F.; Andersson, G. G., Investigation of Ligand-Stabilized Gold Clusters on Defect-Rich Titania. *The Journal of Physical Chemistry C* **2017**, *121* (50), 28007-28016.
- 50. Jianjun, W.; Qunji, X., Effects of synthetic additives on the friction and wear properties of a Cr2O3 coating. *Wear* **1994**, *176* (2), 213-216.
- 51. Alotabi, A. S.; Gibson, C. T.; Metha, G. F.; Andersson, G. G., Investigation of the Diffusion of Cr2O3 into Different Phases of TiO2 upon Annealing. *ACS Applied Energy Materials* **2021**, *4* (1), 322-330.
- 52. Wilcoxon, J. P.; Provencio, P., Etching and Aging Effects in Nanosize Au Clusters Investigated Using High-Resolution Size-Exclusion Chromatography. *The Journal of Physical Chemistry B* **2003**, *107* (47), 12949-12957.
- 53. Al Qahtani, H. S.; Higuchi, R.; Sasaki, T.; Alvino, J. F.; Metha, G. F.; Golovko, V. B.; Adnan, R.; Andersson, G. G.; Nakayama, T., Grouping and aggregation of ligand protected Au9 clusters on TiO2 nanosheets. *RSC Advances* **2016**, *6* (112), 110765-110774.

# Chapter 6: Effect of TiO<sub>2</sub> Film Thickness on the Stability of Au<sub>9</sub> Clusters with a CrO<sub>x</sub> layer

Abdulrahman S. Alotabi, Yanting Yin, Ahmad Redaa, Siriluck Tesana, Gregory F. Metha and Gunther G. Andersson

This chapter is a reformatted version of the paper published in *Nanomaterials*, 2022, Vol. 12, Issue 18, Page 3218. **DOI**: 10.3390/nano12183218

#### Author Contribution:

Abdulrahman S Alotabi: Designed and performed experiments, data analysis and interpretation, and prepared the manuscript for publication.

Yanting Yin: Performed cross-section SEM measurements on samples prepared by A.S.A and contributed to revision of manuscript.

Ahmad Redaa: Performed LSCM measurements on samples prepared by A.S.A

Siriluck Tesana: Synthesised  $Au_9(PPh_3)_8(NO_3)_3$  clusters for this project.

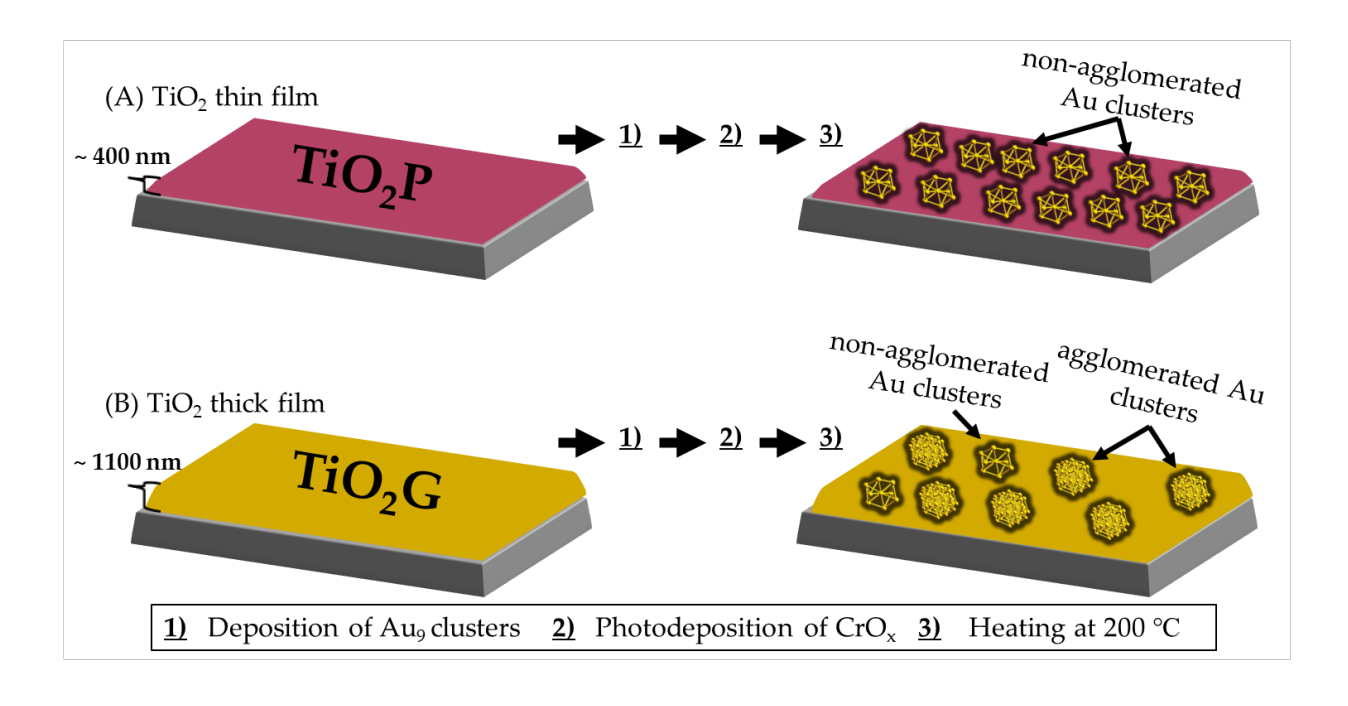
 $Gregory\ F\ Metha:\ Intellectual\ contribution\ in\ revision\ of\ manuscript.$ 

Gunther G Andersson: Intellectual contribution in conceptualising experiments, data interpretation & revision of manuscript

# 6.1 Abstract

Radio frequency (RF) magnetron sputtering allows the fabrication of TiO<sub>2</sub> films with high purity, reliable control of film thickness, and uniform morphology. In the present study, the change of surface roughness upon heating of two different thickness of RF sputter deposited TiO<sub>2</sub> films was investigated. As a measure for the process of the change in surface morphology chemically-synthesised phosphine-protected Au<sub>9</sub> clusters covered by a photodeposited CrO<sub>x</sub> layer were used as a probe. Subsequent to the deposition of the Au<sub>9</sub> clusters and the CrO<sub>x</sub> layer, samples were heated to 200 °C to remove the triphenylphosphine ligands from the Au<sub>9</sub> cluster. After heating, the thick TiO<sub>2</sub> film was found to be mobile, in contrast to the thin TiO<sub>2</sub> film. The influence of the mobility of TiO<sub>2</sub> films on the Au<sub>9</sub> clusters was investigated with X-ray photoelectron spectroscopy. It was found that the high mobility of the thick TiO<sub>2</sub> film after heating leads to a significant agglomeration of the Au<sub>9</sub> clusters, even when protected with the CrO<sub>x</sub> layer. The thin TiO<sub>2</sub> film has a much lower mobility when being heated, resulting in only minor agglomeration of the Au<sub>9</sub> clusters covered with the CrO<sub>x</sub> layer.

# **Graphical Abstract**



# 6.2 Introduction

Titanium dioxide (TiO<sub>2</sub>) is a semiconductor widely used for a large range of photocatalytic applications and is also an ideal model system for various types of study<sup>1, 2</sup>. There are various techniques to prepare TiO<sub>2</sub> films such as sol-gel<sup>3</sup>, evaporation<sup>4</sup>, chemical vapour deposition<sup>5</sup>, atomic layer deposition<sup>6</sup> and radio frequency (RF) magnetron sputtering<sup>7</sup>. Each of these methods has advantages and disadvantages in regard to fabrication costs, uniformity of the film morphology, thermal stability, purity and preparation time. Therefore, the best choice of method for TiO<sub>2</sub> film preparation depends on which application the film will be used.

Amongst the above-named methods, RF magnetron sputtering is known to produce high-purity TiO<sub>2</sub> films with uniform thickness, ease of use and strong film adhesion to the substrate<sup>8</sup>. The properties of these films are significantly impacted by the sputtering conditions such as RF power, gas pressure, substrate type, substrate temperature and target to substrate distance<sup>9-14</sup>. For instance, it has reported that a control of TiO<sub>2</sub> films thickness is possible by modulating the deposition time and the gas sputtering pressure<sup>15</sup>.

TiO<sub>2</sub> films prepared by RF magnetron sputtering method can be amorphous or have rutile, anatase, or brookite crystal structure. It is well known that the physical properties of TiO<sub>2</sub> films depend highly on the post-deposition treatment including heat treatment conditions<sup>16-18</sup>. Çörekçi *et al.* reported that a correlation between heating treatment and surface morphology with different TiO<sub>2</sub> film thicknesses. It was observed that an increase in surface roughness and grain sizes occurred during heating depending on TiO<sub>2</sub> film thicknesses, which also increased with film thickness. This is because increasing temperatures transforms TiO<sub>2</sub> from amorphous to anatase and then to rutile<sup>17</sup> and these phase transitions affect the surface morphology of TiO<sub>2</sub> film, which includes roughness and crystallinity of the surface<sup>19</sup>.

The aim of this study is to investigate the influence of heat treatment on the surface morphology of RF sputter-deposited TiO<sub>2</sub> films with two different thicknesses, and the effect this has on size-specific Au clusters deposited on the surface. TiO<sub>2</sub> films have attracted interest as substrates for investigating the role of Au clusters as co-catalysts in photocatalysis<sup>20, 21</sup>. In these studies, TiO<sub>2</sub> films had been heated as part of the sample preparation procedure. The change of morphology, including surface mobility, upon heating can lead to agglomeration of the Au clusters. Understanding the change in surface morphology upon heating thus is important when using TiO<sub>2</sub> as a substrate for investigating the co-catalyst properties. In the present work, phosphine-protected Au<sub>9</sub> clusters covered by a photodeposited CrO<sub>x</sub> layer are used as probe for the TiO<sub>2</sub> mobility during the change of morphology upon heating. Scanning electron microscopy (SEM), X-ray diffraction (XRD), laser scanning

confocal microscope (LSCM) and X-ray photoelectron spectroscopy (XPS), have been applied to characterize the thickness, crystal structure, surface morphology and chemical composition and size of the Au cluster. The importance of the present work is to show that morphology changes of RF sputter deposited TiO<sub>2</sub> depend on the thickness of the TiO<sub>2</sub> layer and that Au<sub>9</sub> clusters can be used to probe morphology changes

# 6.3 Experimental

# 6.3.1 Material and sample preparation

# Preparation of TiO<sub>2</sub> films

RF sputter-deposited TiO<sub>2</sub> films with two different thickness were fabricated applying the same described procedure in chapter 5 (experimental details, Section 5.3.1). The TiO<sub>2</sub> films had different colours based on light interference<sup>22</sup>: a TiO<sub>2</sub>/Si wafer with a purple colour and a TiO<sub>2</sub>/Si wafer with a gold-like colour (see Figure D1). The difference in colour of the films is related to the difference in light interference patterns within the films due to their difference in film thickness  $^{23}$ . The thickness of TiO<sub>2</sub>P is  $\sim 400$  nm, while TiO<sub>2</sub>G is  $\sim 1100$  nm (*vide infra*). The TiO<sub>2</sub> wafers were cut into 1 cm  $\times$  1 cm pieces and used without further treatment. The two TiO<sub>2</sub> wafers are hereafter referred to as (i) TiO<sub>2</sub>P and (ii) TiO<sub>2</sub>G.

# Deposition of phosphine-protected Au<sub>9</sub> clusters

The deposition procedure of Au<sub>9</sub>(PPh<sub>3</sub>)<sub>8</sub>(NO<sub>3</sub>)<sub>3</sub> (Au<sub>9</sub>) was identical for both the TiO<sub>2</sub>P and TiO<sub>2</sub>G samples. Phosphine-protected Au<sub>9</sub> clusters were synthesised as reported previously<sup>24</sup>. A UV-Vis spectrum of the Au<sub>9</sub> cluster is shown in Figure D2. The TiO<sub>2</sub> films were immersed in Au<sub>9</sub> methanol solutions (2 mL) for 30 minutes at concentrations of 0.006, 0.06 and 0.6 mM. The TiO<sub>2</sub> samples were rinsed by quickly dipping into pure methanol and then dried in a stream of dry nitrogen. These samples are hereafter referred to as (i) TiO<sub>2</sub>P-Au<sub>9</sub> and (ii) TiO<sub>2</sub>G-Au<sub>9</sub>.

#### Photodeposition of Cr<sub>2</sub>O<sub>3</sub> layer

Photodeposition of the  $CrO_x$  layer was the same for both  $TiO_2$ -Au<sub>9</sub> samples ( $TiO_2$ P-Au<sub>9</sub> and  $TiO_2$ G-Au<sub>9</sub>). A 0.5 mM potassium chromate solution was prepared by dissolving  $K_2CrO_4$  ( $\geq$ 99%, Sigma-Aldrich) in deionised water. The  $TiO_2$ -Au<sub>9</sub> samples were immersed into the  $K_2CrO_4$  solution (1 mL) and irradiated for 1h using a UV LED (Vishay, VLMU3510-365-130) with ~1 cm between the sample and the irradiation source. The UV LED had a radiant power of 690 mW at 365 nm wavelength. After photodeposition, the sample was washed by dipping them into deionised water and dried in a stream of dry nitrogen<sup>25</sup>. These samples are hereafter referred to as (i)  $TiO_2$ P-Au<sub>9</sub>-CrO<sub>x</sub> and (ii)  $TiO_2$ G-Au<sub>9</sub>-CrO<sub>x</sub>.

# Heat treatment

To remove the phosphine ligands from Au<sub>9</sub> clusters, all samples were treated with heating at 200 °C for 10 min under ultra-high vacuum ( $1 \times 10^{-8}$  mbar) in the XPS chamber.

#### 6.3.2 Methods

#### Scanning Electron Microscopy

Experimental details for Scanning electron microscopy (SEM) and energy disperse X-ray spectroscopy (EDAX) are discussed in Section 2.6. The thickness of TiO<sub>2</sub> films (TiO<sub>2</sub>P and TiO<sub>2</sub>G) was determined by combining SEM imaging and SEM-EDAX

## X-ray Diffraction

Experimental details for X-ray diffraction (XRD) are discussed in Section 2.4. In this chapter, the crystal and phase structure of the TiO<sub>2</sub> films (TiO<sub>2</sub>P and TiO<sub>2</sub>G) before and after heating were analysed using XRD.

## Laser Scanning Confocal Microscope

Experimental details for laser scanning confocal microscope (LSCM) are discussed in Section 2.8. The surface morphology of TiO<sub>2</sub> films (TiO<sub>2</sub>P and TiO<sub>2</sub>G) was measured using a LSCM

# X-ray Photoelectron Spectroscopy

Experimental details for X-ray photoelectron spectroscopy (XPS) are discussed in Section 2.1. In this chapter, high-resolution XPS spectra were recorded for C, O, P, Si, Ti, Cr and Au using an X-ray source with Mg K $\alpha$  line (hv=1253.6 eV). All XPS binding energy scales were normalised using the C 1s peak at 285 eV. XPS was recorded immediately after sample preparation and heating, thus reducing the number of atmospheric exposures.

#### 6.4 Results and Discussion

#### 6.4.1 Influence of the thickness of the TiO<sub>2</sub> films

The influence of the thickness of the RF sputter deposited TiO<sub>2</sub> on the change of film morphology upon heating is investigated. First, we will determine the thickness of TiO<sub>2</sub> films for TiO<sub>2</sub>P and TiO<sub>2</sub>G and describe the crystallinity and morphology of both samples before and after heating. Then, the XPS results will be reported for both TiO<sub>2</sub>P and TiO<sub>2</sub>G. Subsequently the agglomeration of Au<sub>9</sub> clusters beneath a Cr<sub>2</sub>O<sub>3</sub> overlayer upon heating of the two films is determined and discussed.

# Determination of the TiO<sub>2</sub> film thickness

Figure 6.1 shows cross-section SEM images of TiO<sub>2</sub>P and TiO<sub>2</sub>G with line measurement of the thickness of the TiO<sub>2</sub> films. These SEM images clearly show that the thickness of the film for the

TiO<sub>2</sub>P and TiO<sub>2</sub>G samples is ~400 nm and ~1100 nm, respectively; the film thickness of TiO<sub>2</sub>G is more than two times greater than for TiO<sub>2</sub>P. To confirm the film thickness, EDAX was further processed at the same image spots as SEM. Cross-section SEM-EDAX elemental maps of Ti, O and Si of TiO<sub>2</sub>P and TiO<sub>2</sub>G are shown in Figure D3. The EDAX elemental maps confirm that the thickness of the TiO<sub>2</sub> film for TiO<sub>2</sub>G is larger than TiO<sub>2</sub>P.

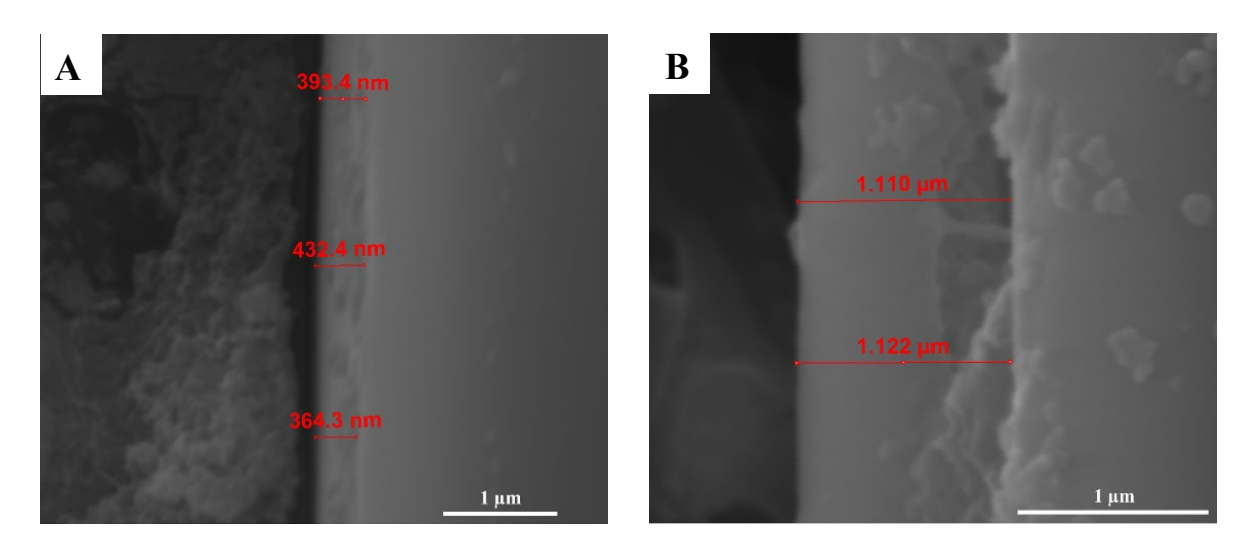


**Figure 6.1**: Cross-section SEM images of the (A)  $TiO_2P^{26}$  and (B)  $TiO_2G$  layer.

# Crystal structure of the TiO<sub>2</sub>P and TiO<sub>2</sub>G before and after heating

To assess the crystal structure of the TiO<sub>2</sub> film for TiO<sub>2</sub>P and TiO<sub>2</sub>G, XRD was conducted (Figure 6.2). There are no observable anatase, rutile or brookite crystal phases peaks<sup>27</sup>, indicating that the films have an amorphous crystal structure. The crystallographic state of TiO<sub>2</sub> is known to be transformed upon heating. The XRD patterns of TiO<sub>2</sub> films (TiO<sub>2</sub>P and TiO<sub>2</sub>G) after heating at 200 °C for 10 min are shown in Figure 6.2. Both spectra show an anatase peak at 29.8°, which confirms the crystal structure of TiO<sub>2</sub>P and TiO<sub>2</sub>G has changed to the anatase phase after heating. The intensity of the anatase diffraction peak for TiO<sub>2</sub>G is more than two times higher than for TiO<sub>2</sub>P, which is due to the difference in the total amount of TiO<sub>2</sub> in each film. The TiO<sub>2</sub>G layer is more than two times thicker than TiO<sub>2</sub>P, so we also expect that there is more than twice as much anatase in the TiO<sub>2</sub>G film. Thus, the percentage change in crystal structure in the films is comparable. The formation of the anatase phase strongly suggests the TiO<sub>2</sub> film could be mobile during the heating process which could influence the morphology of the TiO<sub>2</sub> films, as will be discussed below.

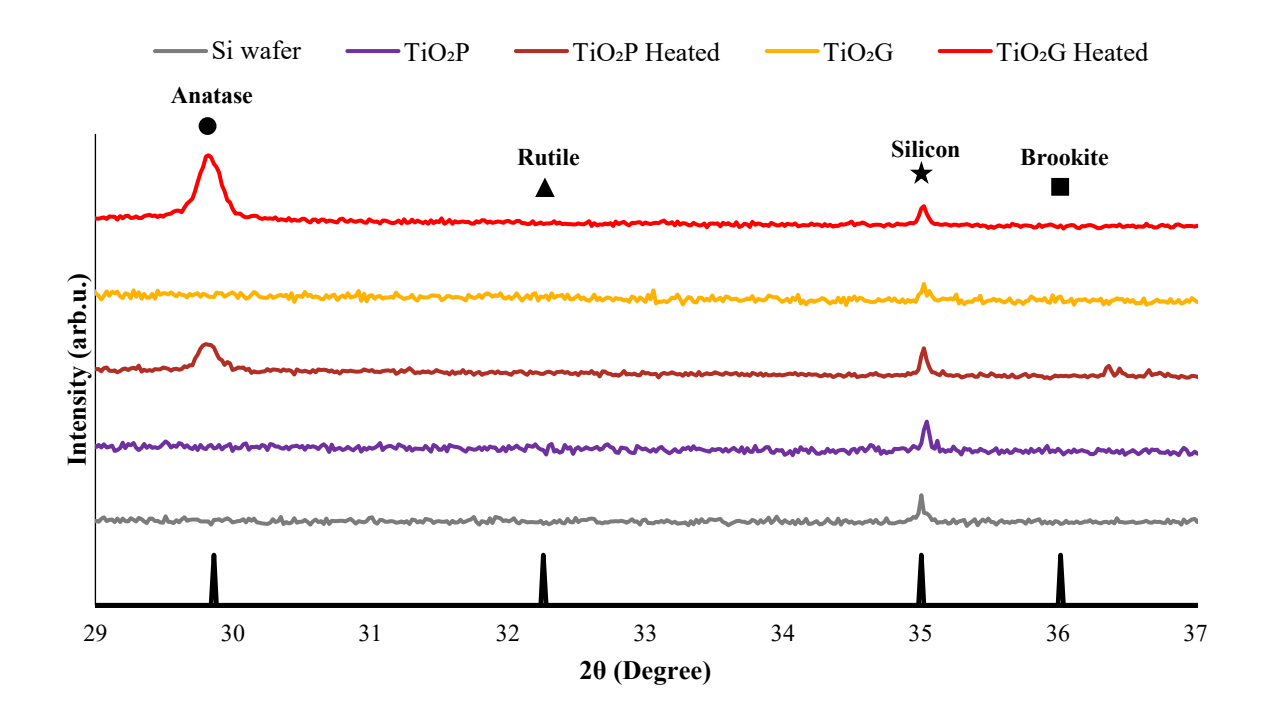


**Figure 6.2**: XRD patterns of the Si wafer, TiO<sub>2</sub>P, TiO<sub>2</sub>P after heating, TiO<sub>2</sub>G and TiO<sub>2</sub>G after heating to 200 °C. The positions of the diffraction peaks for anatase, rutile and brookite, as well as Si, are indicated using the standard XRD patterns (anatase PDF 01-075-1537, rutile PDF 01-071-4809, brookite PDF 04-007-0758 and Si PDF 00-013-0542).

#### Morphology of the TiO<sub>2</sub>P and TiO<sub>2</sub>G layer before and after heating

LSCM was conducted on both TiO<sub>2</sub> films before and after heating to compare their morphology. Figure 6.3 shows the surface morphology of TiO<sub>2</sub>P and TiO<sub>2</sub>G before and after heating over an area of  $16 \times 16$  µm and the determined Ra and Rq values. The 3D profiles of the same spots are displayed in Figure D4. Before heating, the Ra (and Rq) values of the TiO<sub>2</sub>P and TiO<sub>2</sub>G are 0.6 nm (0.8 nm) and 1.0 nm (1.3 nm), respectively. However, after heating, the values become 1.0 nm (1.2 nm) and 12.7 nm (14.7 nm), respectively. The change of Ra (and Rq) for TiO<sub>2</sub>P is small after heating, especially in comparison with TiO<sub>2</sub>G which is 12 times higher after heating. The Ra (and Rq) values were also calculated over a much larger area of 595 × 595 μm and shows a similar change (Figure D5). The change in the Ra (and Rq) values indicate that both the TiO<sub>2</sub>P and TiO<sub>2</sub>G increase in surface roughness after heating. The XRD results shows that the TiO<sub>2</sub>G and TiO<sub>2</sub>P have the same fraction of anatase after heating so the total amount of anatase in TiO<sub>2</sub>G is larger compared to TiO<sub>2</sub>P (vide supra). Çörekçi et al. noted a similar finding in their study of different thicknesses of TiO<sub>2</sub> films heated at different temperatures<sup>19</sup>. The authors reported that the surface roughness of the thicker TiO<sub>2</sub> film (300 nm) increased more compared to thinner films (220 and 260 nm) upon heating. In our study, a large change in the surface roughness is observed clearly with the thicker film (more than two times thicker) by a factor of six. Çörekçi et al. assumed that the increase in surface roughness was due to increases of the grain sizes with increasing film thickness and the recrystallisation in the TiO<sub>2</sub> films during heating. A number of studies have reported comparable findings that the surface morphology of the TiO<sub>2</sub> films changes upon heating<sup>17, 28</sup>. Thus, we conclude that the thicker TiO<sub>2</sub>G film is more mobile during heating in comparison with the thinner film in the TiO<sub>2</sub>P sample.

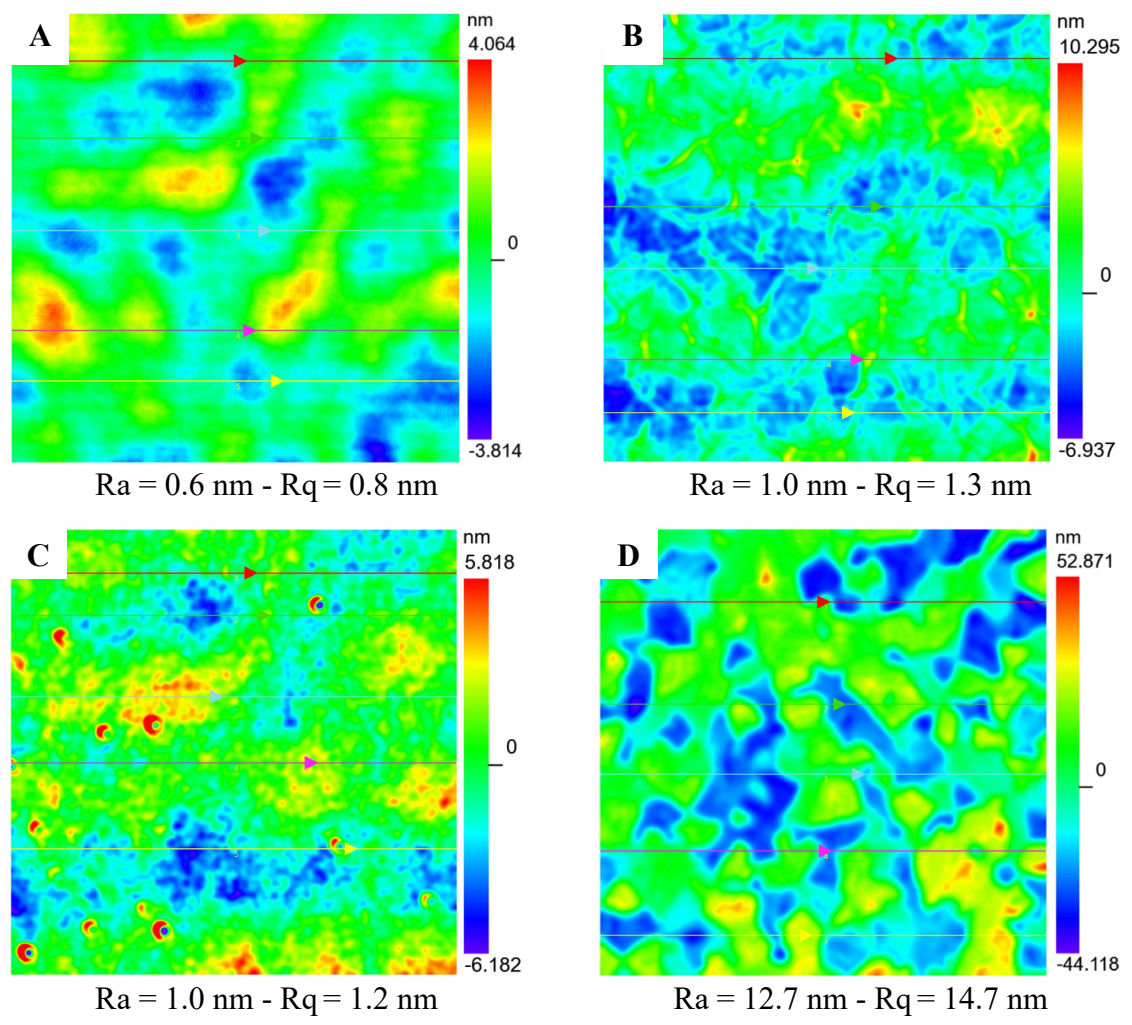


**Figure 6.3**: Surface morphology with the Ra and Rq values of (A)TiO<sub>2</sub>P before heating and (B) TiO<sub>2</sub>P after heating, (C)TiO<sub>2</sub>G before heating and (D) TiO<sub>2</sub>G after heating (area 16 x 16  $\mu$ m). Note that the scale bars are different.

# 6.4.2 Au<sub>9</sub> clusters on TiO<sub>2</sub>P and TiO<sub>2</sub>G; a probe for mobility during heating

In order to provide insight into the mobility of the TiO<sub>2</sub> during the recrystallisation process, Au<sub>9</sub> clusters were deposited onto the TiO<sub>2</sub> films and analysed with XPS. XPS was used to investigate the size of phosphine-protected Au<sub>9</sub> clusters deposited onto TiO<sub>2</sub>P and TiO<sub>2</sub>G. In addition, the effect of the CrO<sub>x</sub> overlayer on the Au<sub>9</sub> clusters was investigated, also with XPS. Figures 6.4 and 6.5 show the peak positions and relative intensities of Au 4f<sub>7/2</sub> peaks in the XPS spectra of three different concentrations (0.006, 0.06 and 0.6 mM) of TiO<sub>2</sub>P-Au<sub>9</sub>, TiO<sub>2</sub>G-Au<sub>9</sub>, TiO<sub>2</sub>P-Au<sub>9</sub>-CrO<sub>x</sub> and TiO<sub>2</sub>G-Au<sub>9</sub>-CrO<sub>x</sub> before and after heating. Tables D1 and D2 show a summary of all the Au 4f<sub>7/2</sub> peak

positions and full-width-half-maximum (FWHM). Note that all the Au 4f spectra for both substrates (TiO<sub>2</sub>P and TiO<sub>2</sub>G) are shown in Figures D6 and D7. The TiO<sub>2</sub>P XPS results will be first presented followed by TiO<sub>2</sub>G results.

# XPS of TiO<sub>2</sub>P sample

Without the  $CrO_x$  layer and before heating, the Au  $4f_{7/2}$  peaks appeared at 85.1 - 85.4 eV with FWHM of 1.7 - 1.8 eV (Figure 6.4A), whereas after heating the Au  $4f_{7/2}$  peaks shift to slightly lower binding energy (84.7 - 84.8 eV) and FWHM (1.5 - 1.6 eV) and also show a decrease in relative Au intensity across all Au<sub>9</sub> concentrations (Figure 6.4B). Results for the samples covered with a CrO<sub>x</sub> layer are shown in Figures 6.4C and 6.4D. The Au 4f<sub>7/2</sub> peak positions of TiO<sub>2</sub>P-Au<sub>9</sub> after CrO<sub>x</sub> deposition but before heating were observed at 85.3 eV and FWHM of 1.6 eV for all three concentrations. Note that the Au relative intensities decrease after the photodeposition of CrO<sub>x</sub> layer, confirming the coverage of Au clusters with CrO<sub>x</sub> layer (Figure 6.4D). After heating, the XPS peak position decreases only slightly to 85.0 eV with no significant change in FWHM. The relative Au intensities also remained unchanged upon heating. XPS has been shown previously to be a reliable indicator of the size of phosphine-protected Au<sub>9</sub> clusters through the final state effect<sup>21, 26, 29-34</sup>. Generally, non-agglomerated Au<sub>9</sub> clusters on TiO<sub>2</sub> appear at a high binding peak (HBP) between 85.0 – 85.4 eV with a FWHM of 1.7 ± 0.2 eV, and agglomerated Au<sub>9</sub> clusters shift toward a low binding peak (LBP) at 84 eV and a decreased FWHM that corresponds to bulk Au<sup>26, 29-33</sup>. This XPS interpretation has been confirmed by correlating the XPS results with other techniques such as high-resolution transmission electron microscopy<sup>31, 32</sup>. Here, the Au 4f<sub>7/2</sub> peak positions of TiO<sub>2</sub>P-Au<sub>9</sub> without CrO<sub>x</sub> layer after heating indicate a small degree of agglomeration of the Au<sub>9</sub> clusters for all concentrations. This is further confirmed by a small decrease in Au intensity after heating, indicating that some of the gold is attenuated due to some larger, agglomerated particles. Electrons emitted from the part of the clusters facing towards the substrate are attenuated when leaving the sample, which decreases the overall Au intensity <sup>29, 30</sup>. Therefore, the same total amount of gold deposited on the surface will have a lower intensity for large gold particles than that of small gold clusters. In contrast, with the CrO<sub>x</sub> layer the Au  $4f_{7/2}$  peaks positions are unchanged after heating and there is no further decrease in the Au relative intensities, indicating that Au clusters remain non-agglomerated clusters with CrO<sub>x</sub> coverage (see Scheme 6.1A). It is important to note that decrease in Au intensity after photodeposition of CrO<sub>x</sub> layer due to the coverage of Au<sub>9</sub> clusters (Figure 6.4D). These results are in agreement with our previous report showing that CrO<sub>x</sub> overlayers inhibit the agglomeration of Au clusters<sup>26</sup>.

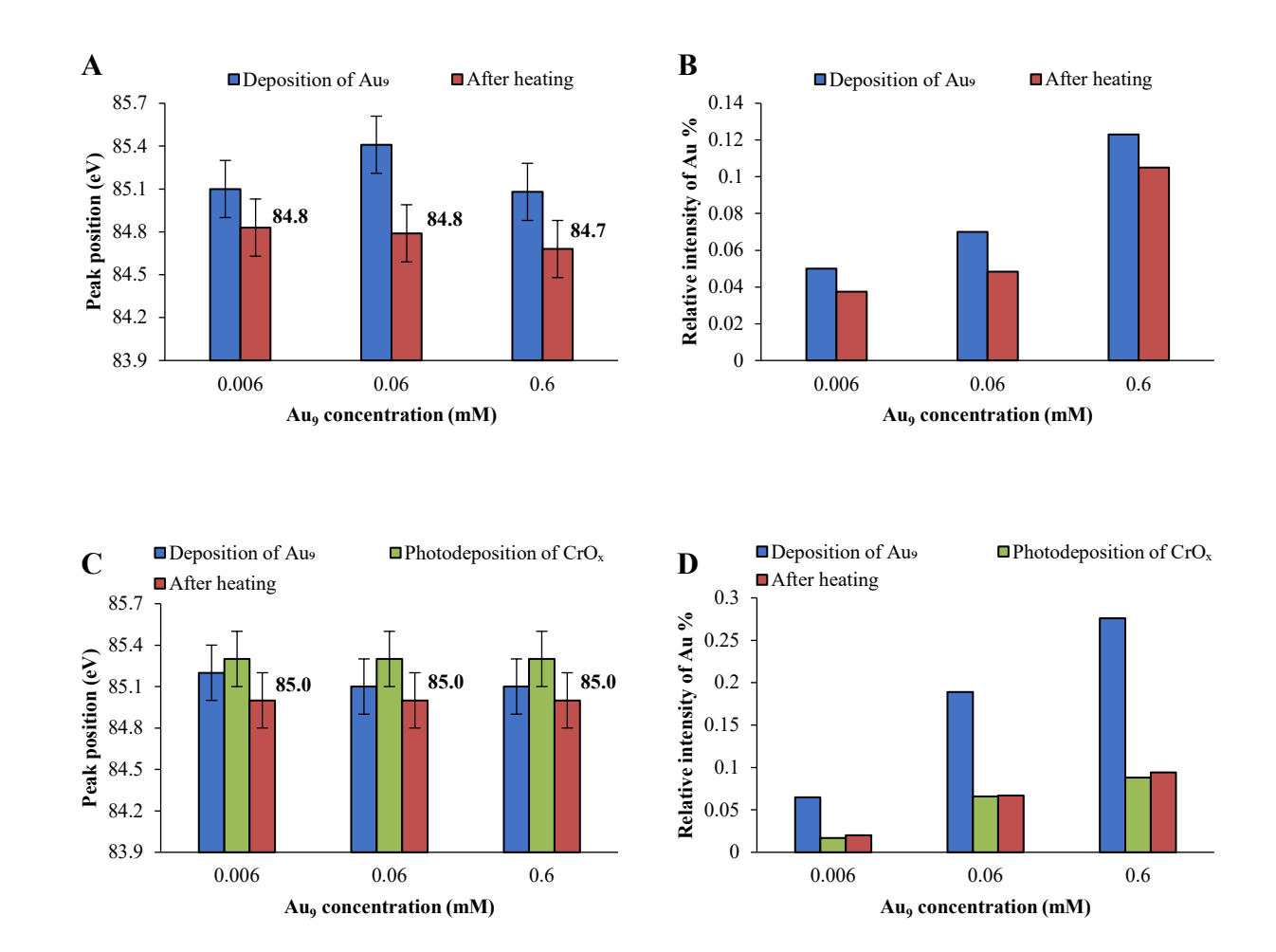
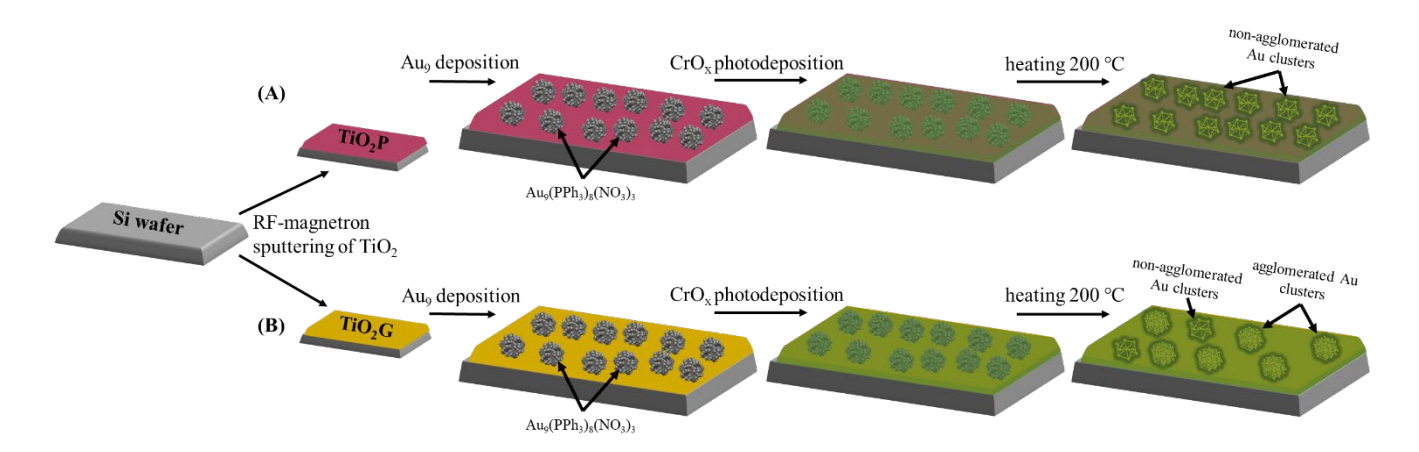


**Figure 6.4**: XPS results of  $TiO_2P$ -Au<sub>9</sub> for three different Au<sub>9</sub> concentrations: (**A**) position of Au  $4f_{7/2}$  and (**B**) relative intensity of Au before and after heating.  $TiO_2P$ -Au<sub>9</sub>-CrO<sub>x</sub> (**C**) position of Au  $4f_{7/2}$  and (**D**) relative intensity of Au before and after photodeposition of  $CrO_x$  layer and after heating. Note that the vertical scales of (**B**,**D**) are different and that the samples in (**A**,**C**) are different but are prepared in the same manner.



**Scheme 6.1:** Schematic illustration of the experimental procedure for preparing (A)  $TiO_2P$ - $Au_9$ - $CrO_x$  and (B)  $TiO_2G$ - $Au_9$ - $CrO_x$ .

The P 2p spectra of TiO<sub>2</sub>P-Au<sub>9</sub> without and with CrO<sub>x</sub> layer before and after heating are shown in Figure D8 and the peak positions are discussed in the appendix section. The Cr 2p spectra for TiO<sub>2</sub>P-Au<sub>9</sub>-CrO<sub>x</sub> before and after heating of the three different concentrations are shown in Figure D9. A summary of all the Cr 2p<sub>3/2</sub> peak positions are shown in Table D3 and the peak positions are discussed in the appendix section.

#### XPS of TiO<sub>2</sub>G sample

For the thicker film, TiO<sub>2</sub>G-Au<sub>9</sub>, the Au 4f<sub>7/2</sub> peak positions before heating for all three different concentrations appeared at the HBP at  $85.3 \pm 0.1$  eV (Figure 6.5A) and FWHM of  $1.8 \pm 0.2$  eV, corresponding to non-agglomerated Au clusters. However, after heating, the Au 4f<sub>7/2</sub> have shifted toward lower energy (84.6 - 84.9 eV) and a FWHM of 1.5 - 1.7 eV with a decrease in Au intensity (Figure 6.5B), indicating that Au clusters are partially agglomerated. With the CrO<sub>x</sub> layer deposited before heating, the Au  $4f_{7/2}$  peak positions are observed at the HBP position at 85.3 - 85.5 eV (Figure 6.5C), with a decrease in Au 4f<sub>7/2</sub> intensity due to the coverage of the CrO<sub>x</sub> layer on Au<sub>9</sub> clusters (Figure 6.5D). There is a slight increase in the binding energy of the Au 4f peak after the photodeposition of CrO<sub>x</sub>, and we do not know if this a significant change or not. However, the position found can be used as an indication of the presence of non-agglomerated Au clusters. With the CrO<sub>x</sub> layer after heating, the Au  $4f_{7/2}$  peak positions have further shifted to lower energy (84.3 - 84.8 eV) position and a FWHM of 1.3 - 1.8 eV with a decrease in Au intensity, which is attributed to further agglomeration of the Au clusters based on the final state effect (see Scheme 6.1B). The degree of agglomeration increases with increasing the Au<sub>9</sub> concentration for both cases (without and with CrO<sub>x</sub> layer). Note here the difference; Au clusters on the surface of TiO<sub>2</sub>G undergo increased agglomeration after heating, even in the presence of the CrO<sub>x</sub> layer. This is different to the TiO<sub>2</sub>P, where Au clusters are less likely to agglomerate under the CrO<sub>x</sub> layer with heating. This difference will be further discussed below.

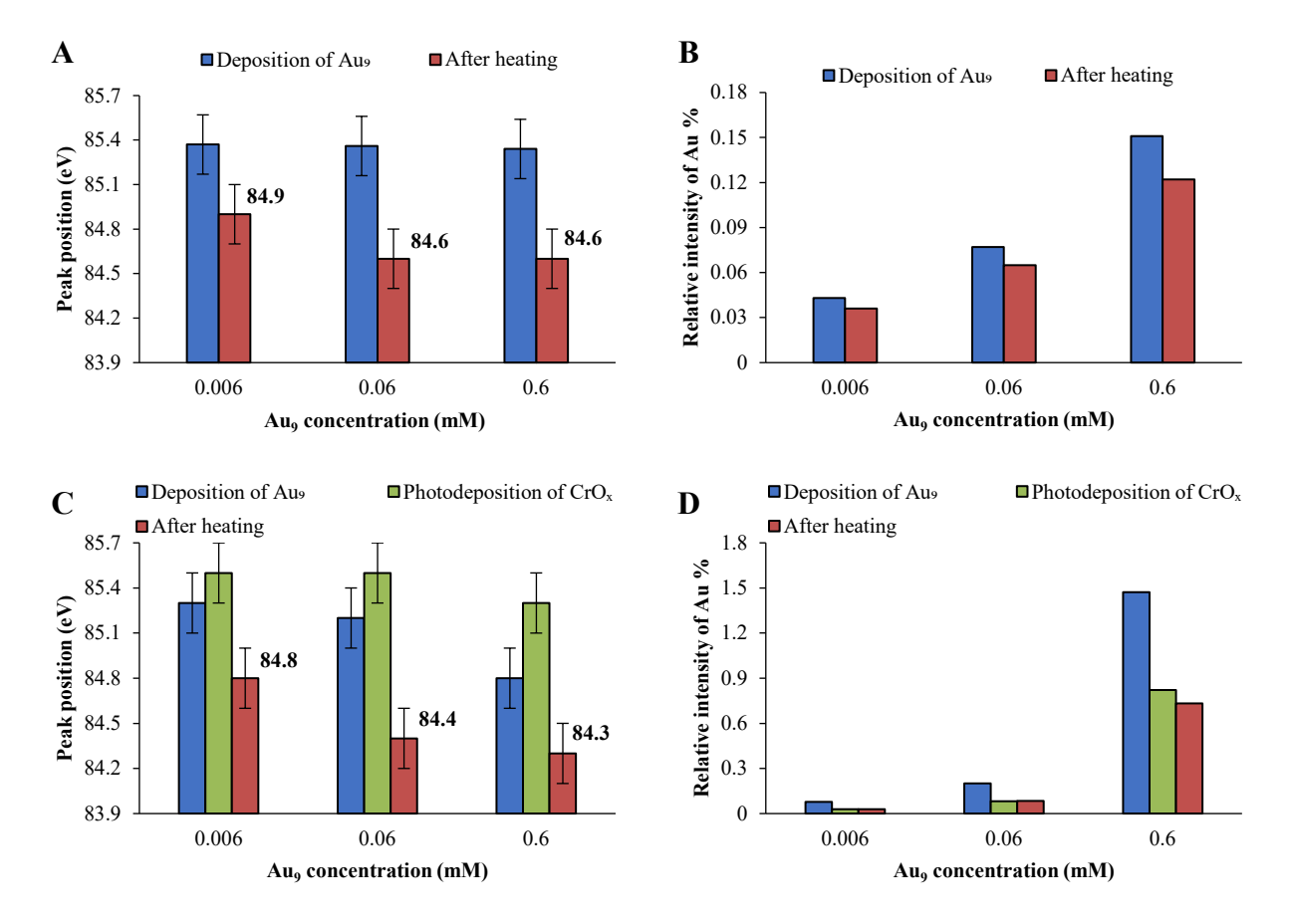


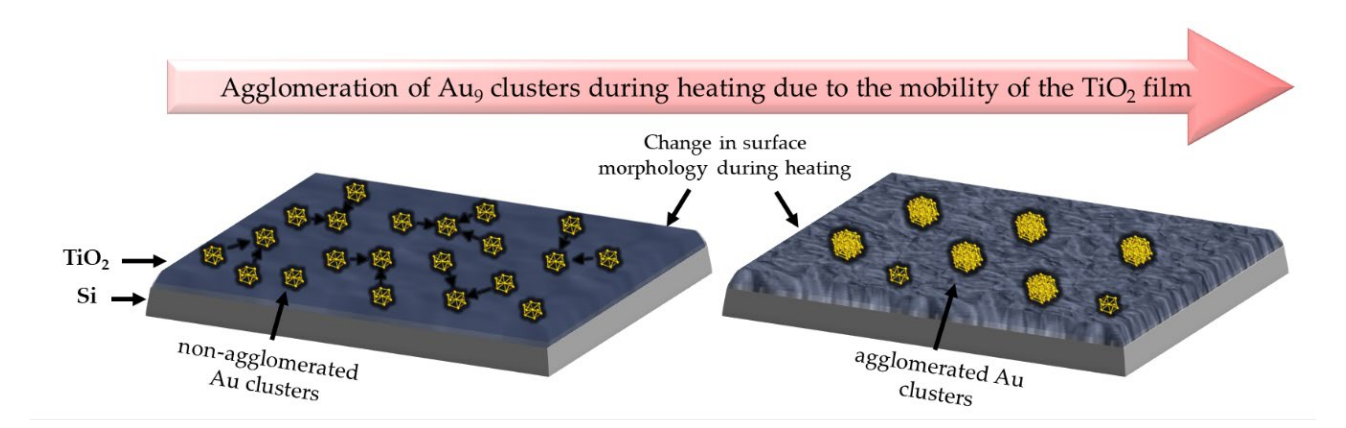
**Figure 6.5**: XPS results of Au<sub>9</sub> deposited on TiO<sub>2</sub>G for three different Au<sub>9</sub> concentrations: (A) position of Au  $4f_{7/2}$  and (B) relative intensity of Au before and after heating. TiO<sub>2</sub>G-Au<sub>9</sub> with CrO<sub>x</sub> layer: (C) position of Au  $4f_{7/2}$  and (D) relative intensity of Au before and after photodeposition of CrO<sub>x</sub> layer and after heating. Note that vertical scales of (B,D) are different and that the samples in (A,C) are different but are prepared in the same manner.

The chemical state of the phosphorous ligands of TiO<sub>2</sub>G-Au<sub>9</sub> without and with CrO<sub>x</sub> layer, both before and after heating, was determined using P 2p region (see Figure D10 for more information and accompanying text). Figure D11 shows the Cr 2p spectra for TiO<sub>2</sub>G-Au<sub>9</sub>-CrO<sub>x</sub> before and after heating of the three different concentrations. All the Cr 2p<sub>3/2</sub> peak positions are given in Table D4. and the peak positions are discussed in the appendix section.

#### 6.4.3 Effect of the TiO<sub>2</sub> film thickness

The protective effect of the  $CrO_x$  layer on agglomeration of  $Au_9$  clusters is not the same for both the  $TiO_2P$  and  $TiO_2G$  substrates. The agglomeration of  $Au_9$  clusters is inhibited on  $TiO_2P$  with the  $CrO_x$  overlayer but not on  $TiO_2G$ , which shows a higher degree of agglomeration. The coverage of the  $CrO_x$  layer on  $Au_9$  clusters for both substrates is demonstrated by the decrease of the Au XPS intensities. After heating, it is observed that the relative amount of  $CrO_x$  decreases for both films (Table D5). Our previous studies on a similar system revealed that the  $CrO_x$  layer diffuses into a  $TiO_2$ 

film after heating to 600°C due to the differences in surface energy between TiO<sub>2</sub> and CrO<sub>x</sub><sup>25</sup>. In this study, both films are heated to only 200 °C, however, CrO<sub>x</sub> on TiO<sub>2</sub>G experienced more diffusion of CrO<sub>x</sub> into the film compared to TiO<sub>2</sub>P. One possibility for the higher degree of Au<sub>9</sub> agglomeration and CrO<sub>x</sub> diffusion is the mobility of the TiO<sub>2</sub> film. Cluster agglomeration can be due to either (i) growth of the clusters over the surface or (ii) mobility of the substrate. In the case of (i), the cluster growth and agglomeration on a substrate can be ascribed to either Smoluchowski ripening and Ostwald ripening mechanisms. For Smoluchowski ripening, agglomeration of clusters is caused by the collision and coalescence of entire clusters to larger particles<sup>35</sup>. For Ostwald ripening, the growth of larger particles takes place by the detachment of single atoms which diffuse onto a nearby cluster or nanoparticle<sup>36</sup>. In the case of (ii), a section of the substrate to which a cluster is adsorbed moves closer to another section of the substrate which has another adsorbed cluster. The significant change in the surface morphology of TiO<sub>2</sub>G after heating (Ra: 11.7 nm and Rq: 13.4 nm) compared to TiO<sub>2</sub>P (Ra: 0.4 nm and Rq: 0.5 nm) strongly suggests that the agglomeration of the Au<sub>9</sub> clusters with different concentrations on TiO2G after heating is due to the high distortion of the surface upon heating. A higher mobility of the TiO<sub>2</sub> substrate during heating means that the local surface beneath a Au cluster moves larger distances compared to a substrate which exhibits lower mobility during heating (see Scheme 6.2). The high mobility of the thick film is assumed to be due to the recrystallisation during heating, which is in agreement with previous studies 17, 19, 28. With increasing mobility, the likelihood for close contact between two or more Au clusters increases and thus the likelihood of agglomeration is also increased. Furthermore, the degree of agglomeration of the Au clusters is larger for the thicker TiO<sub>2</sub>G substrate compared to the thinner TiO<sub>2</sub>P substrate.



**Scheme 6.2:** Schematic illustration showing the agglomeration mechanism of  $Au_9$  clusters on the  $TiO_2G$  film during heating.

# 6.5 Conclusions

In summary, the change in surface morphology of two different film thicknesses of RF sputter deposited TiO<sub>2</sub> (~400 nm and ~1100 nm) were examined and compared upon heating. After heating, the thick TiO<sub>2</sub> film shows a larger change in surface morphology which is associated with a higher mobility during heating compared to the thin TiO<sub>2</sub> film. The difference in mobility is attributed to the differences in the total amount of amorphous TiO<sub>2</sub> transformed to anatase in each of the films, which then results in differences in the morphology of the surface upon heating. Au<sub>9</sub> clusters were used as a probe for the TiO<sub>2</sub> mobility. Au<sub>9</sub> clusters were deposited onto the two different TiO<sub>2</sub> films followed by photodeposition of CrO<sub>x</sub> layer. After heating, the Au clusters on the thicker film showed a larger degree of agglomeration compared to the thinner film. The higher mobility of the thick film during heating increases the probability of close encounters of Au clusters, which results in agglomeration of the Au<sub>9</sub> clusters even in the presence of a CrO<sub>x</sub> overlayer. In contrast, the lower mobility of the thin film resulted in less agglomeration of the Au<sub>9</sub> clusters after heating.

# 6.6 References

- 1. Daghrir, R.; Drogui, P.; Robert, D., Modified TiO2 For Environmental Photocatalytic Applications: A Review. *Industrial & Engineering Chemistry Research* **2013**, *52* (10), 3581-3599.
- 2. Linsebigler, A. L.; Lu, G.; Yates, J. T., Photocatalysis on TiO2 Surfaces: Principles, Mechanisms, and Selected Results. *Chemical Reviews* **1995**, *95* (3), 735-758.
- 3. Brinker, C. J.; Harrington, M. S., Sol-gel Derived Antireflective Coatings for Silicon. *Solar Energy Materials* **1981**, *5* (2), 159-172.
- 4. Lottiaux, M.; Boulesteix, C.; Nihoul, G.; Varnier, F.; Flory, F.; Galindo, R.; Pelletier, E., Morphology and Structure of TiO2 Thin Layers Vs. Thickness and Substrate Temperature. *Thin Solid Films* **1989**, *170* (1), 107-126.
- 5. Yeung, K. S.; Lam, Y. W., A Simple Chemical Vapour Deposition Method for Depositing Thin TiO2 Films. *Thin Solid Films* **1983**, *109* (2), 169-178.
- 6. Aarik, J.; Aidla, A.; Uustare, T.; Kukli, K.; Sammelselg, V.; Ritala, M.; Leskelä, M., Atomic Layer Deposition of TiO2 Thin Films from TiI4 and H2O. *Applied Surface Science* **2002**, 193 (1-4), 277-286.
- 7. Dakka, A.; Lafait, J.; Abd-Lefdil, M.; Sella, C., Optical Study of Titanium Dioxide Thin Films Prepared by RF Sputtering. *Moroccan Journal of Condensed Matter* **1999**, *2*.
- 8. Tanemura, S.; Miao, L.; Wunderlich, W.; Tanemura, M.; Mori, Y.; Toh, S.; Kaneko, K., Fabrication and Characterization of Anatase/Rutile—TiO2 Thin Films by Magnetron Sputtering: A Review. *Science and Technology of Advanced Materials* **2005**, *6* (1), 11-17.
- 9. Miao, L.; Jin, P.; Kaneko, K.; Terai, A.; Nabatova-Gabain, N.; Tanemura, S., Preparation and characterization of polycrystalline anatase and rutile TiO2 thin films by rf magnetron sputtering. *Applied Surface Science* **2003**, *212-213*, 255-263.
- 10. Wang, T. M.; Zheng, S. K.; Hao, W. C.; Wang, C., Studies on photocatalytic activity and transmittance spectra of TiO2 thin films prepared by r.f. magnetron sputtering method. *Surface and Coatings Technology* **2002**, *155* (2), 141-145.
- 11. Ye, Q.; Liu, P. Y.; Tang, Z. F.; Zhai, L., Hydrophilic properties of nano-TiO2 thin films deposited by RF magnetron sputtering. *Vacuum* **2007**, *81* (5), 627-631.
- 12. Huang, C. H.; Tsao, C. C.; Hsu, C. Y., Study on the photocatalytic activities of TiO2 films prepared by reactive RF sputtering. *Ceramics International* **2011**, *37* (7), 2781-2788.
- 13. Yoo, D.; Kim, I.; Kim, S.; Hahn, C. H.; Lee, C.; Cho, S., Effects of annealing temperature and method on structural and optical properties of TiO2 films prepared by RF magnetron sputtering at room temperature. *Applied Surface Science* **2007**, *253* (8), 3888-3892.
- 14. Hou, Y.-Q.; Zhuang, D.-M.; Zhang, G.; Zhao, M.; Wu, M.-S., Influence of annealing temperature on the properties of titanium oxide thin film. *Applied Surface Science* **2003**, *218* (1), 98-106.
- 15. Grilli, M. L.; Yilmaz, M.; Aydogan, S.; Cirak, B. B., Room temperature deposition of XRD-amorphous TiO2 thin films: Investigation of device performance as a function of temperature. *Ceramics International* **2018**, *44* (10), 11582-11590.
- 16. Mathews, N. R.; Morales, E. R.; Cortés-Jacome, M. A.; Toledo Antonio, J. A., TiO2 Thin Films Influence of Annealing Temperature on Structural, Optical and Photocatalytic Properties. *Solar Energy* **2009**, *83* (9), 1499-1508.
- 17. Meng, F.; Xiao, L.; Sun, Z., Thermo-induced hydrophilicity of nano-TiO2 thin films prepared by RF magnetron sputtering. *Journal of Alloys and Compounds* **2009**, *485* (1), 848-852.
- 18. Taherniya, A.; Raoufi, D., Thickness dependence of structural, optical and morphological properties of sol-gel derived TiO2 thin film. *Materials Research Express* **2018**, *6* (1), 016417.
- 19. Çörekçi, Ş.; Kizilkaya, K.; Asar, T.; Öztürk, M.; Çakmak, M.; Ozcelik, S., Effects of Thermal Annealing and Film Thickness on the Structural and Morphological Properties of Titanium Dioxide Films. *Acta Physica Polonica A* **2012**, *121*.
- 20. Pichugina, D. A.; Kuz'menko, N. E.; Shestakov, A. F., Ligand-protected gold clusters: the structure, synthesis and applications. *Russian Chemical Reviews* **2015**, *84* (11), 1114-1144.

- 21. Adnan, R. H.; Madridejos, J. M. L.; Alotabi, A. S.; Metha, G. F.; Andersson, G. G., A Review of State of the Art in Phosphine Ligated Gold Clusters and Application in Catalysis. *Advanced Science* **2022**, *9* (15), 2105692.
- 22. Yuan, X.; Ye, Y.; Lian, M.; Wei, Q., Structural Coloration of Polyester Fabrics Coated with Al/TiO2 Composite Films and Their Anti-Ultraviolet Properties. *Materials* **2018**, *11* (6).
- 23. Diamanti, M. V.; Del Curto, B.; Pedeferri, M., Interference Colors of Thin Oxide Layers on Titanium. *Color Research & Application* **2008**, *33* (3), 221-228.
- 24. Wen, F.; Englert, U.; Gutrath, B.; Simon, U., Crystal Structure, Electrochemical and Optical Properties of [Au9(PPh3)8](NO3)3. *European Journal of Inorganic Chemistry* **2008**, *2008* (1), 106-111.
- 25. Alotabi, A. S.; Gibson, C. T.; Metha, G. F.; Andersson, G. G., Investigation of the Diffusion of Cr2O3 into Different Phases of TiO2 upon Annealing. *ACS Applied Energy Materials* **2021**, *4* (1), 322-330.
- 26. Alotabi, A. S.; Yin, Y.; Redaa, A.; Tesana, S.; Metha, G. F.; Andersson, G. G., Cr2O3 layer inhibits agglomeration of phosphine-protected Au9 clusters on TiO2 films. *The Journal of Chemical Physics* **2021**, *155* (16), 164702.
- 27. Ali, S.; Granbohm, H.; Lahtinen, J.; Hannula, S.-P., Titania Nanotubes Prepared by Rapid Breakdown Anodization for Photocatalytic Decolorization of Organic Dyes under UV and Natural Solar Light. *Nanoscale Research Letters* **2018**, *13* (1), 179.
- 28. Chandra Sekhar, M.; Kondaiah, P.; Jagadeesh Chandra, S. V.; Mohan Rao, G.; Uthanna, S., Substrate temperature influenced physical properties of silicon MOS devices with TiO2 gate dielectric. *Surface and Interface Analysis* **2012**, *44* (9), 1299-1304.
- 29. Anderson, D. P.; Alvino, J. F.; Gentleman, A.; Al Qahtani, H.; Thomsen, L.; Polson, M. I.; Metha, G. F.; Golovko, V. B.; Andersson, G. G., Chemically-Synthesised, Atomically-Precise Gold Clusters Deposited and Activated on Titania. *Physical chemistry chemical physics* **2013**, *15* (11), 3917-3929.
- 30. Anderson, D. P.; Adnan, R. H.; Alvino, J. F.; Shipper, O.; Donoeva, B.; Ruzicka, J.-Y.; Al Qahtani, H.; Harris, H. H.; Cowie, B.; Aitken, J. B., Chemically Synthesised Atomically Precise Gold Clusters Deposited and Activated on Titania. Part II. *Physical chemistry chemical physics* **2013**, *15* (35), 14806-14813.
- 31. Al Qahtani, H. S.; Kimoto, K.; Bennett, T.; Alvino, J. F.; Andersson, G. G.; Metha, G. F.; Golovko, V. B.; Sasaki, T.; Nakayama, T., Atomically resolved structure of ligand-protected Au9 clusters on TiO2 nanosheets using aberration-corrected STEM. *The Journal of Chemical Physics* **2016**, *144* (11), 114703.
- 32. Al Qahtani, H. S.; Metha, G. F.; Walsh, R. B.; Golovko, V. B.; Andersson, G. G.; Nakayama, T., Aggregation Behavior of Ligand-Protected Au9 Clusters on Sputtered Atomic Layer Deposition TiO2. *The Journal of Physical Chemistry C* **2017**, *121* (20), 10781-10789.
- 33. Howard-Fabretto, L.; Andersson, G. G., Metal Clusters on Semiconductor Surfaces and Application in Catalysis with a Focus on Au and Ru. *Advanced Materials* **2020**, *32* (18), 1904122.
- 34. Alotabi, A. S.; Osborn, D. J.; Ozaki, S.; Kataoka, Y.; Negishi, Y.; Tesana, S.; Metha, G. F.; Andersson, G. G., Suppression of phosphine-protected Au9 cluster agglomeration on SrTiO3 particles using a chromium hydroxide layer. *Materials Advances* **2022**, *3* (8), 3620-3630.
- 35. Smoluchowski, M. v., Drei vortrage uber diffusion, brownsche bewegung und koagulation von kolloidteilchen. *Zeitschrift fur Physik* **1916**, *17*, 557-585.
- 36. Ostwald, W., Blocking of Ostwald ripening allowing long-term stabilization. *Phys. Chem* **1901,** *37*, 385.

# Chapter 7: Suppression of Phosphine-Protected Au<sub>9</sub> Clusters Agglomeration on SrTiO<sub>3</sub> Particles Using a Chromium Hydroxide Layer

Abdulrahman S. Alotabi, D. J. Osborn, Shuhei Ozaki, Yuki Kataoka, Yuichi Negishi, Siriluck Tesana, Gregory F. Metha and Gunther G. Andersson

This chapter is a reformatted version of the paper published in *Materials Advances*, 2022, Vol. 3, Issue 8, Page 3620. **DOI**: 10.1039/D1MA01226F

#### Author Contribution:

Abdulrahman S Alotabi: Designed and performed experiments, data analysis and interpretation, and prepared the manuscript for publication.

D. J. Osborn: Performed STEM measurements on samples prepared by A.S.A.

Shuhei Ozaki & Yuki Kataoka: Contributed in photocatalysis measurements on samples prepared by A.S.A

Siriluck Tesana: Synthesised Au<sub>9</sub>(PPh<sub>3</sub>)<sub>8</sub>(NO<sub>3</sub>)<sub>3</sub> clusters for this project.

Yuichi Negishi: Intellectual contribution in revision of manuscript.

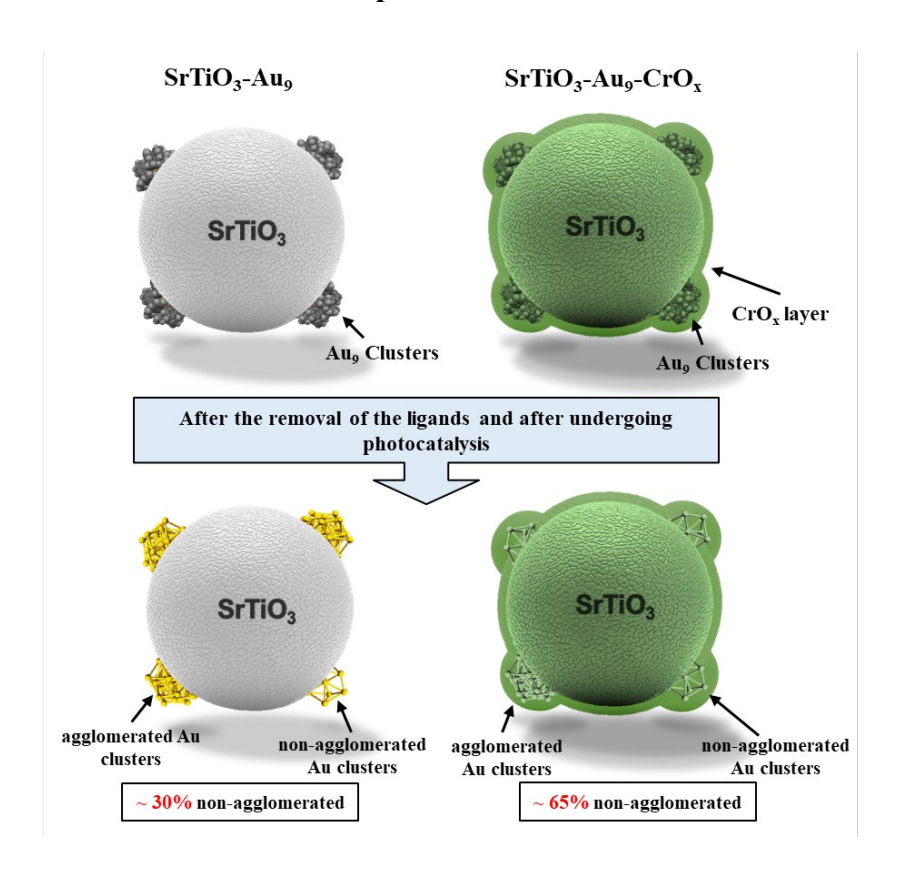
*Gregory F Metha: Intellectual contribution in revision of manuscript.* 

Gunther G Andersson: Intellectual contribution in conceptualising experiments, data interpretation & revision of manuscript.

# 7.1 Abstract

Au clusters have been shown to have great potential for use as co-catalysts in photocatalytic water splitting. Agglomeration of Au clusters deposited onto semiconductor surfaces into larger particles is a major challenge. Metal oxide overlayers can be used to improve the stability of Au clusters on surfaces and avoid their agglomeration. The aim of this work is to investigate the inhibition of phosphine-protected Au<sub>9</sub> clusters beneath a Cr(OH)<sub>3</sub> overlayer to agglomerate under conditions of photocatalytic water splitting (i.e. UV irradiation). Au<sub>9</sub> was deposited on the surface of SrTiO<sub>3</sub> using a solution impregnation method followed by photodeposition of a Cr(OH)<sub>3</sub> layer. After UV light irradiation for 7 hours for photocatalytic water splitting, uncovered Au clusters on SrTiO<sub>3</sub> agglomerated into larger particles. However, agglomeration was inhibited when a thin Cr(OH)<sub>3</sub> layer was deposited onto the SrTiO<sub>3</sub>-Au<sub>9</sub> system. From careful XPS measurements, the chemical state of the overlayer is initially determined to be Cr(OH)<sub>3</sub> but upon heating at 200 °C for 10 mins it converts to Cr<sub>2</sub>O<sub>3</sub>. Through photocatalysis experiments it was found that the Cr(OH)<sub>3</sub> overlayer blocks the sites for O evolution reaction on the SrTiO<sub>3</sub>-Au<sub>9</sub>.

# **Graphical Abstract**



# 7.2 Introduction

Metal clusters are formed by a specific number of metal atoms and are generally less than 2 nm in size. Metal clusters exhibit unique physical and chemical properties which are different to those of nanoparticles formed by the same element and the respective bulk materials 1-4. Clusters can be synthesised with protecting ligands to stabilise the cluster core and prevent agglomeration <sup>5, 6</sup>. In contrast to gas phase generated clusters, ligand protected clusters can be synthesised on a larger scale. Atomically precise chemically synthesised ligated clusters deposited onto metal oxides are known to be photocatalytic active in water splitting <sup>2, 7, 8</sup>. When using chemically synthesised ligated clusters, the ligands need to be removed to generate naked clusters on a surface as active sites of a photocatalyst 9. Au clusters decorated metal oxide surfaces show enhanced photocatalytic water splitting activity due to the size and dispersibility of ultrasmall metal clusters on surfaces <sup>10-16</sup>. However, removal of the ligands of the deposited clusters without causing agglomeration of the clusters is a challenging task <sup>2, 7, 17</sup>. Agglomeration of the clusters render them inefficient as active sites in photocatalysis, particularly when the catalytic performance is based on the size of the clusters. For example, Au<sub>25</sub> clusters on BaLa<sub>4</sub>Ti<sub>4</sub>O<sub>15</sub> surfaces show a strong decrease in photocatalytic activity if the clusters increase in size <sup>13</sup>. It is also known that Au clusters on surfaces exposed to constant irradiation can result in agglomeration of the clusters <sup>18, 19</sup>.

Inhibiting the agglomeration of Au clusters decorated on metal oxide surfaces can be achieved by using surface modification and coating strategies<sup>20, 21</sup>. Krishnan et al. have stabilised Au<sub>9</sub>(PPh<sub>3</sub>)<sub>8</sub>(NO<sub>3</sub>)<sub>3</sub> and Au<sub>13</sub>(dppe)<sub>5</sub>Cl<sub>2</sub>Cl<sub>3</sub> clusters deposited on ALD TiO<sub>2</sub> films by pre-treatment of the surface through heating and sputtering to introduce defects <sup>22, 23</sup>. These defects sites stabilise the Au clusters against agglomeration on the surface. Recently, Xu et al. reported that the photostability of glutathione-protected Au<sub>25</sub> clusters on SiO<sub>2</sub> spheres was increased by addition of multifunctional branched poly-ethylenimine (BPEI)<sup>24</sup>. Subsequent coating with TiO<sub>2</sub> shell produced a photocatalyst with improved efficiency and photostability, even after long periods of light irradiation.

It has been shown that deposition of a CrO<sub>x</sub> overlayer can stabilise nanoparticles and clusters. Domen et al. have developed a method to improve the stability of rhodium nanoparticles using a CrO<sub>x</sub> overlayer <sup>25-28</sup>. CrO<sub>x</sub> overlayers also can prevent the back reaction H<sup>+</sup> and O<sub>2</sub> to H<sub>2</sub>O (oxygen photoreduction reaction) in photocatalysts used for water splitting <sup>29-38</sup>, with the effectiveness of the overlayer depending on its thickness <sup>39</sup>. CrO<sub>x</sub> layers have been applied to a range of co-catalysts deposited on other metal oxide substrates, such as platinum nanoparticles <sup>38, 40</sup>, palladium nanoparticles <sup>41</sup>, silver nanoparticles <sup>39</sup> and metal oxides (NiO<sub>x</sub>, RuO<sub>2</sub>, Rh<sub>2</sub>O<sub>3</sub> and CuO<sub>x</sub>) <sup>28, 42</sup>. Overlayers of other metal oxides have also been employed to stabilise co-catalysts and to prevent the back reaction in photocatalysis <sup>43-46</sup>.

Chemically synthesised phosphine-protected Au clusters have attracted much attention because of their fluxional behaviour and facile removal of the Au-P ligands <sup>2,21,47</sup>. The aim of the present study is to investigate the size of Au<sub>9</sub>(PPh<sub>3</sub>)<sub>8</sub>(NO<sub>3</sub>)<sub>3</sub> (hereafter referred to as Au<sub>9</sub>) deposited onto SrTiO<sub>3</sub> nanoparticles before and after the removal of the ligands and after undergoing photocatalysis. This study includes an investigation of the influence of the chromium oxide (CrO<sub>x</sub>) layer in preventing cluster agglomeration. CrO<sub>x</sub> overlayers are photodeposited, before the removal of the ligands, to inhibit the Au clusters from agglomeration. The size of Au<sub>9</sub> clusters was examined to investigate the effectiveness of the CrO<sub>x</sub> overlayer to stabilising phosphine-protected Au clusters after heating and UV irradiation. Finally, the influence of CrO<sub>x</sub> coverage for Au<sub>9</sub> deposited onto SrTiO<sub>3</sub> on overall photocatalytic water splitting rate is examined.

# 7.3 Experimental

# 7.3.1 Material and sample preparation

#### Material

SrTiO<sub>3</sub> with a purity of 99% (<100 nm particle size) was purchased from Sigma-Aldrich (Australia). Au<sub>9</sub> was synthesised using the procedure reported earlier <sup>48</sup>. Methanol (CH<sub>3</sub>OH) (99.9% super gradient HPLC (ACI labscan)), potassium chromate ( $K_2CrO_4$ ) (purity  $\geq$ 99%, Sigma-Aldrich, Australia) and deionised water were used for sample preparation.

#### Deposition mechanism

Scheme 7.1 depicts the experimental procedure for preparing a) the SrTiO<sub>3</sub>-Au<sub>9</sub> samples and b) the SrTiO<sub>3</sub>-Au<sub>9</sub>-CrO<sub>x</sub> samples via impregnation and photodeposition.

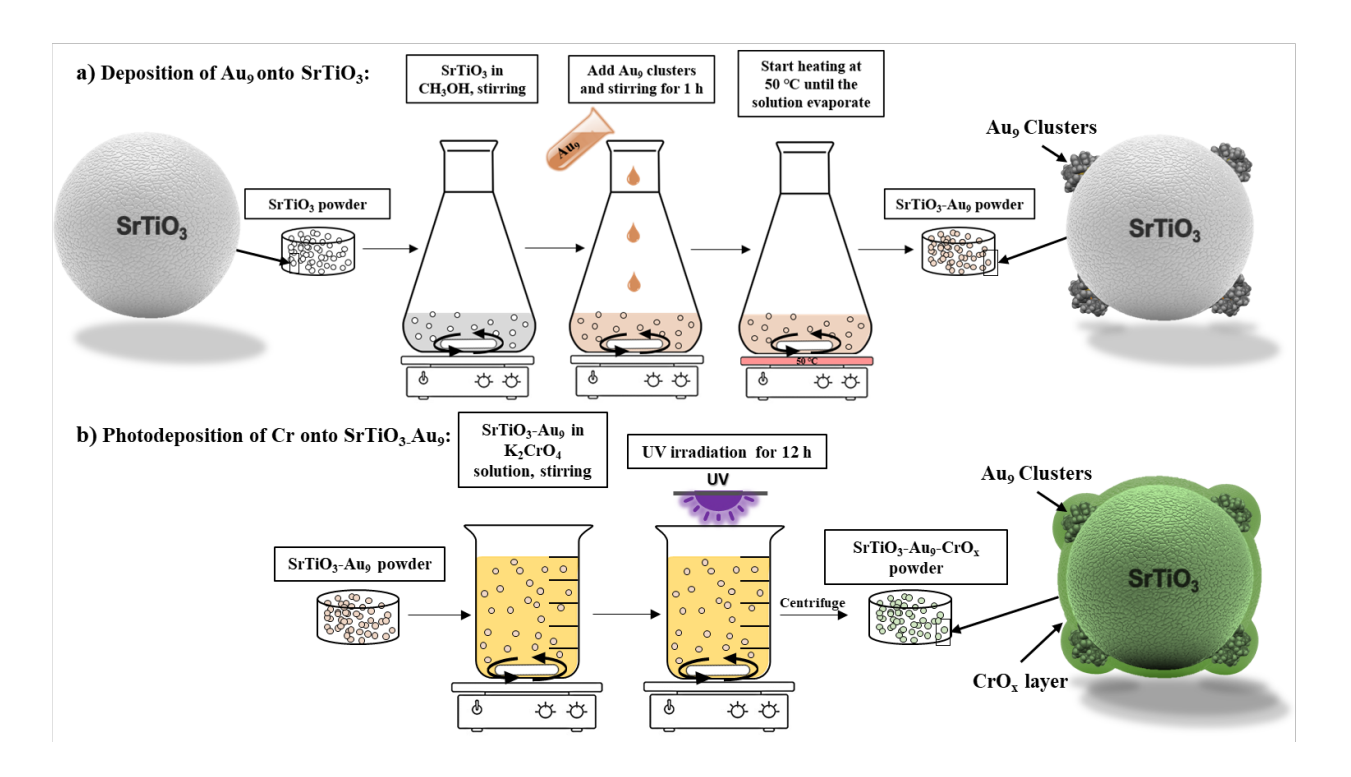
# a) Deposition of Au<sub>9</sub> onto SrTiO<sub>3</sub> (SrTiO<sub>3</sub>-Au<sub>9</sub>)

SrTiO<sub>3</sub>-Au<sub>9</sub> was prepared using an impregnation method (see Scheme 7.1a). First, 1 g of SrTiO<sub>3</sub> was dispersed in 10 mL of CH<sub>3</sub>OH. Subsequently, 10 mL of a Au<sub>9</sub> cluster solution (0.12 mM) was added to a stirred suspension of SrTiO<sub>3</sub> (1 g SrTiO<sub>3</sub>, 10 mL CH<sub>3</sub>OH) and left to stir for 1 h at room temperature. The total volume of a CH<sub>3</sub>OH solution was 20 mL and concentration of Au<sub>9</sub> in the solution was 0.06 mM. Assuming complete adhesion of the clusters onto the substrate, the total Au content of the SrTiO<sub>3</sub>-Au<sub>9</sub> sample is 0.2 wt %Au content. The stirred suspension was heated at 50 °C under N<sub>2</sub> flow until the CH<sub>3</sub>OH had evaporated (approximately 8-10 min for evaporating the CH<sub>3</sub>OH). The SrTiO<sub>3</sub>-Au<sub>9</sub> powder was collected without further treatment.

#### b) Photodeposition of Cr onto SrTiO<sub>3</sub>-Au<sub>9</sub>

CrO<sub>x</sub> was photodeposited onto the SrTiO<sub>3</sub>-Au<sub>9</sub> samples to form an overlayer (see Scheme 7.1b). 500 mg of SrTiO<sub>3</sub>-Au<sub>9</sub> powder was added to a 0.5 mM aqueous K<sub>2</sub>CrO<sub>4</sub> solution (200 mL). The

mixture was irradiated for 12 hours using a UV LED source (Vishay, VLMU3510-365-130) while stirring at a speed of 1000 rpm. The radiant power of the UV LED source was 690 mW at a wavelength of 365 nm. After irradiation, the SrTiO<sub>3</sub>-Au<sub>9</sub>-CrO<sub>x</sub> powder was collected by centrifugation and washed with deionised water. ICP-MS analysis determined that approximately 20 % of all available Cr was deposited onto the SrTiO<sub>3</sub>-Au<sub>9</sub> particles.



**Scheme 7.1:** Experimental procedure of (a)  $Au_9$  deposition on  $SrTiO_3$  particles and (b) photodeposition of  $CrO_x$  onto  $SrTiO_3$ - $Au_9$  particles.

#### Heat treatment

All samples were heated under vacuum (below  $1 \times 10^{-3}$  mbar) at 200 °C for 10 min to remove the ligands before photocatalytic testing <sup>49</sup>. XPS samples were heated at the same temperature and for the same time; spectra were recorded immediately after heating.

#### 7.3.2 Methods

#### X-ray Photoelectron Spectroscopy

Experimental details for X-ray photoelectron spectroscopy (XPS) are discussed in Section 2.1. In this chapter, high-resolution XPS spectra were recorded at a pass energy of 10 eV for Au 4f, Sr 3d, Cr 2p, Ti 2p, P 2p, O 1s and C 1s. At a pass energy of 10 eV the FWHM of the Ag 3d<sub>5/2</sub> peak is < 1 eV. The uncertainty of the peak positions is typically 0.2 eV. The XPS spectra were calibrated using the main carbon peak at 285 eV to correct for charging effects<sup>50</sup>.

# Scanning Transmission Electron Microscopy

Experimental details for Scanning transmission electron microscopy (STEM) are discussed in Section 2.9. In this chapter, it should be noted that STEM imaging can alter the samples due to the energy deposited by the electrons impinging on the sample (vide infra).

#### X-ray Diffraction

Experimental details for X-ray diffraction (XRD) are discussed in Section 2.4.

# Photocatalytic Water Splitting Reactions

Overall Water Splitting. The photocatalytic activity was tested using a high-pressure Hg lamp (400 W, main wavelength at 365 nm) within a quartz cell (see Scheme E1)<sup>19</sup>. The reaction was carried out in a closed gas flow system with Ar flow of 30 mL/min using a solution containing 500 mg of the photocatalyst(i.e. SrTiO<sub>3</sub>, SrTiO<sub>3</sub>-Au<sub>9</sub> and SrTiO<sub>3</sub>-Au<sub>9</sub>-CrO<sub>x</sub> after heating) with 350 mL of water. Before the photocatalysis experiment, the reaction cell was purged with Ar gas bubbling through the water for 1 h to ensure that air was completely removed from the reaction vessel.

<u>Hydrogen Evolution Using a Sacrificial Reagent.</u> This experiment was performed using the same procedure as overall water splitting except that 10% of the water is replaced with methanol.

<u>Oxygen Photoreduction Reaction.</u> Using the same procedure as hydrogen evolution with the sacrificial reagent, oxygen was introduced into the reaction with a closed gas flow system using a 7:3 mixture of Ar to air at a flow rate of 30 mL/min.

# 7.4 Results and Discussion

# 7.4.1 Before heating

# Characterisation of SrTiO<sub>3</sub>-Au<sub>9</sub> and SrTiO<sub>3</sub>-Au<sub>9</sub>-CrO<sub>x</sub>

 phosphine-protected Au<sub>9</sub> clusters is known to be 84.8–85.2 eV, with a typical FWHM of  $1.7 \pm 0.2$  eV. The peak position for agglomerated Au<sub>9</sub> clusters shifts to 83.7–84.1 eV with FWHM of  $1.0 \pm 0.2$  eV<sup>23, 51-55</sup>. The Au 4f spectrum of SrTiO<sub>3</sub>-Au<sub>9</sub> shows 83% of the intensity at the HBP position, corresponding to non-agglomerated Au<sub>9</sub> clusters, and 17% at the LBP, corresponding to agglomerated Au<sub>9</sub> clusters. The SrTiO<sub>3</sub>-Au<sub>9</sub>-CrO<sub>x</sub> shows 90% of the Au 4f spectrum intensity at the HBP position and 10% at the LBP position. The LBP of SrTiO<sub>3</sub>-Au<sub>9</sub> has a slightly higher percentage than SrTiO<sub>3</sub>-Au<sub>9</sub>-CrO<sub>x</sub>, which can be attributed to a somewhat higher degree of agglomeration of the Au<sub>9</sub> clusters in SrTiO<sub>3</sub>-Au<sub>9</sub> without a CrO<sub>x</sub> layer. However, more than 80% of the Au 4f intensity for both samples are at the HBP, indicating that most of the Au<sub>9</sub> clusters remain non-agglomerated. It is important to note that the triphenylphosphine (PPh<sub>3</sub>) ligands are difficult to determine using XPS due to the overlapping energies of P 2p and Sr 3d peaks (see Figure E1)<sup>56</sup>.

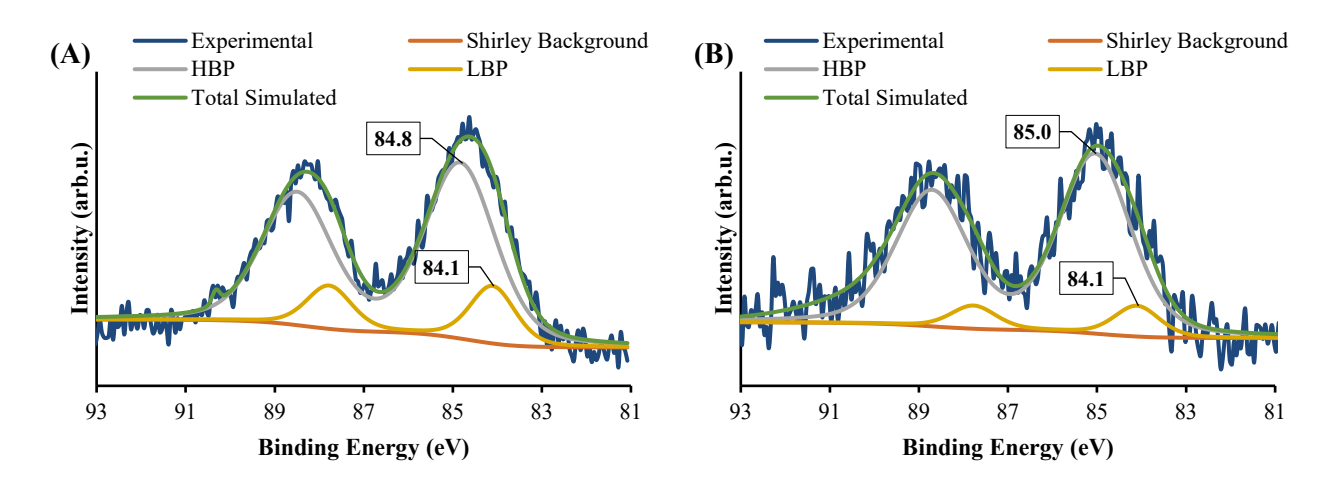


**Figure 7.1**: XPS spectra of Au 4f of (A) Au<sub>9</sub> deposited on  $SrTiO_3$  and (B)  $SrTiO_3$ -Au<sub>9</sub> after photodeposition of a  $CrO_x$  layer.

The state of Cr photodeposited on  $SrTiO_3$ -Au<sub>9</sub> was investigated using XPS. Figure 7.2 shows the Cr 2p spectrum of  $SrTiO_3$ -Au<sub>9</sub>-CrO<sub>x</sub> before heating. The Cr 2p spectrum was fitted with a single doublet peak ( $2p_{3/2}$  and  $2p_{1/2}$ ). It was fitted by including the Ti 2s energy loss peak, which occurs in the same energy region. In our previous work, the Cr 2p peak was described and fitted using a fixed relation between the intensity of the Ti  $2p_{3/2}$  and the Ti 2s loss peak <sup>57</sup>. The Cr  $2p_{3/2}$  peak is found at  $577.4 \pm 0.2$  eV, which can be identified from literature reference data as being  $Cr(OH)_3^{58}$ . It should be noted that this is different to the binding energy of  $Cr_2O_3$  and will be discussed below (vide infra).

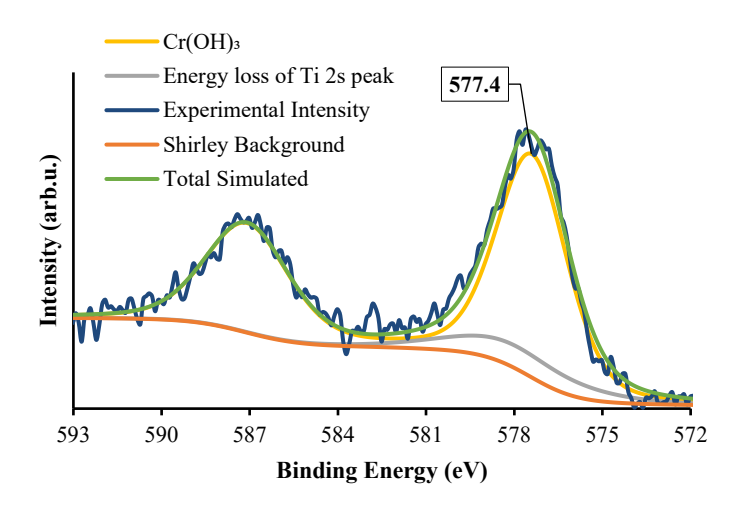


*Figure 7.2*: XPS Cr 2p spectrum of  $SrTiO_3$ -Au<sub>9</sub> after photodeposition of a  $CrO_x$  layer.

Figure 7.3 shows the HAADF-STEM image of Au<sub>9</sub> deposited onto the surface of SrTiO<sub>3</sub>. The figure includes EDX elemental mapping of Au and Ti as well as line analysis of Au. It should be noted that P was difficult to analyse using STEM-EDX due to the intensity of P in EDX being significantly lower than that of Au and due to overlapping of the P  $K_{\alpha}$  and Au  $M_{\alpha}$  peaks<sup>59</sup>. In Figure 7.3A, the HAADF-STEM image shows small bright particles, which can be identified from the EDX mapping as Au features. The line analysis of L1 and L2 confirmed the size of Au features as approximately 5.5 and 1.3 nm, respectively. The HAADF-STEM image shows further small Au clusters, indicated with red circles, that were not detected clearly by EDX mapping (see Figure 7.3A). A possible reason for this is that EDX is not suitable for size analysis due to its lower spatial resolution compared with STEM. The size of these Au clusters in the HAADF image is approximately 0.7 - 0.9 nm. Previous studies have shown that the size of a single Au<sub>9</sub> cluster is approximately  $0.6 \pm 0.2$  nm<sup>54</sup>. In the present experiment, the small Au clusters (0.7 - 0.9 nm) in the HAADF-STEM image are of a similar size as Au<sub>9</sub>. Therefore, we conclude that these are non-agglomerated clusters. The Au feature from the STEM-EDX line analysis (Figure 7.3L1), which is 5.5 nm in size, is due to many adjacent Au<sub>9</sub> clusters or agglomerations of Au clusters. The Au feature from L2 is 1.3 nm in size, suggesting two adjacent clusters or an agglomeration of two clusters due to the effect of the high-energy STEM electron beam (see Figure E2 for more information). This finding is in line with the XPS data that suggested some of the Au clusters had agglomerated on SrTiO<sub>3</sub>-Au<sub>9</sub> STEM shows the Au cluster sizes for only a small selected area of the sample, which could also be subject to electron beam damage of the clusters. Therefore, the XPS data is considered as being more accurate in identifying the fraction of agglomerated and non-agglomerated clusters because XPS averages over a significant larger number of Au cluster compared to STEM and also because XPS does not cause damage to the clusters resulting in their agglomeration 51, 52. XPS shows that 83% of Au clusters remain nonagglomerated.

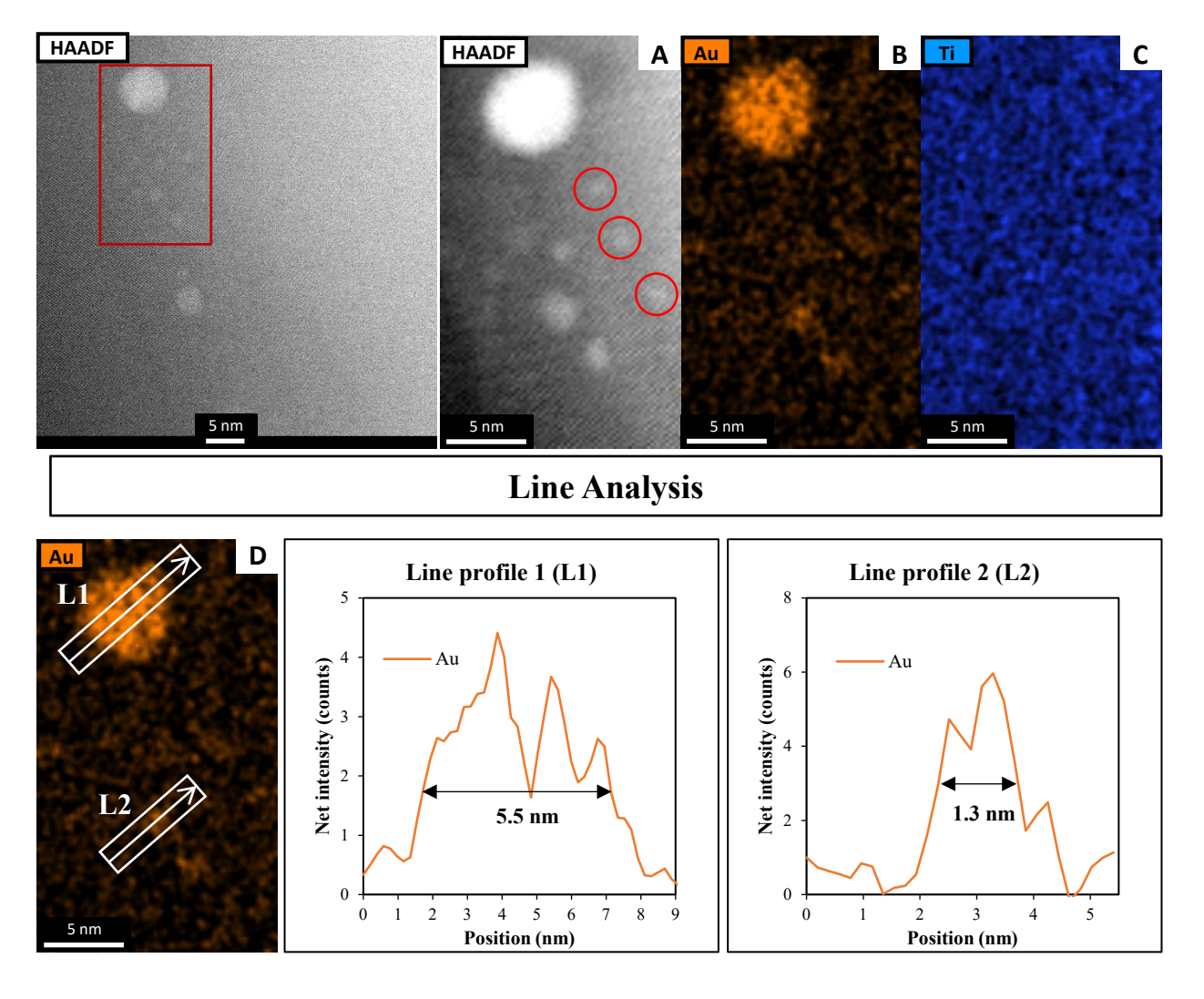


**Figure 7.3**: (A) HAADF-STEM image with EDX elemental mapping of (B) Au and (C) Ti in SrTiO<sub>3</sub>-Au<sub>9</sub> before heating and (D) line analyses of the Au signal.

A HAADF-STEM image of SrTiO<sub>3</sub>-Au<sub>9</sub>-Cr(OH)<sub>3</sub> with EDX elemental mapping and a line analysis of Cr, Au and Ti is shown in Figure 7.4. Figure 7.4A-C shows the first STEM mapping region which is focused on the edge of SrTiO<sub>3</sub>-Au<sub>9</sub>-Cr(OH)<sub>3</sub> to determine the thickness and distribution of Cr(OH)<sub>3</sub> at the surface of SrTiO<sub>3</sub>. The STEM-EDX elemental map L1 at the edge of the SrTiO<sub>3</sub>-Au<sub>9</sub>-Cr(OH)<sub>3</sub> shows that the Cr(OH)<sub>3</sub> layer is distributed over the entire SrTiO<sub>3</sub> surface (Figure 7.4B) and has a thickness of 1.6 nm (Figure 7.4L1). The line analysis of Cr, Ti and Au (L2) shows that the presence of Cr(OH)<sub>3</sub> around the Au clusters (Figure 7.4L2). Using the line analysis of L2 and L3 in Figure 7.4, the Au clusters are shown to be approximately 1.3 – 1.6 nm in diameter. This is similar to the size of the Au clusters determined for SrTiO<sub>3</sub>-Au<sub>9</sub> (i.e. without the Cr(OH)<sub>3</sub> covering layer, Figure 7.3). Note that the STEM-EDX mapping shows Au features with a larger diameter compared to a single Au<sub>9</sub> cluster. Here, the increase in the size of the Au clusters is most likely due to the effect of the highenergy STEM electron beam, (see Figure E2 for further information). Again, XPS is considered to be

the more accurate method for determining the extent of cluster agglomeration, which was determined to be 90% of Au clusters remain non-agglomerated on SrTiO<sub>3</sub> with Cr(OH)<sub>3</sub> coverage.

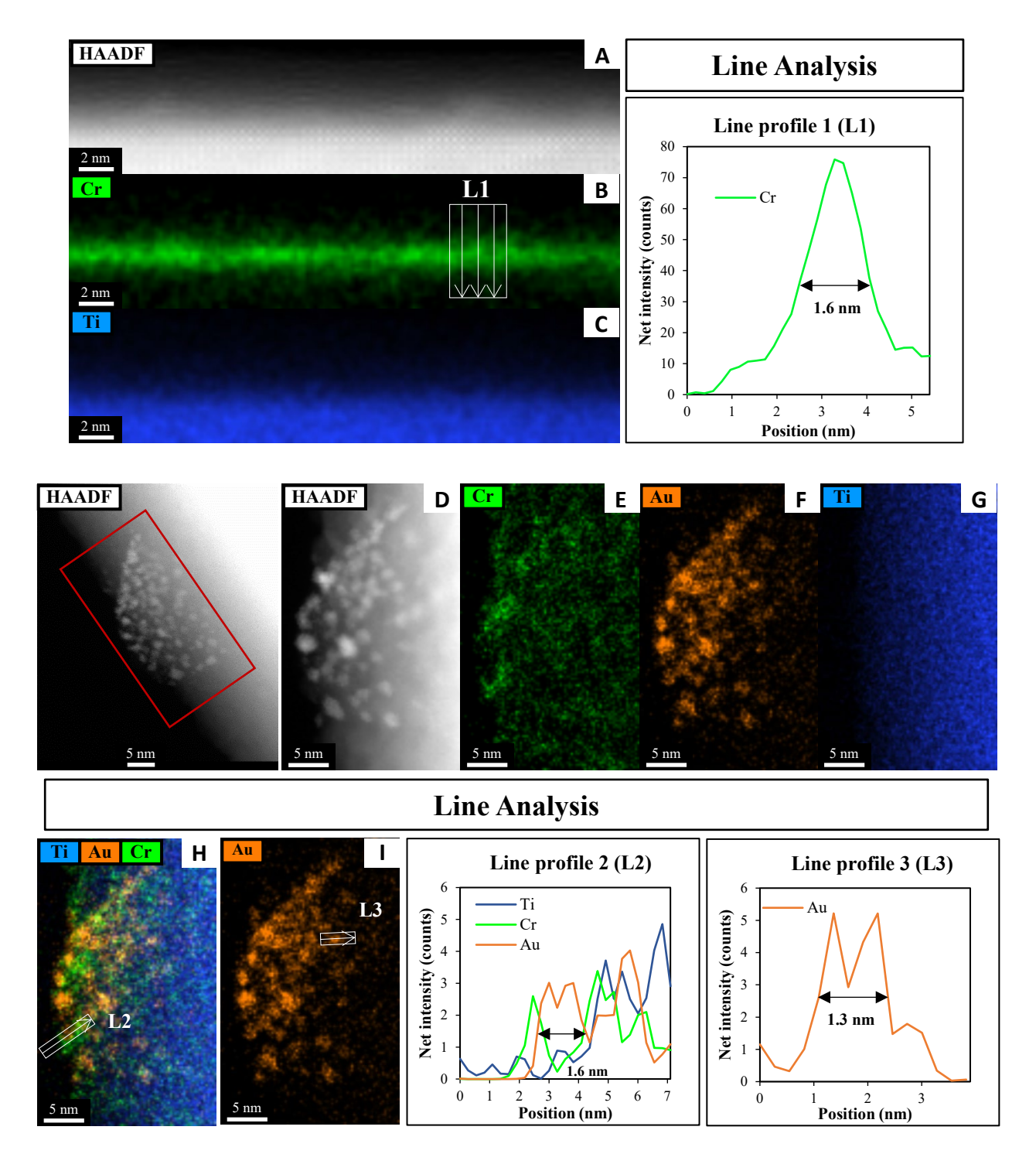


**Figure 7.4**: HAADF-STEM image with EDX elemental mapping and line analyses of the Cr, Au and Ti in SrTiO<sub>3</sub>-Au<sub>9</sub>-Cr(OH)<sub>3</sub>.

#### 7.4.2 After heating

Figure 7.5 shows the XPS Au 4f spectra of SrTiO<sub>3</sub>-Au<sub>9</sub> and SrTiO<sub>3</sub>-Au<sub>9</sub>-CrO<sub>x</sub> after heating (the CrO<sub>x</sub> notation is used again here because heating could change the chemical state of the Cr). The Au 4f

spectra are again fitted with a HBP and LBP doublet. The peak positions and FWHM are summarised in Table E1. As mentioned above, it is difficult to determine the state of PPh<sub>3</sub> ligands on SrTiO<sub>3</sub> using XPS, however, previous studies showed that PPh<sub>3</sub>-ligated Au<sub>9</sub> clusters are removed by heating at 200 °C for 10 min <sup>23, 49, 51-55</sup>. As shown in Figure 7.5A, the Au 4f spectrum for SrTiO<sub>3</sub>-Au<sub>9</sub> after heating is fitted with 50% Au clusters at HBP ( $85.4 \pm 0.2$  eV, FWHM of  $2.0 \pm 0.2$  eV) and 50% agglomerated clusters at LBP ( $83.7 \pm 0.2$  eV, FWHM of  $1.2 \pm 0.2$  eV). The feature at  $89.9 \pm 0.2$  eV corresponds to Ba  $4d_{5/2}$  due to contamination of the commercial SrTiO<sub>3</sub> (see Figure E3). After application of the CrO<sub>x</sub> overlayer and heating, the Au 4f spectrum for SrTiO<sub>3</sub>-Au<sub>9</sub>-CrO<sub>x</sub> is fitted with 65% and 35% of the Au intensity at the HBP ( $84.9 \pm 0.2$  eV, FWHM of  $2.0 \pm 0.2$  eV) and LBP ( $83.8 \pm 0.2$  eV, FWHM of  $1.2 \pm 0.2$  eV), respectively (see in Figure 7.5B). Thus, the comparison of the XPS results between the heated SrTiO<sub>3</sub>-Au<sub>9</sub> and SrTiO<sub>3</sub>-Au<sub>9</sub>-CrO<sub>x</sub> samples indicated that the photodeposition of CrO<sub>x</sub> improves the stability of the phosphine-protected Au<sub>9</sub> clusters, with the majority retaining their size after removal of the ligands through heating to 200 °C.

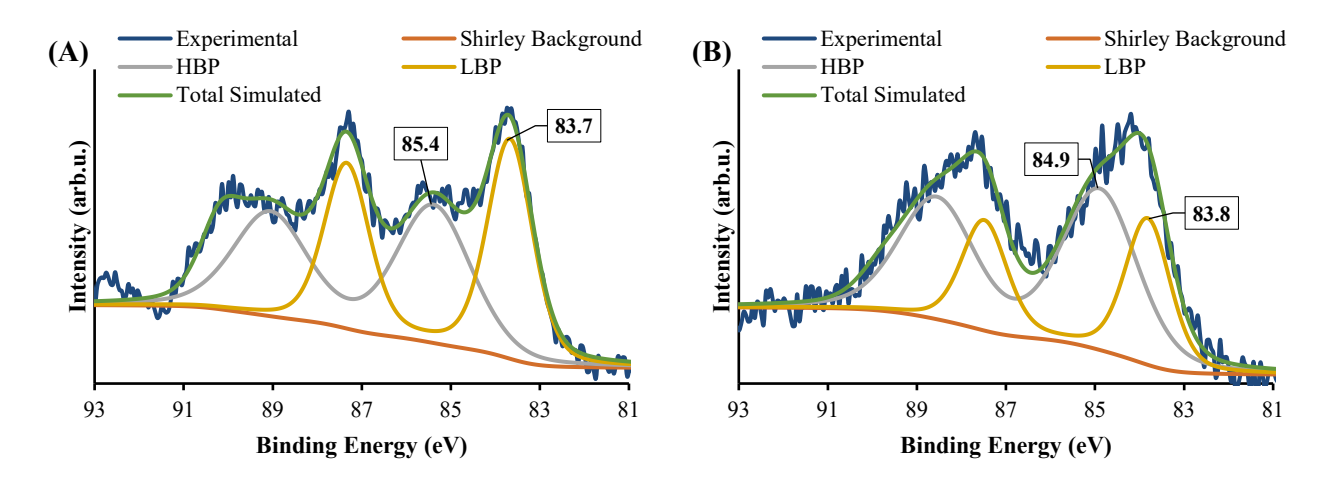
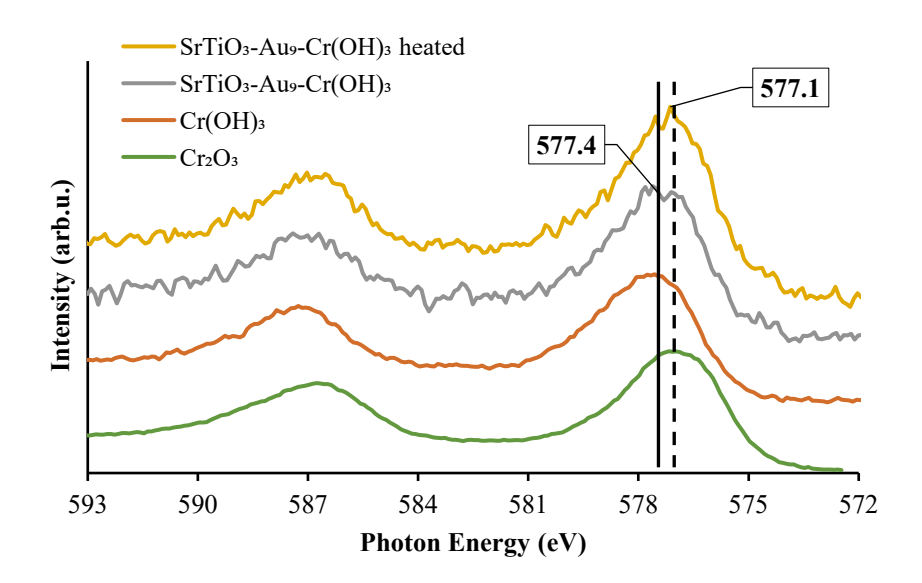


Figure 7.5: XPS spectra of Au 4f after heating of (A) SrTiO<sub>3</sub>-Au<sub>9</sub> and (B) SrTiO<sub>3</sub>-Au<sub>9</sub>-CrO<sub>x</sub>.

XPS Cr 2p spectra of SrTiO<sub>3</sub>-Au<sub>9</sub>-Cr(OH)<sub>3</sub> before and SrTiO<sub>3</sub>-Au<sub>9</sub>-CrO<sub>x</sub> after heating are shown in Figure 7.6, along with reference spectra for  $Cr_2O_3$  and  $Cr(OH)_3$ . A summary of the Cr  $2p_{3/2}$  peak positions is presented in Table E4. The Cr  $2p_{3/2}$  peak for SrTiO<sub>3</sub>-Au<sub>9</sub>-CrO<sub>x</sub> after heating shifts slightly to a low binding energy of 577.1  $\pm 0.2$  eV (Figure E4), corresponding to  $Cr_2O_3$  <sup>60</sup>. This confirms that a reduction of the  $Cr(OH)_3$  layer to  $Cr_2O_3$  occurs by heating. This finding is in agreement with a previous report that heating reduces photodeposited  $Cr(OH)_3$  layer to  $Cr_2O_3$  <sup>16</sup>.



**Figure 7.6**: XPS spectra of  $Cr\ 2p$  of  $SrTiO_3$ - $Au_9$ - $Cr(OH)_3$  before heating and  $SrTiO_3$ - $Au_9$ - $CrO_x$  after heating with reference spectrum of  $Cr_2O_3$  and  $Cr(OH)_3$  (Figure E4 shows complete fitting to all components).

#### Photocatalytic water splitting of SrTiO<sub>3</sub>-Au<sub>9</sub> and SrTiO<sub>3</sub>-Au<sub>9</sub>-Cr<sub>2</sub>O<sub>3</sub>.

Figure 7.7 shows the H<sub>2</sub> production by overall water splitting of SrTiO<sub>3</sub>, SrTiO<sub>3</sub>-Au<sub>9</sub> and SrTiO<sub>3</sub>-Au<sub>9</sub>-Cr<sub>2</sub>O<sub>3</sub> (i.e. after heating at 200 °C for 10 mins to remove the ligands) over a period of seven hours. Note that the O<sub>2</sub> production is not shown due to the very low O<sub>2</sub> production. This suggests that another oxidation reaction is occurring more readily than OH- to O2. One possible reaction is the oxidation of residual PPh<sub>3</sub> ligands on the catalyst surface. Another possibility could be the oxidation of adventitious hydrocarbons absorbed onto the surface when the catalyst is exposed to atmosphere. The H<sub>2</sub> production of SrTiO<sub>3</sub>-Au<sub>9</sub> is observed to be more than two times higher compared with that of SrTiO<sub>3</sub> during the 7 h irradiation period. Surprisingly, SrTiO<sub>3</sub>-Au<sub>9</sub>-Cr<sub>2</sub>O<sub>3</sub> shows decreased H<sub>2</sub> production compared to SrTiO<sub>3</sub>-Au<sub>9</sub> but is higher than SrTiO<sub>3</sub>. In order to better understand the effect of the overlayer, hydrogen evolution using methanol as a sacrificial reagent was performed with and without air (oxygen) in the reaction system to investigate the role of the back reaction (oxygen photoreduction reaction). Figure E5 shows that the SrTiO<sub>3</sub> and SrTiO<sub>3</sub>-Au<sub>9</sub> samples suffer a large drop in H<sub>2</sub> production after O<sub>2</sub> was introduced into the reaction but not the SrTiO<sub>3</sub>-Au<sub>9</sub>-Cr<sub>2</sub>O<sub>3</sub> sample. The drop in H<sub>2</sub> production is due to the oxygen photoreduction reaction occurring at the surface of the cocatalyst. This indicates that the back reaction is suppressed with the Cr<sub>2</sub>O<sub>3</sub> overlayer for SrTiO<sub>3</sub>-Au<sub>9</sub>-Cr<sub>2</sub>O<sub>3</sub>.

While the addition of a CrO<sub>x</sub> overlayer is expected to increase the H<sub>2</sub> production rate for the overall water splitting reaction due to blocking the back reaction <sup>29-38</sup>, there is a possibility for the observed decrease in H<sub>2</sub> production rate due to an even distribution and a too thick Cr<sub>2</sub>O<sub>3</sub> overlayer on the

surface of the photocatalyst (SrTiO<sub>3</sub>). STEM images shows that  $Cr_2O_3$  is deposited in a homogeneous layer with a thickness of c.a. 1.6 nm across the catalyst (Figure 7.4). Having a uniform and too thick  $Cr_2O_3$  layer covering the entire surface could result in stopping the oxidation reaction to occur through blocking the respective sites on the catalyst surface, which blocks the overall water splitting reaction. Kurashige et al. noted a similar result in their study of an  $Au_{25}$ - $CrO_x$ - $BaLa_4Ti_4O_{15}$  system in which  $CrO_x$  was deposited at various concentrations  $(0.1-1.5 \text{ wt \%})^{19}$ . The authors found that higher Cr contents led to an increase in the coverage and thickness of the  $CrO_x$  layer (1.2-2.0 nm), which significantly decreased the water splitting rate. In the above-mentioned studies, this decrease in activity was assumed to be due to a reduction in the numbers of  $O_2$  generation sites<sup>19</sup>. This shows that the amount of  $CrO_x$  deposited impacts here the O reduction sites rather the O reduction sites.

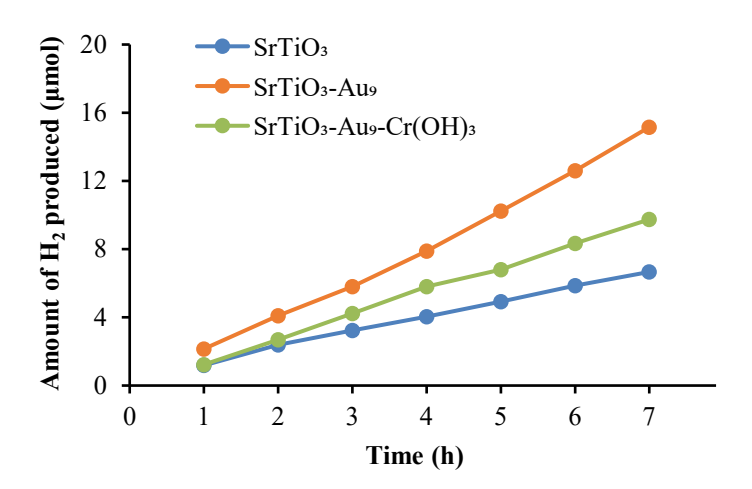


**Figure 7.7**: H<sub>2</sub> evolution by overall photocatalytic water splitting of SrTiO<sub>3</sub>, SrTiO<sub>3</sub>-Au<sub>9</sub> and SrTiO<sub>3</sub>-Au<sub>9</sub>-Cr<sub>2</sub>O<sub>3</sub> (i.e. after heating to remove the ligands).

#### 7.4.3 After photocatalysis

## Determination of $Au_9$ Size After photocatalysis and the influence of the $CrO_x$ layer on agglomeration

Figure 7.8 shows the XPS Au 4f spectra of  $SrTiO_3$ -Au<sub>9</sub> and  $SrTiO_3$ -Au<sub>9</sub>-CrO<sub>x</sub> after 7 h irradiation during the water splitting reaction (the  $CrO_x$  notation is used again here because photocatalysis could change the chemical state of the Cr). A summary of the peak positions and FWHM is presented in Table E1. After 7 h irradiation, the spectrum of  $SrTiO_3$ -Au<sub>9</sub> (Figure 7.8A) shows that 30% of the Au 4f spectrum is at the HBP position (non-agglomerated clusters), and 70% is at the LBP position (agglomerated clusters). The Ba  $4d_{5/2}$  peak appears at  $89.9 \pm 0.2$  eV corresponding to the commercial contamination of  $SrTiO_3$  (see Figure E3). The spectrum of  $SrTiO_3$ -Au<sub>9</sub>-CrO<sub>x</sub> after 7 h irradiation (Figure 7.8B) was fitted with 63% non-agglomerated Au clusters at the HBP and 37% agglomerated Au clusters at the LBP, which is almost the same as after heating (see Figure 7.5B). Thus, the

comparison of the XPS results between the SrTiO<sub>3</sub>-Au<sub>9</sub> and SrTiO<sub>3</sub>-Au<sub>9</sub>-CrO<sub>x</sub> indicated that the photodeposition of CrO<sub>x</sub> significantly improves the stability of the phosphine-protected Au<sub>9</sub> clusters and retains their size after 7 h of water splitting reaction with 10% methanol as a sacrificial reagent (see Figure E6 for additional spectra).

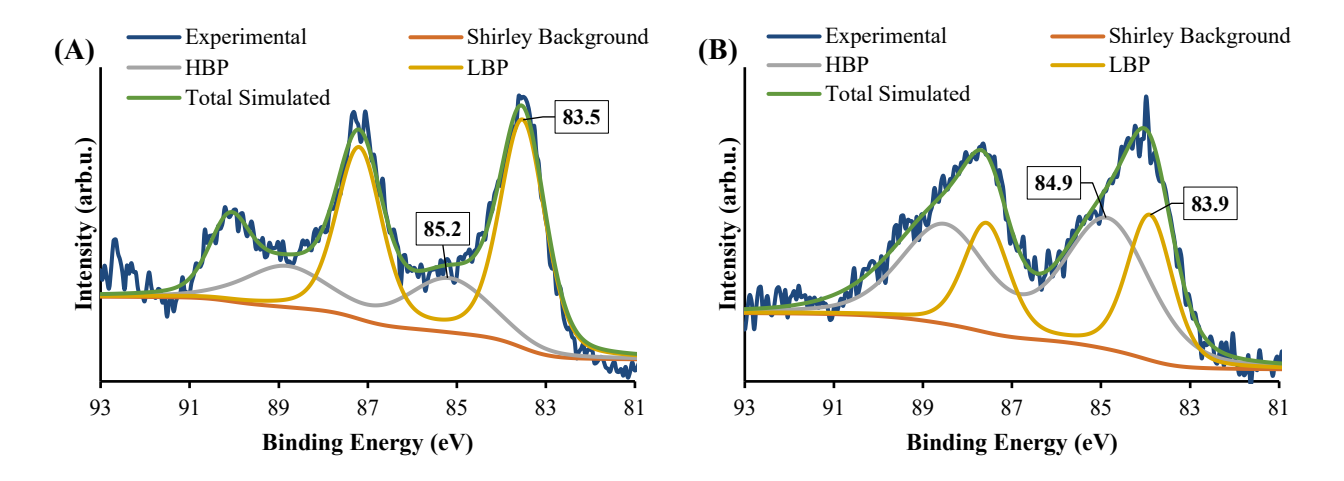
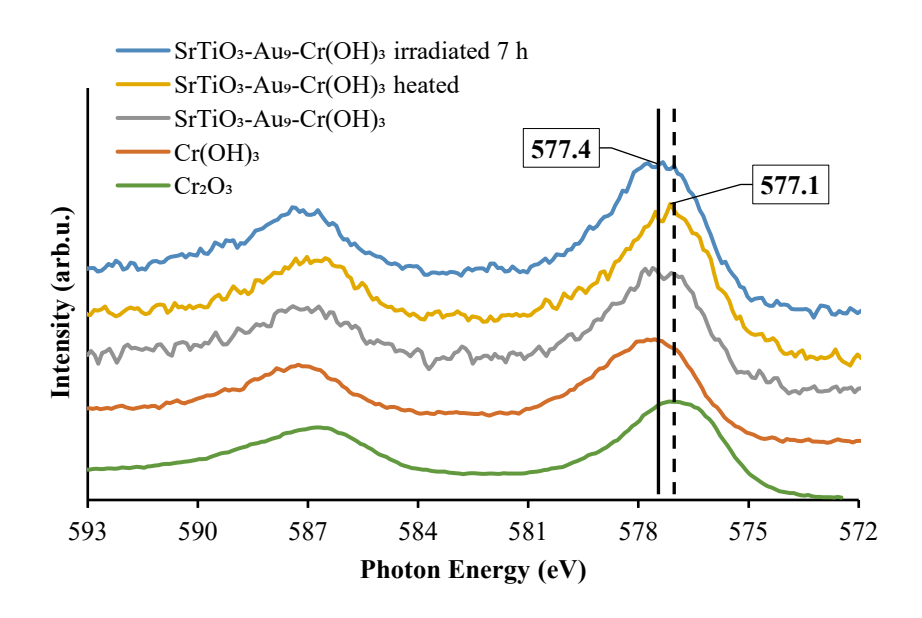


Figure 7.8: XPS spectra of Au 4f after 7 h irradiation of (A) SrTiO<sub>3</sub>-Au<sub>9</sub> and (B) SrTiO<sub>3</sub>-Au<sub>9</sub>-CrO<sub>x</sub>.

XPS Cr 2p spectra of  $SrTiO_3$ - $Au_9$ - $CrO_x$  before and after heating and after 7 h irradiation, with reference spectra of  $Cr_2O_3$  and  $Cr(OH)_3$ , are shown in Figure 7.9 and summarised in Table E4. After 7 h irradiation, the Cr  $2p_{3/2}$  peak for  $SrTiO_3$ - $Au_9$ - $CrO_x$  appears at  $577.4 \pm 0.2$  eV (Figure E7), corresponding to  $Cr(OH)_3$ , indicating that the Cr layer converts back to  $Cr(OH)_3$  during photocatalysis  $^{16}$ .



**Figure 7.9**: XPS spectra of Cr 2p of SrTiO<sub>3</sub>-Au<sub>9</sub>-Cr(OH)<sub>3</sub> before heating, SrTiO<sub>3</sub>-Au<sub>9</sub>-Cr<sub>2</sub>O<sub>3</sub> after heating and SrTiO<sub>3</sub>-Au<sub>9</sub>-CrOx after 7 h irradiation with reference spectrum of Cr<sub>2</sub>O<sub>3</sub> and Cr(OH)<sub>3</sub> (Figure E7 shows complete fitting to all components).

A HAADF-STEM image of SrTiO<sub>3</sub>-Au<sub>9</sub> after 7 h irradiation with EDX elemental mapping of Au and Ti is shown in Figure 7.10 (and summarised in Table E1). The image shows that the Au<sub>9</sub> clusters have agglomerated into large particles after 7 h irradiation with no Au clusters left on the surface. The line analysis of Au particles (L1 and L2) confirmed the size of Au particles as approximately 3.9–4.6 nm, with some Au particles having a size of 5.0–6.9 nm (as indicated with arrows in Figure 7.10D).

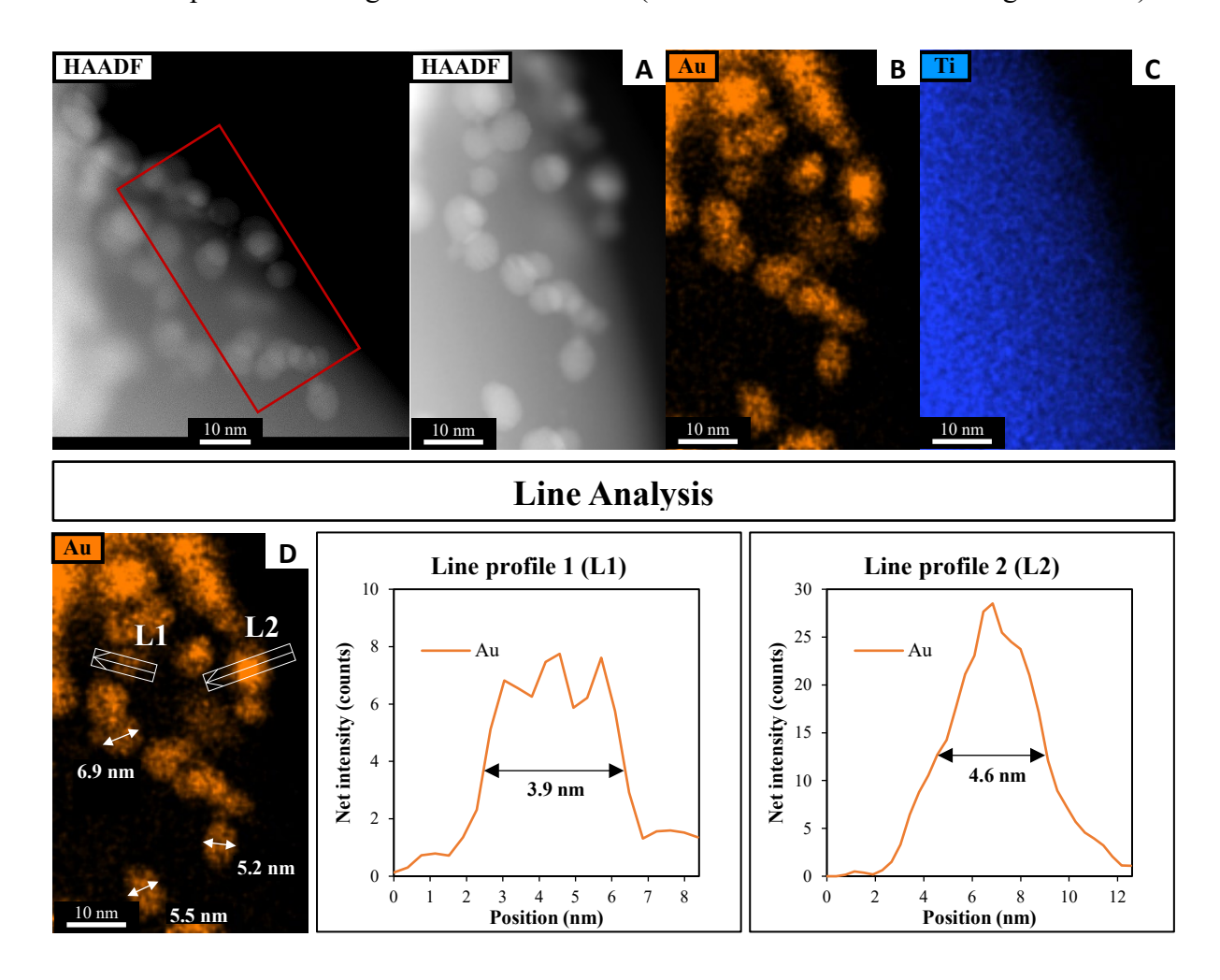


**Figure 7.10**: (A) HAADF-STEM image with EDX elemental mapping of (B) Au and (C) Ti in SrTiO<sub>3</sub>-Au<sub>9</sub> after 7 h irradiation and (D) line analyses of the Au signal

A HAADF-STEM image of SrTiO<sub>3</sub>-Au<sub>9</sub>-Cr(OH)<sub>3</sub> after 7 h irradiation with EDX elemental mapping of Au, Cr and Ti is presented in Figure 7.11. The typical size of the Au clusters as determined using line analysis (L1 and L2) range from 1.4 to 1.6 nm. This size is nearly identical to Au clusters determined before heating and photocatalysis irradiation (Figure 7.4 and Figure E8). Note that STEM-EDX elemental mapping shows that some Au features are 2–2.7 nm in size. As discussed above, the slight increase in the size of the Au clusters is assumed to be caused either by adjacent clusters or agglomeration of Au<sub>9</sub> clusters due to the effect of the STEM electron beam (this is further discussed around Figure E2). As outlined above, XPS is averaged over a significant larger number of Au clusters and is thus considered as being a more representative analysis whereas STEM is averaged over a

small selected area of the sample and also causes beam damage. Through XPS analysis it is shown that 63% of Au clusters remain non-agglomerated (Figure 7.8B, Table E1).

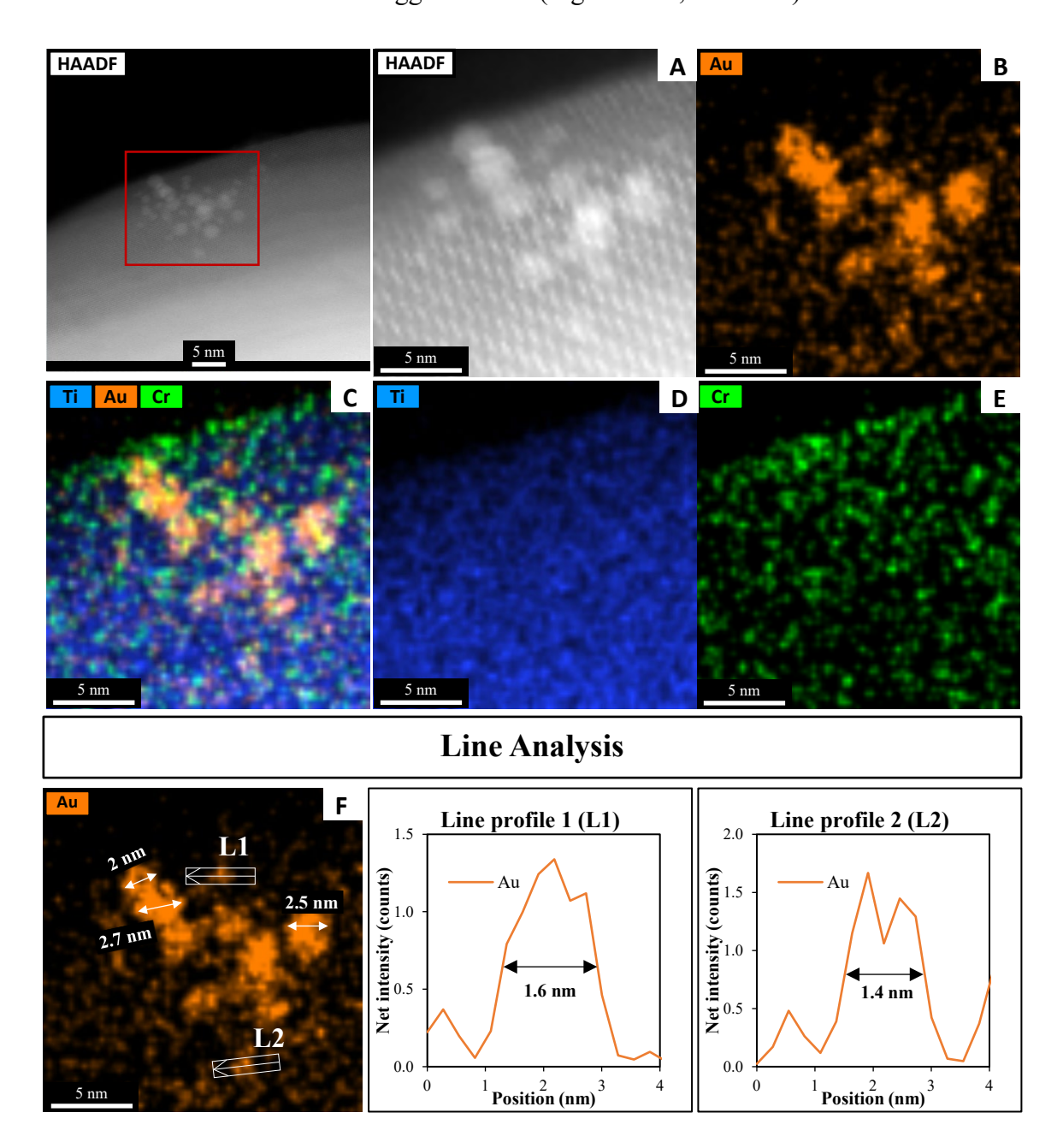


**Figure 7.11**: (A) HAADF-STEM image with EDX elemental mapping of (B) Au, (C) Ti. Au and Cr, (D) Ti and (E) Cr in SrTiO<sub>3</sub>-Au<sub>9</sub>-Cr(OH)<sub>3</sub> after 7 h irradiation and (F) line analyses of the Au signal.

#### 7.5 Conclusions

We have demonstrated that application of a Cr(OH)<sub>3</sub> overlayer before heating and photocatalytic reaction protects the phosphine-ligated Au<sub>9</sub> clusters from agglomeration after the removal of the ligands. The photocatalytic activity of Au clusters deposited on SrTiO<sub>3</sub> was investigated as well as the influence of the addition of a Cr<sub>2</sub>O<sub>3</sub> overlayer. For SrTiO<sub>3</sub>-Au<sub>9</sub>, the Au clusters agglomerated, forming large particles (up to 8 nm in size) after the overall photocatalytic water splitting reaction.

The results show that only 30% of the Au clusters remain non-agglomerated on the SrTiO<sub>3</sub> surface after 7 h irradiation. When a Cr(OH)<sub>3</sub> overlayer was added, more than 60% Au clusters on the surface of SrTiO<sub>3</sub> remained non-agglomerated after heating and with 7 h of photocatalytic water splitting under UV irradiation. The Cr(OH)<sub>3</sub> layer was converted to Cr<sub>2</sub>O<sub>3</sub> upon heating and was found to be returned to Cr(OH)<sub>3</sub> after photocatalytic water splitting. The H<sub>2</sub> production rate reduced after photodeposition of a Cr(OH)<sub>3</sub> layer. It is assumed that the decrease of the H<sub>2</sub> production is due to the even distribution and thickness of the Cr<sub>2</sub>O<sub>3</sub> layer on the surface of the semiconductor photocatalyst, blocking the O<sub>2</sub> generating sites then leading to a decrease of the overall photocatalytic water splitting reaction. Although the deposition of a Cr(OH)<sub>3</sub> protective layer has been demonstrated for Au<sub>9</sub> clusters deposited onto a SrTiO<sub>3</sub> substrate, this approach could be applied to other sized Au clusters on other metal oxide substrates.

#### 7.6 References

- 1. Borman, V.; Pushkin, M.; Tronin, V.; Troyan, V., Evolution of the Electronic Properties of Transition Metal Nanoclusters on Graphite Surface. *Journal of Experimental and Theoretical Physics* **2010**, *110*, 1005-1025.
- 2. Sudheeshkumar, V.; Sulaiman, K. O.; Scott, R. W. J., Activation of atom-precise clusters for catalysis. *Nanoscale Advances* **2020**, *2* (1), 55-69.
- 3. Jin, R., Quantum sized, thiolate-protected gold nanoclusters. *Nanoscale* **2010**, *2* (3), 343-362.
- 4. Castro, T.; Reifenberger, R.; Choi, E.; Andres, R. P., Size-dependent melting temperature of individual nanometer-sized metallic clusters. *Physical Review B* **1990**, *42* (13), 8548-8556.
- 5. Jin, R.; Zeng, C.; Zhou, M.; Chen, Y., Atomically Precise Colloidal Metal Nanoclusters and Nanoparticles: Fundamentals and Opportunities. *Chemical Reviews* **2016**, *116* (18), 10346-10413.
- 6. Liu, L.; Corma, A., Metal Catalysts for Heterogeneous Catalysis: From Single Atoms to Nanoclusters and Nanoparticles. *Chemical Reviews* **2018**, *118* (10), 4981-5079.
- 7. Howard-Fabretto, L.; Andersson, G. G., Metal Clusters on Semiconductor Surfaces and Application in Catalysis with a Focus on Au and Ru. *Advanced Materials* **2020**, *32* (18), 1904122.
- 8. Alarawi, A.; Ramalingam, V.; He, J.-H., Recent advances in emerging single atom confined two-dimensional materials for water splitting applications. *Materials Today Energy* **2019**, *11*, 1-23.
- 9. Kurashige, W.; Mori, Y.; Ozaki, S.; Kawachi, M.; Hossain, S.; Kawawaki, T.; Shearer, C. J.; Iwase, A.; Metha, G. F.; Yamazoe, S.; Kudo, A.; Negishi, Y., Activation of Water-Splitting Photocatalysts by Loading with Ultrafine Rh–Cr Mixed-Oxide Cocatalyst Nanoparticles. *Angewandte Chemie International Edition* **2020**, *59* (18), 7076-7082.
- 10. Yang, S.; Ding, S.; Zhao, C.; Huo, S.; Yu, F.; Fang, J.; Yang, Y., Ligand-free Au nanoclusters/g-C3N4 ultra-thin nanosheets composite photocatalysts for efficient visible-light-driven photocatalytic H2 generation. *Journal of Materials Science* **2021**, *56* (24), 13736-13751.
- 11. Wang, C.; Lv, P.; Xue, D.; Cai, Y.; Yan, X.; Xu, L.; Fang, J.; Yang, Y., Zero-Dimensional/Two-Dimensional Au25(Cys)18 Nanoclusters/g-C3N4 Nanosheets Composites for Enhanced Photocatalytic Hydrogen Production under Visible Light. *ACS Sustainable Chemistry & Engineering* **2018**, *6* (7), 8447-8457.
- 12. Kurashige, W.; Niihori, Y.; Sharma, S.; Negishi, Y., Precise synthesis, functionalization and application of thiolate-protected gold clusters. *Coordination Chemistry Reviews* **2016**, *320-321*, 238-250.
- 13. Negishi, Y.; Mizuno, M.; Hirayama, M.; Omatoi, M.; Takayama, T.; Iwase, A.; Kudo, A., Enhanced Photocatalytic Water Splitting by BaLa4Ti4O15 Loaded with ~1 nm Gold Nanoclusters Using Glutathione-protected Au25 Clusters. *Nanoscale* **2013**, *5* (16), 7188-7192.
- 14. Negishi, Y.; Matsuura, Y.; Tomizawa, R.; Kurashige, W.; Niihori, Y.; Takayama, T.; Iwase, A.; Kudo, A., Controlled Loading of Small Aun Clusters (n = 10–39) onto BaLa4Ti4O15 Photocatalysts: Toward an Understanding of Size Effect of Cocatalyst on Water-Splitting Photocatalytic Activity. *The Journal of Physical Chemistry C* **2015**, *119* (20), 11224-11232.
- 15. Kurashige, W.; Hayashi, R.; Wakamatsu, K.; Kataoka, Y.; Hossain, S.; Iwase, A.; Kudo, A.; Yamazoe, S.; Negishi, Y., Atomic-Level Understanding of the Effect of Heteroatom Doping of the Cocatalyst on Water-Splitting Activity in AuPd or AuPt Alloy Cluster-Loaded BaLa4Ti4O15. *ACS Applied Energy Materials* **2019**, *2* (6), 4175-4187.
- 16. Kawawaki, T.; Kataoka, Y.; Hirata, M.; Akinaga, Y.; Takahata, R.; Wakamatsu, K.; Fujiki, Y.; Kataoka, M.; Kikkawa, S.; Alotabi, A. S.; Hossain, S.; Osborn, D. J.; Teranishi, T.; Andersson, G. G.; Metha, G. F.; Yamazoe, S.; Negishi, Y., Creation of High-Performance Heterogeneous Photocatalysts by Controlling Ligand Desorption and Particle Size of Gold Nanocluster. *Angewandte Chemie International Edition* **2021**, *60* (39), 21340-21350.
- 17. Andersson, G. G.; Golovko, V. B.; Alvino, J. F.; Bennett, T.; Wrede, O.; Mejia, S. M.; Al Qahtani, H. S.; Adnan, R.; Gunby, N.; Anderson, D. P., Phosphine-stabilised Au9 Clusters Interacting with Titania and Silica Surfaces: The First Evidence for the Density of States Signature of the Support-immobilised Cluster. *The Journal of chemical physics* **2014**, *141* (1), 014702.

- 18. Kurashige, W.; Kumazawa, R.; Mori, Y.; Negishi, Y., Au25 cluster-loaded SrTiO3 water-splitting photocatalyst; preparation and elucidation of the effect of cocatalyst refinement on photocatalytic activity. *Journal of Materials and Applications* **2018**, *7* (1), 1-11.
- 19. Kurashige, W.; Kumazawa, R.; Ishii, D.; Hayashi, R.; Niihori, Y.; Hossain, S.; Nair, L. V.; Takayama, T.; Iwase, A.; Yamazoe, S.; Tsukuda, T.; Kudo, A.; Negishi, Y., Au25-Loaded BaLa4Ti4O15 Water-Splitting Photocatalyst with Enhanced Activity and Durability Produced Using New Chromium Oxide Shell Formation Method. *The Journal of Physical Chemistry C* **2018**, *122* (25), 13669-13681.
- 20. Tan, C.-L.; Zhang, F.; Li, Y.-H.; Tang, Z.-R.; Xu, Y.-J., Au clusters-based visible light photocatalysis. *Research on Chemical Intermediates* **2021**, *47* (1), 29-50.
- 21. Adnan, R. H.; Madridejos, J. M. L.; Alotabi, A. S.; Metha, G. F.; Andersson, G. G., A Review of State of the Art in Phosphine Ligated Gold Clusters and Application in Catalysis. *Advanced Science* **2022**, *9* (15), 2105692.
- 22. Krishnan, G.; Eom, N.; Kirk, R. M.; Golovko, V. B.; Metha, G. F.; Andersson, G. G., Investigation of Phosphine Ligand Protected Au13 Clusters on Defect Rich Titania. *The Journal of Physical Chemistry C* **2019**, *123* (11), 6642-6649.
- 23. Krishnan, G.; Al Qahtani, H. S.; Li, J.; Yin, Y.; Eom, N.; Golovko, V. B.; Metha, G. F.; Andersson, G. G., Investigation of Ligand-Stabilized Gold Clusters on Defect-Rich Titania. *The Journal of Physical Chemistry C* **2017**, *121* (50), 28007-28016.
- 24. Weng, B.; Lu, K.-Q.; Tang, Z.; Chen, H. M.; Xu, Y.-J., Stabilizing ultrasmall Au clusters for enhanced photoredox catalysis. *Nature Communications* **2018**, *9* (1), 1543.
- 25. Maeda, K.; Teramura, K.; Lu, D.; Saito, N.; Inoue, Y.; Domen, K., Roles of Rh/Cr2O3 (Core/Shell) Nanoparticles Photodeposited on Visible-Light-Responsive (Ga1-xZnx)(N1-xOx) Solid Solutions in Photocatalytic Overall Water Splitting. *The Journal of Physical Chemistry C* **2007**, *111* (20), 7554-7560.
- 26. Sakamoto, N.; Ohtsuka, H.; Ikeda, T.; Maeda, K.; Lu, D.; Kanehara, M.; Teramura, K.; Teranishi, T.; Domen, K., Highly Dispersed Noble-metal/Chromia (Core/Shell) Nanoparticles as Efficient Hydrogen Evolution Promoters for Photocatalytic Overall Water Splitting under Visible Light. *Nanoscale* **2009**, *1* (1), 106-109.
- 27. Yoshida, M.; Takanabe, K.; Maeda, K.; Ishikawa, A.; Kubota, J.; Sakata, Y.; Ikezawa, Y.; Domen, K., Role and Function of Noble-Metal/Cr-Layer Core/Shell Structure Cocatalysts for Photocatalytic Overall Water Splitting Studied by Model Electrodes. *The Journal of Physical Chemistry C* **2009**, *113* (23), 10151-10157.
- 28. Maeda, K.; Sakamoto, N.; Ikeda, T.; Ohtsuka, H.; Xiong, A.; Lu, D.; Kanehara, M.; Teranishi, T.; Domen, K., Preparation of Core–Shell-Structured Nanoparticles (with a Noble-Metal or Metal Oxide Core and a Chromia Shell) and Their Application in Water Splitting by Means of Visible Light. *Chemistry A European Journal* **2010**, *16* (26), 7750-7759.
- 29. Maeda, K.; Teramura, K.; Lu, D.; Takata, T.; Saito, N.; Inoue, Y.; Domen, K., Photocatalyst Releasing Hydrogen from Water. *Nature* **2006**, *440* (7082), 295-295.
- 30. Maeda, K.; Teramura, K.; Masuda, H.; Takata, T.; Saito, N.; Inoue, Y.; Domen, K., Efficient Overall Water Splitting under Visible-Light Irradiation on (Ga1-xZnx)(N1-xOx) Dispersed with Rh–Cr Mixed-Oxide Nanoparticles: Effect of Reaction Conditions on Photocatalytic Activity. *The Journal of Physical Chemistry B* **2006**, *110* (26), 13107-13112.
- 31. Maeda, K.; Teramura, K.; Lu, D.; Takata, T.; Saito, N.; Inoue, Y.; Domen, K., Characterization of Rh–Cr Mixed-Oxide Nanoparticles Dispersed on (Ga1-xZnx)(N1-xOx) as a Cocatalyst for Visible-Light-Driven Overall Water Splitting. *The Journal of Physical Chemistry B* **2006**, *110* (28), 13753-13758.
- 32. Maeda, K.; Xiong, A.; Yoshinaga, T.; Ikeda, T.; Sakamoto, N.; Hisatomi, T.; Takashima, M.; Lu, D.; Kanehara, M.; Setoyama, T.; Teranishi, T.; Domen, K., Photocatalytic Overall Water Splitting Promoted by Two Different Cocatalysts for Hydrogen and Oxygen Evolution under Visible Light. *Angewandte Chemie International Edition* **2010**, *49* (24), 4096-4099.

- 33. Takata, T.; Jiang, J.; Sakata, Y.; Nakabayashi, M.; Shibata, N.; Nandal, V.; Seki, K.; Hisatomi, T.; Domen, K., Photocatalytic Water Splitting with a Quantum Efficiency of Almost Unity. *Nature* **2020**, *581* (7809), 411-414.
- 34. Maeda, K.; Lu, D.; Domen, K., Direct Water Splitting into Hydrogen and Oxygen under Visible Light by using Modified TaON Photocatalysts with d0 Electronic Configuration. *Chemistry A European Journal* **2013**, *19* (16), 4986-4991.
- 35. Maeda, K.; Domen, K., Photocatalytic Water Splitting: Recent Progress and Future Challenges. *The Journal of Physical Chemistry Letters* **2010**, *1* (18), 2655-2661.
- 36. Soldat, J.; Busser, G. W.; Muhler, M.; Wark, M., Cr2O3 Nanoparticles on Ba5Ta4O15 as a Noble-Metal-Free Oxygen Evolution Co-Catalyst for Photocatalytic Overall Water Splitting. *ChemCatChem* **2016**, *8* (1), 153-156.
- 37. Sanwald, K. E.; Berto, T. F.; Jentys, A.; Camaioni, D. M.; Gutiérrez, O. Y.; Lercher, J. A., Kinetic Coupling of Water Splitting and Photoreforming on SrTiO3-Based Photocatalysts. *ACS Catalysis* **2018**, *8* (4), 2902-2913.
- 38. Qureshi, M.; Shinagawa, T.; Tsiapis, N.; Takanabe, K., Exclusive Hydrogen Generation by Electrocatalysts Coated with an Amorphous Chromium-Based Layer Achieving Efficient Overall Water Splitting. *ACS Sustainable Chemistry & Engineering* **2017**, *5* (9), 8079-8088.
- 39. Pang, R.; Teramura, K.; Tatsumi, H.; Asakura, H.; Hosokawa, S.; Tanaka, T., Modification of Ga2O3 by an Ag-Cr core-shell cocatalyst enhances photocatalytic CO evolution for the conversion of CO2 by H2O. *Chemical Communications* **2018**, *54* (9), 1053-1056.
- 40. Tian, B.; Gao, W.; Zhang, X.; Wu, Y.; Lu, G., Water splitting over core-shell structural nanorod CdS@Cr2O3 catalyst by inhibition of H2-O2 recombination via removing nascent formed oxygen using perfluorodecalin. *Applied Catalysis B: Environmental* **2018**, *221*, 618-625.
- 41. Li, Z.; Zhang, F.; Han, J.; Zhu, J.; Li, M.; Zhang, B.; Fan, W.; Lu, J.; Li, C., Using Pd as a Cocatalyst on GaN–ZnO Solid Solution for Visible-Light-Driven Overall Water Splitting. *Catalysis Letters* **2018**, *148* (3), 933-939.
- 42. Busser, G. W.; Mei, B.; Weide, P.; Vesborg, P. C. K.; Stührenberg, K.; Bauer, M.; Huang, X.; Willinger, M.-G.; Chorkendorff, I.; Schlögl, R.; Muhler, M., Cocatalyst Designing: A Regenerable Molybdenum-Containing Ternary Cocatalyst System for Efficient Photocatalytic Water Splitting. *ACS Catalysis* **2015**, *5* (9), 5530-5539.
- 43. Bau, J. A.; Takanabe, K., Ultrathin Microporous SiO2 Membranes Photodeposited on Hydrogen Evolving Catalysts Enabling Overall Water Splitting. *ACS Catalysis* **2017**, *7* (11), 7931-7940.
- 44. Garcia-Esparza, A. T.; Shinagawa, T.; Ould-Chikh, S.; Qureshi, M.; Peng, X.; Wei, N.; Anjum, D. H.; Clo, A.; Weng, T.-C.; Nordlund, D.; Sokaras, D.; Kubota, J.; Domen, K.; Takanabe, K., An Oxygen-Insensitive Hydrogen Evolution Catalyst Coated by a Molybdenum-Based Layer for Overall Water Splitting. *Angewandte Chemie International Edition* **2017**, *56* (21), 5780-5784.
- 45. Takata, T.; Pan, C.; Nakabayashi, M.; Shibata, N.; Domen, K., Fabrication of a Core–Shell-Type Photocatalyst via Photodeposition of Group IV and V Transition Metal Oxyhydroxides: An Effective Surface Modification Method for Overall Water Splitting. *Journal of the American Chemical Society* **2015**, *137* (30), 9627-9634.
- 46. Yoshida, M.; Maeda, K.; Lu, D.; Kubota, J.; Domen, K., Lanthanoid Oxide Layers on Rhodium-Loaded (Ga1–xZnx)(N1–xOx) Photocatalyst as a Modifier for Overall Water Splitting under Visible-Light Irradiation. *The Journal of Physical Chemistry C* **2013**, *117* (27), 14000-14006.
- 47. Konishi, K., Phosphine-Coordinated Pure-Gold Clusters: Diverse Geometrical Structures and Unique Optical Properties/Responses. In *Gold Clusters, Colloids and Nanoparticles I*, Mingos, D. M. P., Ed. Springer International Publishing: Cham, 2014; pp 49-86.
- 48. Wen, F.; Englert, U.; Gutrath, B.; Simon, U., Crystal Structure, Electrochemical and Optical Properties of [Au9(PPh3)8](NO3)3. *European Journal of Inorganic Chemistry* **2008**, *2008* (1), 106-111.

- 49. Alotabi, A. S.; Yin, Y.; Redaa, A.; Tesana, S.; Metha, G. F.; Andersson, G. G., Cr2O3 layer inhibits agglomeration of phosphine-protected Au9 clusters on TiO2 films. *The Journal of Chemical Physics* **2021**, *155* (16), 164702.
- 50. Briggs, D., Practical surface analysis. *Auger and X-Ray Photoelecton Spectroscory* **1990,** *I*, 151-152.
- 51. Anderson, D. P.; Alvino, J. F.; Gentleman, A.; Al Qahtani, H.; Thomsen, L.; Polson, M. I.; Metha, G. F.; Golovko, V. B.; Andersson, G. G., Chemically-Synthesised, Atomically-Precise Gold Clusters Deposited and Activated on Titania. *Physical chemistry chemical physics* **2013**, *15* (11), 3917-3929.
- 52. Anderson, D. P.; Adnan, R. H.; Alvino, J. F.; Shipper, O.; Donoeva, B.; Ruzicka, J.-Y.; Al Qahtani, H.; Harris, H. H.; Cowie, B.; Aitken, J. B., Chemically Synthesised Atomically Precise Gold Clusters Deposited and Activated on Titania. Part II. *Physical chemistry chemical physics* **2013**, *15* (35), 14806-14813.
- 53. Ruzicka, J.-Y.; Abu Bakar, F.; Hoeck, C.; Adnan, R.; McNicoll, C.; Kemmitt, T.; Cowie, B. C.; Metha, G. F.; Andersson, G. G.; Golovko, V. B., Toward Control of Gold Cluster Aggregation on TiO2 via Surface Treatments. *The Journal of Physical Chemistry C* **2015**, *119* (43), 24465-24474.
- 54. Al Qahtani, H. S.; Kimoto, K.; Bennett, T.; Alvino, J. F.; Andersson, G. G.; Metha, G. F.; Golovko, V. B.; Sasaki, T.; Nakayama, T., Atomically resolved structure of ligand-protected Au9 clusters on TiO2 nanosheets using aberration-corrected STEM. *The Journal of Chemical Physics* **2016**, *144* (11), 114703.
- 55. Al Qahtani, H. S.; Metha, G. F.; Walsh, R. B.; Golovko, V. B.; Andersson, G. G.; Nakayama, T., Aggregation Behavior of Ligand-Protected Au9 Clusters on Sputtered Atomic Layer Deposition TiO2. *The Journal of Physical Chemistry C* **2017**, *121* (20), 10781-10789.
- 56. Zong, S.; Tian, L.; Guan, X.; Cheng, C.; Shi, J.; Guo, L., Photocatalytic overall water splitting without noble-metal: Decorating CoP on Al-doped SrTiO3. *Journal of Colloid and Interface Science* **2022**, *606*, 491-499.
- 57. Alotabi, A. S.; Gibson, C. T.; Metha, G. F.; Andersson, G. G., Investigation of the Diffusion of Cr2O3 into Different Phases of TiO2 upon Annealing. *ACS Applied Energy Materials* **2021**, *4* (1), 322-330.
- 58. Moulder, J. F., Handbook of x-ray photoelectron spectroscopy: a reference book of standard data for use in x-ray photoelectron spectroscopy. *Handbook of x-ray photoelectron spectroscopy*: **1992**.
- 59. Mousavi, H.; Yin, Y.; Howard-Fabretto, L.; Sharma, S. K.; Golovko, V.; Andersson, G. G.; Shearer, C. J.; Metha, G. F., Au101–rGO nanocomposite: immobilization of phosphine-protected gold nanoclusters on reduced graphene oxide without aggregation. *Nanoscale Advances* **2021**, *3* (5), 1422-1430.
- 60. Jianjun, W.; Qunji, X., Effects of synthetic additives on the friction and wear properties of a Cr2O3 coating. *Wear* **1994**, *176* (2), 213-216.

## **Chapter 8:** Conclusions and Future work

#### 8.1 Conclusions

Metal oxide overlayer has been widely used to improve the efficiency of photocatalysis reactions by blocking the back reactions and protecting the co-catalyst from agglomeration. This thesis makes an original contribution to the knowledge by performing physical, chemical, electronic and catalytic studies on chromium oxide formed as an overlayer onto photocatalysts and Au cluster-modified photocatalysts. The significant findings are summarised below.

The stability of Cr<sub>2</sub>O<sub>3</sub> as a protective layer on the photocatalyst is essential to maintain the protective feature of Cr<sub>2</sub>O<sub>3</sub>. In Chapter 3, evidence was established showing that when Cr<sub>2</sub>O<sub>3</sub> deposited onto TiO<sub>2</sub> films was heated to 600 °C, the Cr<sub>2</sub>O<sub>3</sub> layer remained stable on the rutile phase but not the amorphous and anatase phases. This finding was attributed to the differences in surface energy between Cr<sub>2</sub>O<sub>3</sub> and the different crystal phases of titania. The surface energy of Cr<sub>2</sub>O<sub>3</sub> is higher than the amorphous and anatase surface energies of TiO<sub>2</sub>, which led to the diffusion of Cr<sub>2</sub>O<sub>3</sub> upon heating. However, Cr<sub>2</sub>O<sub>3</sub> has a lower surface energy than the rutile, which resulted in the stability of the Cr<sub>2</sub>O<sub>3</sub> layer upon heating. Reduction of some of the Cr<sub>2</sub>O<sub>3</sub> layer to Cr metal was observed by annealing up to 600 °C under vacuum, but there was no observation of higher oxidised forms of chromium oxide.

Expanding on the work performed in Chapter 3, in Chapter 4, the stability, oxidation state and bulk and surface electronic structure of CrO<sub>x</sub> photodeposited onto P25, BaLa<sub>4</sub>Ti<sub>4</sub>O<sub>15</sub>, and Al:SrTiO<sub>3</sub> particles as a function of the annealing process were investigated. The CrO<sub>x</sub> layer was coated with the three photocatalysts particles with a 1.2–1.7 nm thickness. After annealing, Cr<sub>2</sub>O<sub>3</sub> was mostly diffused into P25, while for BaLa<sub>4</sub>Ti<sub>4</sub>O<sub>15</sub>, the degree of Cr<sub>2</sub>O<sub>3</sub> diffusion was less than that into P25. Interestingly, the Cr<sub>2</sub>O<sub>3</sub> layer was very stable on the surface of Al:SrTiO<sub>3</sub> particles. The lack of Cr<sub>2</sub>O<sub>3</sub> diffusion here was believed to be due to the higher surface energy of Al:SrTiO<sub>3</sub> compared to Cr<sub>2</sub>O<sub>3</sub>. Further, NEXAFS, XPS and UPS provided evidence that some of the Cr<sub>2</sub>O<sub>3</sub> had been reduced to metallic Cr after annealing with no presence of CrO<sub>2</sub> or CrO<sub>3</sub> states on the surface. The surface and bulk band gaps of the three photocatalysts particles were influenced by the formation and diffusion of Cr<sub>2</sub>O<sub>3</sub>. UPS and IPES measurements showed that the surface band gaps were narrowed by the formation of Cr<sub>2</sub>O<sub>3</sub> and then increased upon diffusion of Cr<sub>2</sub>O<sub>3</sub>. DRS absorption spectra showed the presence of undoped Cr<sub>2</sub>O<sub>3</sub> electronic structure on the photocatalyst surfaces after the formation of Cr<sub>2</sub>O<sub>3</sub>. However, upon diffusion of Cr<sub>2</sub>O<sub>3</sub> into P25 and BaLa<sub>4</sub>Ti<sub>4</sub>O<sub>15</sub>, a step in the absorption tail at lower energies of the bulk band gap was observed. This step in the absorption tail was less noticeable for Al:SrTiO<sub>3</sub>. This observation was interpreted as due to the stability of Cr<sub>2</sub>O<sub>3</sub> on the surface. Photocatalytic water splitting was performed with two light sources providing evidence that the changes in the surface and bulk band gaps before and after annealing have not contributed to improving photocatalytic activity. These results supported the conclusion that the Cr<sub>2</sub>O<sub>3</sub> layer is

beneficial for photocatalytic activity by preventing the back reactions with less chance of contributing to the photocatalytic reaction.

A major challenge is to protect Au clusters deposited onto a metal oxide surface from agglomeration to form Au nanoparticles. The first successful experiment on stabilising a Au cluster-modified surface by depositing a protective  $Cr_2O_3$  layer on top of the Au clusters was reported in Chapter 5. The phosphine-protected  $Au_9$  clusters were deposited onto a RF-sputter deposited  $TiO_2$  film, followed by photodeposition of the  $Cr_2O_3$  layer. A 1.1 nm—thick  $Cr_2O_3$  layer was formed over the surface. After the removal of the phosphine ligands, it was proved, using synchrotron XPS, that the  $Cr_2O_3$  layer completely blocked the agglomeration of the  $Au_9$  clusters. Interestingly, even with an extensive loading of  $Au_9$  clusters, the  $Cr_2O_3$  layer improved the resistance of  $Au_9$  clusters to agglomerate. Overall, this study provides an innovative use of a thin  $Cr_2O_3$  layer in stabilising phosphine-protected Au clusters on  $TiO_2$ .

In Chapter 6, the effect of RF-sputter deposited TiO<sub>2</sub> film thickness on the stability of Au<sub>9</sub> clusters with a chromium oxide layer was also investigated. It was shown that the surface morphology of the thick TiO<sub>2</sub> film was significantly changed compared to the thin TiO<sub>2</sub> film after heating. This change is due to the recrystallisation and high mobility of the thick TiO<sub>2</sub> film during heating. The high mobility of the thick TiO<sub>2</sub> film led to a significant agglomeration of the Au<sub>9</sub> clusters, even when protected with the CrO<sub>x</sub> layer. This work raises a new possibility of cluster agglomeration due to the mobility of the substrate.

It is well known that clusters on photocatalysts exposed to constant irradiation can result in agglomeration. In Chapter 6, the stability of the Au<sub>9</sub> clusters on SrTiO<sub>3</sub> was examined after UV light irradiation for seven hours for photocatalytic water splitting and improved with a chromium hydroxide layer. After UV irradiation, only 30% of Au<sub>9</sub> clusters remained stable at the surface of SrTiO<sub>3</sub>. Interestingly, with Cr(OH)<sub>3</sub> layer, more than 60% of Au<sub>9</sub> clusters on the surface of SrTiO<sub>3</sub> remained stable after UV irradiation. This finding confirmed that the agglomeration of Au<sub>9</sub> clusters was inhibited during the seven-hour UV light irradiation for photocatalytic water splitting by the chromium hydroxide layer. Moreover, it was confirmed that the back reaction on the SrTiO<sub>3</sub>-Au<sub>9</sub> system was suppressed using Cr(OH)<sub>3</sub> layer. However, the H<sub>2</sub> production rate was reduced with the Cr(OH)<sub>3</sub> layer. This was assumed to be due to the even distribution and thickness of the Cr(OH)<sub>3</sub> layer on the surface of the SrTiO<sub>3</sub>, which blocks the O<sub>2</sub> generating sites, then leading to a decrease in the overall photocatalytic water splitting reaction. The chemical state of the photodeposited layer was confirmed to be Cr(OH)<sub>3</sub>. However, upon heating to remove the ligands, it was converted to Cr<sub>2</sub>O<sub>3</sub>,

then returned to  $Cr(OH)_3$  after photocatalytic water splitting. This change was assumed to be due to the interaction between the  $H_2O$  and  $Cr_2O_3$  layers.

The overall outcome of this thesis is an improved understanding of the nature of the photodeposited  $CrO_x$  layer on photocatalysts and Au cluster-modified photocatalysts treated at various conditions. This thesis provides an investigation and novel use of the  $CrO_x$  layer on the top of Au cluster-modified photocatalysts for photocatalysis reaction, where the size of Au-P clusters has been preserved successfully after the removal of the ligands. Moreover, it has demonstrated that the  $CrO_x$  layer with the small band gap did not contribute to the photocatalytic water splitting activity as a generation of electron-hole pairs. However, it has confirmed the ability of the  $CrO_x$  layer to block the back reaction. The photodeposition method of  $CrO_x$  layer has shortcomings such as controlling the thickness and distribution of  $CrO_x$  layer. These limitations have shown an effect on the overall photocatalytic water splitting reaction. Also, another limitation of photodeposition of  $CrO_x$  layer is that the deposition using the same experimental setup did not result in equal formation on all photocatalysts. This variability could be a substrate-dependent change. These findings are of general interest to researchers utilising a protective overlayer on photocatalysts for efficient photocatalysis reactions.

#### 8.2 Future Works

There is plenty of scope for further research on overlayer for photocatalysis reactions, particularly in utilising other metal oxides as a layer on metal cluster-modified photocatalysts. In Chapter 4, the reduction and diffusion of the  $Cr_2O_3$  layer into photocatalysts were observed upon annealing, causing a loss of the protection feature, which led to a change in the electronic structure of the photocatalysts. Further studies can be carried out to explore more stable metal oxides with lower surface energy to be used as a protective layer for catalysts. In Chapter 1, we listed a summary of other metal oxide layers that have been used to block the back reactions reported to date. These metal oxides can be an alternative protective layer for  $CrO_x$  on metal cluster-modified photocatalysts, but further research on this is needed.

Another research opportunity is the development of the preparation method for the  $CrO_x$  layer. In Chapter 6,  $Cr(OH)_3$  formed as a uniform and overly thick layer on the catalyst surface, which blocked the overall water splitting reaction rather than the back reaction only. One way to improve this system is to selectively deposit a  $CrO_x$  layer of controllable thickness on the Au clusters as a core/shell structure to obtain the benefits of  $CrO_x$  without influencing the overall water splitting. Very recently, it was reported that the  $V_2O_5$  layer was deposited selectively on Pt nanoparticles on carbon electrodes through atomic layer deposition (ALD). \(^1\). ALD is a powerful technique to deposit thin oxide layers with a highly controllable depth. This advantage allows the ALD technique to be applied to cluster-

modified photocatalysts to form the core/shell structure of the metal oxide layer on clusters that will improve the photocatalytic activity.					

### 8.3 References

1. Hardisty, S. S.; Frank, S.; Zysler, M.; Yemini, R.; Muzikansky, A.; Noked, M.; Zitoun, D., Selective Catalyst Surface Access through Atomic Layer Deposition. *ACS Applied Materials & Interfaces* **2021**, *13* (49), 58827-58837.

## Appendices

# Appendix A: Investigation of the Diffusion of Cr<sub>2</sub>O<sub>3</sub> into Different Phases of TiO<sub>2</sub> upon Annealing

This appendix contains a detailed description, additional figures and tables:

#### Additional figures and tables:

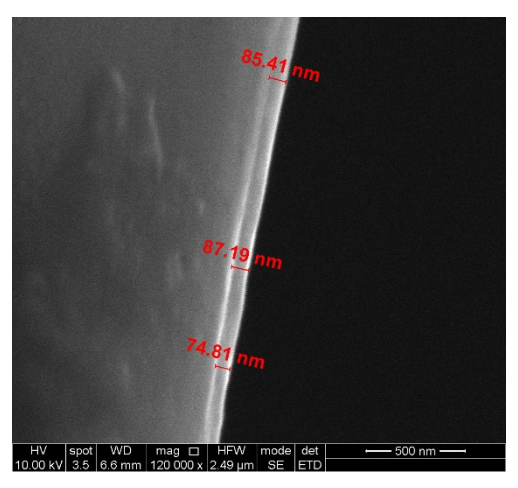


**Figure A1**: SEM cross-section image of the  $TiO_2$  film deposited using the magnetron sputtering technique. The thickness of the  $TiO_2$  film was determined to be  $82 \pm 5$  nm.

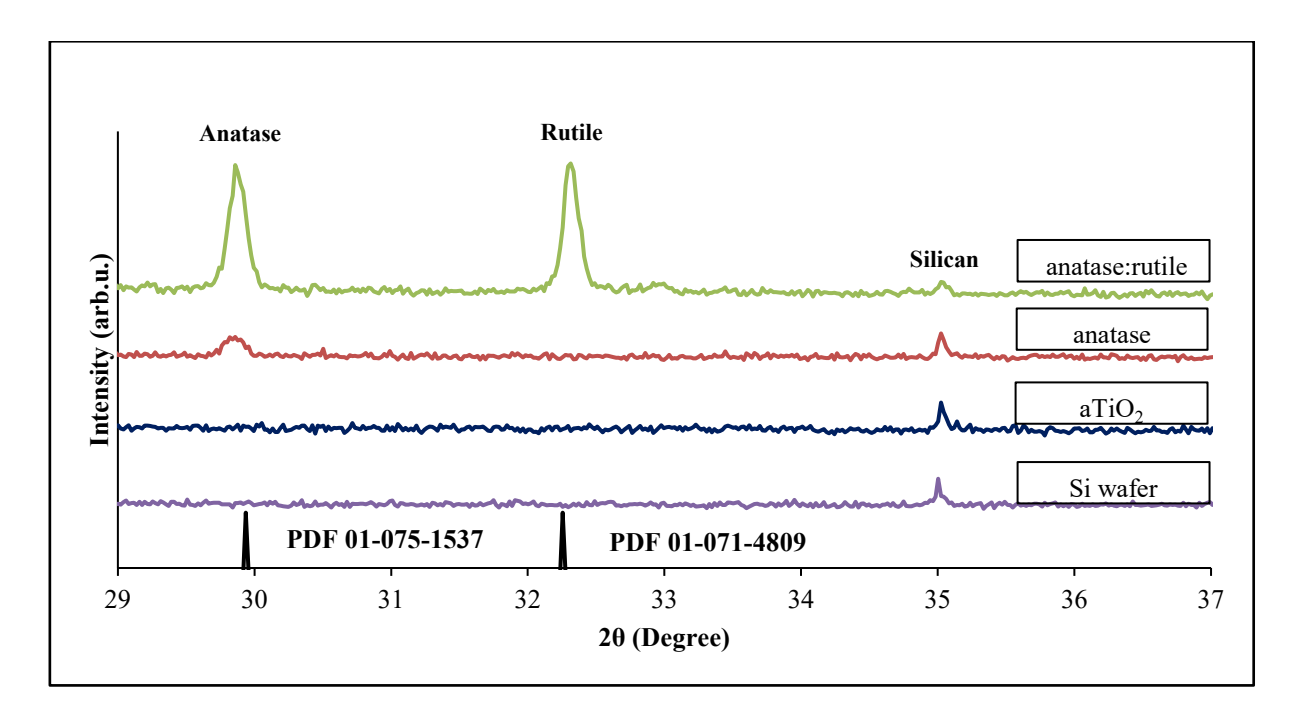


**Figure A2**: XRD patterns of Si wafer, aTiO<sub>2</sub>, anatase, and anatase:rutile. The standard XRD patterns for anatase is PDF 01-075-1537, and rutile is PDF 01-071-4809.

Crystalline domain size can be calculated using the Scherrer equation. Figure A3 shows XRD pattern of anatase:rutile sample with the Scherrer equation  $\tau = \frac{0.9\lambda}{B\cos\theta}$ : where  $\tau$  is the average crystalline

domain size in Å,  $\lambda$  the wavelength of the X-ray source, B the full width at half maximum(FWHM) and  $\theta$  the diffraction angle. The average crystalline domain size of anatase in anatase:rutile sample is:  $\tau = \frac{0.9x0.179}{0.144\cos 29.88} = 66.3 \text{ Å} = 6.63 \pm 0.1 \text{ nm}$ . The average crystalline domain size of rutile in anatase:rutile sample is:  $\tau = \frac{0.9x0.179}{0.126\cos 32.32} = 76.2 \text{ Å} = 7.62 \pm 0.1 \text{ nm}$ .

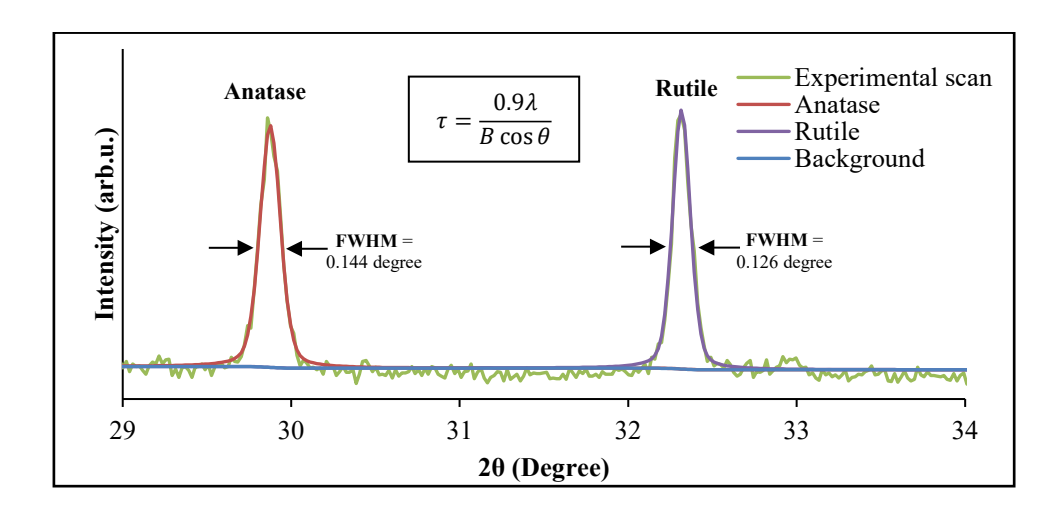
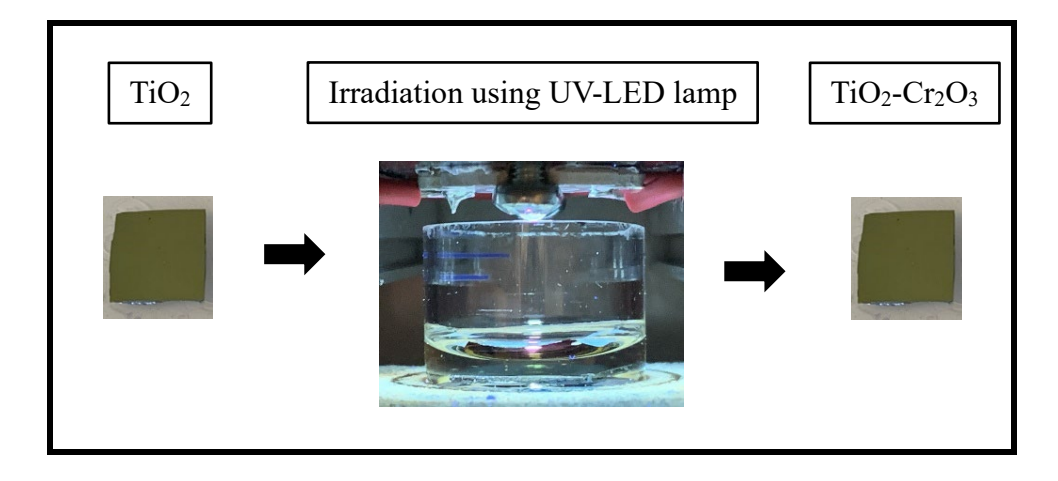


Figure A3: XRD pattern of anatase:rutile sample with Scherrer equation.



*Figure A4:* Experimental procedure of photodeposition of the  $Cr_2O_3$  layer.

The binding energies of the XPS spectra of the aTiO<sub>2</sub>-Cr<sub>2</sub>O<sub>3</sub> and the anatase-Cr<sub>2</sub>O<sub>3</sub> samples were used as measured and not calibrated by setting the main C 1s peak to 285 eV. The binding energies are shown in Table A1. The reason is twofold. Firstly, it can be seen from the UP spectra shown in Figure A5 that both samples are not subject to charging while acquiring UP spectra. In Figures A5A and A5B, three consecutive spectra of both samples are shown. The shape of the three immediately consecutive spectra is identical and the secondary electron cut-off does not shift. Secondly, the position of O 1s and Ti 2p<sub>3/2</sub> is the same within experimental uncertainty as well as the C 1s for the

samples heated to 200°C and higher temperatures. Note that the C 1s peak for the non-heated sample is found at 285.4 eV. We assume that the C 1s peak of the non-heated sample stems from slightly oxidised hydrocarbons found on the sample, which could be due to solvent molecules remaining on the sample surface following cleaning of the sample, or photo-oxidation of hydrocarbons on the titania surface. If the energy scale of these two samples were calibrated by setting the main C 1s peak to 285 eV, the binding energies of O and Ti would move upon heating. Such a change in O and Ti binding energies upon mild heating cannot be rationalised by a chemical process. Based on this procedure, the binding energy of Ti is found at  $459.2 \pm 0.2$  eV and can be assigned to Ti in  $TiO_2^{-1}$ . The binding energy of O is found at  $530.5 \pm 0.2$  eV and can be assigned to O in TiO<sub>2</sub>, which is the same binding energy of O in Cr<sub>2</sub>O<sub>3</sub><sup>1, 2</sup>. A second and smaller O 1s peak is found for the non-heated sample at 532.2 eV, which could be related to H<sub>2</sub>O or OH<sup>-</sup> from the Cr deposition process. The binding energy of C for the non-heated sample is found at  $285.4 \pm 0.2$  eV and is assumed to represent slightly oxidised C. The binding energy of C after annealing to 200°C and higher temperatures is found at 284.8  $\pm$  0.2 eV and can be assigned to C in C-C bonds<sup>3, 4</sup>. The binding energy of Cr of the non-heated sample is found at  $577.9 \pm 0.2$  eV and can be assigned to  $Cr_2O_3$  or could also be  $Cr(OH)_3^{5,}$ <sup>6</sup>. The binding energy of Cr after annealing to 200°C and higher temperatures, is found at 577.1  $\pm$  0.2 eV and can be assigned to Cr<sub>2</sub>O<sub>3</sub><sup>5, 6</sup>.

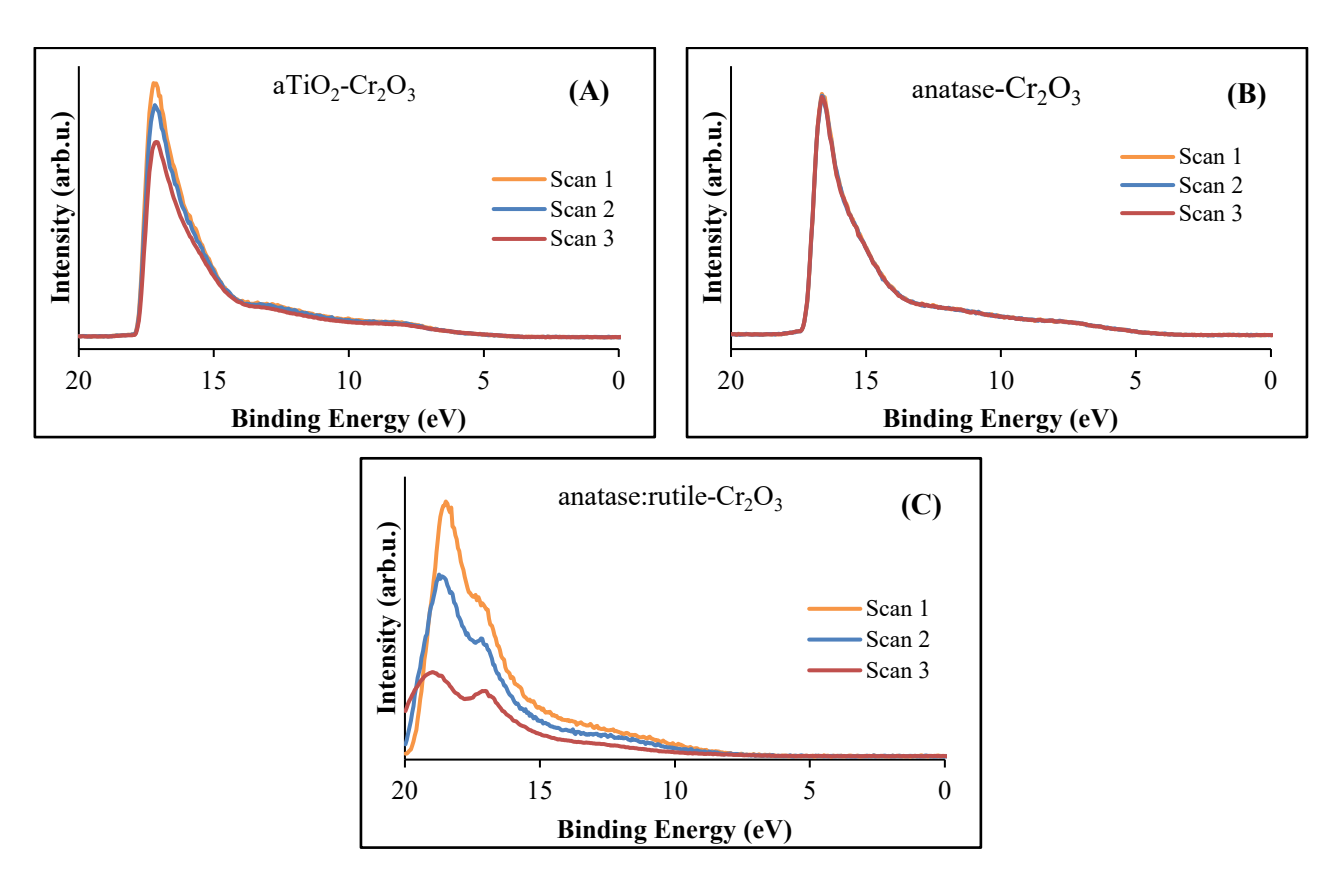
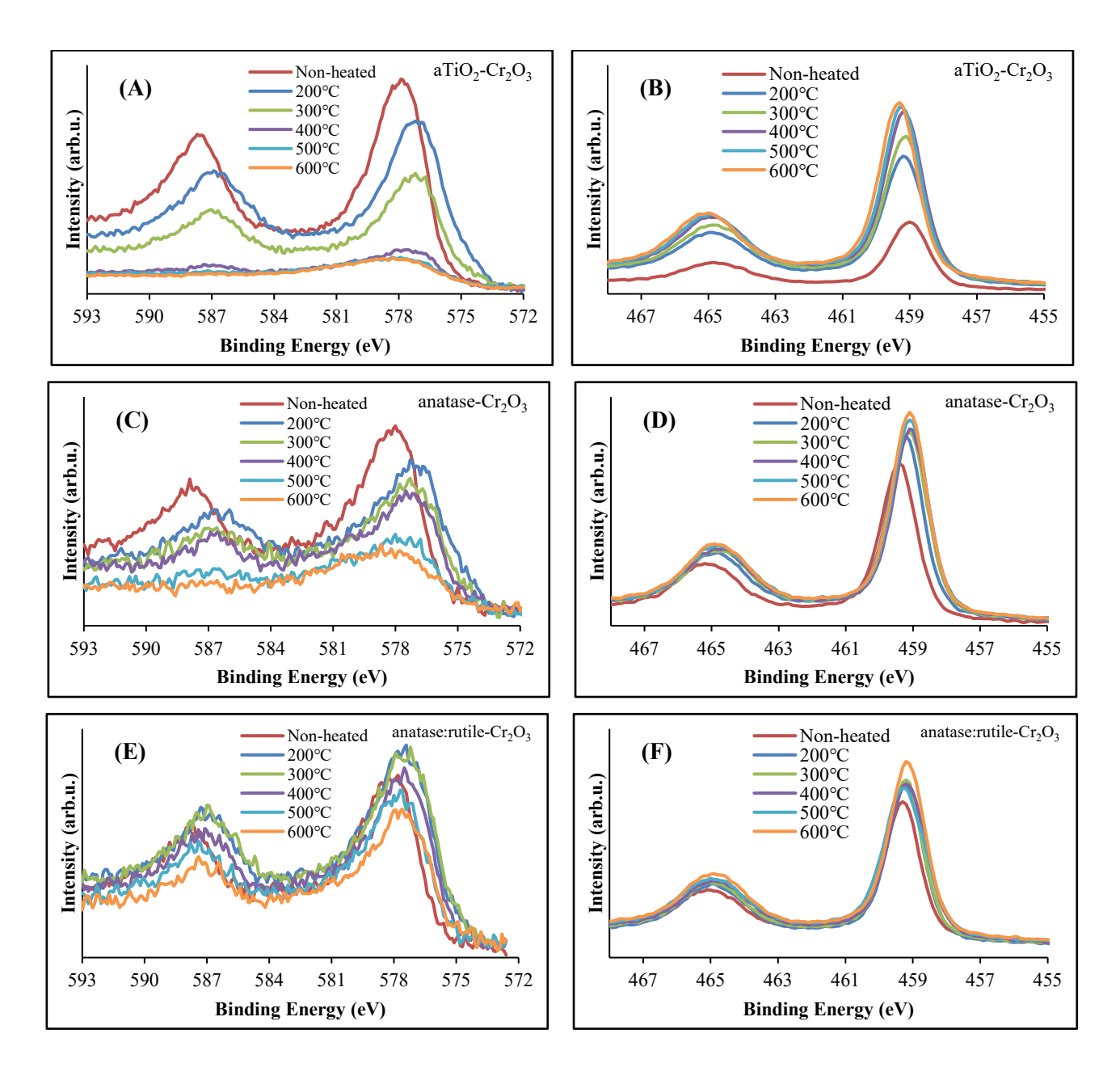


Figure A5: UPS spectra of (A) aTiO2-Cr2O3, (B) anatase-Cr2O3, and (C) anatase:rutile-Cr2O3.

**Table A1**: XPS peak positions of C 1s, O 1s,  $Cr 2p_{3/2}$  and  $Ti 2p_{3/2}$  of  $aTiO_2$ - $Cr_2O_3$ , anatase- $Cr_2O_3$ , and anatase:rutile- $Cr_2O_3$  samples as a function of annealing temperature. For C and O, the position of the main peak is shown.

	Element	Peak position (eV)				
Sample		C 1s	O 1s	Ti 2p <sub>3/2</sub>	Cr 2p <sub>3/2</sub>	
aTiO <sub>2</sub> -Cr <sub>2</sub> O <sub>3</sub>	Non-heated	$285.4 \pm 0.2$	$530.4 \pm 0.2$	$459.0 \pm 0.2$	$577.9 \pm 0.2$	
	200°C	$284.9 \pm 0.2$	$530.6 \pm 0.2$	$459.2 \pm 0.2$	$577.1 \pm 0.2$	
	300°C	$284.7 \pm 0.2$	$530.6 \pm 0.2$	$459.2 \pm 0.2$	$577.2 \pm 0.2$	
	400°C	$284.7 \pm 0.2$	$530.5 \pm 0.2$	$459.2 \pm 0.2$	$577.2 \pm 0.2$	
	500°C	$284.7 \pm 0.2$	$530.6 \pm 0.2$	$459.2 \pm 0.2$	$577.1 \pm 0.2$	
	600°C	$284.8 \pm 0.2$	$530.7 \pm 0.2$	$459.3 \pm 0.2$		
anatase-Cr <sub>2</sub> O <sub>3</sub>	Non-heated	$285.4 \pm 0.2$	$530.6 \pm 0.2$	$459.4 \pm 0.2$	$578.1 \pm 0.2$	
	200°C	$284.8 \pm 0.2$	$530.5 \pm 0.2$	$459.2 \pm 0.2$	$576.9 \pm 0.2$	
	300°C	$284.5 \pm 0.2$	$530.4 \pm 0.2$	$459.1 \pm 0.2$	$577.1 \pm 0.2$	
	400°C	$284.5 \pm 0.2$	$530.3 \pm 0.2$	$459.1 \pm 0.2$	$577.0 \pm 0.2$	
	500°C	$284.4 \pm 0.2$	$530.3 \pm 0.2$	$459.1 \pm 0.2$	$577.2 \pm 0.2$	
	600°C	$285.4 \pm 0.2$	$530.4 \pm 0.2$	$459.1 \pm 0.2$		
anatase:rutile-Cr <sub>2</sub> O <sub>3</sub>	Non-heated	$285.6 \pm 0.2$	$530.5 \pm 0.2$	$459.3 \pm 0.2$	$578.1 \pm 0.2$	
	200°C	$285.3 \pm 0.2$	$530.5 \pm 0.2$	$459.2 \pm 0.2$	$577.4 \pm 0.2$	
	300°C	$285.0 \pm 0.2$	$530.5 \pm 0.2$	$459.2 \pm 0.2$	$577.3 \pm 0.2$	
	400°C	$284.8 \pm 0.2$	$530.5 \pm 0.2$	$459.2 \pm 0.2$	$577.5 \pm 0.2$	
	500°C	$284.9 \pm 0.2$	$530.5 \pm 0.2$	$459.3 \pm 0.2$	$577.7 \pm 0.2$	
	600°C	$285.1 \pm 0.2$	$530.5 \pm 0.2$	$459.1 \pm 0.2$	$577.5 \pm 0.2$	

In contrast, the anatase:rutile- $Cr_2O_3$  sample did show charging and the above procedure cannot be applied to this sample. As can be seen in Figure A5C, the UP spectra of this sample show a change in shape of the spectra and a shift to the left on the binding energy scale from scan 1 to 3. From this observation, it can be concluded that the sample is charging during electron spectroscopy. This could be due to various reasons like mounting of the sample on the sample holder or poor electrical contact between the  $TiO_2$  layer and the Si substrate. For this sample we have calibrated the XPS spectra by setting the O 1s peak to the average of the binding energy of the O 1s peak in the  $aTiO_2$ - $Cr_2O_3$  and anatase- $Cr_2O_3$  samples. With this calibration, the binding energy of  $Ti 2p_{3/2}$  is found at  $459.2 \pm 0.2$  eV, which is the same as for the  $aTiO_2$ - $Cr_2O_3$  and the anatase- $Cr_2O_3$  samples. The  $Cr 2p_{3/2}$  is found for the heated samples at  $577.4 \pm 0.2$  eV, which is within error the same as for the  $aTiO_2$ - $Cr_2O_3$  and the anatase- $Cr_2O_3$  samples. The binding energy of Cr of the non-heated sample is somewhat higher and could also indicate the presence of  $Cr(OH)_3$ . The C 1s peak is found for the non-heated sample at  $285.6 \pm 0.2$  eV, and for the heated sample at  $284.8 \pm 0.2$  eV, which is the same as for the  $aTiO_2$ - $Cr_2O_3$  and the anatase- $Cr_2O_3$  samples. The C species of this sample are thus assigned to the same compounds as for the  $aTiO_2$ - $Cr_2O_3$  and the anatase- $Cr_2O_3$  samples.



**Figure A6**: XPS spectra of Cr 2p regions of (A)  $aTiO_2$ - $Cr_2O_3$ , (C) anatase- $Cr_2O_3$ , and (E) anatase:rutile- $Cr_2O_3$  and Ti 2p regions of (B)  $aTiO_2$ - $Cr_2O_3$ , (D) anatase- $Cr_2O_3$ , and (F) anatase:rutile- $Cr_2O_3$  as a function of annealing temperature.

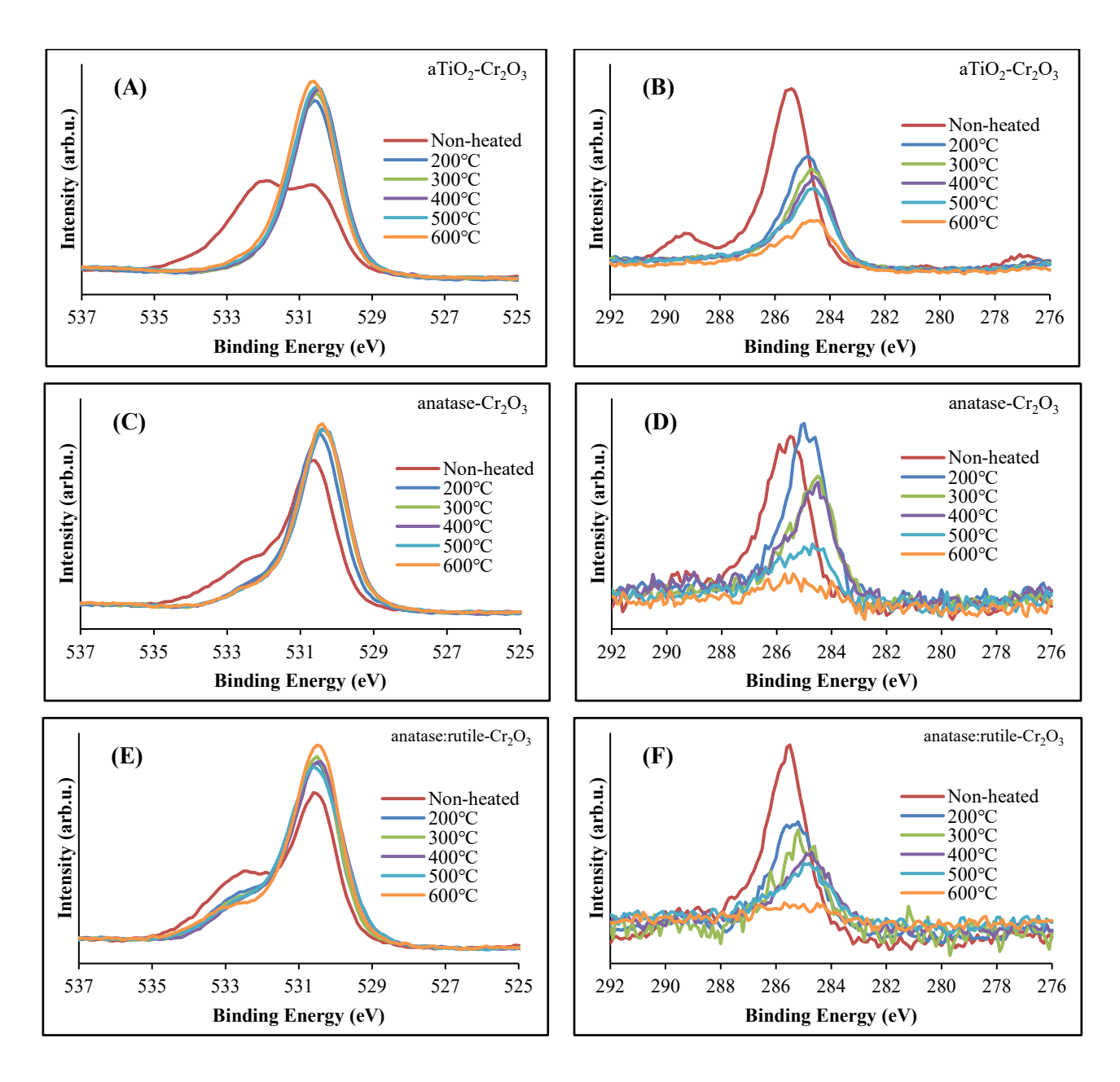


**Figure A7**: XPS spectra of O 1s regions of (A)  $aTiO_2$ - $Cr_2O_3$ , (C) anatase- $Cr_2O_3$ , and (E) anatase:rutile- $Cr_2O_3$  and C 1s regions of (B)  $aTiO_2$ - $Cr_2O_3$ , (D) anatase- $Cr_2O_3$ , and (F) anatase:rutile- $Cr_2O_3$  as a function of annealing temperature.

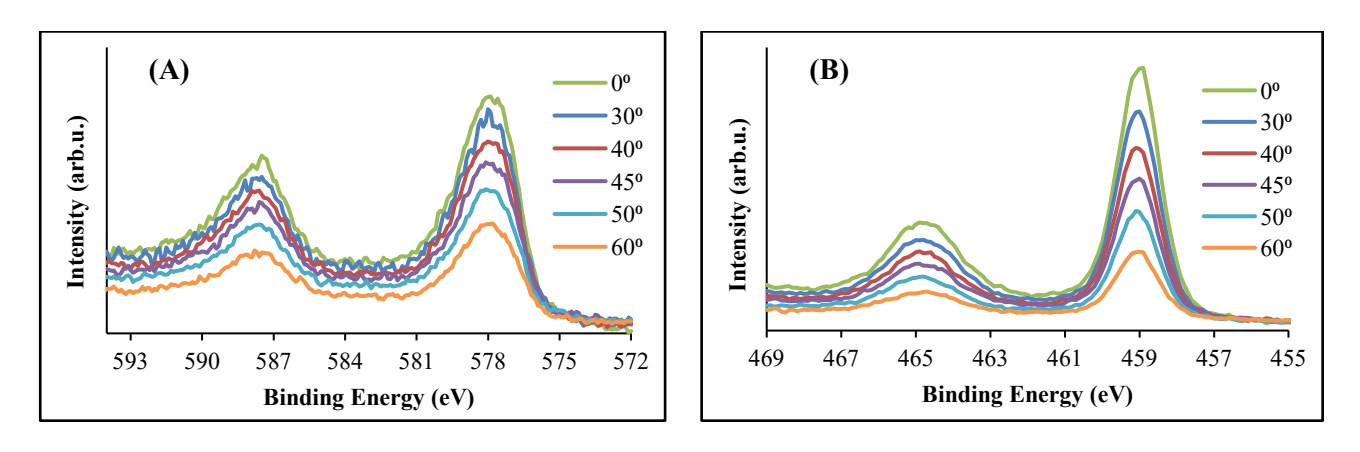
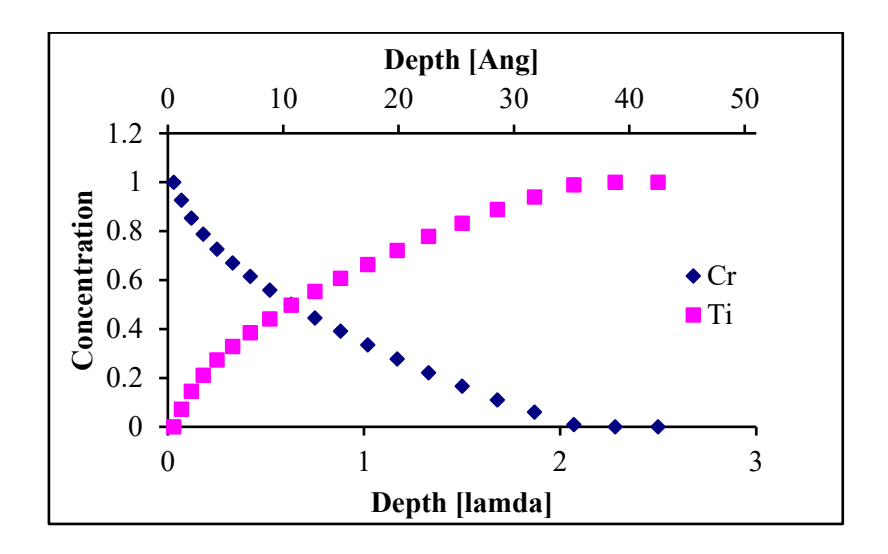


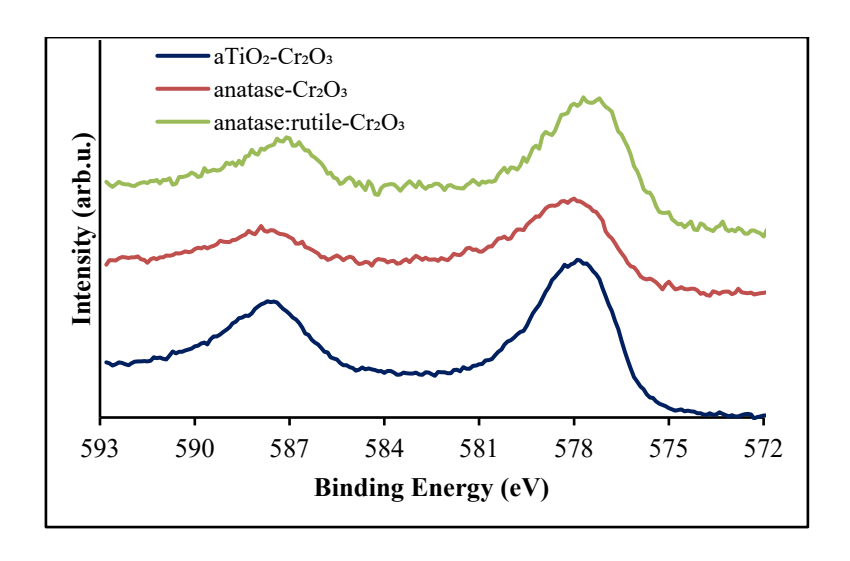
Figure A8: AR-XPS spectra of (A) Cr 2p and (B) Ti 2p regions of aTiO2-Cr2O3 at different angles.

The concentration depth profile of Cr and Ti of a  $TiO_2$ - $Cr_2O_3$  sample determined using AR-XPS is shown in Figure A9. We have applied the procedure described in detail by Eschen et al  $^7$  using a single excitation energy  $^8$  to determine the thickness of Cr layer. The depth profile for a $TiO_2$ - $Cr_2O_3$  interpreted that Cr has a thickness of  $\sim 11$  Å (1.1 nm). The usual crystal structure of  $Cr_2O_3$  is corundum. 11 Å correspond to approximately two unit cells of  $Cr_2O_3$ . We have no evidence which crustal structure  $Cr_2O_3$  forms in the present experiments.



**Figure A9**: Concentration depth profiles deter of Cr and Ti of the  $Cr_2O_3$  deposited onto the  $TiO_2$  ( $aTiO_2-Cr_2O_3$ ).

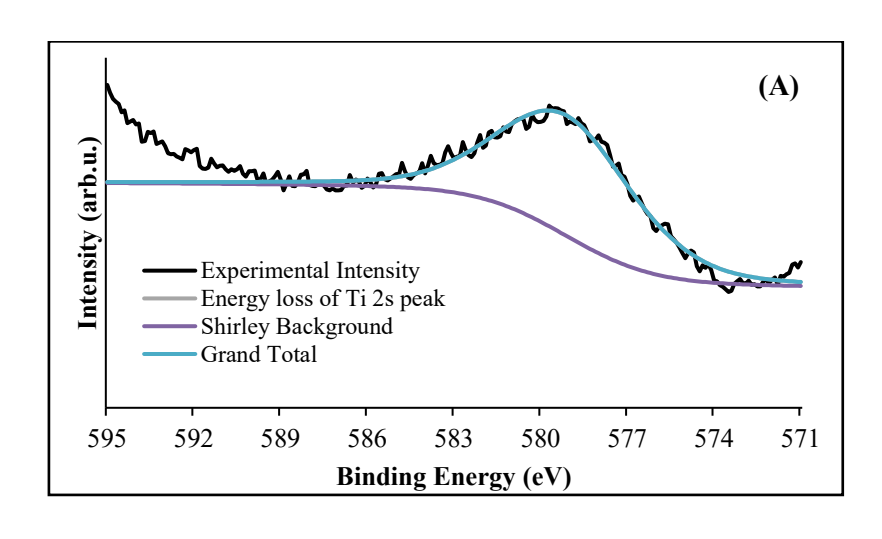
Figure A10 shows the Cr 2p spectra of aTiO<sub>2</sub>-Cr<sub>2</sub>O<sub>3</sub>, anatase-Cr<sub>2</sub>O<sub>3</sub>, and anatase:rutile-Cr<sub>2</sub>O<sub>3</sub>. The binding energy of Cr  $2p_{3/2}$  appear at  $577.8 \pm 0.2$  eV for Cr photodeposited onto various substrates, which corresponding to Cr<sub>2</sub>O<sub>3</sub>.

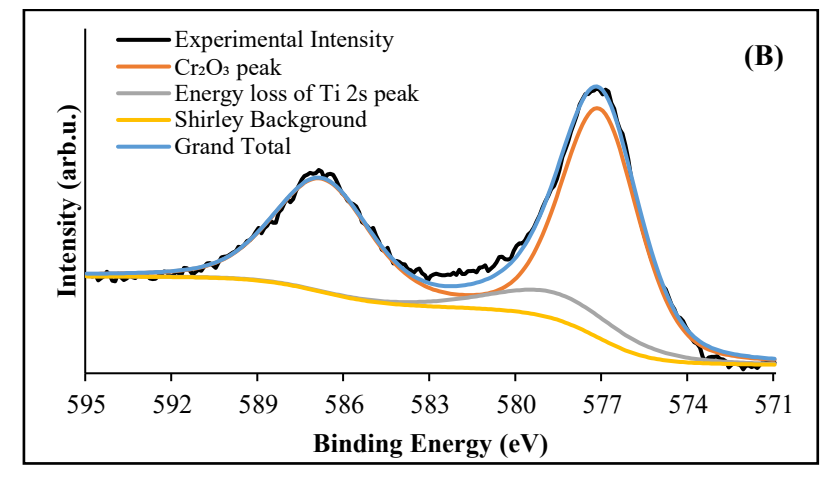


**Figure A10**: XPS spectra of (A)  $Cr\ 2p$  of  $aTiO_2-Cr_2O_3$ , anatase- $Cr_2O_3$ , and anatase:rutile- $Cr_2O_3$  before annealing.

Figure A11A shows the spectrum in the Cr 2p region for the aTiO<sub>2</sub> sample. It shows a peak with broad FWHM, which is the energy loss peak of the Ti 2s peak. This peak was also observed by Trenczek-Zajac  $^9$ . Figure A11B shows the Cr 2p spectrum after the photodeposition of a chromium oxide layer and heating at ultrahigh vacuum conditions for 10 min at 200°C. The position of the Cr  $2p_{3/2}$  peak at  $577.2 \pm 0.2$  eV allows for identifying this peak as  $Cr_2O_3$   $^6$ .

The energy loss peak of the Ti 2s peak overlaps with the Cr  $2p_{3/2}$  peak at ~578.8 eV. The binding energy of this energy loss peak was calibrated according to Ti  $2p_{3/2}$  (~459.4 eV) with the addition of 119.4 eV, and the FWHM was fixed at 5.4 eV. The area of the energy loss peak was identified by dividing the fitted area of Ti  $2p_{3/2}$  on a relative factor of 8.35. Estimation of the Ti 2s energy loss peak was essential to correctly determine the chemical state of Cr.

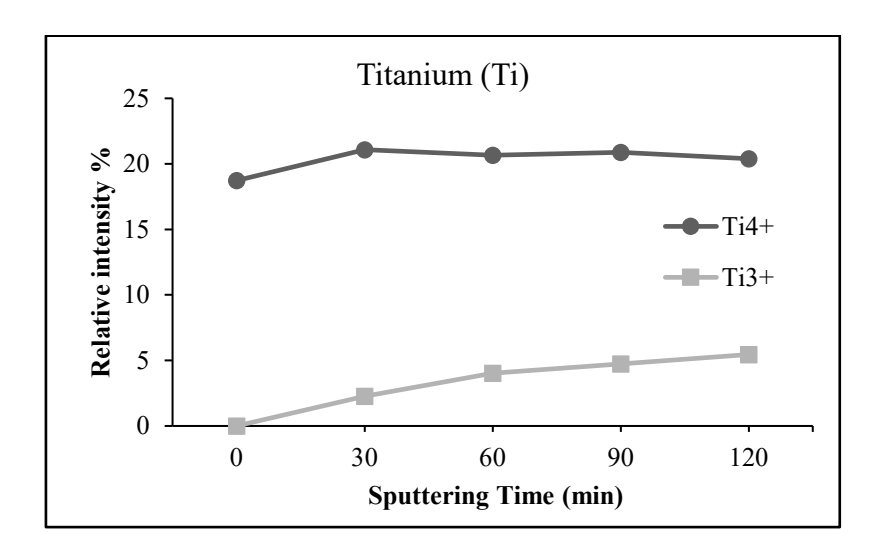




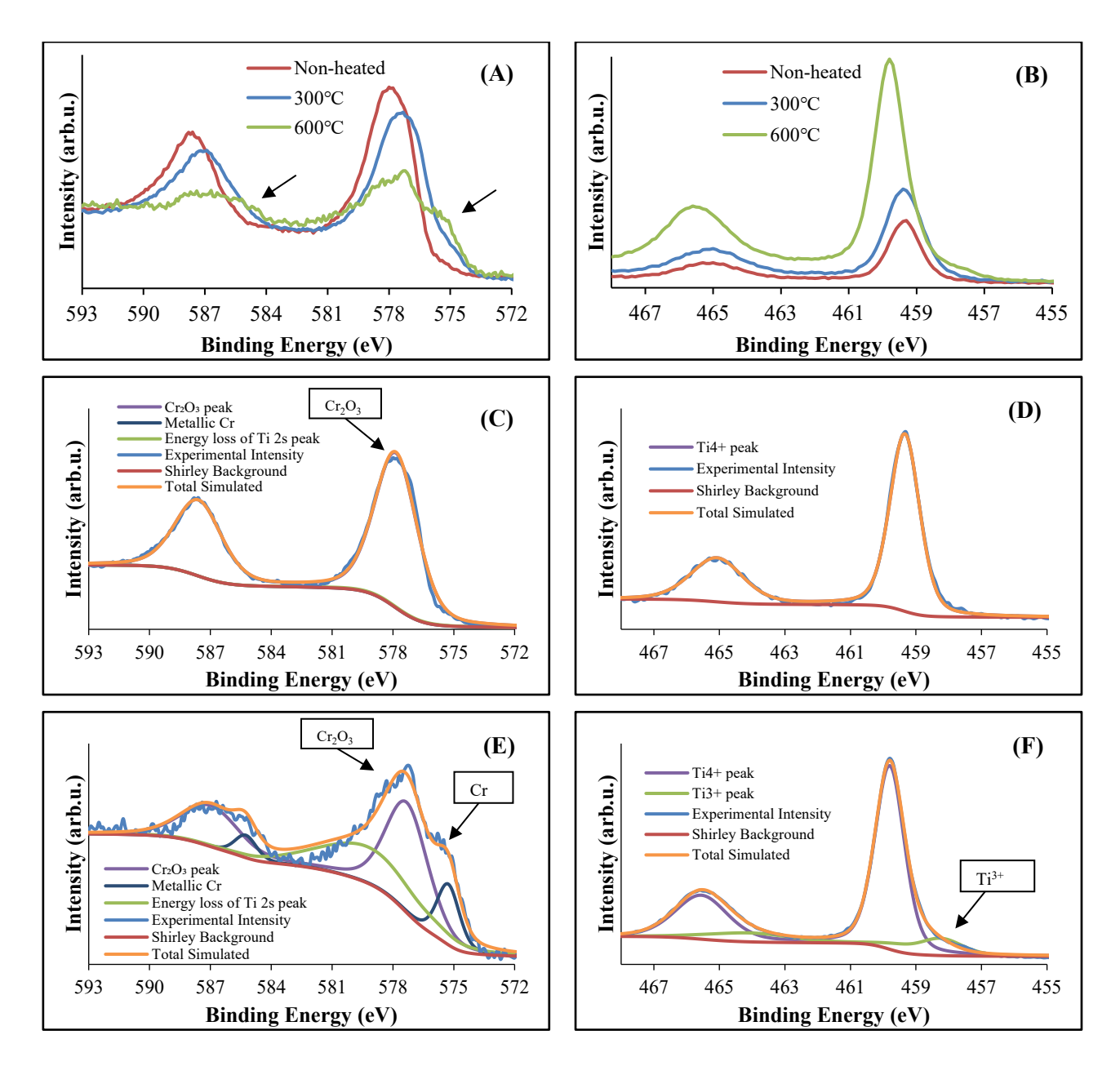
**Figure A11**:  $Cr\ 2p\ XPS\ spectra\ of\ (A)\ aTiO_2\ and\ (B)\ aTiO_2\ after\ photodeposition\ of\ the\ Cr_2O_3\ layer$  and calcining the sample at 200°C for 10 min.

Figure A12 shows the relative intensity of  $TiO_2$  peaks at different sputtering dose for both  $Ti^{4+}$  and  $Ti^{3+}$ . When the  $TiO_2$  is sputtered, a second Ti  $2p_{3/2}$  doublet was found at  $457.6 \pm 0.2$  eV that

corresponds to  $Ti^{3+}$  and the presence of O vacancies due to the sputtering  $^{10}$ . Figure A12 shows that  $Ti^{4+}$  decreased slightly and  $Ti^{3+}$  increased with increasing sputter dose.



**Figure A12**: XPS relative intensity of Ti 2p of  $aTiO_2$ - $Cr_2O_3$  and subsequently annealed to  $600^{\circ}C$ . Then, the sample was sputtered for various times.



**Figure A13**: Synchrotron XPS spectra of (A) Cr 2p and (B) Ti 2p regions of aTiO<sub>2</sub>-Cr<sub>2</sub>O<sub>3</sub> before and after annealing at 300°C and 600°C. Fitted synchrotron XPS spectra of (C and E) Cr 2p and (D and F) Ti 2p of aTiO<sub>2</sub>-Cr<sub>2</sub>O<sub>3</sub> before and after annealing at 600°C. A small amount of  $Ti^{3+}$  is formed when heating the samples to 600°C.

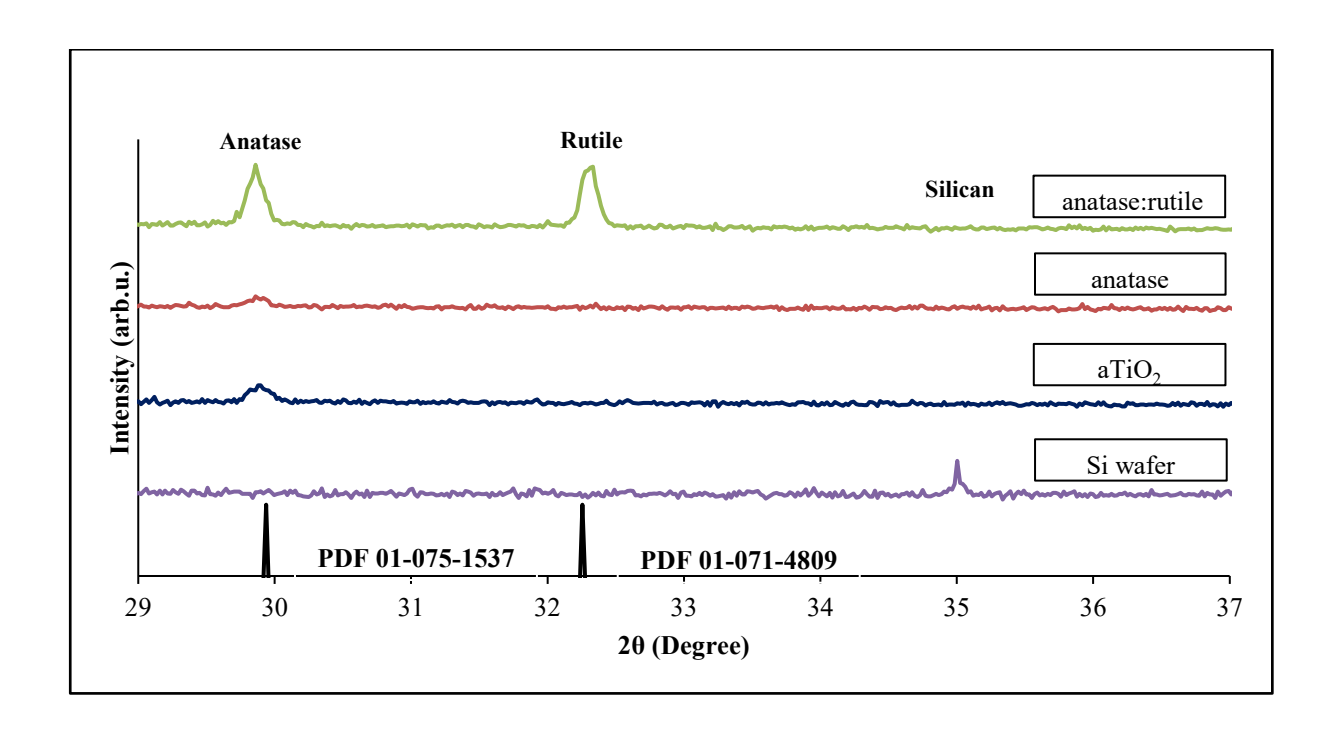


**Figure A14**: XRD patterns of Si wafer, aTiO<sub>2</sub>-Cr<sub>2</sub>O<sub>3</sub>, anatase-Cr<sub>2</sub>O<sub>3</sub>, and anatase:rutile-Cr<sub>2</sub>O<sub>3</sub> after annealing to 600°C. The standard XRD patterns for anatase is PDF 01-075-1537 and rutile is PDF 01-071-4809.

Figure A15 shows the valence electron spectra (UPS) of aTiO<sub>2</sub> and aTiO<sub>2</sub>-Cr<sub>2</sub>O<sub>3</sub> as function of annealing temperatures. The edge of the valences band is indicated in the figures with a dash line (the blue dash line is aTiO<sub>2</sub> and green dash line is aTiO<sub>2</sub>-Cr<sub>2</sub>O<sub>3</sub>). After annealing at 200°C, the valence band is found for aTiO<sub>2</sub> and aTiO<sub>2</sub>-Cr<sub>2</sub>O<sub>3</sub> at ~ 3.1 eV and ~ 3.4 eV, respectively. Annealing to 300°C up to 500°C shows same valence band for both samples around ~ 3.4 eV. The valence band shifted to higher binding energy after annealing at 600°C to ~ 3.9 eV and ~ 3.7 eV for aTiO<sub>2</sub> and aTiO<sub>2</sub>-Cr<sub>2</sub>O<sub>3</sub>. UPS valence band structure measurements of aTiO<sub>2</sub> and aTiO<sub>2</sub>-Cr<sub>2</sub>O<sub>3</sub> as function of annealing temperatures did not observe much change of the valence band edge. Therefore, no doping of Cr in TiO<sub>2</sub> occurred in the sample after annealing.

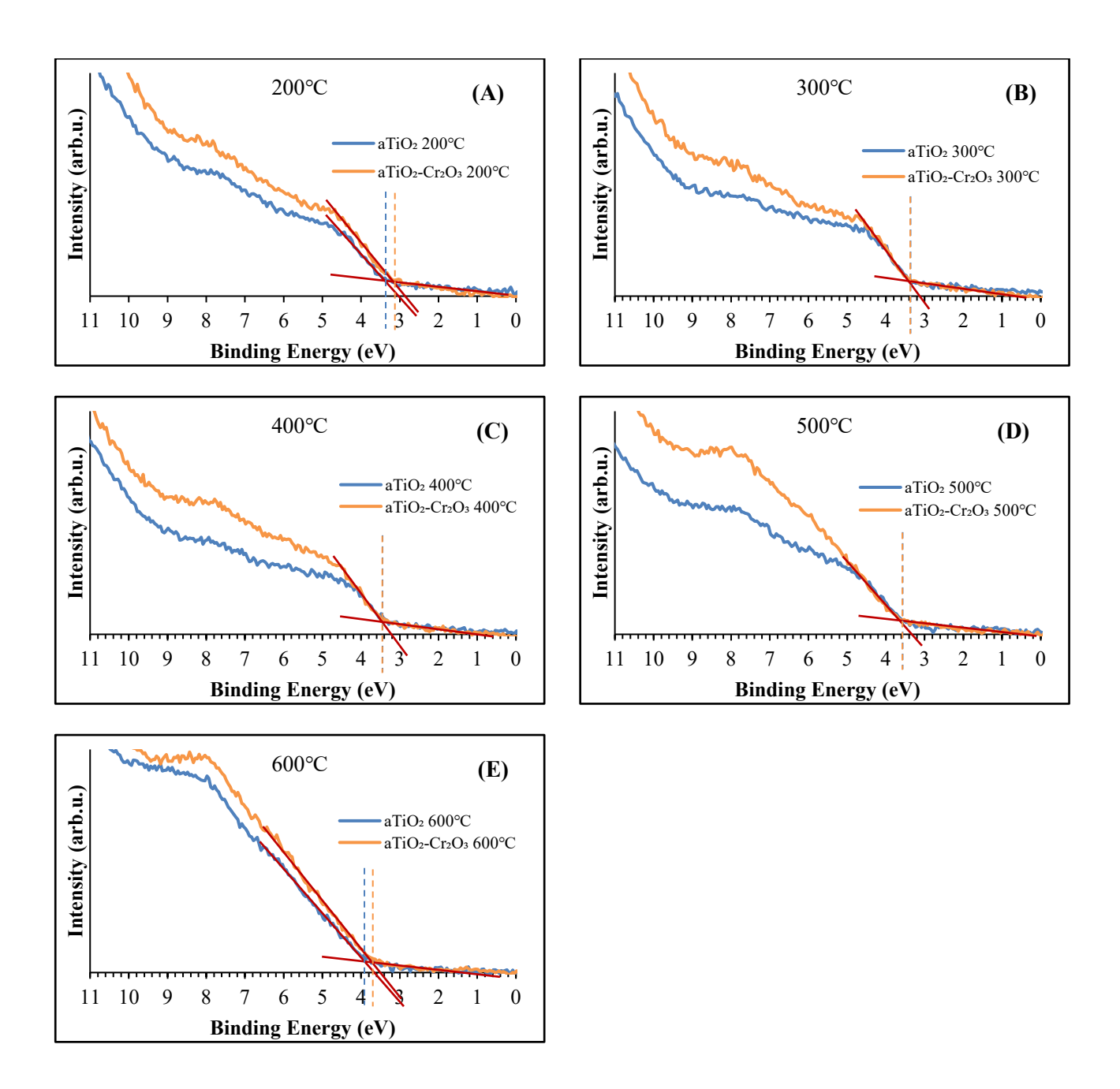


Figure A15: UPS spectra of aTiO<sub>2</sub> and aTiO<sub>2</sub>-Cr<sub>2</sub>O<sub>3</sub> after annealing at various temperatures (A)  $200^{\circ}$ C, (B)  $300^{\circ}$ C, (C)  $400^{\circ}$ C, (D)  $500^{\circ}$ C and (E)  $600^{\circ}$ C.

Figure A16 shows AFM images of aTiO<sub>2</sub> and aTiO<sub>2</sub>-Cr<sub>2</sub>O<sub>3</sub>. Three  $4 \times 4 \mu m$  images were acquired on each sample at separate locations (i.e., the tip was disengaged from the surface and moved some hundreds of microns in the X and Y directions before re-engaging). The average Ra value of the images acquired on the aTiO<sub>2</sub> surface was  $1.1\pm0.03$  nm, while the average Ra value for the aTiO<sub>2</sub> surface after the photodeposition of Cr<sub>2</sub>O<sub>3</sub> layer was  $1.16\pm0.17$  nm. Note that the white particles increase the overall roughness and excluding these particles lead to the decrease the Ra to  $0.94\pm0.04$  nm.

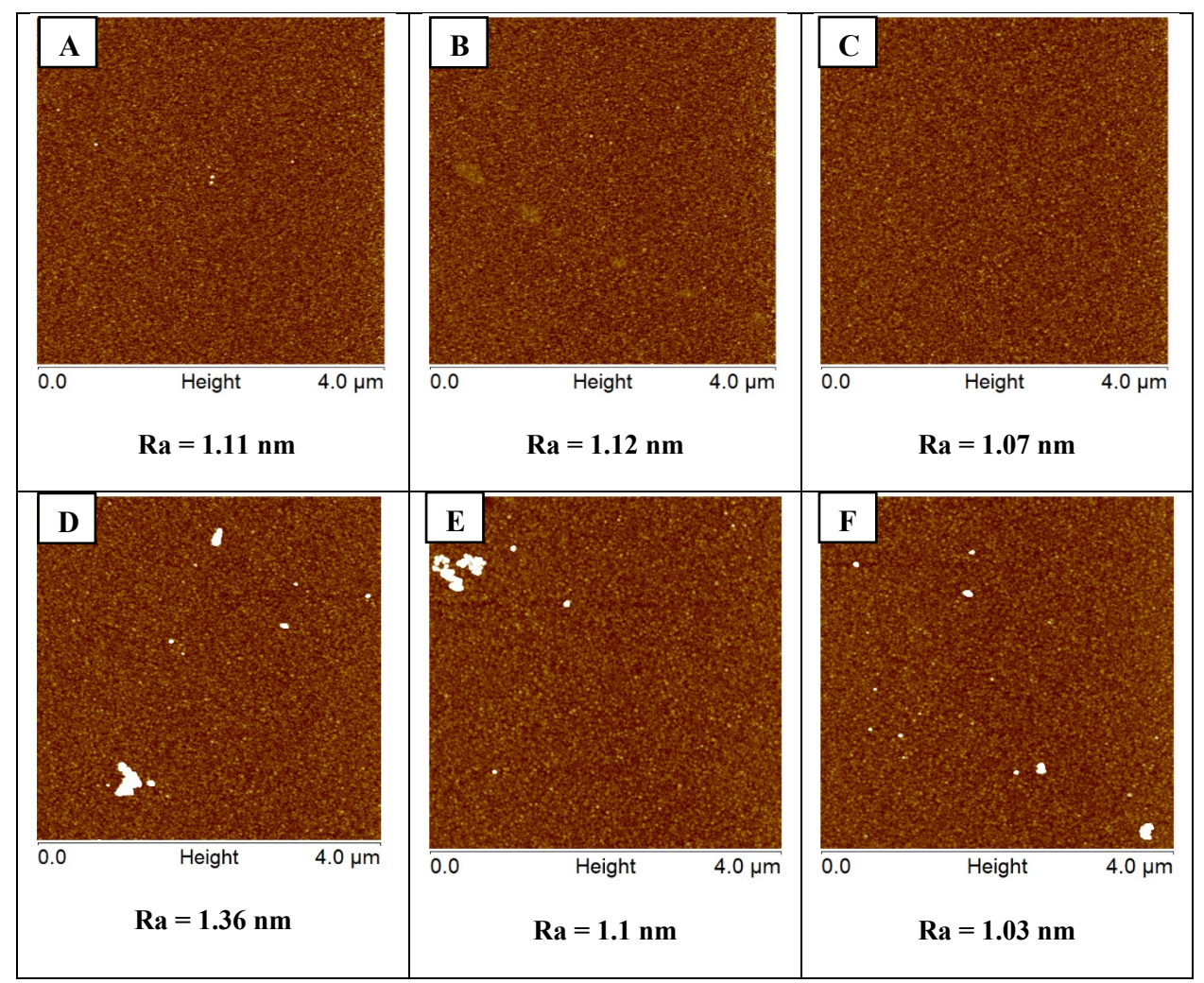


Figure A16: AFM images of (A, B and C) aTiO<sub>2</sub> and (D, E and F) aTiO<sub>2</sub>-Cr<sub>2</sub>O<sub>3</sub>. (The height scale for each image is the same and is 20 nm)

#### References

- 1. Andersson, G. G.; Golovko, V. B.; Alvino, J. F.; Bennett, T.; Wrede, O.; Mejia, S. M.; Al Qahtani, H. S.; Adnan, R.; Gunby, N.; Anderson, D. P., Phosphine-stabilised Au9 Clusters Interacting with Titania and Silica Surfaces: The First Evidence for the Density of States Signature of the Support-immobilised Cluster. *The Journal of chemical physics* **2014**, *141* (1), 014702.
- 2. Nefedov, V. I. G., D.; Dzhurinskii, B. F.; Sergushin, N. P.; Salyn, Ya. V., The X-ray Electronic Studies of Oxides of Certain Elements. *Zh. Neorg. Khimii* **1975**, (0044-457X), 20, 2307.
- 3. Baikie, T.; Ahmad, Z.; Srinivasan, M.; Maignan, A.; Pramana, S. S.; White, T. J., The crystallographic and magnetic characteristics of Sr2CrO4 (K2NiF4-type) and Sr10(CrO4)6F2 (apatite-type). *Journal of Solid State Chemistry* **2007**, *180* (5), 1538-1546.
- 4. Torras, J.; Azambuja, D. S.; Wolf, J. M.; Alemán, C.; Armelin, E., How Organophosphonic Acid Promotes Silane Deposition onto Aluminum Surface: A Detailed Investigation on Adsorption Mechanism. *The Journal of Physical Chemistry C* **2014**, *118* (31), 17724-17736.
- 5. Biesinger, M. C.; Brown, C.; Mycroft, J. R.; Davidson, R. D.; McIntyre, N. S., X-ray photoelectron spectroscopy studies of chromium compounds. *Surface and Interface Analysis* **2004**, *36* (12), 1550-1563.
- 6. Jianjun, W.; Qunji, X., Effects of synthetic additives on the friction and wear properties of a Cr2O3 coating. *Wear* **1994**, *176* (2), 213-216.
- 7. Eschen, F.; Heyerhoff, M.; Morgner, H.; Vogt, J., The concentration-depth profile at the surface of a solution of tetrabutylammonium iodide in formamide, based on angle-resolved photoelectron spectroscopy. *Journal of Physics: Condensed Matter* **1995**, 7 (10), 1961-1978.
- 8. Wang, C.; Andersson, G. G., Measuring concentration depth profiles at liquid surfaces: Comparing angle resolved X-ray photoelectron spectroscopy and neutral impact collision scattering spectroscopy. *Surface Science* **2011**, *605* (9), 889-897.
- 9. Trenczek-Zajac, A.; Radecka, M.; Jasinski, M.; Michalow, K. A.; Rekas, M.; Kusior, E.; Zakrzewska, K.; Heel, A.; Graule, T.; Kowalski, K., Influence of Cr on structural and optical properties of TiO2:Cr nanopowders prepared by flame spray synthesis. *Journal of Power Sources* **2009**, *194* (1), 104-111.
- 10. Al Qahtani, H. S.; Metha, G. F.; Walsh, R. B.; Golovko, V. B.; Andersson, G. G.; Nakayama, T., Aggregation Behavior of Ligand-Protected Au9 Clusters on Sputtered Atomic Layer Deposition TiO2. *The Journal of Physical Chemistry C* **2017**, *121* (20), 10781-10789.

# Appendix B: Reduction and Diffusion of Cr-oxide Layer into P25, BaLa<sub>4</sub>Ti<sub>4</sub>O<sub>15</sub> and Al:SrTiO<sub>3</sub> Particles upon High-Temperature Annealing

This appendix contains a detailed description, additional figures and tables:

#### Additional figures and tables:

### Photodeposition of Cr<sub>2</sub>O<sub>3</sub>

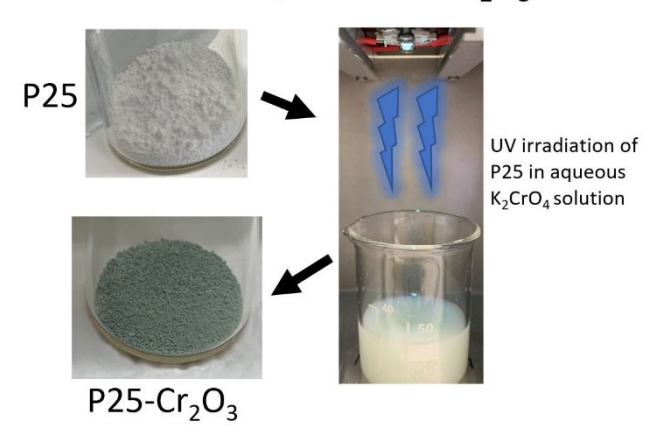


*Figure B1*: Experimental procedure of photodeposition of the Cr<sub>2</sub>O<sub>3</sub> on P25 particles.

STEM-EDX elemental mapping of Cr, Ti and O for P25-Cr<sub>2</sub>O<sub>3</sub> are shown in Figure B2 with line analysis for Cr and Ti. The line analysis shows that the thickness of the Cr-oxide layer is 1.2 - 1.5 nm.

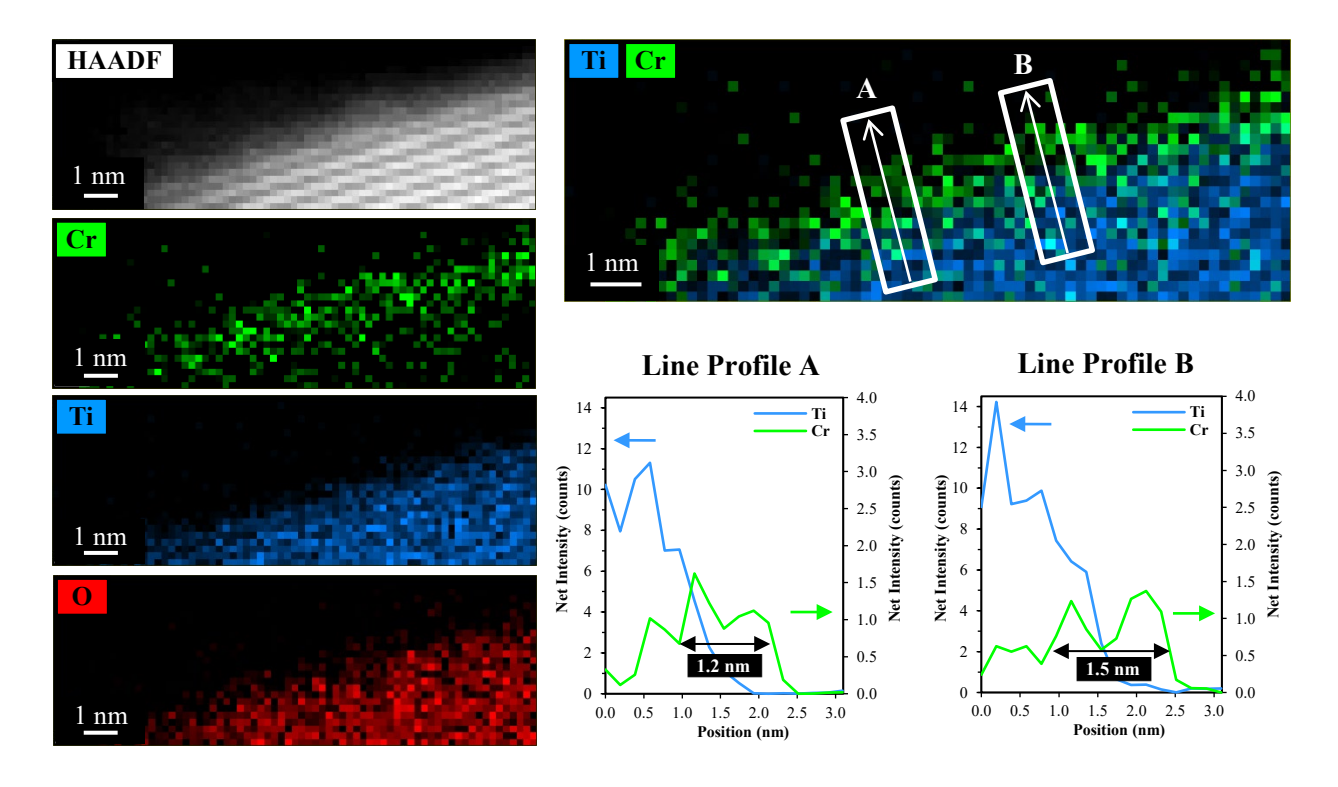


**Figure B2**: STEM-EDX elemental mapping of Cr, Ti and O with line analysis of Ti and Cr for P25- $Cr_2O_3$  before annealing.

Figure B3 shows the Cr L-edge spectra of Cr<sub>2</sub>O<sub>3</sub>, CrO<sub>2</sub> and CrO<sub>3</sub> reference samples reproduced from literature<sup>1</sup>.

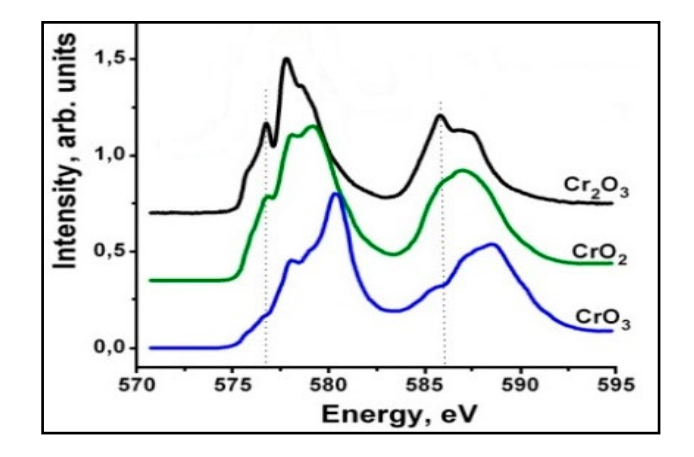
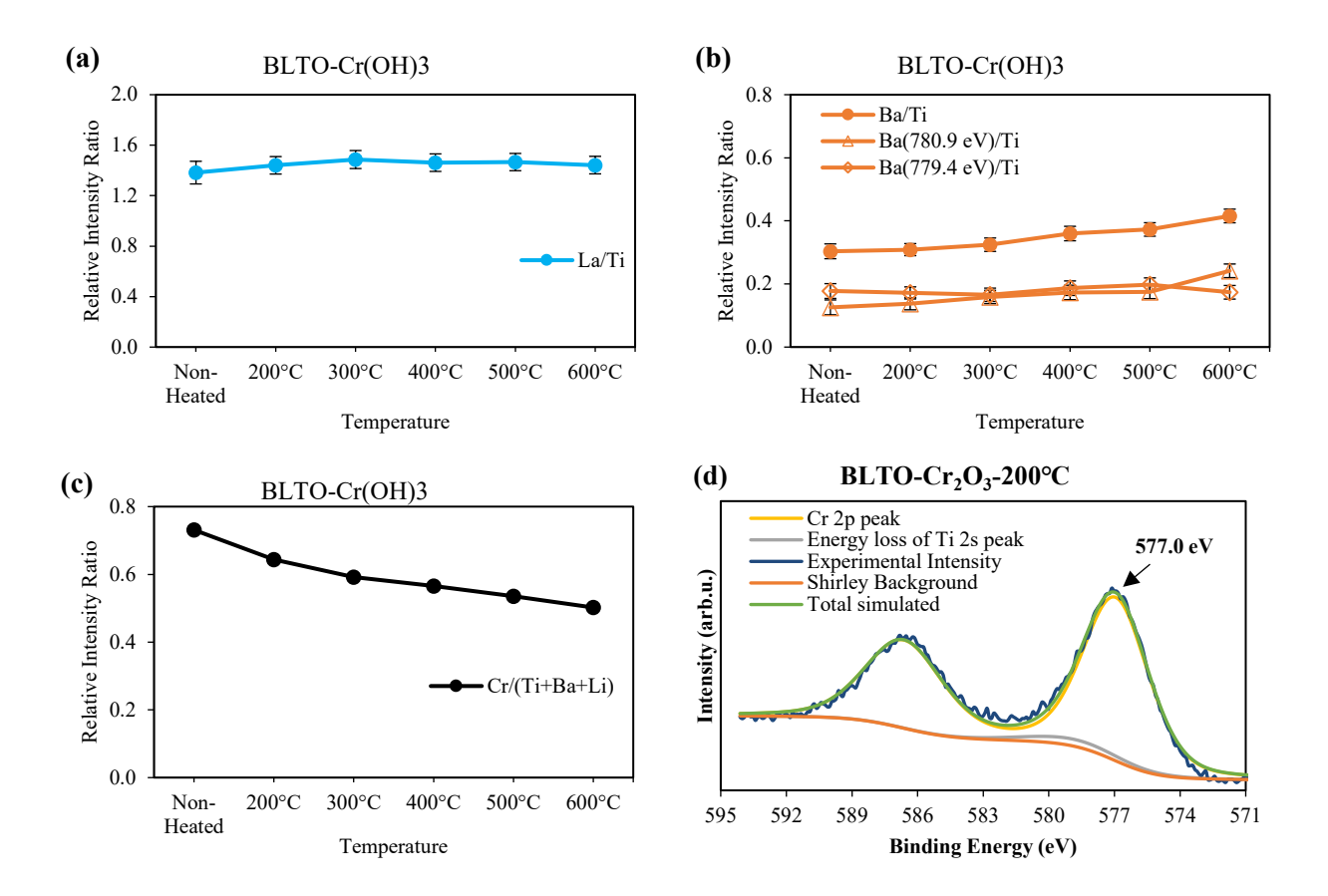


Figure B3: Cr L-edge NEXAFS spectra of Cr<sub>2</sub>O<sub>3</sub>, CrO<sub>2</sub>, and CrO<sub>3</sub> from ref <sup>1</sup>

Figures B4a and B4b show the relative intensity ratio of La and Ba to Ti of BLTO-Cr(OH)<sub>3</sub> annealed at various temperatures. Figure B4a shows a stable La to Ti ratio, while Figure B4b shows a slight increase in the Ba to Ti ratio.



**Figure B4**: XPS relative intensity ratio of (a) La 3d to Ti 2p, (b) Ba 3d to Ti 2p and (c) Cr 2p to (Ti 2p, Ba 3d and La 3d) of BLTO-Cr<sub>2</sub>O<sub>3</sub> annealed at various temperatures. (d) Cr 2p XP spectra of (c) BLTO-Cr<sub>2</sub>O<sub>3</sub>-200°C

The relative intensity ratio of Cr to Ti of SrTiO<sub>3</sub>-Cr<sub>2</sub>O<sub>3</sub> annealed at various temperatures is shown in Figure B5 with a stable ratio.

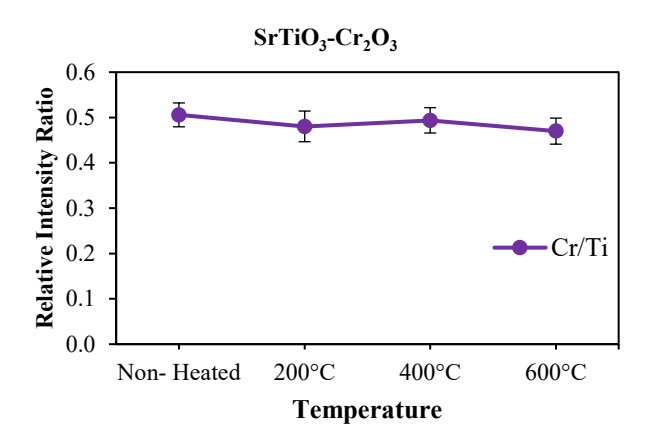


**Figure B5**: XPS relative intensity ratio of Cr 2p to Ti 2p of SrTiO<sub>3</sub>-Cr<sub>2</sub>O<sub>3</sub> annealed at various temperatures.

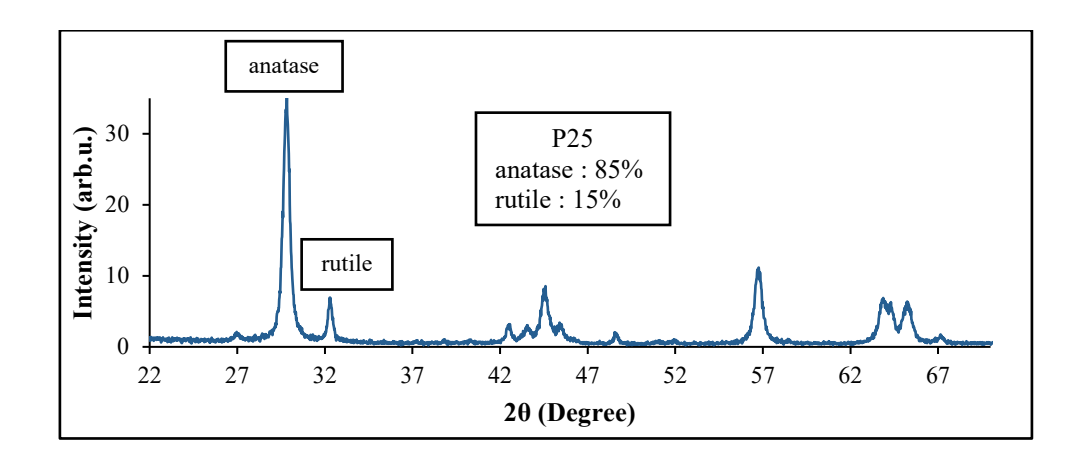


*Figure B6*: XRD pattern of P25 with a rough estimation of the anatase and rutile amount in P25. The standard XRD patterns for anatase is PDF 01-075-1537 and rutile is PDF 01-071-4809.

Figure B7 shows the Cr L-edge of Cr metal and  $Cr_2O_3$  reference spectra with the features of the Cr metal spectrum identified<sup>2</sup>. These features (indicated by black arrows in Figure B7) are the start of the Cr L<sub>3</sub>-edge spectrum just below 575 eV, the less sharp peaks in the Cr L<sub>3,2</sub>-edges spectrum and interference of a small peak in the tail of the Cr L<sub>2</sub>-edge. These features were also described in our previous publication<sup>2</sup>. These features distinguish Cr metal from  $Cr_2O_3$  in the Cr L<sub>3,2</sub>-edges spectrum.

A high-resolution XPS spectrum of Cr 2p of the Cr metal reference sample demonstrates that Cr 2p has a mix of Cr and  $Cr_2O_3$  peaks  $(30.70)^2$ . It has been found that the presence of  $Cr_2O_3$  at the surface of Cr metal was due to exposing the sample to air, which causes the Cr atoms at the surface to oxidise and forming  $Cr_2O_3$  at the surface<sup>3</sup>. This result means that the Cr L-edge spectrum of Cr metal is considered a mixture of Cr and  $Cr_2O_3$ 

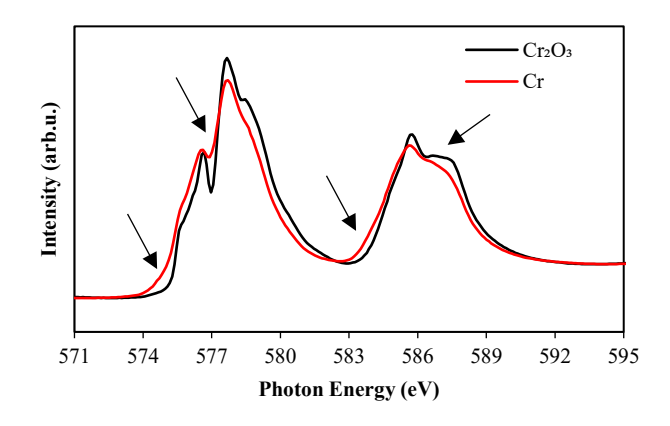
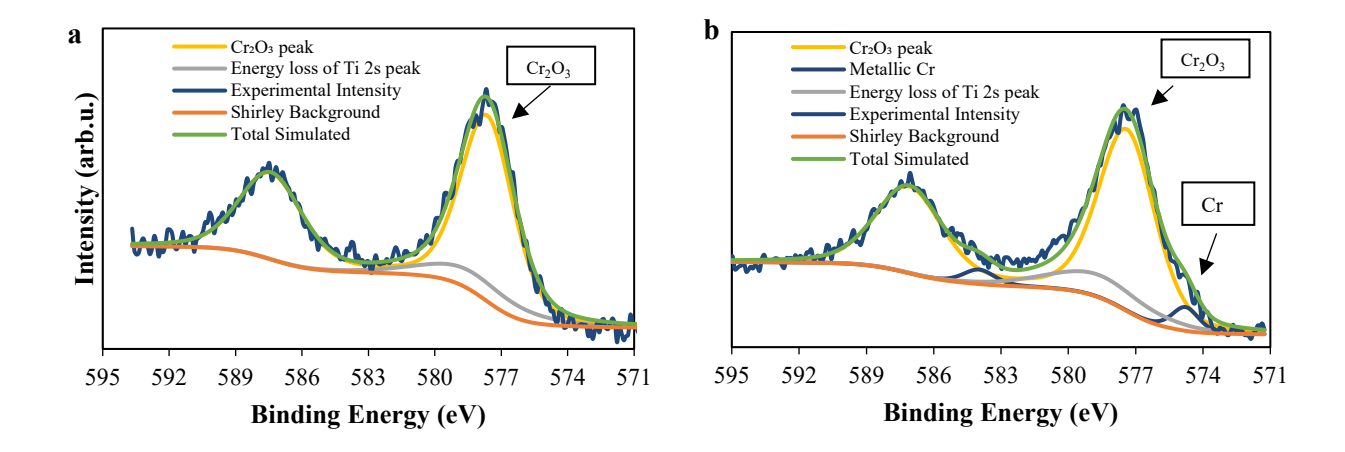


Figure B7: Cr L-edge NEXAFS spectra of chromium metal and chromium oxide reference samples

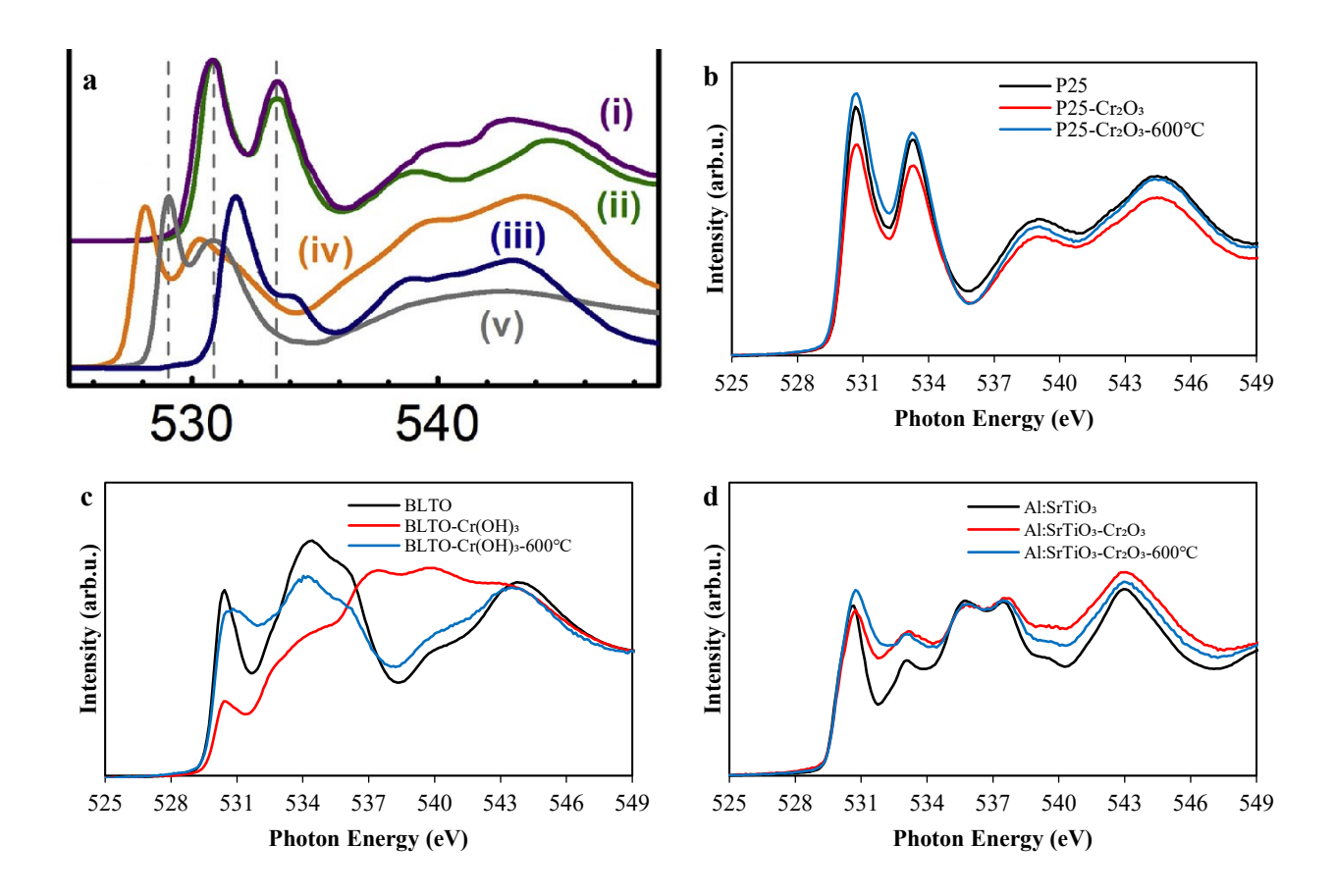


**Figure B8**: Cr 2p XP spectra of (a) SrTiO<sub>3</sub>-Cr<sub>2</sub>O<sub>3</sub> before annealing and (b) SrTiO<sub>3</sub>-Cr<sub>2</sub>O<sub>3</sub> after annealing at 600°C.

NEXAFS O K-edge spectrum can be used to determine the chemical state of the Cr-oxide layer. Figure B9a shows the O K-edge reference spectra of anatase, rutile, Cr<sub>2</sub>O<sub>3</sub>, CrO<sub>2</sub> and CrO<sub>3</sub><sup>4</sup>. The O K-edge spectrum has a different lineshape for the different oxidation states of Cr. The O K-edge spectra of Cr<sub>2</sub>O<sub>3</sub>, CrO<sub>2</sub> and CrO<sub>3</sub> are observed with main peaks at 532 eV, 528 eV and 529 eV respectively. These main peaks can be used as fingerprints to indicate the oxidation state of Cr in the O K-edge spectrum. Note that the anatase and rutile have two similar main peaks observed at 531 eV and 533 eV.

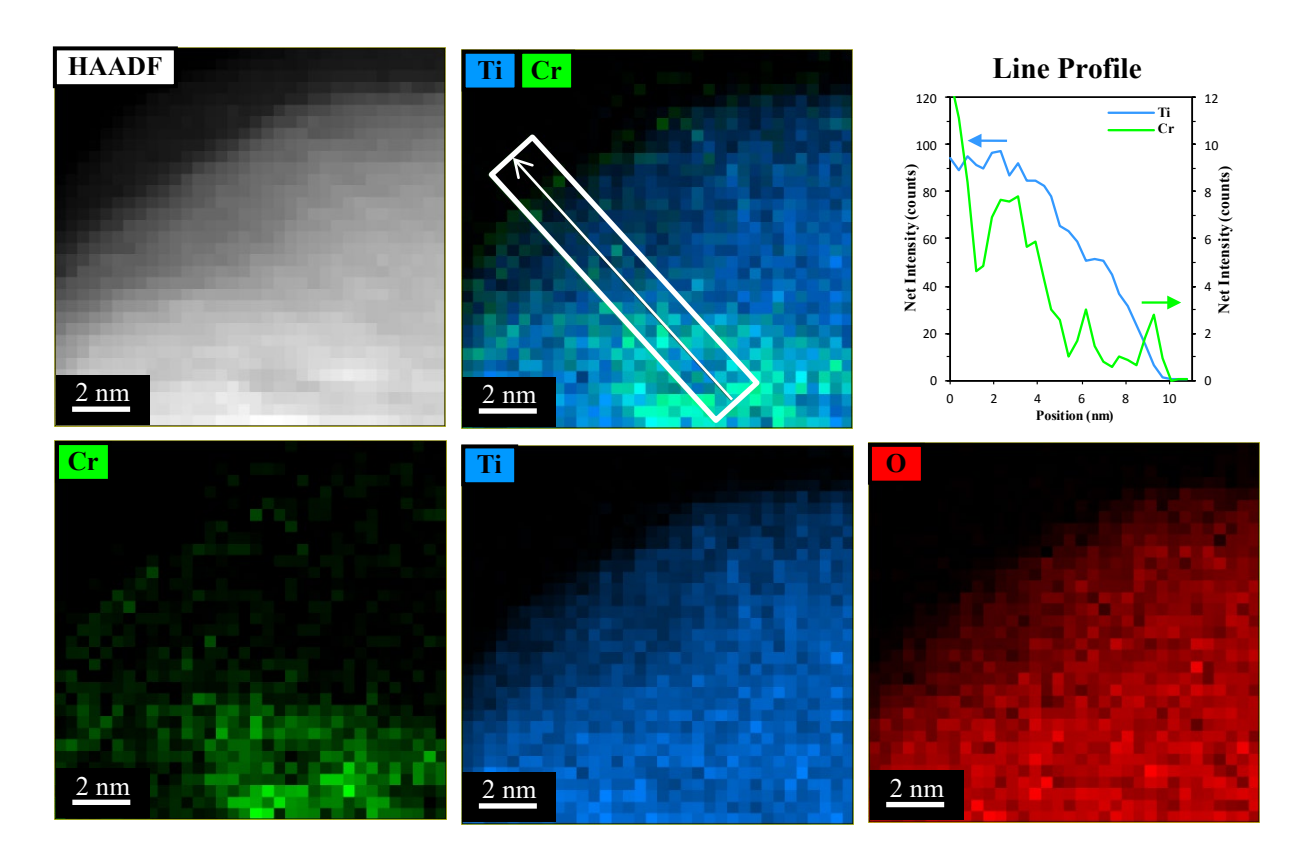
Figure B9b shows the O K-edge spectra of P25-Cr<sub>2</sub>O<sub>3</sub> before and after annealing at 600°C. The O K-edge spectra have two main peaks at 531 eV and 533 eV, similar to the two main peaks observed in Figure B9a, which correspond to anatase and rutile. It can be seen that the O K-edge spectra of P25-Cr<sub>2</sub>O<sub>3</sub> before and after annealing have no indication of a peak below 530 eV, which is the region in the spectrum where the CrO<sub>2</sub> and CrO<sub>3</sub> main peaks occur.

Figure B9c shows the O K-edge spectra of BLTO, BLTO-Cr(OH)<sub>3</sub> and BLTO-Cr<sub>2</sub>O<sub>3</sub> after annealing at 600°C. There is no observation of any peak at an energy below 530 eV, where the main peaks of O in CrO<sub>2</sub> and CrO<sub>3</sub> occur. Figure B9d shows the O K-edge spectra of Al:SrTiO<sub>3</sub>, Al:SrTiO<sub>3</sub>-Cr<sub>2</sub>O<sub>3</sub> and Al:SrTiO<sub>3</sub>-Cr<sub>2</sub>O<sub>3</sub> after annealing at 600°C. There is also no presence of O in CrO<sub>2</sub> or CrO<sub>3</sub> main peaks. Figure B9 confirm the absence of CrO<sub>2</sub> and CrO<sub>3</sub> species in in P25-Cr<sub>2</sub>O<sub>3</sub>, BLTO-Cr(OH)<sub>3</sub> and Al:SrTiO<sub>3</sub>-Cr<sub>2</sub>O<sub>3</sub> before and after annealing at 600°C.



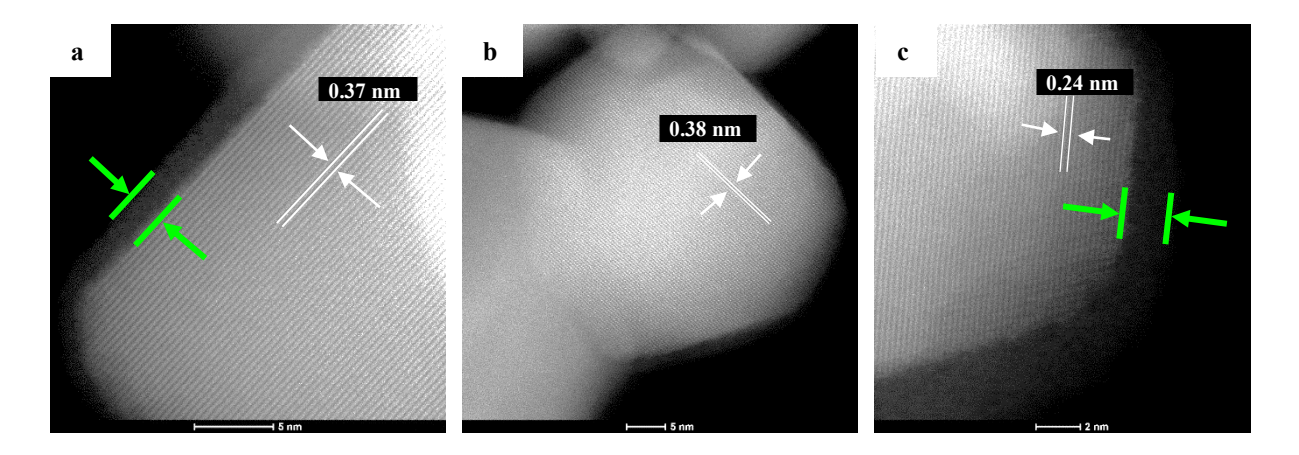
**Figure B9**: O K-edge NEXAFS spectra of (a) (i) anatase, (ii) rutile, (iii)  $Cr_2O_3$ , (iv)  $CrO_2$  and (v)  $CrO_3$  from the literature <sup>4</sup>, (b) P25- $Cr_2O_3$  and P25- $Cr_2O_3$  after annealing at  $600^{\circ}$ C, (c) BLTO, BLTO- $Cr(OH)_3$  and BLTO- $Cr_2O_3$ - $600^{\circ}$ C and (d)  $Al:SrTiO_3$ ,  $Al:SrTiO_3$ - $Cr_2O_3$  and  $Al:SrTiO_3$ - $Cr_2O_3$ - $600^{\circ}$ C. British Crown Owned Copyright 2022/AWE. Published with permission of the Controller of Her Britannic Majesty's Stationery Office

Figure B10 shows an elemental mapping of the P25-Cr<sub>2</sub>O<sub>3</sub> particle after annealing at 600°C. It can be seen that Cr has diffused into the P25 particle with high intensity of Cr in the inner part of the P25 particle.



**Figure B10**: STEM-EDX elemental mapping of Cr, Ti and O with line analysis of Cr and Ti for P25- $Cr_2O_3$  after annealing at 600°C.

Figure B11 shows STEM images of P25-Cr<sub>2</sub>O<sub>3</sub> particles before and after annealing. Figures B11a and B11b show P25 particles with lattice spacing of 0.37 nm and 0.38 nm. These match with anatase TiO<sub>2</sub> (101) and (100) crystal planes<sup>5, 6</sup>. Figure B11a shows the Cr<sub>2</sub>O<sub>3</sub> layer formed on the anatase particle (before annealing). However, Figure B11b shows the anatase particle with no Cr<sub>2</sub>O<sub>3</sub> layer at the surface (after annealing at 600°C). Figure B11c shows a P25 particle (after annealing at 600°C) with a lattice spacing of 0.24 nm, which corresponding to the rutile (001) crystal plane<sup>7</sup>. It is clear that the Cr<sub>2</sub>O<sub>3</sub> layer remains at the surface of a rutile particle after annealing at 600°C. Therefore, the STEM images are consistent with our explanation that annealing P25-Cr<sub>2</sub>O<sub>3</sub> at 600°C causes Cr<sub>2</sub>O<sub>3</sub> to diffuse into anatase particles but remain on the surface of rutile particles due to difference in surface energy (*vide supra*).



**Figure B11** STEM images of (a) P25-Cr<sub>2</sub>O<sub>3</sub> before annealing and (b and c) P25-Cr<sub>2</sub>O<sub>3</sub> after annealing at 600°C.

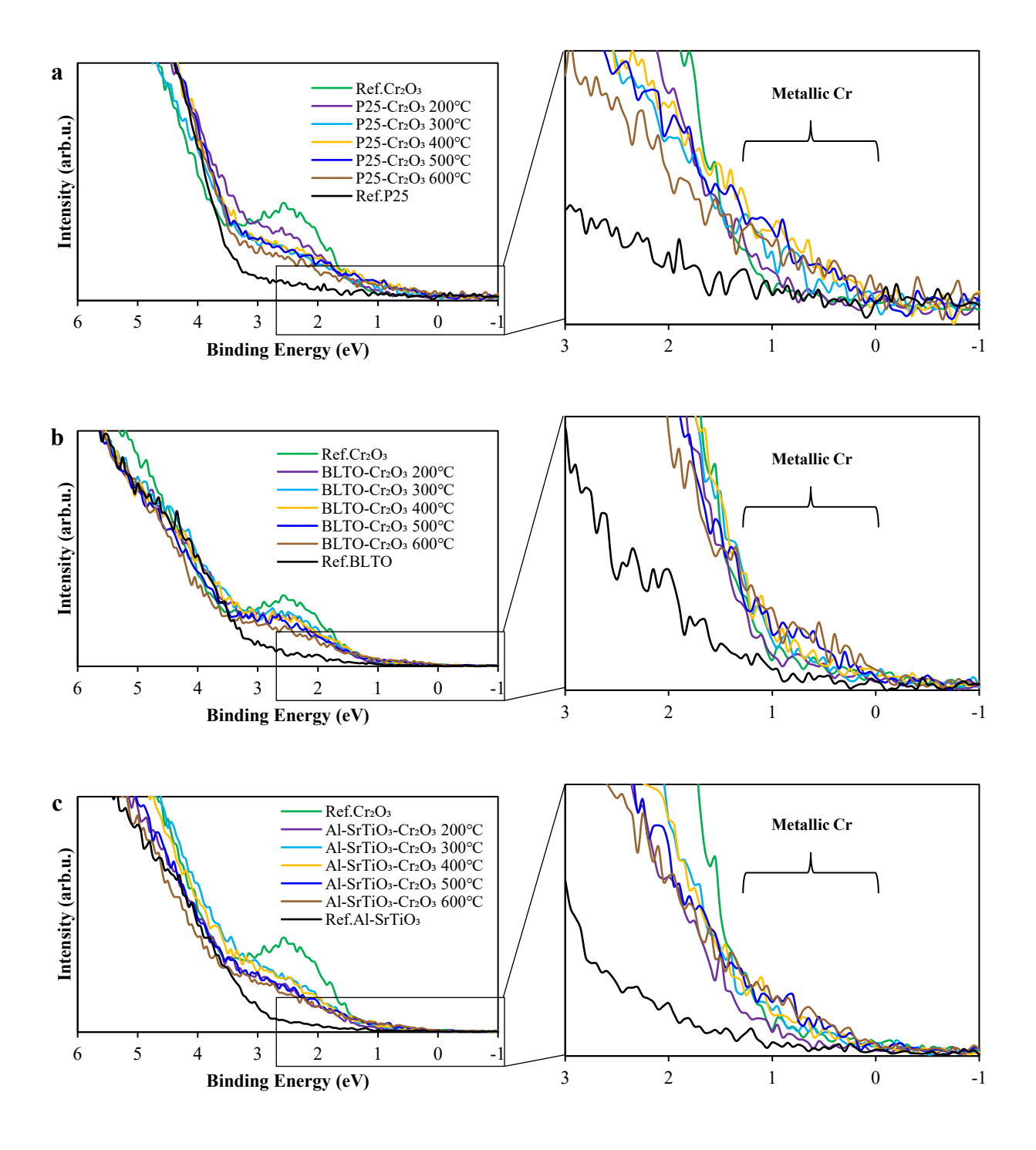


**Figure B12**: UPS spectra of (a) P25,  $Cr_2O_3$  and P25- $Cr_2O_3$  after annealing at various temperatures, (b) BLTO,  $Cr_2O_3$  and BLTO- $Cr_2O_3$  after annealing at various temperatures and (c) Al:SrTiO<sub>3</sub>,  $Cr_2O_3$  and Al:SrTiO<sub>3</sub>- $Cr_2O_3$  after annealing at various temperatures.

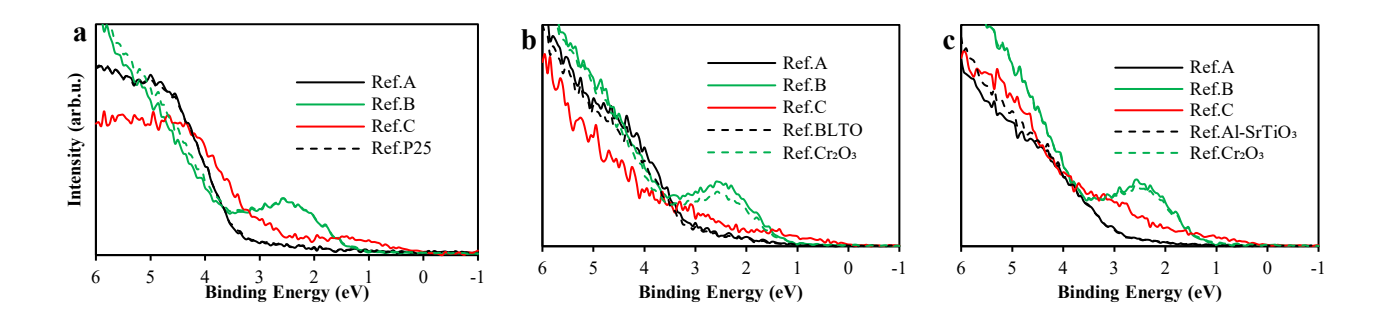


**Figure B13**: UPS reference spectra identified via SVD of (a) P25-Cr<sub>2</sub>O<sub>3</sub> after annealing at various temperatures with UPS spectra of P25 and Cr<sub>2</sub>O<sub>3</sub>, (b) BLTO-Cr<sub>2</sub>O<sub>3</sub> after annealing at various temperatures with UPS spectra of BLTO and Cr<sub>2</sub>O<sub>3</sub> and (c) Al:SrTiO<sub>3</sub>-Cr<sub>2</sub>O<sub>3</sub> after annealing at various temperatures with UPS spectra of Al:SrTiO<sub>3</sub> and Cr<sub>2</sub>O<sub>3</sub>.

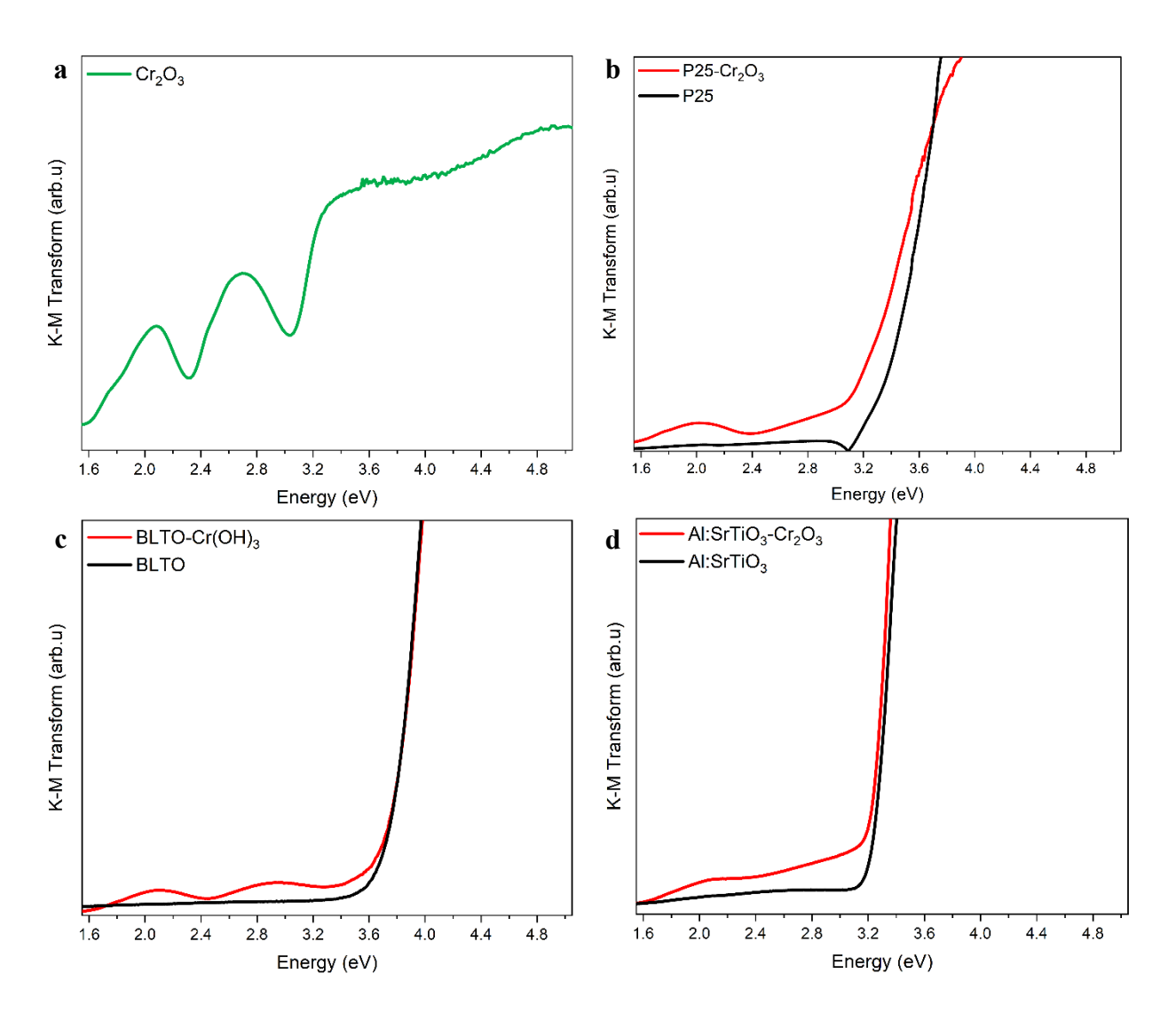


**Figure B14:** Comparison of as deposited  $Cr_2O_3$ -doped samples with pure  $Cr_2O_3$ . Kubelka-Munk Transformed UV-visible diffuse reflectance spectra of (a)  $Cr_2O_3$ , (b) P25, (c) BLTO and (d)  $Al:SrTiO_3$ .

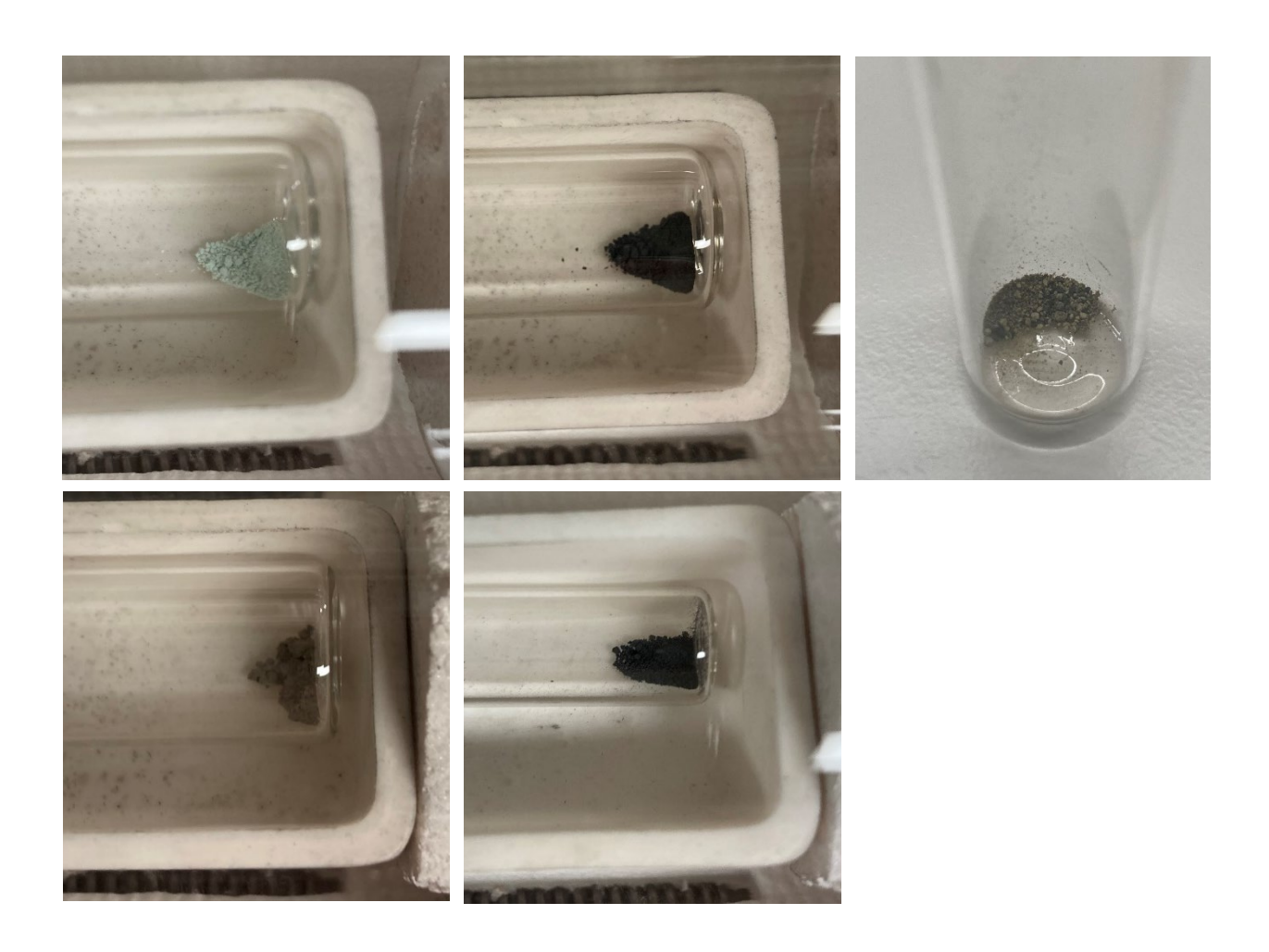


**Figure B15:** P25-Cr<sub>2</sub>O<sub>3</sub> as-deposited (top left), after annealing to 600 °C (top middle) and upon mixing (top right) Al:SrTiO<sub>3</sub>-Cr<sub>2</sub>O<sub>3</sub> (bottom left) and BLTO-Cr<sub>2</sub>O<sub>3</sub> (bottom right) after annealing to 600 °C

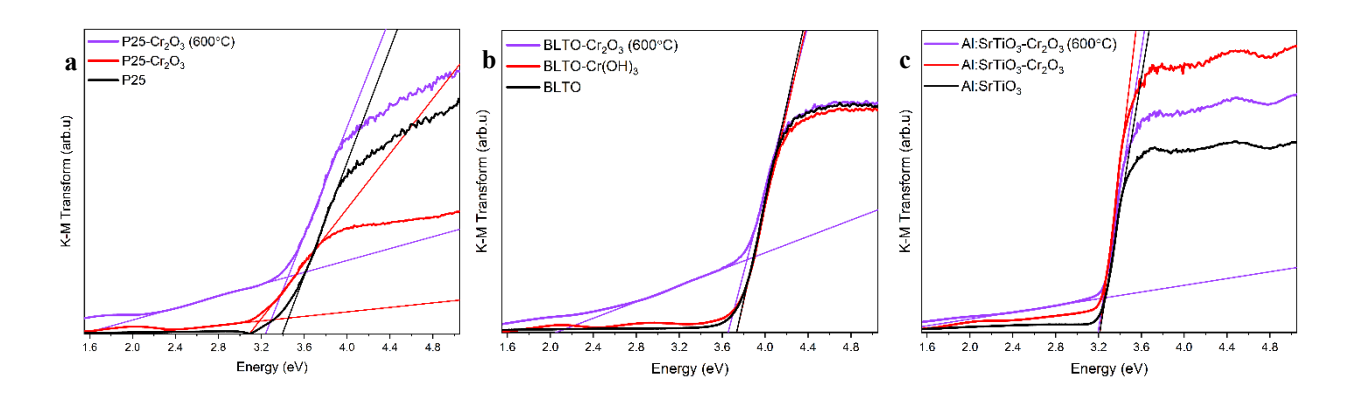


**Figure B16:** Kubelka-Munk Transformed UV-visible diffuse reflectance spectra of (a) P25, (b) BLTO and (c) Al:SrTiO<sub>3</sub> with the band gap cut-off.

 Table B1:
 UV-visible diffuse reflectance derived bandgaps for photocatalysts with Cr-oxide

Photocatalyst	Before photodeposition	Cr-oxide photodeposited	After annealing
	Bandgap (eV)	Bandgap (eV)	Bandgap (eV)
P25	3.40	3.18	3.45
BLTO	3.74	3.76	3.83
Al:SrTiO <sub>3</sub>	3.21	3.21	3.23

**Table B2:** Photocatalytic hydrogen production rate of P25 and BLTO using methanol as sacrificial reagent.

Photocatalyst	Before photodeposition	Cr-oxide photodeposited	After annealing 600 °C
	I	Light Source - 405 nm (649 mW	)
P25	0.015 μmoles	No H <sub>2</sub> produced	No H <sub>2</sub> produced
BLTO	No H <sub>2</sub> produced	No H <sub>2</sub> produced	No H <sub>2</sub> produced
	I	Light Source - 365 nm (408 mW	)
Pt(1 wt%)/P25	2.8 µmoles	0.12 μmoles	0.23 μmoles
Pt(1 wt%)/BLTO	No H <sub>2</sub> produced	No H <sub>2</sub> produced	No H <sub>2</sub> produced

#### References

- 1. Sivkov, D.; Petrova, O.; Mingaleva, A.; Ob'edkov, A.; Kaverin, B.; Gusev, S.; Vilkov, I.; Isaenko, S.; Bogachuk, D.; Skandakov, R.; Sivkov, V.; Nekipelov, S., The Structure and Chemical Composition of the Cr and Fe Pyrolytic Coatings on the MWCNTs' Surface According to NEXAFS and XPS Spectroscopy. *Nanomaterials (Basel)* **2020**, *10* (2), 374.
- 2. Alotabi, A. S.; Gibson, C. T.; Metha, G. F.; Andersson, G. G., Investigation of the Diffusion of Cr2O3 into Different Phases of TiO2 upon Annealing. *ACS Applied Energy Materials* **2021**, *4* (1), 322-330.
- 3. Thurner, G.; Holloway, P. H., Oxidation of Polycrystalline Chromium between 30° C and 400° C. *Acta Physica Polonica A* **1992**, *81* (2), 273-283.
- 4. Gago, R.; Prucnal, S.; Pérez-Casero, R.; Caretti, I.; Jiménez, I.; Lungwitz, F.; Cornelius, S., Structural impact of chromium incorporation in as-grown and flash-lamp-annealed sputter deposited titanium oxide films. *Journal of Alloys and Compounds* **2017**, *729*, 438-445.
- 5. Xu, Q.; Yu, J.; Zhang, J.; Liu, G., Cubic anatase TiO2 nanocrystals with enhanced photocatalytic CO2 reduction activity. *Chemical Communications* **2015**, *51* (37), 7950-7953.
- 6. Tan, H.; Zhao, Z.; Niu, M.; Mao, C.; Cao, D.; Cheng, D.; Feng, P.; Sun, Z., A facile and versatile method for preparation of colored TiO2 with enhanced solar-driven photocatalytic activity. *Nanoscale* **2014**, *6* (17), 10216-10223.
- 7. An, X.; Liu, H.; Qu, J.; Moniz, S. J. A.; Tang, J., Photocatalytic mineralisation of herbicide 2,4,5-trichlorophenoxyacetic acid: enhanced performance by triple junction Cu–TiO2–Cu2O and the underlying reaction mechanism. *New Journal of Chemistry* **2015**, *39* (1), 314-320.

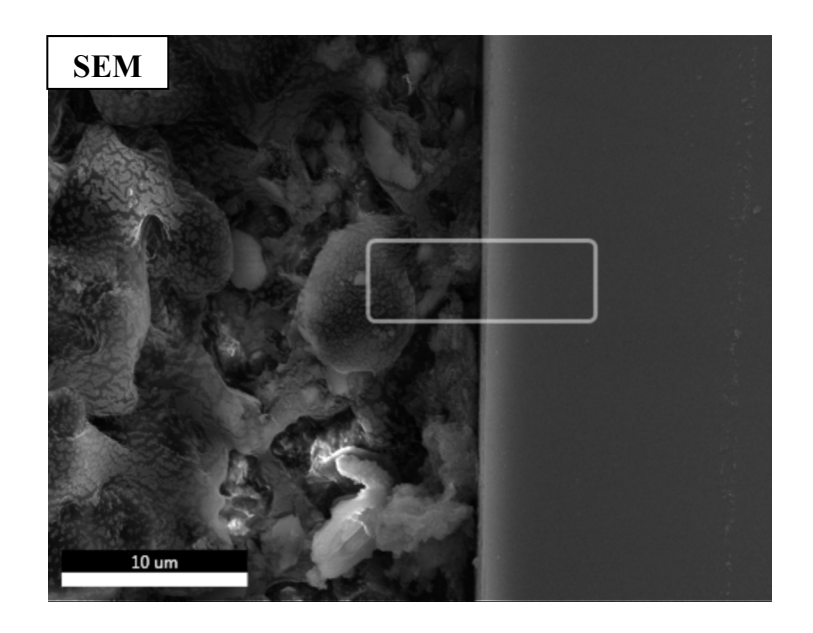
# Appendix C: Cr<sub>2</sub>O<sub>3</sub> Layer Inhibits Agglomeration of Phosphine-Protected Au<sub>9</sub> Clusters on TiO<sub>2</sub> Films

This appendix contains a detailed description, additional figures and tables:

#### Additional figures and tables:



*Figure C1:* A photo of the  $TiO_2P$  film.



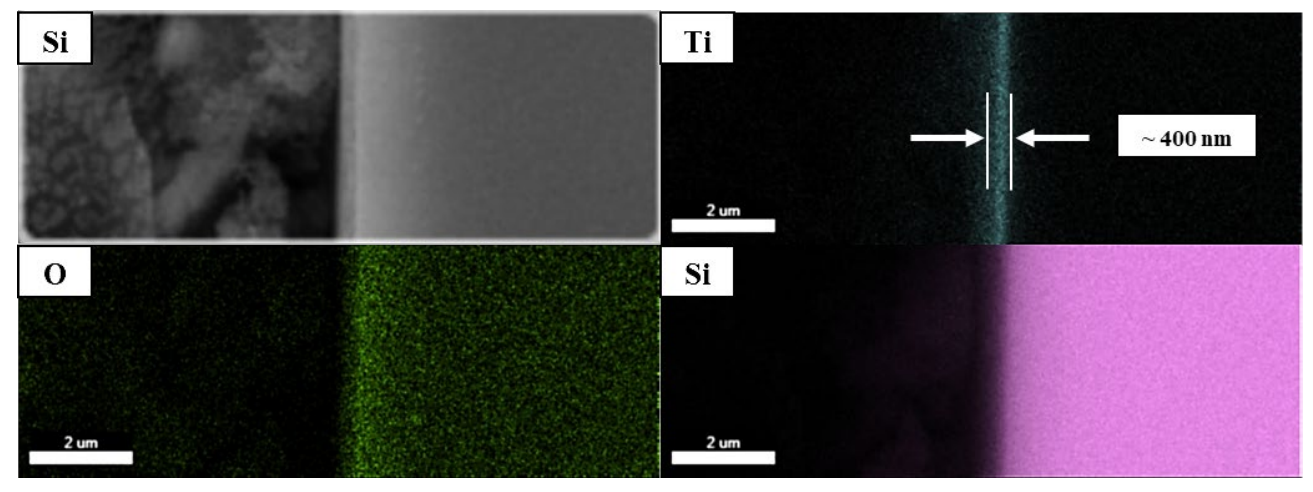
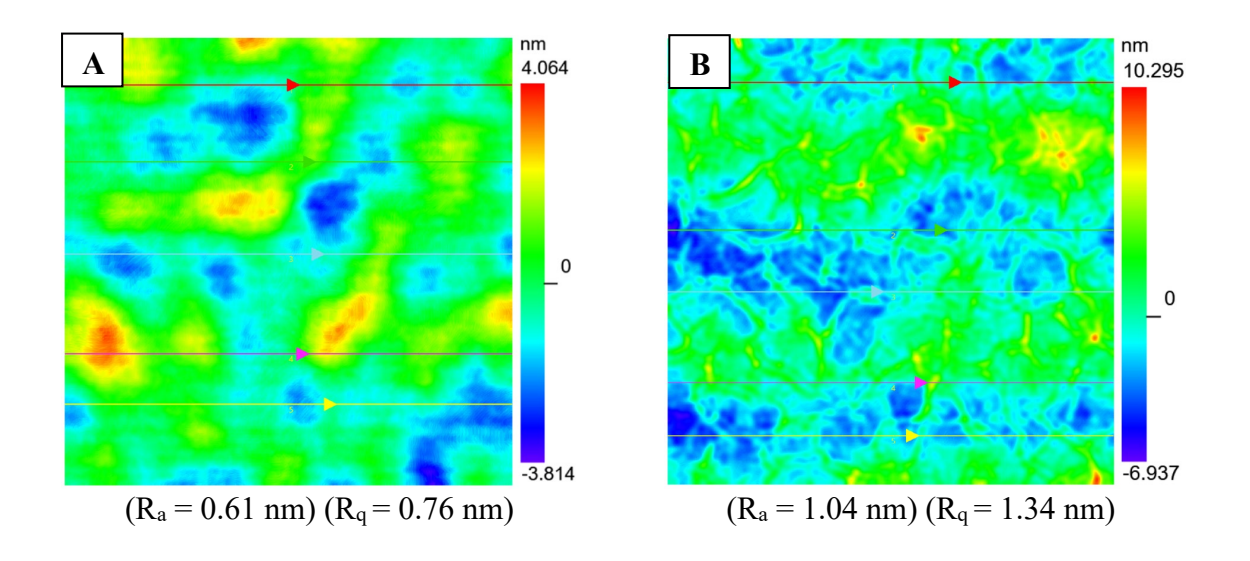
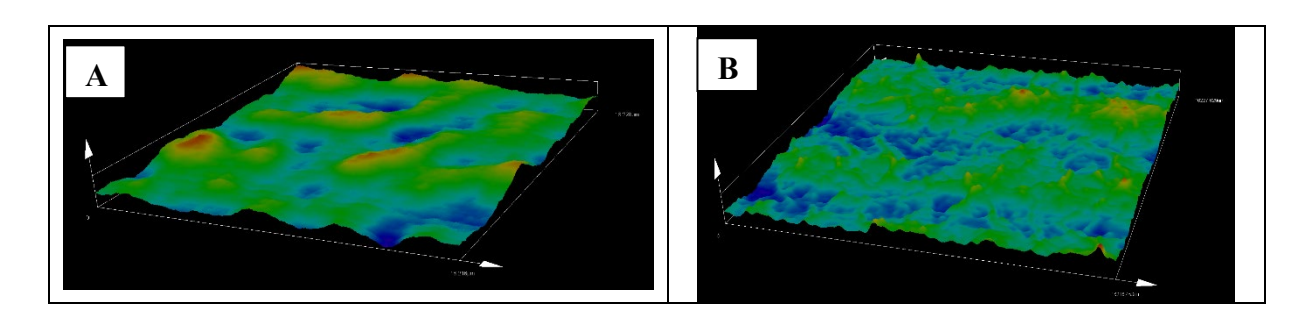


Figure C2: Cross-section SEM-EDAX elemental mapping of TiO<sub>2</sub>P.



**Figure C3**: Surface topography with the average of Ra and Rq values of  $TiO_2P$  (A) before heating and (B) after heating. Note that the scale bars are different. (area  $16 \times 16 \mu m$ ).



**Figure C4:** 3D Profile of  $TiO_2P$  (A) before heating and (B) after heating (area  $16 \times 16 \mu m$ ).

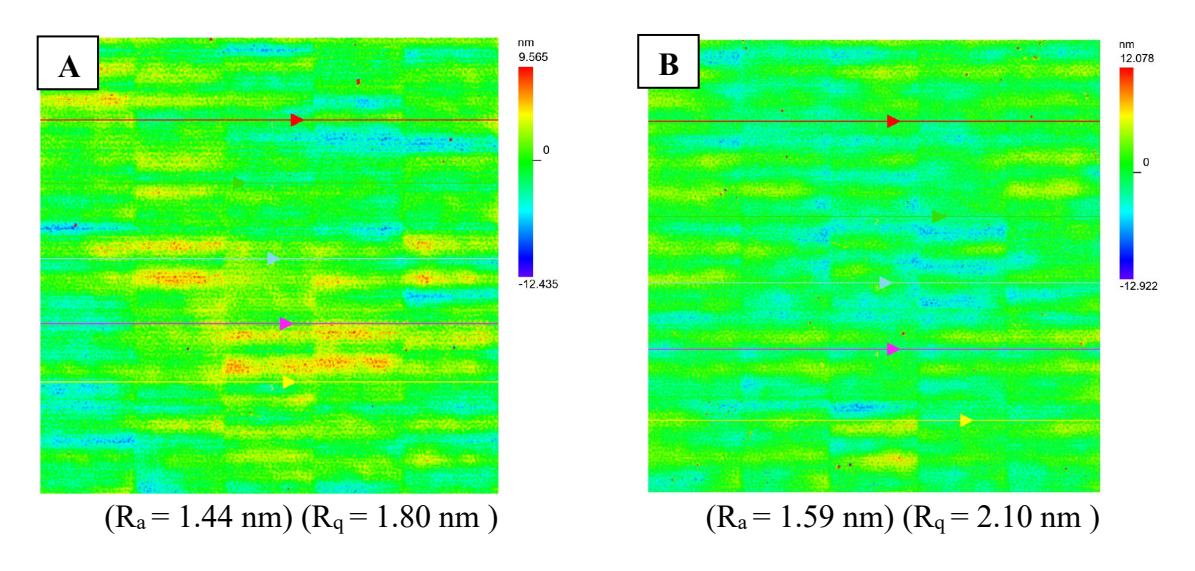


**Figure C5**: Surface topography with the average of Ra and Rq values of  $TiO_2P$  (A) before heating and (B) after heating. (area  $595 \times 595 \mu m$ ).

**Table C1**: Synchrotron XPS Au  $4f_{7/2}$  peak positions, FWHM and relative HBP:LBP intensities.

		Before	e heating		After	· heating	
Au <sub>9</sub> concentration		Peak position (eV)	FWHM	Intensity %	Peak position (eV)	FWHM	Intensity %
			Wi	thout Cra	2O <sub>3</sub> layer		
	HBP	$85.3 \pm 0.2$	$1.7 \pm 0.2$	83	$85.3 \pm 0.2$	$1.5 \pm 0.2$	55
0.006 mM	LBP	$84.1 \pm 0.2$	$1.0 \pm 0.2$	17	$84.3 \pm 0.2$	$1.1 \pm 0.2$	45
0.000 iiivi			V	Vith Cr <sub>2</sub> C	O <sub>3</sub> layer		
	HBP	$85.3 \pm 0.2$	$1.6 \pm 0.2$	100	$85.2 \pm 0.2$	$1.5 \pm 0.2$	100
	LBP	_			—		_
			Wi	thout Cr2	2O <sub>3</sub> layer		
	HBP	$84.7 \pm 0.1$	$1.5 \pm 0.2$	100	$85.2 \pm 0.1$	$1.1 \pm 0.2$	20
0.6 mM	LBP	<u>—</u>			$84.2 \pm 0.1$	$1.0\pm0.2$	80
0.0 IIIVI			V	Vith Cr <sub>2</sub> C	O <sub>3</sub> layer		
	HBP	$84.8 \pm 0.1$	$1.7 \pm 0.2$	100	$85.3 \pm 0.1$	$1.6 \pm 0.2$	53
	LBP	_			$84.3 \pm 0.1$	$0.9 \pm 0.2$	47

Table C2: Synchrotron XPS peak positions of 0.006 mM samples.

	Element	(	C	A	u	P	Т	ì	(	)	Si	Cr
Sample		Peak 1	Peak 2	HBP	LBP	Peak 1	Peak 1	Peak 2	Peak 1	Peak 2	Peak 1	Peak 1
TiO <sub>2</sub> P-Au <sub>9</sub>	Before heating	285	286.2	85.3	84.1	134.1	459	457.4	531.9	530.5	102.4	
11O2F-Au9	After heating	285	286.3	85.3	84.3	134.7	459.1	457.6	531.9	530.6	102.5	
TiO <sub>2</sub> P-	Before heating	285	285.5	85.3		134.6	458.9		531.9	530.4	102.3	577.2
Au <sub>9</sub> -Cr <sub>2</sub> O <sub>3</sub>	After heating	285	285.2	85.2		133.9	458.9		532.1	530.5	102.3	576.9

Table C3: Synchrotron XPS elemental composition of 0.006 mM samples.

	Element	(		A	u	P	T	'i	(	)	Si	Cr	
Sample	Element	Peak 1	Peak 2	НВР	LBP	Peak 1	Peak 1	Peak 2	Peak 1	Peak 2	Peak 1	Peak 1	Au/Ti
TiO2P-Au9	Before heating	23.7	6.4	0.017	0.004	0.02	15.2	1.2	16.7	33.4	3.3		0.00 128
1102F-Au9	After heating	29.6	4.7	0.011	0.009	0.005	14.6	1.2	13.2	33.3	3.4		0.00 126
TiO <sub>2</sub> P-	Before heating	10.4	9.9	0.013	-	0.04	7.7		35.1	25.1	1.6	10.2	0.00 169
Au <sub>9</sub> -Cr <sub>2</sub> O <sub>3</sub>	After heating	40.5	11	0.015		0.03	5		14.2	21.6	1.4	6.3	0.00 300

Table C4: Synchrotron XPS peak positions of 0.6 mM samples.

	Element	(		A	u	P	Т	ì	(	)	Si	Cr
Sample		Peak 1	Peak 2	HBP	LBP	Peak 1	Peak 1	Peak 2	Peak 1	Peak 2	Peak 1	Peak 1
T:O D A	Before heating	285	285.5	84.7		131.6	458.9	457.4	531.8	530.4	102.2	
TiO <sub>2</sub> P-Au <sub>9</sub>	After heating	285	285.5	85.2	84.2	131.6	459.2	458.2	532.1	530.7	102.5	
TiO <sub>2</sub> P-	Before heating	285	285.4	84.8	1	131.6	458.6	-	531.7	530.1	102	577
Au <sub>9</sub> -Cr <sub>2</sub> O <sub>3</sub>	After heating	285	285.5	85.3	84.3	131.7	458.9		532	530.4	102.1	576.9

*Table C5*: Synchrotron XPS elemental composition of 0.6 mM samples.

	Element	(	C	A	u	P	Т	ì	C	)	Si	Cr	
Sample		Peak 1	Peak 2	НВР	LBP	Peak 1	Peak 1	Peak 2	Peak 1	Peak 2	Peak 1	Peak 1	Au/Ti
TiO <sub>2</sub> P-Au <sub>9</sub>	Before heating	45.7	9.7	2.3		2.2	8.5	0.7	8.7	19.9	2.4		0.25
11O2F-Au9	After heating	30.5	10.1	0.4	1.8	0.7	11.4	1.1	10.4	30.4	3.1	-	0.18
TiO <sub>2</sub> P-	Before heating	29.7	11.5	0.6		0.6	4.6		32.3	11.8	1.3	7.5	0.13
Au <sub>9</sub> -Cr <sub>2</sub> O <sub>3</sub>	After heating	33.7	14.7	0.3	0.3	0.2	4.5		18.6	18.1	1.4	7.3	0.13

It can be seen that in Figures 5.3C and 5.3D the Au  $4f_{5/2}$  is larger in intensity than  $4f_{7/2}$  that due to the overlapping of the energy loss peak of the Cr 3s peak with Au  $4f_{5/2}$  peak at ~88.6 eV. This peak was observed by a high-resolution scan of Au 4f region on Cr<sub>2</sub>O<sub>3</sub> reference sample (see Figure C6).

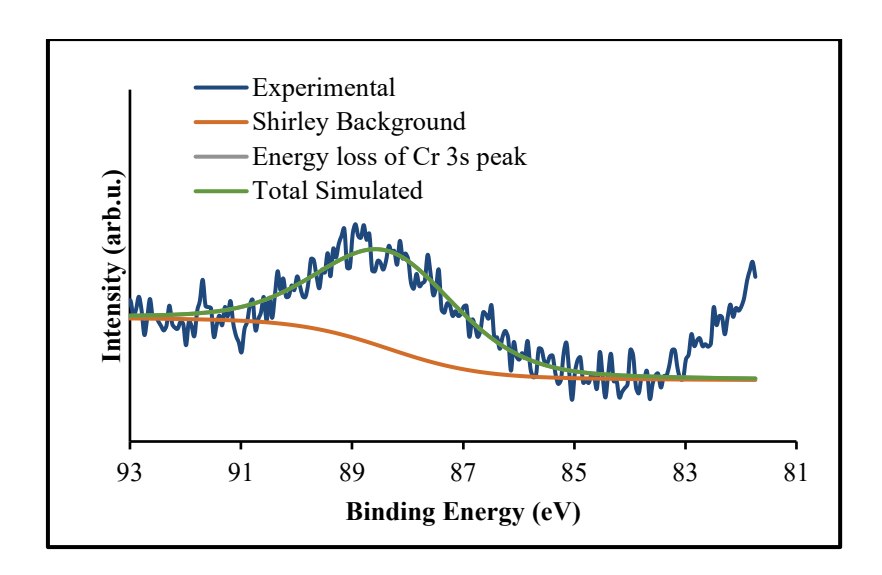


*Figure C6:* Au 4f spectrum of  $Cr_2O_3$  reference sample.

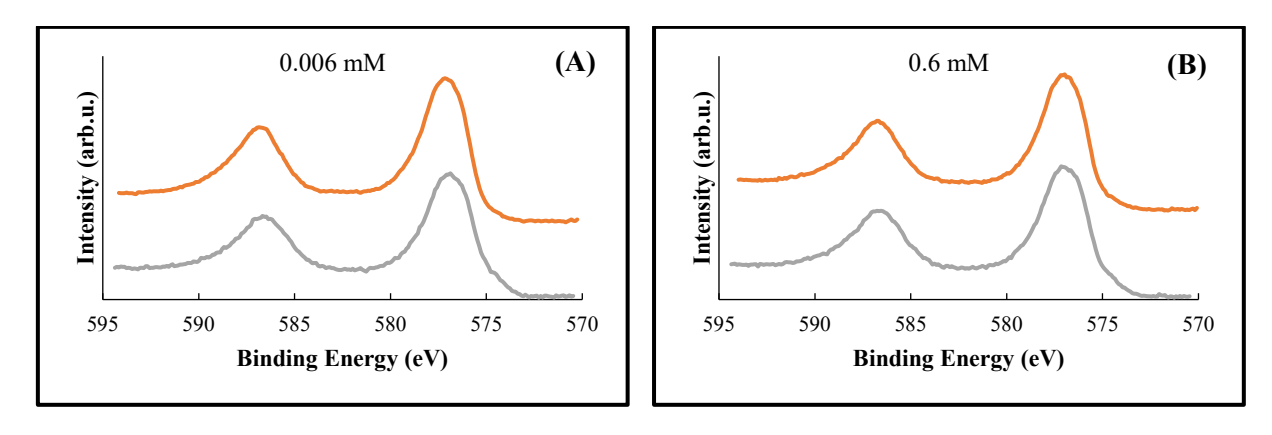


**Figure C7:** Synchrotron XPS spectra of Cr 2p of the  $TiO_2P$ - $Au_9$ - $Cr_2O_3$  sample of **(A)** 0.006 mM sample and **(B)** 0.6 mM sample: after  $Cr_2O_3$  layer photodeposited (orange) and after heating (grey).

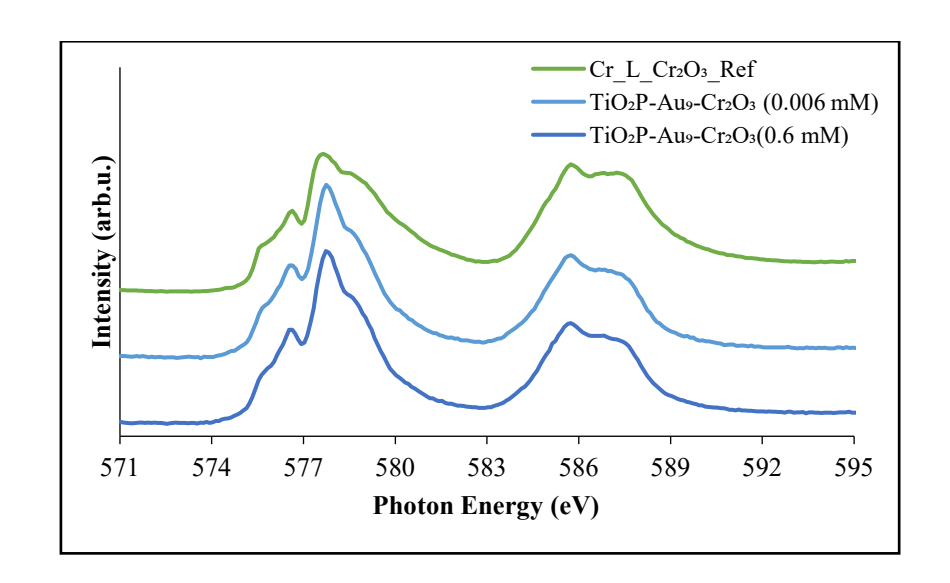


**Figure C8:** Cr L-edge NEXAFS spectra of Cr<sub>2</sub>O<sub>3</sub> reference sample, TiO<sub>2</sub>P-Au<sub>9</sub>-Cr<sub>2</sub>O<sub>3</sub> (0.006 mM) and TiO<sub>2</sub>P-Au<sub>9</sub>-Cr<sub>2</sub>O<sub>3</sub> (0.6 mM).

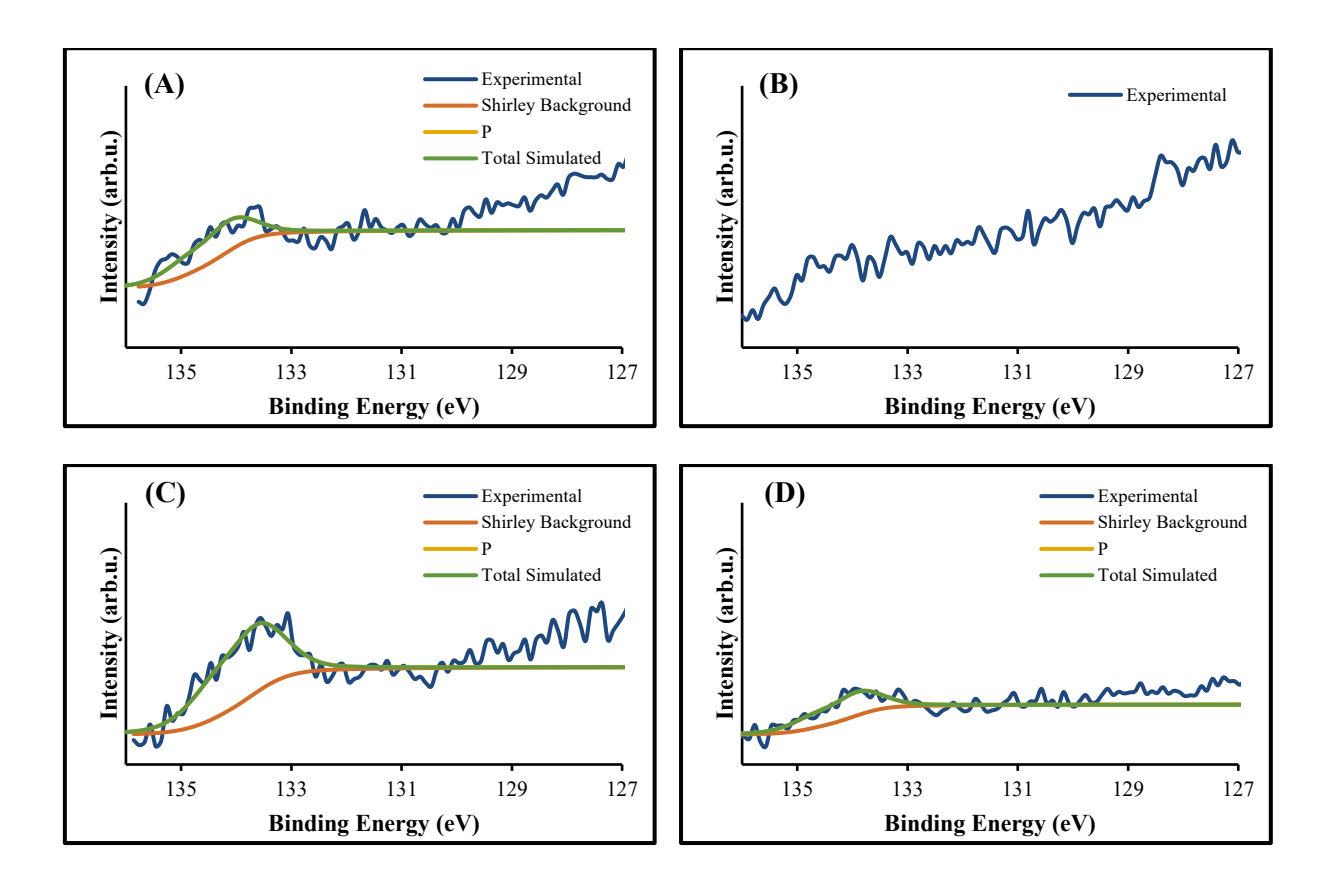


**Figure C9:** Synchrotron XPS spectra of the 0.006 mM sample of P 2p of (A) TiO<sub>2</sub>P-Au<sub>9</sub> before heating, (B) TiO<sub>2</sub>P-Au<sub>9</sub> after heating, (C) TiO<sub>2</sub>P-Au<sub>9</sub>-Cr<sub>2</sub>O<sub>3</sub> before heating and (D) TiO<sub>2</sub>P-Au<sub>9</sub>-Cr<sub>2</sub>O<sub>3</sub> before heating.

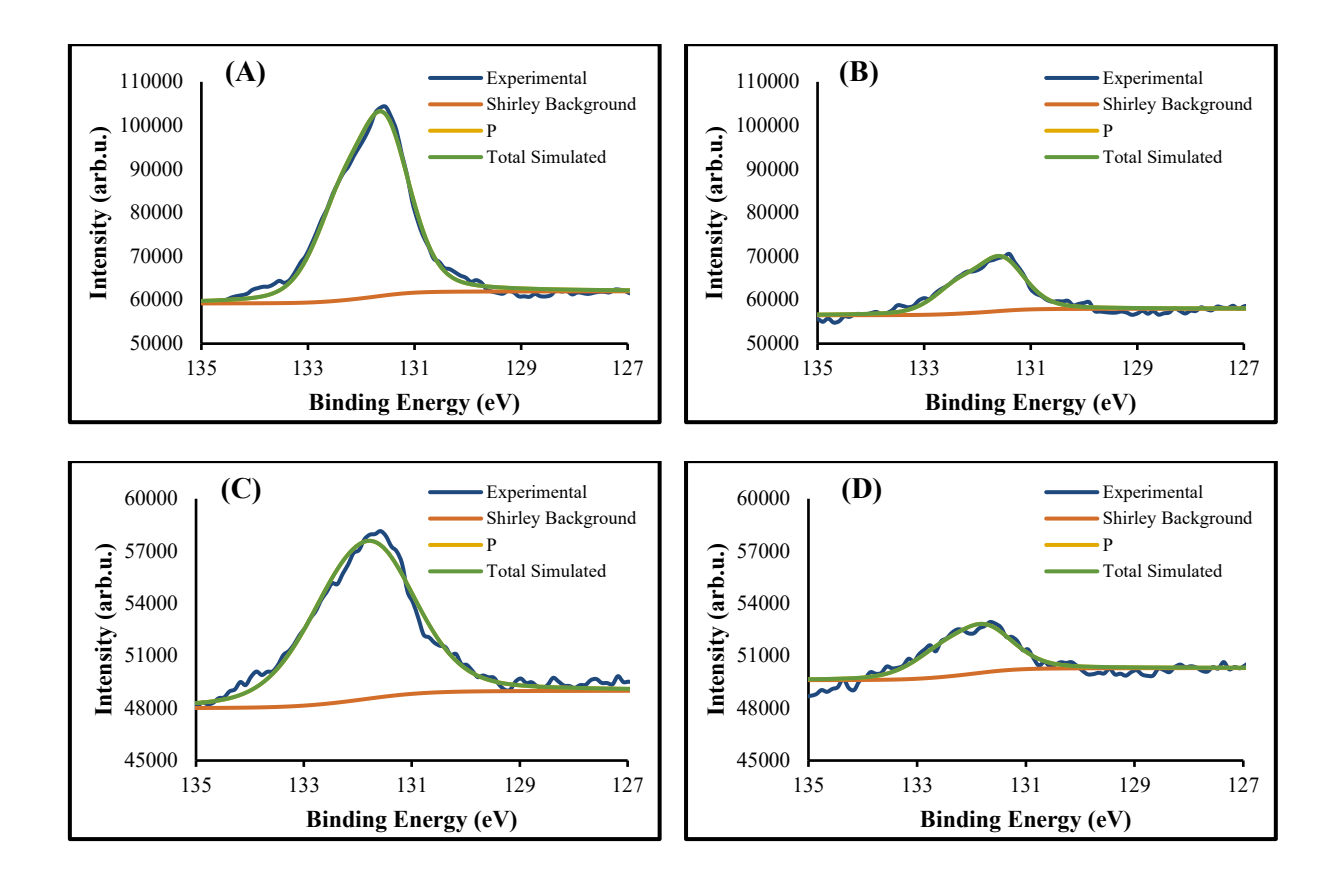


**Figure C10:** Synchrotron XPS spectra of the 0.6 mM sample of P 2p of (A) TiO<sub>2</sub>P-Au<sub>9</sub> before heating, (B) TiO<sub>2</sub>P-Au<sub>9</sub> after heating, (C) TiO<sub>2</sub>P-Au<sub>9</sub>-Cr<sub>2</sub>O<sub>3</sub> before heating and (D) TiO<sub>2</sub>P-Au<sub>9</sub>-Cr<sub>2</sub>O<sub>3</sub> after heating.

# Appendix D: Effect of TiO<sub>2</sub> Film Thickness on the Stability of Au<sub>9</sub> Clusters with a CrO<sub>x</sub> layer

This appendix contains a detailed description, additional figures and tables:

#### Additional figures and tables:



Figure D1: A photo of the  $TiO_2P$  (lift) and  $TiO_2G$  (right) films.

Figure D2 shows the UV-Vis spectrum of synthesised Au<sub>9</sub>(PPh<sub>3</sub>)<sub>8</sub>(NO<sub>3</sub>)<sub>3</sub> clusters with four peaks around 315, 350, 375 and 440 nm. The UV-Vis spectrum is in agreement with those obtained from literatures of Au<sub>9</sub>(PPh<sub>3</sub>)<sub>8</sub>(NO<sub>3</sub>)<sub>3</sub>, confirming the synthesis of Au<sub>9</sub> clusters<sup>1, 2</sup>.

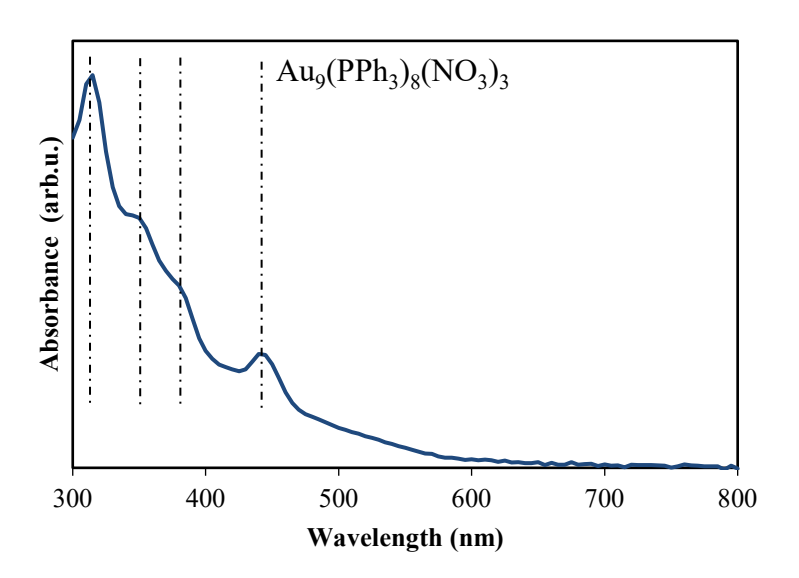
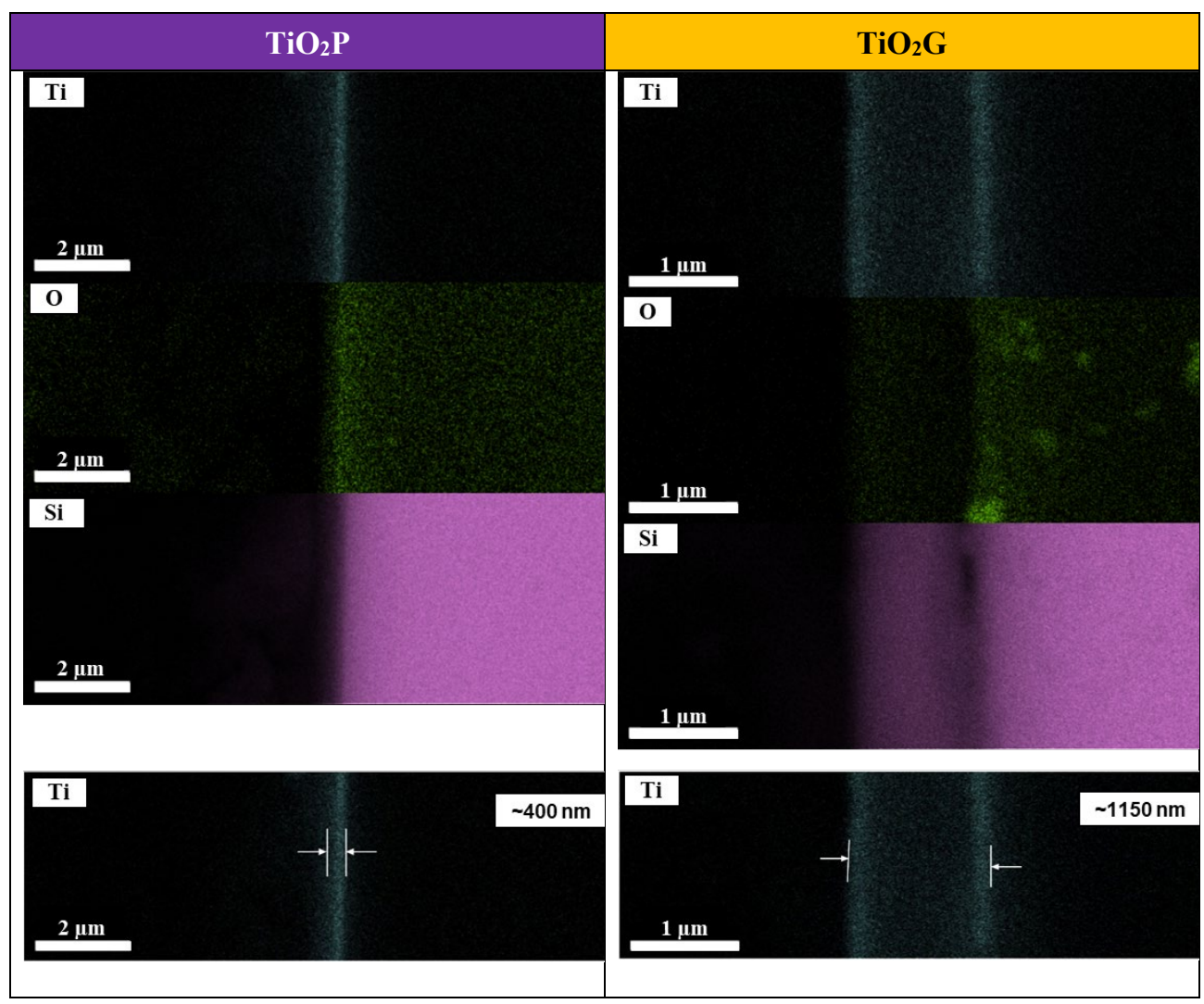
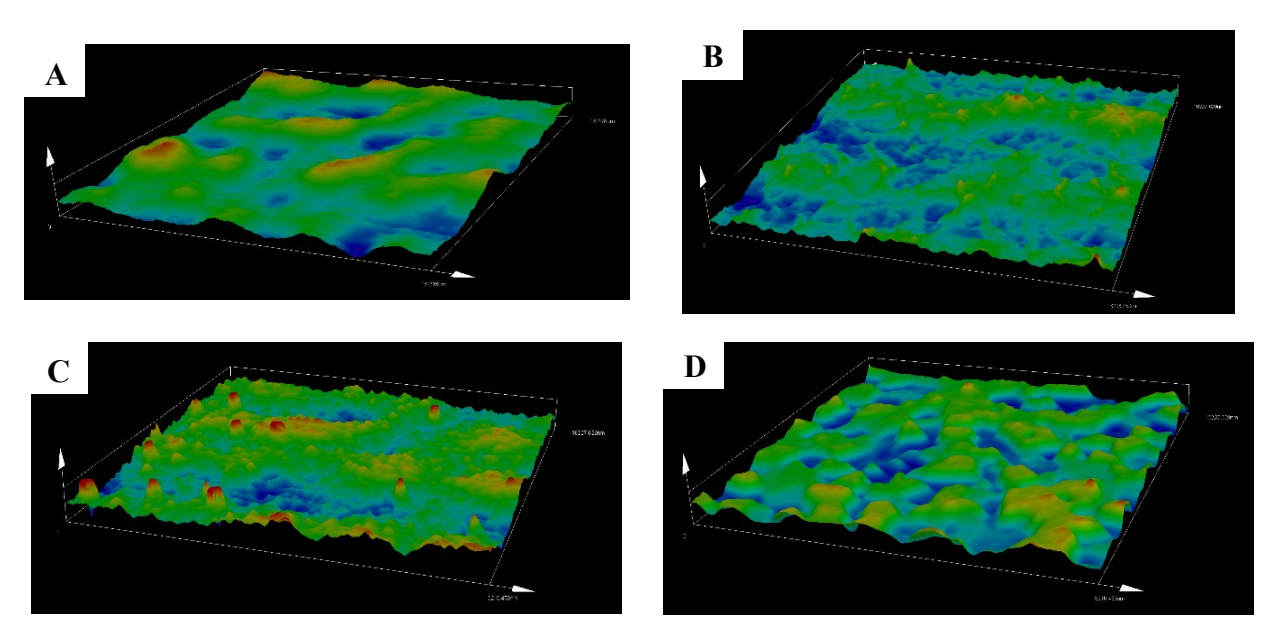


Figure D2: UV-Vis spectrum of Au<sub>9</sub>(PPh<sub>3</sub>)<sub>8</sub>(NO<sub>3</sub>)<sub>3</sub> in Methanol.



**Figure D3**: Cross-section SEM-EDAX elemental maps of Ti, O and Si of  $TiO_2P$  and  $TiO_2G$ . Note that the scale bars are different.



**Figure D4:** 3D Profile of (A)  $TiO_2P$  before heating, (B)  $TiO_2P$  after heating, (C) before heating,  $TiO_2G$  and (D)  $TiO_2G$  after heating (area  $16 \times 16 \mu m$ ).

Figure D5 shows the average Ra and Rq values with a large area scan  $595 \times 595 \,\mu\text{m}$  of  $TiO_2P$  and  $TiO_2G$  before and after heating. For  $TiO_2P$  before heating, the Ra and Rq values are 1.4 nm and 1.8 nm, while after heating are 1.6 nm and 2.1 nm. For  $TiO_2G$  before heating, the Ra and Rq values are 2.8 nm and 4.6 nm, while after heating are 15.0 nm and 17.4 nm. The change in the Ra and Rq values after heating are 0.2 nm and 0.3 nm. for the thin  $TiO_2$  layer ( $TiO_2P$ ), however, the thick  $TiO_2$  layer ( $TiO_2G$ ) are 12.2 nm and 12.8 nm. The Ra and Rq values of  $TiO_2G$  after heating are 12 times higher compared to before heating. The change in the surface morphology of  $TiO_2$  films after heating is due to the transformation of  $TiO_2$  films from amorphous to anatase<sup>3-5</sup>. Çörekçí et al, showed that the change in the surface morphology of  $TiO_2$  film is higher for the thicker film than a thin film after heating. This due to the high mobility (recrystallisation) of the thicker film during the thermal heating<sup>4</sup>. Here, the significant change in the morphology of  $TiO_2G$  after heating is due to the high mobility of  $TiO_2G$  during heating, which is affected by the transformation to anatase phase.

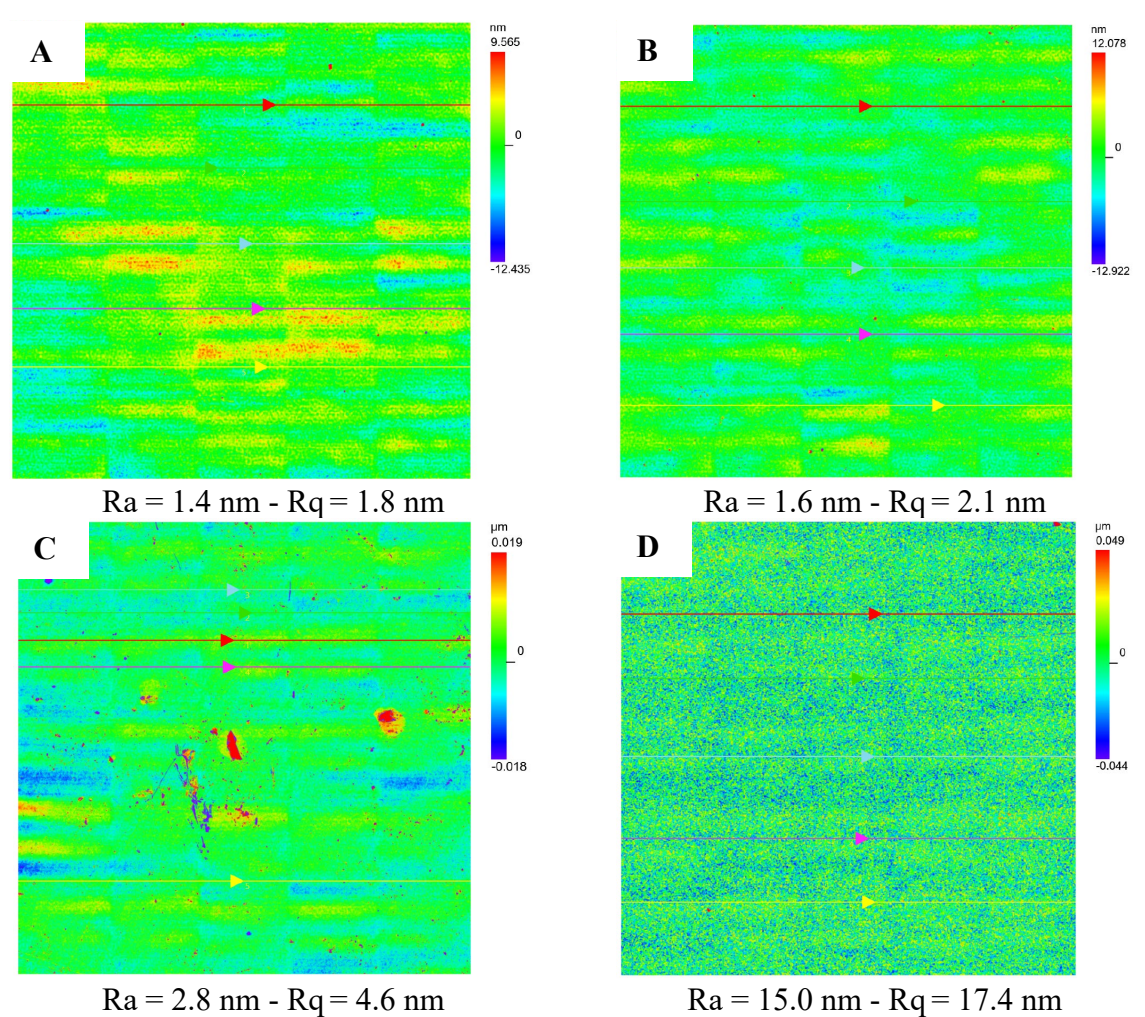


**Figure D5**: Surface morphology with the average of Ra and Rq values of (A)  $TiO_2P$  before heating, (B)  $TiO_2P$  after heating, (C) before heating,  $TiO_2G$  and (D)  $TiO_2G$  after heating. (area  $595 \times 595 \, \mu m$ ). It is important to know that the scale bars are different.

Table D1: XPS Au 4f7/2 peak positions and FWHM of TiO2P-Au9 and TiO2P-Au9-CrOx.

	Before	heating	After CrO <sub>x</sub> ph	otodeposition	After h	eating
Au <sub>9</sub> concentration	Peak position (eV)	FWHM	Peak position (eV)	FWHM	Peak position (eV)	FWHM
			Without C	CrO <sub>x</sub> layer		
0.006 mM	$85.1 \pm 0.2$	$1.7 \pm 0.2$	-	-	$84.8 \pm 0.2$	$1.5 \pm 0.2$
0.06 mM	$85.4 \pm 0.2$	$1.7 \pm 0.2$	-	-	$84.8 \pm 0.2$	$1.6 \pm 0.2$
0.6 mM	$85.1 \pm 0.2$	$1.8 \pm 0.2$	-	-	$84.7 \pm 0.2$	$1.6 \pm 0.2$
			With Cr	O <sub>x</sub> layer		
0.006 mM	$85.2 \pm 0.2$	$1.8 \pm 0.2$	$85.3 \pm 0.2$	$1.6 \pm 0.2$	$85.0 \pm 0.2$	$1.7 \pm 0.2$
0.06 mM	$85.1 \pm 0.2$	$1.8\pm0.2$	$85.3 \pm 0.2$	$1.6 \pm 0.2$	$85.0 \pm 0.2$	$1.7 \pm 0.2$
0.6 mM	$85.1 \pm 0.2$	$1.8\pm0.2$	$85.3 \pm 0.2$	$1.6 \pm 0.2$	$85.0 \pm 0.2$	$1.7 \pm 0.2$

Table D2: XPS Au 4f7/2 peak positions and FWHM of TiO2G-Au9 and TiO2G-Au9-CrOx.

	Before	heating	After CrO <sub>x</sub> ph	otodeposition	After h	eating
Au <sub>9</sub> concentration	Peak position (eV)	FWHM	Peak position (eV)	FWHM	Peak position (eV)	FWHM
			Without C	CrO <sub>x</sub> layer		
0.006 mM	$85.4 \pm 0.2$	$1.8 \pm 0.2$	-	-	$84.9 \pm 0.2$	$1.7 \pm 0.2$
0.06 mM	$85.4 \pm 0.2$	$1.8 \pm 0.2$	-	-	$84.6 \pm 0.2$	$1.6 \pm 0.2$
0.6 mM	$85.3 \pm 0.2$	$1.8\pm0.2$	-	-	$84.6 \pm 0.2$	$1.5 \pm 0.2$
			With Cr	O <sub>x</sub> layer		
0.006 mM	$85.3 \pm 0.2$	$1.6 \pm 0.2$	$85.5 \pm 0.2$	$1.6 \pm 0.2$	$84.8 \pm 0.2$	$1.8 \pm 0.2$
0.06 mM	$85.2 \pm 0.2$	$1.6 \pm 0.2$	$85.5 \pm 0.2$	$1.6 \pm 0.2$	$84.4 \pm 0.2$	$1.6 \pm 0.2$
0.6 mM	$84.9 \pm 0.2$	$1.8\pm0.2$	$85.3 \pm 0.2$	$1.6 \pm 0.2$	$84.3 \pm 0.2$	$1.3 \pm 0.2$

Figure D6 shows the Au 4f spectra of TiO<sub>2</sub>P-Au<sub>9</sub> and TiO<sub>2</sub>P-Au<sub>9</sub>-CrO<sub>x</sub>. The blue line is after the Au<sub>9</sub> cluster deposition, green line is after the photodeposition of CrO<sub>x</sub> layer and red line is after heating at 200°C for 10min to remove the Au<sub>9</sub> clusters ligands. The black lines indicate the binding energy at 85 eV.

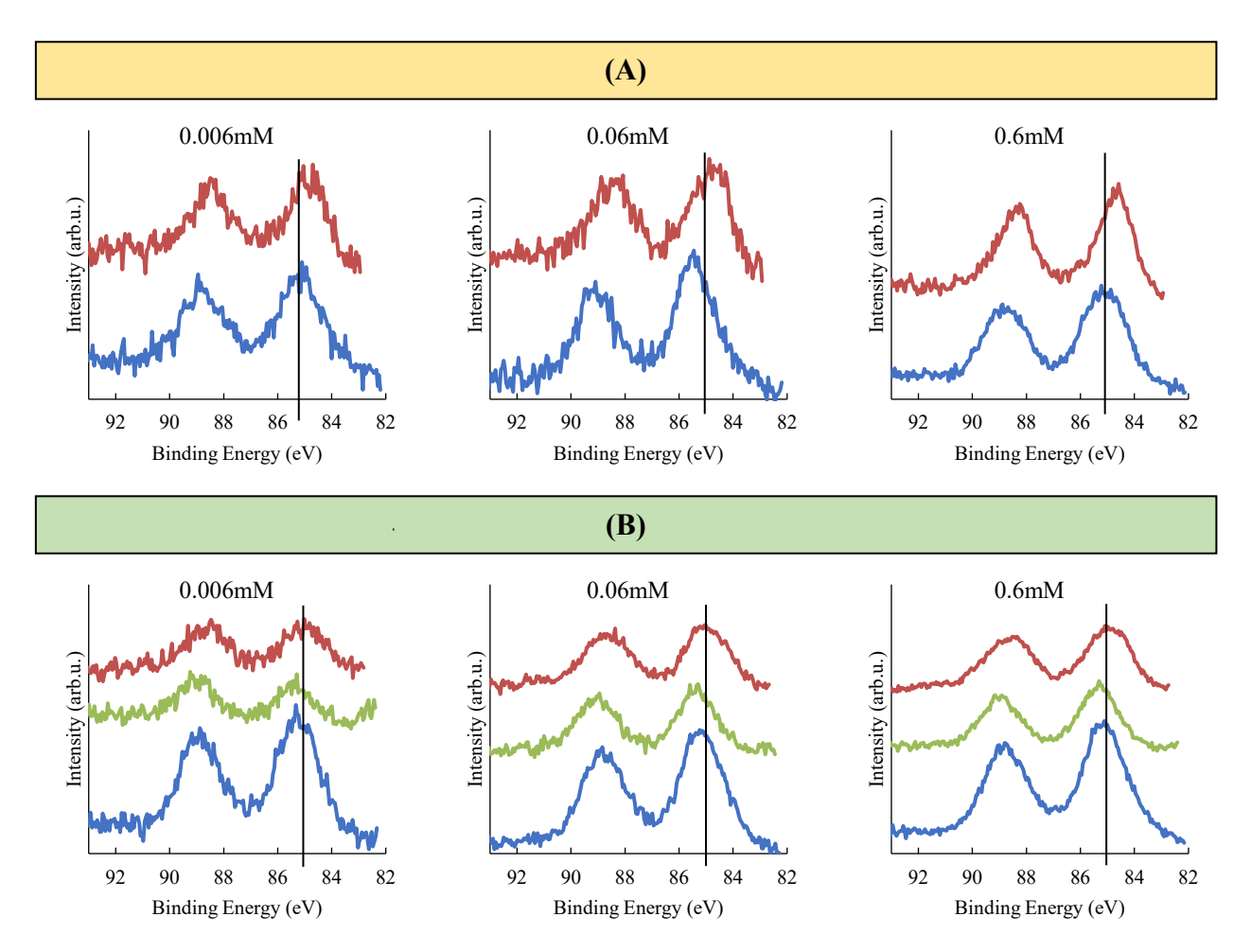


**Figure D6:** XPS spectra of Au 4f of **(A)**  $TiO_2P$ -Au<sub>9</sub>: after Au<sub>9</sub> deposition (blue) and after heating (red) **(B)**  $TiO_2P$ -Au<sub>9</sub>- $CrO_x$ : after Au<sub>9</sub> deposition (blue), after  $CrO_x$  layer photodeposited (green) and after heating (red).

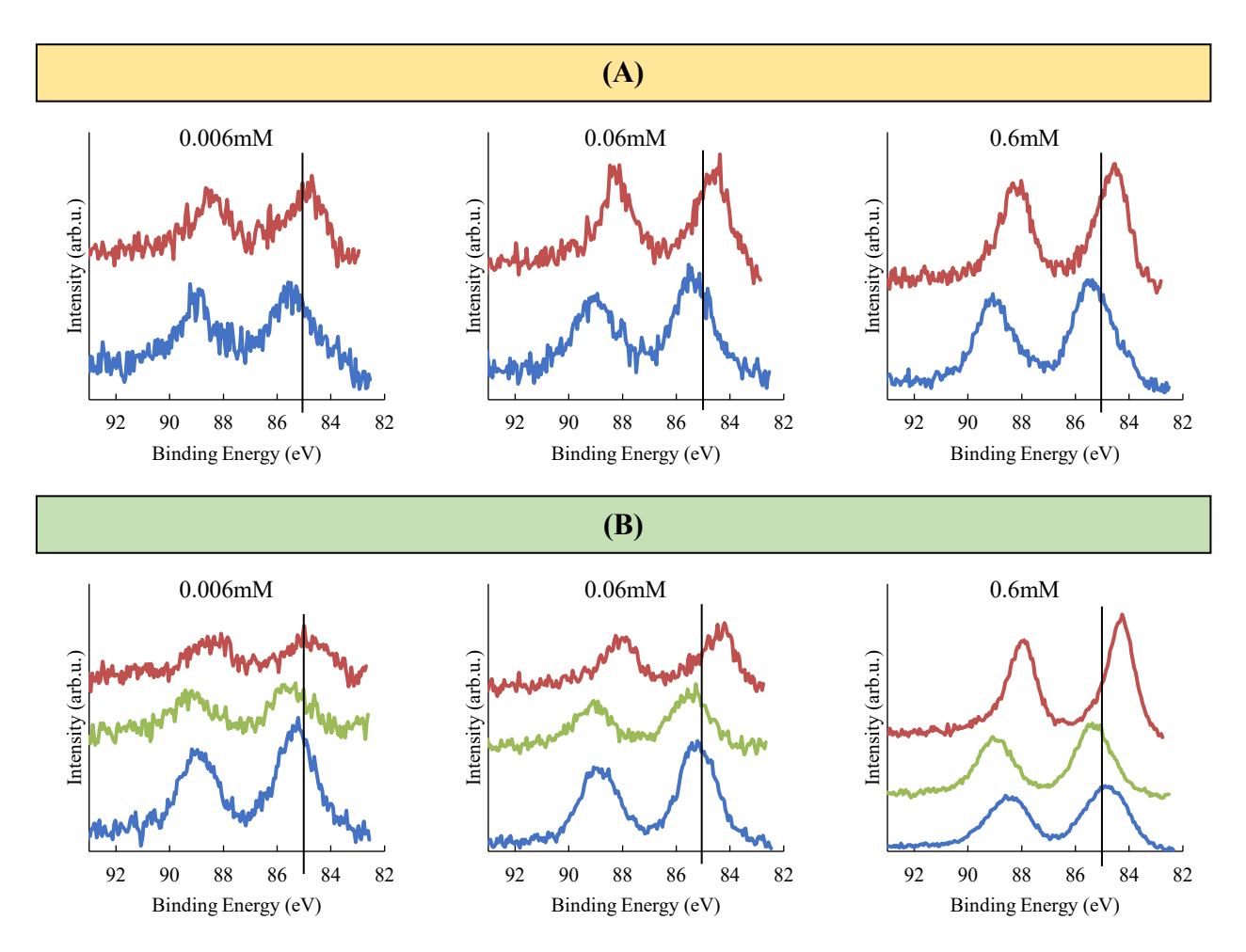


**Figure D7:** XPS spectra of Au 4f of **(A)**  $TiO_2G$ -Au<sub>9</sub>: after Au<sub>9</sub> deposition (blue) and after heating (red) **(B)**  $TiO_2G$ -Au<sub>9</sub>- $CrO_x$ : after Au<sub>9</sub> deposition (blue), after  $CrO_x$  layer photodeposited (green) and after heating (red)

Figure D8 shows the P 2p spectra of  $TiO_2P$ -Au<sub>9</sub> and  $TiO_2P$ -Au<sub>9</sub>-CrO<sub>x</sub>. The blue line is after the Au<sub>9</sub> cluster deposition, green line is after the photodeposition of  $CrO_x$  layer and red line is after heating. The black lines indicate the position of triphenylphosphine ligands at 131.8 eV<sup>6, 7</sup>. The P 2p spectrum can be fitted with doublet ( $2p_{3/2}$  and  $2p_{1/2}$ ), the splitting was fixed at 0.84 eV. Before heating, for 0.6 mM, the P  $2p_{3/2}$  peak is appeared at  $131.8 \pm 0.2$  eV, which relates to the peak position of PPh<sub>3</sub> ligands bounds to Au<sub>9</sub> clusters<sup>6, 7</sup>. After heating, no peak is detected, indicating that phosphorous ligands were removed by heating for 0.6 mM. For the lower concentrations of 0.06 and 0.006 mM with the addition of the  $CrO_x$  overlayer, the P 2p signal is below the detection limit. However, the same phenomenon of ligand removal via heating is expected for these lower concentrations <sup>8, 9</sup>.

The size of Au<sub>9</sub> clusters were more stable using the laboratory based XPS instrument comparing to synchrotron XPS. This assumed to be due to ageing of the Au<sub>9</sub> clusters with the Synchrotron XPS results, where the samples were measured a week after the deposition of Au<sub>9</sub> and the photodeposition of CrO<sub>x</sub><sup>10</sup>. While using the laboratory based XPS instrument, the measurements were performed

directly after the deposition of  $Au_9$  and followed by photodeposition of  $CrO_x$  layer. The conclusion is similar to that reported previously from synchrotron data that the agglomeration of  $Au_9$  clusters was inhibited with  $CrO_x$  layer.

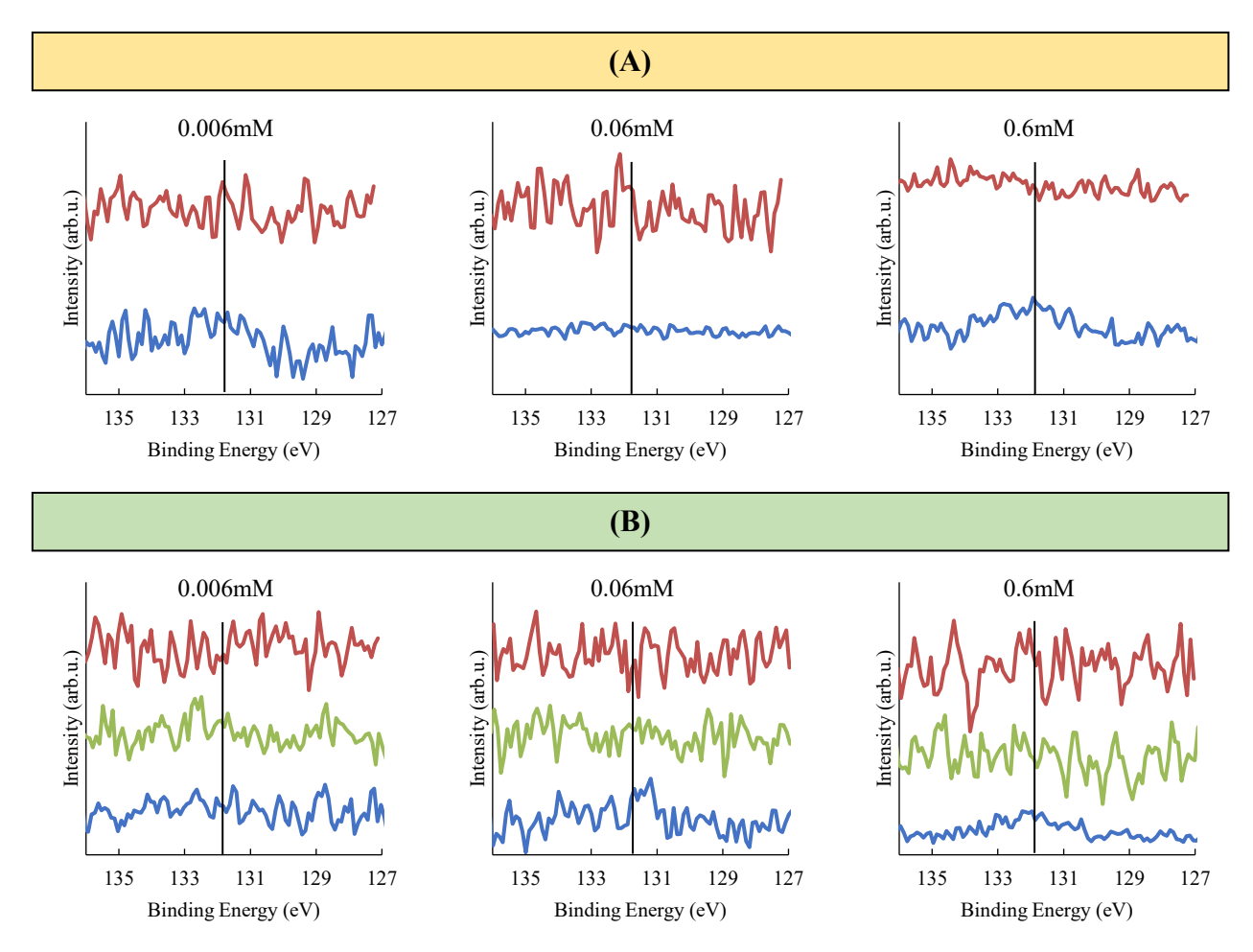


**Figure D8:** XPS spectra of P 2p of **(A)**  $TiO_2P$ - $Au_9$ : after  $Au_9$  deposition (blue) and after heating (red) **(B)**  $TiO_2P$ - $Au_9$ - $CrO_x$ : after  $Au_9$  deposition (blue), after  $CrO_x$  layer photodeposited (green), and after heating (red)

Figure D9 shows the Cr 2p spectra of  $TiO_2P$ -Au<sub>9</sub> and  $TiO_2P$ -Au<sub>9</sub>-CrO<sub>x</sub>. Before heating, the Cr  $2p_{3/2}$  peak is appeared at  $577.7 \pm 0.2$  eV, which relates to the peak position of  $Cr(OH)_3^{11}$ . After heating, the Cr  $2p_{3/2}$  peak position shifts to a low binding energy at  $577.1 \pm 0.2$  eV, which corresponds to  $Cr_2O_3^{12, 13}$ . This confirms that the  $CrO_x$  layer is reduced by heating from  $Cr(OH)_3$  to  $Cr_2O_3$ . This in agreement to previous studies report that heating reduces  $Cr(OH)_3$  layer to  $Cr_2O_3^{14}$ .

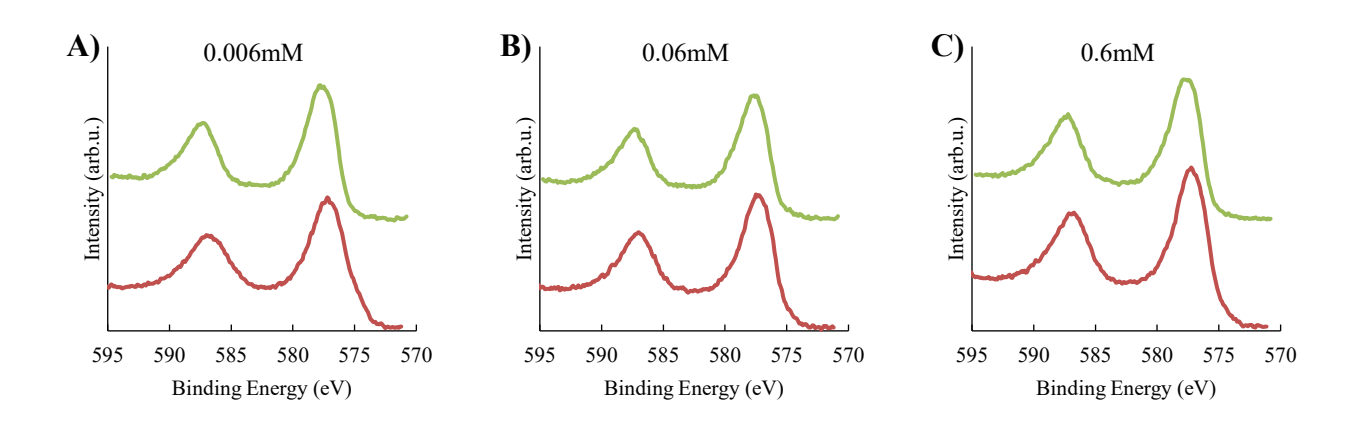
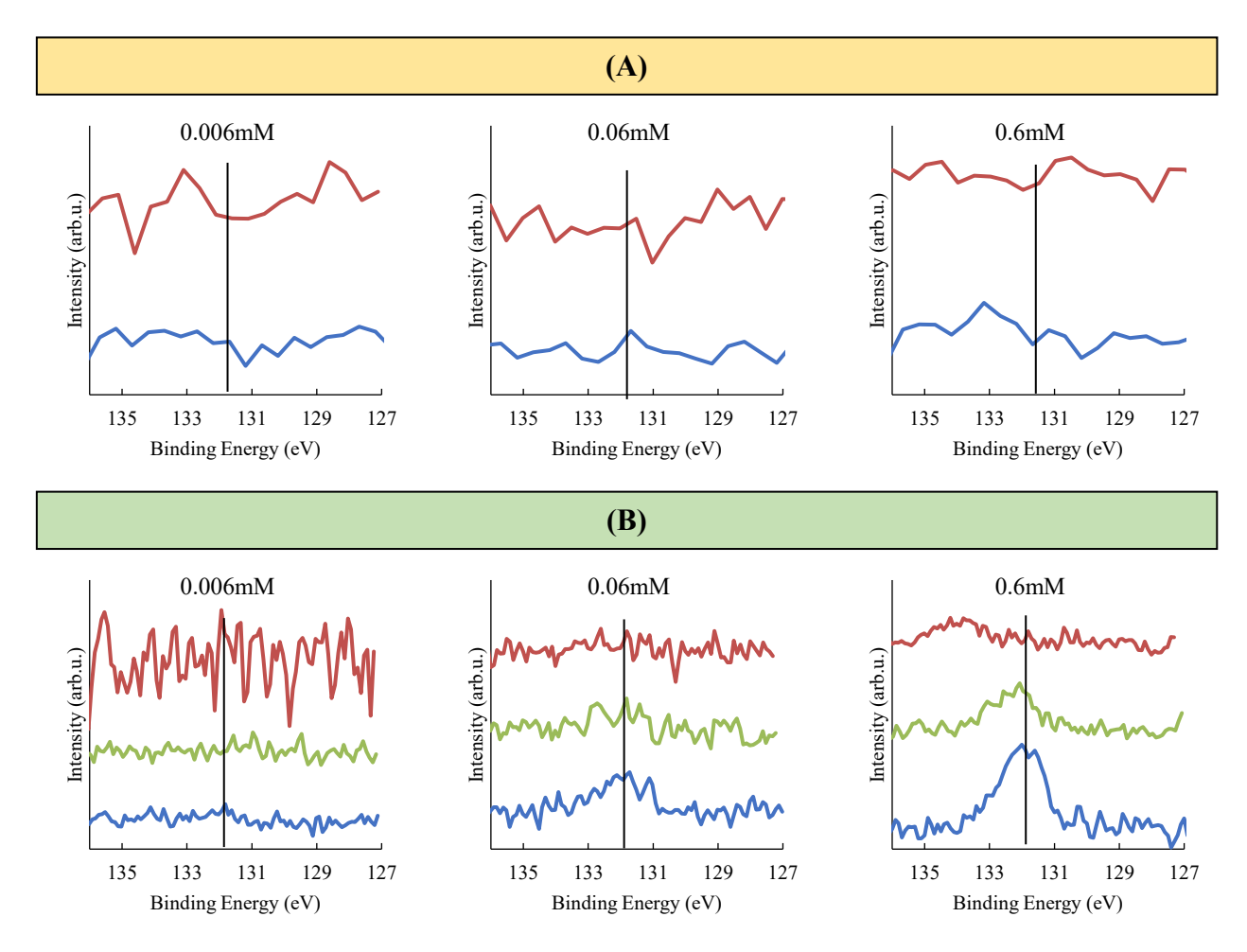


**Figure D9:** XPS spectra of Cr 2p of the  $TiO_2P$ - $Au_9$ - $CrO_x$  sample of **(A)** 0.006mM sample, **(B)** 0.06mM sample and **(C)** 0.6mM sample: after  $CrO_x$  layer photodeposited (green) and after heating (red).

**Table D3**: XPS Cr  $2p_{3/2}$  peak positions and FWHM of  $TiO_2P$ -Au<sub>9</sub>-CrO<sub>x</sub>.

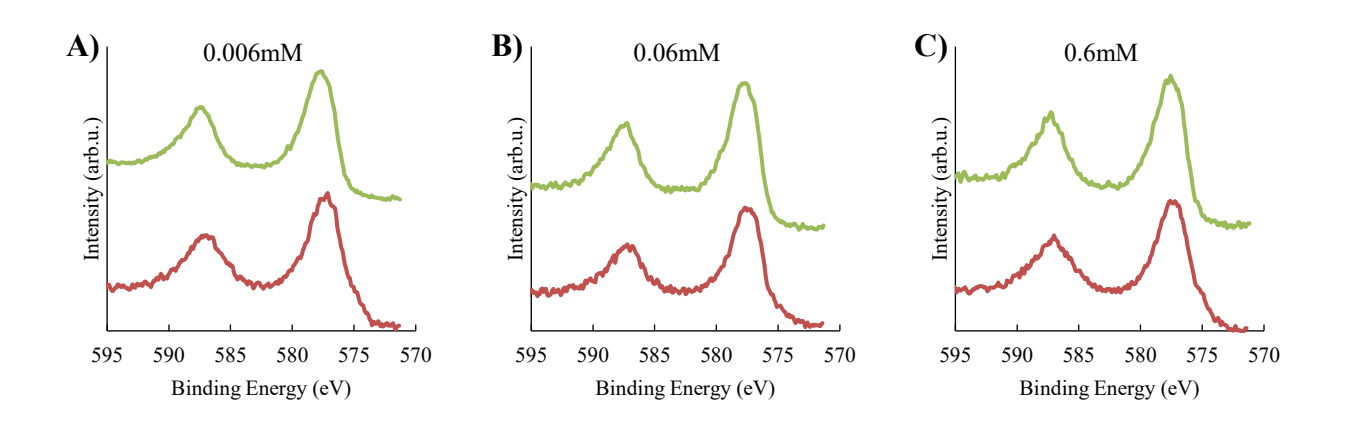
	TiO <sub>2</sub> P							
	Before h	eating	After heating					
	Peak position (eV)	FWHM	Peak position (eV)	FWHM				
0.006 mM	$577.7 \pm 0.2$	$2.7\pm0.2$	$577.1 \pm 0.2$	$3.4 \pm 0.2$				
0.06 mM	$577.7 \pm 0.2$	$2.9 \pm 0.2$	$577.1 \pm 0.2$	$3.0 \pm 0.2$				
0.6 mM	$577.7 \pm 0.2$	$2.9 \pm 0.2$	$577.2 \pm 0.2$	$3.0\pm0.2$				

Figure D10 shows the P 2p spectra of  $TiO_2G$ -Au<sub>9</sub> without and with  $CrO_x$  layer before and after heating. For 0.6 mM, the P  $2p_{3/2}$  peak before heating are found at  $131.8 \pm 0.2$  eV for both without and with  $CrO_x$  layer, referring to the peak of PPh<sub>3</sub> ligands<sup>6, 7</sup>. After heating, the P  $2p_{3/2}$  peak is found at  $133.7 \pm 0.2$  eV, which attribute to removed ligands from the Au<sub>9</sub> clusters and oxidised by attaching to  $TiO_2$  substrate as previously reported<sup>6, 9</sup>. For 0.06 and 0.006 mM, the signal of the P 2p is below the detection limit but it is expected that same behaviour occurs for these lower concentrations.



**Figure D10:** XPS spectra of P 2p of **(A)**  $TiO_2G$ -Au<sub>9</sub>: after Au<sub>9</sub> deposition (blue) and after heating (red) **(B)**  $TiO_2G$ -Au<sub>9</sub>-CrO<sub>x</sub>: after Au<sub>9</sub> deposition (blue), after CrO<sub>x</sub> layer photodeposited (green), and after heating (red)

Figure D11 shows the Cr 2p spectra of  $TiO_2G$ -Au<sub>9</sub> and  $TiO_2G$ -Au<sub>9</sub>-CrO<sub>x</sub>. The Cr  $2p_{3/2}$  peak is appeared at  $577.8 \pm 0.2$  eV before heating for all samples. This binding energy is similar to that of  $Cr(OH)_3^{11}$ . The peak position of  $Cr 2p_{3/2}$  shifts to a low binding energy at  $577.3 \pm 0.2$  eV after heating, which relates to the binding energy of  $Cr_2O_3^{13}$ . This in consistent with  $TiO_2P$  substrate that  $CrO_x$  layer is reduced from  $Cr(OH)_3$  to  $Cr_2O_3$  by heating.



**Figure D11:** XPS spectra of Cr 2p of the  $TiO_2G$ - $Au_9$ - $CrO_x$  sample of **(A)** 0.006mM sample, **(B)** 0.06mM sample and **(C)** 0.6mM sample: after  $CrO_x$  layer photodeposited (green) and after heating (red).

Table D4: XPS Cr 2p<sub>3/2</sub> peak positions and FWHM of TiO<sub>2</sub>G-Au<sub>9</sub>-CrO<sub>x</sub>.

	TiO₂G							
	Before h	eating	After heating					
	Peak position (eV)	FWHM	Peak position (eV)	FWHM				
0.006 mM	$577.8 \pm 0.2$	$2.8 \pm 0.2$	$577.3 \pm 0.2$	$3.3 \pm 0.2$				
0.06 mM	$577.8 \pm 0.2$	$2.8 \pm 0.2$	$577.5 \pm 0.2$	$2.8 \pm 0.2$				
0.6 mM	$577.6 \pm 0.2$	$2.7 \pm 0.2$	$577.3 \pm 0.2$	$3.0 \pm 0.2$				

**Table D5**: XPS relative amount of  $Cr\ 2p_{3/2}$  to  $Ti\ 2p_{3/2}$  of  $TiO_2P$ -Au<sub>9</sub>- $CrO_x$  and  $TiO_2G$ -Au<sub>9</sub>- $CrO_x$ .

		Cr/Ti								
	T	iO2P-Au9-Cr	$O_{\mathbf{x}}$	Ti	O <sub>2</sub> G-Au <sub>9</sub> -Cr	Ox				
	Before	After	Difference	Before	After	Difference				
	heating	heating	%	heating	heating	%				
0.006 mM	2.74	1.47	47	1.48	0.62	58				
0.06 mM	1.54	1.14	26	1.30	0.40	69				
0.6 mM	3.12	1.99	36	1.82	0.72	61				

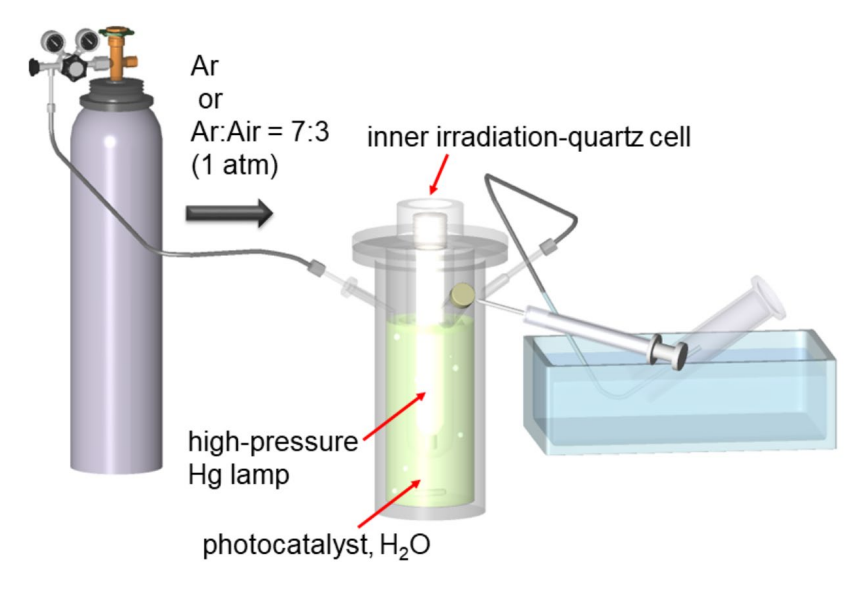
#### References

- 1. Adnan, R. H.; Madridejos, J. M. L.; Alotabi, A. S.; Metha, G. F.; Andersson, G. G., A Review of State of the Art in Phosphine Ligated Gold Clusters and Application in Catalysis. *Advanced Science* **2022**, *9* (15), 2105692.
- 2. Madridejos, J. M. L.; Harada, T.; Falcinella, A. J.; Small, T. D.; Golovko, V. B.; Andersson, G. G.; Metha, G. F.; Kee, T. W., Optical Properties of the Atomically Precise C4 Core [Au9(PPh3)8]3+ Cluster Probed by Transient Absorption Spectroscopy and Time-Dependent Density Functional Theory. *The Journal of Physical Chemistry C* **2021**, *125* (3), 2033-2044.
- 3. Mathews, N. R.; Morales, E. R.; Cortés-Jacome, M. A.; Toledo Antonio, J. A., TiO2 Thin Films Influence of Annealing Temperature on Structural, Optical and Photocatalytic Properties. *Solar Energy* **2009**, *83* (9), 1499-1508.
- 4. Çörekçi, Ş.; Kizilkaya, K.; Asar, T.; Öztürk, M.; Çakmak, M.; Ozcelik, S., Effects of Thermal Annealing and Film Thickness on the Structural and Morphological Properties of Titanium Dioxide Films. *Acta Physica Polonica A* **2012**, *121*.
- 5. Chandra Sekhar, M.; Kondaiah, P.; Jagadeesh Chandra, S. V.; Mohan Rao, G.; Uthanna, S., Substrate temperature influenced physical properties of silicon MOS devices with TiO2 gate dielectric. *Surface and Interface Analysis* **2012**, *44* (9), 1299-1304.
- 6. Anderson, D. P.; Adnan, R. H.; Alvino, J. F.; Shipper, O.; Donoeva, B.; Ruzicka, J.-Y.; Al Qahtani, H.; Harris, H. H.; Cowie, B.; Aitken, J. B., Chemically Synthesised Atomically Precise Gold Clusters Deposited and Activated on Titania. Part II. *Physical chemistry chemical physics* **2013**, *15* (35), 14806-14813.
- 7. Anderson, D. P.; Alvino, J. F.; Gentleman, A.; Al Qahtani, H.; Thomsen, L.; Polson, M. I.; Metha, G. F.; Golovko, V. B.; Andersson, G. G., Chemically-Synthesised, Atomically-Precise Gold Clusters Deposited and Activated on Titania. *Physical chemistry chemical physics* **2013**, *15* (11), 3917-3929.
- 8. Al Qahtani, H. S.; Metha, G. F.; Walsh, R. B.; Golovko, V. B.; Andersson, G. G.; Nakayama, T., Aggregation Behavior of Ligand-Protected Au9 Clusters on Sputtered Atomic Layer Deposition TiO2. *The Journal of Physical Chemistry C* **2017**, *121* (20), 10781-10789.
- 9. Krishnan, G.; Al Qahtani, H. S.; Li, J.; Yin, Y.; Eom, N.; Golovko, V. B.; Metha, G. F.; Andersson, G. G., Investigation of Ligand-Stabilised Gold Clusters on Defect-Rich Titania. *The Journal of Physical Chemistry C* **2017**, *121* (50), 28007-28016.
- 10. Wilcoxon, J. P.; Provencio, P., Etching and Aging Effects in Nanosize Au Clusters Investigated Using High-Resolution Size-Exclusion Chromatography. *The Journal of Physical Chemistry B* **2003**, *107* (47), 12949-12957.
- 11. Moulder, J. F., Handbook of x-ray photoelectron spectroscopy: a reference book of standard data for use in x-ray photoelectron spectroscopy. *Handbook of x-ray photoelectron spectroscopy*: **1992**.
- 12. Alotabi, A. S.; Gibson, C. T.; Metha, G. F.; Andersson, G. G., Investigation of the Diffusion of Cr2O3 into Different Phases of TiO2 upon Annealing. *ACS Applied Energy Materials* **2021**, *4* (1), 322-330.
- 13. Biesinger, M. C.; Brown, C.; Mycroft, J. R.; Davidson, R. D.; McIntyre, N. S., X-ray photoelectron spectroscopy studies of chromium compounds. *Surface and Interface Analysis* **2004**, *36* (12), 1550-1563.
- 14. Kawawaki, T.; Kataoka, Y.; Hirata, M.; Akinaga, Y.; Takahata, R.; Wakamatsu, K.; Fujiki, Y.; Kataoka, M.; Kikkawa, S.; Alotabi, A. S.; Hossain, S.; Osborn, D. J.; Teranishi, T.; Andersson, G. G.; Metha, G. F.; Yamazoe, S.; Negishi, Y., Creation of High-Performance Heterogeneous Photocatalysts by Controlling Ligand Desorption and Particle Size of Gold Nanocluster. *Angewandte Chemie International Edition* **2021**, *60* (39), 21340-21350.

## Appendix E: Suppression of Phosphine-Protected Au<sub>9</sub> Clusters Agglomeration on SrTiO<sub>3</sub> Particles Using a Chromium Hydroxide Layer

This appendix contains a detailed description, additional figures and tables:

#### Additional figures and tables:



**Scheme E1**: Schematic of the measurement of the photocatalytic activity in this study. Ref. <sup>1</sup>. Copyright 2018 American Chemical Society.

Figure E1 shows the Sr 3d and P 2p spectra of SrTiO<sub>3</sub> and SrTiO<sub>3</sub>-Au<sub>9</sub> before and after heating. The Sr 3d<sub>5/3</sub> peak for SrTiO<sub>3</sub> appeared at a binding energy of 133.6 eV. The significant intensity of the Sr 3d peak overlapped with the P 2p region, which meant that it was more difficult to fit and determine the chemical state of triphenylphosphine ligands.

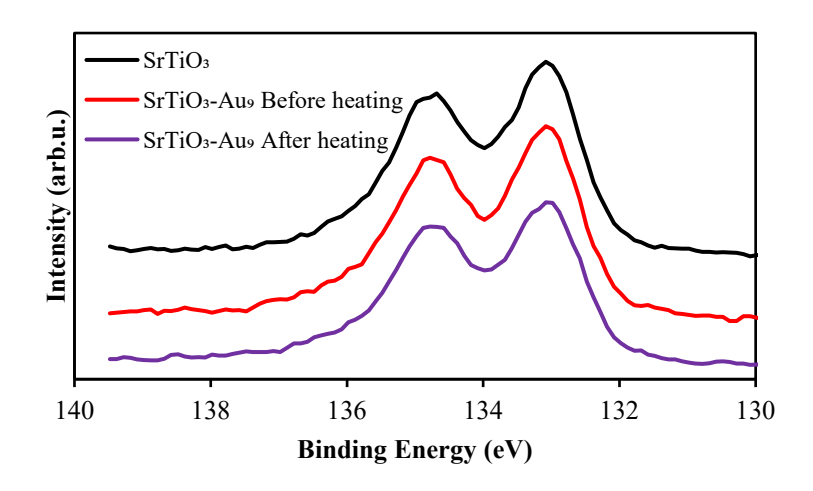
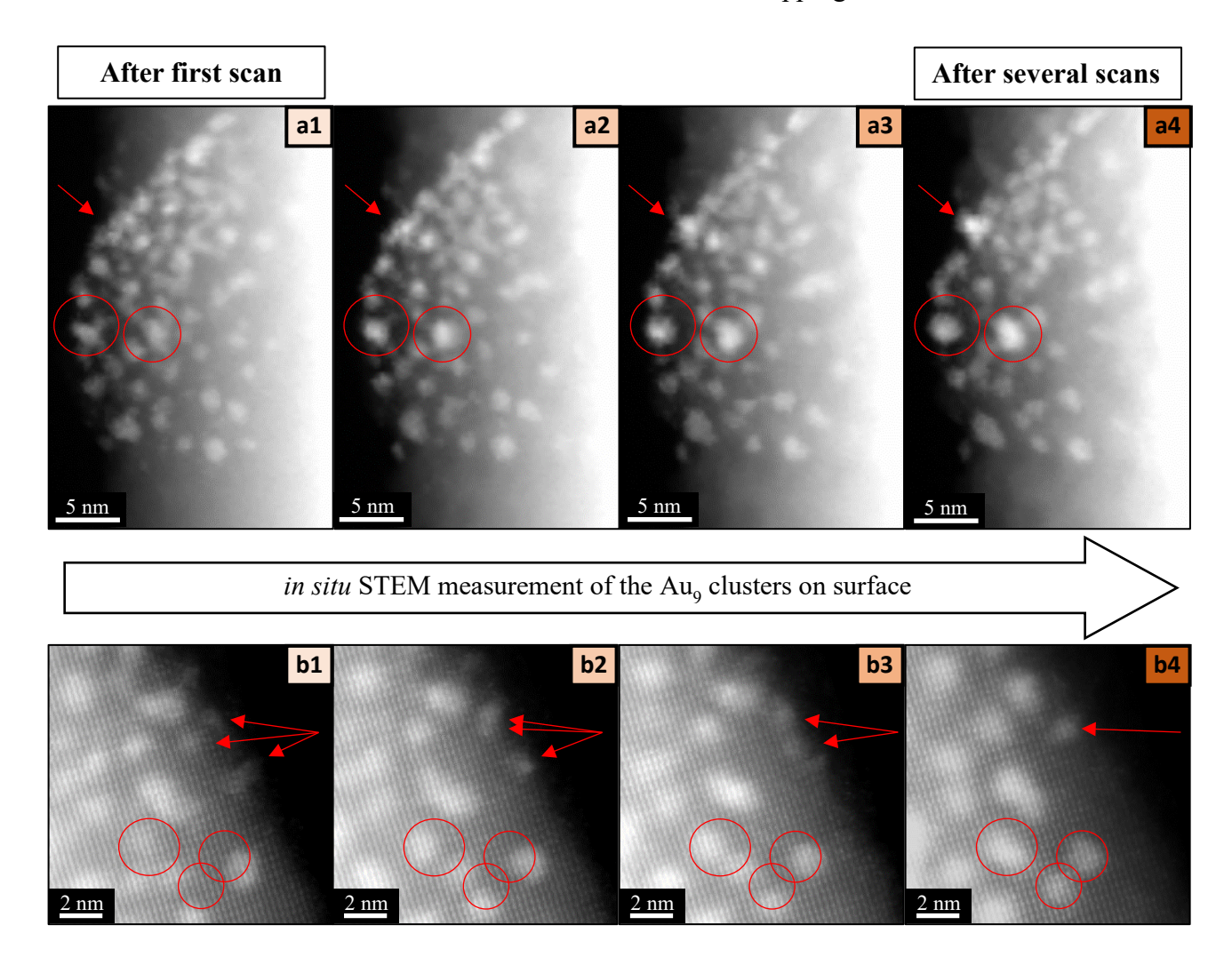


Figure E1: XPS Sr 3d and P 2p spectra of SrTiO3 and SrTiO3-Au9 before and after heating

#### Effect of high-energy STEM electron beam irradiation on Au<sub>9</sub> clusters.

Figure E2 shows HAADF-STEM images after successive EDX elemental mapping measurements. These images show the effect of the high-energy STEM electron beam on the Au<sub>9</sub> clusters at the surface. Drift and agglomeration of Au<sub>9</sub> clusters were observed; the former is attributed to heating of the sample and the latter to beam damage. This effect must be considered for the size analysis of Au clusters from STEM-HAADF and the STEM EDX elemental mapping data.



**Figure E2**: HAADF-STEM images of in situ STEM measurements of the Au<sub>9</sub> clusters on SrTiO<sub>3</sub>-Au<sub>9</sub>-Cr(OH)<sub>3</sub> before heating (**a** and **b**). The images display after the first and several scans with red circles and arrows indicated the clusters damaged by the STEM electron beam.

Figure E3 shows the Ba 3d spectrum of  $SrTiO_3$ -Au<sub>9</sub> after heating. The binding energy of Ba  $3d_{5/2}$  appears at  $780.5 \pm 0.2$  eV corresponding to Ba metal. The presence of barium in the  $SrTiO_3$ -Au<sub>9</sub> sample due to the commercial contamination of  $SrTiO_3$  (99%, Sigma-Aldrich). Using XPS relative intensity, the amount of barium contamination is approximately < 1%.

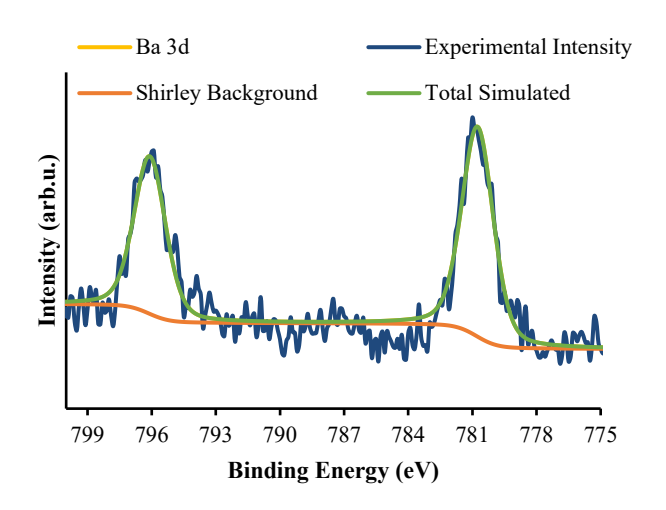
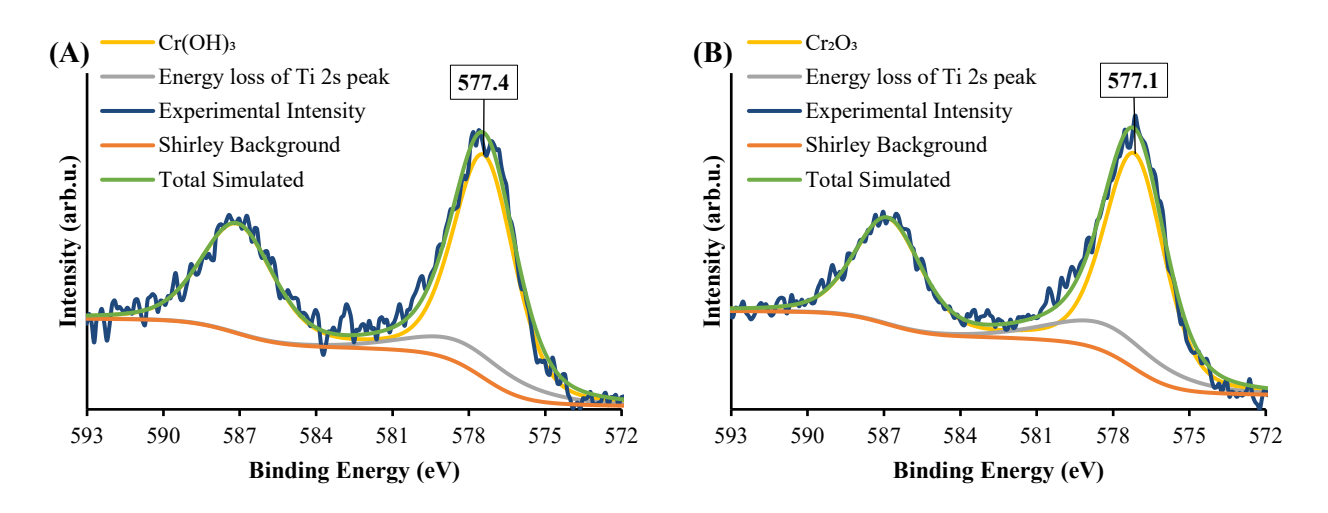
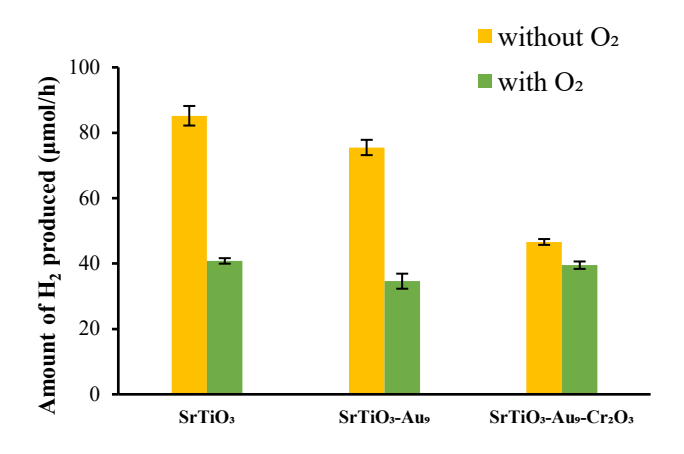


Figure E3: XPS Ba 3d spectrum of SrTiO<sub>3</sub>-Au<sub>9</sub> after heating.



**Figure E4**: XPS Cr 2p spectra of **(A)** SrTiO<sub>3</sub>-Au<sub>9</sub> after photodeposition of a CrO<sub>x</sub> layer and **(B)** after heating.

Figure E5 shows the H<sub>2</sub> production after 1 h irradiation using 10% methanol as a sacrificial reagent under two conditions: (1) using Ar gas flow during the irradiation (without O<sub>2</sub>) and (2) using Ar gas and air (7:3) mixture flow during the irradiation (with O<sub>2</sub>) to investigate the back reaction process. For SrTiO<sub>3</sub> and SrTiO<sub>3</sub>-Au<sub>9</sub>, the level of H<sub>2</sub> production reduced by a factor of two after introducing air into the reactor. This was due to the recombination of H<sub>2</sub> and O<sub>2</sub> (from air) to water, which reduces the H<sub>2</sub> evaluation reaction. For SrTiO<sub>3</sub>-Au<sub>9</sub> with a Cr(OH)<sub>3</sub> layer, the level of H<sub>2</sub> production did not show a significant reduction after introducing air into the reactor, which indicated that Cr(OH)<sub>3</sub> inhibited the back reaction.



**Figure E5**: Comparison of the  $H_2$  evolution reactions of  $SrTiO_3$ ,  $SrTiO_3$ - $Au_9$  and  $SrTiO_3$ - $Au_9$ - $Cr(OH)_3$  using 10% methanol as a sacrificial reagent under flow of Ar gas (without  $O_2$ ) and flow of Ar and air 7:3 mixture (i.e. with  $O_2$ ). The values are average of two hours irradiation.

**Table E1**: XPS Au 4f<sub>7/2</sub> peak positions, full width at half maximum (FWHM) and relative HBP:LBP intensities with the size of Au features from STEM.

		SrTi	O3-Au9		SrTiO3-Au9-Cr(OH)3						
	Peak	FWHM	Intensity	HAADF-STEM	Peak position	FWHM	Intensity	HAADF-STEM			
	position (eV)		%	Size of Au features	(eV)	1 ***111*1	%	Size of Au features			
				Before	heating						
HBP	$84.8 \pm 0.2$	$1.8 \pm 0.2$	83	0.7–1.3 nm	$85.0 \pm 0.2$	$1.9 \pm 0.2$	90	1.3–1.6 nm			
LBP	$84.1 \pm 0.2$	$1.2 \pm 0.2$	17	0.7–1.3 mm	$84.1 \pm 0.2$	$1.2 \pm 0.2$	10	1.5–1.0 IIII			
				After l	neating						
HBP	$85.4 \pm 0.2$	$2.0 \pm 0.2$	50		$84.9 \pm 0.2$	$2.0\pm0.2$	65				
LBP	$83.7 \pm 0.2$	$1.2 \pm 0.2$	50	-	$83.8 \pm 0.2$	$1.2 \pm 0.2$	35	-			
	After 7 h irradiation										
HBP	$85.2 \pm 0.2$	$2.2 \pm 0.2$	30	2060	$84.9 \pm 0.2$	$2.2 \pm 0.2$	63	1.4.2.7			
LBP	$83.5 \pm 0.2$	$1.2\pm0.2$	70	3.9–6.9 nm	$83.9 \pm 0.2$	$1.2\pm0.2$	37	1.4–2.7 nm			

**Table E2**: XPS peak positions of SrTiO<sub>3</sub>-Au<sub>9</sub> and SrTiO<sub>3</sub>-Au<sub>9</sub> after photodeposition of a Cr(OH)<sub>3</sub> layer.

Element	C 1s		Au 4f <sub>7/2</sub>		Sr 3d <sub>5/2</sub>	Ti 2p <sub>3/2</sub>	O 1s		Ba 3d <sub>5/2</sub>	Cr 2p <sub>3/2</sub>	
Sample	P1	P2	Р3	HBP	LBP	P1	P1	P1	P2	P1	P1
SrTiO <sub>3</sub> -Au <sub>9</sub>											
Before heating	285	286.0		84.8	84.1	133.0	458.6	531.8	529.7	780.3	
After heating	285	285.7	290.7	85.4	83.7	133.3	458.8	531.8	529.9	780.5	
After photocatalysis	285	285.8	290.1	85.2	83.5	133.2	458.7	531.6	529.9	780.5	
	SrTiO <sub>3</sub> -Au <sub>9</sub> -CrO <sub>x</sub>										
Before heating	285	286.4	289.8	85.0	84.1	133.0	458.5	531.6	529.7	780.4	577.4
After heating	285	290.5		84.9	83.8	133.1	458.6	531.4	529.8	780.1	577.1
After photocatalysis	285	285.7	289.8	84.9	83.9	133.2	458.7	531.5	529.9	780.4	577.5

<sup>\*</sup> P1: Peak 1

**Table E3**: XPS elemental composition of  $SrTiO_3$ -Au<sub>9</sub> and  $SrTiO_3$ -Au<sub>9</sub> after photodeposition of a  $Cr(OH)_3$  layer.

Element	C 1s		Au 4f <sub>7/2</sub>		Sr 3d <sub>5/2</sub>	Ti 2p <sub>3/2</sub>	О	1s	Ba 3d <sub>5/2</sub>	Cr 2p <sub>3/2</sub>	
Sample	P1	P2	Р3	HBP	LBP	P1	P1	P1	P2	P1	P1
SrTiO <sub>3</sub> -Au <sub>9</sub>											
Before heating	10.81	2.15		0.54	0.11	12.32	13.48	23.77	36.58	0.24	
After heating	7.12	2.50	1.01	0.17	0.17	13.10	13.62	23.36	38.47	0.47	
After photocatalysis	6.31	2.37	1.09	0.07	0.16	14.28	14.09	19.12	41.96	0.56	
	SrTiO3-Au9-CrOx										
Before heating	8.78	2.01	1.22	0.21	0.02	10.59	10.66	31.33	29.42	0.35	5.41
After heating	6.97	1.36		0.13	0.07	11.99	12.02	28.19	33.97	0.24	5.06
After photocatalysis	5.64	3.85	0.54	0.12	0.07	11.72	10.86	31.47	30.39	0.20	5.15

<sup>\*</sup> P1: Peak 1

<sup>\*\*</sup>HBP: High binding peak. LBP: Low binding peak

<sup>\*\*</sup>HBP: High binding peak. LBP: Low binding peak

**Table E4:** Summary of  $Cr\ 2p_{3/2}$  peak position of various samples.

Sample	Cr 2p <sub>3/2</sub> peak position (eV)
$\mathrm{Cr_2O_3}$	$576.9 \pm 0.2$
Cr(OH) <sub>3</sub>	$577.5 \pm 0.2$
SrTiO <sub>3</sub> -Cr(OH) <sub>3</sub>	$577.6 \pm 0.2$
SrTiO <sub>3</sub> -Au <sub>9</sub> -Cr(OH) <sub>3</sub>	$577.4 \pm 0.2$
SrTiO <sub>3</sub> -Au <sub>9</sub> -Cr <sub>2</sub> O <sub>3</sub> heated	$577.1 \pm 0.2$
SrTiO <sub>3</sub> -Au <sub>9</sub> -Cr(OH) <sub>3</sub> after 7 h irradiation	$577.5 \pm 0.2$
SrTiO <sub>3</sub> -Au <sub>9</sub> -Cr <sub>2</sub> O <sub>3</sub> after irradiation (without O <sub>2</sub> )	$577.5 \pm 0.2$
SrTiO <sub>3</sub> -Au <sub>9</sub> -Cr <sub>2</sub> O <sub>3</sub> after irradiation (with O <sub>2</sub> )	$577.5 \pm 0.2$

XPS Au 4f spectra of SrTiO<sub>3</sub>-Au<sub>9</sub> and SrTiO<sub>3</sub>-Au<sub>9</sub>-Cr(OH)<sub>3</sub> after irradiation during water splitting reaction for without O<sub>2</sub> and with O<sub>2</sub> samples are shown in Figure E6. Table E5 showed a summary of the Au 4f peak positions and FWHM. A full elemental composition analyses and peak positions are presented in Tables E6 and E7. The Au 4f spectrum for SrTiO<sub>3</sub>-Au<sub>9</sub> without O<sub>2</sub> was fitted with 59% of the intensity at HBP (84.9  $\pm$  0.2 eV with an FWHM of 2.0  $\pm$  0.2 eV) corresponding to Au clusters and 41% agglomerated clusters at LBP (83.6  $\pm$  0.2 eV with an FWHM of 1.2  $\pm$  0.2 eV) (Figure E6A). As shown in Figure E6B, for SrTiO<sub>3</sub>-Au<sub>9</sub> with O<sub>2</sub>, the Au 4f spectrum was fitted with 26% and 74% at HBP(84.9  $\pm$  0.2 eV with an FWHM of 2.0  $\pm$  0.2 eV) and LBP (83.5  $\pm$  0.2 eV with an FWHM of  $1.2 \pm 0.2$  eV), which represented the non-agglomerated and agglomerated clusters. In Figure E6C, the HBP and LBP of Au  $4f_{7/2}$  SrTiO<sub>3</sub>-Au<sub>9</sub>-Cr(OH)<sub>3</sub> without O<sub>2</sub> were observed at  $85.1 \pm 0.2$  eV (62%) and  $84.0 \pm 0.2$  eV (38%) with an FWHM of  $2.0 \pm 0.2$  eV and  $1.2 \pm 0.2$  eV, respectively. In Figure E6D, with O<sub>2</sub>, the HBP and LBP were observed at  $84.9 \pm 0.2$  eV (55%) and  $83.9 \pm 0.2$  eV (45%) with an FWHM of  $2.0 \pm 0.2$  eV and  $1.2 \pm 0.2$  eV, respectively. In SrTiO<sub>3</sub>-Au<sub>9</sub>-Cr(OH)<sub>3</sub> catalyst, more than a half of the Au clusters were stable at the surface of SrTiO<sub>3</sub> in the present experiment (without and with O<sub>2</sub>). This demonstrated that the Cr(OH)<sub>3</sub> helped inhibit the agglomeration of Au<sub>9</sub> clusters during the water splitting reaction with a sacrificial reagent (10% methanol).

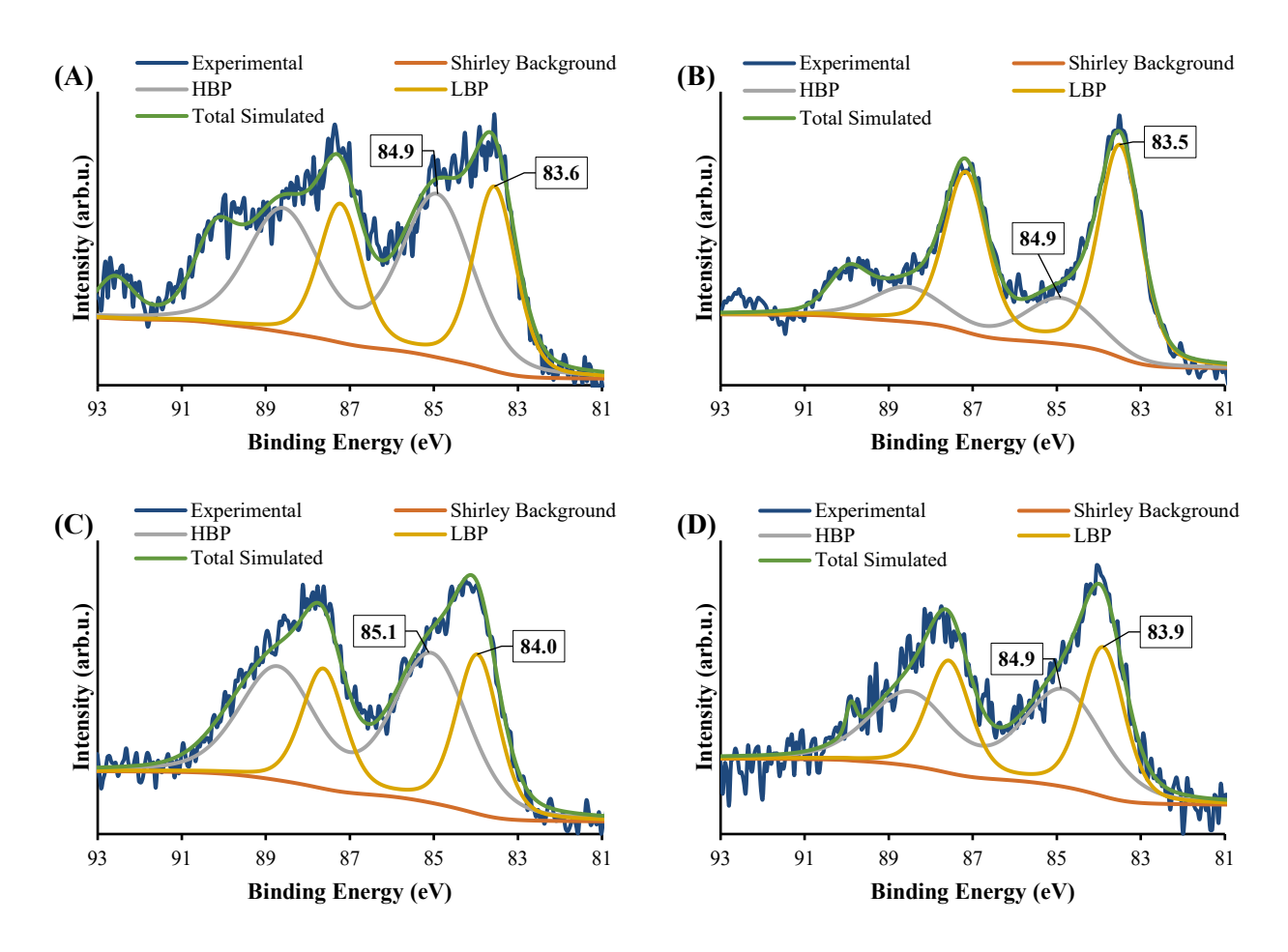


**Figure E6**: XPS spectra of Au 4f of SrTiO<sub>3</sub>-Au<sub>9</sub> after photocatalytic water-splitting reaction with (A) 10% CH<sub>3</sub>OH (without O<sub>2</sub>), and (B) 10% CH<sub>3</sub>OH + (7:3 Ar:air) mixture (with O<sub>2</sub>). (C) SrTiO<sub>3</sub>-Au<sub>9</sub>-Cr(OH)<sub>3</sub> after photocatalytic water-splitting reaction with 10% CH<sub>3</sub>OH (without O<sub>2</sub>), and (D) 10% CH<sub>3</sub>OH + (7:3 Ar:air) mixture (with O<sub>2</sub>).

**Table E5**: XPS Au 4f<sub>7/2</sub> peak positions, FWHM and relative HBP:LBP intensities.

	Sı	rTiO3-Au9	SrTiO3-Au9-Cr(OH)3								
	Peak position (eV)	FWHM	Intensity %	Peak position (eV)	FWHM	Intensity %					
	After photocatalysis (without O2)										
HBP	$84.9 \pm 0.2$	$2.0 \pm 0.2$	59	$85.1 \pm 0.2$	$2.1 \pm 0.2$	62					
LBP	$83.6 \pm 0.2$	$1.2\pm0.2$	41	$84.0 \pm 0.2$	$1.2 \pm 0.2$	38					
	After photocatalysis (with O2)										
HBP	$84.9 \pm 0.2$	$2.0 \pm 0.2$	26	$84.9 \pm 0.2$	$2.2 \pm 0.2$	55					
LBP	$83.5 \pm 0.2$	$1.2\pm0.2$	74	$83.9 \pm 0.2$	$1.2 \pm 0.2$	45					

**Table E6**: XPS peak positions of SrTiO<sub>3</sub>-Au<sub>9</sub> and SrTiO<sub>3</sub>-Au<sub>9</sub> after photodeposition of a Cr(OH)<sub>3</sub> layer.

Element	C 1s		Au 4f <sub>7/2</sub>		Sr 3d <sub>5/2</sub>	Ti 2p <sub>3/2</sub>	O 1s		Ba 3d <sub>5/2</sub>	Cr 2p <sub>3/2</sub>	
Sample	P1	P2	P3	HBP	LBP	P1	P1	P1	P2	P1	P1
SrTiO <sub>3</sub> -Au <sub>9</sub>											
After photocatalysis (without O <sub>2</sub> )	285	286.1		84.9	83.6	134.8	460.3	533.1	531.4	781.8	
After photocatalysis (with O <sub>2</sub> )	285	285.6	290.4	84.9	83.5	133.3	458.8	531.6	530.0	780.5	
	SrTiO <sub>3</sub> -Au <sub>9</sub> -CrO <sub>x</sub>										
After photocatalysis (without O <sub>2</sub> )	285	285.7		85.1	84.0	133.2	458.8	531.7	529.9	780.4	755.5
After photocatalysis (with O <sub>2</sub> )	285	285.9	289.5	84.9	83.9	133.2	458.8	531.7	529.9	780.3	577.5

<sup>\*</sup> P1: Peak 1

**Table E7**: XPS elemental composition of SrTiO<sub>3</sub>-Au<sub>9</sub> and SrTiO<sub>3</sub>-Au<sub>9</sub> after photodeposition of a Cr(OH)<sub>3</sub> layer.

Element	C 1s		Au 4f <sub>7/2</sub>		Sr 3d <sub>5/2</sub>	Ti 2p <sub>3/2</sub>	O 1s		Ba 3d <sub>5/2</sub>	Cr 2p <sub>3/2</sub>	
Sample	P1	P2	Р3	HBP	LBP	P1	P1	P1	P2	P1	P1
SrTiO <sub>3</sub> -Au <sub>9</sub>											
After photocatalysis (without O <sub>2</sub> )	5.20	0.27		0.19	0.13	15.08	14.87	17.16	46.51	0.60	
After photocatalysis (with O <sub>2</sub> )	4.37	6.08	0.74	0.07	0.20	13.99	14.29	19.92	39.91	0.43	
	SrTiO3-Au9-CrOx										
After photocatalysis (without O <sub>2</sub> )	7.60	4.65		0.14	0.08	11.52	10.44	28.31	31.73	0.16	5.37
After photocatalysis (with O <sub>2</sub> )	3.74	0.87	0.40	0.10	0.09	12.29	11.60	29.87	35.48	0.23	5.32

<sup>\*</sup> P1: Peak 1

<sup>\*\*</sup>HBP: High binding peak. LBP: Low binding peak

<sup>\*\*</sup>HBP: High binding peak. LBP: Low binding peak

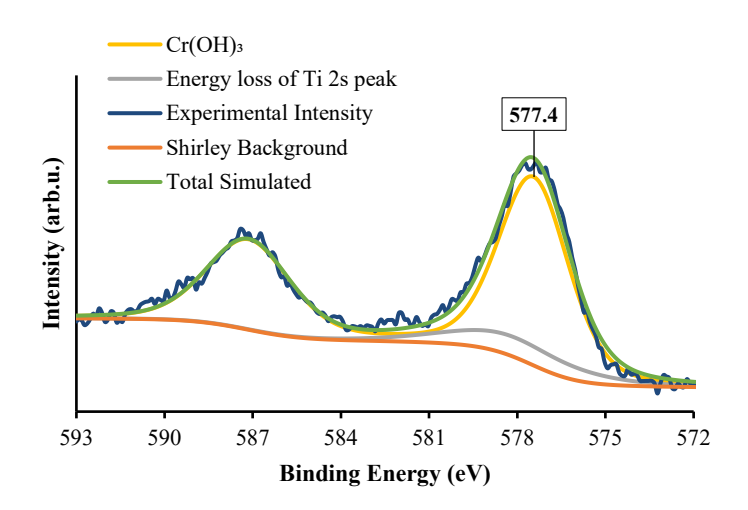
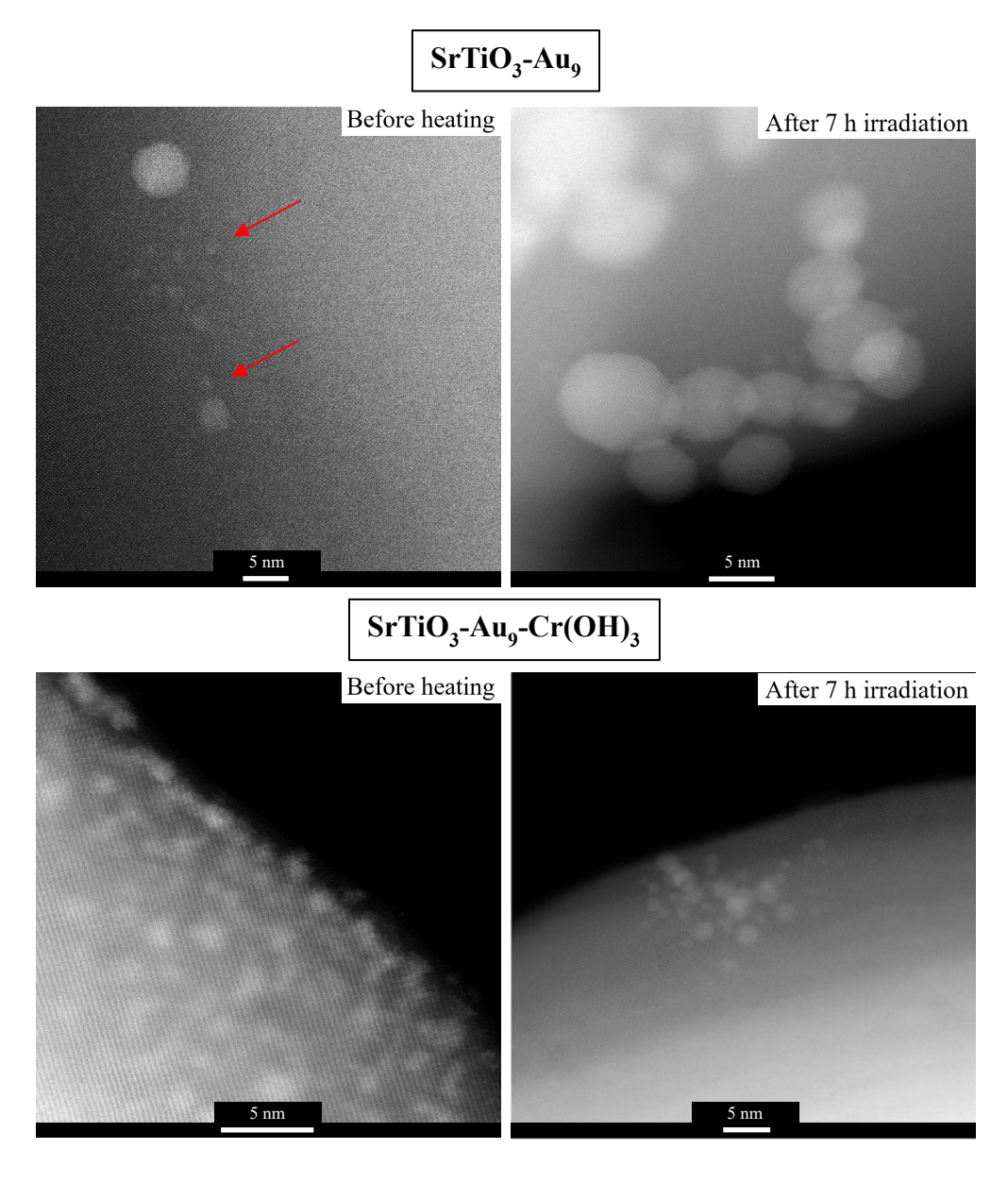
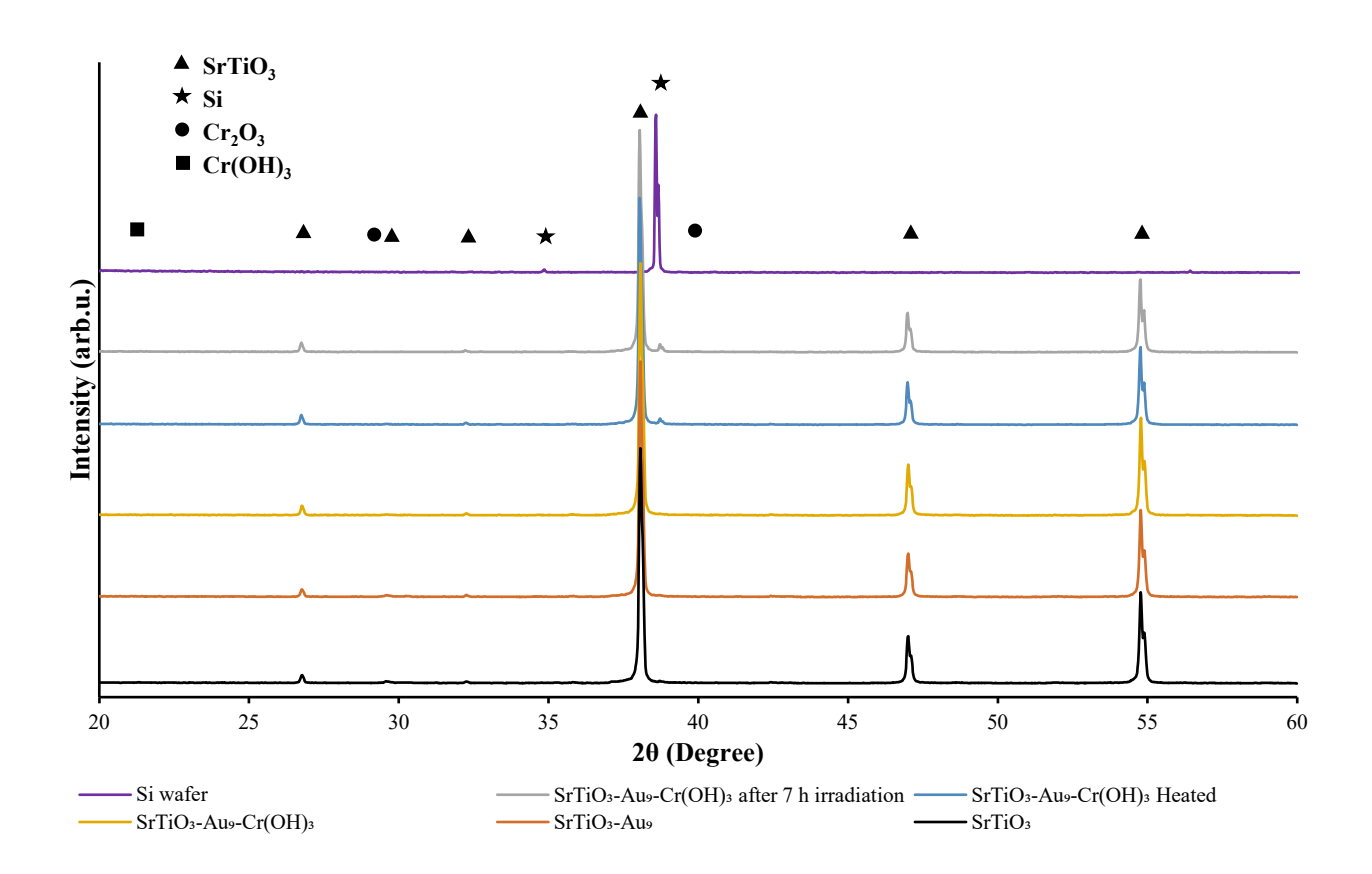


Figure E7: XPS spectrum of Cr 2p of SrTiO<sub>3</sub>-Au<sub>9</sub>-Cr(OH)<sub>3</sub> after 7 h irradiation.

HAADF-STEM images of SrTiO<sub>3</sub>-Au<sub>9</sub> and of SrTiO<sub>3</sub>-Au<sub>9</sub>-Cr(OH)<sub>3</sub> before heating and after 7 h irradiation are presented in Figure E8 for comparison. As shown in the images, the size of the Au clusters increases up to 8 nm for SrTiO<sub>3</sub>-Au<sub>9</sub> after 7 h irradiation due to the aggregation of Au clusters under the ultraviolet (UV) irradiation<sup>2</sup>. However, in terms of SrTiO<sub>3</sub>-Au<sub>9</sub>-Cr(OH)<sub>3</sub>, the Au clusters remain more stable on the surface of SrTiO<sub>3</sub> after 7 h irradiation, up to 2.7 nm.



**Figure E8**: HAADF-STEM images of SrTiO<sub>3</sub>-Au<sub>9</sub> and SrTiO<sub>3</sub>-Au<sub>9</sub>-Cr(OH)<sub>3</sub> before heating and after 7 h irradiation.



**Figure E9**: X-ray diffraction pattern of Si wafer,  $SrTiO_3$ ,  $SrTiO_3$ -Au<sub>9</sub>,  $SrTiO_3$ -Au<sub>9</sub>-Cr<sub>(OH)3</sub>,  $SrTiO_3$ -Au<sub>9</sub>-Cr<sub>(2</sub>O<sub>3</sub> heated and  $SrTiO_3$ -Au<sub>9</sub>-Cr<sub>(OH)3</sub> after 7 h irradiation.

#### References

- 1. Kurashige, W.; Kumazawa, R.; Ishii, D.; Hayashi, R.; Niihori, Y.; Hossain, S.; Nair, L. V.; Takayama, T.; Iwase, A.; Yamazoe, S.; Tsukuda, T.; Kudo, A.; Negishi, Y., Au25-Loaded BaLa4Ti4O15 Water-Splitting Photocatalyst with Enhanced Activity and Durability Produced Using New Chromium Oxide Shell Formation Method. *The Journal of Physical Chemistry C* **2018**, *122* (25), 13669-13681.
- 2. Ruzicka, J.-Y.; Abu Bakar, F.; Hoeck, C.; Adnan, R.; McNicoll, C.; Kemmitt, T.; Cowie, B. C.; Metha, G. F.; Andersson, G. G.; Golovko, V. B., Toward Control of Gold Cluster Aggregation on TiO2 via Surface Treatments. *The Journal of Physical Chemistry C* **2015**, *119* (43), 24465-24474.